

(NASA-CR-197448) NASA/ASEE SUMMER
FACULTY FELLOWSHIP PROGRAM. 1994
RESEARCH REPORTS (University of
Central Florida) 567 p

N95-18166
--THRU--
N95-18186
Unclas

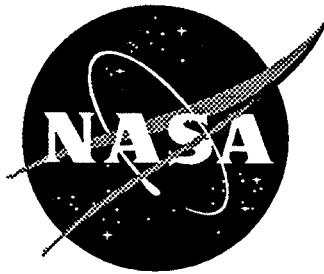
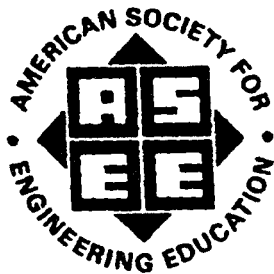
NASA CR-197448

G3/80 0033960

1994 Research Reports

NASA/ASEE Summer Faculty Fellowship Program

John F. Kennedy Space Center
and
University of Central Florida



1995/11/751
351409
68

1994 RESEARCH REPORTS

NASA/ASEE SUMMER FACULTY FELLOWSHIP PROGRAM

JOHN F. KENNEDY SPACE CENTER

UNIVERSITY OF CENTRAL FLORIDA

EDITORS:

Dr. Loren A. Anderson, University Program Director
Dr. E. Ramon Hosler, University Program Co-Director
Department of Mechanical and Aerospace Engineering
College of Engineering
University of Central Florida

Mr. Warren Camp, NASA/KSC Program Director
Human Resources & Management Systems Office
John F. Kennedy Space Center

PREPARED FOR:

John F. Kennedy Space Center
Merritt Island, Florida

NASA Grant NGT-60002 Supplement: 17

Contractor Report No. CR-197448

October 1994

PREFACE

This document is a collection of technical reports on research conducted by the participants in the 1994 NASA/ASEE Summer Faculty Fellowship Program at Kennedy Space Center (KSC). This was the tenth year that a NASA/ASEE program has been conducted at KSC. The 1994 program was administered by the University of Central Florida in cooperation with KSC. The program was operated under the auspices of the American Society for Engineering Education (ASEE) with sponsorship and funding from the Office of Educational Affairs, NASA Headquarters, Washington, D.C. The KSC program was one of nine such Aeronautics and Space Research Programs funded by NASA Headquarters in 1994. The basic common objectives of the NASA/ASEE Summer Faculty Fellowship Program are:

- a. To further the professional knowledge of qualified engineering and science faculty members;
- b. To stimulate an exchange of ideas between participants and NASA;
- c. To enrich and refresh the research and teaching activities of participants' institutions; and,
- d. To contribute to the research objectives of the NASA centers.

The KSC Faculty Fellows spent ten weeks (May 31 through August 5, 1994) working with NASA scientists and engineers on research of mutual interest to the University faculty member and the NASA colleague. The editors of this document were responsible for selecting appropriately qualified faculty to address some of the many problems of current interest to NASA/KSC. A separate document reports on the administrative aspects of the 1994 program. The NASA/ASEE program is intended to be a two-year program to allow in-depth research by the University faculty member. In most cases a faculty member has developed a close working relationship with a particular NASA group that has provided funding beyond the two-year limit.

TABLE OF CONTENTS

	<u>PAGE</u>
1. ANDRAWIS, Alfred S. "The Development of a Fiber Optics Communication Network for Controlling a Multidegree-Of-Freedom Serpentine Truss"	1
2. BREWER, William V. "Space Station Racks Weight & C.G. Measurement Using the Rack Insertion End-Effector"	31
3. BYERS, Robert M. "Automated Path Planning of the Payload Inspection and Processing System"	61
4. CALLE, Luz M. "Evaluation of Inorganic Zinc-Rich Primers Using Electrochemical Impedance Spectroscopy (EIS) in Combination with Atmospheric Exposure"	91
5. CENTENO, Martha A. "Assessment of the SFC Database for Analysis and Modeling"	113
6. CHANG, Chia-Bo "Experiments with the Mesoscale Atmospheric System (MASS) Using the Synthetic Relative Humidity"	139
7. DEITZER, Gerald F. "Physiological and Genetic Characterization of Plant Growth and Gravitropism in LED Light Sources"	159
8. FORBES, Gregory S. "Lightning Studies Using LDAR and Companion Data Sets"	205
9. GLASSCOCK, Barbara H. "Investigation of New Hypergol Scrubber Technology"	235

10.	JOGLEKAR, Prafulla N. "Applying Costs, Risks, and Values Evaluation (CRAVE) Methodology to Engineering Support Request (ESR) Prioritization"	263
11.	KIM, Rhyn H. "Design Optimization of a Brush Turbine with a Cleaner/Water Based Solution"	313
12.	MALLADI, Narasimha S. "Rack Insertion End Effector (RIEE) Guidance"	339
13.	RAKOW, Allen L. "Ethylene Dynamics in the CELSS Biomass Production Chamber"	349
14.	ROSA, Ferdinand "Mechanical Behavior of Precipitation Hardenable Steels Exposed to Highly Corrosive Environment"	379
15.	RUSSELL, John M. "Modeling and Measurement of the Performance of a Branched Conduit Sampling System in a Mass Spectrometer Leak Detector"	419
16.	SWANSON, Sr., James R. "Assessment of a Career Development Program for Executive and Mid-Level Managers"	449
17.	THOMAS, Stan J. "Enhancements to the KATE Model-Based Reasoning System"	485
18.	WANG, Pao-lien "Outgassing of Solid Material into Vacuum Thermal Insulation Spaces"	509
19.	WHITE III, Preston A. "Feasibility Study of Transmission of OTV Camera Control Information in the Video Vertical Blanking Interval"	521
20.	ZOBRIST, George W. "Performance Evaluation of the NASA/KSC CAD/CAE and Office Automation LAN's"	545

N95-18167

357413
11252
51-74
33961
p. 29
399

1994 NASA/ASEE SUMMER FACULTY FELLOWSHIP PROGRAM

JOHN F. KENNEDY SPACE CENTER
UNIVERSITY OF CENTRAL FLORIDA

THE DEVELOPMENT OF A FIBER OPTICS COMMUNICATION NETWORK FOR
CONTROLLING A MULTIDEGREE-OF-FREEDOM SERPENTINE TRUSS

PREPARED BY:	Dr. Alfred S. Andrawis
ACADEMIC RANK:	Assistant Professor
UNIVERSITY AND DEPARTMENT:	South Dakota State University Electrical Engineering Department
NASA/KSC	
DIVISION:	Networks/Robotics
BRANCH:	DL-ESS-12/DM-MED-12
NASA COLLEAGUE:	Ray Pecaut Gabor Tamasi
DATE:	July 22, 1994
CONTRACT NUMBER:	University of Central Florida NASA-NGT-60002 Supplement: 17

ACKNOWLEDGMENTS

This research would not have been possible without the participation in the NASA/ASEE Summer Faculty Program. Assistance, cooperation of a number of people is greatly appreciated. Appreciation is extended to all those who organized and gave tours to the Faculty Fellows. The tours made the Faculty Fellows aware of the magnitude and complexity of operations that takes place in the Kennedy Space Center. Special thanks are extended to Dr. Loren Anderson, Program Director, and to Ms. Kari Stiles, Administrator Assistant for all their efforts, help, coordination and cheerful smiles.

The author gratefully acknowledge the efforts of Gabor Tamasi in organizing and planning research activities.

The author is very appreciative of the support of Raymond Pecaut and for his helpful hints.

Furthermore, the author extends his appreciation to Bill Jones for his encouragement and support. Working with the I-NET group was the most fun and rewarding experience, the author extends his thanks to all the staff of TRM-052 for all their support, help, warmth and generosity.

Last but not least, the author extends his gratitude to his wife, family, kids and specially his brother Victor for their help and support.

ABSTRACT

The problem addressed by this report is the large size and heavy weight of the cable bundle, used for controlling a Multidegree-Of-Freedom Serpentine Truss Manipulator arm, which imposes limitations on the manipulator arm maneuverability. This report covers a design of an optical fiber network to replace the existing copper wire network of the Serpentine Truss Manipulator. This report proposes a fiber network design which significantly reduces the bundle size into two phases. The first phase does not require any modifications for the manipulator architecture, while the other requires major modifications. Design philosophy, hardware details and schematic diagrams are presented.

TABLE OF CONTENTS

<u>Section</u>	<u>Title</u>	<u>page</u>
I.	INTRODUCTION.....	3
II.	PRESENT SYSTEM.....	4
III.	DESIGN PHILOSOPHY.....	6
IV.	DESIGN DETAILS.....	8
	<i>a. Phase I:</i>	8
	<i>(i) Transmitter</i>	9
	<i>(ii) Receiver</i>	10
	<i>b. Phase II</i>	19
	APPENDIX A.....	26

LIST OF FIGURES

<u>Figure</u>	<u>Title</u>	<u>Page</u>
1	Serepentine Truss with phase 1 fiber links	7
2a	Block Diagram of the Serpentine Truss Fiber Optic Link 1 (Tx)	11
2b	Block Diagram of the Serpentine Truss Fiber Optic Link 2 (Tx)	12
3a	Schematic of the Serpentine Truss Fiber Optic Link 1 (Tx).....	13
3b	Schematic of the Serpentine Truss Fiber Optic Link 2 (Tx).....	14
4a	Block Diagram of the Serpentine Truss Fiber Optic Link 1 (Rx)	15
4b	Block Diagram of the Serpentine Truss Fiber Optic Link 2 (Rx)	16
5a	Schematic of the Serpentine Truss Fiber Optic Link 1 (Rx).....	17
5b	Schematic of the Serpentine Truss Fiber Optic Link 2 (Rx).....	18
6	Logic Diagram of 32-Bit Multiplexed Transmitter	24
7	Logic Diagram of 32-Bit Demultiplexed Receiver.....	25

The Development of a Fiber Optics Communication Network for Controlling a Multidegree-Of-Freedom Serpentine Truss

I. INTRODUCTION

The Serpentine Truss is an eight degrees of freedom (DOF) robot manipulator which is presently in the KSC Robotic Applications Development Laboratory. This truss is used as a development prototype. The problem addressed by this project is the large size and heavy weight of the cable bundle which imposes limitations on the manipulator arm maneuverability. This problem could be avoided by developing an optical-fiber communications link between the robot central controller, actuators and sensors. Optical-fibers are characterized with several advantages, some of them are the following:

- **Weight**

Because of their small volume and lower density, optical-fiber cables enjoy considerable weight advantages over typical copper cables. Hence, optical-fibers will certainly reduce the weight and the size of the cable bundle of the present Serpentine Truss.

- **Immunity to Electromagnetic Interference**

Since optical fibers are nonconducting, they will neither generate nor receive *electromagnetic interference* (EMI). The final Serpentine Truss is planned to operate in the vicinity of the Space Orbiter where electromagnetic emissions may be high or/and restricted. Therefore, a transmission system which neither generate nor receive electromagnetic interference is highly desirable.

- **Lack of Sparking**

For special purpose applications that require transmission of information through hazardous places (such as The Space Orbiter Cargo Bay), fibers offer a potential advantage of not sparking in case of breakage in the transmission line.

- **Bandwidth**

Optical-fibers are characterized with very wide bandwidth. Historically, bandwidth requirements for communications have shown increasing trend. The traditional way of meeting this requirement has been to increase the carrier frequency, as the information bandwidth is constrained to be, at most, equal to

the carrier or some fraction of the carrier frequency. Hence, to meet the increase bandwidth demands, information carriers have transitioned from HF to VHF to UHF to microwave to millimeter waves and finally, to light waves. Wide bandwidth may not be crucial for the present prototype Serpentine Truss, but with the addition of more degrees of freedom (DOF), proximity sensors, and distributed controllers, the demand for a wider bandwidth is expected to increase.

- **Compatibility with Solid-State Sources**

The physical dimensions of the fiber-optic sources, detectors, and connectors, as well as the fiber itself, are compatible with modern miniaturized electronics. Most components are available in dual in-line packaging (DIP packs), making mounting on a printed board extremely easy.

- **No Emission Licenses**

Since fiber optics is a nonradiating means of information transfer, no special licenses are required to implement a network for controlling the Serpentine Truss.

Along with the several advantages of optical-fibers, come some potential disadvantages. These include **radiation darkening**. Optical glass darkens under the exposure to nuclear radiation. Although the specifics of the interaction depend on the dose rate and time history of the dose, as well as the type of radiation and the material dopants of the glass, optical-fibers are generally susceptible to interruption to nuclear radiation. Hence, precautions should be taken in similar situations.

II. PRESENT SYSTEM

The serpentine truss system has eight feedback loops six of them are to control six truss arm *servo systems*. Each servo system consists of a DC motor, fail-safe brake, a primary position sensor, and a secondary absolute position sensor. All DC motors are powered by pulse-width modulated (PWM) amplifiers located at the central control and processing unit. On the truss arm, the primary position sensor is a linear quadrature encoder. The secondary absolute position sensor is a linear film potentiometer.

Each servo system is connected to the central control and processing unit via a bundle of wire busses (sixteen wires per servo system). A detailed description for this bundle is as follows:

<u>Device</u>	<u>Number of wires used</u>
DC motor	2
Fail-safety brakes	2
Linear film potentiometer sensor	3
Linear quadrature encoder	9
Total	16

This bundle consists of two types of busses:

1. Power bus; the type of signal carried by this bus is a power signal. The following wires belong to this bus type:
 - two lines from the PWM amplifier in the central control and processing unit to the DC motor,
 - two lines from the DC output module (OPTO-22) to the DC motor,
 - two lines from *Power One* power supply to the linear film potentiometer sensor (± 10 V),
 - one line to analog input *Keithley DAS-15* from the linear film potentiometer sensor, and
 - two lines, from encoder input *Tech 80* board to *Futaba* linear quadrature encoder (+5 V and ground)
2. Timing bus; this bus is intended to carry timing information back from the *Futaba* linear quadrature encoder to the *Tech 80* encoder inputs at the central processing unit. Six wires out from the quadrature encoder are of the timing bus type (the rest are of the power bus type). The six wires consists of; three analog timing signals A, B, and Z and their compliments \bar{A} , \bar{B} , and \bar{Z} . Timing relationship between the three signals A, B, and Z, determines the direction and the relative location of displacement.

III. DESIGN PHILOSOPHY

Present Serpentine Truss moves data from sensors to the central control and processing unit using multiple wire lines (parallel bus). Parallel bus provides, fast data transfer and compatibility with most computer architecture. However, it is bulky, and it has low performance issues such as crosstalk, radio frequency interference (RFI), bit-to-bit skew and other concerns associated with multiple wire interfaces. Serial data links, although simpler and less costly, have not traditionally provided sufficient bandwidth to compete with the high data transfer rates of parallel links. Recent technological advances in optical fibers technology permit very high speed digital transmission over extended distances, at increasingly level of reliability of the connection. In order to maximize the benefits of the bandwidth made available by optical fiber technology, new high speed serial transmission links are being developed. These recent developments have altered the cost/performance trade-off between serial and parallel data transfer techniques.

The optimum and the best design is replacing all copper cables with one optical-fiber network. This requires major modifications of manipulator's architecture from centralized control architecture to distributed control architecture. The intention of this design is to reduce the cable bundle size and weight with the least possible modifications of manipulator's architecture. Network development process will be divided into two phases.

The first phase is to develop fiber serial links to replace all existing Timing Bus parallel wires coming out of the *Futaba* linear encoder. This should reduce the cable bundle size and weight by a factor of almost 30%. The second phase is to replace all other motor controls and sensing signals with another network similar to the one developed for the first phase. The size of the cable bundle of this phase is dominated by the size of the power bus which is directly proportional to the number of actuators. For the present manipulator, with 6 DOF in the arm, cable bundle size is expected not to exceed ~ 1 inch diameter instead of present ~ 3 inch diameter bundle.

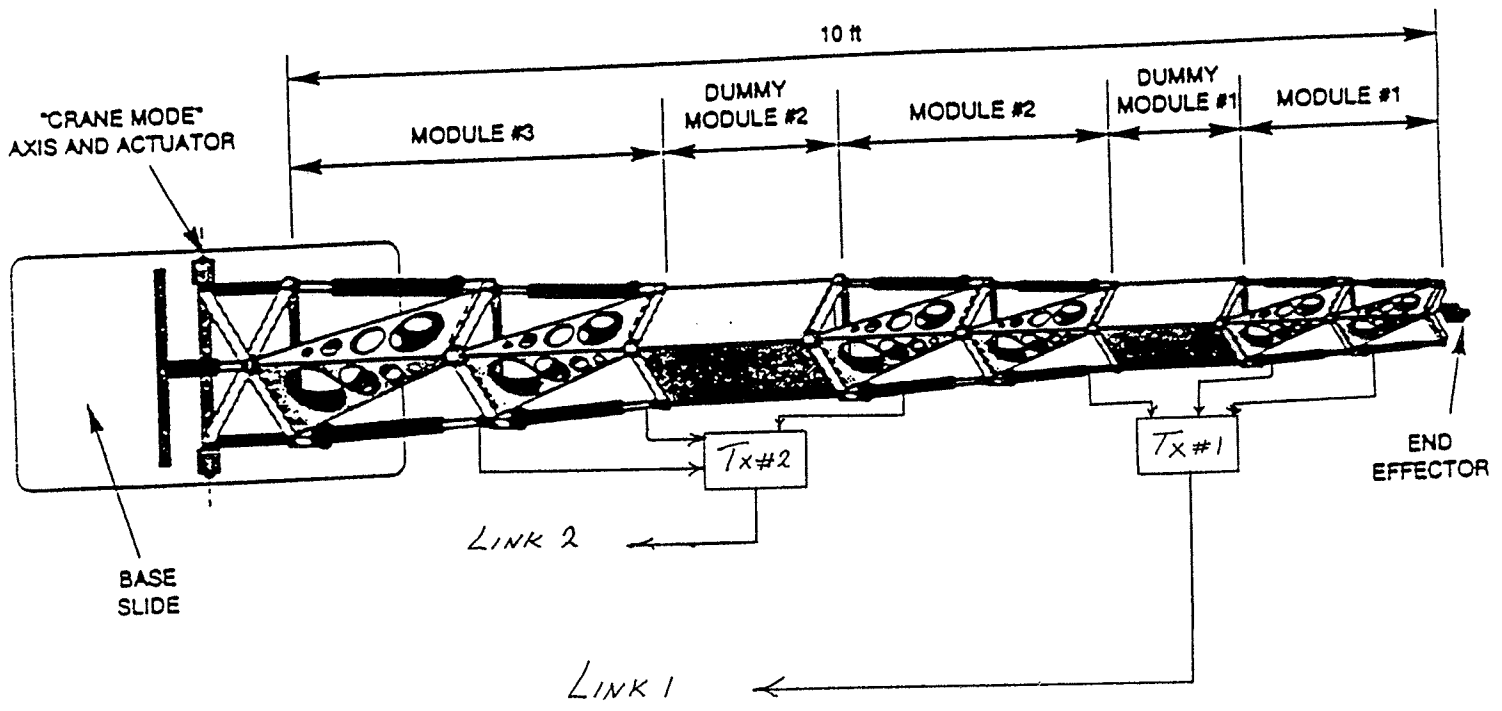


Figure 1: Serpentine Truss with phase 1 fiber links

IV. DESIGN DETAILS

The proposed optical fiber design is divided into two phases; the first phase do not require any modifications to the Truss architecture while the second phase requires major modifications of the Truss.

a. Phase I:

This phase is to replace Timing Bus parallel wires, between the *Futaba* linear encoder and the quadrature encoder board *Tech 80*, with two optical-fiber links.

The quadrature encoder board *Tech 80* accepts quadrature signals in a single-ended mode as well as differential mode. Therefore, the three signals A, B, and Z are sent in a single-ended mode format rather than differential mode format. These are sufficient to completely decode displacement parameters. These three signals are sampled, at the quadrature encoder board *Tech 80*, with a frequency of 0.625 MHz. Three timing signals are multiplexed (each consists of three analog signals A, B, and Z, generated by the *Futaba* quadrature encoder) and transmitted to the central control and processing unit over a digital optical-fiber link. The digital link is transparent, that is to say, the analog signal is over sampled with a rate six times (exactly 6.4x) greater than the sampling rate of the quadrature encoder board.

The link uses a point-to-point configuration using HP FOXIchipTM set (Fiber Optic Xmitter-Receiver Interface with TAXITM). The DLT6000-ST FOXIchip Transmitter and DLR6000-ST Receiver chipset is a general purpose interface for very high-speed interface (up to 12.5 Mbytes/sec) point-to-point communications over fiber-optic make. They include the necessary data handling, timing and control functions together with the optical transducers. The link is unidirectional: a parallel word is sent one end and recovered at the other end. For each point-to-point direction a pair of FOXIs and a separate fiber are required.

(i) *Transmitter:*

The DLT6000-ST data link transmitter provides a high performance transparent fiber optic interface. The DLT6000-ST converts parallel TTL data into serial lightwaves in the 1.3 μm band. When used in conjunction with the complementary DLR6000-ST, in point to point applications, data transfer rates are up to 12.5 Mbytes/sec with minimum power budget of 6 dB. Both, the FOXI parallel interface inputs and the *Futaba* linear quadrature encoder outputs are TTL compatible. Data to be transmitted is latched in the transmitter, encoded, serialized, converted into light, and sent over the fiber.

In the FOXI sense, "Data" means a group of 8, 9, or 10 bits (depending on the "data mode selector". Another group, called "Command", has 4, 3, or 2 bits, correspondingly. The mode used in this design is 9 *Data* + 3 *Command* mode, accordingly, "Data Mode Select" input is connected to V_{cc} .

Present Serpentine Truss arm has six *Futaba* quadrature encoders. Three analog signals A, B, and Z, generated by each encoder, are transmitted, to the central control and processing unit, for a total of 18 signals. Hence, two FOXI links are needed to handle all quadrature encoder signals. Figure 1 illustrates an approximate position for the two transmitters mounted on the two dummy modules. The first FOXI transmitter chip (Tx#1), mounted on dummy module #1, is connected via copper wires to Box1A, Box1B, and Box2A. A block diagram for the Tx#1 is shown in Figure 2a. Pin 17, 16, and 15 are connected to Ch A, Ch B, and Ch Z of Box2A; pin 23, 24, and 25 to Box1B; and pin 26, 27, and 28 to Box1A. The second FOXI transmitter chip (Tx#2), mounted on dummy module #1, is connected via copper wires to Box2B, Box3A, and Box3B. Tx#2 is identical to Tx#1. A block diagram for the Tx#2 is shown in Figure 2b. Pin 17, 16, and 15 are connected to Ch A, Ch B, and Ch Z of Box2B; pin 23, 24, and 25 to Box3A; and pin 26, 27, and 28 to Box3B. In addition to the two fiber links, a +5 V power bus is needed to distribute power to the *Futaba* encoders and the FOXI transmitters.

Detailed schematics for TX#1 and TX#2 are shown in Figure 3a and Figure 3b respectively. For DLT6000 Transmitters, DMS (Data Mode Select) determines the data pattern width. When it is wired to V_{cc} , the DLT600 will

assume Data to be nine bits wide, with three bits of command. In this mode, transmitters use one 5B/6B encoder and one 4B/5B encoder to decode nine data bits into an 11-bit pattern. Only Data bits are used and command pins are not connected. TLS (Test Local Select) should always be grounded during normal operation, and CLK output should be always connected to STRB (strobe) input. Furthermore, X1 and X2 are connected to a crystal oscillator with a frequency of 4 MHz, this frequency is FOXI's minimum operating frequency.

(ii) *Receiver:*

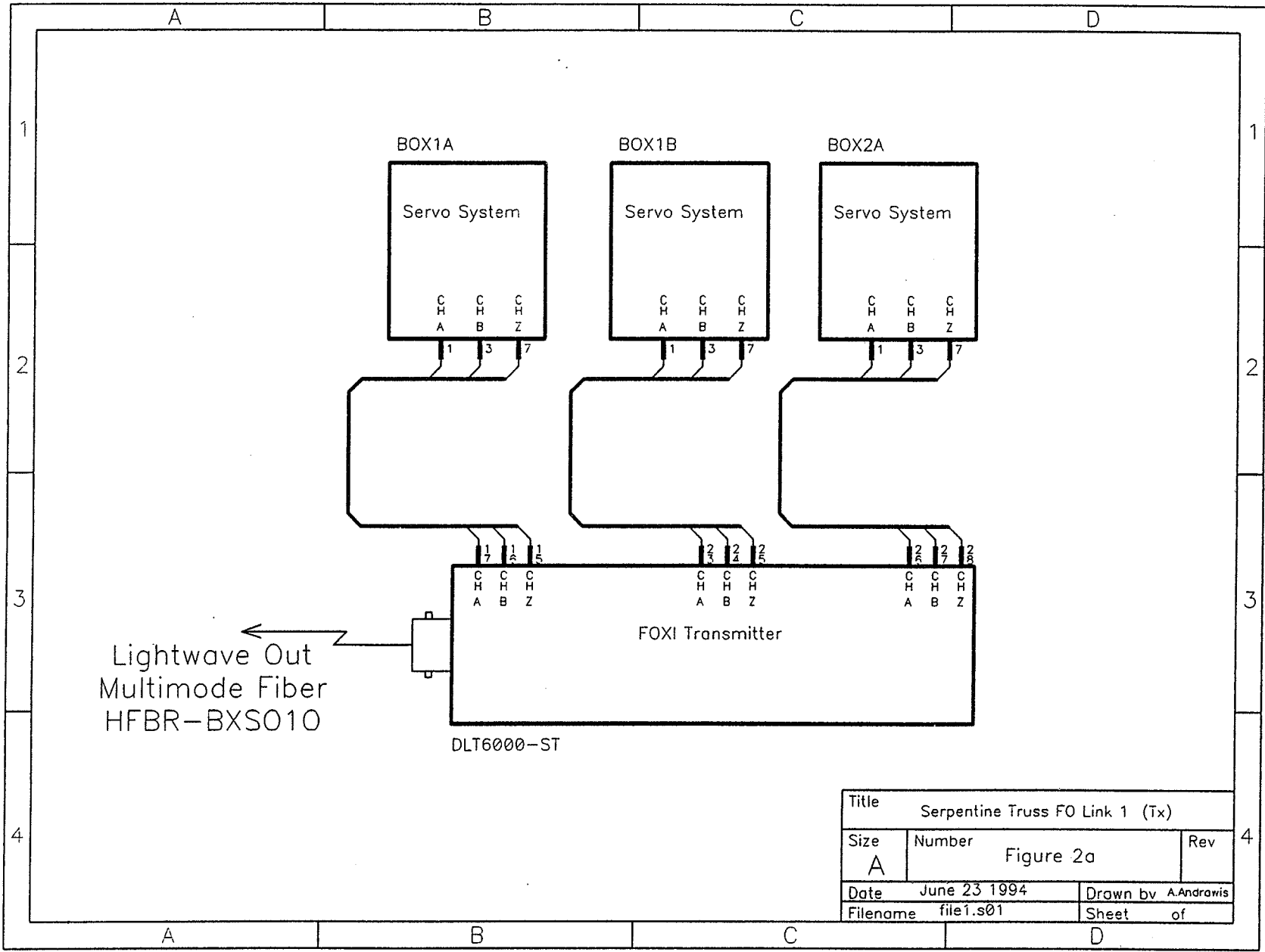
At the receiver end, the serial string of optical symbols is converted into electrical signal, deserialized, decoded and clocked out as parallel words.

Two DLR6000-ST FOXI receivers located in the control rack feed position sensing signals to *Tech 80* encoder inputs. Figure 4a and Figure 4b illustrates block diagrams for the Serpentine Truss Fiber Optic Network Rx1 and Rx2 respectively.

The network features both error detection and error correction capabilities. The capability of detecting simple errors is built in the chip, while correcting errors is done externally.

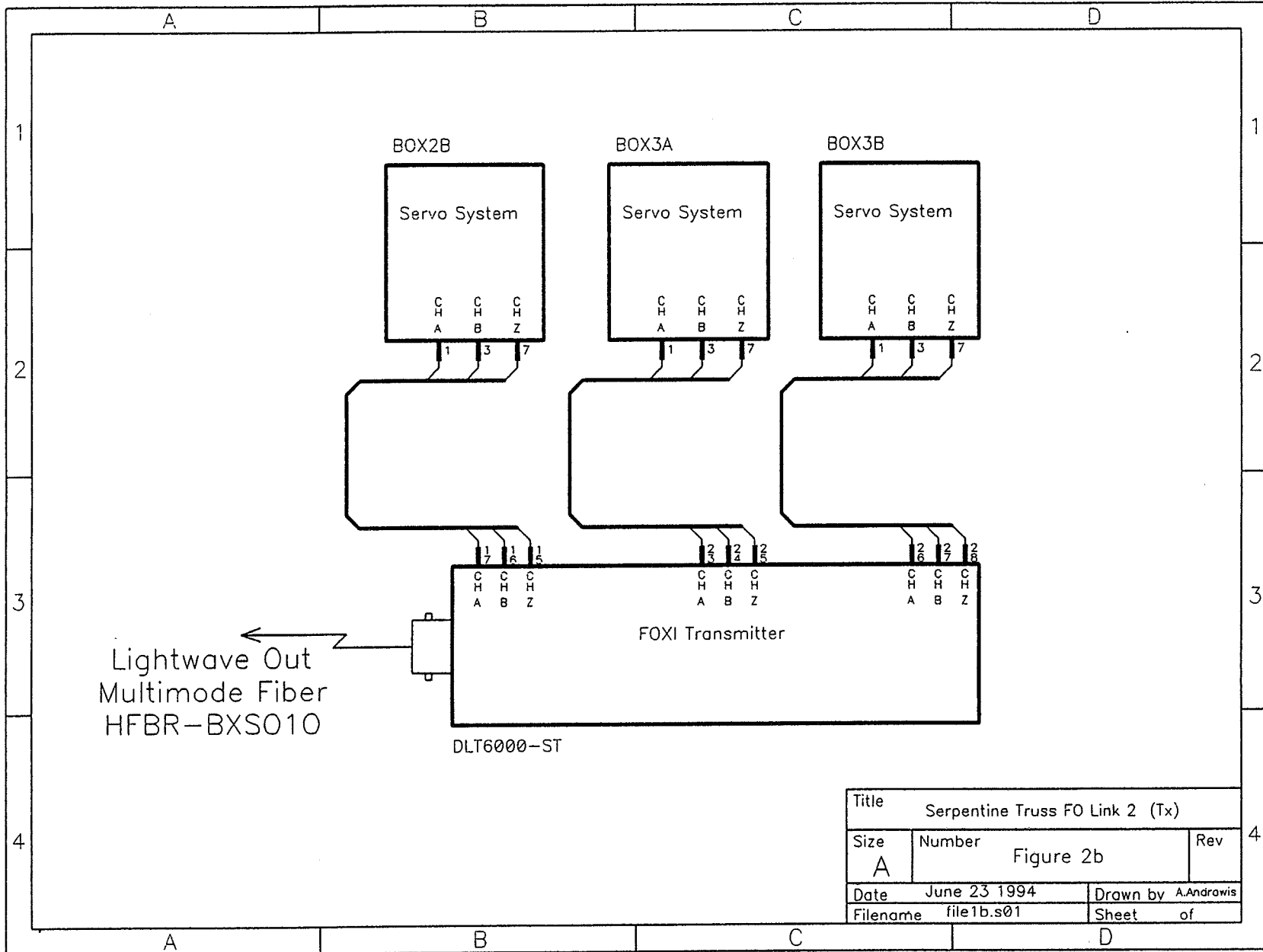
The receiver logic detects the most common types of transmission errors. It detects these errors by completely decoding the incoming data patterns, and recognizes several types of violations. The rising edge of VLTN (Violation) output signals that a transmission error has been detected. Consequently, SN74116 latches ignore the erroneous word and the previous word is considered valid for one more clock cycle. Meanwhile, the LED connected to the SN74121 Monostable Multivibrator blinks for a duration of one second. If the error rate is bigger than $\sim 2 \times 10^{-8}$, then the LED will remain on continuously.

LED blinking rate is not a measure of the end-to-end link error rate, but it is a good indication about the condition of the fiber optic part of the link. Only six consecutive violations causes an end-to-end error. In normal operating conditions, the probability of six consecutive violations is negligible.



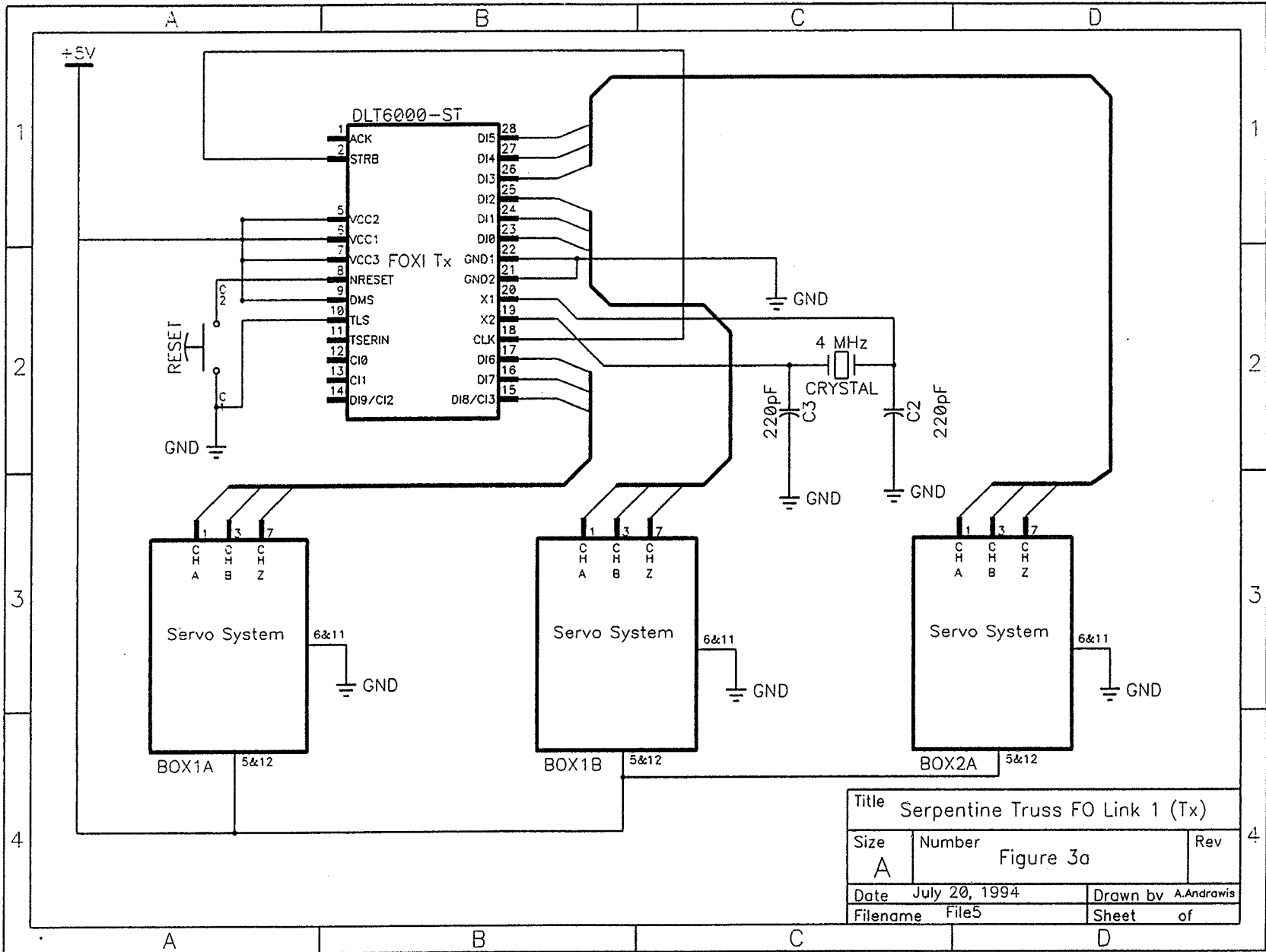
Title			Serpentine Truss FO Link 1 (Tx)		
Size	Number		Rev		
A	Figure 2a				
Date	June 23 1994		Drawn by A.Andrawis		
Filename	file1.s01		Sheet of		

15

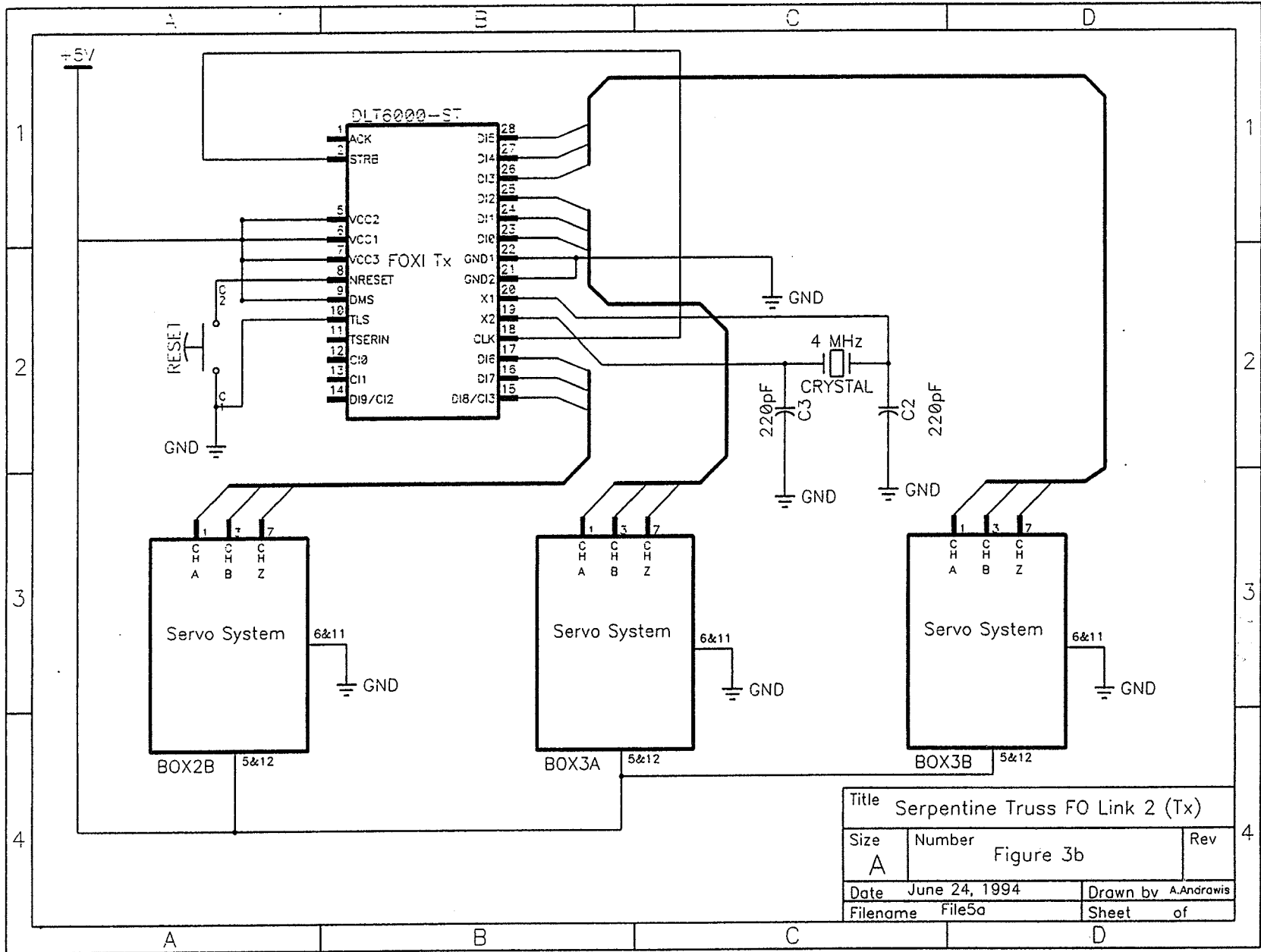


Title			Serpentine Truss FO Link 2 (Tx)		
Size	Number	Rev			
A	Figure 2b				
Date	June 23 1994	Drawn by		A.Androwis	
Filename	file1b.s01	Sheet		of	

12



Title Serpentine Truss FO Link 1 (Tx)		
Size A	Number Figure 3a	Rev
Date July 20, 1994	Drawn by A.Andrawis	
Filename File5	Sheet of	



Title			Serpentine Truss FO Link 2 (Tx)		
Size	Number			Rev	
A	Figure 3b				
Date	June 24, 1994	Drawn by	A.Andrawis		
Filename	File5a	Sheet	of		

Lightwave In
Multimode Fiber
HFBR-BXS010

DLR6200-ST

FOXI Receiver

C
H
A

C
H
B

C
H
Z

C
H
A

C
H
B

C
H
Z

C
H
A

C
H
B

C
H
Z

1

2

3

4

3

2

2

5

3

2D

C
H
A

C
H
B

C
H
Z

Encoder Input

6

7

8

2C

C
H
A

C
H
B

C
H
Z

Encoder Input

6

7

8

2B

C
H
A

C
H
B

C
H
Z

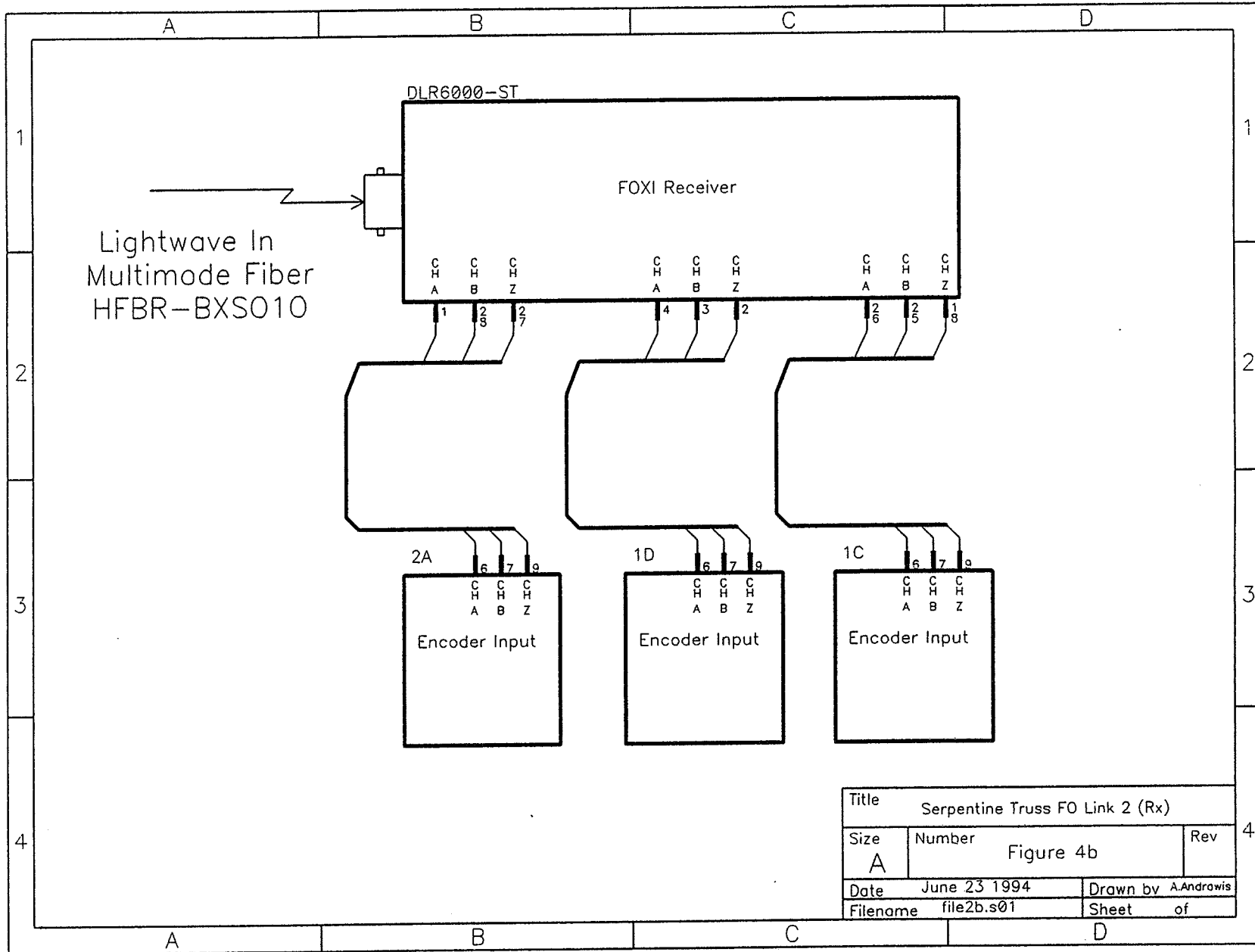
Encoder Input

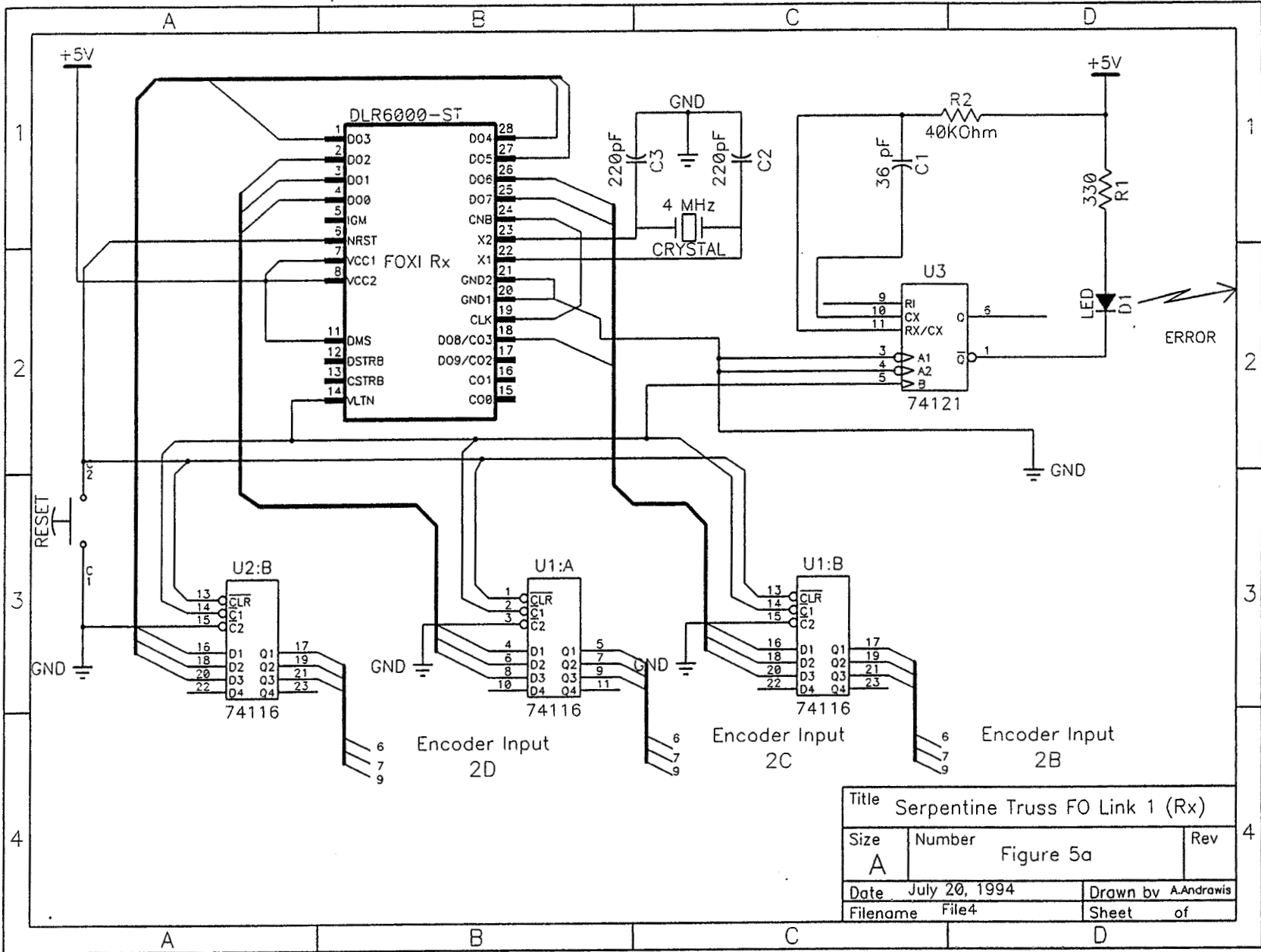
6

7

8

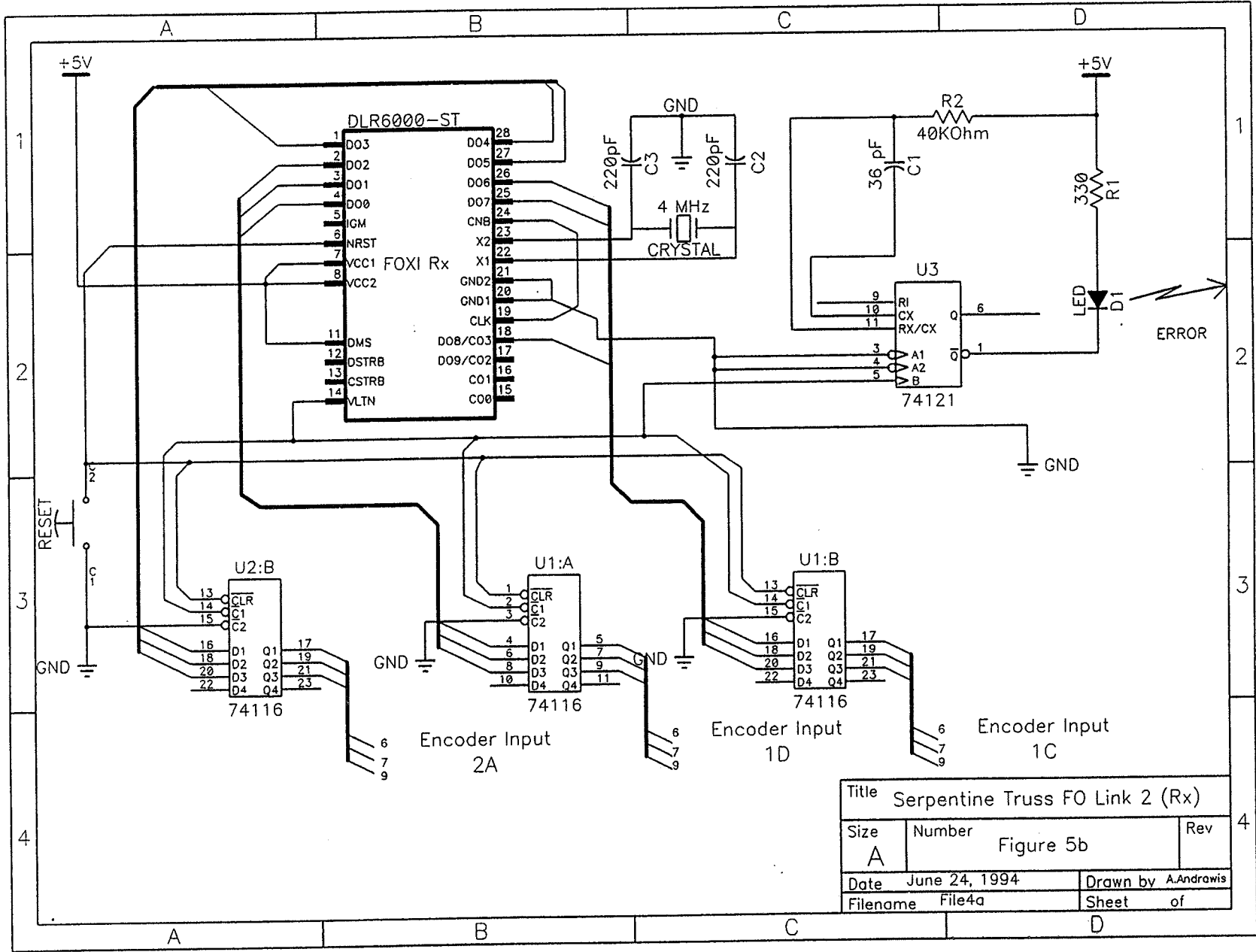
Title			Serpentine Truss FO Link 1 (Rx)		
Size	Number			Rev	
A	Figure 4a				
Date	July 20, 1994		Drawn by	A.Andrawis	
Filename	file2.s01		Sheet	of	





20

Title Serpentine Truss FO Link 1 (Rx)			Rev 4
Size A	Number Figure 5a		
Date July 20, 1994	Drawn by A.Andrawis		
Filename File4	Sheet	of	



Title Serpentine Truss FO Link 2 (Rx)		
Size A	Number Figure 5b	Rev
Date June 24, 1994	Drawn by A.Andrawis	
Filename File4a	Sheet of	

21

FOXI parallel interface outputs and *Tech 80* quadrature encoder board inputs are TTL compatible. Both are connected to SN74116 latches as shown in Figure 5a and Figure 5b. Similar to the transmitter, the DMS pin is connected to V_{cc} for the data to be nine bits wide. CLK is a free-running clock output which runs at the byte rate, and is synchronous with the serial data input. When the CLK output is connected to the CNB (Catch Next Byte) input, the receiver operates in the local mode, and each byte is captured, decoded and latched to the output.

b. Phase II:

As mentioned earlier, present Serpentine Truss architecture is a centralized control and processing (industrial-grade 386DX PC with passive backplane). This design requires the transmission of power signals (from the central control and processing unit to actuators) which can not be transmitted through fiber. Phase I of this design report, requires no major design modifications to be implemented. On the contrary, the second phase requires major design modifications for the Serpentine Truss. Considering potential NASA applications at the Kennedy Space Center, the Advanced Systems Section is interested to increase the truss' degrees of freedom (DOF) from 8 to 18. Moreover, the Truss architecture is to be changed to distributed control configuration instead of being a central control configuration. The central processing and control unit in the new upgraded truss acts as a mater computer, while distributed controllers act as slave computers. To achieve the required upgrade, the following has to be implemented;

- **Ball Drive Linear Actuators:**

An extra 10 degrees of freedom has to be added to the existing Serpentine Truss Manipulator Arm. Reference to Figure 1, the Serpentine Truss Manipulator Arm consists of five modules, three active modules, and two dummy modules. Each active module consists of two boxes, Box A and Box B. Each box is equipped with two Linear Ball Drive Actuators, one is active while the other is passive. Activating the passive actuators will add six degrees of freedom to the truss. Replacing the two dummy modules with two active boxes adds an additional four degrees of freedom. Only four Ball Drive Linear Actuators are in need to activate the two dummy modules.

- Linear Variable Differential Transformers (LVDTs):

The Truss is equipped with six *Futaba* linear encoders, an extra 10 units are needed. Since *Futaba's* encoders are bulky and expensive they are to be replaced with Lucas LVDTs. Therefore, a total of sixteen LVDTs is required for the new added DOF and to replace existing *Futaba* encoders and potentiometers.

- DC Servo Amplifiers:

These amplifiers are to provide DC power to the Ball Drive Linear Actuators.

- Microcontroller Boards (Slave Computers):

These boards should be able to; convert the analog DC voltage level output from the LVDT to at least 12-bit digital word (12-bit A/D); execute instructions given by the Master Computer; provide PWM signal and direction signal to the servo control.

Table 1 estimates cost of materials and labor needed to upgrade Existing Serpentine Truss from 8 DOF to 18 DOF.

The optical fiber network consists of two directions; from the master computer to the slave computer and visa-versa. Optical fiber links developed for phase 1 will be integrated in network upgrade of phase 2. Exact network configuration depends on the microcontroller chip used for distributed control units. Material and labor cost needed for the development of a fiber optics communication network for controlling the upgraded multidegree-of-freedom Serpentine Truss is included in Table 2. A complete vendor list, along with contact persons, is attached in Appendix A.

TABLE 1
Serpentine Truss
Distributed Control and 18 DOF Upgrade

Materials:

• Ball Screw Actuators	
MOTION Ball Drive Actuator 85261 (2 pcs)	\$ 550.00
MOTION Ball Drive Actuator 85199 (2 pcs)	\$ 500.00
• LUCAS CONTROL SYSTEMS	
Linear Variable Differential Transformers (LVDTs)	
Coil Assembly and Core	
DC-E-2000 (4 pcs)	\$ 1664.00
DC-E-3000 (12 PCS)	\$ 5736.00
Rods (242 inches)	\$ 363.00
• Cannibalize existing MOTION 85151 actuators to parallel mount, and Reinstall Ball Screws to reduce backlash of all existing MOTION actuators by ~ 50%	\$ 400.00
• Copley 422 PWM Amplifier (16 pcs)	\$ 4640.00
• AMDEX Industrial Computer Passiveboard CPU 80-5866	\$ <u>3595.00</u>
<u>Total</u>	<u>\$17448.00</u>

Development and Labor:

• Development of the Motor Control Boards, 120 hrs@\$40/hr	\$ 4800.00
• Expansion of control program, 320 hrs@\$40/hr	\$12800.00
• Technician Laboratory Work, 400 hrs@\$40/hr	\$ <u>16000.00</u>
<u>Total</u>	<u>\$33600.00</u>

TABLE 2
Serpentine Truss
Fiber Optic Upgrade

Materials:

• HP DLT6000-ST Transmitter (10 pcs)	\$ 2060.00
• HP DLR6000-ST Receiver (10 pcs)	\$ 2240.00
• FUTABA PC2455 Female Connectors (6 pcs)	\$ 150.00
• Amphenol 953-101-5010 ST multimode connector (20 pcs)	\$ 121.00
• Spec-TRAN G1-62.5-A04RB-500 Fiber cable (60 meters)	\$ <u>120.00</u>
<u>Total</u>	\$ 4691.00

Development and Labor:

• Technician Laboratory Work, 320 hrs@\$40/hr	\$12800.00
--------------------------------------------------	------------

The following example design [Ref. Advanced Micro Systems publication 17490A] multiplexes 32-bit data words using one DLT6000-ST Transmitter. This design can easily be applicable to systems with wider or narrower data paths with or without command. If we assuming that the microcontroller used has 16 bits wide asynchronous output port, then this example design can serve two distributed control units, i.e. one FOXI Transmitter/Receiver pair is needed for each box. Implementation of the 32-bit multiplexed Transmitter circuit is shown in Figure 6. In addition to the DLT600-ST Transmitter, the following parts are required:

- 74LS00 quadraple 2-input positive NAND gates
- 74LS04 hex inverters
- 74LS20 dual 4-input positive NAND gates
- 74LS174 hex D-type flip-flops
- Am29C821 tri-state registers

The design can be optimized to save board space by fitting it into PAL16R6 device or equivalent.

Figure 7 illustrates the basic concepts involved in demultiplexing data from the FOXI receiver. The particular example design demultiplexes four bytes of data and commands into one 32-bit word

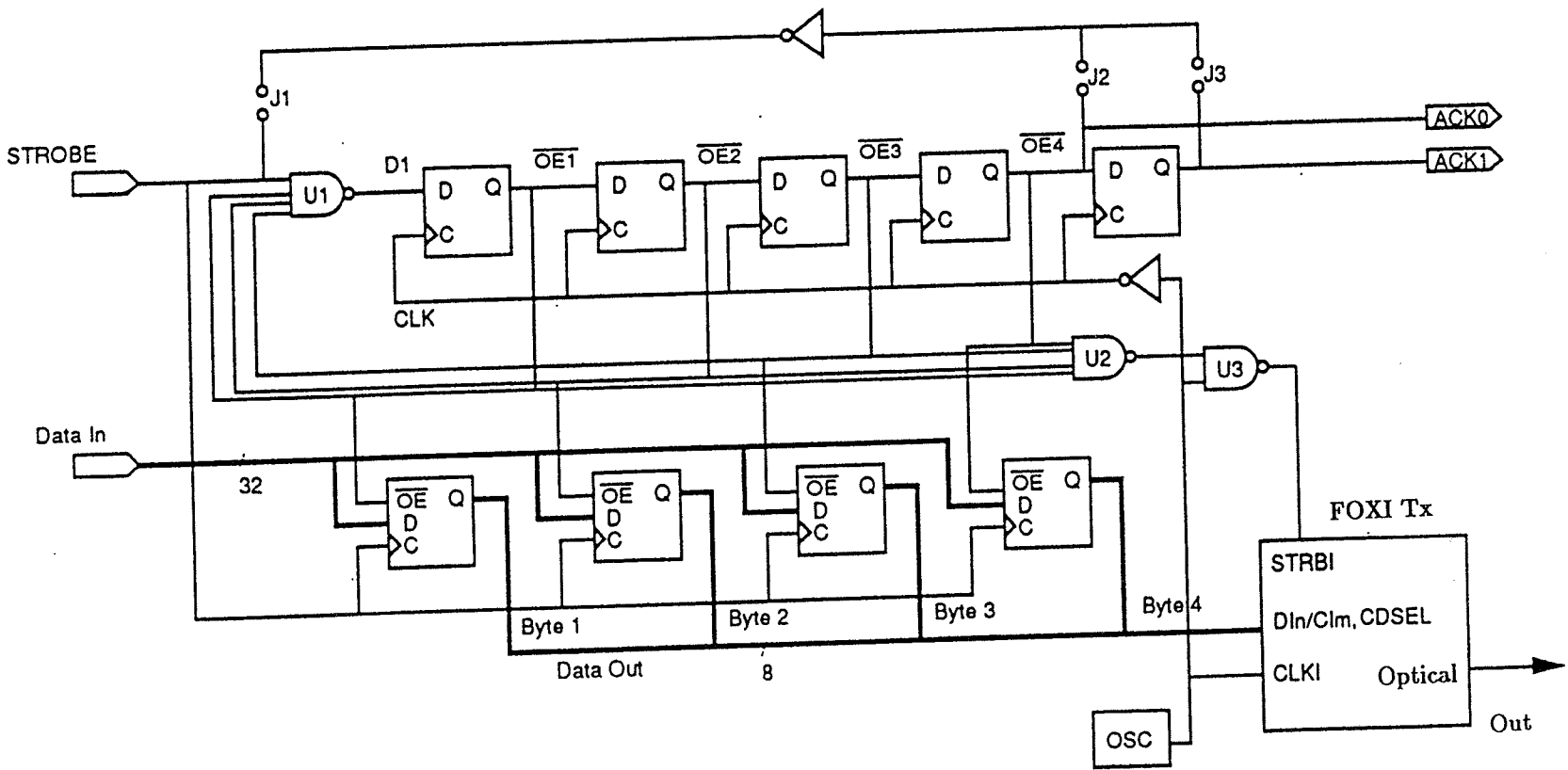


Figure 6: Logic Diagram of 32-Bit Multiplexed Transmitter

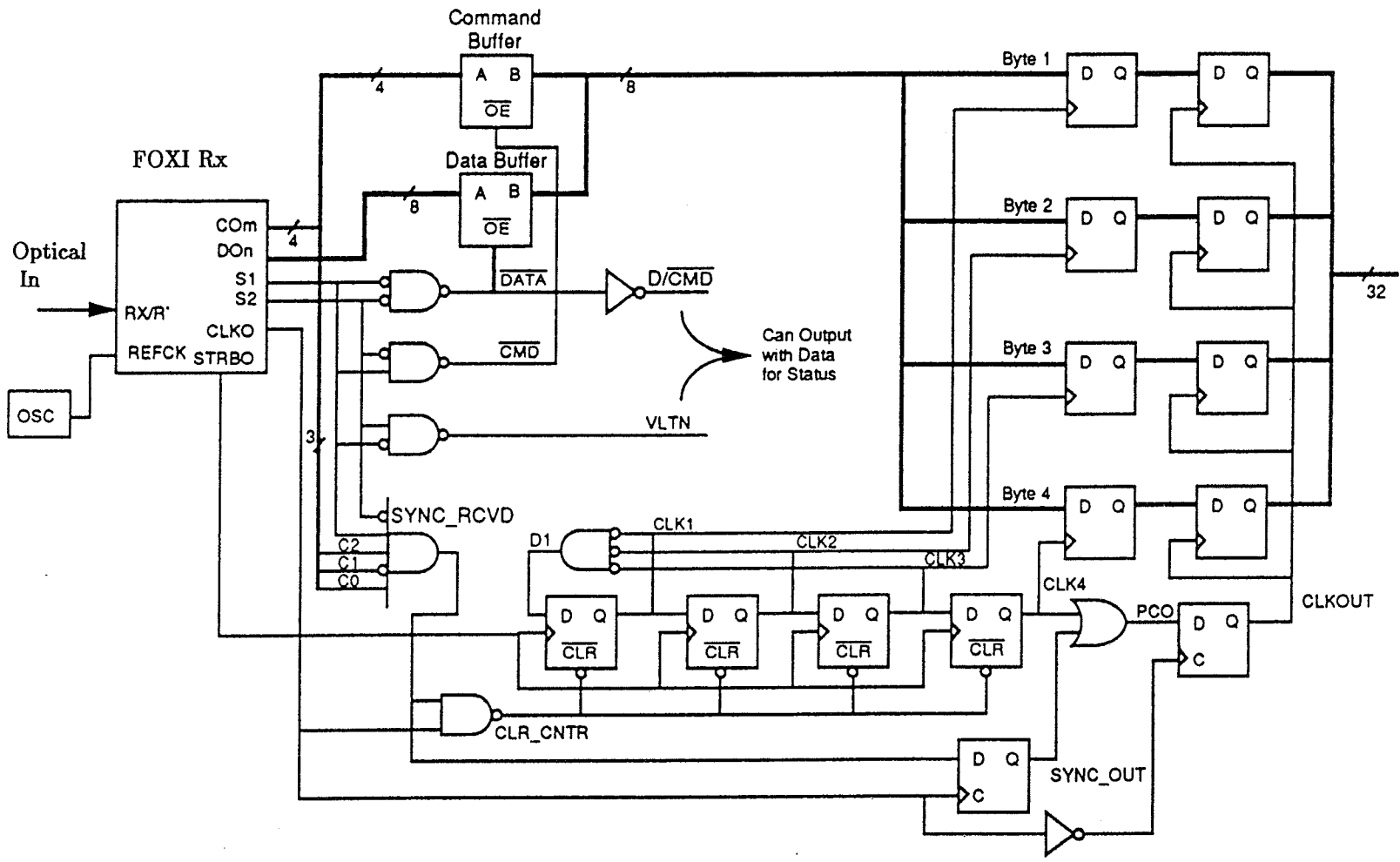


Figure 7: Logic Diagram of 32-Bit Demultiplexed Receiver

APPENDIX A

CONTACT LIST

<u>VENDOR</u>	<u>CONTACT PERSON</u>	<u>TELEPHONE</u>
1. MOTION Systems Corporation Box 11 Shrewsbury New Jersey 07702	Bill Tyrrell	(201)222-1800
2. Lucas Control Systems Products 1000 Lucas Way Hampton, VA 23666	Valerie Wharton (Sales) Martin Aronow (Application Eng)	(804)766-4490 (804)766-1500
3. FUTABA Corporation of America 14492 Sheldon Road, Suite 350 Plymouth, Michigan 48170	Don Mikros	(313)459-2830
4. Spec-TRAN P.O. Box1260 Avon, CT 06001	Sylvia Digey	(203)678-0371
5. Hewlett Packard Company 6177 Lake Ellenor Drive Orlando, FL 32859-3910	Sandy Vehonsky (Sales)	(407)826-9291 (800)933-4395
6. Copely Controls Corp. 410 University Ave. Westwood, MA 02090	Mark Connoly	(617)329-8200
7. AMDEX Division Aerodyne Products Corporation 76 Treble Cove Rd N.Billerica, MA 01862	Walter Stewart	(203)268-8000

1994 NASA/ASEE SUMMER FACULTY FELLOWSHIP PROGRAM 11753

S2-18

JOHN F. KENNEDY SPACE CENTER
UNIVERSITY OF CENTRAL FLORIDA

33962

p. 30

351451

SPACE STATION RACKS WEIGHT & C.G. MEASUREMENT
USING THE RACK INSERTION END-EFFECTOR

PREPARED BY:	Dr. William V. Brewer
ACADEMIC RANK:	Professor
UNIVERSITY AND DEPARTMENT:	Jackson State University Technology Department
NASA/KSC	
DIVISION:	Mechanical Engineering
BRANCH:	Special Projects
NASA COLLEAGUE:	Eduardo Lopez Alan Littlefield
DATE:	August 1, 1994
CONTRACT NUMBER:	University of Central Florida NASA-NGT-60002 Supplement: 17

ACKNOWLEDGEMENTS

Eduardo Lopez provided a good work environment upon arrival here at the robotics lab. He framed the problem well and got the project off to a good start. Alan Littlefield shared time and information to keep the effort focused on the customers perspective. N.S.Malladi offered advice, alternatives and assistance whenever asked. Carey Cooper vastly improved the graphics of this presentation by making the relevant computer drawings available in a usable form. He also shared his experience regarding strut linkage attachment hardware. My appreciation goes to these and many others who made the work here a pleasure. My thanks to Loren Anderson and Kari Styles for putting up with us and answering all the same questions over and over. It's been fun guys and I hope we can do it again.

ABSTRACT

Objective: Design a method to measure weight and center of gravity (C.G.) location for Space Station Modules by adding sensors to the existing Rack Insertion End Effector (RIEE).
Accomplishments: Alternative sensor placement schemes are organized into categories. Vendors were queried for suitable sensor equipment recommendations. Inverse mathematical models for each category determine expected maximum sensor loads. Sensors are selected using these computations, yielding cost and accuracy data. Accuracy data for individual sensors are inserted into forward mathematical models to estimate the accuracy of an overall sensor scheme. Cost of the schemes can be estimated. Ease of implementation and operation are discussed.

SUMMARY

Scope: Non-experimental assessment of competing sensor placement schemes to determine accuracy, cost, installation and operational characteristics of selected alternatives.

Range of variables: Measured weight within $\pm 0.2\%$ of actual weight
" C.G. " " 0.4 in. of " C.G.

Constraints: Rack weight: $250 < W_r < 1750$ lbs.
C.G. envelope: 6.3 x 4.6 x 11.4 ins.
Sensor ranges: 500, 1000, 2000 lbs. (off-the-shelf)
" accuracies: 0.05 % of full scale (" " "maximum)

Results: Selected sensor schemes are evaluated for accuracy, cost, ease of integration with the existing RIEE, and impact on operations. Selections were based on the ability of a scheme to provide features contributing to one or more of the above benefits: accuracy is improved if the ratio of rack to lift weight is maximized; sensor cost is minimized by using Load Cells; integration is easiest with Load Pins replacing those in the existing RIEE; operations are easier if the Interface Plate (500 lbs.) is included in the lift weight. Separate sensor schemes maximizing each of these desirable features are compared.

Accuracy specifications could only be satisfied for rack weights approaching the upper limit (1750 lbs.) of the load range using "off-the-shelf" sensor equipment.

Locating the C.G. within the specified 0.4" was within the capability of "off-the-shelf" sensors.

TABLE OF CONTENTS

Section	Title	Page
I	INTRODUCTION	1-1
1.1	Objective	1-1
1.2	Motivation	
1.3	Scope	
1.4	Module	
1.5	Rack	1-4
1.6	Rack Insertion	
1.7	RIEE	
II	SENSOR SCHEMES	2-1
2.1	Alternatives	2-1
2.2	Accuracy	2-3
2.3	Models	2-4
III	RESULTS	3-1
3.1	Samples	3-1
3.2	Ranges	
3.3	Accuracies	3-2
3.4	Allowables	3-3
IV	CONCLUSIONS	4-1
4.1	Summary of Results	4-1
4.2	Conclusions	
4.3	Recommendations	
APPENDIX A	PLATE MOUNTED SENSORS	A-1
APPENDIX B	ARM MOUNTED SENSORS	B-1

LIST OF ILLUSTRATIONS

Figure	Title	Page
1.1	RACK COORDINATE SYSTEM	
1.2	END EFFECTOR / MODULE CLEARANCES	
1.3	C.M. ENVELOPE FOR INTEGRATED RACK with 1543 lbm PAYLOAD	
1.4	RACK ATTACH POINTS	
2.1	SENSOR PLACEMENT SCHEMES	
2.2	RACK & BAR SUSPENSION	
2.3	ORTHO - STRUT PAIR INTERSECTION	
2.4	RACK & PLATE SUSPENSION	
2.5	RACK-PLATE & ARMS SUSPENSION	

INTRODUCTION

1.1 OBJECTIVE

Design a method to measure weight and center of gravity (C.G.) location for Space Station Resupply Module Racks by adding sensors to the existing Rack Insertion End Effector (RIEE).

1.2 MOTIVATION

Current plans for weight and C.G. measurement require placement of the 1 x 1 x 2 m, half moon shaped racks (weighing as much as 1750 lbs.), Figure 1.1, in a special stand instrumented with load cells. Racks will have to be located on the stand in two positions if two sets of readings are required. Then the racks are to be transferred to the RIEE for installation into the space station resupply module. Measuring weight and C.G. while the rack is attached to the RIEE will eliminate the need for a separate measurement stand. Time will be reduced by one rack reposition and two rack transfer operations.

1.3 SCOPE

Non-experimental assessment of competing sensor placement schemes to determine accuracy, cost, installation and operational characteristics of selected alternatives.

Range of variables:

Specified by NASA:

Accuracy:

Measured weight	within	+/--	0.2 %	of actual weight
" C.G.	"	"	0.4 in.	of " C.G.

Constraints:

Rack weight:	250 < W_r < 1750	lbs.
C.G. envelope:	6.3 x 4.6 x 11.4	ins.

Specified by vendors:

Sensor ranges:	500, 1000, 2000	lbs.	(off-the-shelf)
" accuracies:	0.05 %	of full scale	(" " "maximum)

1.4 MODULE

Space station resupply modules are pressurized cylindrical containments of approximately 4m diameter x 4m length. They contain 16 quarter cylinder, moon shaped segments called racks, Figure 1.2 . Racks are 1m in axial thickness so that 4 sets of 4 segments fill the module. Access to the module is thru a 2.4m diameter hatch in the bulkhead at the end.

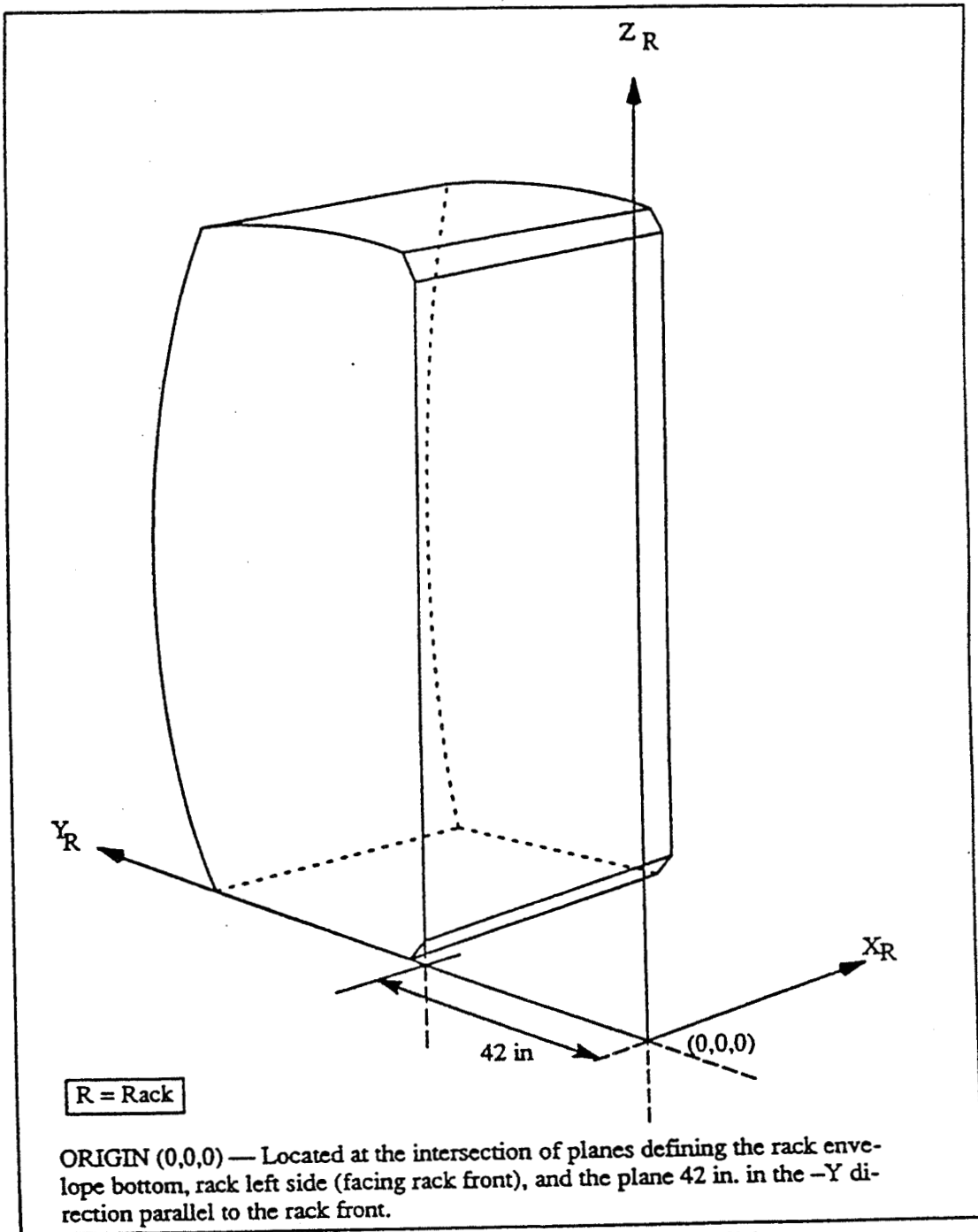


FIGURE 1.1 RACK COORDINATE SYSTEM

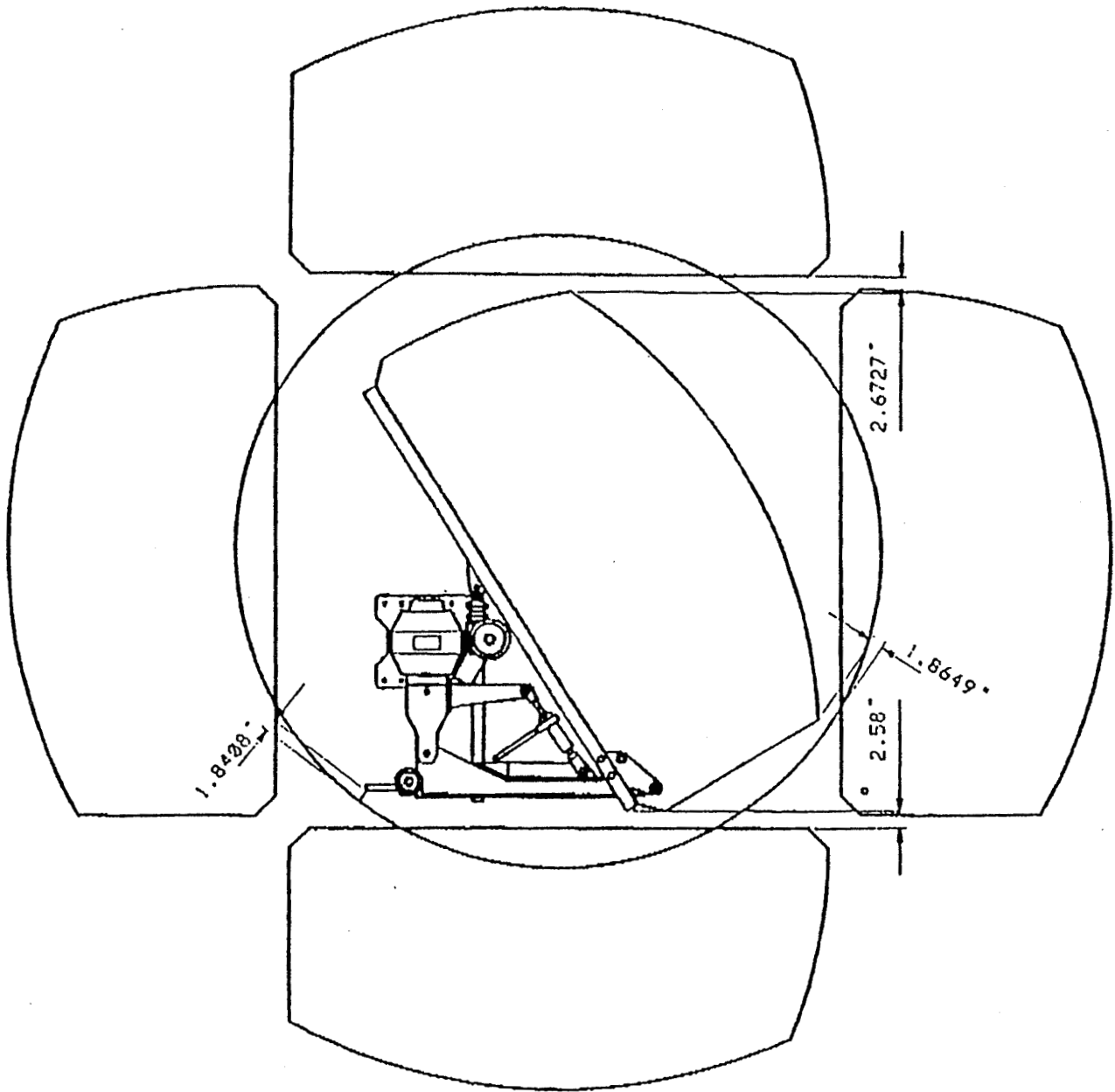


FIGURE 1.2 END EFFECTOR / MODULE CLEARANCES

1.5 RACK

"U.S. Standard Equipment Rack (is described in the) Interface Development Document",[1].

Figure 1.1 shows the coordinate system used for the rack. X_r coordinate measures from the left side of the rack in the direction of the module cylindrical axis. Y_r coordinate measures parallel to a radius, perpendicular to a plane thru the module center line. Z_r measures from the rack base orthogonal to X_r and Y_r .

Figure 1.2 shows the rack attached to the Rack Insertion End Effector (RIEE) in the inclined position necessary for insertion thru the bulkhead access hatch.

Figure 1.3 shows the specified C.M. (Center of Mass is the same as the Center of Gravity, C.G.) envelope for the larger (1543 lbm) of 2 rack specifications. The envelop for the smaller (882 lbm) is slightly more generous.

Figure 1.4 shows the location of Rack Attach Points. Only points G,H,E,F, at the corners of the frontal plane can be used by the RIEE to manipulate the rack.

1.6 RACK INSERTION

Semi-robotic installation of racks into the module is accomplished with a large, 3 d.o.f. (degree of freedom), robotic positioning device supporting a 6 d.o.f., manually operated end-effector weighing 2 tons.

ORU Handling Device is the designation of the robot [2]. Its main feature is a large beam, telescoping in the X_r direction, on which the end-effector is mounted. Smaller Y_r & Z_r translations are permitted.

RIEE is the designation of the manual end-effector [3]. The rack is mounted on the RIEE interface plate by 4 bolts that pass thru holes at the corners of the 1 x 2m plate to screw into threaded holes in the rack at attach points G,H,E,F on the rack front panel. Rack and Plate thus assembled in a vertical position are then tilted by the RIEE to an angle of 35 deg (as on the left in Figure 1.5) so that both may pass thru the module access hatch as shown in Figure 1.2 . On the inside, the rack is returned to vertical as it is placed into its functional location.

1.7 RIEE

Rack and interface plate combination are supported at 3 points. A retractable jack strut between end-effector frame and plate cross-member controls tilt angle. Two variable length arm beams lift pivot points at the base of the plate. These are in turn lifted by 2 turnbuckle tensile struts. Varying degrees of displacement are provided in surge and heave adjustments. Pitch of 35 deg with much smaller amounts of roll and yaw rotations are also accommodated.

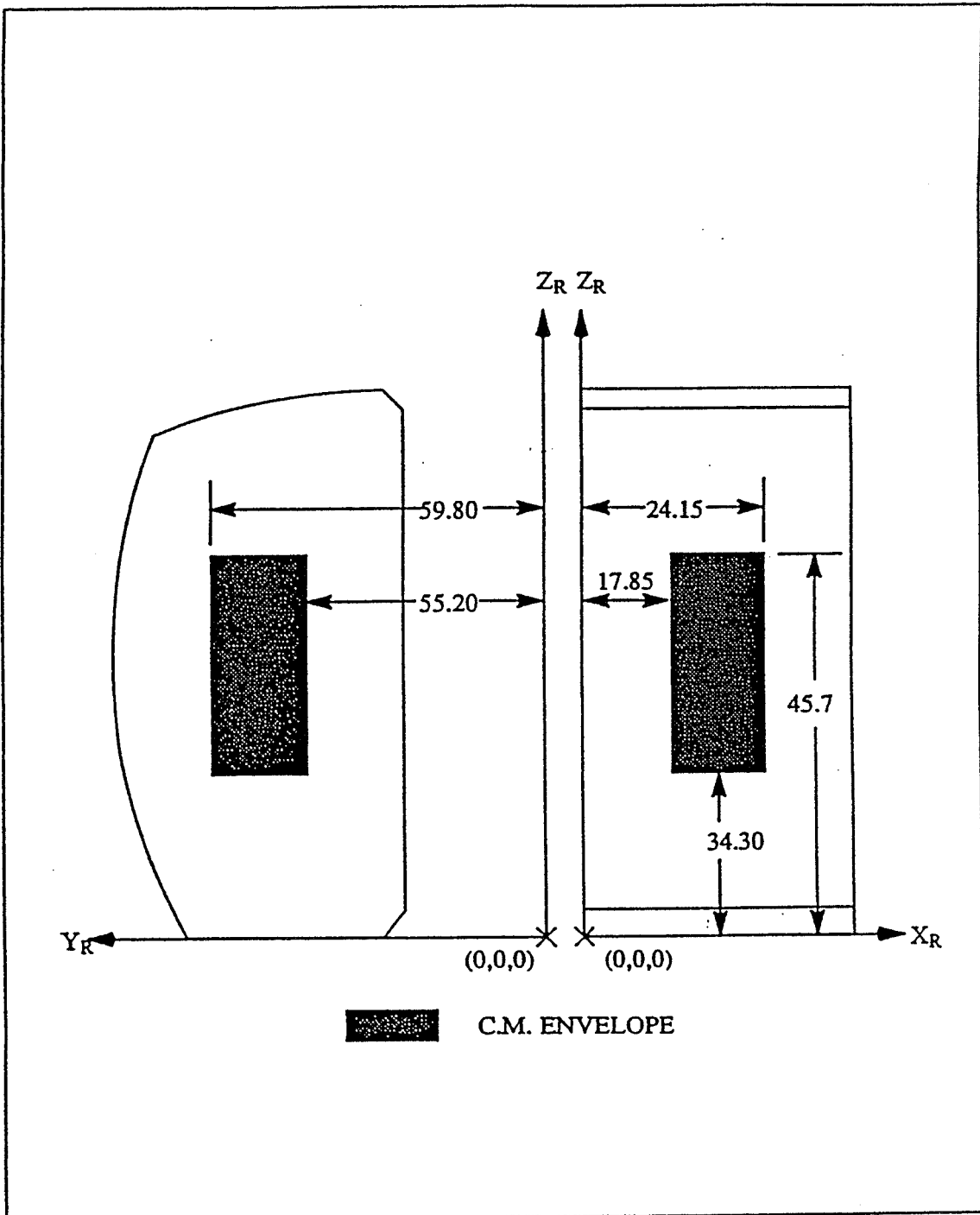


FIGURE 1.3 C.M. ENVELOPE FOR INTEGRATED RACK
WITH 1543 LBM PAYLOAD

POINT	X_R	Y_R	Z_R
A	1.350	69.866	1.678
B	40.650	69.866	1.678
C	1.260	46.020	79.315
D	40.740	46.020	79.315
E	1.300	42.000	2.750
F	40.700	42.000	2.750
G	1.300	42.000	74.840
H	40.700	42.000	74.840
I	0.500	45.500	3.800
J	41.500	45.500	3.800

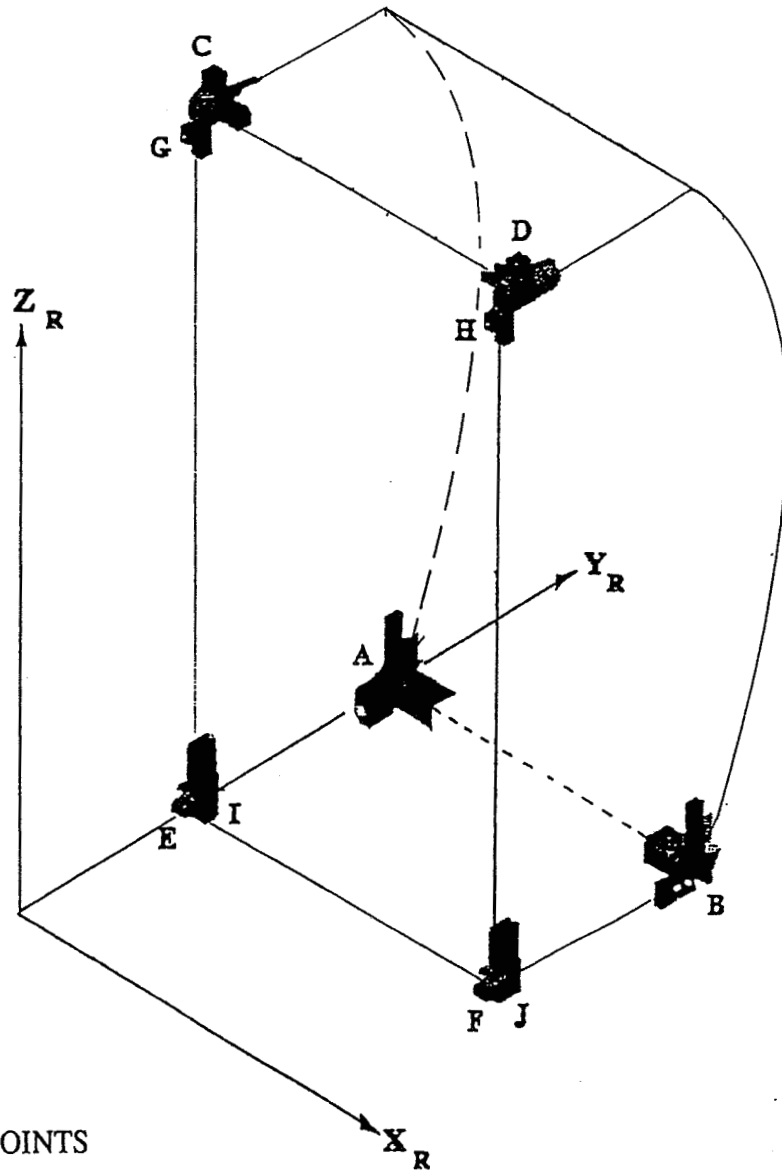


FIGURE 1.4 RACK ATTACH POINTS

II

SENSOR SCHEMES

2.1 ALTERNATIVES

Sensor placement schemes, suggested by interested personnel from NASA/KSC Special Projects Branch / Robotics Laboratory, were organized into 4 categories, Figure 2.1, with some variations on each theme:

2.1.1 ONE BIG F / T. A single, heavy lift, Force / Torque sensor placed between robot and end-effector offers simplicity of installation requiring no modifications to either. Servicing the sensor is facilitated by its location, remote from higher activity areas close to the rack.

Off-the-shelf F/T sensors of the specification required ($F = 4,000$ lbs / $T = 96,000$ lb-ins) are unavailable. Custom construction of such a sensor has been estimated at \$150,000 with a 36" diameter and measurement error on the order of ± 100 lbs.

Another approach calls for building the F/T device from 6 load cells statically arranged in a Stewart Platform configuration. Load cells are relatively inexpensive. Their would be flexibility to trade-off bending against torque capacity using strut angle parameters to achieve a design tailored to this application. I am told this scheme has been tried unsuccessfully before but I have no information on the details of the trial.

2.1.2 TWO PIVOT F / T. Placing sensors at the interface plate pivot points puts them within the commercially available range ($F = 2000$ lbs / $T = 2000$ lb-ins) with several vendors from which to choose. Costs range from \$15 to 30,000 for the pair depending on the extent of customization. Accuracies on the order of 1.0 lb. or less are possible. Choice of 2 computational procedures depends on whether the sensors are fixed to the interface plate, or arm support beam part of the pivot hinges. Some measurement redundancy can be added by installing a load pin at the upper end of the jack strut.

2.1.3 THREE LOAD PINS. Replacing ball-clevis pins in the RIEE with load pins offers the potential of minimum impact on the existing hardware. Cost on the order of \$4,000 renders this the least expensive of all alternatives. Redundant computation is possible but no redundant measurements are available without abandoning the simplicity of just replacing the pins.

2.1.4 FOUR LOAD CELLS mounted in orthogonal pairs at the lower outside corners of the interface plate such that they support only the rack and a load bar, read the lowest lift forces (as seen by sensors), therefore offer the highest potential accuracy. Cost of approximately \$5,000 is expected. Computations for this method (and 2.1.2 interface mounted F/T) do not depend on knowing the plate tilt angles precisely as do other computational methods.

1 BIG F/T sensor
between robot
& end-effector

2 F/T sensors
at interface
plate pivots

SPACE STATION
PROCESSING FACILITY
RACK INSTL/REMOVAL
END EFFECTOR
WEIGHT
&
C.G.
SENSOR SCHEMES

3 Load Pins
replacing
existing pins

4 Load Cells in
2 pairs on
interface plate

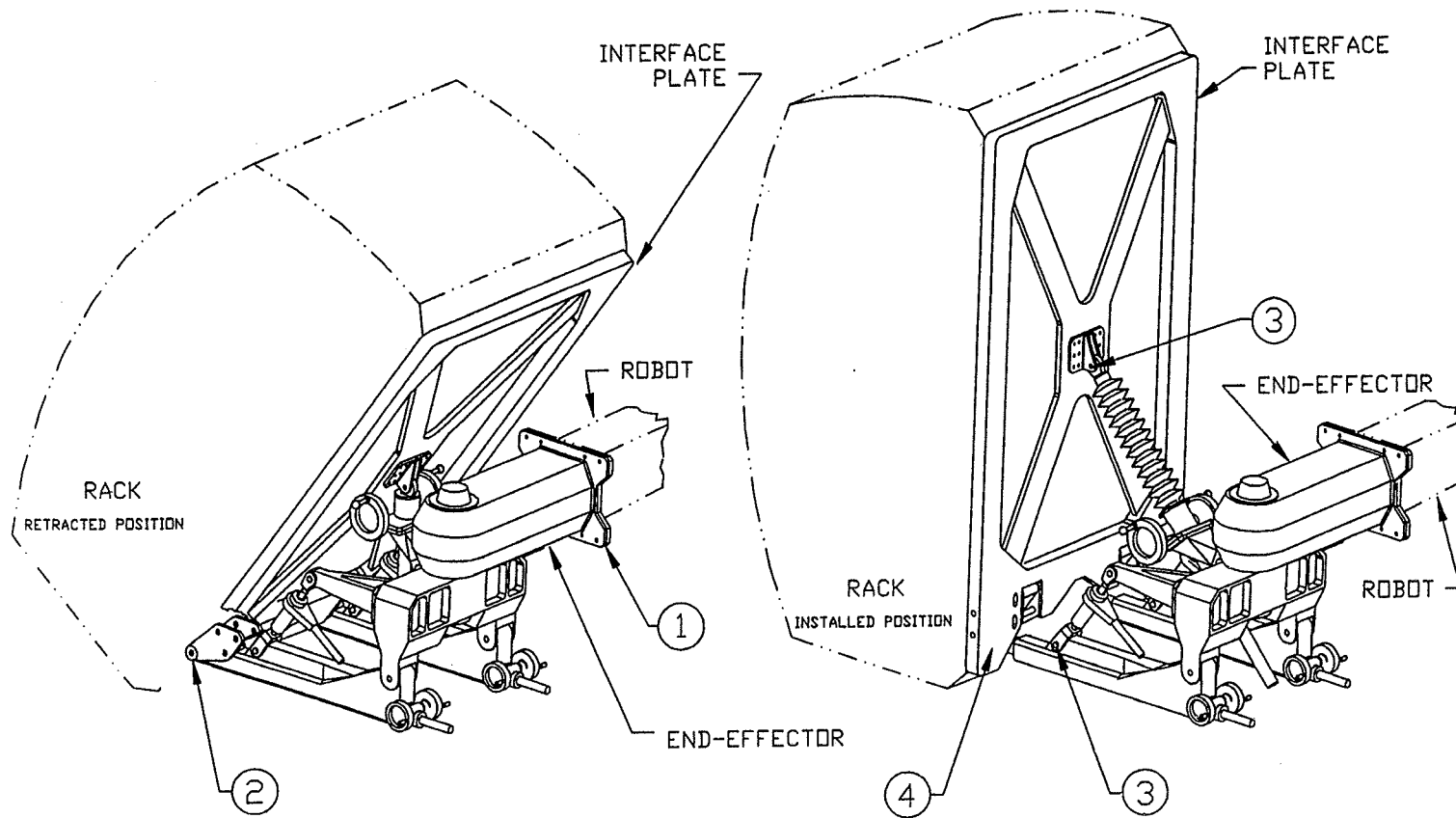


FIGURE 2.1 SENSOR PLACEMENT SCHEMES

2.2 ACCURACY

Sensor scheme error is dependant on component errors in: force measurement, dimensional parameters (c.g. of end-effector parts and load point locations) and friction effects. This non-experimental study attempts to access only the overall effect on accuracy that might be expected as a result of errors in force measurement. Dimensions are still in a state of flux. Approximations have been made, where required, based on information made available. No attempt has been made to measure or quantify errors that may be introduced by dimensional uncertainty or friction in suspension linkages.

2.2.1 RANGE DEPENDANCE. Scheme accuracy is dependant on component sensor error. Sensor load range must be specified before error (almost universally a % of range) can be known. Range is determined by the maximum load a sensor will experience over the total measurement process. An inverse computation (i.e. given rack weight and C.G. location, find forces in the end-effector where sensors are located) is used to establish range information. This is done by assuming the maximum allowable rack weight and C.G. off-set (from geometric symmetry plane of both rack and end-effector). Sensor placements that result in statically indeterminant inverse solutions make range determination a function of structural rigidity. This would be true, for example, with sensors placed between rack and plate at all 4 Rack Attach Points in Figure 1.4 . Simplicity suggests these be excluded from consideration.

2.2.2 SENSOR SELECTION. Nominal range specifications are usually in increments of 100, 500, 1000, 5000 etc. for off-the-shelf equipment. Maximum expected sensor load is thus rounded up to the nearest available range. This and the physical sensor dimensions that will fit in the space available are absolute requirements. Beyond these, trade-offs between cost, accuracy, availability, service, ease of installation and operation are among considerations that are less clear cut.

2.2.3 SENSOR ACCURACY. Error components are normally broken down into various categories: non-linearity, hysteresis, non-repeatability, temperature effects on output and zero. These are usually expressed as a percent of the specified full scale sensor range. An overall error parameter is obtained by combining the various categories as the square root of the sum of squared component values. This emphasizes larger error sources and minimizes the impact of minor ones. It is less conservative than simple summation of component errors.

2.2.4 SCHEME ACCURACY. Forces at sensor locations are found using the inverse solutions discussed in 2.2.1 above. The overall error parameter multiplied by the sensor range at each sensor location is added to the force there computed from the inverse solution. Thus modified to reflect possible error, these forces are inputs to the forward solutions resulting in an estimate(s) of weight and C.G. location. Comparison with the original values, assumed as inputs to the inverse solution, yields an estimate of errors the chosen sensor scheme might produce. These can be compared with specified allowable error. Maximum error can be explored by examining the extremes of allowable weight at the vertices of the C.G. envelope.

2.3 MODELS

2.3.1 IMPLEMENTATION. All model computations were made with MathCAD version 2.5. Final models to be used with the hardware should include "if - then" logic for testing +/- conditions. This would allow a better assessment of "worst case" accuracy where force errors combine with true values so they amplify rather than cancel thus reflecting maximum error that may be expected. Further investigation would be expedited with "do-loop" capability.

As matters stand, force error magnitude is merely added to the actual force regardless of its sign. To obtain maximum possible error estimates, manual insertion of error signs is required after signs of actual forces have been computed. Exploration of all possibilities would result in a sizable matrix of solutions. Time permits only sample solution development with tools currently being used. Sample computations are appended and referenced where appropriate.

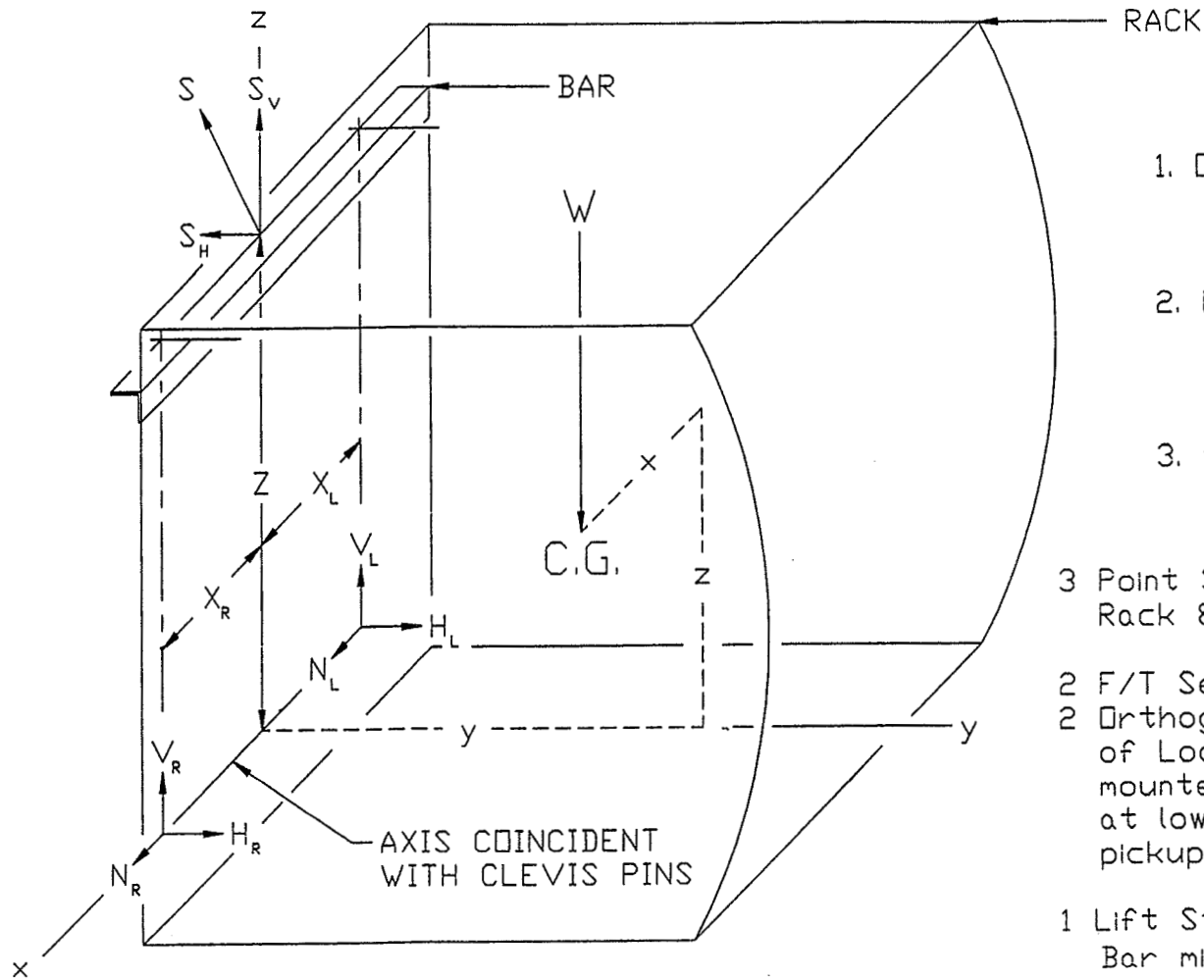
2.3.2 SAMPLES. Preliminary investigation indicated the most difficult specification to satisfy would be measuring weight to within .2% of the actual value as the rack approaches an empty weight ($W_r=250$ lbs). As the ratio of pay-load / lift-load approaches zero the errors become unbounded. For this reason schemes that minimize tare weight are considered first:

2.3.2.1 Rack Alone. Suspension of the rack alone was not possible within given constraints. Suspension from the 4 attach points shown in Figure 1.4 and discussed in section 1.5 above would result in a statically indeterminant problem rendering an inverse model difficult to solve. Using only 3 attach points would be determinant. This was disallowed because such an asymmetric lift could distort (or deform) the rack frame.

2.3.2.2 Rack & Bar. Approximation of rack alone suspension uses a lift bar spanning the upper 2 attach points, Figure 2.2. A bar-mounted, load bearing strut is placed perpendicular to the longitudinal axis of the bar at its middle. This allows a symmetric, 3 point, determinant suspension. Strut angle can be adjusted to balance loads on sensors as the interface plate moves from the vertical to an inclined position. Reduction of the required load range to improve accuracy is the result. A load cell in this strut would supply a redundant reading as a check.

Orthogonal pairs of load cell struts between rack and interface plate at the lower attach points completes the suspension and measurement scheme. Suspension of the rack without bolting it to the interface plate presents some installation and operational complications. An adequate, determinant suspension would permanently join the pair of ball/clevis ended ortho-struts to each other at a single ball with a hollow pin, Figure 2.3 . An additional clevis yoke would be bolted to the rack attach point with a revolute joint between. At the time of mating rack to plate, this yoke would be attached to the permanently assembled ortho-struts with a "slip-pin" thru the permanent hollow pin. This arrangement allows both concentric clevis pins to share the same axis. A "sway bar" along the plate bottom constrains the ortho-strut pairs so their axes remain in a vertical plane, Figure 2.3 . An alternative to load cells substitutes a single F/T sensor for each load cell pair. Only one ball/clevis at each location is required. See Appendix A.

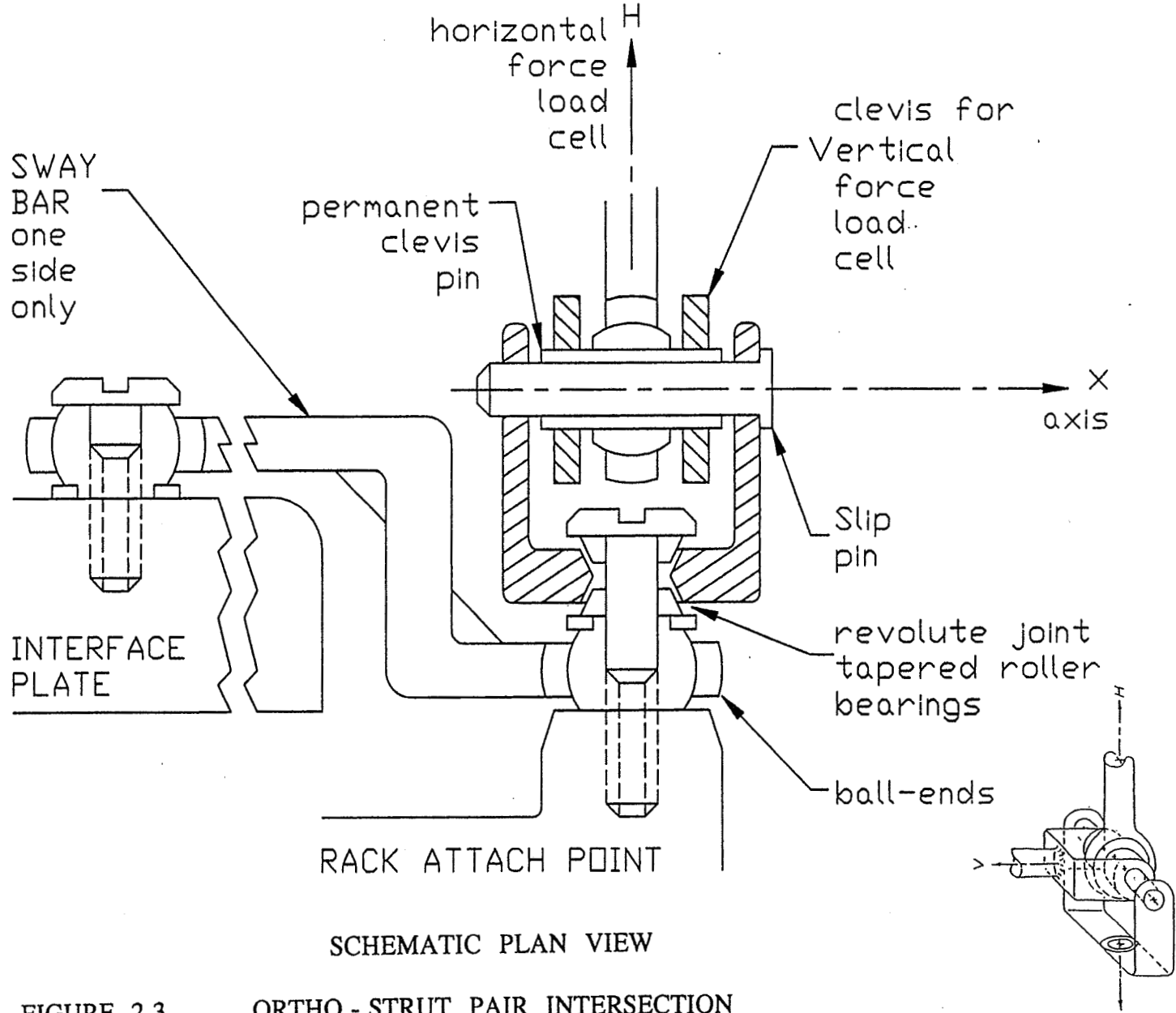
3 Point Suspension Scheme RACK & BAR Plate Mounted Sensors



NOTE

1. ONLY fixed dimensions required
 2. NO Angle of inclination measurements required
 3. LOW lift weight
- 3 Point Suspension of Rack & Support Bar
- 2 F/T Sensors or 2 Orthogonal Pairs of Load Cells mounted on Plate at lower Rack pickup points
- 1 Lift Strut at Bar mid-point

FIGURE 2.2 RACK & BAR SUSPENSION



2.3.2.3 Rack & Plate. Bolting rack to plate as intended by the RIEE designers simplifies the attachment operation. Plate weight of 500 lbs increases the lift and therefore sensor range required. Modification of the plate, though not required, would be beneficial if the tare weight could be significantly reduced. The rack-plate unit may be treated as a 3 point determinant suspension with the jack-strut supporting in the middle of the plate and 2 plate-pivot hinges providing reactions at the bottom of the plate, Figure 2.4. One F/T sensor at each pivot hinge is sufficient to extract all necessary information. A load-pin at the upper end of the jack would give a redundant check.

Plate mounted sensors may be attached to the plate side of the pivot hinge. Model computations would be similar to those in Appendix A for the Rack & Bar case but with different geometric parameters and mass combinations. Since the sensors tilt with the rack-plate so does the reference frame. The sensors see a weight vector that changes its angle of incidence equal to the tilt. Plate angles need not be known (except for the redundant check) but should be separated as far as possible.

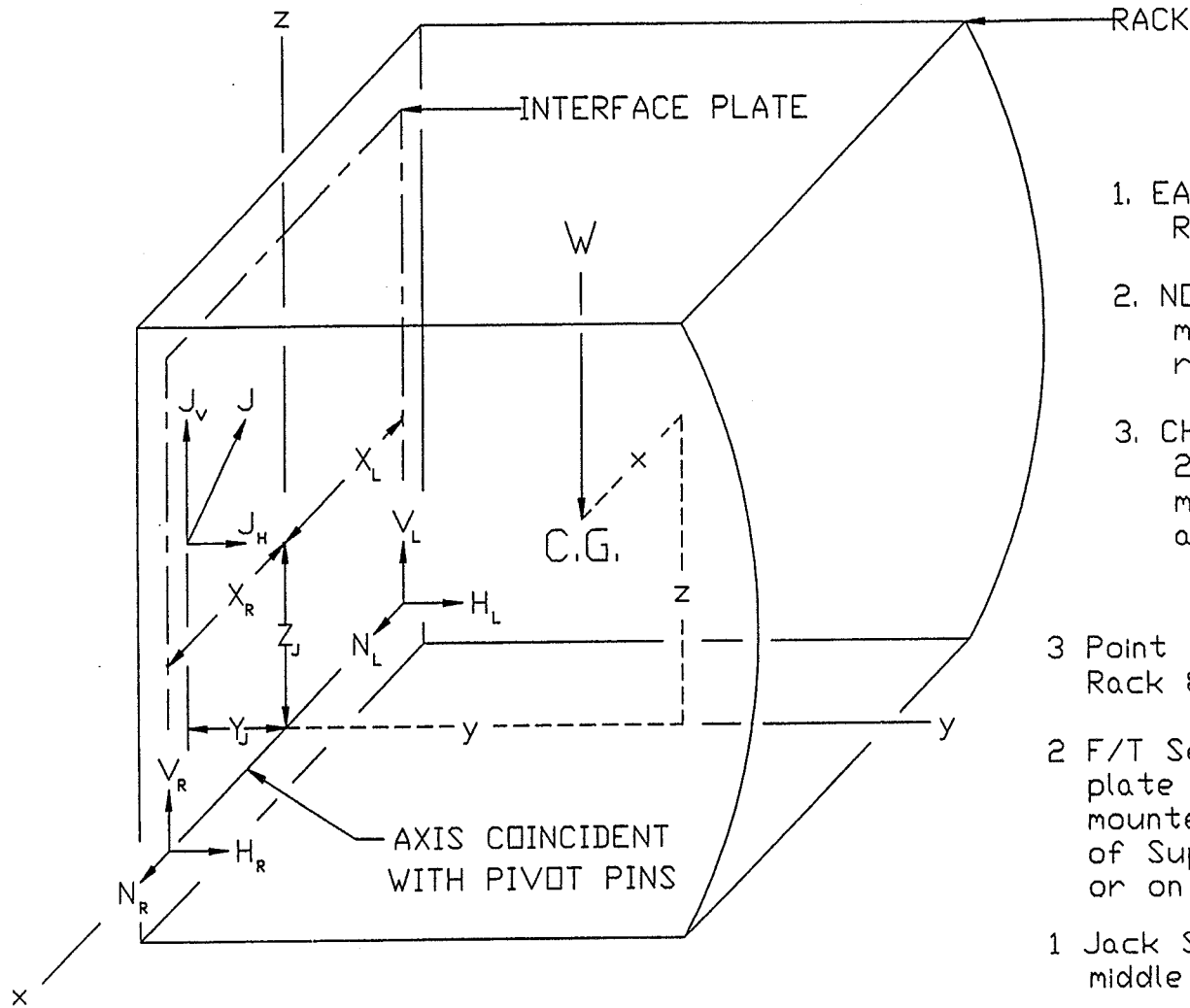
Arm mounted sensors may be attached to the arm side of the pivot hinge. Model computations are given in Appendix B. Sensors are fixed as is the reference frame. When the plate tilts, computational procedure is the same but a coordinate transformation is required to relate back to the vertical position of the plate. The method depends on interface-plate and jack-strut angles, one set of which must be for the vertical position. This introduces an additional source of operational error. Information on expected angular measurement error is not currently available. Accuracy assessments made here do not reflect this possibility.

2.3.2.4 Rack-Plate & Arms. Replacement of existing ball-clevis pins with load-pins would require the least modification of existing hardware. Load pins are unidirectional. If the direction of applied load differs from pin orientation by more than 15 deg, readings are unpredictable. This limits their use to struts (i.e. 2-force members) where the load direction is known to be parallel to a line between the end attach points. Plate pivot and arm-elbow pins do not qualify. A 5-point suspension of 3 rigid members, consisting of the rack-plate and both arms, is determinant. Pins are replaced at the jack-strut upper end and lower ends of the 2 turnbuckle struts. These 3 members are the only 2-force members in the end effector. They are sufficient for all computations. Any attempt at adding redundancy would destroy the simplicity of the installation. More geometric information is required for this computation than the previous ones. It depends, as does the Rack & Plate with arm mounted sensors, on the accuracy of angles, locations of plate & arm centers of mass, and load points, Figure 2.5. It is difficult to obtain both forward and inverse solutions from the Rack-Plate & Arms taken as a single unit. Rather writing equations for the individual members is more fruitful especially since the solutions for the Rack & Plate in Appendix B can be used as part of the solution for this problem together with additional equations representing the arm beams.

2.3.2.5 Higher Tare Weights. All other schemes involving higher lift weights have not been evaluated because of the adverse trend of error measured as a percent of rack weight.

3 Point Suspension Scheme RACK & PLATE

Arm or Plate Mounted Sensors



NOTE

1. EASY 4 bolt Rack mounting
2. NO plate modifications required
3. CHOICE of 2 sensor mount/compute arrangements

- 3 Point Suspension of Rack & Plate
- 2 F/T Sensors at plate pivots mounted on ends of Support Arms or on Plate Hinge
- 1 Jack Strut behind middle of Plate

FIGURE 2.4 RACK & PLATE SUSPENSION

ASSUMPTIONS
during all sensor readings

1. Pin axes horizontal
2. Arm axes horizontal
3. y-z plane is vertical
4. y-z plane is a plane of interface plate symmetry
5. Both symmetry planes of interface plate are vertical
 $l = 0$

Rack Weight & C.G. SENSOR SCHEME
5 Point Suspension

Coordinate Origins and Geometric Parameter Identification

NOTE

5 point scheme depends on **RELATIVE** rather than only **FIXED** dimensions

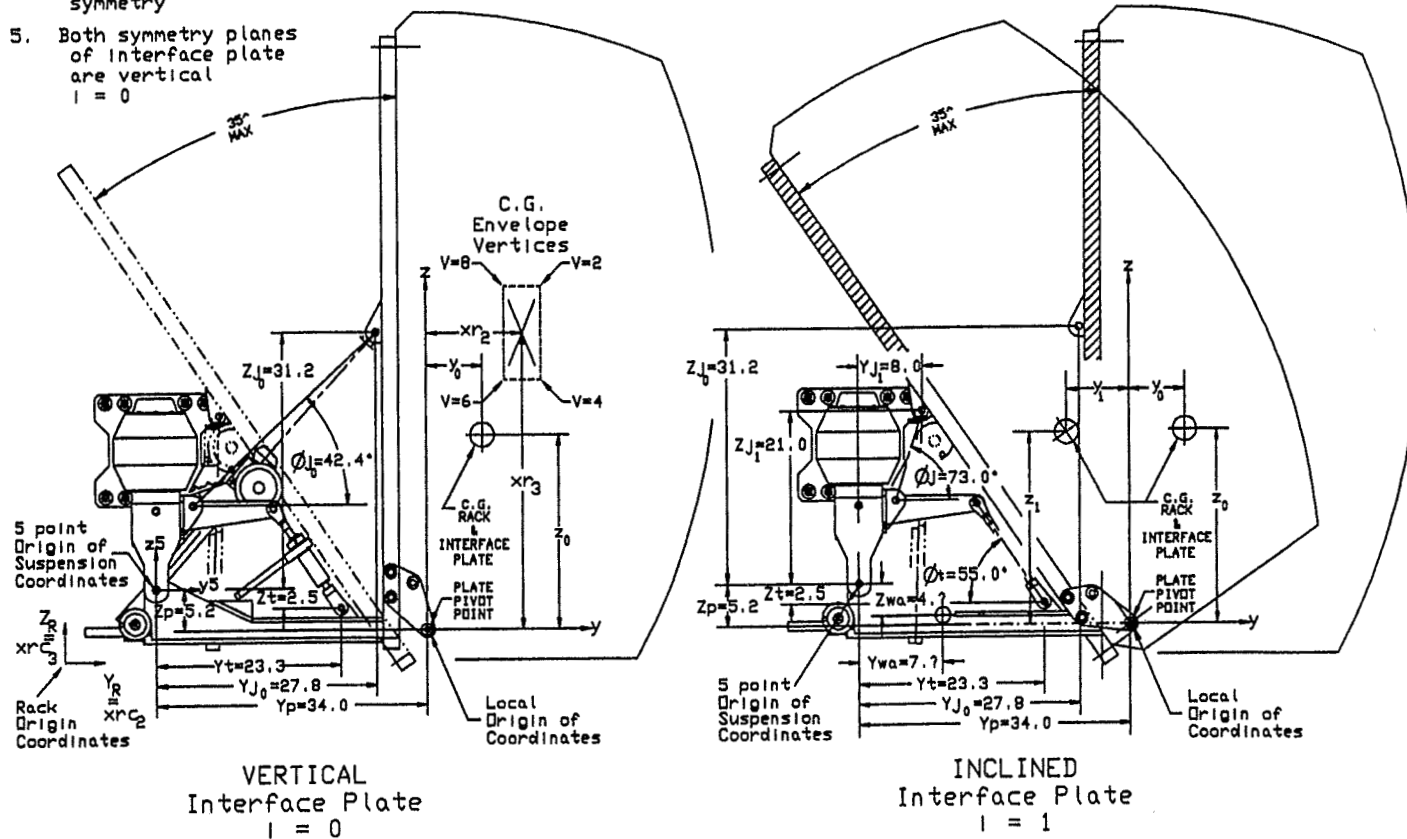


FIGURE 2.5 RACK-PLATE & ARMS SUSPENSION

III

RESULTS

3.1 SAMPLES

Computations exhibited in the appendices were for the largest rack weight with a maximum allowed off-center C.G. at an upper right vertex No. 2. These give a good indication of maximum sensor load. Sensor ranges were determined by rounding up to the next available size. Vendors were queried for suitable sensor equipment recommendations.

3.2 RANGES

3.2.1 RACK & BAR. (with the least tare weight has the lowest ranges)

Vertical Load Cell range:	913 lbs max	rounded up to:	1000 lbs
Horizontal " " " :	490 " "	" " "	500 "

3.2.2 RACK & PLATE.

Vertical F/T range:	1592 lbs max	rounded up to:	2740 lbs
Horizontal " " "	197 " "	" " "	1140 "

Note: The F/T data is for a custom sensor. It is a package that does not allow independent choice of vertical and horizontal force ranges. To achieve the indicated performance this 3.1" diameter unit must be oriented with its axis in the direction of maximum load. It may be worth exploring the possibility of a custom F/T sensor with lower ranges that are closer to those needed.

3.2.3 RACK - PLATE & ARMS.

Jack Strut Load Pin range:	994 lbs max	rounded up to:	1000 lbs
Turnbuckle " " " :	3313 " "	" " "	3500 "

Note: Ranges for off-the-shelf Load Pins were 1500, 3000, 6000 lbs which are so far from the required ranges as to prejudice any comparison with the other alternatives. Values shown were substituted assuming that custom load pins would be possible and worth the effort if this case is selected for further development.

3.3 ACCURACIES

3.3.1 MAXIMUM RACK WEIGHT. The best accuracies are expected using the load for which the range was selected, $W_r=1750$ lbs. The sample calculations in the appendices compute these results for Vertex 2 of the C.G. envelope ($x_r=24.15$, $y_r=59.80$, $z_r=45.7$).

Note that two estimates, one for each plate angle, are produced for most quantities. However when the sensors are plate mounted, equations from both plate positions are needed to obtain a single assessment of the y and z-coordinates.

3.3.1.1 Rack & Bar. $erW_r = .074 \%$, $.064 \%$ compared with $.2 \%$ allowable
 $er_x = -.002$ in. both " " $.4$ in. "
 $er_y = .006$ " " " "
 $er_z = .009$ " " " "
 $er_v = .011$ " (vector sum of coordinate errors)

Weight error is about a third of that allowed.
 C.G. error is more than an order of magnitude less than the requirement.

3.3.1.2 Rack & Plate. $erW_r = .059 \%$, $-.164 \%$ compared with $.2 \%$ allowable
 $er_x = -.001$ in., $.003$ in. " " $.4$ in. "
 $er_y = .016$ " $.035$ " " " " "
 $er_z = .038$ " $.022$ " " " " "
 $er_v = .041$ " $.041$ " (vector sum of coordinate errors)

Weight error is about a third of that allowed.
 C.G. error is about an order of magnitude less than the requirement.

3.3.1.3 Rack-Plate & Arms. $erW_r = 1.839 \%$, 1.928% compared with $.2 \%$ allowable
 $er_x = -.035$ in., $-.036$ in. " " $.4$ in. "
 $er_y = -.242$ " $.118$ " " " " "
 $er_z = -.551$ " $-.590$ " " " " "
 $er_v = .603$ " $.603$ " (vector sum of coordinate errors)

Weight error violates the allowable by nearly an order of magnitude.
 C.G. error violates the allowable by about 50 %.

3.3.2 DATA TREND. For these three quite different sensor placement schemes, desirable performance correlates inversely with sensor range and directly with the ratio of pay-load / lift-load. These are, of course, both manifestations of the same phenomenon.

Correlation with the pay/lift ratio is very evident as it approaches zero.

3.3.3 MINIMUM RACK WEIGHT. The worst accuracies can be expected with minimum rack weight, $W_r=250$ lbs. Results given below are for Vertex 2 of the C.G. envelope.

Note the envelope for smaller rack weights of mass less than 882 lbm, is larger than that for maximum rack weight. Vertex 2 moves out to ($x_r=26.50$, $y_r=61.50$, $z_r=50.00$).

3.3.3.1 Rack & Bar. $erW_r = .515 \%$, $.448 \%$ compared with $.2 \%$ allowable
 $er_x = -.020$ in., $-.017$ in. " " $.4$ in. "
 $er_y = .039$ " " " "
 $er_z = .024$ " " " "
 $er_v = .050$ " (vector sum of coordinate errors)

Weight error is more than double the allowable.
 C.G. error is less than allowed by nearly an order of magnitude.

3.3.3.2 Rack & Plate. $erW_r = .411 \%$, -1.166% compared with $.2 \%$ allowable
 $er_x = -.003$ in., $.007$ in. " " $.4$ in. "
 $er_y = .053$ " $.165$ " " " " "
 $er_z = -.212$ " $-.143$ " " " " "
 $er_v = .219$ " $.218$ " (vector sum of coordinate errors)

Weight error is more than double the allowable.
 C.G. error is about half of that allowed.

3.3.3.3 Rack-Plate & Arms. $erW_r = 12.87 \%$, 13.50% compared with $.2 \%$ allowable
 $er_x = -.075$ in., $-.079$ in. " " $.4$ in. "
 $er_y = -.385$ " $.547$ " " " " "
 $er_z = -1.503$ " -1.452 " " " " "
 $er_v = 1.553$ " 1.554 " (vector sum of coordinate errors)

Weight error violates the allowable by more than an order of magnitude.
 C.G. error violates the allowable by nearly a factor of 4.

3.4 ALLOWABLES

Data presented indicates that it is much easier to satisfy the absolute limit for C.G. error of $.4$ in than the variable $.2 \%$ error for the weight. The problem is measurement range. Percent error is a difficult standard to apply to measurement when the range of interest approaches zero. If zero is included it is impossible. The cost is not accompanied by a commensurate benefit. Empty racks are less likely to affect the overall resupply module's weight and C.G. yet the cost of their measurement is likely to be high if error is expressed as a fixed percent of the true value.

IV CONCLUSIONS

4.1 SUMMARY OF RESULTS

- o Three models representing different sensor placement schemes, each with its own computational method, were developed.
- o Inverse solutions, assuming known weight and C.G. location extremes, were used to determine maximum expected sensor load so that sensor load ranges could be selected.
- o Forward solutions predict overall expected sensor error from each scheme based solely on component errors of sensors employed. Other error sources such as friction, dimensional and angular measurement error were not investigated.

4.2 CONCLUSIONS

- o Sensor load range is the major determinant of component sensor error. Lift weight determines load range therefore low lift weight is desirable.
- o Error limits are easily satisfied for the highest rack weights but are far more difficult to satisfy for an empty rack.
- o Error as a percent of weight increases rapidly as the weight approaches zero. It becomes unbounded if the load range includes zero.
- o Cost of measuring near empty racks to the current specification is not accompanied by a commensurate benefit.

4.3 RECOMMENDATIONS

- o Retain the simple four bolt mating of rack to interface plate as intended by the designers of the rack insertion end effector.
- o Isolate the rack-plate with plate mounted force/torque sensors at the plate pivots.
- o Lighten the interface plate.
- o Negotiate fixed error limits based on maximum or expected rack weights rather than the current variable limits based on percent of weight measured.

APPENDIX A
 PLATE MOUNTED SENSORS
 3 Point Suspension of Rack and Bar
 with Inclined Central Support Strut

Vertex := 2

INVERSE COMPUTATION

Weights:

Rack: $W_r := 1750$ lbs. Support Strut Bar: $w_b := 50$ lbs.

Total Lift: $W := W_r + w_b$ $W = 1.8 \cdot 10^3$ lbs.

Angle of Tilt: $i := 0 \dots 1$ $\theta :=$ $\text{deg} := \frac{\pi}{180}$

Angle of Strut: $\phi := 30 \cdot \text{deg}$

0
35 deg

 Coordinate Indices: $j := 1 \dots 3$

Center of Mass Location:

Rack

Coordinates:

$x_{rc} :=$
j
24.15
59.80
45.70

Local Rack

Coordinates:

$x_r := x_{rc} - 21$
1
$x_r := x_{rc} - 42 + 3$
2
$x_r := x_{rc} - 2.75$
3

Support Strut Bar

Coordinates:

$X_b :=$
j
0.0
0.0
72.0

Total Lift
Coordinates:

$x_t := \frac{x_r \cdot W_r + X_b \cdot w_b}{W}$
j
3.062
20.222
43.757

Center of Mass Location:

$x := x_t$ $y := x_t$ $z := x_t$
 1 2 3

Load Point Distances:

$X := 19.7$ $Y := 0.0$ $Z := 72.0$

Weight Components:

$W_y := W \cdot \sin[\theta]$ $W_z := W \cdot \cos[\theta]$
 i i

Reaction at Strut:

$S := \frac{y \cdot W_z - z \cdot W_y}{Z \cdot \cos(\phi)}$

S
i
583.765
-246.323

Reactions Right:

$V_r := \frac{W_z}{2} \left[1 + \frac{x}{X} \right] - \frac{S}{2} \sin(\phi)$ $H_r := \frac{W_y}{2} \left[1 + \frac{x}{X} \right] + \frac{S}{2} \cos(\phi)$
 i i i i

V_r
i
893.97
913.426

H_r
i
252.778
489.808

Reactions Left:

$V_l := V_r - \frac{x}{X} W_z$ $H_l := H_r - \frac{x}{X} W_y$
 i i i i

V_l
i
614.148
684.209

H_l
i
252.778
329.308

Vertex = 2
3
Wr = 1.75·10

3 Point Suspension of Rack and Bar
with Inclined Central Support Strut

page 2

FORWARD COMPUTATION

Measurement Error
Allowance:

Load Cell
Accuracy:

Ac := .05 %

Force Error:

Range: Vrng := 1000 Hrng := 500 lbs

$$\delta V := \text{Vrng} \cdot \frac{\text{Ac}}{100} \quad \delta H := \text{Hrng} \cdot \frac{\text{Ac}}{100}$$

Reaction Readings with Maximum Errors:

$$Vr_i := Vr_i + \delta V \quad Hr_i := Hr_i + \delta H \quad Vl_i := Vl_i + \delta V \quad Hl_i := Hl_i + \delta H$$

Reaction Combinations:

Reaction Differences:

$$Vs_i := Vr_i + Vl_i \quad Hs_i := Hr_i + Hl_i \quad Vd_i := Vr_i - Vl_i \quad Hd_i := Hr_i - Hl_i$$

Reaction at Strut,
Computed:

$$S_i := \frac{Vd_i \cdot Hs_i - Vs_i \cdot Hd_i}{Vd_i \cdot \cos(\phi) + Hd_i \cdot \sin(\phi)}$$

$$S_i = \begin{bmatrix} 584.343 \\ -246.488 \end{bmatrix}$$

Weights, Computed:

$$Wy_i := Hs_i - S_i \cdot \cos(\phi) \quad Wz_i := Vs_i + S_i \cdot \sin(\phi)$$

$$Wyz_i := \sqrt{Wy_i^2 + Wz_i^2}$$

$$Wyz = \begin{bmatrix} 1.801 \cdot 10^3 \\ 1.801 \cdot 10^3 \end{bmatrix}$$

Center of Mass,
Computed:

$$xv_i := \frac{X}{Wz_i} \cdot Vd_i \quad xh_1 := \frac{X}{Wy_1} \cdot Hd_1$$

$$xv_i = \begin{bmatrix} 3.06 \\ 3.061 \end{bmatrix}$$

$$y01 := y$$

$$z01 := z$$

$$xh_1 = 3.061$$

Given

xh₀ = singular

$$y01 \cdot Wz_0 - z01 \cdot Wy_0 \approx Z \cdot S_0 \cdot \cos(\phi)$$

$$y01 \cdot Wz_1 - z01 \cdot Wy_1 \approx Z \cdot S_1 \cdot \cos(\phi)$$

$$\begin{bmatrix} y01 \\ z01 \end{bmatrix} := \text{Find}(y01, z01)$$

$$y01 = 20.228 \\ z01 = 43.766$$

Vertex = 2
 3
 Wr = 1.75·10

3 Point Suspension of Rack and Bar
 with Inclined Central Support Strut

page 3

ERROR ESTIMATES

Weight Error:

Center of Mass Error:

$$erWr_i := \frac{Wyz_i - W}{Wr} \cdot 100$$

erWr_i

0.074
0.064

 .2 %
 % compared with allowable

$$erx_i := xv_i - x_i$$

erx_i

-0.002
-0.002

 .4 in.
 compared with allowable

$$ery := y01 - y$$

$$erz := z01 - z$$

ery = 0.006
 erz = 0.009
 .4 in.

APPENDIX B
ARM MOUNTED SENSORS
 Rack & Plate, 3 Point Suspension
 with Inclined Central Support Jack

Vertex := 2

INVERSE COMPUTATION

Weights:

Rack: $W_r := 1750$ lbs. Plate: $W_p := 500$ lbs.

Total Lift: $W := W_r + W_p$ Indices: $i := 0 \dots 1$ $j := 1 \dots 3$
 $W = 2.25 \cdot 10^3$ Conversion: $\text{deg} := \frac{\pi}{180}$

Angles: Plate: $\theta :=$ Jack: $\phi :=$

Angle of Strut: $\begin{matrix} 0.00 \cdot \text{deg} \\ 35.0 \cdot \text{deg} \end{matrix}$ $\begin{matrix} 44.2 \cdot \text{deg} \\ 78.5 \cdot \text{deg} \end{matrix}$?

Center of Mass Location:

Rack
Coordinates:

$x_{rc} :=$
 $\begin{matrix} 24.15 \\ 59.80 \\ 45.70 \end{matrix}$

Local Rack
Coordinates:

$x_r := x_{rc} - 21$
 $\begin{matrix} 1 \\ 2 \\ 3 \end{matrix}$
 $x_r := x_{rc} - 42 - 3.5$
 $\begin{matrix} 1 \\ 2 \\ 3 \end{matrix}$
 $x_r := x_{rc} - 3.8$ according to

Local Plate
Coordinates:

$x_p :=$
 $\begin{matrix} 0.0 \\ -4.5 \\ 33.0 \end{matrix}$?

Total Lift Local
Coordinates:

$x_r \cdot W_r + x_p \cdot W_p$
 $\begin{matrix} j \\ j \end{matrix}$
 $x_t := \frac{\quad}{W}$

x_t
 $\begin{matrix} 2.45 \\ 7.622 \\ 58.256 \end{matrix}$

When let

$\theta_0 = 0$
 $\theta_1 = 0.611$

$x_0 := x_t$
 $x_1 := x_0$

$y_0 := x_t$
 $y_1 := y_0 \cdot \cos[\theta_1] - z_0 \cdot \sin[\theta_1]$
 $z_1 := y_0 \cdot \sin[\theta_1] + z_0 \cdot \cos[\theta_1]$

Load Point Locations
Local Coordinates:

When let

$\theta_0 = 0$
 $\theta_1 = 0.611$

Side:
 $X_0 := 10.0$
 $X_1 := 10.0$

Center:

$Y_0 := -6.625$ $Z_0 := 37.16$
 $Y_1 := Y_0 \cdot \cos[\theta_1] - Z_0 \cdot \sin[\theta_1]$
 $Z_1 := Y_0 \cdot \sin[\theta_1] + Z_0 \cdot \cos[\theta_1]$

Reactions at Jack:

$J_{h_i} := \frac{y_i \cdot W}{Y_i \cdot \tan[\phi_i] - Z_i}$

J_{h_i}
 $\begin{matrix} -393.326 \\ 386.732 \end{matrix}$

x_i
 $\begin{matrix} 2.45 \\ 2.45 \end{matrix}$

y_i
 $\begin{matrix} 7.622 \\ -27.17 \end{matrix}$

z_i
 $\begin{matrix} 58.256 \\ 52.092 \end{matrix}$

$J_{v_i} := J_{h_i} \cdot \tan[\phi_i]$

J_{v_i}
 $\begin{matrix} -382.493 \\ 1.901 \cdot 10^3 \end{matrix}$

X_i
 $\begin{matrix} 10 \\ 10 \end{matrix}$

Y_i
 $\begin{matrix} -6.625 \\ -26.741 \end{matrix}$

Z_i
 $\begin{matrix} 37.16 \\ 26.64 \end{matrix}$

Vertex = 2
 3
 Wr = 1.75·10

Rack & Plate, 3 Point Suspension
 with Inclined Central Support Jack

page 2

Reactions at Hinges:

$$Pvr_i := \frac{W}{2} \left[1 + \frac{x_i}{X_i} \right] - \frac{Jv_i}{2}$$

$$Pvl_i := Pvr_i - \frac{x_i}{X_i} \cdot W$$

$$Phr_i := -.5 \cdot Jh_i$$

$$Phl_i := -.5 \cdot Jh_i$$

$1.592 \cdot 10^3$
450.2

$1.041 \cdot 10^3$
-101.05

196.663
-193.366

FORWARD COMPUTATION

Resolutions of

Force/Torque $\delta Fz := 1.0$ lbs.
 Sensors: $\delta Fxy := 0.5$ lbs.

Force Readings with Maximum Errors:

$Pvr_i := Pvr_i + \delta Fz$ $Pvl_i := Pvl_i + \delta Fz$
 $Phr_i := Phr_i + \delta Fxy$ $Phl_i := Phl_i + \delta Fxy$

Load Point Off-Set Limit:

$$Fz_i := Pvr_i$$

$$Fxy_i := Phr_i$$

$$Zo_i := \frac{2000}{Fxy_i} \left[1 - \frac{Fz_i}{2740} \right]$$

4.247
-8.662

(use minimum absolute value)

Reaction Jack
 Computed:

$$Jh_i := -[Phr_i + Phl_i]$$

-394.326
385.732

$$Jv_i := Jh_i \cdot \tan[\phi_i]$$

-383.465
$1.896 \cdot 10^3$

Weight, Computed:

$$Wc_i := Pvr_i + Pvl_i + Jv_i$$

Center of Mass,
 Computed:

$$xc_i := \frac{X_i}{Wc_i} [Pvr_i - Pvl_i]$$

$$yc_i := \frac{Y_i \cdot Jv_i - Z_i \cdot Jh_i}{Wc_i}$$

$$zc_0 := \frac{yc_0 \cdot \cos[\theta_1] - yc_1}{\sin[\theta_1]}$$

$$zc_1 := \frac{yc_0 - yc_1 \cdot \cos[\theta_1]}{\sin[\theta_1]}$$

xc_i	yc_i	zc_i	Wc_i								
<table border="1"><tr><td>2.449</td></tr><tr><td>2.453</td></tr></table>	2.449	2.453	<table border="1"><tr><td>7.638</td></tr><tr><td>-27.135</td></tr></table>	7.638	-27.135	<table border="1"><tr><td>58.217</td></tr><tr><td>52.07</td></tr></table>	58.217	52.07	<table border="1"><tr><td>$2.251 \cdot 10^3$</td></tr><tr><td>$2.247 \cdot 10^3$</td></tr></table>	$2.251 \cdot 10^3$	$2.247 \cdot 10^3$
2.449											
2.453											
7.638											
-27.135											
58.217											
52.07											
$2.251 \cdot 10^3$											
$2.247 \cdot 10^3$											

Vertex = 2
 3
 Wr = 1.75 · 10

Rack & Plate, 3 Point Suspension
 with Inclined Central Support Jack

page 3

ERROR ESTIMATES

Weight Error:

$$erWr_i := \frac{Wc_i - W}{Wr} \cdot 100$$

$erWr_i$

0.059
-0.167

 % compared with allowable
 .2 %

Center of Mass Error:

$$erx_i := xc_i - x_i$$

erx_i

-0.001
0.003

 compared with allowable
 .4 in.

$$ery_i := yc_i - y_i$$

ery_i

0.016
0.035

 .4 in.

$$erz_i := zc_i - z_i$$

erz_i

-0.038
-0.022

 .4 in.

REFERENCES

- [1] Boeing, U. S. STANDARD EQUIPMENT RACK INTERFACE DEVELOPMENT DOCUMENT, NASA / MSFC, SSP 41090, Draft 6, 6/30/92
- [2] McDonnell - Douglas, ORU HANDLING DEVICE, NASA / KSC, design file No. D0392900, dwg. No. 82K03929, 11/20/92
- [3] McDonnell - Douglas, RACK INSTL / REMOVAL END EFFECTOR ASSY / INSTL, NASA / KSC, design file No. D0393100, dwg. No. 82K03931, 9/30/92

1994 NASA/ASEE SUMMER FACULTY FELLOWSHIP PROGRAM

351455

JOHN F. KENNEDY SPACE CENTER
UNIVERSITY OF CENTRAL FLORIDA

53-37

33963

P-30

11754

AUTOMATED PATH PLANNING OF THE PAYLOAD
INSPECTION AND PROCESSING SYSTEM

PREPARED BY:	Dr. Robert M. Byers
ACADEMIC RANK:	Assistant Professor
UNIVERSITY AND DEPARTMENT:	University of Central Florida Department of Mechanical and Aerospace Engineering
NASA/KSC	
DIVISION:	Advanced Systems
BRANCH:	Automation Group
NASA COLLEAGUE:	Eduardo Lopez Gabor Tamasi
DATE:	August 12, 1994
CONTRACT NUMBER:	University of Central Florida NASA-NGT-60002 Supplement: 17

Automated Path Planning of the Payload Inspection and Processing System

R.M. Byers

University of Central Florida, Orlando, FL

Abstract

The Payload Changeout Room Inspection and Processing System (PIPS) is a highly redundant manipulator intended for performing tasks in the crowded and sensitive environment of the Space Shuttle Orbiter payload bay. Its dexterity will be exploited to maneuver the end effector in a workspace populated with obstacles. A method is described by which the end effector of a highly redundant manipulator is directed toward a target via a Lyapunov stability function. A cost function is constructed which represents the distance from the manipulator links to obstacles. Obstacles are avoided by causing the the vector of joint parameters to move orthogonally to the gradient of the workspace cost function. A C language program implements the algorithm to generate a joint history. The resulting motion is graphically displayed using the Interactive Graphical Robot Instruction Program (IGRIP) produced by Deneb Robotics. The graphical simulation has the potential to be a useful tool in path planning for the PIPS in the Shuttle Payload Bay environment.

<i>CONTENTS</i>	2
-----------------	---

Contents

1 Introduction	3
2 Manipulator Kinematics	4
3 Lyapunov Stability Approach to Manipulator Control	7
4 Joint Motion Weighting	8
5 Obstacle Avoidance	8
6 Graphical Representation with the IGRIP software	10
7 The Payload Inspection and Processing System	10
8 Algorithm Implementation	11
9 Conclusions and Recommendation	11
A Appendix: Collision Avoidance Path Planner Source Code Listing	13

List of Figures

1 General Transform of a Vector	5
2 Denavitt-Hartenberg Coordinate Transform Convention	5
3 Obstacle Cost Functions	9
4 Foster Miller Serpentine Truss	11
5 Notional PIPS	27
6 CAPP Program Flow	28
7 Simulated PIPS Maneuver	29

1 Introduction

The range of motion achievable by a robot manipulator's end effector is a function of the number and type of joints or degrees of freedom it possesses. Any degrees of freedom in excess of the minimum number required to reach an arbitrary end effector position and orientation within the reachable workspace are considered "redundant". Commercial manipulators typically possess six or fewer DOF for primarily "anthropomorphic" tasks such as industrial assembly and are therefore not redundant.

There are some tasks for which such standard manipulators are not well suited, such as those requiring an extended reach in a confined workspace. For that reason, so-called "serpentine" manipulators have attracted interest. Their designation and appearance suggest the long reach and dexterity associated with snakes or tentacles. They achieve this snake-like ability by possessing a high degree of redundancy. This redundancy allows them, theoretically, to "wriggle" an end effector into a confined or difficult to reach point while allowing the robot arm to be configured in such a way as to not contact the surrounding environment.

The Payload Processing and Inspection System seeks to exploit the dexterity of the serpentine truss to service space shuttle orbiter payloads in the Payload Changeout Room (PCR). Because of the dimensions of the PCR and the sensitivity of shuttle payloads, there are specific tasks which are difficult, costly or hazardous to perform by humans due to lack of access. These tasks include:

- photographic inspections.
- visual inspections
- spot cleaning
- cover installation and removal
- line replaceable unit (LRU) installation and removal
- connector installation and removal.

References [2] and [1] discuss the requirements for inspection and processing of space related payloads and the feasibility for employing a manipulator to perform such tasks.

Several approaches for achieving collision avoidance with redundant manipulators have been suggested. Maciejewski and Klein [3], Nakamura [4], and Wegerif, et al [5] make use of the Moore-Penrose pseudo-inverse [6] to generate the joint rates to move the end effector and null motion to avoid obstacles. The pseudo-inverse solution is hampered by the existence of singularities for which the pseudo-inverse is undefined. Under these circumstances, no motion in the specified direction is possible. Sciavicco, and Siciliano [7] make use of a Lyapunov stability function to track a prescribed trajectory and augment the configuration space to accommodate obstacle avoidance constraints. An alternative approach is used by Pasch [2] and Asano [8]. They prescribe an obstacle free end effector path and cause each joint to adhere to that path in a "follow the leader" mode. All of these methods require that at least the end effector's trajectory and velocity be prescribed. This presumes that a suitable velocity function for the end effector is readily determined. Only Wegerif [5], who makes use of sensors to detect obstacle proximity, allows for the end effector to deviate from the prescribed path as an emergency measure.

There are several limitations inherent in these approaches. The pseudo inverse kinematic solution may result in singular configurations for which some small motions of the end effector require excessive and physically unrealizable joint speeds. Although redundant degrees of freedom seem to offer some potential for singularity avoidance, Baker and Wampler [9] show that singularity free trajectories cannot be guaranteed. The requirement to specify the end effector trajectory and velocity

presumes that a suitable trajectory is easily determined. Such a trajectory must not only itself be obstacle and singularity free, but must allow for the permissible motion of the entrained links. Null motion may not be sufficient to cause the entrained links to avoid obstacles because such motion is constrained by the end effector trajectory requirements. Furthermore, as discussed by Doty, et al, [10] the pseudoinverse solution to robot manipulator kinematics can lead to inconsistent results (i.e. results that are not invariant with respect to changes in the reference frame and/or changes in the dimensional units used to express the problem).

In Ref. [11] the principal investigator presented an alternative method for determining an acceptable robot trajectory which allows the end effector's path, as well as the entrained link's to be free to move around obstacles. The control algorithm uses a Lyapunov stability approach to generate a family of joint rates which will move the end effector toward a desired target. The relative motion of the joints can be weighted to meet operational requirements such as rate or deflection limits. Because the end effector path is not specified, there are no requirements for inverse solutions, and singular joint configurations are only encountered at the reachable workspace boundaries.

Obstacles are avoided by determining the distance from each link to the surface of each obstacle in the workspace. An obstacle gradient vector, indicates the direction, in the joints space toward the obstacle array. By selecting only joint motion which is orthogonal to this direction, collisions with obstacles are avoided.

In the current work, the collision avoidance algorithm is applied to a notional PIPS based on the Foster-Miller serpentine truss [2] with sixteen degrees of freedom. Both the end effector's desired final position and orientation may be specified. The algorithm is coded in the C programming language and graphically displayed using the IGRIP software.

2 Manipulator Kinematics

Typically, robot motion is sufficiently slow so that it is adequately controlled by commanding joint velocities in response to the robot kinematics. Serpentine motion and the requirements for collision avoidance are especially complex. It is sufficient to describe the motion in terms of the end effector position and velocity.

The end effector position is a function of the vector of generalized joint displacements \underline{q} .

$$\underline{r} = \underline{r}(\underline{q}(t), t) \in \mathfrak{R}^m \quad (1)$$

Figure 1 illustrates that the location of a point in space given by the 3×1 vector \underline{r} can be expressed in terms of an inertial frame by its position in an intermediate frame, \underline{r}_B , the location of the origin of the intermediate frame, \underline{r}_A and the orientation of that frame with respect to the inertial frame, given by the 3×3 direction cosine matrix R_O^A .

$$\underline{r} = R_O^A \underline{r}_B + \underline{r}_A \quad (2)$$

It is appealing to express the transformation in the form

$$\underline{r} = T_O^A \underline{r}_B \quad (3)$$

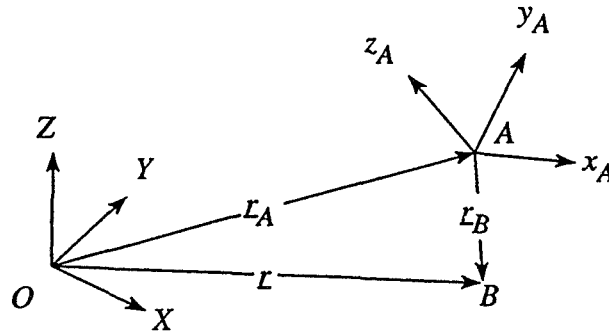


Figure 1: General Transform of a Vector

This is accomplished by defining the 4×4 transformation matrix relationship

$$\begin{bmatrix} \underline{r} \\ 1 \end{bmatrix} = \begin{bmatrix} \text{---} & R_O^A & \text{---} \\ 0 & 0 & 0 \end{bmatrix} \begin{bmatrix} \underline{r}_A \\ 1 \end{bmatrix} \begin{bmatrix} \underline{r}_B \\ 1 \end{bmatrix} \quad (4)$$

The well known Denavit-Hartenberg convention [13], is a convenient convention for describing the transformation between link coordinate frames and is shown in Fig. 2. The length a_i is the

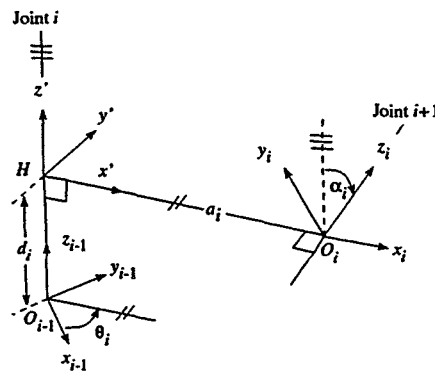


Figure 2: Denavit-Hartenberg Coordinate Transform Convention

length of the common normal between the frames. For a revolute joint this is link length. The length d_i is the distance between the origin O_{i-1} and the point H_i . In a prismatic joint, this is the variable component. The angle α_i is the rotation of the joint axis i and the z_i axis, about the common normal; the "twist" of the link. The angle θ_i is the rotation angle between the x_{i-1} axis and the common normal $H_i O_i$; measured about the z_{i-1} axis in the right-hand sense. In a revolute joint, this is the variable parameter. In the D-H convention, the 4×4 transformation between link

frames is given by

$$T_{i-1}^i = \begin{bmatrix} \cos \theta_i & -\sin \theta_i \cos \alpha_i & \sin \theta_i \sin \alpha_i & a_i \cos \theta_i \\ \sin \theta_i & \cos \theta_i \cos \alpha_i & -\cos \theta_i \sin \alpha_i & a_i \sin \theta_i \\ 0 & \sin \alpha_i & \cos \alpha_i & d_i \\ 0 & 0 & 0 & 1 \end{bmatrix} \quad (5)$$

For a manipulator consisting of n links, the position and orientation of the end effector (frame n) with respect to an inertial frame (frame 0), is expressed in terms of the link transformations

$$\begin{aligned} T_0^n &= \prod_{i=1}^n T_{i-1}^i \\ &= \left[\begin{array}{ccc|c} & R_O^{target} & & \underline{r}_{target} \\ \hline 0 & 0 & 0 & 1 \end{array} \right] \\ &= \begin{bmatrix} \underline{r}_{n_1} & \underline{r}_{n_2} & \underline{r}_{n_3} & \underline{r}_{n_4} \\ 0 & 0 & 0 & 1 \end{bmatrix} \end{aligned} \quad (6)$$

The vectors \underline{r}_{n_1} , \underline{r}_{n_2} , and \underline{r}_{n_3} are unit column vectors of the direction cosine matrix which relates the end effector's orientation to the inertial frame. The vector \underline{r}_{n_4} gives the end effectors location with respect to the origin of the base frame.

The velocity of the end effector is given by

$$\frac{d\underline{r}}{dt} = \frac{\partial \underline{r}}{\partial \underline{q}} \frac{d\underline{q}}{dt} = J \dot{\underline{q}} \quad (7)$$

where J is the *Jacobian* matrix. For an end effector trajectory specified by $\dot{\underline{r}}$ the required joint rates are given by

$$\dot{\underline{q}}_r = J^* \dot{\underline{r}} \quad (8)$$

where

$$J^* = J^T (J J^T)^{-1} \quad (9)$$

is the pseudo-inverse for $n > 3$. Equation (8) gives the minimum norm joint rates which satisfy the end effector trajectory $\dot{\underline{r}}$. When $|J J^T| = 0$ the pseudo inverse is undefined and infinite joint rates are required to satisfy the specified end effector velocity. Obviously, even when the manipulator is in a singular configuration, it is still possible to move the end effector in directions other than the singular direction.

There are several limitations to the pseudo inverse velocity kinematics solution of robot motion. As with all pseudo inverse kinematic solutions, the end effector's trajectory must be specified and takes priority over obstacle avoidance. Choosing an acceptable end effector path can be a difficult task in a complex workspace and it sometimes occurs that the specified path precludes obstacle avoidance. To further complicate matters, null motion for obstacle avoidance may be incompatible with the task of singularity avoidance. Finally, Doty, et al [10] notes that noninvariant results may be obtained from the pseudo-inverse solution.

3 Lyapunov Stability Approach to Manipulator Control

As an alternative to the operator prescribing the end effector path, the end effector may be driven to its target by use of a Lyapunov stability function. The desired end effector position may be represented by a target transformation

$$\begin{aligned} T_O^{target} &= \left[\begin{array}{ccc|c} & R_O^{target} & & \underline{L}_{target} \\ \hline 0 & 0 & 0 & 1 \end{array} \right] \\ &= \left[\begin{array}{cccc} \underline{L}_{T_1} & \underline{L}_{T_2} & \underline{L}_{T_3} & \underline{L}_{T_4} \\ 0 & 0 & 0 & 1 \end{array} \right] \end{aligned} \quad (10)$$

where \underline{L}_{T_i} , $i = 1, 2, 3$, are the unit column vectors of R_O^{target} and $\underline{L}_{T_4} = \underline{L}_{target}$. The difference between the manipulator's actual configuration and the desired configuration is given by the array of vectors

$$\underline{\epsilon}_i = \underline{L}_{T_i} - \underline{L}_{n_i} \quad (11)$$

The scalar Lyapunov function is chosen

$$V = \sum_{i=1}^4 \frac{1}{2} \underline{\epsilon}_i^T \underline{\epsilon}_i \quad (12)$$

V may be viewed as the "energy" of the system and is always positive. To drive V to zero, and hence the end effector to the target position and orientation, it is sufficient that $\dot{V} < 0$ for every subinterval of time on $t_0 \leq t \leq t_f$.

Taking the time derivative of V gives

$$\begin{aligned} \dot{V} &= \sum_{i=1}^4 \underline{\epsilon}_i^T \dot{\underline{\epsilon}}_i \\ &= - \sum_{i=1}^4 \underline{\epsilon}_i^T \dot{\underline{L}}_{n_i} \\ &= - \sum_{i=1}^4 \underline{\epsilon}_i^T (J_i \dot{\underline{q}}_r) \end{aligned} \quad (13)$$

where

$$J_i = \frac{\partial r_{n_i}}{\partial \underline{q}} \quad i = 1, \dots, 4 \quad (14)$$

It is obvious that $\dot{V} < 0$ is guaranteed by choosing the joint rate vector

$$\dot{\underline{q}}_r = M \sum_{i=1}^4 \left(\frac{J_i^T \underline{\epsilon}_i}{\|J_i^T \underline{\epsilon}_i\|} \right) = M \hat{\underline{\epsilon}}_i \quad (15)$$

where M is a $n \times n$ positive definite scaling matrix, Eq. (13) becomes

$$\dot{V} = - \sum_{i=1}^4 \frac{\underline{\epsilon}_i^T J_i M J_i^T \underline{\epsilon}_i}{\|J_i^T \underline{\epsilon}_i\|} \quad (16)$$

which is always negative. Substituting Eq. (15) into Eq. (7) gives

$$\dot{\mathbf{r}} = \sum_{i=1}^4 J_i M \dot{\mathbf{e}}_i \quad (17)$$

No matrix inversion is required, and therefore the control is not sensitive to singularities. In contrast to Eq. (8) which gives joint rate to satisfy a desired trajectory, Eq. (17) moves the end effector in response to a family of joint rates which depend on the relative priority of joint motion caused by the matrix M . In addition, this matrix enforces appropriate unit transformations.

4 Joint Motion Weighting

Generally, the boundary conditions and obstacle avoidance requirements can be satisfied by an infinite number of joint trajectories by modification of the M matrix. The composition of the M matrix is determined by the various requirements on the hardware or end effector task.

In addition to avoiding obstacles, manipulator arms are frequently limited by the manipulator architecture in the magnitude of the joint deflections and joint rates which can be achieved. The M matrix may be selected to enforce joint rate and joint displacement limits.

It is useful to think of the M matrix as the non-linear stiffness matrix. The deflection of the i th joint is bounded by $q_{i_{min}} \leq q_i \leq q_{i_{max}}$. Defining

$$\begin{aligned} \Delta_i &= q_{i_{max}} - q_{i_{min}} \\ \Gamma_i &= q_{i_{max}} + q_{i_{min}} \\ f_i &= \frac{2q_i - \Gamma_i}{\Delta_i} \\ \eta_i &= \text{sign}(e_i) \\ k_i &\leq \frac{\dot{q}_{i_{max}}}{2} \end{aligned}$$

The elements of M are given by

$$m_{ij} = \begin{cases} k_i(1 - \eta_i f_i) & i = j \\ 0 & i \neq j \end{cases} \quad (18)$$

Equation (18) causes the i th joint rate toward the joint limit to approach zero near the limit and the rate to be near the maximum if away from the limit.

5 Obstacle Avoidance

With the end effector motion no longer prescribed, much greater latitude is allowed in obstacle avoidance. Joint motion which moves the manipulator away from obstructions is no longer subordinated the end effector path.

Obstacle avoidance requires that the distance to obstacles *vis-a-vis* the manipulator links be known. In a realistic environment, devices in the workspace may be numerous and complexly shaped. CAD models of high complexity, such as exist in the Payload Changeout Room may be imported to IGRIP. The MIN_DISTANCE function in the GSL language returns the minimum designated

links and devices in the CAD environment. IGRIP can be set to disregard any devices outside of a selected radius.

The cost function C_{ij} is the minimum distance between the i th link and the j th obstacle (Fig. 3). Contact of the i th link with the j th obstacle is indicated by $C_{ij} = 0$.

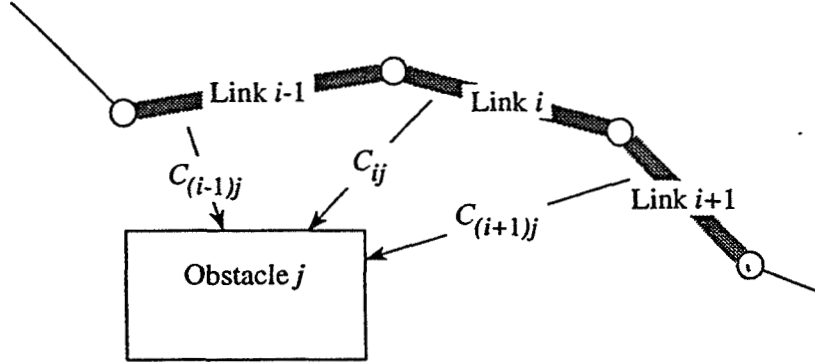


Figure 3: Obstacle Cost Functions

The potential function

$$P = \sum_{i=1}^{nl} \sum_{j=1}^{no} \frac{1}{C_{ij}} \quad (19)$$

where nl is the number of links and no is the number of obstacles. $P \rightarrow \infty$ upon contact with an obstacle. The gradient of the potential function with respect to the joint space vector is given by

$$\underline{\mu} = \frac{\partial P}{\partial \underline{q}} \quad (20)$$

The time rate of change of P can thus be expressed

$$\frac{dP}{dt} = \underline{\mu}^T \dot{\underline{q}} \quad (21)$$

Assuming that a trajectory exists which allows the end effector to reach the target without penetrating any obstacles, then if $\dot{P} \leq 0$ throughout the maneuver, the collision avoidance points will not encounter the obstacle surfaces. The component of $\dot{\underline{q}}_r$ which is orthogonal to $\underline{\mu}$ is found via the Gram-Schmidt orthogonalization method.

$$\dot{\underline{q}} = \dot{\underline{q}}_r - (\dot{\underline{q}}_r^T \hat{\underline{\mu}}) \hat{\underline{\mu}} \quad (22)$$

where $\hat{\underline{\mu}}$ is a unit vector in the direction $\underline{\mu}$. Equation (22) may be written

$$\begin{aligned} \dot{\underline{q}} &= [E_3 - (\hat{\underline{\mu}} \hat{\underline{\mu}}^T)] \dot{\underline{q}}_r \\ \Rightarrow \dot{\underline{q}} &= \tilde{M} \dot{\underline{q}}_r \end{aligned} \quad (23)$$

where

$$\tilde{M} = (E_n - \hat{\underline{\mu}} \hat{\underline{\mu}}^T) M \quad (24)$$

\bar{M} is the obstacle avoidance metric. This matrix is positive semi-definite. The fact that this matrix possess a zero eigenvalue becomes evident when $\underline{\mu}$ is parallel to $\underline{\hat{q}}_r$. In this circumstance, it is impossible for the end effector to move closer to the target. The most obvious case occurs when the target is unreachable or the manipulator has entered a dead-end path. The operator may take some steps to avoid the manipulator from entering a dead-end by designating intermediate targets, or waypoints.

As an alternative to measuring distances from the links to devices in the workspace, obstacles may be modelled as primitive solids. In this approach, the centroid of the j th object is located at $\underline{o}_j = [x_j \ y_j \ z_j]^T$ and has the dimensions $2a_j, 2b_j, 2c_j$, along its principal axes. The orientation of the solid with respect to the inertial frame is given by a direction cosine matrix. Obstacle avoidance points $p_i, i = 1, \dots, n_p$ are designated along the manipulator arm. In the simulation model, these points are the joints and the link midpoints. The location of the j th obstacle *vis-a-vis* the i th obstacle avoidance point is approximated by the super-ellipsoid function

$$C_j(p_i) = \left(\frac{x_i - x_j}{a_j} \right)^{k_j^x} + \left(\frac{y_i - y_j}{b_j} \right)^{k_j^y} + \left(\frac{z_i - z_j}{c_j} \right)^{k_j^z} \quad (25)$$

The the desired shape of the j th obstacle is approximated by selecting appropriate values for k_j^x, k_j^y , and k_j^z greater than or equal to one. For $k_j^x = k_j^y = k_j^z = 1$ the surface is an octahedron. Setting $k_j^x = k_j^y = k_j^z = 8$ approximates a rectangular parallelepiped. Contact with the surface of the j th obstacle by the i th collision avoidance point is approximated by $C_j(p_i) = 1$. The workspace potential function is defined by

$$P = \sum_j^{n_o} \sum_i^{n_p} [C_j(p_i) - 1]^{-1} \quad (26)$$

where n_p is the number of collision avoidance points. The gradient vector $\underline{\mu}$ is generated by a finite difference method as described above.

6 Graphical Representation with the IGRIP software

The Interactive Graphical Robot Instructional Program is a product of Deneb Robotics Inc. [12] It is a computer graphics based package for workcell layout, simulation and offline programming which permits the graphical simulation of virtually any robotic device. Devices used in the workcells may be added by modelling them with any of several CAD systems. A device has both geometric and non-geometric information stored with it. Non-geometric information including kinematics, dynamics, velocities, etc., can be entered through interactive menus.

IGRIP allows robot programming via the Graphical Simulation Language (GSL), which in turn, can communicate with programs written in C programming language. This capability will eventually be exploited to imbed the robot control algorithm into the IGRIP simulation.

7 The Payload Inspection and Processing System

The Payload Inspection and Processing System (PIPS) is conceived as a highly redundant manipulator with a serpentine truss configuration. It is based on the Foster-Miller Serpentine Truss currently under development at the Kennedy Space Center. The truss shown in Fig. 4 can accomodate up to twelve degrees of freedom.

For the purposes of examining the efficacy of control algorithms, a notional PIPS, shown in Fig 5 has been designed. The illustration was generated in IGRIP. The Foster Miller Truss, with twelve

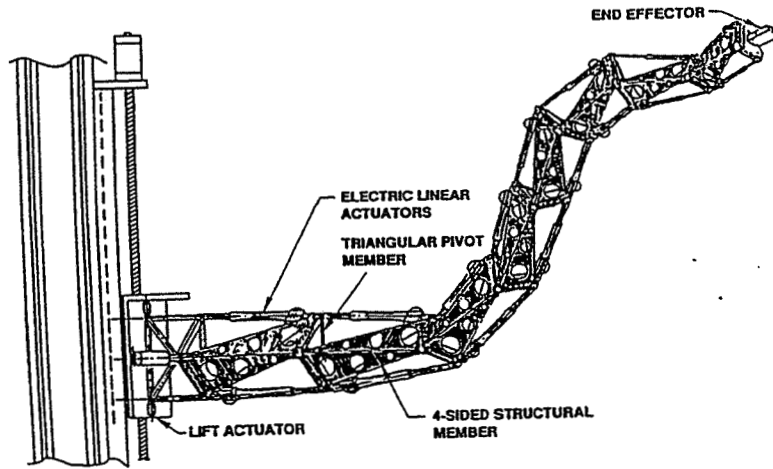


Figure 4: Foster Miller Serpentine Truss

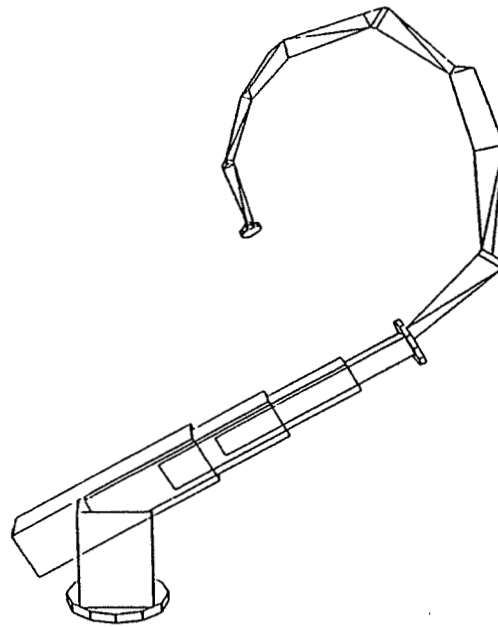


Figure 5; Notional PIPS

degrees of freedom, is mounted to a pedestal with two revolute joints and three telescoping prismatic joints. At the end of the truss, a revolute wrist is mounted, giving the complete system eighteen joints and sixteen independent degrees of freedom. The table of the Denavit–Hartenberg parameters for the nominal “home” position, is shown in Table 1.

Table 1: Denevitt–Hartenberg Parameters for Notional PIPS

i	α_i (deg)	θ_i (deg)	a_i (in)	d_i (in)	joint type
1	90.0	90.0	0.0	22.0	revolute
2	90.0	0.0	0.0	0.0	revolute
3	0.0	0.0	-2.593	20.0	prismatic
4	0.0	-45.0	0.0	1.0	prismatic
5	-90.0	90.0	0.0	0.0	prismatic
6	90.0	0.0	20.0	0.0	revolute
7	-90.0	0.0	1.25	0.0	revolute
8	90.0	0.0	20.0	0.0	revolute
9	-90.0	0.0	16.003	0.0	revolute
10	90.0	0.0	16.004	0.0	revolute
11	-90.0	0.0	1.188	0.0	revolute
12	90.0	0.0	16.004	0.0	revolute
13	-90.0	0.0	12.006	0.0	revolute
14	90.0	0.0	12.004	0.0	revolute
15	-90.0	0.0	.813	0.0	revolute
16	90.0	0.0	12.004	0.0	revolute
17	-90.0	90.0	.833	-.833	revolute
18	0.0	45.0	0.0	1.793	revolute

8 Algorithm Implementation

The algorithm described above is executed in the *C* language program, Collision Avoidance Path Planner (CAPP.c). The program flow is shown in Fig.6(a). In order to make use of utilities imbedded in IGRIP, CAPP will itself become a library utility which can be accessed by a program written in a GSL program which directly controls the graphical simulation and shown in Fig. 6(b).

The CAPP program has demonstrated the ability to generate obstacle free trajectories for the PIPS model. In Fig7 the PIPS is shown maneuvering in a simple representation of the PCR/Shuttle Payload Bay environment. In the simulation, it is desired to view a point, to the aft of the large cylindrical payload from a distance of six inches.

9 Conclusions and Recommendation

An algorithm has been presented which will move the end effector of a redundant manipulator toward a target state while avoiding collisions of the arm with obstacles in the workspace. Allowing the end effector path to be free avoids the problem of singularities found in the pseudo-inverse solution of the robot kinematics. In addition, it simplifies the operator’s workload and allows greater latitude for obstacle avoidance. The algorithm is straightforward and requires only modest computing power.

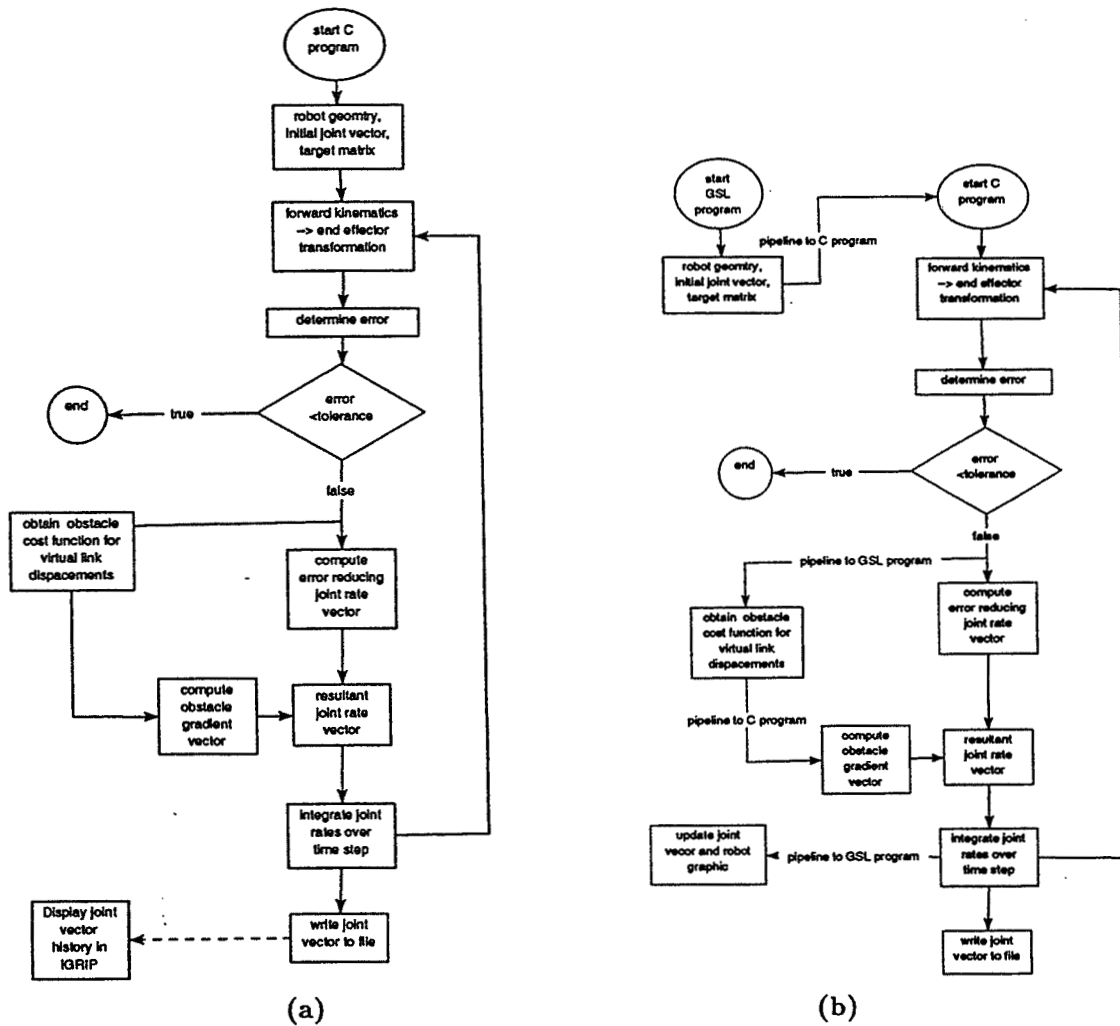


Figure 6: CAPP Program Flow
 (a) Current Flow, (b) IGRIP Imbedded Flow

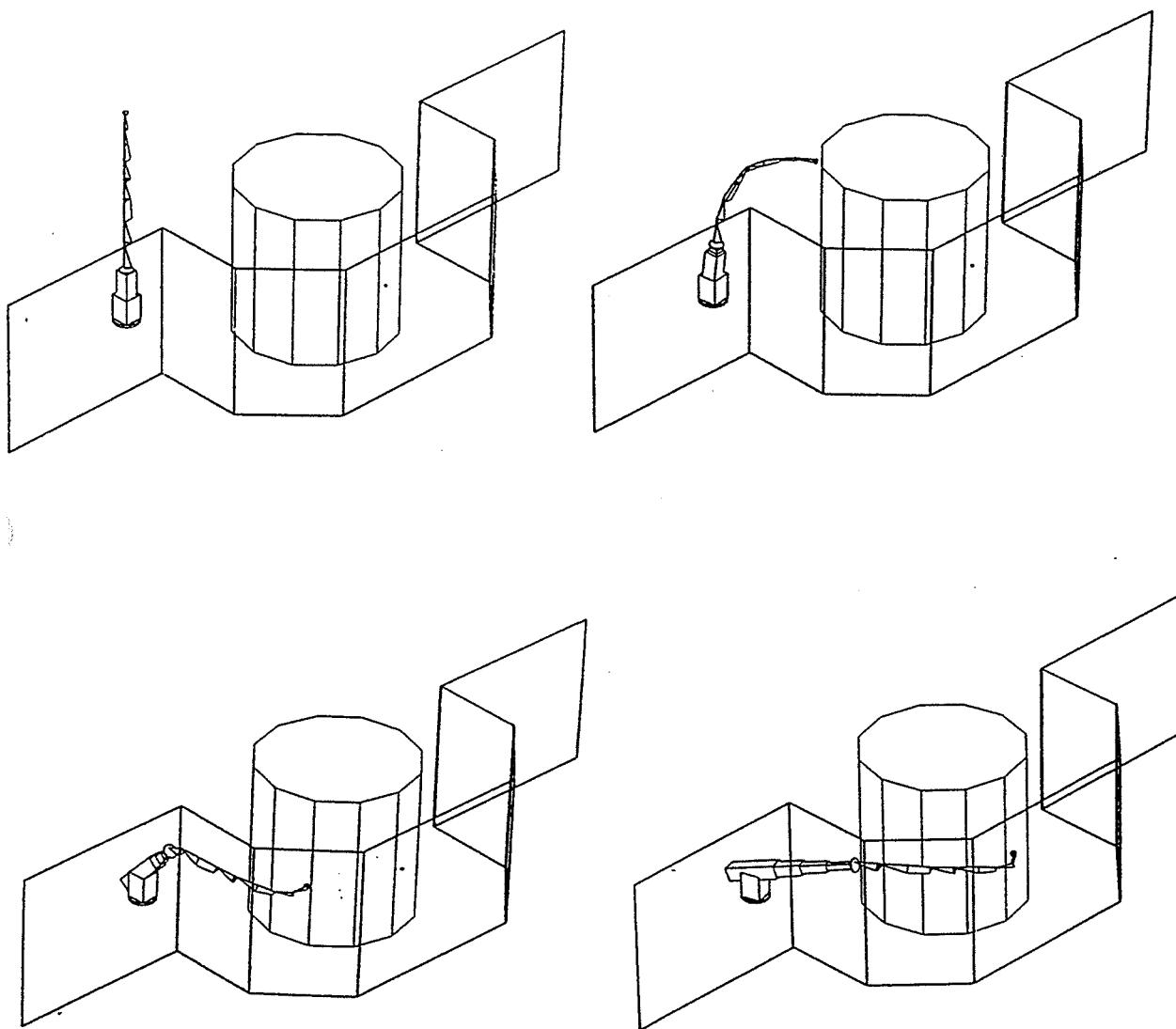


Figure 7: Simulated PIPS Maneuver

Although it is applied here to a highly redundant manipulator, redundancy is not explicitly required for its implementation.

Serpentine manipulators such as the PIPs are envisioned for employment in complex and costly environments. This method provides a tool for path planning by which specific maneuvers may be simulated without risk. A nominal joint history may be generated which is subsequently used as an open loop trajectory to be tracked by a robot with distributed control.

Offline processing of the robot trajectory, while sufficient to demonstrate the efficacy of the CAPP algorithm, is cumbersome and has severe shortcomings. Equation (25) has only limited utility to model a complex environment, such as exists in the shuttle payload bay. Processing time increases dramatically as the number and complexity of obstacles increases beyond a few simple shapes.

For that reason, it is recommended that future research be directed at various methods of interactively linking the GSL and C languages in IGRIP. This will allow the algorithm to interrogate IGRIP for distance information given by the MIN_DISTANCE utility. This should allow very complex and realistic CAD models to be exploited and greatly reduced execution time.

There are several unresolved problems with automated path planning. In its current incarnation, the manipulator path is influenced to a great degree by its initial configuration with respect to the workspace. Heretofore, the "home" configuration has been chosen arbitrarily. It would be useful to the operator to have specific rules by which to choose an optimal configuration. The weighting of the joint motion is also somewhat arbitrary, currently only enforcing joint rate limits. The scaling between revolute and prismatic joints requires a more rigorous basis.

Currently, the operator may designate way-points which assist the algorithm in finding a collision free path. However, heuristics should be developed which help the manipulator avoid dead-ends and to choose between multiple paths around an obstacle.

A Appendix: Collision Avoidance Path Planner Source Code Listing

```

/*****
*      COLLISION AVOIDANCE PATH PLANNER
*      Dr. Robert M. Byers, University of Central Florida
*      8/4/94
*      Robot end effector directed to a point in space with
*      a desired orientation .
*      Obstacles are modelled by hyperellipsoids
*      and may be oriented via 1-2-3 euler angles
*      Robot parameters contained in 'input.dat'
*      joint angles written to 'joints.dat'
*****/
#include <stdio.h>
#include <math.h>
/*****
*      function prototypes
*****/
void matrix_mult(float**matrix1,float**matrix2);
void end_effector(int n, float*q_p, float target_p[3][4],float error_p[3][4],float err_mag[4]);
void integrate(int n, float *var1, float *var2, float err, float err_dot, float step_s);
void joints_print(int n,float *var, FILE *file);
void **obstacle_transformation(int n, float **obst, float vector_n[3]);
float **IdentityMatrix(int n);
float **JacobianMatrix(int n_dof, int n_obs,float *q_p, float **ob);
float **transformation_matrix(int n, float *var);
float *joint_rates(int n, float *metric_p, float error_p[3][4], float target_p[3][4],
float**jb, float step_s);
float *mem_alloc_1(int n);
float **mem_alloc_2(int nrows, int ncols);

int *flag;
float *alpha,*theta,*a,*d;
/*****MAIN*****/

main()
{
/*****
* local variables *
*****/
int i, j,k, num_dof, num_obstacles, num_waypoints, waypoint_counter;
float **jacobian;
float *rate,*q;
float *metric;
float **obstacle;
float **waypoint;
float target[3][4], error[3][4];
float rate_mag, tolerance, move_dist;
float error_mag[4],step_size, error_mag_old,error_prod, error_prod_old,error_prod_dist;
float error_step=-1.0;
FILE *data;
FILE *joints;
joints=fopen("joints.dat","w");

if((data=fopen("input.dat", "r"))==NULL)
{
printf("input file could not be opened\n");
exit(-1);
}

/* *****
* input data

```

```

*****/

fscanf(data, "%d", &num_dof);

alpha=mem_alloc_1(num_dof);
theta=mem_alloc_1(num_dof);
a=mem_alloc_1(num_dof);
d=mem_alloc_1(num_dof);
metric=mem_alloc_1(num_dof);
q=mem_alloc_1(num_dof);

if((flag=(int*)malloc(sizeof(int)*num_dof)) == (int *) NULL)
{
    fprintf(stderr, "Error mallocing flag\n");
    exit(-1);
}

for (i=0;i<num_dof;i++)
{
    fscanf(data, "%f %f %f %f %f %d\n", &alpha[i], &theta[i], &a[i], &d[i],
&metric[i], &flag[i]);

    if(flag[i]==1)
        q[i]=theta[i];
    else
        q[i]=d[i];
}

/*****
*   read in target information
*   and way points
*****/
waypoint_counter=0;
fscanf(data, "%f %f %d", &step_size, &tolerance, & num_waypoints);
waypoint=mem_alloc_2(3,num_waypoints);

for(i=0;i<num_waypoints;i++)
    for(j=0;j<3;j++)
        fscanf(data, "%f ", &waypoint[j][i]);
for(i=0;i<3;i++)
    target[i][3]=waypoint[i][0];

for(i=0;i<3;i++)
    for (j=0;j<3;j++)
        fscanf(data, "%f ", &target[i][j]);

/*****
*   read obstacle array
*****/
fscanf(data, "%d", &num_obstacles);

obstacle=mem_alloc_2(12,num_obstacles);

for(i=0;i<num_obstacles;i++)
    for(j=0;j<12;j++)
        fscanf(data, "%f", &obstacle[j][i]);

fclose(data);

```

```

joints_print(num_dof,q,joints);

/* *****
*       for loop until all waypoints passed
***** */

while (waypoint_counter<num_waypoints)
{

/* *****
*       determine end effector position
***** */
end_effector( num_dof, q, target,error,error_mag);

for(j=0;j<4;j++)
    printf("%f ",error_mag[j]);
    printf("\n");
error_mag_old=error_mag[3];
move_dist=error_mag_old;
error_prod=sqrt(error_mag[0]*error_mag[0]+error_mag[1]*error_mag[1]+error_mag[2]*error_mag[2]);
error_prod_old=error_prod;
/* *****
*       while loop until error within tolerance
***** */
while (error_mag[3]>tolerance||error_prod>.4)
{

/* *****
*       form the jacobian matrix
***** */
jacobian=JacobianMatrix(num_dof,num_obstacles, q, obstacle);

/* *****
*       determine joint rate vector toward target
***** */
rate=joint_rates(num_dof,metric, error, target,jacobian,step_size);

/* *****
*       integrate joint rates to update joint parameters
***** */
integrate(num_dof, rate, q,error_mag[3],error_step, step_size);

/* *****
*       recompute position vector and error vector
***** */
end_effector( num_dof, q, target,error,error_mag);
for(j=0;j<4;j++)
    printf("%f ",error_mag[j]);
printf("\n");
error_step=error_mag[3]-error_mag_old;
error_mag_old=error_mag[3];
error_prod=sqrt(error_mag[0]*error_mag[0]+error_mag[1]*error_mag[1]+error_mag[2]*error_mag[2]);
error_prod_old=error_prod;

/* *****
*       print joint angles to "joints.dat"
***** */
if(fabs(move_dist-error_mag[3])>1.0 ||fabs(error_prod_dist-error_prod)>.1)
{
    move_dist=error_mag[3];
    error_prod_dist=error_prod;
    joints_print(num_dof,q,joints);
}
}
}
}

```

```

    )

    } /* end error tolerance while*/
/*****
if(waypoint_counter==num_waypoints-1)
    printf("Target point reached\n");
else
    printf("\n Waypoint %d reached\n ", waypoint_counter);

waypoint_counter+=1;

for(i=0;i<3;i++)
    target[i][3]=waypoint[i][waypoint_counter];

} /*close waypoint counter while loop */

/*****
*   print final joint angles to "joints.dat"
*****/
joints_print(num_dof,q,joints);

fclose(joints);

free(alpha);
free(theta);
free(a);
free(d);
free(metric);
free(flag);
free(q);
free(rate);

for(i=0;i<12;i++)
    free(obstacle[i]);
free(obstacle);
for(i=0;i<3;i++)
    free(waypoint[i]);
free(waypoint);

for(i=0;i<3;i++)
{
    for(j=0;j<num_dof;j++)
        free(jacobian[i][j]);
    free(jacobian[i]);
}
free(jacobian);

}
/*****
*   end of main program
*****/
/*****TRANSFORMATION MATRIX*****/
float **transformation_matrix(int n, float *var)
{
    static float **transform;

    int i;

    if(!(transform)){
        transform=(float **)malloc(sizeof(float*)*4);
        for(i=0;i<4;i++)

```

```

if((transform[i]=(float *)malloc(sizeof(float)*4)) == (float *) NULL)
    fprintf(stderr, "Error mallocing transform\n");
}

/*rotation matrix*/
if(flag[n]==1)
{
    transform[0][0]=cos(var[n]);
    transform[0][1]=-cos(alpha[n])*sin(var[n]);
    transform[0][2]=sin(alpha[n])*sin(var[n]);
    transform[0][3]=a[n]*cos(var[n]);
    transform[1][0]=sin(var[n]);
    transform[1][1]=cos(alpha[n])*cos(var[n]);
    transform[1][2]=-sin(alpha[n])*cos(var[n]);
    transform[1][3]=a[n]*sin(var[n]);
    transform[2][0]=0;
    transform[2][1]=sin(alpha[n]);
    transform[2][2]=cos(alpha[n]);
    transform[2][3]=d[n];
    transform[3][0]=0;
    transform[3][1]=0;
    transform[3][2]=0;
    transform[3][3]=1;
}
else
{
    transform[0][0]=cos(theta[n]);
    transform[0][1]=-cos(alpha[n])*sin(theta[n]);
    transform[0][2]=sin(alpha[n])*sin(theta[n]);
    transform[0][3]=a[n]*cos(theta[n]);
    transform[1][0]=sin(theta[n]);
    transform[1][1]=cos(alpha[n])*cos(theta[n]);
    transform[1][2]=-sin(alpha[n])*cos(theta[n]);
    transform[1][3]=a[n]*sin(theta[n]);
    transform[2][0]=0;
    transform[2][1]=sin(alpha[n]);
    transform[2][2]=cos(alpha[n]);
    transform[2][3]=var[n];
    transform[3][0]=0;
    transform[3][1]=0;
    transform[3][2]=0;
    transform[3][3]=1;
}

return(transform);
}

```

```

/*****MATRIX MULTIPLICATION*****/

```

```

void matrix_mult(float**matrix1, float**matrix2)
{
    float **matrix3=mem_alloc_2(4,4);
    int i,j,k;

    for(i=0;i<4;i++)
        for (j=0;j<4;j++){
            matrix3[i][j]=0;
            for (k=0;k<4;k++)
                matrix3[i][j]+=matrix1[i][k]*matrix2[k][j];}

    for(i=0;i<4;i++)
    {

```

```

        free(matrix1[i]);
        matrix1[i]=matrix3[i];
    }
}

/*****IDENTITY MATRIX*****/
float **IdentityMatrix(int n)
{
    float **matrix=mem_alloc_2(n,n);
    int i,j;

    for(i=0;i<n;i++)
        for(j=0;j<n;j++)
            if(i==j)
                matrix[i][j]=1;
            else
                matrix[i][j]=0;

    return(matrix);
}

/*****JACOBIAN MATRIX*****/
float ***JacobianMatrix(int n_dof, int n_obs, float *q_p,float **ob)
{
    float ***jacobian;
    float ***temp;
    float **result_plus, **result_minus;
    float *q_plus=mem_alloc_1(n_dof);
    float *q_minus=mem_alloc_1(n_dof);
    float *gradient=mem_alloc_1(n_dof);
    float cost_minus;
    float cost_plus;
    float **mu_matrix=mem_alloc_2(n_dof,n_dof);
    float potential_plus, potential_minus;
    float end_point_plus[3],end_point_minus[3];
    float mid_point_plus[3],mid_point_minus[3];
    float gradient_mag=0.0;
    int i, j, k,kk;

    jacobian=(float***)malloc(sizeof(float**)*3);
    for (i=0;i<3;i++)
    {
        jacobian[i]=(float**)malloc(sizeof(float*)*n_dof);
        for(j=0;j<n_dof;j++)
            jacobian[i][j]=(float*)malloc(sizeof(float)*4);
    }
    temp=(float***)malloc(sizeof(float**)*3);
    for (i=0;i<3;i++)
    {
        temp[i]=(float**)malloc(sizeof(float*)*n_dof);
        for(j=0;j<n_dof;j++)
            temp[i][j]=(float*)malloc(sizeof(float)*4);
    }

    /*****
    * virtual joint displacement loop
    *****/
}

```

```

for(j=0;j<n_dof;j++) /* outer loop start*/
{
  for (i=0;i<n_dof;i++)
    if(i==j)
    {
      q_plus[i]=q_p[i]+.005;
      q_minus[i]=q_p[i]-.005;
    }
    else
    {
      q_plus[i]=q_p[i];
      q_minus[i]=q_p[i];
    };

result_plus=IdentityMatrix(4);
result_minus=IdentityMatrix(4);
potential_plus=0.0;
potential_minus=0.0;
for(i=0;i<3;i++)
{
  end_point_plus[i]=0.0;
  end_point_minus[i]=0.0;
}

/*find change in r for a plus/minus permutation of q*/

for(i=0;i<n_dof;i++)
{
  /*****
  * cost function for joint locations
  *****/
  matrix_mult(result_plus,transformation_matrix(i, q_plus));
  matrix_mult(result_minus,transformation_matrix(i,q_minus));

  for(kk=0;kk<3;kk++)
  {
    mid_point_plus[kk]=(result_plus[kk][3]+end_point_plus[kk])/2.0;
    mid_point_minus[kk]=(result_minus[kk][3]+end_point_minus[kk])/2.0;
    end_point_plus[kk]=result_plus[kk][3];
    end_point_minus[kk]=result_minus[kk][3];
  }
  /*****
  * link endpoint collision avoidance cost function
  *****/
  for(k=0;k<n_obs;k++)
  {
    obstacle_transformation(k, ob,end_point_plus);
    obstacle_transformation(k,ob,end_point_minus);
    obstacle_transformation(k, ob,mid_point_plus);
    obstacle_transformation(k,ob,mid_point_minus);

    cost_plus= -1.0;
    cost_minus= -1.0;
    for(kk=0;kk<3;kk++)
    {
      cost_plus+=pow((end_point_plus[kk]-ob[kk][k])/(ob[kk+3][k]+6.0),ob[kk+6][k]);
      cost_minus+=pow((end_point_minus[kk]-ob[kk][k])/(ob[kk+3][k]+6.0),ob[kk+6][k]);
    }
    potential_plus+=1.0/cost_plus;
    potential_minus+=1.0/cost_minus;
  }
}

```

```

/*****
*   link midpoint collision avoidance cost function
*****/
cost_plus= -1.0;
cost_minus= -1.0;
for(kk=0;kk<3;kk++)
{
    cost_plus+=pow((mid_point_plus[kk]-ob[kk][k])/(ob[kk+3][k]+3.0),ob[kk+6][k]);
cost_minus+=pow((mid_point_minus[kk]-ob[kk][k])/(ob[kk+3][k]+3.0),ob[kk+6][k]);
}
    potential_plus+=1.0/cost_plus;
    potential_minus+=1.0/cost_minus;
}

/*****
*   obstacle gradient vector
*****/
gradient[j]=(potential_plus-potential_minus)/.01;
gradient_mag+=gradient[j]*gradient[j];

/*****
*   rate only jacobian
*****/
for(i=0;i<3;i++)
    for(k=0;k<4;k++)
        temp[i][j][k]=(result_plus[i][k]-result_minus[i][k])/0.01;

} /* end virtual displacement loop */

/*****
*   normalize gradient vector
*****/

gradient_mag=sqrt(gradient_mag);
for(i=0;i<n_dof;i++)
    gradient[i]=gradient[i]/gradient_mag;

for(i=0;i<n_dof;i++)
    for(j=0;j<n_dof;j++)
    {
        if(i==j)
            mu_matrix[i][j]=1.0-gradient[i]*gradient[j];
        else
            mu_matrix[i][j]=-gradient[i]*gradient[j];
    }

/*****
*   obstacle avoidance jacobian
*****/

for(k=0;k<4;k++)
{
    for(i=0;i<3;i++)
    for(j=0;j<n_dof;j++)
    {
        jacobian[i][j][k]=0.0;
        for(kk=0;kk<n_dof;kk++)
            jacobian[i][j][k]+=mu_matrix[j][kk]*temp[i][kk][k];
    }
}

```



```

for(i=0;i<4;i++)
    {
        free (result_plus[i]);
        free (result_minus[i]);
    }
free (result_plus);
free (result_minus);

for(i=0;i<3;i++)
    {
        for(j=0;j<n_dof;j++)
            free(temp[i][j]);
        free(temp[i]);
    }
free(temp);
free (q_plus);
free (q_minus);
free (gradient);

return(jacobian);
}
/*****END EFFECTOR POSITION AND ERROR*****/
void end_effector(int n, float*q_p, float target_p[3][4],float error_p[3][4], float err_mag[4])
{
    int i,j;
    float **result;

    result=IdentityMatrix(4);                /*initialize transformation matrix*/
        for(i=0;i<n;i++)                    /*carry out sequential matrix multiplication*/
            matrix_mult(result,transformation_matrix(i, q_p));
        printf("%.2f   %.2f   %.2f\n", result[0][3], result[1][3], result[2][3]);
/*****
*   determine end effector error
*****/

for(j=0;j<4;j++)
    {
        for(i=0;i<3;i++)
            error_p[i][j]=target_p[i][j]-result[i][j];

err_mag[j]=sqrt(error_p[0][j]*error_p[0][j]+error_p[1][j]*error_p[1][j]+error_p[2][j]*error_p[2][j]);
    }
for(i=0;i<4;i++)
    free(result[i]);
free(result);

}
/*****JOINT RATES*****/
float *joint_rates(int n, float *metric_p, float error_p[3][4], float target_p[3][4],
float**jb, float step_s)
{
    float rate_mag=0;
    float *rate_p,error_mag;

    int i,j,k;
    rate_p=mem_alloc_1(n);

    error_mag=sqrt(error_p[0][3]*error_p[0][3]+error_p[1][3]*error_p[1][3]+error_p[2][3]*error_p[2][3]);

/*****
*   target position approach rates

```

```

*****/
for(i=0;i<n;i++)
{
    rate_p[i]=0;
    for(j=0;j<3;j++)
        rate_p[i]+=metric_p[i]*jb[j][i][3]*error_p[j][3]/error_mag;
    rate_mag+=rate_p[i]*rate_p[i];
}

/*****
*   target orientation rates
*****/

for(i=0;i<n;i++)
{
    for(j=0;j<3;j++)
        for(k=0;k<3;k++)
            rate_p[i]+=10*jb[j][i][k]*target_p[j][k];

    rate_mag+=rate_p[i]*rate_p[i];
}

rate_mag=sqrt(rate_mag);

/*****
*   rate limit 10 degrees /sec
*****/

for(i=0;i<n;i++)
{
    rate_p[i]=rate_p[i]/rate_mag;
    if (flag[i]==1 && fabs(rate_p[i])>.175*step_s)
        rate_p[i]=.175*step_s*rate_p[i]/sqrt(rate_p[i]*rate_p[i]);
}
return(rate_p);
}

/*****NUMERICAL INTEGRATION*****/
void integrate(int n, float *var1, float *var2, float err, float err_dot, float max_step)
{
    int i;
    float step;
    float step_s;

    /* first order euler's method integration */
    step_s=max_step;
    if(err>10*step_s)
    {
        if (err>fabs(err_dot))
            step=step_s;
        else
            step=fabs(err/err_dot)*step_s;
    }
    else
        step=.25*step_s;

    printf("%.2f \n",step);

    for(i=0;i<n; i++)
        var2[i]+=var1[i]*step;
}

```

```

/*****PRINT OUTPUT*****/
void joints_print(int n, float *var, FILE *file)
{
  int i;
  for(i=0;i<n/2;i++)
    fprintf(file, "%f ", var[i]);
  fprintf(file, "\n");

  for(i=n/2;i<n;i++)
    fprintf(file, "%f ", var[i]);
  fprintf(file, "\n");
}
/*****MEMORY ALLOCATION 1*****/

float *mem_alloc_1(int n)
{
  float *var;

  if((var = (float *)malloc(sizeof(float)*n)) == (float *) NULL)
  {
    fprintf(stderr, "mallocing error\n");
    exit(-1);
  }
  return(var);
}
/*****MEMORY ALLOCATION 2*****/

float **mem_alloc_2(int nrows, int ncols)
{
  float **var;
  int i;
  if((var=(float **)malloc(sizeof(float*)*nrows)) == (float **) NULL)
  {
    fprintf(stderr, " mallocing error\n");
    exit(-1);
  }
  for(i=0;i<nrows;i++)
  {
    if((var[i]=(float*)malloc(sizeof(float)*ncols)) == (float *) NULL)
    {
      fprintf(stderr, " mallocing error\n");
      exit(-1);
    }
  }
  return(var);
}
/*****OBSTACLE ORIENTATION TRANSFORMATION*****/
void **obstacle_transformation(int n, float **obst, float vector_n[3])
{
  float pry[3][3];
  float vector_r[3];
  int i, j;

  pry[0][0]=cos(obst[11][n])*cos(obst[10][n]);
  pry[0][1]=cos(obst[11][n])*sin(obst[10][n])*sin(obst[9][n])-sin(obst[11][n])*cos(obst[9][n]);
  pry[0][2]=cos(obst[11][n])*sin(obst[10][n])*cos(obst[9][n])+sin(obst[11][n])*sin(obst[9][n]);

  pry[1][0]=sin(obst[11][n])*cos(obst[10][n]);
  pry[1][1]=sin(obst[11][n])*sin(obst[10][n])*sin(obst[9][n])+cos(obst[11][n])*cos(obst[9][n]);
  pry[1][2]=sin(obst[11][n])*sin(obst[10][n])*cos(obst[9][n])-cos(obst[11][n])*sin(obst[9][n]);
}

```

```
pry[2][0]=--sin(obst[10][n]);
pry[2][1]=cos(obst[10][n])*sin(obst[9][n]);
pry[2][2]=cos(obst[10][n])*cos(obst[9][n]);

for(i=0;i<3;i++)
{
    vector_r[i]=0;
    for(j=0;j<3;j++)
        vector_r[i]+=pry[i][j]*vector_n[j];
}
for(i=0;i<3;i++)
    vector_n[i]=vector_r[i];
}
```

References

- [1] Richardson, B., Sklar, M., and Fresa, M., "PCR Inspection and Processing Robot Study, Final Report", McDonnell Douglas Space Systems - Kennedy Space Division, Nov 5 1993
- [2] Pasch, K., "Self-Contained Deployable Serpentine Truss for Prelaunch Access of the Space Shuttle Orbiter Payloads", NAS -2659-FM-9106-387, Final Report, Contract No. NAS 10-11659, NASA, Kennedy Space Center, FL Aug. 1990.
- [3] Maciejewski, A., and Klein, C., "Obstacle Avoidance for Kinematically Redundant Manipulators in Dynamically Varying Environments", *The International Journal for Robotics Research*, Vol. 4, No. 3, Fall 1985, pp. 109-117.
- [4] Nakamura, Y., *Advanced Robotics, Redundancy and Optimization*, Addison-Wesley Publishing Co., Inc., Redwood City, C, 1991.
- [5] Wegerif, D., Rosinski, D., and Parton, W., "Results of Proximity Sensing Research for Real-Time Collision Avoidance of Articulated Robots Working Near the Space Shuttle", *Proceedings of the 6th Annual Conference on Recent Advances in Robotics*, University of Florida, Gainesville, FL, 19-20 April 1993.
- [6] Penrose, R., "On the Best Approximate Solutions of Linear Matrix Equations", *Proceedings, Cambridge Philosophy Society*, 52:17-19.
- [7] Sciavicco, L., Siciliano, B., "A Solution Algorithm to the Inverse Kinematic Problem for a Redundant Manipulator", *IEEE Journal of Robotics and Automation*, Vol. 4., No. 4., Aug. 1988, pp. 403-410.
- [8] Asano, K., et al, "Multi-Joint Inspection Robot", *IEEE Transactions on Industrial Electronics*, Vol. IE-30, No. 3, August 1983, pp. 277-281.
- [9] Baker, D.R., and Wampler, C.W., "On the Inverse Kinematics of Redundant Manipulators", *The International Journal of Robotics Research*, Vol. 7., No. 2., March/April 1988.
- [10] Doty K., Melchiorri, C., and Bonivento, C., "A Theory of Generalized Inverses Applied to Robotics", *The International Journal of Robotics Research*, Vol. 12, No. 1, Feb. 1993, pp 1-19.
- [11] Byers, R., "Control of a Serpentine Manipulator with Collision Avoidance" Final Report, 1993 NASA/ASEE Summer Faculty Fellowship Program, NASA CR-194678, Contract NGT 60002 Suppl. #11, Kennedy Space Center, FL.
- [12] "IGRIP Users Reference Manual", Deneb Robotics, Inc. 1990.
- [13] Denavit, J. and Hartenberg, R.S., "A Kinematic Notation for Lower-Pair Mechanisms Based on Matrices," *Journal of Applied Mechanics*, pp. 215-221, June 1955.
- [14] Khatib, O., and Le Maitre, J.-F., "Dynamic Control of Manipulators Operating in a Complex Environment", *3rd Symp. Theory and Practice of Robot Manipulators*, Elsevier, pp. 267-282.

REFERENCES

29

- [15] Luenberger, D., *Optimization by Vector Space Methods*, John Wiley & Sons, Inc., New York, 1969.
- [16] Nakamura, Y., and Hanafusa, H., "Optimal Redundancy Control of Robot Manipulators", *International Journal of Robotics Research*, vol. 6, No. 1., Spring 1987. pp 32-42.

1994 NASA/ASEE SUMMER FACULTY FELLOWSHIP PROGRAM

111755

JOHN F. KENNEDY SPACE CENTER
UNIVERSITY OF CENTRAL FLORIDA

54-25
33964
p. 22
351459

EVALUATION OF INORGANIC ZINC-RICH PRIMERS USING
ELECTROCHEMICAL IMPEDANCE SPECTROSCOPY (EIS) IN COMBINATION
WITH ATMOSPHERIC EXPOSURE

PREPARED BY:	Dr. Luz M. Calle
ACADEMIC RANK:	Associate Professor
UNIVERSITY AND DEPARTMENT:	Randolph-Macon Woman's College Department of Chemistry
NASA/KSC	
DIVISION:	Material Science Laboratory
BRANCH:	Failure Analysis and Materials Evaluation
NASA COLLEAGUE:	Louis MacDowell III
DATE:	August 12, 1994
CONTRACT NUMBER:	University of Central Florida NASA-NGT-60002 Supplement: 17

ACKNOWLEDGMENT

I would like to express my appreciation to NASA/ASEE for providing me with the wonderful opportunity to spend the last two summers engaged in what I consider a fascinating area of research. The expert leadership of Loren A. Anderson, the program director, and the professionalism and enthusiasm of Kari Styles, the administrative assistant, made participating in the program a very pleasurable and rewarding experience. I would also like to thank my NASA colleague, Louis G. MacDowell, III, for his expert guidance and support throughout the duration of the project. I am also indebted to Irby Moore, Cole Bryan, and specially , Scott Murray and the rest of the materials section for making me feel welcome.

ABSTRACT

This investigation explored the use of Electrochemical Impedance spectroscopy (EIS) in combination with atmospheric exposure as a short term method for analyzing the performance of twenty-one commercially available zinc-rich primers. The twenty-one zinc-rich primers were: Carboline CZ-11, Ameron Devoe-Marine Catha-Coat 304, Briner V-65, Ameron D-21-9, Sherwin Williams Zinc Clad II, Carboline CZ-D7, Ameron D-4, Dupont Ganicin 347WB, Porter TQ-4374H, Inorganic Coatings IC-531, Subox Galvanox IV, Southern Coatings Chemtec 600, Glidden Glidzinc 5530, Byco SP-101, Tnemec 90E-75, Devoe Catha-Coat 302H, Glidden Glidzinc 5536, Koppers 701, Ameron D-21-5, Coronado 935-152, and Subox Galvanox V. Data were also collected on galvanized steel for comparison purposes. A library of Bode magnitude plots was generated for each coating including curves for the initial time and after each week of atmospheric exposure at the Beach Corrosion Test Site near the Space Shuttle launch pad at the Kennedy Space Center for up to four weeks. Subsequent measurements were collected after 8 weeks and after one year of atmospheric exposure. Analysis of the impedance data was performed with the purpose of identifying parameters that could be used to predict the long-term performance of zinc-rich primers. It has been shown that there is a correlation between the long-term performance of zinc-rich primers and several parameters obtained from EIS measurements in combination with atmospheric exposure. The equivalent circuit $R_1(R_2C(R_3W))$ provided a satisfactory fit for the EIS data. The corrosion potential and the R_2 resistance are parameters indicative of the galvanic mechanism of protection. The capacitance of the coating is related to the barrier mechanism of protection.

SUMMARY

This investigation explored the use of Electrochemical Impedance spectroscopy (EIS) in combination with beach exposure as a short term method for analyzing the performance of twenty-one zinc-rich primers. The twenty-one zinc-rich primers were: Carboline CZ-11, Ameron Devoe-Marine Catha-Coat 304, Briner V-65, Ameron D-21-9, Sherwin Williams Zinc Clad II, Carboline CZ-D7, Ameron D-4, Dupont Ganicin 347WB, Porter TQ-4374H, Inorganic Coatings IC-531, Subox Galvanox IV, Southern Coatings Chemtec 600, Glidden Glidzinc 5530, Byco SP-101, Tnemec 90E-75, Devoe Catha-Coat 302H, Glidden Glidzinc 5536, Koppers 701, Ameron D-21-5, Coronado 935-152, and Subox Galvanox V. Data were also collected on galvanized steel for comparison purposes.

Electrochemical Measurements were performed on 10.16 cm x 15.24 cm x 0.32 cm (4-inch x 6-inch x 1/8 inch) test panels. The panel included in this investigation had been rated previously to determine their degree of corrosion performance on a scale of 1 to 10, with 10 being the highest rating. The twenty-one primers chosen represent a wide range of performance. AC impedance data were collected after one hour immersion time in 3.55% NaCl. Data were gathered in the frequency range from 100 kHz to 0.01 Hz.

A library of Bode magnitude, Nyquist, and Bode magnitude/phase angle was generated for each coating including curves for the initial time and after each week of atmospheric exposure for up to four weeks. Subsequent measurements were collected after 8 weeks and after one year of atmospheric exposure.

Analysis of the impedance data was performed with the purpose of identifying parameters that could be used to predict the long-term performance of zinc-rich primers. It has been shown that there is a correlation between the long-term performance of zinc-rich primers and several parameters obtained from EIS measurements in combination with atmospheric exposure. The equivalent circuit $R_1(R_2C(R_3W))$ provided a satisfactory fit for the EIS data. The corrosion potential and the R_2 resistance are parameters indicative of the galvanic mechanism of protection. A corrosion potential below -0.735 V Ag/AgCl [-0.780 V (SCE)] and an R_2 value that starts around 10^{-2} ohms and increases gradually with time of atmospheric exposure is indicative of good galvanic activity that results in the formation of a protective layer that has a higher resistance. The capacitance of the coating is related to the barrier mechanism of protection. Good coatings have capacitances that decrease gradually as the protective film formed by zinc corrosion products becomes less porous. This decrease in porosity is accompanied by a decrease in the water content of the film which results in lower capacitance values.

TABLE OF CONTENTS

<u>Section</u>	<u>Title</u>	<u>Page</u>
I.	INTRODUCTION	7
II.	MATERIALS AND METHODS	8
III.	RESULTS AND DISCUSSION	10
IV.	CONCLUSIONS	13
V.	REFERENCES	20

LIST OF ILLUSTRATIONS

<u>Figure</u>	<u>Title</u>	<u>Page</u>
1	Exploded View of Model K0235 Flat Cell	14
2	Variation of Corrosion Potential with Time of Atmospheric Exposure for Coatings A, P, R, and T	15
3	Nyquist Plot for Coating A in 3.55% NaCl prior to Atmospheric Exposure	16
4	Nyquist Plot for Coating A in 3.55% NaCl after One Week of Atmospheric Exposure	16
5	Equivalent Circuit Used to Fit Impedance Data of Inorganic Zinc-Rich Primers	17
6	Dependence of R_2 on Time of Atmospheric Exposure for Coatings A, P, R, and T	18
7	Dependence of C on Time of Atmospheric Exposure for Coatings A, P, R, and T	19

LIST OF TABLES

<u>Table</u>	<u>Title</u>	<u>Page</u>
1	Materials Tested, Code, Type, Rust Grade Evaluation, Zinc Content, and Thickness	9
2	Variation of Corrosion Potential with Time of Atmospheric Exposure	11
3	Equivalent Circuit Components for Coatings P, A, R, and T	12

I. INTRODUCTION

For over 25 years, the process of coating testing at the Kennedy Space Center (KSC) to identify materials for the long term protection of carbon steel structures has taken place at the Beach Corrosion Test Site near the launch pad. The atmosphere at the launch pad is highly corrosive due to the proximity of the ocean, high heat from rocket exhaust, and now with the Space Shuttle, the acidic combustion products of the Solid Rocket Boosters (SRB's). As a result of previous tests, zinc-rich primers were identified as the best choice to provide long term protection of launch structures and ground support equipment at KSC^{1,2,3}.

Exposure at the beach site provides very valuable data but it takes a long time. Testing requires 18 months for preliminary approval and continued good performance for 5 years for final approval. This investigation explores the use of Electrochemical Impedance spectroscopy (EIS) in combination with atmospheric exposure at the beach corrosion test site as a short term method for analyzing the performance of zinc-rich primers. EIS has been used before on bare metals⁴, and on zinc-rich primers⁵. The samples tested previously were flat, 0.16 cm (1/16 inch) thick coupons, 1.59 cm (5/8 inch) in diameter and did not include atmospheric exposure.

The initial stage of this investigation included EIS measurements in combination with atmospheric exposure for up to three weeks⁶. Subsequent measurements were collected after four weeks, eight weeks, and one year of atmospheric exposure.

Inorganic zinc-rich primers contain a high percentage of zinc particles (between 75% and 90%) dispersed in inorganic binders. Initially, the zinc provides cathodic protection to the steel substrate (galvanic effect). As exposure time increases, the galvanic action becomes less effective. The deposition of inhibiting zinc compounds at the base of the coating pores, followed by the sealing of the porous structure by the zinc corrosion products, results in what is referred to as the barrier mechanism of protection. The galvanic and the barrier effect must undoubtedly occur to ensure long-term protection of the steel substrate^{7, 8}.

II. MATERIALS AND METHODS

A model 378 Electrochemical Impedance system manufactured by EG&G Princeton Applied Research Corporation was used for all electrochemical measurements. Electrochemical Measurements were performed on 10.16 cm x 15.24 cm x 0.32 cm (4-inch x 6-inch x 1/8 inch) test panels. Twenty-one panels were coated with the inorganic zinc-rich primers listed in Table 1. The panel rating corresponds to the degree of corrosion judged on a scale of 1 to 10, with 10 being the highest rating⁹. The 21 primers chosen represent a wide range of performance. Also listed on the table is the zinc content, and the thickness when available.

The panels were mounted on an EG&G Princeton Applied Research Model KO235 Flat Cell with a working electrode area of 1 cm². The flat cell (see Figure 1) consists of a flat cylinder clamped horizontally between two end plates. One end plate houses the working electrode and the other houses the platinum counter electrode. The reference silver/silver chloride electrode is housed in a Luggin well with a Luggin capillary protruding from the bottom of the well.

AC impedance data were collected after one hour immersion time in aerated 3.55% NaCl. Data were gathered in the frequency range from 100 kHz to 0.01 Hz using the Auto Execute option of the M388 electrochemical analysis software. Three experiments were performed in a sequence covering the specified frequency range and the data were automatically merged and saved. The frequency ranges for the three experiments were 100 kHz to 5 Hz, 10 Hz to 0.1 Hz, and 0.1 Hz to 0.01 Hz. The ac amplitude was 10 mV. After each set of measurements, the panels were mounted on a rack and taken to the beach corrosion test site and left there for a week. At the end of the week, the panels were brought back to the laboratory for a new set of measurements and the cycle was repeated for up to four weeks of exposure. Subsequent measurements were performed after eight weeks and after one year of atmospheric exposure.

TABLE 1. MATERIALS TESTED, TYPE, RUST GRADE EVALUATION, ZINC CONTENT, AND THICKNESS

COATING	CODE	TYPE	RATING	% ZINC	COATING THICKNESS (μm)
AMERON D-21-9	A	SB	10.00	N/A	152
DEVOE CATHACOAT 302H	B	SB	1.25	N/A	102
SHERWIN WILLIAMS ZINC CLAD II	C	SB	10.00	N/A	127
AMERON D-4	D	WB	9.50	N/A	114
AMERON D-21-5	E	WB	5.75	N/A	114
BRINER V-65	F	WB	10.00	N/A	76
CARBOLINE CZ-D7	G	WB	10.00	N/A	89
DuPONT GANICIN 347 WB	H	WB	10.00	86	89
INORGANIC COATINGS IC-531	I	WB	9.75	90	89
PORTER TQ-4374H	J	WB	8.63	N/A	76
SOUTHERN COATINGS CHEMTEC 600	K	WB	9.88	90	76
SUBOX GALVANOX IV	L	SB	8.75	N/A	89
BYCO SP-101	M	SB	8.13	N/A	89
CARBOLINE CZ-11	N	SB	10.00	N/A	127
CORONADO 935-152	O	SB	5.25	84	114
DEVOE-MARINE CATHA-COAT 304	P	SB	10.00	N/A	127
GLIDDEN GLID-ZINC 5530	Q	SB	8.50	86	127
GLIDDEN GLID-ZINC 5536	R	SB	2.00	76	102
KOPPER 701	S	SB	7.00	N/A	102
SUBOX GALVANOX V	T	SB	2.75	N/A	102
TNEMEC 90E-75	U	SB	7.00	76	89
GALVANIZED STEEL	Z				
WB = Water-based (inorganic silicate)					
SB = Solvent-based (ethyl silicate)					

III. RESULTS AND DISCUSSION

Due to the limitations on the length of this paper and the large amount of data generated in this investigation, this discussion will be focused on four coatings that are representative of the group of twenty-one included in this research. A and P were chosen as typical examples of those coatings that have a rust grade evaluation of 10.00 (good performers). R and T were chosen as typical examples of those coatings that had a poor performance (rust grade evaluation of 2.00 and 2.75 respectively).

The variation of the corrosion potential with time of atmospheric exposure for the twenty-one coatings included in this investigation is presented in Table 2. Graphical presentation of the variation of the corrosion potential with time of atmospheric exposure is presented in Figure 2 for coatings A, P, R, and T.

The evolution of the corrosion potential with time is a useful indicator of the galvanic mechanism of protection of the coating. The corrosion potential of steel quoted in various Standards and codes of practice¹⁰ is $-0.735 \text{ V Ag/AgCl} [-0.780 \text{ V (SCE)}]$. At or below this potential the corrosion of the steel is reduced to approximately zero. Coatings A and P exhibit galvanic protection for up to eight weeks at least. Coatings R and T exhibit corrosion potentials above the protection potential for steel after two weeks of atmospheric exposure thus indicating their failure at protecting the steel galvanically. However, corrosion potential variation with time measurements provide no estimate of the performance of the coating after the cessation of the cathodic protection mechanism.

Another indication of the galvanic mechanism of protection is obtained by analyzing the EIS data. Figure 3 is typical of the Nyquist plots obtained for zinc-rich primers upon initial immersion in 3.55% NaCl prior to atmospheric exposure. Since at this time, the coating is protecting the steel galvanically, the Nyquist plot represents the corrosion of the zinc dust in the coating. The magnitude of the diameter of the semicircle is related to the rate of corrosion of the zinc dust: The smaller the diameter, the greater the rate of corrosion of the zinc and its protective galvanic effect. Upon atmospheric exposure, the Nyquist plot evolves to include what has been described as the barrier mechanism of protection. Figure 4 shows the appearance of a second semicircle in the low frequency range of the Nyquist plot. The parameters extracted from this region are associated with the barrier mechanism of protection.

To extract information on the galvanic as well as on the barrier mechanism of protection from the Nyquist plots generated in this investigation, the impedance spectra were analyzed using a computer simulation program¹¹. The equivalent circuit $R_1(R_2C(R_3W))$ ¹² shown in Figure 5 provided a satisfactory fit for the data (see simulation curves in Figures 3 and 4). The letters R, C, and W denote a resistor, capacitor, and Warburg impedance respectively.

TABLE 2. VARIATION OF CORROSION POTENTIAL (VOLTS) WITH TIME OF ATMOSPHERIC EXPOSURE

COATING	INITIAL	ONE WEEK	TWO WEEKS	THREE WEEKS	FOUR WEEKS	EIGHT WEEKS	ONE YEAR
A	-1.029	-1.025	-0.980	-0.947	-0.947	-0.898	-0.409
B	-0.004	-0.894	-0.143	-0.328	0.002	-0.084	-0.536
C	-1.015	-1.024		-0.923	-0.907	-0.836	-0.520
D	-0.990	-0.899	-0.767	-0.816	-0.625	-0.800	-0.727
E	-0.249	-0.552	-0.575	-0.155	-0.248	-0.457	-0.769
F	-1.009	-1.030	-0.995	-0.976	-0.904	-0.877	-0.561
G	-0.777	-0.117	-0.829	-0.869	-0.789	-0.879	-0.394
H	-0.895	-0.758	-0.968	-0.903	-0.692	-0.853	-0.688
I	-0.846	-0.725	-0.881	-0.867	-0.692	-0.810	-0.720
J	-0.992	-0.982	-0.944	-0.935	-0.766	-0.852	-0.414
K	-0.524	-0.571	-0.560	-0.616	-0.305	-0.499	-0.742
L	-0.988	-0.999	-0.979	-0.935	-0.968	-0.889	-0.603
M	-1.013	-1.025	-0.964	-0.965	-0.718	-0.788	-0.270
N	-0.814	-1.021	-1.008	-0.949	-0.796	-0.925	-0.913
O	-1.035	-1.022	-0.956	-0.926	-0.959	-0.862	-0.407
P	-0.987	-0.995	-0.939	-0.930	-0.766	-0.894	-0.449
Q	-1.016	-1.011	-0.957	-0.929	-0.953	-0.888	-0.393
R	-0.768	-1.015	-0.490	-0.771	-0.269	-0.909	-0.460
S	-0.975	-0.999	-0.937	-0.950	-0.821	-0.901	-0.524
T	-1.002	-1.020	-0.244	-0.584	-0.468	-0.843	-0.651
U	-0.983	-0.686	-0.861	-0.773	-0.520	-0.513	-0.336
Z	-1.024	-0.966	-0.959	-0.959	-0.788	-0.788	-0.865

Table 3 lists the values obtained for R_2 and C for coatings A, P, R, and T. The variation of R_2 with time of atmospheric exposure is shown in Figure 6. During the early stages of atmospheric exposure, R_2 represents the galvanic mechanism of protection involving the corrosion of the zinc. After this period, the resistance is equivalent to the magnitude of the film resistance. Its increase is due to the build up of zinc corrosion products responsible for the barrier effect. This trend holds for coating P (up to 56 days of atmospheric exposure), and for coatings A and T (up to 28 days of atmospheric exposure). The change in the value of R_2 for T was not as gradual as it was for A and

P perhaps resulting in the formation of a barrier that was not as effective in protecting the steel as indicated by the poor performance of the coating.

TABLE 3. EQUIVALENT CIRCUIT COMPONENTS FOR COATINGS P, A, R AND T

Coating	P	P	A	A	R	R	T	T
Days	R ₂ (ohms)	C (Farad)	R ₂ (ohms)	C (Farad)	R ₂ (ohms)	C (Farad)	R ₂ (ohms)	C (Farad)
0	1.89E+02	5.52E-04	3.72E+02	3.06E-04	1.65E+06	2.78E-10	3.77E+02	2.76E-07
7	4.97E+02	1.03E-05	1.50E+02	1.51E-06	9.28E+02	2.10E-08	5.29E+02	2.80E-07
14	9.88E+02	4.30E-08	1.14E+04	8.66E-10	1.07E+05	2.41E-09	1.68E+06	1.31E-10
21	2.33E+03	1.27E-08	1.14E+04	8.66E-10	4.49E+04	3.81E-09	1.49E+06	2.01E-10
28	3.70E+03	5.23E-09	2.50E+05	2.29E-10	2.98E+06	3.01E-10	1.21E+06	2.18E-10
56	2.58E+04	5.28E-09	1.52E+04	1.37E-08	8.67E+04	3.42E-10	3.51E+03	8.23E-08
365	2.22E+04	2.04E-10	5.19E+04	2.14E-10	5.57E+06	3.59E-10	2.21E+04	2.45E-08

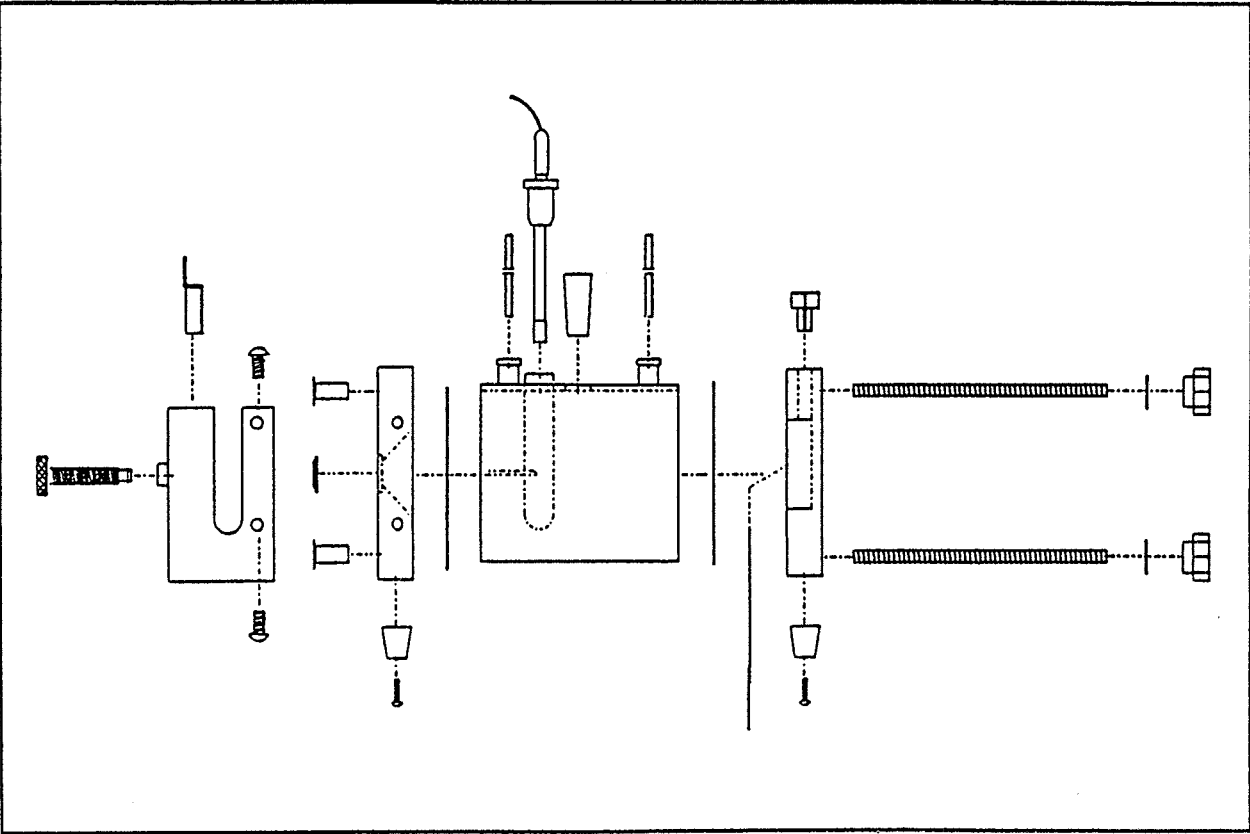
The capacitance variation with time of atmospheric exposure is shown graphically in Figure 7. Coatings A and P exhibit initial capacitances on the order of 10^{-4} Farad. Both coatings show a gradual change toward lower values of capacitance in the order of 10^{-10} Farads. Lower capacitance values can be attributed to a decrease in the water contents of the protective film formed by the zinc corrosion products. Coatings R and T exhibit initial capacitances that are lower than those for A and P. The change in capacitance with time of atmospheric exposure is not as pronounced as it was observed for A and P. This behavior may be attributed to the fact that coatings R and T do not form a barrier that is as effective at protecting the steel as the barrier formed by A and P.

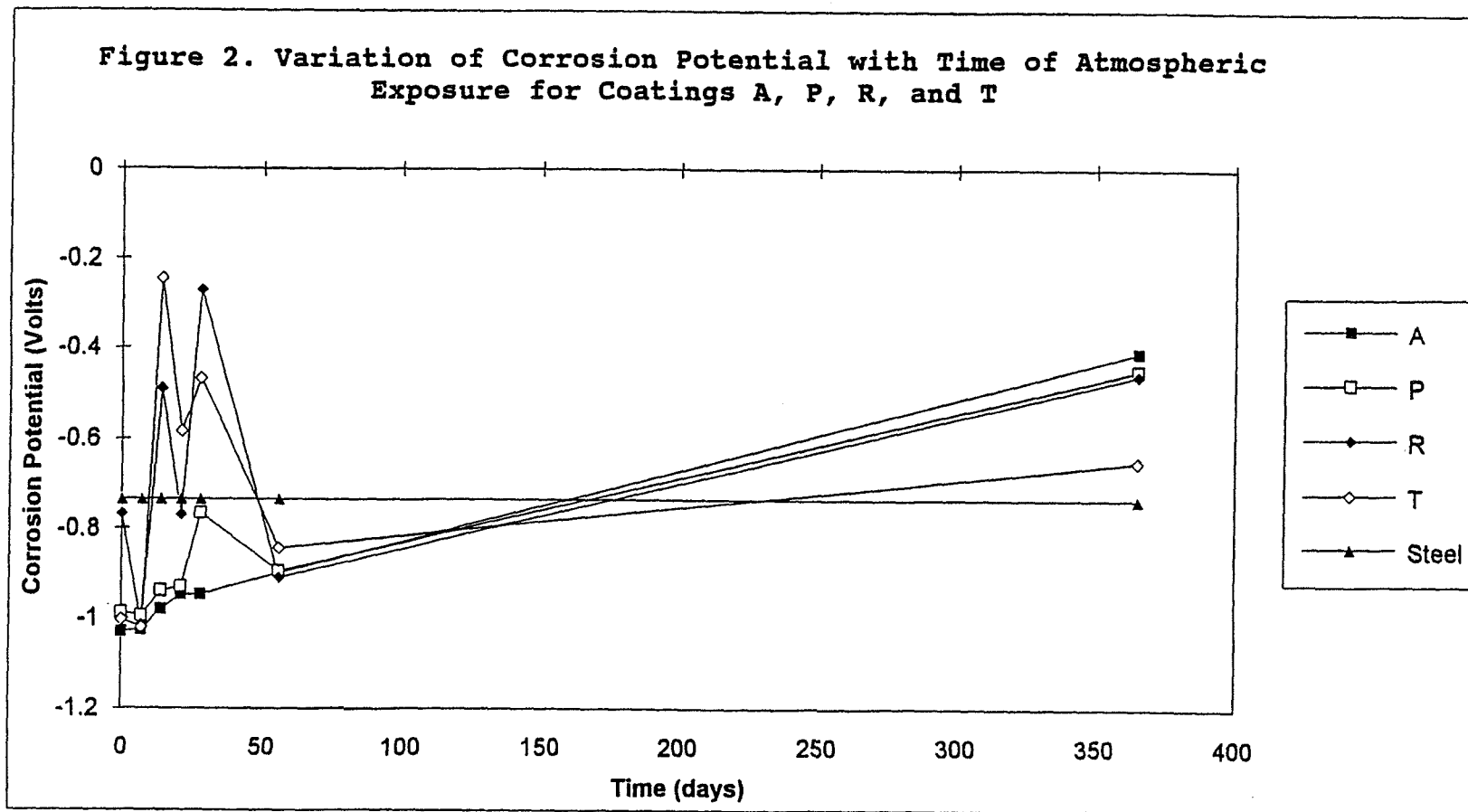
IV. CONCLUSIONS

It has been shown that there is a correlation between the long-term performance of zinc-rich primers and several parameters obtained from EIS measurements in combination with atmospheric exposure. The equivalent circuit $R_1(R_2C(R_3W))$ provided a satisfactory fit for the EIS data. The corrosion potential and the R_2 resistance are parameters indicative of the galvanic mechanism of protection. A corrosion potential below -0.735 V Ag/AgCl [-0.780 V (SCE)] and an R_2 value that starts around 10^{-2} ohms and increases gradually with time of atmospheric exposure is indicative of good galvanic activity that results in the formation of a protective layer that has a higher resistance. The capacitance of the coating is related to the barrier mechanism of protection. Good coatings have capacitances that decrease gradually as the protective film formed by zinc corrosion products becomes less porous. This decrease in porosity is accompanied by a decrease in the water content of the film which results in lower capacitance values. The two coatings with a high rating had capacitance values that varied from around 10^{-4} to around 10^{-10} Farads. The coatings with the low ratings had initial capacitances that were significantly lower than 10^{-4} .

It is suggested that a flow chart based on the above conclusions can be used to predict the long-term performance of inorganic zinc-rich primers. The chart could be used in order to select those coatings that are expected to perform well under atmospheric conditions similar to those present near the Space Shuttle launch site. The chart is being developed and tested with the available data and will appear in Report No. 94-2082, NASA, Kennedy Space Center, Materials Testing Branch¹³

Figure 1. Exploded View of Model K0235 Flat Cell





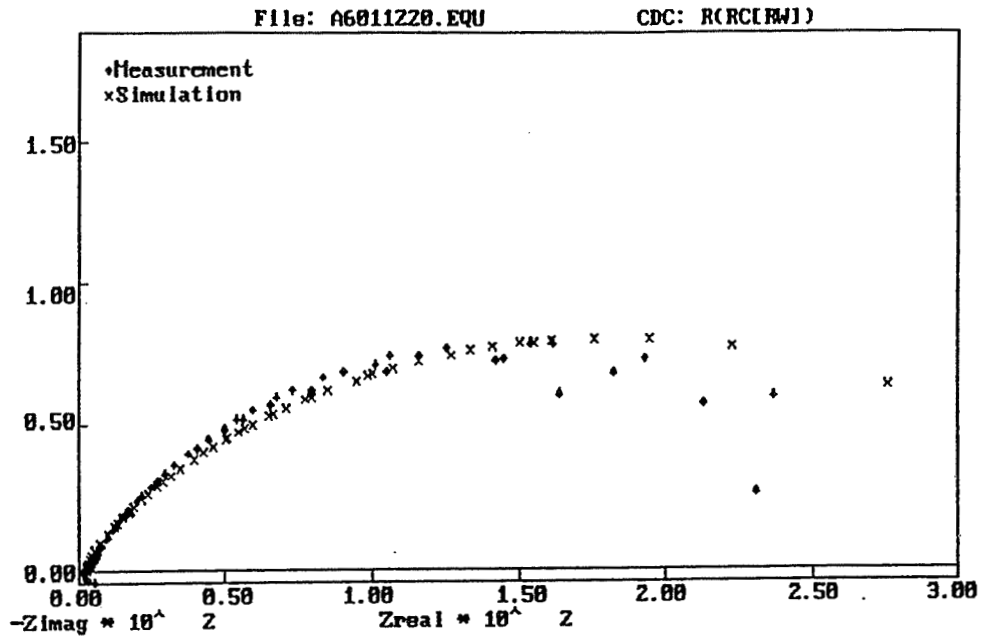


Figure 3. Nyquist Plot for Coating A in 3.55% NaCl prior to Atmospheric Exposure

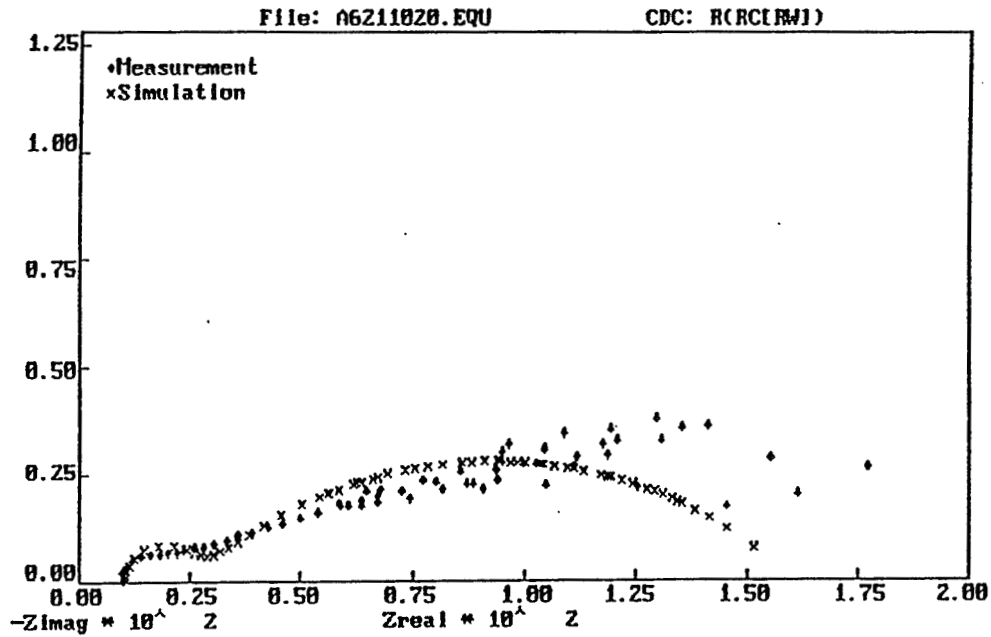


Figure 4. Nyquist Plot for Coating A in 3.55% NaCl after One Week of Atmospheric exposure

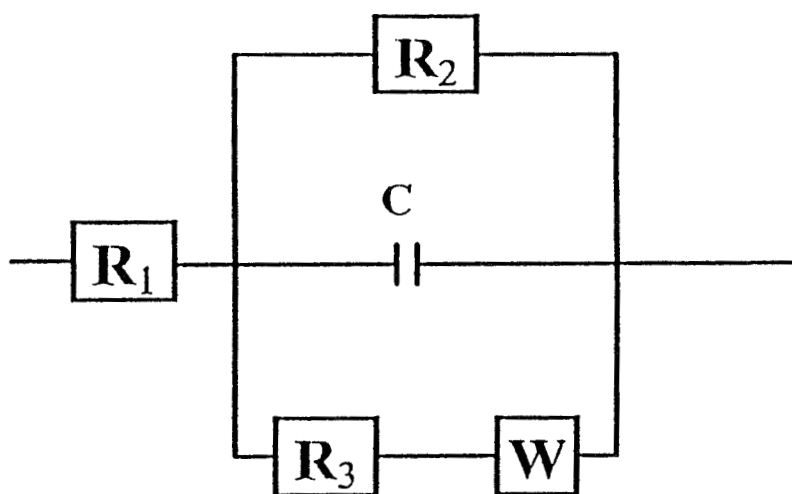


Figure 5. Equivalent Circuit Used to Fit Impedance Data of Inorganic Zinc-Rich Primers

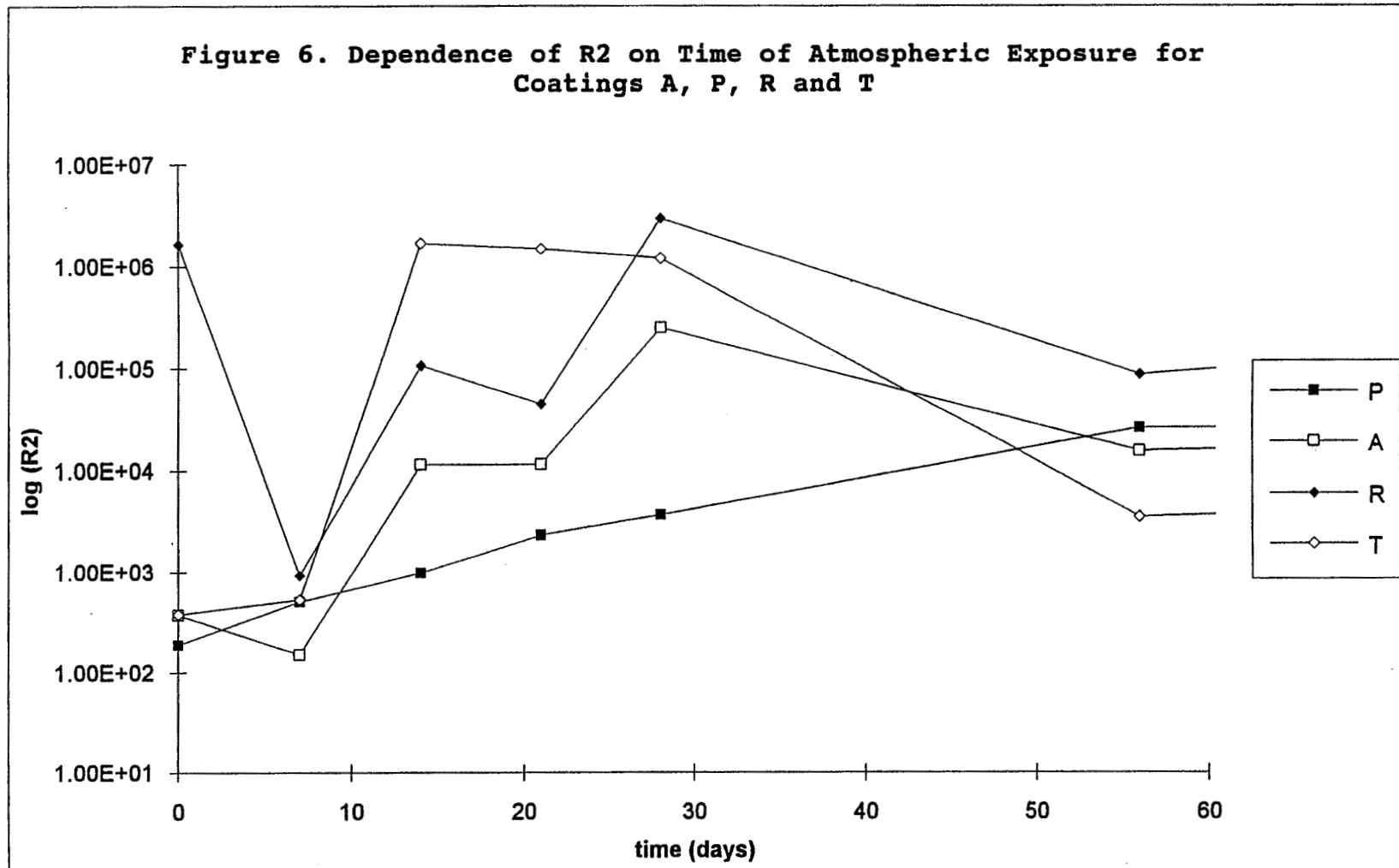
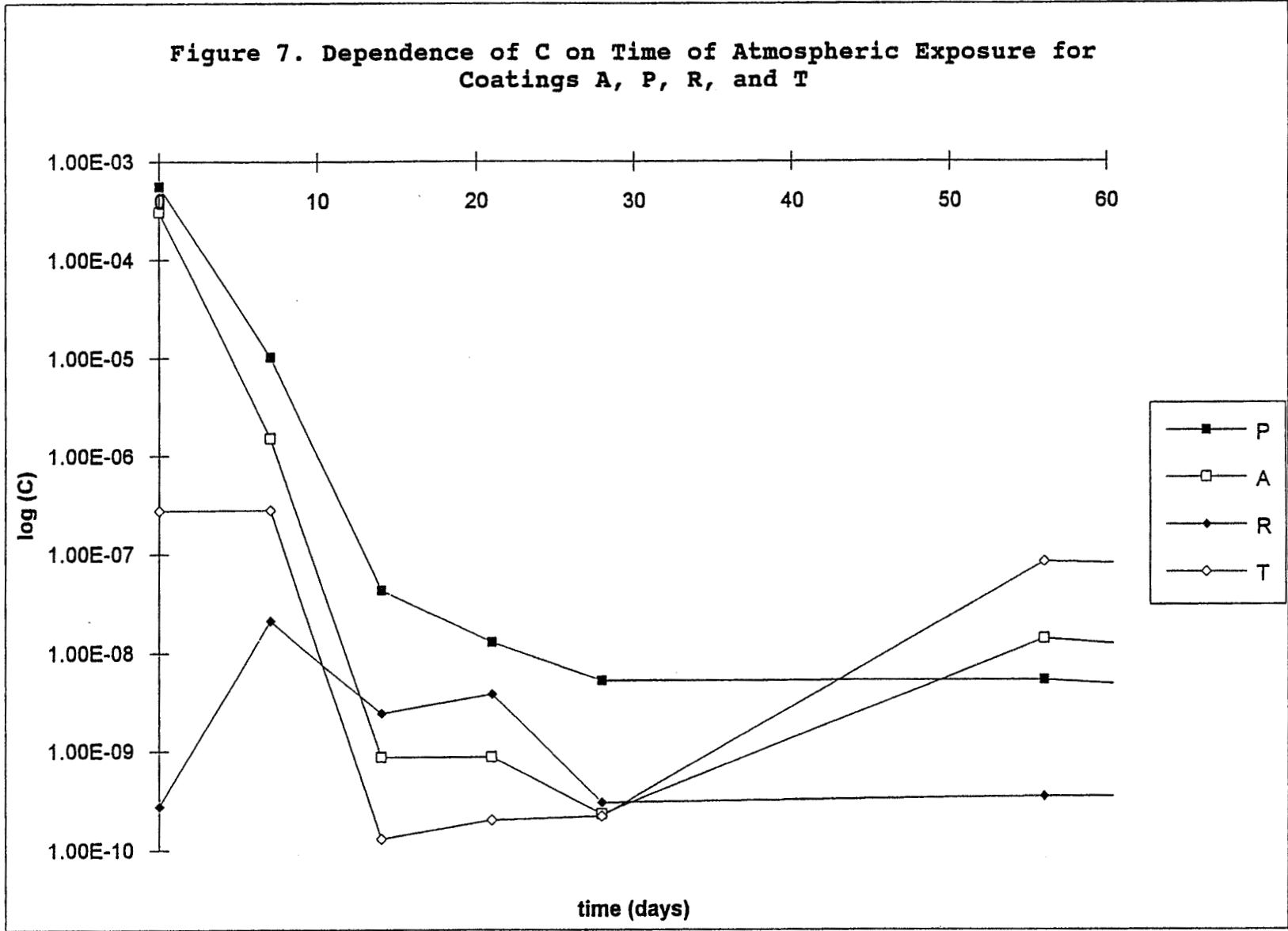


Figure 7. Dependence of C on Time of Atmospheric Exposure for Coatings A, P, R, and T



IV. REFERENCES

- ¹L. G. MacDowell, Evaluation of Protective Coating Systems for Carbon Steel Exposed to Simulated SRB Effluent After Eighteen Months of Seacoast Exposure, Document No. MTB-268-86B, NASA, Kennedy Space Center, Materials Testing Branch, February 16, 1988.
- ²L. G. MacDowell, Status Report on Protective Coating Systems for Carbon Steel Exposed to Simulated SRB Effluent - 36 Month Exposure, Document No. MTB 268-86C, NASA, Kennedy Space Center, Materials Testing Branch, September 19, 1989.
- ³L. G. MacDowell, Volatile Organic Content (VOC) Compliant Coating Systems for Carbon Steel Exposed to the STS Launch Environment - Application, Laboratory and 18 Month Exposure results, Study No. 93-2004, NASA, Kennedy Space Center, Materials Testing Branch, February 22, 1993.
- ⁴L. G. MacDowell, L. M. Calle, Evaluation of High Performance Metal Alloys in the STS Launch Environment Using Electrochemical Impedance Spectroscopy, Document No. MTB-610-89A, NASA, Kennedy Space Center, Materials Testing Branch, August 16, 1990
- ⁵C. Ontiveros, L. G. MacDowell, Electrochemical Impedance Spectroscopy for Evaluating Inorganic Zinc Rich Primers on Steel in the STS launch Environment, Interim Report, Document No. 91-4336, NASA, Kennedy Space Center, Materials Testing Branch, July 31, 1991.
- ⁶L. M. Calle, Evaluation of Inorganic Zinc-Rich Primers Using Electrochemical Impedance Spectroscopy, NASA/ASEE research Reports, NASA CR-194678, E. R. Hosler, Ed., October 1993.
- ⁷S. Feliu, R. Barajas, J. M. Bastidas and M. Morcillo, J. Coatings Technol. **61**, 63 (1989).
- ⁸S. Feliu, R. Barajas, J. M. Bastidas and M. Morcillo, J. Coatings Technol. **61**, 71 (1989).
- ⁹L. G. MacDowell, Final Report on Protective Coating Systems for Carbon Steel Exposed to Simulated Solid Rocket Booster (SRB) Effluent -60 Month Exposure, Report No. 91-4821, NASA, Kennedy Space Center, Materials Testing Branch, October 18, 1991.
- ¹⁰N.A.C.E, RP-01-69, RP-05-75, RP-06-75, RP-01-76, U.S.A.
- ¹¹B. Boukamp, Equivalent Circuit Programme, University of Twente, Netherlands.

¹²S. E. Faidi, J. D. Scantlebury, P. Bullivant, N. T. Whittle, and R. Savin, *Corrosion Science*, 35, 1319 (1993).

¹³L. G. MacDowell, L. M. Calle, *Evaluation of Inorganic Zinc-Rich Primers Using Electrochemical Impedance Spectroscopy (EIS) in Combination with Atmospheric Exposure*, Document No. MTB-94-2082, NASA, Kennedy Space Center, Materials Testing Branch, (in preparation).

1994 NASA/ASEE SUMMER FACULTY FELLOWSHIP PROGRAM

111756

JOHN F. KENNEDY SPACE CENTER
UNIVERSITY OF CENTRAL FLORIDA

55-82
33965 24
P-25
357464

ASSESSMENT OF THE SFC DATABASE FOR ANALYSIS AND MODELING

PREPARED BY:	Dr. Martha A. Centeno
ACADEMIC RANK:	Assistant Professor
UNIVERSITY AND DEPARTMENT:	Florida International University Industrial & Systems Engineering Department
NASA/KSC	
DIVISION:	TP-OAO
BRANCH:	
NASA COLLEAGUE:	Amanda Mitskevich
DATE:	August 18, 1994
CONTRACT NUMBER:	University of Central Florida NASA-NGT-60002 Supplement: 17

ACKNOWLEDGMENTS

I would like to acknowledge and thank you the following person for making this summer experience a reality: Kari Stiles, Amanda Mitskevich, Timothy Barth, William Bastedo, and anyone else who contributed to make my appointment reinstatement possible.

To the former TP-OAO staff: Amanda, Bill, JoAnn, Kathy, Laura, and Tim **GRACIAS!!** Thanks are specially given to Amanda for keeping me on my toes with her questions, and for re-directing me with her insightful comments. Thank you, Boss!☺

TABLE OF CONTENTS

	Acknowledgments	ii
	List of figures	iii
	List of tables	iv
1.	Introduction	1
2.	SFC records that need to be updated	2
3.	Setting up historical summaries	6
4.	Continuous gathering of historical summaries	15
4.1.	Updating cleaning statistics	16
4.2.	Cleaning downloaded files	17
4.3.	Multiple flow basic summaries - work	17
4.4.	Single flow basic summaries - delays	18
5.	Preparing inputs for SCRAM	19
6.	The SMART Prototype	20
7.	Results and Recommendations	20

LIST OF FIGURES

No.		Page
1	Distribution of <i>tasks worked</i> records	3
2	Distribution of <i>delays</i> records	3
3	Distribution of <i>wad_type</i> in <i>tasks worked</i> records	3
4	Distribution of <i>wad_type</i> in <i>delays</i> records	3
5	Distribution of wads with inconsistencies in <i>partn</i> per <i>depch</i>	5
6	Distribution of wads with inconsistencies over time	5
7	Frequency of wads with inconsistencies over time per OPF	6
8	Deleted Records - Tasks Worked	8
9	Deleted Records - Delays	8
10	Deleted Records - Tasks Worked Per OPF	8
11	Deleted Records - Delays Per OPF	8
12	Deleted Records - Tasks Worked Per Criterion	9
13	Deleted Records - Delays Per Criterion	10
14	Layout for multiple flow file	12
15	Sample of multiple flow basic summaries	13
16	Example of naming problem	13
17	Frequency and accumulated time - STS-56	14
18	Frequency and accumulated time - STS-57	14
19	Frequency and accumulated time - STS-58	14
20	Layout for delays - Single flow	15
21	Layout of SCRAM Input File	19

LIST OF TABLES

No.		Page
1	Tasks Worked and Delays records in ACTVEMPL per sts_no	2
2	Number of orphan records per flow	8
3	Records with one blank space in sts_no	8
4	Key to Table #2	9
5	Name of queries to extract data per flow	13
6	Cleaning results - tasks worked	14
7	Cleaning results - delays	16
8	Sample flows for multiple flow comparison	17

1. INTRODUCTION

This effort is a continuation of the one initiated during the summer of 1993, concerning the utilization of the SFC data. During the summer of 1993, we discovered the actual configuration of the SFC database and found out the several aspects of the data entry process; i.e. the actual *form* of the SFC database. This summer we set out to do some actual analysis with the SFC contents. In order to do that, however, we had to know the *actual values* that are being stored in the SFC database.

SFC is one of the four clusters that make up the Integrated Work Control System (IWCS), which will integrate the shuttle processing databases at Kennedy Space Center (KSC). The IWCS framework will enable communication among the four clusters and add new data collection protocols. The Shop Floor Control (SFC) module has been operational for two and a half years; however, at this stage, automatic links to the other 3 modules have not been implemented yet; except for a partial link to IOS (CASPR). SFC revolves around a DB/2 database with PFORMS acting as the database management system (DBMS). PFORMS is an off-the-shelf DB/2 application that provides a set of data entry screens and query forms. The main dynamic entity in the SFC and IOS database is a *task*; thus, the physical storage location and update privileges are driven by the status of the WAD. Complete discussion of the 1993 effort is found in the report "*Issues Regarding Data Collection, Data Extraction, and Data Analysis*" by Centeno and Colucci (1993).

As we explored the SFC values, we realized that there was much to do before actually engaging in continuous analysis of the SFC data. Half way into this effort, it was realized that full scale analysis would have to be a future third phase of this effort. So, we concentrated in *getting to know the contents* of the database, and in *establishing an initial set of tools* to start the continuous analysis process. Specifically, we set out to

1. Provide specific procedures for statistical models, so as to enhance the TP-OAO office analysis and modeling capabilities
2. Design a data exchange interface
3. Prototype the interface to provide inputs to SCRAM
4. Design a modeling database

These objectives were set with the expectation that, if met, they would provide former TP-OAO engineers with tools that would help them demonstrate the importance of process-based analyses. The latter, in return, will help them obtain the cooperation of various organizations in charting out their individual processes.

Sections 2 and 3 address most of the issues that raised new questions regarding the contents of SFC's database, and their impact on analysis. Sections 4, 5, and 6 describe the initial set of tools developed. Section 8 summarizes results and recommendations.

2. SFC RECORDS THAT NEED TO BE UPDATED

As part of the data retrieval process, it was found that many records do not have complete information. Although this situation is relatively normal in a software system of the magnitude of SFC, it must be corrected in as much as possible. It has been found, for instance, that there are approximately 111,000 ! ⊗ *tasks worked* (ACTTRNID = '31') records which have either a null, a non-printable character, a 0, or a blank space in the STS_NO field of the ACTVEMPL table. In the early stages of SFC implementation, there was no STS_NO field in the table; it was added later on. A similar situation was found for *delays* records. Furthermore, since some of the analyses will be done on a "per wad type" basis, the completeness of ACTVEMPL on the WAD_TYPE field was checked. It was found that 26% of the *tasks worked* records and 41% of the *delays* records do not have a value in this field. Identifying the wad type is a feasible, yet cumbersome task that, at this time, may not be worth pursuing because losing those *wad_type*-less records will not have an adverse effect on the various analyses (Figures #3 and #4).

Table #1 gives a tally of the *tasks worked* and *delays* records in ACTVEMPL (as of July 6, 1994) for each one of the flows, including those unidentified flows. It can be seen from this table that about 111,000 (~42%) *tasks worked* records belong to *unknown* flows (Figure #1). Similarly, only 887 records were found to belong to STS-52 and STS-53 combined, which is an abnormally low value for completed flows. Similarly, 53% of *delays* records (Figure #2) belong to *unknown* flows.

Table #1: TASKS WORKED and DELAYS records in ACTVEMPL per STS_NO

STS_NO	COUNT() for tasks worked	COUNT() for delays	STS_NO	COUNT() for tasks worked	COUNT() for delays
	159	9216	56	9956	1119
<i>weird</i>	1		57	11455	1010
—	2		58	15581	1208
	71066		59	12953	580
<i>weird</i>	1		60	16471	954
<i>TBD</i>	2270	206	61	19321	893
0	41870	2051	62	13278	635
5	5	1	63	132	2
15	7		64	11499	525
16	3		65	14734	656
17	4		66	3605	225
18	1		67	4	
19	6		68	8717	407
47	1093	3	69	4	
51	12284	987	73	34	1
52	739	4			
53	166	3			
54	2359	50			
55	7989	895	Grand Total	277,769	21,631

Figure #1: Distribution of *tasks worked* records

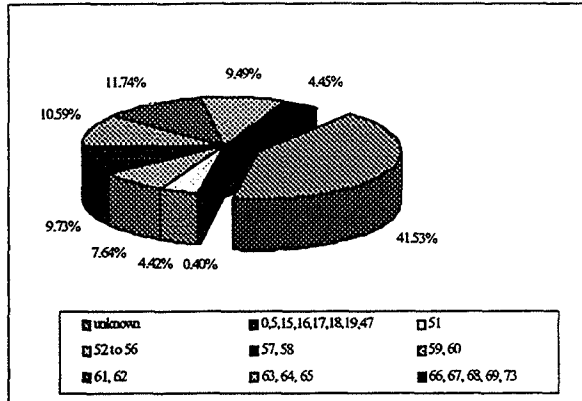


Figure #2: Distribution of *delays* records

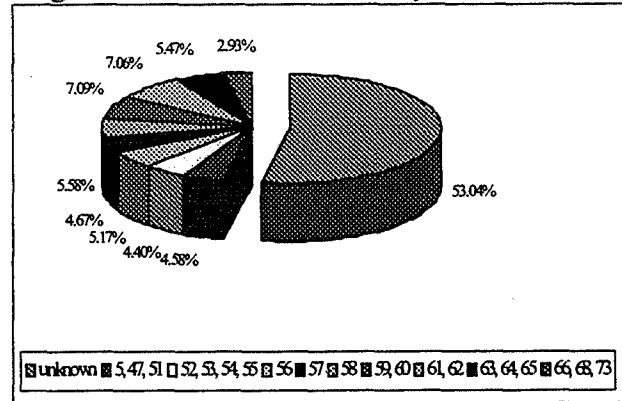


Figure #3: Distribution of *wad_types* in *tasks worked* records

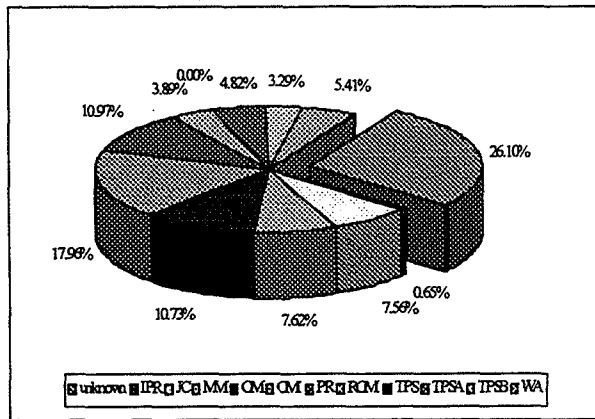
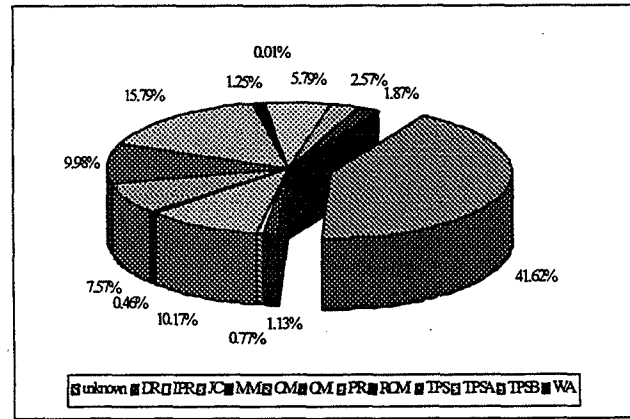


Figure #4: Distribution of *wad_type* in *delays* records



To identify the *flow-less* records, a series of queries have been run against ACTVEMPL (KSC3) using the dates of each flow at the OPF (Table #3). The results of these queries have been summarized in Table #2. About 70,000 of these flow-less records have one blank space or a '000' in STS_NO. However, there are records from 1993 and 1994 that have a '000' in the STS_NO field. The latter situation should not be occurring especially since the software has been upgraded to automatically download the *sts_no* from IOS.

Sometimes an orbiter is processed at two OPF facilities. To keep track of the data downloaded for each facility, Table #3 assigns a sequential key to each *flow/OPF* pair to be used in Table #2.

A counting query was issued to check how many of the records with '000%' in STS_NO were *notes or remarks*. This was done to assess whether the extra mainframe processing time was worthwhile, or if these records could be easily removed using a PC-based tool (e.g. Excel 5.0 or a Visual Basic (or C) program). A comment on the subject of notes is that their entry in the database does not seem to be consistent with the overall design of SFC. ACTVEMPL contains various types of records: tasks worked, delays, and so forth. Each transaction has a different

value for *acttrnid*, yet when it comes to *notes*, they get the same *acttrnid* as *tasks worked*.

Table #2: Number of orphan records per flow

Key	flow	Tasks Worked		Delays	
		records with sts_no = ''	records with sts_no = '000'	records with sts_no = ''	records with sts_no = '000'
4	sts-49	---	---	---	---
2	sts-46	2112	---	188	---
7	sts-52	7751	---	918	---
10	sts-54	5773	---	563	---
1	sts-45	2	---	---	---
8	sts-53	10728	---	1964	---
11	sts-55	2158	13	360	3
5	sts-50	2386	---	904	---
3	sts-47	7988	---	1034	---
9	sts-53	6607	---	1071	---
13	sts-57	---	10	---	---
6	sts-51	---	19	---	1
16	sts-61	---	59	---	5
	Total	45,505	101	7,002	9

Table #3: Key to Table #2¹

Key	flow	orbiter	OPF	Dates at OPFs		Dates at VAB & Pad	
				In	Out	In	Out
1	sts-45	OV-104	2	1-Dec-91	13-Feb-92		
2	sts-46	OV-104	1	3-Apr-92	5-Jun-92		
3	sts-47	OV-105	3	1-Jun-92	16-Aug-92	17-Aug-92	12-Sep-92
4	sts-49	OV-105	1	1-Dec-91	7-Mar-92	7-Mar-92	9-May-92
5	sts-50	OV-102	3	9-Feb-92	30-May-92		
6	sts-51	OV-103	3	16-Apr-93	24-Jun-93	24-Jun-93	12-Sep-93
7	sts-52	OV-102	1	10-Jul-92	20-Sep-92		
8	sts-53	OV-103	2	17-Feb-92	8-Aug-92		
9	sts-53	OV-103	3	17-Aug-92	3-Nov-92		
10	sts-54	OV-105	1	21-Sep-92	23-Nov-92	23-Nov-92	13-Jan-93
11	sts-55	OV-102	2	12-Nov-92	27-Jan-93		
12	sts-56	OV-103	3	9-Dec-92	3-Mar-93	3-Mar-93	8-Apr-93
13	sts-57	OV-105	1	19-Jan-93	24-Mar-93	24-Mar-93	21-Jun-93
14	sts-58	OV-102	2	6-May-93	12-Aug-93	12-Aug-93	7-Oct-93
15	sts-59	OV-105	1	13-Dec-93	15-Mar-94	15-Mar-94	9-Apr-94
16	sts-61	OV-105	1	1-Jul-93	21-Oct-93		
17	sts-62	OV-102	2	1-Nov-93	27-Jan-94	27-Jan-94	24-Feb-94
18	sts-65	OV-102	2	10-Mar-94	21-Jun-94	21-Jun-94	7/8/94

¹ Dates were taken from Volume II of Schedule and Status Summary Enhancement Analysis KSC Processing Summary Data, May 18, 1993. This table should be updated as the flows are processed through the OPF facilities.

In reviewing extracted data for *tasks worked* and *delays*, it was found that some wads have a *blank* space in their name (PARTN), or they have a double hyphen ('--'). The rule of the majority seems to indicate that these cases are not supposed to exist. A possible reason for this situation is a bar coding error since the error is consistent across the same wad. Specific examples of this situation are given below. In these examples the '^' symbol represents a *blank* space.

V1262.002-C-R0^1	V30-14343-B-R0^1	V9002.10E/2-01^18
V41-10017-B-R0^1	V63-50006-H-R0^1	V5C06.001-B01-R^0
V02-50002-H-R0^1	V1008.001-Q-R0^1	V1165.013-S-R0^1
V9023.001/5-111692-15	APU-4-12-^293	RMS-201-^202-018
V9001^VL^1	V9028/5-092492-02	V9023.001/3-0614
V9045C/3-042693-^^		

The importance of knowing if the names of the wads (*partn*) in SFC are correct is critical to automatically group them for various types of analyses. A wad that differs just by one character in its *partn* field will be considered a different wad. To alleviate this problem, either the contents of SFC must be corrected, or the grouping routines have to be built with pseudo smart grouping capabilities, using a cross referencing table. Since the wads are mostly downloaded from IOS, it seems reasonable that *partn* be corrected directly into the database, so that future occurrences of the wad do not exhibit the same problem. Furthermore, by correcting these discrepancies at the source (database), future software applications will not have to take care of it over and over again.

The high number of wads with inconsistencies in *partn*, led us to run a query to identify all '31' and '37' entries in SFC which contain a "/" or a "\" in *partn* for the OPFs and the VAB/PAD. The results of this query show that there are 7,625 records (as of 8/8/94) under this situation. 97.1% of them are type '31', with the rest being type '37'. Most of these records were posted by the OPFs (94.57%) (Figure #5), with the VAB/PAD posting the other ones. Figure #6 shows the incidence of this situation over time, and Figure #7 shows it per OPF.

Figure #5: Distribution of wads with inconsistencies

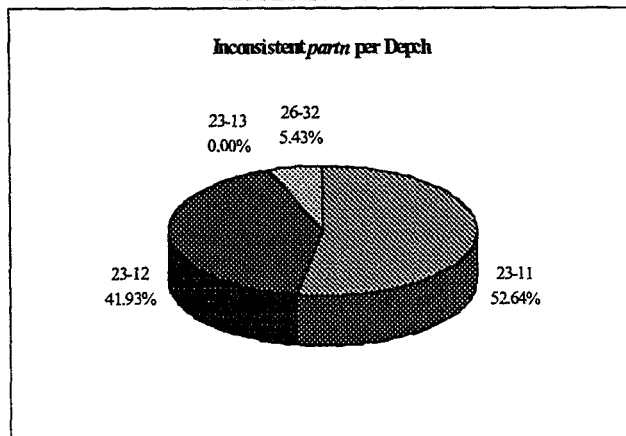


Figure #6: Frequency of wads w/inconsistencies over time

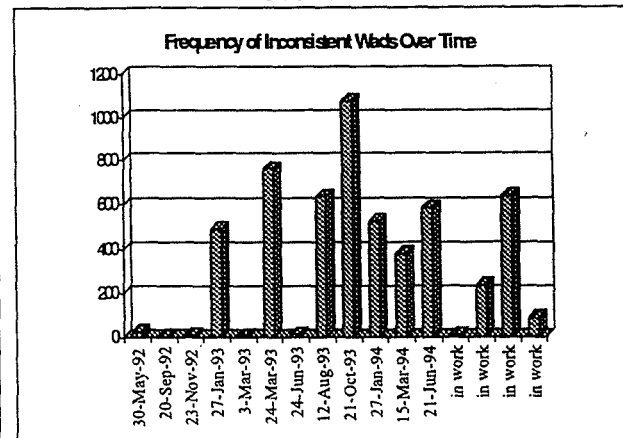
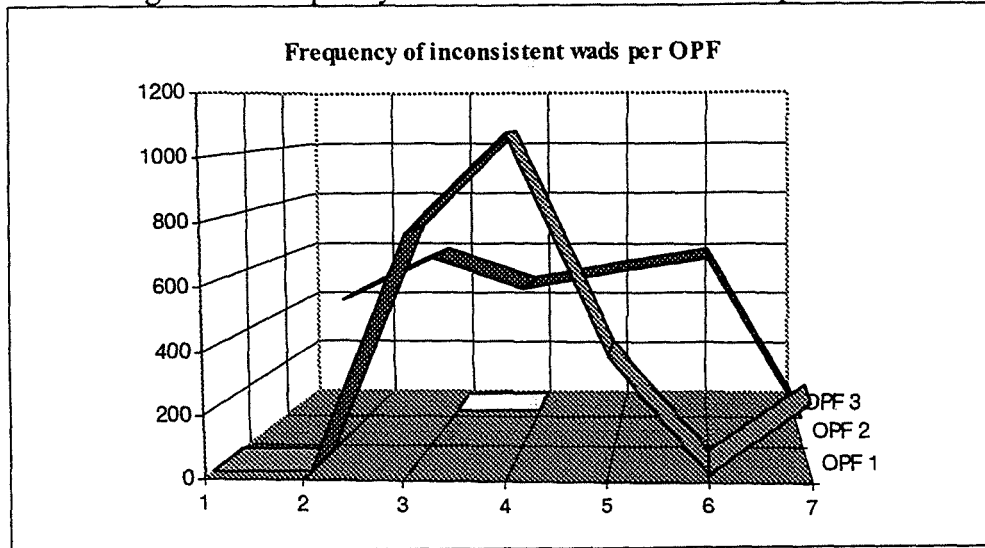


Figure #7: Frequency of wads with inconsistencies per OPF



It is clear from Figure #7 that for some unknown reason, OPFs 1 and 2 have a higher incidence of discrepancies with the value for *partn*. This needs further investigation.

4. SETTING UP HISTORICAL SUMMARIES

This section describes an initial set of historical summaries for each one of the shuttle flights for which there was data. Summaries are for both *delays* as well as *tasks worked* records.

Setting up these initial set of summaries, and enabling the mechanisms to make it a continuous process, required a thorough exploration of the SFC database contents. This exploration helped us to better understand how to manipulate the SFC data, but at the same time, like any other exploration, it raised new interesting questions.

It was learned that, confidence aside, many of the records in the SFC database cannot be used for analysis. Specifically, it was found that many '31' and '37' type entries

1. were done as *trial* records. During the early stages of implementation, engineers at various facilities needed to practice with the system, so they entered records which have a *non-wad* value in *partn*.
2. were not logged off until months later or were never logged off. In the beginning the technicians were not given the appropriate training to deal with the system. This resulted in very *long* or *negative* delay and work duration.

3. were not updated appropriately when converted from a type '31' record to a type '37' record. Some *delay* records show a "CD", "SQ" or other invalid delay code in *p_sub_stat*, which should represent the delay category in a type '37' record.
4. seem to have been entered accidentally. Their delay or work duration is less than one minute.
5. are *notes* or *remarks*.

Some of these problems can be readily overcome by conditioning the query (e.g. **where partn not like "%NOTE%"**.) The other ones have to be taken care of once the data has been imported into Excel 5.0. The following criteria has been implemented in the Excel 5.0 templates to get rid of non-useful records:

tasks worked (type '31')

1. TIME ELAPSED BETWEEN TECHNICIANS *CLOCKING OUT* OF THE TASK IS MORE THAN 7 HOURS. $\{\max(sdate+stime) - \min(sdate+stime)\} > 7 \text{ hours}$
2. TIME ELAPSED BETWEEN TECHNICIANS *CLOCKING IN* OF THE TASK IS MORE THAN 7 HOURS. $\{\max(actcdate+actctime) - \min(actcdate+actctime)\} > 7 \text{ hours}$
3. WORKED TIME IS LESS THAN 10 MINUTES (INCLUDING NEGATIVE). $\{\max(sdate+stime) - \min(actcdate+actctime)\} < 0.167 \text{ hours}$
4. WORKED TIME IS MORE THAN 60 DAYS $\{\max(sdate+stime) - \min(actcdate+actctime)\} > 1440 \text{ hours}$
5. RECORD IS A TRIAL RECORD. TRIAL RECORDS HAVE A NUMBER AS THE FIRST CHARACTER AND A "-" AS THE SECOND CHARACTER OF *PARTN* **examples:** 2-111692-5
3-011293-6
6. THE *CLOCK OUT* DATE IS 2 OR MORE DAYS AFTER THE ROLL OVER DATE. $\max(sdate+stime) > \text{roll over date} + 2$

delays (type '37')

1. DELAY CODE IS INVALID. **examples:** null, one blank space, CD, SQ, C24, ACT, SQ, PA, ST, NW
2. DELAY TIME IS LESS THAN 5 MINUTES (INCLUDING NEGATIVE). $(sdate+stime) - (actcdate+actctime) < 0.083 \text{ hours}$
3. DELAY TIME IS MORE THAN 60 DAYS $(sdate+stime) - (actcdate+actctime) > 1440 \text{ hours}$
4. THE *CLOCK IN* DATE IS AFTER THE ROLL OVER DATE. $actcdate+actctime > \text{roll over date}$

5. RECORD IS A TRIAL RECORD.

(See explanation given for *tasks worked*)

Data was downloaded for as many flows as possible. There were only two records for *sts-45*, so no further processing was done for this flow. All queries used to extract data have been stored in *sf0110*. All extracted files are saved on floppy diskettes.

Each extracted file was cleaned up using the criteria given before. It can be stated that the data entry process (overall) has been improving as SFC reaches steady state conditions. This can be seen in Figure #8 (*tasks worked*) and Figure #9 (*delays*). The same thing can be said for each OPF although their individual learning curve differs greatly as shown in Figure #10 and Figure #11.

Figure #8: Deleted records (Tasks worked)

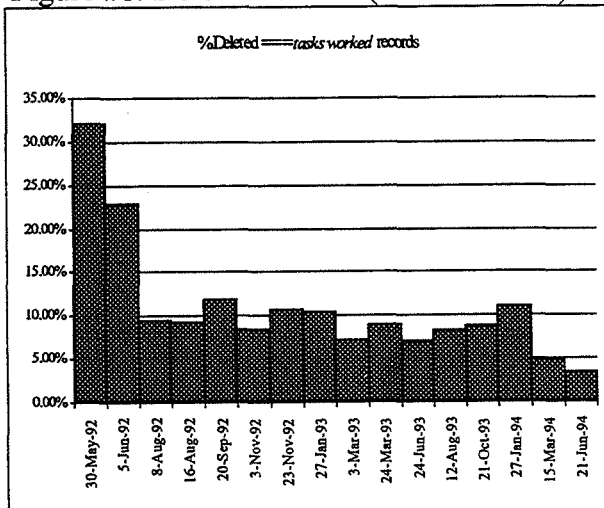


Figure #9: Deleted records (Delays)

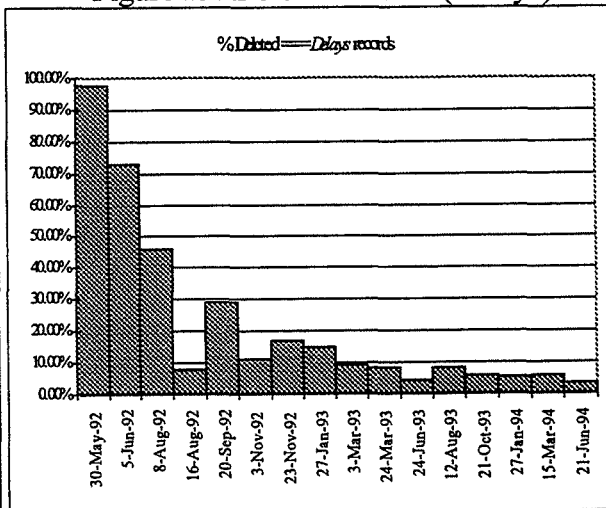


Figure #10: Deleted records (per OPF)

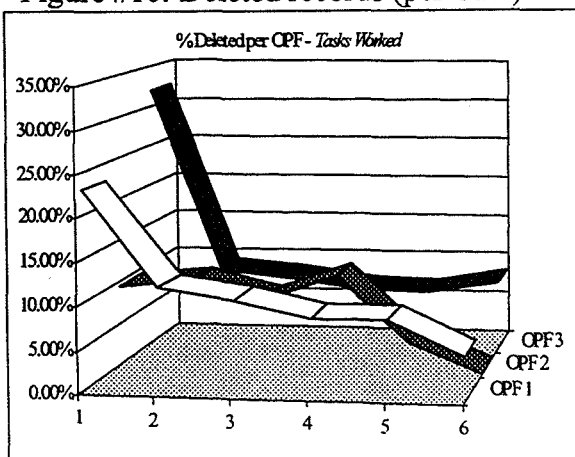
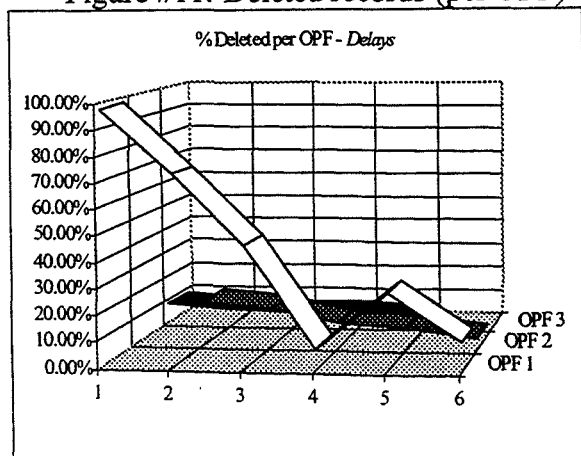


Figure #11: Deleted records (per OPF)

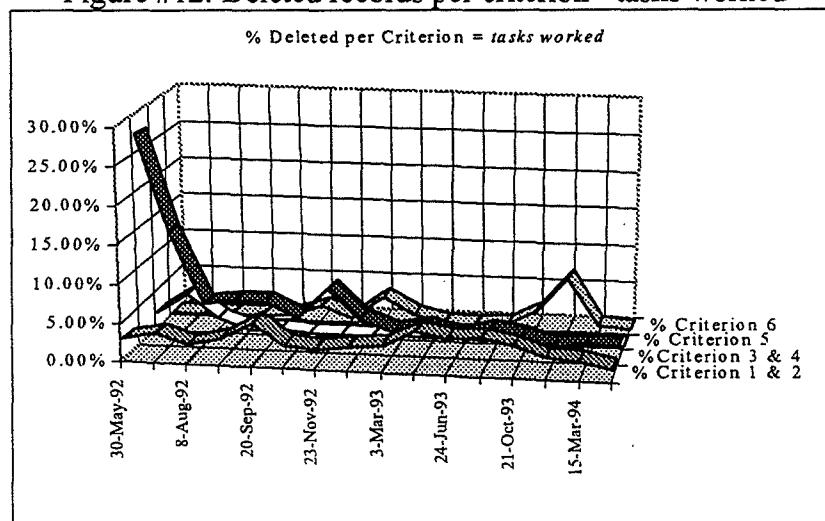


It is interesting to see from Table #4 and Figure #12 how the relevance of each criterion has changed over time. Entries with too small or too large work duration have steadily decreased, whereas technicians clocking in/out at different times for the same task has maintained the same level. The latter may be an indicator for further investigation (*why are technicians clocking in/out at significantly different times for the same task? Are they still using the "assigned" shift of the technicians to update actscode?*). Most of the improvements seen with regards to criterion 1 & 2 and 3 & 4 are mostly due to better training and software improvements respectively.

Table #4: Cleaning results - tasks worked

sts_no	Date Out of OPF	Records left	Criterion 1 & 2	Criterion 3 & 4	Criterion 5	Criterion 6	Total Deleted	% Deleted
sts-50	30-May-92	1223	46	492	38	0	576	32.02%
sts-46	5-Jun-92	1145	51	218	70	0	339	22.84%
sts-53(a)	8-Aug-92	6607	156	405	112	16	689	9.44%
sts-47	16-Aug-92	4508	150	308	0	0	458	9.22%
sts-52	20-Sep-92	4453	270	302	16	10	598	11.84%
sts-53(b)	3-Nov-92	2097	59	93	0	39	191	8.35%
sts-54	23-Nov-92	3201	85	288	1	8	382	10.66%
sts-55	27-Jan-93	3897	116	188	0	145	449	10.33%
sts-56	3-Mar-93	3421	117	106	2	38	263	7.14%
sts-57	24-Mar-93	3128	176	126	1	0	303	8.83%
sts-51	24-Jun-93	782	37	22	0	0	59	7.02%
sts-58	12-Aug-93	4840	242	183	4	3	432	8.19%
sts-61	21-Oct-93	6077	252	189	0	138	579	8.70%
sts-62	27-Jan-94	3768	105	75	0	290	470	11.09%
sts-59	15-Mar-94	3727	84	89	0	17	190	4.85%
sts-65	21-Jun-94	4036	52	83	1	5	141	3.38%

Figure #12: Deleted records per criterion - tasks worked



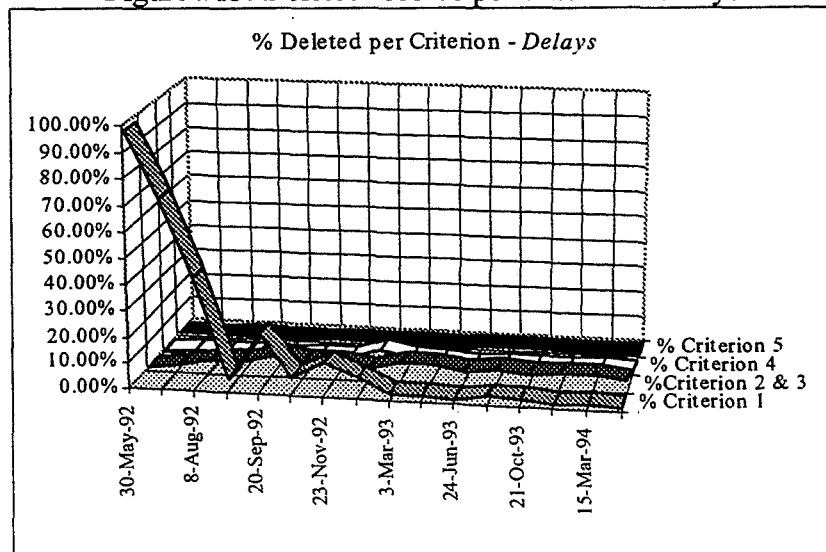
Not surprisingly, criterion #5 (trial records) has maintained a very low profile. What came as a surprise is the rise of the level of criterion 6 (posting entries after the roll over date). Again this must be further investigated.

For delays records, the situation has greatly improved as far as non-usable records are concerned (Table #5 and Figure #13). It must be pointed out, however, that the number of recorded delays seem to be steadily decreasing. This should be a great news if one were confident on the reliability of the data. There are strong reasons to believe that such a decrease is due to willful avoidance of entering delays and not due to an improvement of the shuttle assembly process. This is another issue that needs further investigation.

Table #5: Cleaning results - delays

sts_no	Date Out of OPF	records left	Criterion 1	Criterion 2 & 3	Criterion 4	Criterion 5	Total Deleted	% Deleted
sts-50	30-May-92	22	880	0	0	1	881	97.56%
sts-46	5-Jun-92	51	135	2	0	0	137	72.87%
sts-53(a)	8-Aug-92	1061	831	75	0	0	906	46.06%
sts-47	16-Aug-92	951	36	41	0	0	77	7.49%
sts-52	20-Sep-92	650	207	63	0	1	271	29.42%
sts-53(b)	3-Nov-92	939	64	53	0	0	117	11.08%
sts-54	23-Nov-92	470	68	27	1	0	96	16.96%
sts-55	27-Jan-93	952	78	40	46	0	164	14.70%
sts-56	3-Mar-93	770	13	52	13	1	79	9.31%
sts-57	24-Mar-93	545	9	36	2	0	47	7.94%
sts-51	24-Jun-93	617	2	27	0	0	29	4.49%
sts-58	12-Aug-93	851	21	52	0	0	73	7.90%
sts-61	21-Oct-93	640	13	26	1	0	40	5.88%
sts-62	27-Jan-94	451	1	23	1	0	25	5.25%
sts-59	15-Mar-94	380	3	20	1	0	24	5.94%
sts-65	21-Jun-94	476	0	16	0	0	16	3.25%

Figure #13: Deleted records per criterion - delays



From the cleaning exercise, one must learn whether the data entry process keeps on improving until it reaches a steady state. In a manufacturing setting, the rule of thumb is to accept a batch if it has, statistically speaking, at most π_0 percentage of *defective* (non-usable records in this case). The π_0 value is never more than 10%, with the preferred value being less than 5%. Establishing whether a batch of *products* is acceptable (good batch) is done by taking a sample of size n and using the percentage of defectives (P) found in the sample as the *estimator* of the batch's true percent defective (π). In the SFC case, even though one may think of the *records* being the product to *inspect*, one does not need to sample because the capability for a 100% inspection is readily available. Therefore, one only needs to use the Excel 5.0 templates to find the true π value for the given batch. Once the value of π is known, if it is too high, the reasons for the increase must be investigated. At the same time, if the number of records left is too little, no further analyses can be done for that flow. To update the cleaning statistics, see Section 5.1 of this report.

Tables #4 and #5 clearly show that a great improvement has occurred since the inception of SFC. Because a starting point is needed, it is recommended that any flow yielding at most $\pi = 10\%$ be used to set up and revise analyses. As the SFC software, IWCS, and the data entry process settle, the π value should be revised down until it reaches less than 2%. Putting this rationale to work, the paragraphs below present initial assessment of the following flows: STS-56, STS-57, STS-58. These flows, although chosen arbitrarily, provided the basis to exemplify some of the problems that inconsistent wad naming brings into analysis. More on this later on.

A point of clarification is that the cleaning process does not assess thoroughly the quality of the data entry process; hence, it does not say the whole story regarding the reliability of the data. The cleaning process deals only with records that were actually *entered*. If records of delays, for instance, are not entered, there is no way that the cleaning process herein described will detect that. This cleaning process is done to remove from the data those records that are an obvious data entry error due to a weak implementation of the data entry process.

Due to time constraints, the assessment is limited to gathering basic summaries for these three initial flows. The varied nature of wad work contents, in conjunction with the fact that many wads are unique to a flow, it was decided that only wads which begin with the letter "V" would be taken into consideration to conduct the multiple flow analysis. However, this is not true for generating inputs for SCRAM. SCRAM input file will contain all the wads that experienced a delay, even if they are IPR or PR or TSPB.

Table #6 gives a summary of the historic processing of the three flows. As it can be seen, each one of these flows was processed at a different OPF (1, 2, and 3), and each involved a different orbiter (Columbia, Discovery, and Endeavour). Time constraints prevented a multiple flow analysis where the orbiter (or the OPF) was the same; however, this kind of summaries can be done by simply choosing the flows for the same OPF.

STS-56 had a total of 2151 *tasks worked* records (for wads starting with a "V") for a total of 737 distinct wads processed. STS-57 had a total 1902 *tasks worked* records for a total of 593

distinct wads processed. STS-58 had a total of 2286 *tasks worked* records for a total of 663 distinct wads. To understand what is meant by distinct wads, keep in mind that a wad may be completed in multiple sessions. Although it is suspected that multiple session may also indicate multiple runs of the same wad (which means the wad suffix should be different), there is no way to know, at the moment, the truth about this situation until the data entry processes is consolidated. Therefore, the work duration for a wad is the sum of the individual records work duration.

Table #6: Sample flows for multiple flow comparison

STS-56	Orbiter:	OV-103	(querya14.dat)	
	OPF	3	Delays Deleted	xx
	Left OPF	3-Mar-93	Tasks Work Deleted	xxx
STS-57	Orbiter:	OV-105	(querya14.dat)	
	OPF	1	Delays Deleted	7.94%
	Left OPF	24-Mar-93	Tasks Work Deleted	8.83%
STS-58	Orbiter:	OV-105	(querya14.dat)	
	OPF	2	Delays Deleted	7.90%
	Left OPF	8-Aug-93	Tasks Work Deleted	8.19%

Given the fact that STS-56 processed 737 wads (set A), STS-57 processed 593 (set B) wads, and STS-58 (set C) processed 663, one might expect to find a great deal of overlapping among set A, b, and C that, when laid out as in Figure #14, the number of rows in that matrix would be no more than a 1,000 (roughly). Unfortunately, this is not the case with these three flows. When the information for the flows was re-arranged as in Figure #14, there were 1516 rows in the matrix. About 1100 of these rows had only one observation; thus, several of the basic statistical summaries (e.g. standard deviation, mode) could not be computed (see Figure #15).

Figure #14: Layout for multiple flow file

<i>partn</i>	<i>flow 1</i>	<i>flow 2</i>	<i>flow n</i>
<i>wad₁</i>	duration ₁₁	duration ₁₂		duration _{1n}
<i>wad_i</i>	duration _{i1}	duration _{i2}		duration _{in}
<i>wad_m</i>	duration _{m1}	duration _{m2}		duration _{mn}

These findings led us to try to include an additional flight, so we included STS-59 (Endeavour, OPF 1). It was found that it had a total of 2219 *tasks worked* records for a total of 703 distinct wad. Yet, despite the fact that the number of wads processed in this flight seems to be a "normal" count, the number of wads in the multiple flow matrix grew from 1516 to 2040, which means that about 75% of the wads in STS-59 were **new wads**. This may be true, but it needs to be further investigated, especially because the naming inconsistencies may be the cause

of this situation. An example is given in Figure #16. Wad V1047 seems to have a date attached to it. What does this mean? Should this be the same wad? Multiple runs of the same wad in the same flow? This situation must be clarified; otherwise, we will keep getting nowhere in our analysis: even with the information from four flows, for only 25% of the records it was possible to compute something as simple as the standard deviation of the work duration.

Figure #15: Sample of multiple flow basic summaries (part 1)

sample size	minimum	maximum	range	standard deviation	arithmetic average	mode	5th percentile	median
1	3.60	3.60	0.00	Can't Compute	3.60	#N/A	3.60	3.60
1	22.98	22.98	0.00	Can't Compute	22.98	#N/A	22.98	22.98
2	8.38	24.30	15.92	11.25	16.34	#N/A	9.18	16.34
1	9.05	9.05	0.00	Can't Compute	9.05	#N/A	9.05	9.05
1	21.98	21.98	0.00	Can't Compute	21.98	#N/A	21.98	21.98
1	0.93	0.93	0.00	Can't Compute	0.93	#N/A	0.93	0.93
1	5.02	5.02	0.00	Can't Compute	5.02	#N/A	5.02	5.02
1	3.67	3.67	0.00	Can't Compute	3.67	#N/A	3.67	3.67
1	18.00	18.00	0.00	Can't Compute	18.00	#N/A	18.00	18.00
1	22.05	22.05	0.00	Can't Compute	22.05	#N/A	22.05	22.05
1	0.92	0.92	0.00	Can't Compute	0.92	#N/A	0.92	0.92

Figure #15: (continued - part 2)

95th percentile	95% C.I. - lower bound	95% C.I. - upper bound	partn	56	57	58
3.60	0.00	0.00	V00-10071-F-R01	3.60		
22.98	0.00	0.00	V00-10072-A-R01			22.98
23.50	0.00	0.00	V00-10072-R01	8.38	24.30	
9.05	0.00	0.00	V02-40002-J-R01	9.05		
21.98	0.00	0.00	V02-50002-H-R01	21.98		
0.93	0.00	0.00	V05-50004-E-R01	0.93		
5.02	0.00	0.00	V070-2-15-153			5.02
3.67	0.00	0.00	V070-2-15-158			3.67
18.00	0.00	0.00	V070-3-16-175	18.00		
22.05	0.00	0.00	V070-5-04-0054		22.05	
0.92	0.00	0.00	V10-00001-B-R01			0.92

Figure #16: Sample of naming problem

V1047 /2-051193-03			4.883	
V1047/3-011993-18	1.783			
V1047/3-021993-12	1.050			
V1047/5-020893-0		6.900		
V1047/5-020894-12			9.750	
V1047/5-022293-0		11.167		
V1047/5-022494-01			2.450	
V1047/5-022594-11			8.467	
V1047/5-031093-0		3.200		
V1047/5-031293-0		8.217		

Delay records for STS-56, STS-57, STS-58 confirm what was long known: the frequency of a delay category does not tell the whole story; rather the accumulated time of such delay category is a better indicator of reality. This can be seen in Figure #17 and #18 where B31 was the delay category with the highest frequency, but it was not the highest contributor to the total stoppage hours in these flows. Figure #19 further confirms this situation, but with another delay category.

Figure #17: Frequency and accumulated time - STS 56

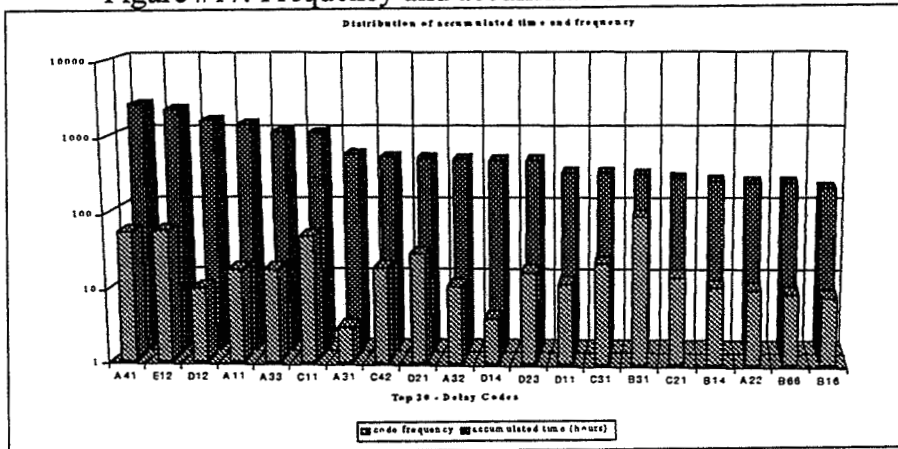


Figure #18: Frequency and accumulated time - STS 57

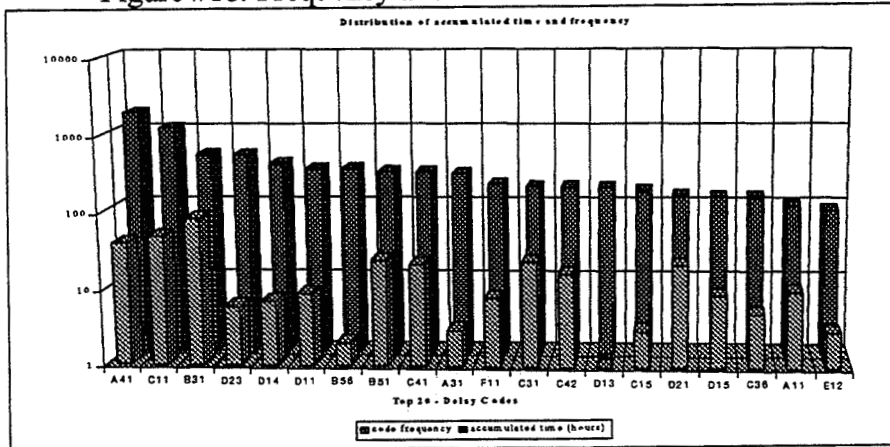
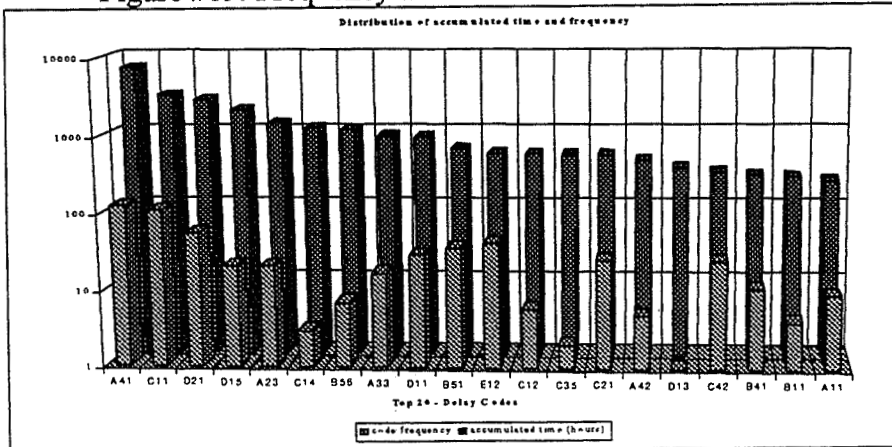


Figure #19: Frequency and accumulated time - STS 58



Based on only these three flows, nothing reliable can be said about the regularity with which delays occurred; however, these types of charts can help in identifying possible bottleneck organizations. One must be careful in drawing conclusions from these charts because the numeric measurement does not necessarily remove the need to improve an organization's process. There is always room for improvement, but most importantly, perception of being a bottleneck must be taken into consideration. An example of this can be found in the *snnndlyb.xls* templates for these flows, under the *logistics* worksheet. Logistics has always been among the organizations with high frequency codes (25% of all the delays count are related to Logistics); yet, Logistics is not the highest contributor to the total number of hold hours (about 10% all delays accumulated time), but Logistics has been perceived as a major bottleneck. This findings were presented to the NASA side of Logistics, and A. Mitskevich has began to collaborate with Logistics, so that they can chart out their process.

Although time did not permit any further analysis, the capability to possibly build probability functions for the top 30 delay categories exists. A third Excel 5.0 template (*snnndlyc.xls*) computes basic summaries of the top 30 delay categories, but because of the way it is laid out (Figure #20), some of its information may be exported as a text, and then imported into SIMAN IV's INPUT module.

Figure #20: Layout for delays - Single flow

<i>code 1</i>	<i>code 2</i>		<i>code 30</i>
<i>duration₁</i>	<i>duration₁₁</i>	<i>duration₁₂</i>		<i>duration_{1n}</i>
<i>duration_i</i>	<i>duration_{i1}</i>	<i>duration_{i2}</i>		<i>duration_{in}</i>
		<i>duration_{m2}</i>		
	<i>duration_{m1}</i>			<i>duration_{mn}</i>

4. CONTINUOUS GATHERING OF HISTORICAL SUMMARIES

The generic process to gather summaries for one OPF-related flight operations consists of 4 macro steps:

1. EXTRACT DATA: After roll over, the OPF is expected to have closed all pending tasks regarding that particular flight. To ensure that all tasks are closed, allow for a couple of days before data is extracted.
 - a) Edit appropriate generic query.
 - b) Run query in QMF

- c) Export results from query to a PC diskette
2. CLEAN EXPORTED FILE: QMF reporting facility adds about 20 rows of heading and formatting information that is needed only if the file is to be printed from the mainframe. It also places information, at the beginning of each line in the resulting set, which identifies the characteristics of the "record". This extra information needs to be removed before any analysis is done. This cleaning can be done using Excel 5.0 or the *clean* option of SMART.
 3. REMOVE NON-USABLE RECORDS: Many records in the SFC database cannot and should not be used in any type of analysis because of data entry problems. Some of the data entry problems can be readily detected from the data itself, so the Excel 5.0 templates *snnnrka.xls* and *snnndlya.xls* should be used to applied the appropriate criteria. More on this step later in this section.
 4. COMPUTE BASIC SUMMARIES: The basic summaries are done by using the various Excel 5.0 templates and the SMART prototype
 5. CONDUCT FURTHER ANALYSIS: This may be done by using the SMART interface, if and when fully implemented. The actual analysis will depend on the objective of the modeling activity.

4.1. Updating the Cleaning Statistics

Updating the cleaning statistics requires some manual data transfer. This could be later automated if the SMART concept is further pursued. In the mean time, use the *cleansfc.xls* production Excel 5.0 file. These file has four worksheets named tasksworked, delays, chartswork, and chartsdelay. The name of the worksheets is self explanatory as far as what they contain. This is what needs to be done:

1. As you interact with the template *snnnrka.xls* and *snnndlya.xls*, write down how many records were deleted with each criterion.
2. Write down how many records were left after the cleaning exercise.
3. Open the *cleansfc.xls* production file. Enter data accordingly based on the data being *delays* or *tasks worked*.

The *cleansfc.xls* file is setup to handle 26 flows. Except for the charts per OPF, everything is setup to pick up the data as soon as the data is entered in the appropriate place. For the "per OPF" charts, enter the data under the appropriate OPF work area. Charts will be updated automatically.

4.2. Cleaning Downloaded Files

At this point in time, the *clean data* option of SMART has not been implemented, yet data can be processed using Excel 5.0. Every extracted file needs to be "*cleaned*" meaning that any header information that QMF places at the top and left of the data must be removed. It also means that records that are suspected of being "*not useful*" records must be eliminated before any analysis is done.

The *snnnrka.xls* template is designed to clean up the *tasks worked* file downloaded from the mainframe. This template has a series of conditional Excel 5.0 statements to implement the delete criteria (as given in Section 4 of this report) for *tasks worked* records. The first three rows of the template are used for general headings and control data. Beginning column I is where the conditional formulas are entered. Data exported from SFC is to be stored beginning on row 4 of columns A to H. At the same time that this templates cleans the downloaded data, it creates a subset of the data that will, later on, be used to generate inputs for SCRAM.

This template should be used to clean data after a flow, OPF section, has concluded. Detail instructions are in another report submitted to NASA. Once there is a "clean" file of *tasks worked* records. From here, the ScramWorkTime worksheet could be exported (comma delimited) in preparation for the interaction with SMART. However, remember that SCRAM requires a *delays* files too. Cleaning *delays* files is very similar to cleaning *tasks worked*.

The *snnndlya.xls* template is designed to clean up the *delays* file downloaded from the mainframe. This template has a series of conditional Excel 5.0 statements to implement the delete criteria (as given in Section 4 of this report) for *delays* records. The first three rows of the template are used for general headings and control data. Beginning column I is where the conditional formulas are entered. Data exported from SFC is to be stored beginning on row 4 of columns A to H. At the same time that this templates cleans the downloaded data, it creates a subset of the data that will, later on, be used to generate inputs for SCRAM.

This templates is similar in nature to *snnnrka.xls*. Consequently, the instructions to work with this template are very similar. they have been fully detailed in another report submitted to NASA.

4.3. Multiple Flow Basic Summaries

Work records can be used to estimate how long is actually taken to complete a wad. The varied nature of wads, however, does not allow (at the moment) for such estimation directly from the SFC data. Many wads (e.g. IPR, PR) are unique to a flow; thus, there will always be only ONE observation for these wads, across all the flows. Other wads (e.g. OMI) change in contents from flow to flow, which makes them illegible for across flows comparisons. Taking these facts into account, it was decided that, at the moment, only those wads that begin with a "V" would be used. Other types of wads could be added later on.

To conduct the multiple flow basic summaries calculations, you must interact with the *snnnrwka.xls* (already a clean *task work* records file), *snnnrwkb.xls* (already containing the worksheet with wads that begin with "V" only), SMART (to re-arranged all the flows in a single file), and with *snnnrwkc.xls* (a new template onto which you will paste the multiple flow single file).

The *snnnrwkb.xls* is a template that must be used after the files for all the flows to processed have been cleaned. This template must be given a unique name, making sure that no other file is overwritten. This template has an Excel 5.0 condition to eliminate those records with wads not beginning with a "V". It has 3 worksheets: *basetable*, *countofwads*, and *multiflowexport*. The *basetable* is the one that has the conditional excel function to identify if the wad begins with a "V" or not. *CountOfWads* has the necessary conditional Excel 5.0 function to found out how many unique wads were processed in the flow. *MultiFlowExport* has the necessary data columns to be used by the SMART interface in building the multiple flow single file.

The SMART interface has one option on the main menu that refers to *tasks worked*. Under such option, you will find another option that refers to multiple flows. Again, the SMART interface is very straight forward to use.

The *snnnrwkc.xls* is a template that has all the statistical functions to compute the basic summaries across the flows, for each wad. These basic summaries include a confidence interval, which will be computed only if there are enough data points for the wad (more than 5). If there are enough data points, the confidence interval will be computed using the *t-student* distribution for sample sizes less than 25 observations, and it will use the normal distribution otherwise.

Steps to follow have been detailed in another report submitted to NASA.

4.4. Single flow basic summaries -delays

The *snnndlyb.xls* is a template that must be used after the delay file for a flow has been cleaned. This template must be given a unique name, making sure that no other file is overwritten. This template has a series of Excel 5.0 conditions and graphs to summarized the behavior of delays. It also has two worksheets to export data, so that the SMART interface can generate a file to gather basic statistical summaries about each one of the top 30 delay code.

The SMART interface has one option on the main menu that refers to *delays*. Under such option, you will find another option that refers to single flow. Again, the SMART interface is very straight forward to use.

The *snnndlyc.xls* is a template that has all the statistical functions to compute the basic summaries across the codes. These basic summaries include a confidence interval, which will be computed only if there are enough data points for the wad (more than 5). If there are enough data points, the confidence interval will be computed using the *t-student* distribution for sample sizes less than 25 observations, and it will use the normal distribution otherwise.

Details on the interaction are part of another report submitted to NASA

5. PREPARING INPUTS FOR SCRAM

SCRAM is a modeling tool that is being developed by Lumina, Inc. through a SBIR contract. The main purpose of SCRAM is to identify and quantify the contributors to overall costs and schedule risk in a shuttle processing flow. Once the initial model is constructed, SCRAM will use Bayes' Theorem to revise the probabilities of wads experiencing delays and delay duration as data is collected in the SFC database. These revised probability functions are then utilized to update the network of shuttle processing activities, including those activities in the critical path.

Inputs for SCRAM must be provided in a "spread-sheet" like format, with data laid out as shown in Figure #21; therefore, it is necessary to download the data from SFC and process it, so that such format is complied with. Necessary Excel 5.0 templates and Visual Basic routines have been set up to carry out this process. The Visual Basic routine has been incorporated into the SMART (Shop Floor Modeling, Analysis, and Reporting, Tool) prototype.

Figure 21: Layout of SCRAM input file

wad_1	workd ₁	delcod ₁₁	deldur ₁₁	...	delcod _{1k}	deldur _{1k}
wad_2	workd ₂	delcod ₂₁	deldur ₂₁		delcod _{2k+1}	deldur _{2k+1}
:	:	:	:	:	:	:		:
wad_i	workd _i	delcod _{i1}	deldur _{i1}		delcod _{in}	deldur _{in}
:	:	:	:	:	:	:		:
wad_m	workd _m	delcod _{m1}	deldur _{m1}	...	delcod _{mn}	deldur _{mn}		...

There are two possible ways in which the process is initiated: 1) data has just been downloaded from SFC, and 2) data has been downloaded from SFC and it has been cleaned using the Excel 5.0 templates. The inner works of these templates has already been addressed in another section of this report; however, it is necessary to *emphasize* that once the records have been cleaned up, the resulting Excel 5.0 file must be **cleared up** in those cells that have no data (*ScramDelayTime* and *ScramWorkTime* sheets of Excel 5.0 files *snnnwrka.xls* and *snnndlya.xls*). To clear cells up, highlight the appropriate cells, click on edit, clear, all in Excel 5.0.

Details on the interaction are part of another report submitted to NASA

A decision to create the *s65wrka.txt* file was made because when testing the Visual Basic procedure, it was found that many records were not being included in the *s65wrka.out* file. The

reason for delay records not to be included is the lack of at least one matching work record. The initial testing of the Visual Basic routine was done using data for *sts 51* which, for an unknown reason, had a large number of delay records (≈ 350 out of 617) without a matching work record. However, this situation does not seem to be the law of the land because when *sts65* was processed, only 2 delay records (out of 476) were excluded. Appendix C gives samples of the SCRAM input files for *sts-51* and *sts-65*

6. THE SMART PROTOTYPE

The main idea of the S.M.A.R.T. (Shop floor Modeling, Analysis, and Reporting Tool) framework is to have a cohesive and integrated environment that supports analysis and modeling using the SFC data. To avoid re-inventing the wheel, the S.M.A.R.T. framework would use off-the-shelf data processing and analysis tools in as much as possible. Where these tools fail to meet specific requirements, the S.M.A.R.T. framework would integrate customized data processing and analysis routines.

To facilitate various analyses, such as ANOVA test, time series and so forth, the S.M.A.R.T. framework proposes to utilize a database to maintain a history of the analysis results and decisions made. Full implementation of the S.M.A.R.T. framework requires an in-depth study of several issues (such as feasibility of integrating heterogeneous tools in this context, and the development or modification of analysis techniques to better handle the uniqueness of the SFC data), which are beyond the scope of this effort. However, steps toward enabling the *data exchange* capabilities of the S.M.A.R.T. framework have been taken. The data exchange interface was pursued because of the large amount of data that need to be re-arranged, once downloaded from the mainframe, before any kind of analysis can be done (e.g. SCRAM, multiple flows). It is expected that the working option of the S.M.A.R.T. framework will facilitate the processing of these large quantities of information.

The current implementation of the S.M.A.R.T. is limited to read in files exported from Excel 5.0 (comma delimited) and re-arranging these files, with some basic computations (e.g. work time per wad), so that they can be used with other tools. Specifically the following options are operational in the S.M.A.R.T. framework:

The documentation of the prototype can be found in another report submitted to NASA

7. RESULTS AND RECOMMENDATIONS

Results of this effort include:

- A thorough consensus of the completeness (or incompleteness) of the SFC data. We learned that a lot of the data in SFC cannot be used for a variety of reasons, including the

natural evolution of SFC, and misunderstanding of the data entry process on the part of the technicians. We also learned that things have been improving over time.

- An understanding of the ACCESS database management system (DBMS), and its potential as the DBMS of choice for fully designing and developing the modeling database (if so desired)
- An understanding of the Visual Basic programming language, and its potential as development tool for the S.M.A.R.T. (Shop floor Modeling, Analysis, and Reporting Tool) framework.
- A set of Excel 5.0 templates that, in conjunction with Visual Basic routines, enable the "cleaning" of downloaded data, the generation of inputs for SCRAM, across flows descriptive statistics of *tasks worked*, monitoring improvements in the SFC data entry process, gathering of descriptive statistics for delay categories. Further, various files could be exported into SIMAN IV's Input module to establish probability functions for the delay category.
- Last, but not least, once again, Dr. Centeno goes back with a bag full of great experiences to use in her future research and teaching endeavours.

Among the recommendations of this effort are:

- Pursue the update of as many SFC records as possible.
- Request that the *notes* records be given another *acttrnid*, not '31' or '37', and that the existing records be updated.
- Thoroughly investigate the issue of inconsistent *partn*. This is very crucial to accumulate observations.
- Thoroughly investigate why some delays are never put in work.
- Clarify why records are being posted against a flow that has already landed. Take appropriate corrective actions to make this situation disappear.
- Acquire a new computer workstation with at least 24 Mb of RAM, preferably 32 Mb, and with at least 900 Mb of hard disk. This workstation is necessary to maintain a history of the various analyses that will eventually be done.
- Acquire Excel 5.0 as soon as possible. Schedule the acquisition of Visual Basic and ACCESS.

1994 NASA/ASEE SUMMER FACULTY FELLOWSHIP PROGRAM

111757

JOHN F. KENNEDY SPACE CENTER
UNIVERSITY OF CENTRAL FLORIDA

56-47

33966

9-20

35/490

EXPERIMENTS WITH THE MESOSCALE ATMOSPHERIC
SIMULATION SYSTEM (MASS) USING THE
SYNTHETIC RELATIVE HUMIDITY

PREPARED BY:	Dr. Chia-Bo Chang
ACADEMIC RANK:	Associate Professor
UNIVERSITY AND DEPARTMENT:	Texas Tech University Department of Geosciences
NASA/KSC	
DIVISION:	Launch & Landing Projects
BRANCH:	Weather Projects Management
NASA COLLEAGUE:	John Madura
DATE:	August 5, 1994
CONTRACT NUMBER:	University of Central Florida NASA-NGT-60002 Supplement: 17



ACKNOWLEDGEMENTS

I am grateful to the NASA/ASEE Summer Faculty Fellowship Program for this research opportunity at the Kennedy Space Center. I wish to express my appreciation to Dr. L. Anderson, Program Director, and Kari L. Stiles, Administrative Assistant for their help in all administrative and directional aspects of this program, and for arranging many enlightening tours and presentations. Thanks to the University of Central Florida for providing us with faculty ID and allowing us to use the University library and other facilities.

It has been an enjoyable experience to work with John Madura, Chief, Weather Projects Office; Dr. Frank Merceret, Chief of the Applied Meteorology Unit (AMU); Mrs. Faulkenberry. I am indebted to them for providing work space and administrative support. I benefit from many informative conversations with John Madura, in particular, his insight into the impact of weather-related hazards on the Center operations. Dr. Merceret was always available to answer questions concerning the IBM PC operating system.

I am indebted to Dr. John Manobianco of AMU for setting up the MASS preprocessor programs, Ms. Launa Maier of Weather Lab. for lending me her computer, and Mr. Mark Wheeler of AMU for installing OS/2 on the computer. Dr. Manobianco has also provided valuable suggestions during the early preparation of this work.

ABSTRACT

This study is intended to examine the impact of the synthetic relative humidity on the model simulation of mesoscale convective storm environment. The synthetic relative humidity is derived from the National Weather Services surface observations, and non-conventional sources including aircraft, radar, and satellite observations. The latter sources provide the mesoscale data of very high spatial and temporal resolution. The synthetic humidity data is used to complement the National Weather Services rawinsonde observations. It is believed that a realistic representation of initial moisture field in a mesoscale model is critical for the model simulation of thunderstorm development, and the formation of non-convective clouds as well as their effects on the surface energy budget. The impact will be investigated based on a real-data case study using the mesoscale atmospheric simulation system developed by Mesoscale Environmental Simulations Operations, Inc.

The mesoscale atmospheric simulation system consists of objective analysis and initialization codes, and the coarse-mesh and fine-mesh dynamic prediction models. Both models are a three dimensional, primitive equation model containing the essential moist physics for simulating and forecasting mesoscale convective processes in the atmosphere. The modeling system is currently implemented at the Applied Meteorology Unit, the Kennedy Space Center. Two procedures involving the synthetic relative humidity to define the model initial moisture fields are considered. It is proposed to perform several short-range (~ 6 hours) comparative coarse-mesh simulation experiments with and without the synthetic data. They are aimed at revealing the model sensitivities to the changes in the initial moisture conditions. Investigations of these sensitivities should allow us both to refine the specification of the observational requirements, and to develop more accurate and efficient objective analysis schemes. The goal is to advance the MASS modeling expertise so that the model output can provide reliable guidance for thunderstorm forecasting.

SUMMARY

Thunderstorm-related hazards such as hail, lightning, heavy rain, and strong winds represent a major threat to the space shuttle operations at the Kennedy Space Center (KSC). The operational forecasting needs at KSC require an accurate portrayal of mesoscale convective storm environment in the vicinity of the center for the period of 2 to 12 hours. Version 5.5 of mesoscale atmospheric simulation system (MASS) is currently under evaluation at the Applied Meteorology Unit (AMU) for its practicability in providing reliable short-range thunderstorm forecasting. There are many environmental factors influencing the development of thunderstorms. One of the most significant factors is three-dimensional (3-D) moisture structure. For the Florida peninsula, because of the adjacent data sparse waters it is difficult to obtain a realistic initial moisture field for mesoscale modeling from the regular National Weather Services (NWS) rawinsonde and surface observations. An alternative is the use of the so-called synthetic relative humidity (RH). This study examines the impact of the synthetic RH on the MASS model simulation of convective storm environment.

Two procedures involving the synthetic RH in the moisture analysis are considered. One is the approach currently employed at AMU. It invokes a bogus and enhancing procedure to assimilate the synthetic RH data into the objectively analyzed moisture field based on the NWS rawinsonde observations. The bogus RH soundings are derived from the surface and aircraft observations, while the enhancing process is carried out according to the satellite images and radar data. Small scale features as a result of the enhancement are present in the final analysis. The other procedure is to combine the rawinsonde and synthetic RH observations as part of the objective analysis of the moisture field. The second approach is designed to test whether the small-scale features, which are too fine to be resolved in the model, can be suppressed.

It is proposed to construct the 3-D profiles of convection-related humidity parameters including precipitable water, low-level moisture flux convergence, and moist static energy. These parameters are often well correlated temporally and spatially with convective activity; for example, the low-level moisture flux convergence and the resultant rapid increase in precipitable water frequently occur prior to the outbreak of convective storms. It is proposed to examine in detail the differences in the horizontal and vertical profiles of these parameters between the analyses with and without the

synthetic RH. The purpose is to reveal whether the synthetic RH significantly alters the fundamental structure of the humidity field.

It is proposed to perform several short-range (~ 6 hours) comparative experiments using the MASS coarse-mesh (45-km grid interval) model over a domain of 55 by 50 grid points in the horizontal and 20 levels in the vertical. The experiments will include one without and the others with the synthetic RH. It is intended to find out how much information from the synthetic RH observations persists in the first 6 h simulation. RH signals incompatible with the model dynamics could be considerably reduced in a short time period. It is proposed to invoke scale decomposition technique to isolate the model dynamic responses to the inclusion of the synthetic RH data.

The plan was to process and analyze the data using the MASS preprocessor on the IBM personal computer (PC), and to perform the coarse-mesh model simulations on the UNIX-based Stardent 3000 workstation at AMU. However, because of many unexpected difficulties with the preprocessor we were not able to complete the data analysis. One primary cause of the delay is that the PC was not a suitable tool for this work.

TABLE OF CONTENTS

1. INTRODUCTION

2. MODELING SYSTEM

3. PROPOSED WORK

3.1 Analysis

3.2 Diagnosis and Model Experiments

3.3 Scale Decomposition

4. SUMMARY REMARKS

REFERENCES

ABBREVIATIONS AND ACRONYMS LIST

AMU	Applied Meteorology Unit
KSC	Kennedy Space Center
MASS	Mesoscale Atmospheric Simulation System
MCS	Mesoscale Convective System
MDR	Manually Digitized Radar
MESO	Mesoscale Environmental Simulations Operations
NMC	National Meteorological Center
NWP	Numerical Weather Prediction
NWS	National Weather Services
OI	Optimum Interpolation
PBL	Planetary Boundary Layer
PC	Personal Computer
RAM	Random Access Memory
RH	Relative Humidity
SST	Sea Surface Temperature
3-D	Three-Dimensional

I. INTRODUCTION

Meteorological knowledge and operational forecasting techniques were revolutionized during the 1960s by dynamical model forecasting, also known as numerical weather prediction (NWP). Numerical modeling enables us to have a quantitative understanding and prediction of large scale (~1000 km) weather systems. However, NWP has had limited impact on the forecast problems associated with mesoscale convective systems (MCSs). The characteristic scale of convective storms varies from less than 10 km (e.g., isolated cumulonimbus cells) to 100 km (e.g., mesoscale convective complex and hurricane). One of the crucial factors determining NWP model performance in simulating convective storms is the model mesh size. The limitation of large mesh size prevents model from resolving the fine scale structure of MCSs. Consequently, the models cannot respond dynamically to the concentrated latent heat release, which is the principal energy source responsible for the continued existence of MCSs.

Because of the enormous number of calculations involved, the development of supercomputers in the late 1970s made the mesoscale NWP of convective storms practical (Pielke 1984). During the past years, the National Meteorological Center (NMC) and various mesoscale research groups at universities have moved progressively toward finer mesh size in their NWP models. Numerical experiments using the models of mesh sizes ranging from 30 to 100 km have indicated significant improvements in the simulation of MCSs. Recently, the rapid development of inexpensive workstation computers allows atmospheric scientists to conduct mesoscale NWP for research and operational applications aimed at regional meteorological forecasting problems. Advanced workstations are capable of executing complex large-scale model integrations at a comparable speed to that of supercomputers at a much lower cost.

The characteristics and development of mesoscale systems are strongly influenced by the regional environmental conditions. KSC is located in the area dominated by relatively unstable tropical maritime air mass and hence has one of the highest frequency of thunderstorm occurrences in the United States. Slightly upper-air forcings or the sea- and land-breeze circulations often lead to the rapid development of thunderstorms. It has been suggested that KSC has the most lightning strikes per unit area in the whole world. At KSC the most critical issue concerning the weather support to the center operations is the prediction of hazardous conditions (e.g., hail, lightning, heavy rain, and strong

winds) caused by convective storms. In particular, such conditions represent a major threat to the space shuttle launch and landing operations. The regional operational models currently available at the National Meteorological Center (NMC) are not designed for providing thunderstorm-scale forecast. To enhance the weather support, NASA funded Mesoscale Environmental Simulations Operations (MESO) Inc. to develop a version of MASS for operational applications at KSC. The version 5.5 of MASS is recently implemented on the UNIX-based Stardent 3000 workstation and under evaluation for its performance at AMU.

One of the major difficulties associated with mesoscale NWP is model initialization. To have a successful and timely prediction of future atmospheric state for operational forecasting, the present state of the atmosphere must be characterized as accurately as possible. However, the NWS upper-air network with the average spacing of about 400 km and observation frequency of twice per day is not aimed at resolving mesoscale structure. The NWS surface network with the average spacing of about 150 km provides more complete and frequent observations, but the relatively high resolution surface data alone is insufficient for initializing a 3-D mesoscale model. For the Florida peninsula, the problem is further compounded by the lack of data over the adjacent waters.

In order to obtain an improved estimate of model initial state, MASS adopts an approach known as 4-D data assimilation. The approach is designed to blend data of various sources at different spatial and temporal resolutions into a 3-D data set that consists of synoptic-scale as well as mesoscale features desirable for mesoscale model initialization. The data sources include the NWS synoptic upper-air and surface networks, and data taken at asynoptic times such as radar, satellite, and aircraft observations.

This research focuses on the impact of the synthetic RH, a 3-D product of the MASS data assimilation cycle, on the MASS model simulation of convective storm environment in the vicinity of KSC. It is believed that the development and evolution of convection in Florida are strongly influenced by the fine-scale detail in the 3-D moisture structure over the peninsula and surrounding waters. It is intended to address the impact using real-data model simulation experiments on the 2 June 1994 case. The research goal is to improve MASS modeling expertise so that the model output can provide reliable guidance for thunderstorm forecasting.

2. MODELING SYSTEM

Several versions of MASS have been developed since the early 1980s. Version 5.5 currently used at AMU/KSC has two major components, a preprocessor for data processing and analysis, and a dynamic prediction system consisting of coarse-mesh (~ 45 km grid size) and fine-mesh (~ 11 km grid size) models. A brief description of the modeling system summarized from the MASS reference manual (MESO Inc. 1993) is presented below.

2.1 Data Preprocessor

The data preprocessor prepares 3-D gridded fields including temperature, horizontal wind, surface pressure, and humidity for the coarse-mesh model initial state. The following tasks are performed.

- a. Generation of grid and surface characteristics data
- b. Ingestion of atmospheric data
- c. Data analysis and initialization
- d. Synthesizing RH based on indirect observations
- e. Processing of lateral boundary condition data
- f. Preparation of nudging data sets

In Task a, the model domain and grid size are specified. Over land surface parameters include land/water distribution, terrain elevation, and types of canopy at individual grid points are determined. Over the waters, monthly mean sea surface temperature (SST) data is prepared for the use as a first-guess field in the SST analysis. These surface variables specify the lower boundary conditions for the model, and they are also required in the parameterization of the model PBL processes.

In Task b, gridded first-guess fields to be used in objective analysis are prepared. The NWS surface and upper air data, and SST data are checked for errors and written out in a standard format that can be used in Task c. Two options are available for the objective analysis: the optimum interpolation (OI) scheme and the Barnes' scheme. Both schemes, using a linear estimate, interpolate the values of a observed variable at irregularly distributed observation sites to a set of regularly spaced grid points. The linear estimate can be expressed as follow:

$$\phi_a(i,j) = \sum_{k=1}^N w_k \phi_{ok}$$

where $\phi_a(i,j)$ is the analyzed value at grid point (i,j), ϕ_{ok} is the observed value at site k, N is the number of observations. In the current MASS preprocessor, N = 8 indicating that the eight closest stations are involved in defining the gridded value. The principal difference between the two schemes is in the determination of weight functions (w_k) in the linear estimate. The weights are determined using a spatial correlation function derived from raw data in the OI scheme, while the weights are specified in the Barnes' scheme as a function of the distance between the grid point and observations.

In Task d, the synthetic RH is derived from four sources of cloud and precipitation information. They are the NWS surface observations, pilot reports, satellite infrared and visible images, and radar data. The surface observations used to retrieve the vertical profile of RH include the height of clouds (low, middle, high), the cloud coverage (scattered, broken, overcast), and the weather (precipitation, no precipitation, fog). The pilot reports used are the cloud base and top, and sky coverage. The empirical formulae are employed to estimate RH values from the information. Bogus RH soundings are created from the surface observations and the pilot reports. Using the Barnes' scheme, these bogus soundings are merged into the RH analysis obtained from the regular NWS rawinsonde data. Adjustments of the analyzed RH field are then performed based on the satellite images and manually digitized radar (MDR) data. For example, the entire air column for those grid points under deep convective clouds detected in the satellite infrared images will be moistened.

Task e is to generate time-dependent lateral boundary conditions to be used in the MASS model research simulations or operational forecasts. In the case of research simulations of past weather events, the model boundary conditions can be defined from observations. In the forecast mode, one approach is to generate such conditions from global or much larger domain model forecasts. Task f is to prepare nudging data sets for the MASS model 4-D data assimilation, which will not be considered in this research.

The initial and time dependent boundary conditions of the fine-mesh model, usually covering a much smaller area of interest than the coarse-mesh model, are obtained by interpolating the coarse-mesh model simulations onto the fine-mesh model grid points. The boundary conditions provide large-scale forcing for the fine-mesh simulation. This so-called one-way nesting method, which is

relatively simple and straightforward, has been employed by many research groups in studying mesoscale meteorological processes (Anthes 1983; Chang et al. 1981). As mentioned earlier, for this study our interest is in the coarse-mesh model.

2.2 Dynamic Models

The MASS dynamic prediction system is a limited-area multi-level primitive equation model. A complete description of the model equations and physics can be found in the MASS user reference manual (MESO Inc. 1993). The early versions of MASS prediction system were developed in 1980s and have been used in many successful real-data simulation studies (Kaplan et al. 1982; Kaplan et al. 1985; Zack and Kaplan 1987). Major improvements in the model convective parameterization and surface physics were made in 1992.

The model equations are:

- a. Conservation of horizontal momentum,
- b. Hydrostatic equation in the vertical,
- c. Conservation of energy,
- d. Conservation of mass,
- e. Conservation of moisture including water vapor, cloud water, and rain water,
- f. Equation of state.

These equations are formulated in a (x, y, σ_p) coordinate system, in which x and y are Cartesian coordinates on a plane and σ_p (a normalized pressure) is a terrain following vertical coordinate. The six basic grid-scale prognostic variables are the u ($= dx/dt$) and v ($= dy/dt$) components of the wind, temperature, air density, humidity, cloud water content, and rain water content. For most mesoscale models, the basic equations are generally very similar, however, the treatment of physical processes varies considerably among the models.

The model physical processes include:

- a. Surface energy budget,
- b. Solar and infrared radiation,
- c. PBL processes,
- d. Soil hydrology,

- e. Grid scale moisture physics,
- f. Sub-grid moist convective parameterization.

The surface energy budget used to predict the ground temperature involves sensible and latent heat fluxes, solar heating and infrared cooling, and ground heat flux. The effects of cloudiness on the model radiative transfer are considered. The model PBL is divided into the surface layer and mixed layer. In the surface layer, similarity theory is used to determine the eddy mixing coefficients, while in the mixed layer, the K-theory and mass exchange approach are applied in stable and unstable air, respectively. The PBL processes, radiative transfer, and surface heat budget are closely interrelated.

The soil is divided into two layers, a 5-cm layer at the surface and a layer of 5 cm to 30 cm deep below. The model soil hydrology involves the prediction of soil moisture fractions for the two layers as well as the parameterization of moisture reservoir on the surface.

Two methods are available for resolving the grid-scale moist physics: a diagnostic scheme computing latent heating as a function of water vapor mixing ratio and a prognostic scheme preferred in fine-mesh simulations based on the conservation of cloud and rain water. Three different schemes may be invoked for parameterizing sub-grid scale convection. Two are modified Kuo schemes, of which Kuo-MESO incorporates the cloud-scale downdraft plumes, and the third one is the Fritsch-Chappell scheme most suitable for simulating meso- β systems.

The major numerical aspects of the model are as follows:

- a. Arakawa "A" grid in the horizontal and staggered grid in the vertical,
- b. Fourth order centered difference in the horizontal and second order centered difference in the vertical,
- c. Split time integration scheme with a longer timestep used for integrating the advection terms and a shorter timestep for integrating gravity-inertial terms,
- d. Either Kreitzberg-Perkey sponge condition or Orlanski radiative formulation may be applied along the lateral boundaries,
- e. Lateral diffusion to remove short-wave ($2\Delta x$ to $4\Delta x$) oscillations.

3. PROPOSED WORK

3.1 Analysis

Two procedures involving the synthetic RH data to obtain moisture analysis will be adopted. The first is the approach mentioned earlier and currently employed at AMU. It invokes two steps, bogusing and moistening, as summarized in 2.1. Small scale features associated with the satellite infrared and MDR data are present in the final analysis. Example of moisture analyses with and without the synthetic RH is shown in Figs. 1 and 2. Clearly, the first-order discontinuity is indicated in the analysis with the synthetic RH (Fig. 1).

The second procedure proposed by Dr. John Manobianco of AMU is to combine the rawinsonde and synthetic RH including satellite and radar observations as part of the objective analysis of moisture field. This approach is designed to test whether the small-scale features, which are too fine to be resolved in the coarse-mesh model, can be suppressed. However, the author feels that the first procedure in conjunction with spatial smoothing, i. e., applying a digital filter to the gridded field will have the similar effect on eliminating the discontinuity.

3.2 Diagnosis and Model Experiments

The horizontal maps and vertical cross-sections of analyzed humidity fields (e.g. specific humidity) before and after incorporating the synthetic RH will be carefully compared. For a quantitative comparison, a display code capable of mapping the difference fields between the RH analyses will be most useful. The convection-related humidity parameters including the precipitable water, low-level moisture flux convergence, and moist static energy will be computed. These parameters are correlated well temporally and spatially with convective activity; for example, the low-level moisture flux convergence and resultant rapid increase in precipitable water often occur prior to the outbreak of convective storms. Again, differences in the horizontal and vertical profiles of the parameters between the analyses with and without the synthetic RH will be examined. The purpose is to reveal any significant improvements in the basic structure of humidity field when the synthetic RH is invoked.

Several short-range (~ 6 hours) comparative experiments using the coarse-mesh MASS model over a relatively small domain will be conducted. The experiments include one with and the other without the synthetic RH. We like

to find out how much information from the synthetic RH observations persists in the 6 h simulation. The RH signal incompatible with the model dynamics could be considerably reduced in a short time period. Also, we will have an in-depth examination of the thermodynamic and dynamic responses of the model to the enhanced moisture content.

3.3 Scale Decomposition

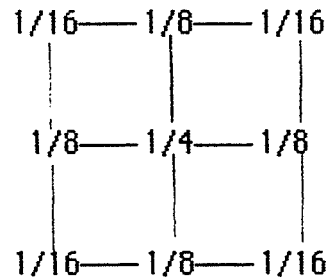
In the model simulated solutions, there exist complex interactions between motions of different scales. Such scale interactions will be further complicated by latent heat release, which is of course directly related to the moisture distribution in the model. The synthetic RH possesses scales different from those of motion and thermal fields derived from the NWS regular networks. The comparisons of model solutions may not explain physically the role of the synthetic RH in the simulations. In order to reveal the true impact the characteristic scales of the synthetic RH have to be identified, and the model simulated motion and temperature fields may be decomposed into selected space-scale ranges using a digital filter. The correlation between the enhanced RH and model responses can then be examined in a more meaningful way.

Figure 2 shows primarily the large-scale RH patterns, while Fig. 1 shows many meso- β scale (on the order of 100 km) features, for example, over the southeastern states and Florida. The circulation of the comparable scale may be generated in the model in response to the mesoscale features. It is also possible that both model simulations regardless of with and without the synthetic RH produce the similar mesoscale circulation. However, whether there is impact can be determined by the relative intensity of such motions between the two model simulations. In this case study, a digital band-pass filter centered around 300 km may be desired to isolated the mesoscale motion field.

A simple 2-D digital filter can be expressed in the following form.

$$\langle Z \rangle_{i,j} = \sum_{L=-n}^n w_L Z_{i+L,j+L}$$

where L is the filter length and $z_{i,j}$ represents a gridded field at point (i,j) , w_L represents smoothing weight factors. For this study, we may set $n = 2$, and the above filter represents a 9-point operator as follows:



where $1/4$, $1/8$, $1/16$ are the weight factors.

The response function of the filter is

$$R(\lambda) = [1 - \sin^4(\pi\Delta/\lambda)]^2$$

where λ is wavelength, Δ grid size. For m number of repeated applications of the filter, the response function will be $R^m(\lambda)$. We can produce two different low-pass filters by choosing two values of m and then isolate any band-pass filter by taking differences between the two low-pass filters. For example, two low-pass filters are made by taking $m = 3$ and 50 which remove the small scale features up to the wavelength of 3Δ and 8Δ , respectively. The difference between the two low-pass filters gives the band-pass filter whose peak response is located near 8Δ with a bandwidth of about 12Δ , i.e., 4 to 16Δ . The waves of length less than 4Δ are not examined because they are suppressed strongly by the fourth-order lateral diffusion.

4. SUMMARY REMARKS

The comprehensive mesoscale modeling system (MASS) and multiple data sources available at KSC provide a unique opportunity to address many pressing issues concerning the weather forecasting support for the space operations. However, this study is intended to focus on the sensitivities of the MASS model simulation of convective storm environment to the use of the synthetic RH. The synthetic RH provides very high resolution data for initializing the model moisture field. Investigations of the sensitivities should help us both to refine the specification of the observational requirements, and to develop more accurate and efficient objective analysis schemes in dealing with multiple sources of observations.

The proposed work is well-defined. We anticipated a certain degree of success. The plan was that using the MASS preprocessor the author performed data processing and analysis on the IBM PC, while Dr. Manobianco performed the proposed coarse-mesh model simulations on the Stardent 3000 workstation at AMU. But the author encountered considerable difficulties during the earlier phase of the work partially due to our inexperience in the PC and MS-DOS operating system.

The MASS preprocessor codes are fairly well structured and documented. However, because of its size and complexity (involving about 50 sub-programs with nearly 5000 lines of codes) to shift the codes from the UNIX-based workstation to the DOS-based PC was indeed a major undertaking for a first-time user of MASS. The 3-D analysis as well as model domain consisted of 55 by 50 grid points in the horizontal and 20 levels in the vertical. The size of grid points was not unusually large for a mesoscale model. Nevertheless, it was discovered unexpectedly that to execute the preprocessor analysis codes required a computer of more than ten megabytes of random access memory (RAM) far exceeding the PC's capacity. Furthermore, after considerable efforts, we eventually realized that with the FORTRAN application programs, MS-DOS did not provide an easy access to the so-called extended memory, which was the bulk of RAM.

We were fortunately able to locate a sixteen megabyte PC in conjunction with IBM Operating System 2 (OS-2). This enabled the author to tackle the preprocessor programs. But the PC was extremely slow in processing the satellite data; it took more than twelve hours to complete one run for the 2 June 1994 case. Also, the machine lacked sophisticated graphics software

(e.g., contouring capability) for displaying the analyzed results. In any event the PC was not a proper tool for MASS; a more advanced computer was needed to carry out the proposed work. Because of many unexpected obstacles and difficulties we have not reached the point of conducting the model simulations.

Finally, the role of high-resolution non-conventional data in mesoscale NWP is a worthwhile research topic. A quantitative understanding of such role is essential to the further improvement of mesoscale model initialization and forecast.

REFERENCES

- Anthes, R. A. 1983: A review of regional models of the atmosphere in middle latitudes. *Mon. Wea. Rev.*, **111**, 1306-1335.
- Chang, C.-B., D. J. Perkey, and C. W. Kreitzberg, 1981: A numerical case study of the squall line of 6 May 1975. *J. Atmos. Sci.*, **38**, 1601-1615.
- Pielke, R. A., 1984: *Mesoscale Meteorological Modeling*. Academic Press, 612 pp.
- Kaplan, M. L., J. W. Zack, V. C. Wong, and J. J. Tuccillo, 1982: Initial results from a mesoscale atmospheric simulation system and comparisons with an AVE-SESAME I data set, *Mon. Wea. Rev.*, **110**, 1564-1590.
- Kaplan, M. L., J. W. Zack, V. C. Wong, and J. J. Tuccillo, 1985: The interactive role of subsynoptic scale jet streak and planetary boundary layer adjustments in organizing an isolated convective complex, *Mon. Wea. Rev.*, **113**, 2212-2238.
- MESO, Inc., 1993: MASS Version 5.5 Reference Manual. MESO, Inc., 185 Jordan Road, Troy, NY 12180, 120 pp.
- Zack, J. W., and M. L. Kaplan, 1987: Numerical simulation of the subsynoptic features associated with the AVE-SESAME I Case, Part I: The preconvective environment, *Mon. Wea. Rev.*, **115**, 2367-2394.

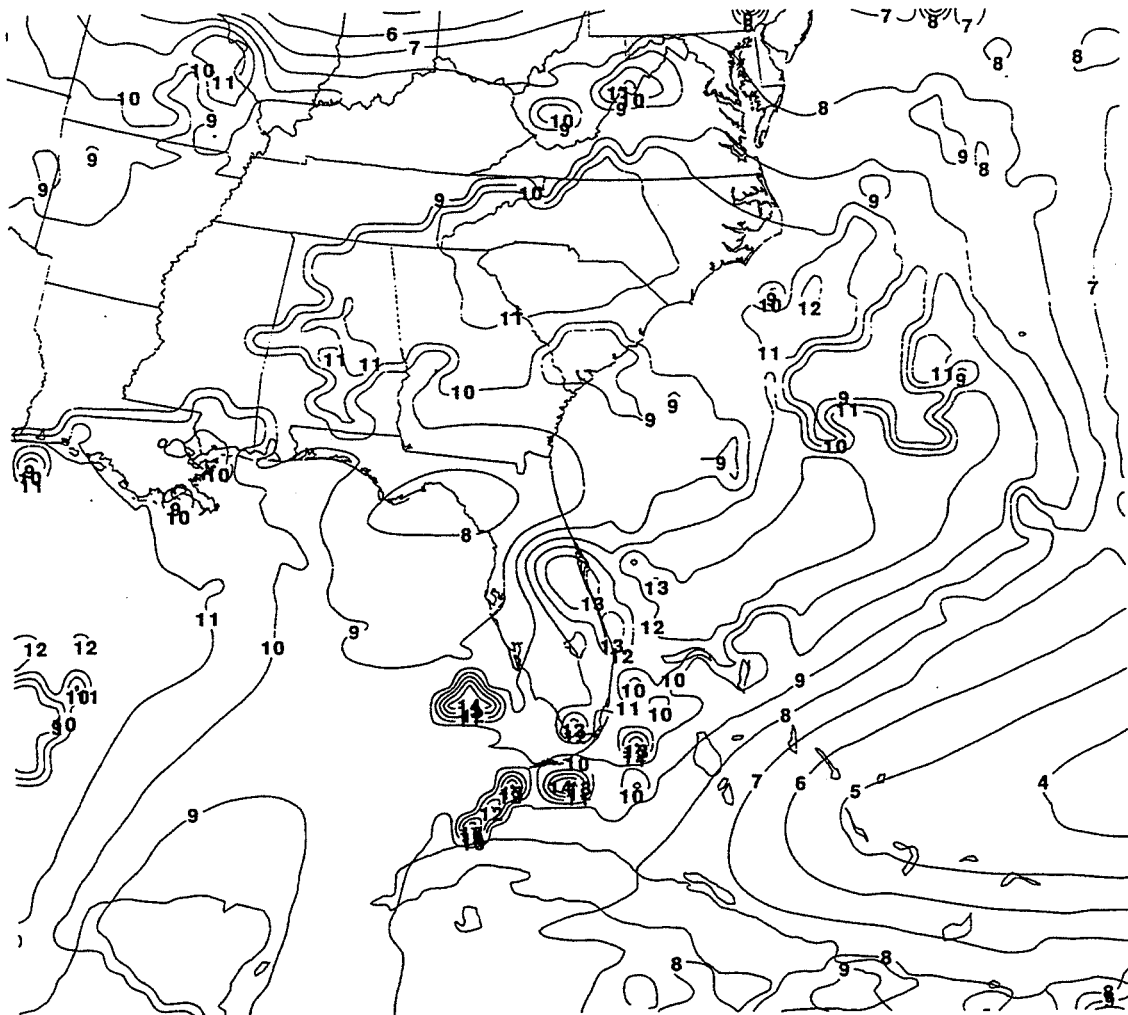


Fig. 1. 850 mb specific humidity (gm/kg) analysis with the synthetic RH at 1200 GMT 1 June 1994.

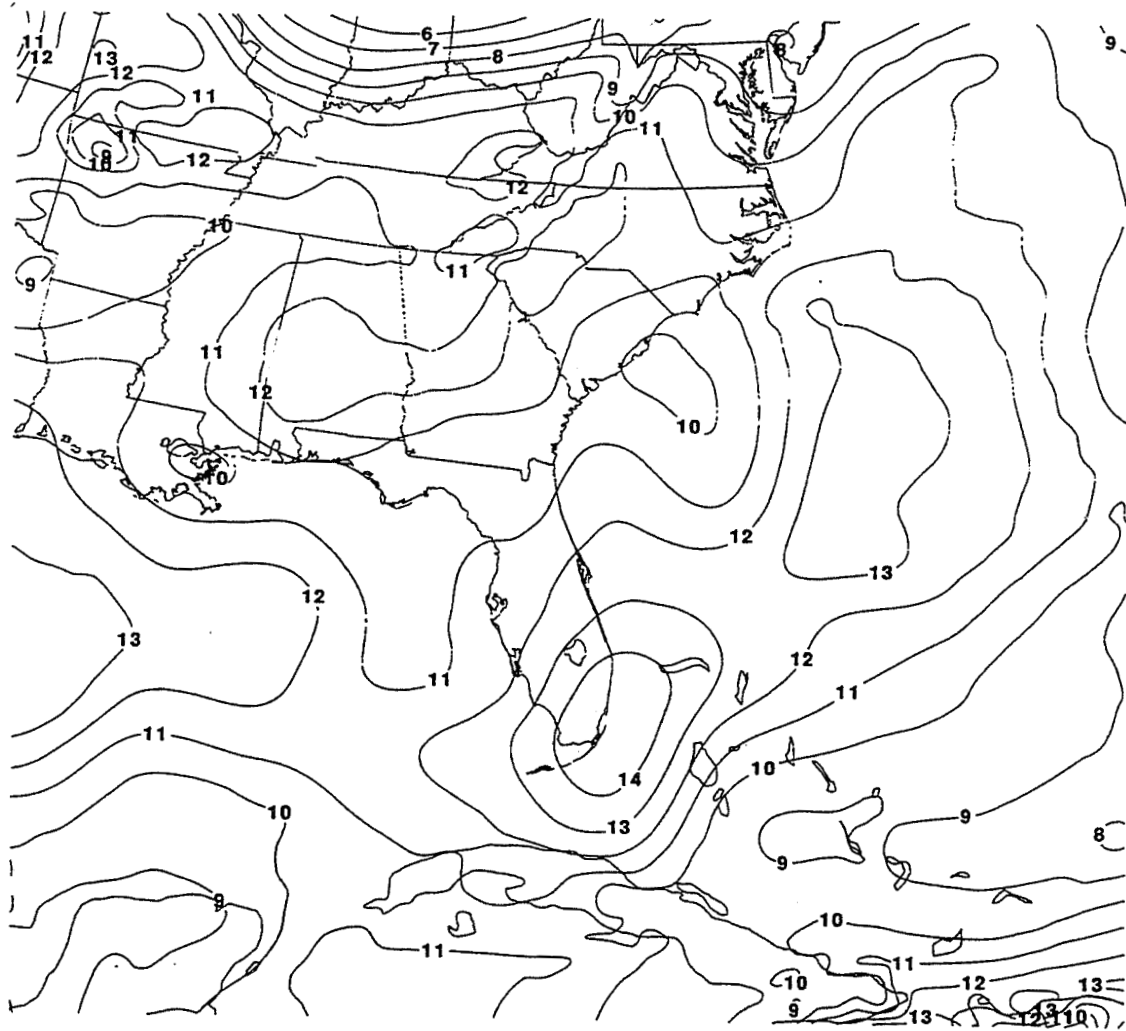


Fig. 2. As in Fig. 1 except without the synthetic RH.

1994 NASA/ASEE SUMMER FACULTY FELLOWSHIP PROGRAM

141858

57-51

JOHN F. KENNEDY SPACE CENTER
UNIVERSITY OF CENTRAL FLORIDA

33967

8-46

351474

PHYSIOLOGICAL AND GENETIC CHARACTERIZATION OF PLANT
GROWTH AND GRAVITROPISM IN LED LIGHT SOURCES

PREPARED BY:	Dr. Gerald F. Deitzer
ACADEMIC RANK:	Associate Professor
UNIVERSITY AND DEPARTMENT:	University of Maryland Department of Horticulture
NASA/KSC	
DIVISION:	Biomedical Operations and Research
BRANCH:	Biological Research and Life Support
NASA COLLEAGUE:	John Sager
DATE:	August 24, 1994
CONTRACT NUMBER:	University of Central Florida NASA-NGT-60002 Supplement: 17

ACKNOWLEDGEMENTS

Interaction with several NASA and Bionetics Corporation personnel, who are part of the Biological Research and Life Sciences Office was vital to the success achieved during the ten week period of this Fellowship. Drs. John Sager, William Knott and Christopher Brown were especially supportive in arranging to make space and facilities available to me to carry out the work reported in this document. Most important to the direction and success of this research was Ms. Corey Johnson, who was kind enough to allow me to utilize her extraordinary LED and clinostat facilities, and who spent countless hours helping with the conduct of the experiments and analyses of the results. Special thanks are also extended to Dr. Baishnab Tripathy for sharing his office with me and Dr. Gary Stutte for providing me with housing, hospitality and freindship. Finally, I wish to express my gratitude to the staff of the University of Central Florida, especially Dr. Loren Anderson and Ms. Kari Stiles, who were involved in making every aspect of the NASA/ASEE Summer Fellowship exceptionally rewarding.

ABSTRACT

Among the many problems of growing plants in completely controlled environments, such as those anticipated for the space station and the CELSS program, is the need to provide light that is both adequate for photosynthesis and of proper quality for normal growth and development. NASA scientists and engineers have recently become interested in the possibility of utilizing densely packed, solid state, light emitting diodes (LEDs) as a source for this light. Unlike more conventional incandescent or electrical discharge lamps, these sources are highly monochromatic and lack energy in spectral regions thought to be important for normal plant development. In addition, a recent observation by NASA scientists has suggested that infra-red LEDs, that are routinely used as photographic safelights for plants grown in darkness, may interact with the ability of plants to detect gravity.

In order to establish how plants respond to light from these LED light sources we carried out a series of experiments with known pigment mutants of the model mustard plant, *Arabidopsis thaliana*, growing in either a gravity field or on a clinostat to simulate a micro-gravity environment. Results indicate that only red light from the 665 nm LEDs disrupts the ability of normal wildtype seedlings to detect a gravity stimulus. There was no consistent effect found for the far-red (735 nm) LEDs or either of the infra-red (880 nm or 935 nm) LED sources but both showed some effect in one or more of the genotypes tested. Of the five members of the phytochrome multigene family in *Arabidopsis*, only the phytochrome B pigment mutant (hy3) lacked the ability to detect gravity under all conditions. There was no effect of either micro-gravity (clinostat) or the infra-red LEDs on the light induced inhibition of hypocotyl elongation. Measurements of the pigment phytochrome in oats also showed no photoconversion by 15 min irradiations with the infra-red LEDs. We conclude that phytochrome B is required for the perception of gravity and that only red light is able to disrupt this perception. The infra-red LEDs also do not appear to interact with gravity perception in *Arabidopsis*, but caution should be exercised if infra-red LEDs are to be used as photographic safelights for these types of experiments.

SUMMARY

In order to investigate the interaction of light and gravity using LED light sources, we chose several single gene point mutations in *Arabidopsis thaliana* that represented either deletions of individual members of the phytochrome pigment multigene family or loss of phytochrome function. The genotypes used were: (1) hy 8-2, which lacks a light-labile phytochrome A gene product (PhyA) that predominates in dark grown, etiolated tissue and (2) its wildtype ecotype RLD; (3) hy 3, which lacks a light-stable phytochrome B gene product (PhyB) that predominates in light grown, deetiolated tissue and (4) its wildtype ecotype Landsberg erecta (Ler); (5) elf 3, which is an unknown mutation thought to affect phytochrome B function and (6) its wildtype ecotype Columbia (Col).

Approximately 50 seeds of each of these genotypes were surface sterilized and sown on agar in small (3 cm dia.) petri dishes. Velcro™ was attached to the bottoms of the dishes and they were stuck to vertically oriented platters that could be rotated at 1.0 RPM to simulate micro-gravity (clinostat). The clinostats (whether rotated or not) were located inside light-tight, ventilated boxes which were allowed to remain dark for 48 hrs to provide uniform germination. Following germination, the LEDs in each box were turned on to a preset intensity of $100 \mu\text{mol m}^{-2} \text{s}^{-1}$ for the 665 and 735 nm LEDs, $90 \mu\text{mol m}^{-2} \text{s}^{-1}$ for the 880 nm and $65 \mu\text{mol m}^{-2} \text{s}^{-1}$ for the 935 nm LEDs. One box was left in the dark as a control. The seedlings were allowed to grow for 48 hrs, harvested, photographed with a CCD camera and stored as a digital image for hypocotyl length and growth angle (deviation from vertical) analysis.

Results show that there is no interaction between gravity (\pm clinostat) and the effect of light on the inhibition of hypocotyl elongation in any of the genotypes tested. There is also no inhibition of hypocotyl elongation by the infra-red LEDs. Continuous far-red light strongly inhibits elongation in all genotypes except hy 8-2 whereas continuous red light significantly inhibits all genotypes, including hy 3 and elf 3. The ability to detect gravity (small deviation from the vertical) is normal in the dark and far-red light for all genotypes except hy 3, which behaves agravitropically in all conditions. None of the genotypes are able to detect gravity (large deviation from the vertical) in continuous red light. The data support the conclusion that the Pr form of phytochrome B (which seems to have activity only for this response) is essential for gravity perception. In addition to hy 3, the ecotypes Landsberg erecta and RLD, both of which are normal wildtypes, appear to respond to the 880 nm LEDs while elf 3 appears to respond to the 935 nm LEDs. The latter two responses are not understood, but caution should be used in applications requiring use of infra-red LEDs in gravity experiments.

TABLE OF CONTENTS

<u>Section</u>	<u>Title</u>	<u>Page</u>
I.	INTRODUCTION.....	8
II.	EXPERIMENTAL PROCEDURES	
2.1	Seeds.....	11
2.2	Surface Sterilization.....	11
2.3	Experimental Protocol	
2.3.1	Stationary.....	11
2.3.2	Clinorotated.....	12
2.4	Light Sources.....	12
2.5	Image Analysis.....	14
2.6	Phytochrome Measurements.....	14
III.	RESULTS AND DISCUSSION	
3.1	Hypocotyl Elongation	
3.1.1	hy 8-2.....	15
3.1.2	hy-3.....	17
3.1.3	elf-3.....	17
3.2	Gravity Perception	
3.2.1	hy 8-2.....	17
3.2.2	hy-3.....	21
3.2.3	elf-3.....	21
3.3	Phytochrome Measurements.....	21
IV.	SUMMARY COMMENTS.....	26
V.	REFERENCES.....	27
VI.	APPENDIX.....	29

LIST OF ILLUSTRATIONS

<u>Figure</u>	<u>Title</u>	<u>Page</u>
1	Emission Spectrum of the LED Light Sources.....	13
2	Hypocotyl Elongation of RLD and hy 8-2 in various light conditions with and without clinorotation.....	16
3	Hypocotyl Elongation of Ler and hy-3 in various light conditions with and without clinorotation.....	18
4	Hypocotyl Elongation of Col and elf-3 in various light conditions with and without clinorotation.....	19
5	Growth angle of RLD and hy 8-2 in various light conditions with and without clinorotation.....	20
6	Growth angle of Ler and hy-3 in various light conditions with and without clinorotation.....	22
7	Growth angle of Col and elf-3 in various light conditions with and without clinorotation.....	23

LIST OF TABLES

<u>Table</u>	<u>Title</u>	<u>Page</u>
1	Phytochrome Photoconversion in oats after 15 min of irradiation with various light sources.....	24

I. INTRODUCTION

In order for plants to acclimate to changes in their environment, they must be able to detect such changes and respond by altering internal biochemical and molecular pathways that lead to physiological and morphological differences. One of the most important of these environmental signals is light. Changes in the quality of light provide a plant with information about seasonal variation, spatial orientation, temporal organization, proximity of competing vegetation, etc.. Changes in these parameters are collectively referred to as photomorphogenesis. Photomorphogenetic responses are dependent on the ability of the plant to detect changes in light quality by absorption of light in specific wavelength ranges of the electromagnetic spectrum. Only three pigments have been identified that lead to photomorphogenetic changes: (1) a red/far-red absorbing pigment called phytochrome, (2) a blue light absorbing pigment(s) referred to as cryptochrome(s) and (3) a UV-B absorbing pigment. Of these, only phytochrome has been isolated and characterized.

Phytochrome is present as a multigene family (1) consisting of five separate gene products in *Arabidopsis*. Mutations in two of these genes has indicated that each phytochrome species may control separate photomorphogenetic responses (2). In order to dissect which phytochrome species is responsible for which photomorphogenetic response, we have compared a number of different physiological responses in six different *Arabidopsis* genotypes. One of these genotypes (hy 8-2) (3) lacks the gene product for the light-labile phytochrome A protein, another (hy 3) lacks the gene product of the light-stable phytochrome B protein (4), while a third (elf 3) is a mutant at an unknown locus that has an early flowering phenotype (5). The other three genotypes are all normal wildtype *Arabidopsis* plants with different genetic backgrounds.

Phytochrome is known to regulate the rate of elongation of the embryonic shoot axis known as the hypocotyl. When grown in continuous darkness, the hypocotyls elongate very rapidly; becoming extremely long and spindly. Light inhibits this elongation; producing normal, very short, rosette plants. Continuous, monochromatic far-red light, despite being very dim ($<20 \mu\text{mol m}^{-2} \text{s}^{-1}$) causes the same level of inhibition as bright white fluorescent light ($>200 \mu\text{mol m}^{-2} \text{s}^{-1}$). Null mutants lacking the light-labile product of the phytochrome A gene (*phyA*), which predominates in etiolated tissue, completely lack this far-red response and are indistinguishable from the dark controls (3). However, they remain strongly inhibited in both continuous red and white light. Null mutants lacking the light-stable product of the phytochrome B gene (*phyB*), which predominates in light-grown, de-etiolated tissue (4,6), fail to respond to continuous red light

(7). We have noticed; however, that this inhibition is incomplete (unpublished results) either because some other phytochrome species (*phyC*, *phyD* or *phyE*) participates in this response or that our red light source (red phosphor fluorescent filtered through red cellophane) contains enough far-red light to produce *phyA* mediated inhibition. The red LEDs, which do not have any far-red emission, will allow us to distinguish between these alternatives. The *phyB* mutant, like the *phyA* mutant, is also strongly inhibited by white light. We believe that this is a blue light rather than a phytochrome mediated response.

A recent report (8) demonstrated that the shoots of wildtype *Arabidopsis* seedlings were able to detect, and respond to, gravity when grown in complete darkness, but were unable to do so when irradiated with continuous red light. Interestingly, the *phyB* mutant *hy-3* was unable to detect gravity even in continuous darkness. The red light induced disruption of the gravitropic response was found to be red/far-red reversible, confirming that phytochrome was required. Since the mutant only lacks phytochrome B, and since it was unable to detect gravity in the dark (where only the "inactive" Pr form of phytochrome is present), it was argued that the Pr form of phytochrome B was required for gravitropic perception in *Arabidopsis* shoots. Red light would lead to a reduction in the pool of "active" Pfr in the wildtype and increase the pool of "inactive" Pr; causing it to lose its ability to respond to a gravity stimulus. This is an extremely controversial conclusion because it is the only instance where the Pr form of the phytochrome molecule has been shown to have biological activity. They further confirmed this by showing that *hy-2*, which is defective in chromophore biosynthesis leading to a reduction in all phytochrome species, also failed to detect gravity in the dark, but could be rescued by feeding the immediate precursor of the chromophore, biliverdin.

Scientists at KSC and the Bionetics Corporation have discovered that energy from infra-red emitting LEDs is able to cause a number of responses in oat seedlings that may be attributable to phytochrome (9, Appendix). They found that, when seedlings were irradiated with either 880 nm or 935 nm LEDs, mesocotyl (embryonic shoot in grasses equivalent to the hypocotyl in *Arabidopsis*) growth was inhibited, coleoptile (embryonic sheath covering the leaves) growth was increased and leaves emerged earlier than seedlings grown in darkness. In addition, the IR irradiated plants had mesocotyls oriented in an orthogravitropic (growth parallel to, but away from the gravity vector) direction while the dark controls were oriented in a diagravitropic (perpendicular to the gravity vector) direction. This has caused concern since the use of such LEDs as "safelight" sources for infra-red sensitive cameras has been recommended for monitoring biological experiments aboard the Space Station (10).

We have; therefore, undertaken an investigation of the phytochrome involvement in both the growth responses and the gravitropic responses in *Arabidopsis* using red (665 nm), far-red (735 nm) and infra-red LEDs (both 880 nm and 935 nm). Also, in order to characterize which members of the phytochrome multigene family are responsible for these responses, we have examined all of the responses in the phytochrome pigment mutants hy 8-2, which lacks phy A, hy-3, which lacks phyB and elf-3, which is unable to respond to phyB stimulation.

II. EXPERIMENTAL PROCEDURES

2.1 SEEDS

Six different genotypes were used during the course of these experiments. The elf-3 seeds were obtained from Dr. D. Rye Meeks-Wagner at the University of Oregon, hy 8-2 seeds were obtained from Dr. Peter H. Quail at the University of California at Berkeley and the hy-3 seeds were obtained from Richard Amasino at the University of Wisconsin. All seed stocks were maintained by selfing the homozygous recessive plants in the growth chamber facility at the University of Maryland. All seed were stored in a dry condition at 4 °C until use.

2.2 SURFACE STERILIZATION

Approximately 300 seed of each genotype were added to 15 ml sterile, disposable Falcon tubes to which was added 10 ml of a 20% Chlorox™ solution (1.5% NaClO₄). These were stirred on a vortex stirrer and allowed to incubate for 20 min. at room temperature in a laminar flow hood. At the end of this period all of the seed was rapidly transferred by filtration through a presterilized Whatman™ No. 1 filter paper and washed three times with 10 ml each of sterile distilled water. The filters were then removed and allowed to air dry in the laminar flow hood overnight. This procedure was found to be necessary to stimulate germination of seeds in darkness which otherwise have a light requirement.

2.3 EXPERIMENTAL PROTOCOL

2.3.1 STATIONARY. Approximately 50 seed of each genotype were transferred to small (3.5 cm) sterile, disposable petri dishes containing 0.7% (w/v) Sigma No. A-7002 agar in deionized water under a dim ($<2.0 \mu\text{mol m}^{-2} \text{s}^{-1}$) green (2 x 15 in green phosphor fluorescent tubes wrapped with several layers of green cellophane) safelight in a photographic darkroom. The dishes were then sealed with Parafilm™ and a strip of Velcro™ was applied to the bottom of each dish. The dishes were transferred in darkness to one of five specially constructed 245 cm x 368 cm light-tight wooden boxes that contained an LED board at one end and a 15 cm diameter round Velcro™ covered platter at the other. The LED end of the chamber was separated from the remainder of the chamber by a 1/8 in thick clear acrylic barrier and air was circulated over the LEDs using a centrifugal blower with a light trapped opening. The platter was mounted vertically and attached to an electrical motor mounted outside of the box. The boxes were maintained at 23 °C inside a Conviron E-36 growth chamber (Dark, 880 and 935 nm LEDs) or in the photographic darkroom (red and far-red LEDs).

Seeds were allowed to germinate in darkness for 48 hrs before the

lights were turned on so that the light conditions would not influence the time or percentage of germination. Following germination the LEDs were switched on to preset irradiances corresponding to calibrated currents on the power supplies. The plants were then irradiated for an additional 48 hrs and then removed in darkness, covered with aluminum foil and placed at 4 °C. As soon as possible thereafter, each dish was captured as a digital image using a CCD camera and the image stored in the computer. The dishes were then returned to 4 °C in the dark.

2.3.2 CLINOROTATED. One half of the experimental series was treated in exactly the same way as those described above for the stationary response, but after placing the dishes on the platter, the electrical motor connected to it was switched on. The motor was chosen to provide a constant 1.0 RPM throughout the experiment. Since seedlings germinated on agar in a vertical direction grow along the surface of the agar, clinorotated seedlings experience a uniform gravitational field in the direction of growth.

2.4 LIGHT SOURCES

The 880 nm LEDs consisted of 100 Honeywell # 840-3470-001 gallium-aluminum arsenide diodes (Micro Switch Division, Richardson, TX) mounted in a 21 cm² matrix and provided a maximal fluence rate of 90 $\mu\text{mol m}^{-2} \text{s}^{-1}$. The 935 nm LEDs consisted of the same configuration as the 880 nm LEDs but were gallium arsenide (Honeywell # 840-3445-004) and provided a maximal fluence rate of 65 $\mu\text{mol m}^{-2} \text{s}^{-1}$. Red LED light was obtained from a monolithic array of diodes sold commercially by Quantum Devices, Inc. (Barneveld, WI) as their Model QBE AM 2000 which provided 100 $\mu\text{mol m}^{-2} \text{s}^{-1}$ at 8.0 Amps measured at the center of the clinostat. The far-red LEDs were obtained as part of a prototype array containing both red and far-red LEDs from NASA Ames, but were also fabricated by Quantum Devices, Inc. 144 of the far-red LEDs were removed and mounted in a single circuit board and set at 2.3 Amps to provide 100 $\mu\text{mol m}^{-2} \text{s}^{-1}$ at the center of the clinostat. The spectral distribution, measured with an LI-1800 spectroradiometer (LiCor, Lincoln NE), of all of these sources is shown in Fig. 1.

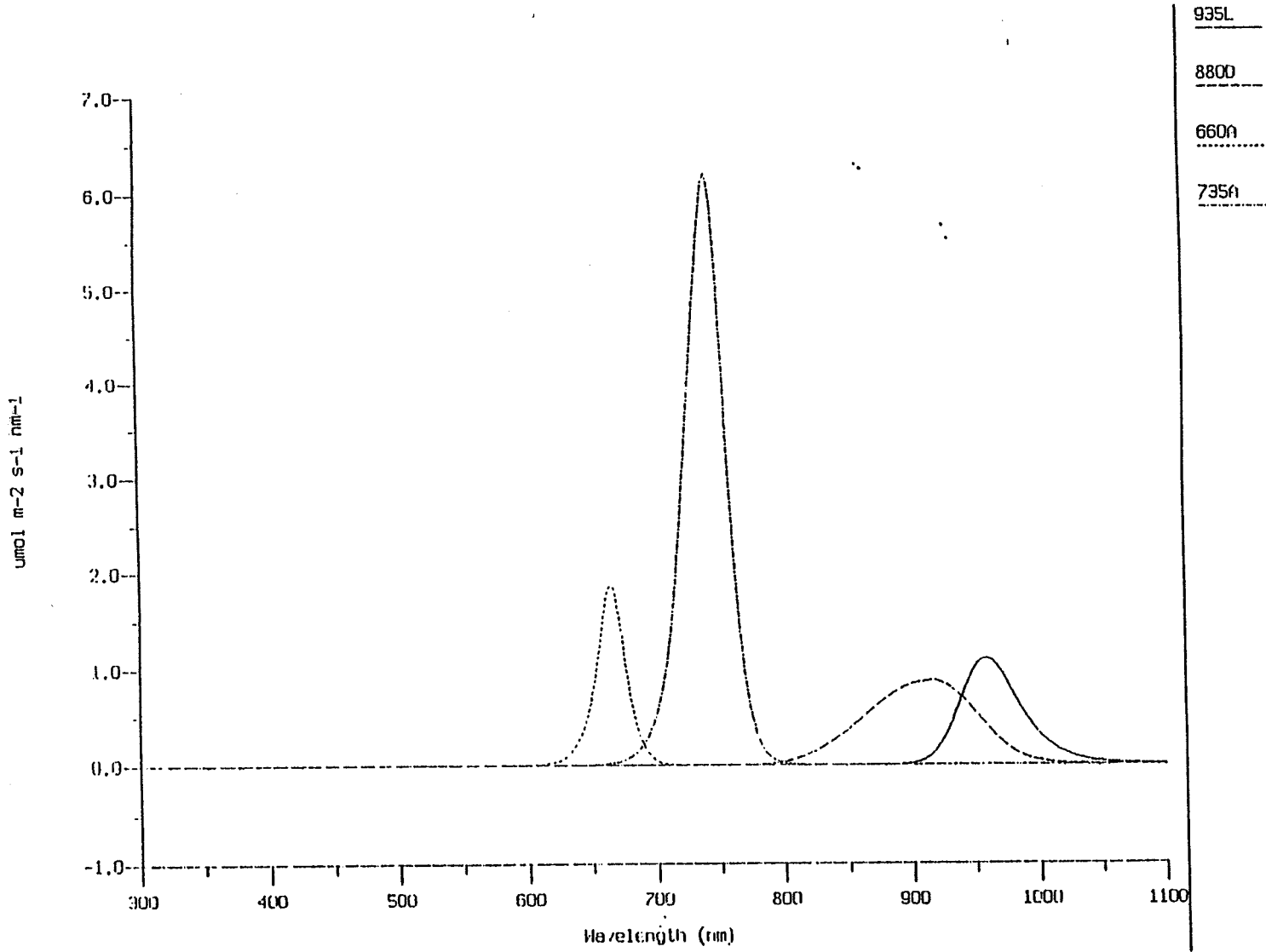


Figure 1

Emission Spectrum of the LED Light Sources

2.5 IMAGE ANALYSIS

Immediately following harvest, the petri dishes were opened and the Velcro removed from the bottom to allow the seedling images to be captured by CCD camera and the digitized image was stored on a Macintosh Quadra 950 computer. A millimeter ruler image was captured next to each dish in order to calibrate the hypocotyl length measurements. Each image was then analyzed for hypocotyl length and angle using NIH Image software, a public domain program developed for Macintosh by Wayne Rasband of the National Institutes of Health. Each seedling is simultaneously analyzed for length and angle and the results transferred to Excel for statistical analysis. All experiments were repeated three times and the means and standard deviations calculated.

2.6 PHYTOCHROME MEASUREMENTS

Phytochrome was measured using a custom-built ratio-spectrophotometer as the difference in absorbance between 660 nm and 730 nm before and after actinic irradiation with red and far-red light. Oat seedlings were grown on moistened KimpackTM in the dark for 4-6 days. At the end of this time, the upper 1.5 cm of several hundred coleoptiles were harvested and 1.0 g of fresh weight were placed in petri dishes on ice. These samples were then transferred to each of the LED light conditions and irradiated for 15 min. on ice to prevent thermal destruction of the labile Pfr pool. Following irradiation the coleoptiles were chopped into 0.5 mm sections with a razor blade and placed into a cylindrical aluminum cuvette which is open at the top and has a clear plastic window on the bottom. This cuvette was then placed in the ratio-spectrophotometer and the difference in absorbance recorded. The sample is then irradiated from above by a high irradiance far-red source for 1.5 min. and then the difference in absorbance was immediately measured again. This was then repeated for five cycles alternating red and far-red irradiations between measurements. The Pfr/Ptotal photoequilibrium was then calculated.

III RESULTS AND DISCUSSION

3.1 HYPOCOTYL ELONGATION

When allowed to germinate and grow in continuous darkness, virtually all plants will respond by elongating very rapidly and by displaying a whole host of characteristics that are typical of growth in the absence of light. This condition is known as etiolation and is a transient condition since, without light, plant cells elongate but do not divide to produce new cells for growth. Thus they can survive only until internal energy stores are exhausted. Light immediately inhibits this rapid cell elongation, initiates the synthesis of chlorophyll and causes leaves to expand and begin photosynthesizing to provide new energy from external sources. While these changes involve the synthesis of chlorophyll and the development of the photosynthetic apparatus, the light signal is not detected by chlorophyll itself. The pigment responsible is phytochrome, a photointerconvertible photoreceptor molecule that exists in two isomeric forms. One of these forms, which has an absorption maximum in the far-red region of the spectrum at 730 nm, is known as Pfr and is thought to be the active form of the molecule. The other, which has an absorption maximum at 667 nm is known as Pr and is considered to be inactive. Absorption of light by one form converts it to the other form and so a photoequilibrium is established by irradiation with any light source. The relative proportion of Pfr to the total pool of phytochrome is important in determining the extent of the response to light.

3.1.1 HY 8-2. Not only does phytochrome exist in two isomeric forms, but there are at least five different phytochrome genes expressed in *Arabidopsis*. One of these predominates in etiolated plants and is known to be encoded by the phytochrome A gene (11) and is characterized by being light labile as Pfr and so it disappears very rapidly following irradiation. It is also known to be both necessary and sufficient for the far-red mediated inhibition of hypocotyl elongation. This was deduced following the isolation and characterization of a mutant called hy 8, especially the hy 8-2 allele, which was found to have a stop codon in the gene encoding phytochrome A (3) resulting in the complete loss of inhibition by far-red light.

Results reported in Fig. 2 show that hy 8-2 elongates normally in the dark (DD) as well as after 48 hrs of irradiation with far-red (FR) light. In contrast, the wildtype RLD, with which it is isogenic, is completely inhibited by 48 hrs of far-red light. There is also no apparent inhibition by either of the IR LEDs (880 or 935 nm) in either the mutant or the wildtype, but both are strongly inhibited by 48 hrs of irradiation with red (RR) light. There is also absolutely no effect of clinorotation on any of

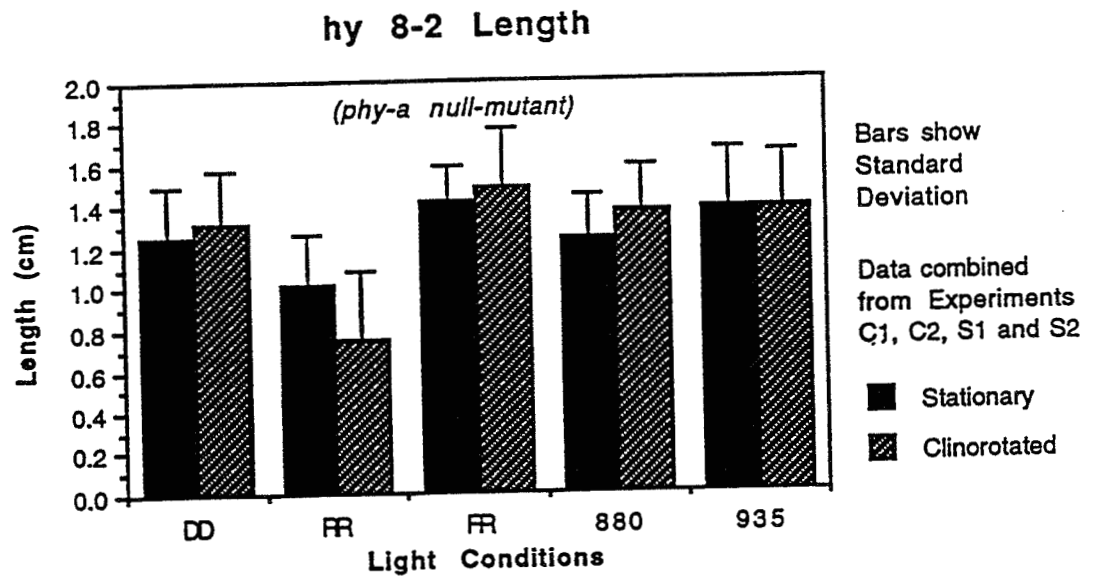
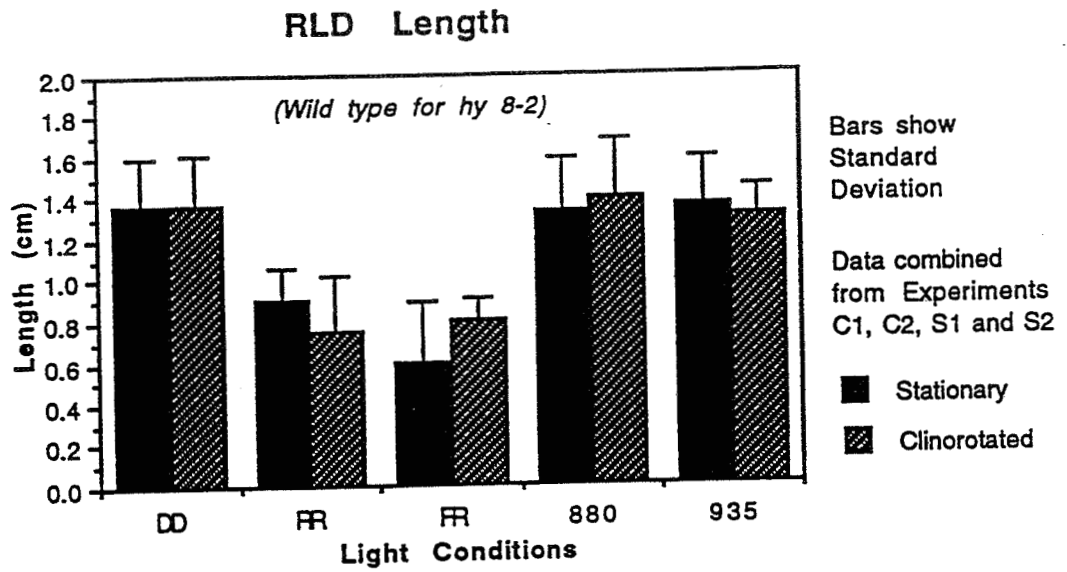


Figure 2

Hypocotyl Elongation of RLD and hy 8-2 in various light conditions with and without clinorotation

these responses. Thus phytochrome A is responsible for the detection of continuous far-red light but not continuous red light and neither infra-red nor gravity interact with this response.

3.1.2 HY-3. Hy-3 was originally isolated in 1980 by Maarten Koornneef (12) as one of a group of mutants that developed long hypocotyls in the light that were characteristic of etiolated plants. It was subsequently found (6) that this mutant was devoid of phytochrome B and was characterized by its failure to be inhibited by continuous red-light (13). Fig 3 shows that the response of hy-3 to red light (RR) is completely normal. This suggests that at high irradiances ($100 \mu\text{mol m}^{-2} \text{s}^{-1}$) that some other type of phytochrome can assume this function, possibly even phytochrome A as suggested recently by Reed et al. (14). Again, as with hy 8-2, there was no significant effect of either the infra-red LEDs nor gravity for both the mutant and its isogenic wildtype, Landsberg erecta.

3.1.3 ELF-3. When this mutant was isolated in 1992 (5), it was characterized as an early flowering mutant, but it was noted that it also produced very long hypocotyls when grown under short photoperiods. In this respect, these plants resembled the hy mutants, especially hy-3. However, when the levels of phytochrome were examined on Western blots, they were found to have normal levels of phytochromes A, B and C (Zagotta, Meeks-Wagner and Quail, unpublished results). In addition, the elf-3 mutation was found not to map to any of the known chromosomal locations for phytochrome (5). When compared under our conditions, elf-3 was found to behave exactly like hy-3 (Fig. 4) and did not differ significantly from its isogenic wildtype Columbia. Also, as was found for hy 8-2 and hy-3, there was no effect detected for either gravity or infra-red irradiation. Since both elf-3 and hy-3 appear to be phytochrome B mutations, we have suggested that elf-3 is a mutation in one of the biochemical events downstream from photoreception but within a common pathway leading to a number of phytochrome B mediated responses. The normal inhibition of hypocotyl elongation in elf-3 is also interpreted as being due to overlapping functions of photoreceptors, especially at high irradiances.

3.2 GRAVITY PERCEPTION

Although it is questionable to what extent rotation on a clinostat simulates the effects of micro-gravity, it at least provides a first approximation where the effects of a gravitational field are at least equalized in all directions. Deviations from a uniform direction of growth may reasonably be assumed to conform to a failure to perceive a gravity stimulus.

3.2.1 HY 8-2. When hy 8-2 was grown on the clinostat it grew randomly in all directions (Fig. 5) in all of the light treatments. This was also true for its wildtype RLD and so may be regarded as an internal control for the interaction of light with

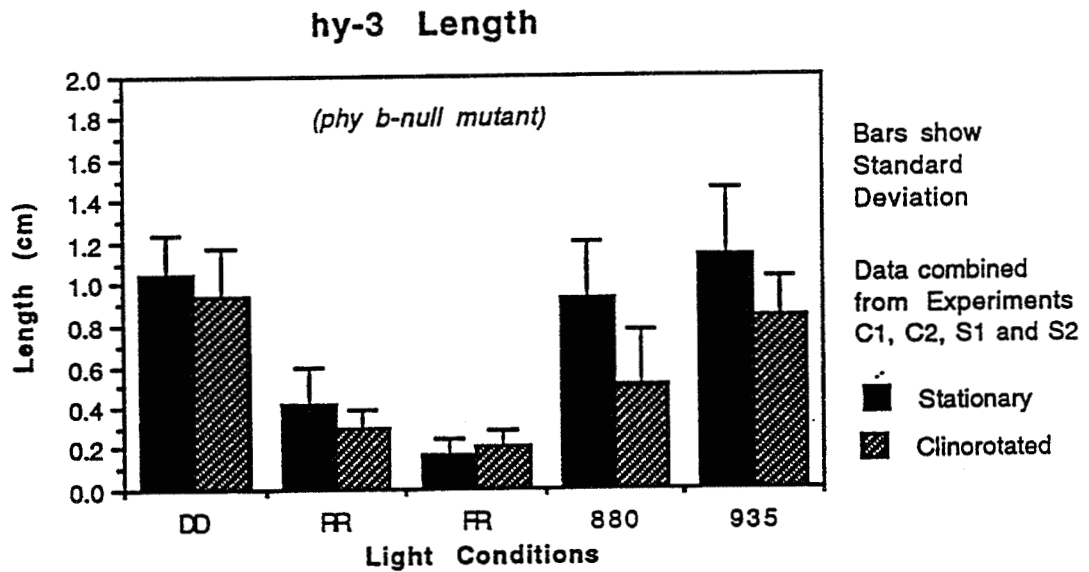
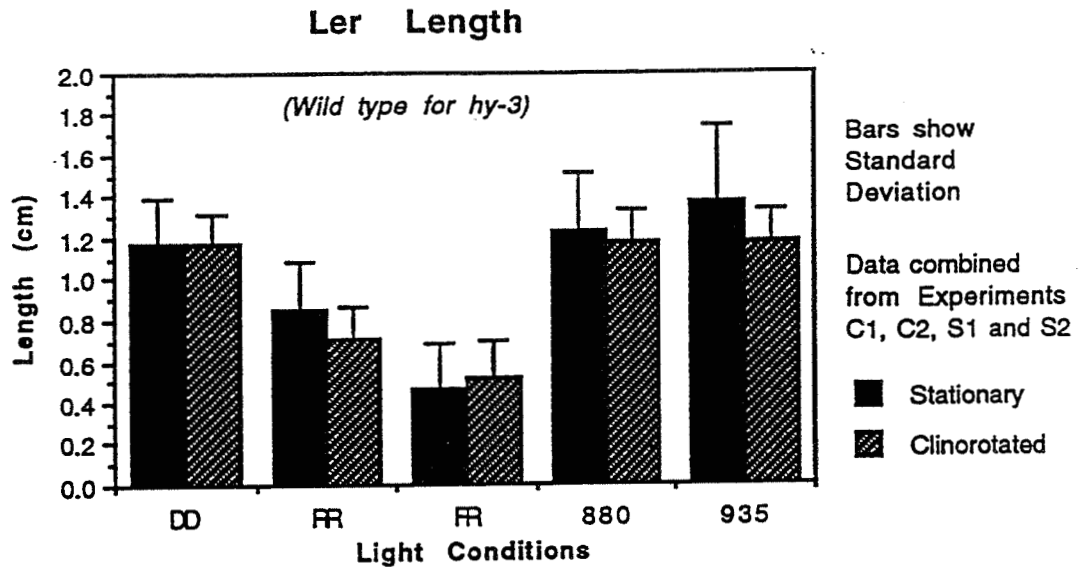
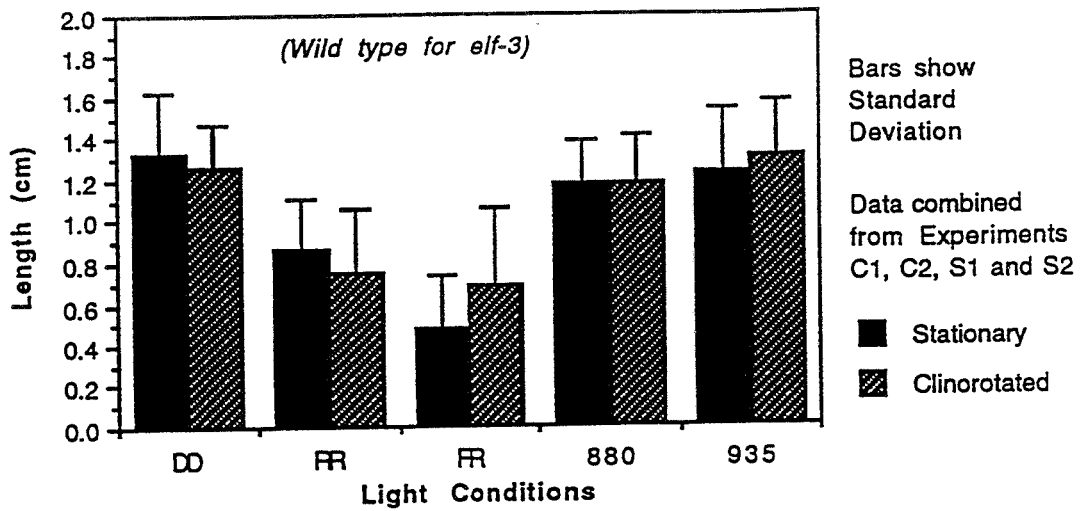


Figure 3

Hypocotyl Elongation of Ler and hy-3 in various light conditions with and without clinorotation

Columbia Length



elf-3 Length

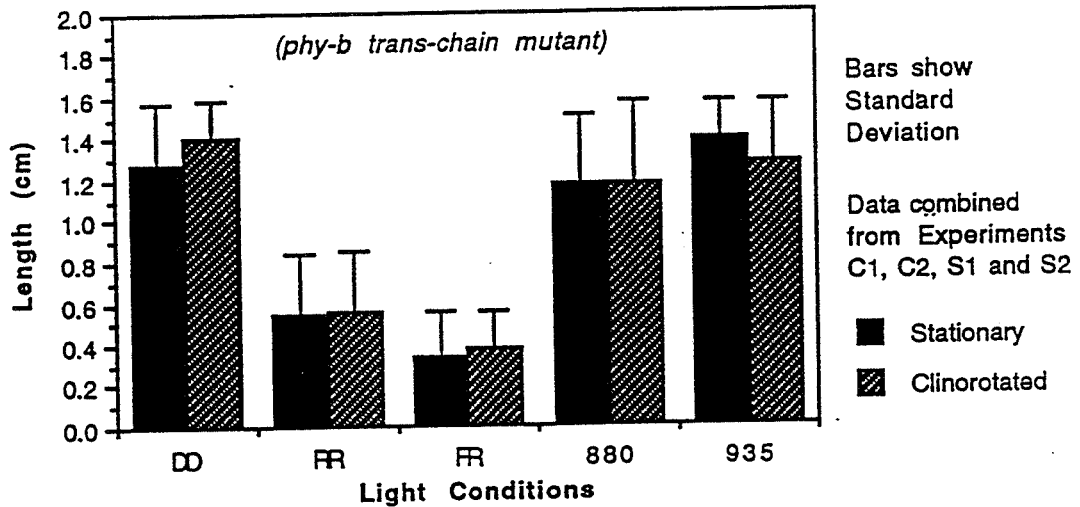


Figure 4

Hypocotyl Elongation of Col and *elf-3* in various light conditions with and without clinorotation

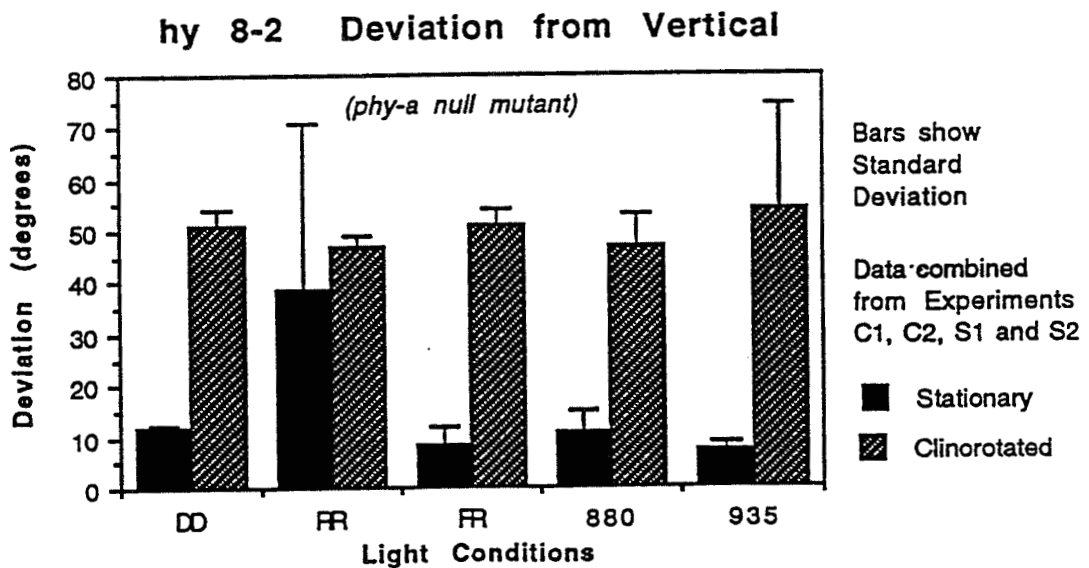
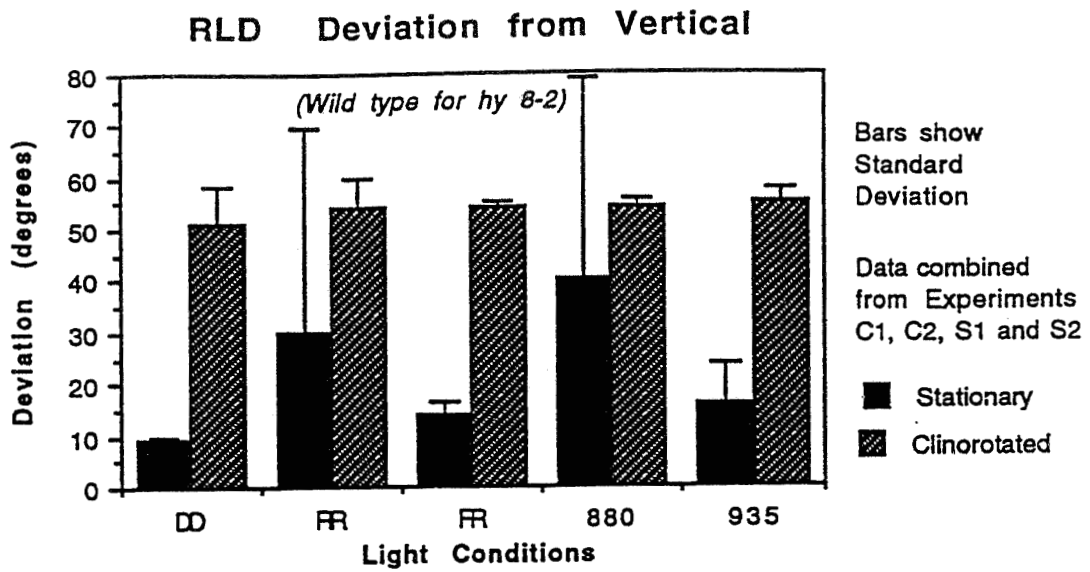


Figure 5

Growth angle of RLD and hy 8-2
in various light conditions with and
without clinorotation

gravity perception. When the clinostat was switched off and the seedlings grew in a stationary vertical orientation, both hy 8-2 and RLD were able to orient to the gravity vector in continuous darkness (DD), far-red (FR), 880 nm (880) and 935 nm (935) LEDs. They were both; however, completely randomized when grown in continuous red (RR) light. Thus, the ability to respond to gravity is not a phytochrome A mediated response because both the mutant and wildtype are normally oriented in continuous far-red light which was clearly demonstrated to differ in section 3.2.1. Thus, the disruption of gravity perception by red light must be mediated by another species of phytochrome. The failure of either 880 nm or 935 nm LED energy to disrupt gravitropism clearly indicates that they do not interfere with gravity perception through phytochrome A.

3.2.2 HY-3. Unlike hy 8-2, hy-3 is completely agravitropic under all conditions including darkness (DD) (Fig. 6). Landsberg erecta, on the other hand only fails to respond to gravity only when grown in continuous red (RR) and so behaves like hy 8-2 and RLD. This confirms the report of Liscum and Hangarter (8) that phytochrome B is required for the perception of gravity. It is also consistent with the suggestion that the Pr form of phytochrome B is required for this response. Here, the infra-red LEDs, while they both fail to respond to gravity, nevertheless behave exactly like the dark control. Thus, there is no apparent effect of infra-red on the gravity response in hy-3 either.

3.2.3 ELF-3. If elf-3 is a mutation in the biochemical transduction chain initiated by phytochrome B, as is apparent in section 3.1.3, then it should behave exactly like hy-3. Figure 7; however, shows a very different picture. Elf-3 is completely normal when grown in continuous darkness (DD) but is randomized when grown in continuous red (RR) light. The responses to far-red (FR) and infra-red (880 and 935) are; however, ambiguous. They appear to be partially gravitropic under these conditions, but are clearly not as agravitropic as hy-3. The ability to perceive gravity normally in the dark in elf-3 suggests that, while phytochrome B may be required for this response, the light dependent transduction chain is not. Hence the interpretation by Liscum and Hangarter (8) that the Pr form of phytochrome B is required is not supported by these data. The effect of red light on the disruption of this response remains to be explained, but it does not appear to be a simple case of converting the Pfr form of phytochrome B back to the Pr form.

3.3 PHYTOCHROME MEASUREMENTS

Although only elf-3 showed a partial effect when plants were grown in infra-red energy, the question of whether the 880 nm and 935 nm LEDs could photoconvert phytochrome from Pr to Pfr was addressed by measuring the photoequilibrium directly. Unfortunately, the

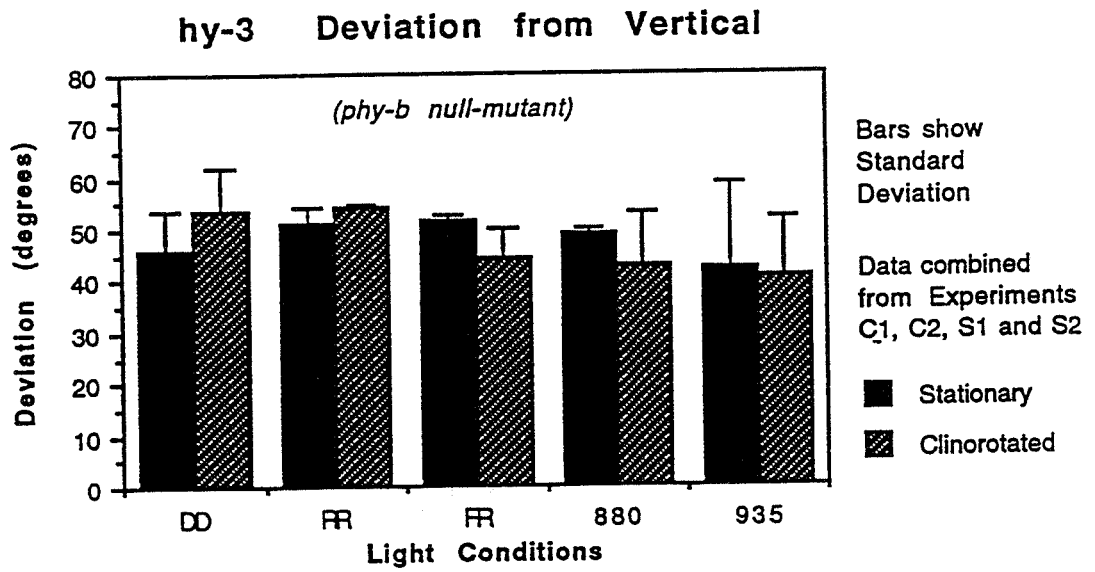
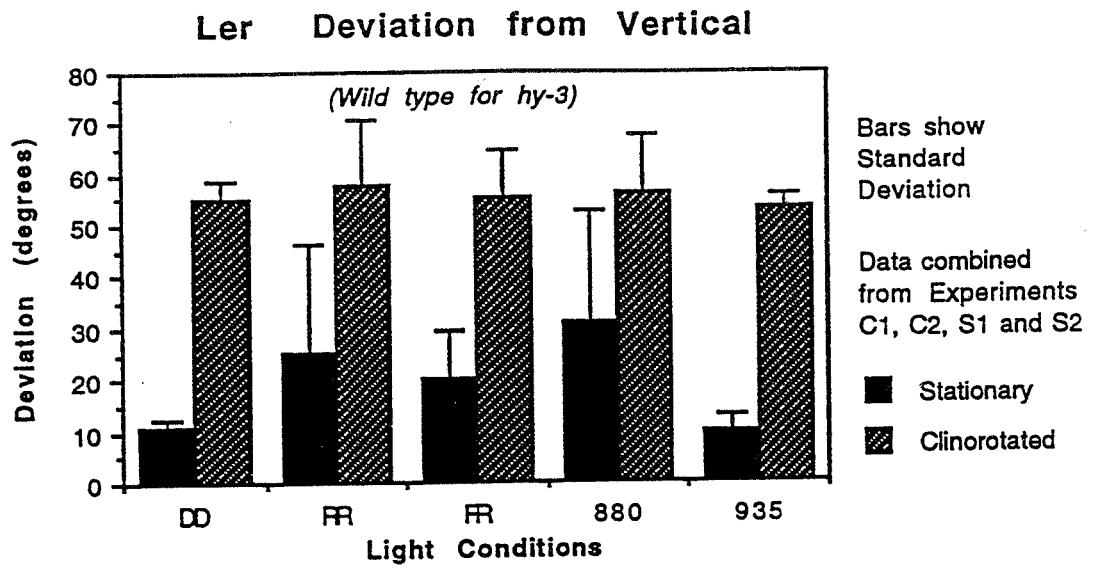


Figure 6
 Growth angle of Ler and hy-3
 in various light conditions with and
 without clinorotation

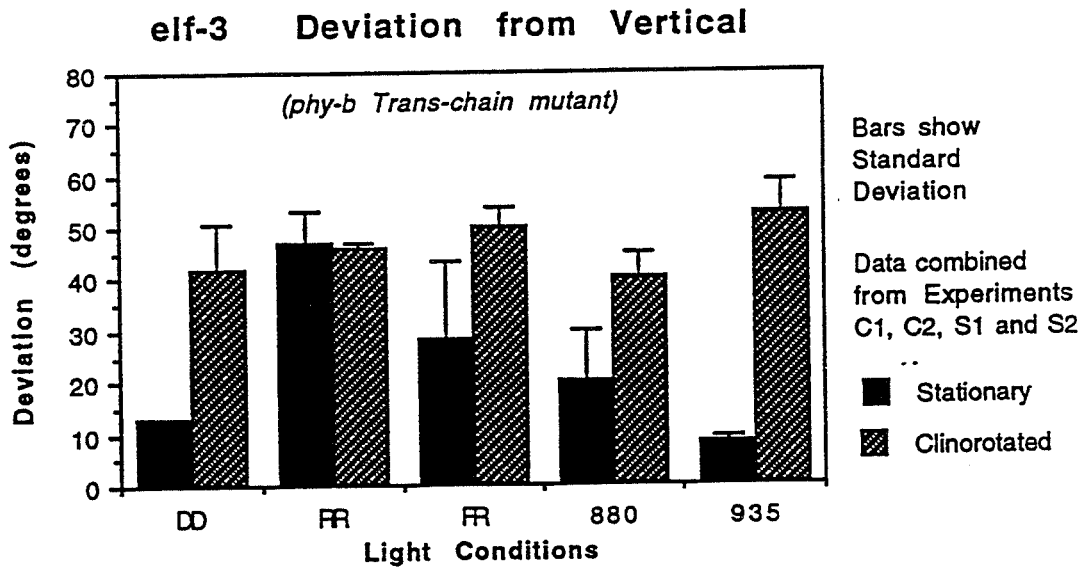
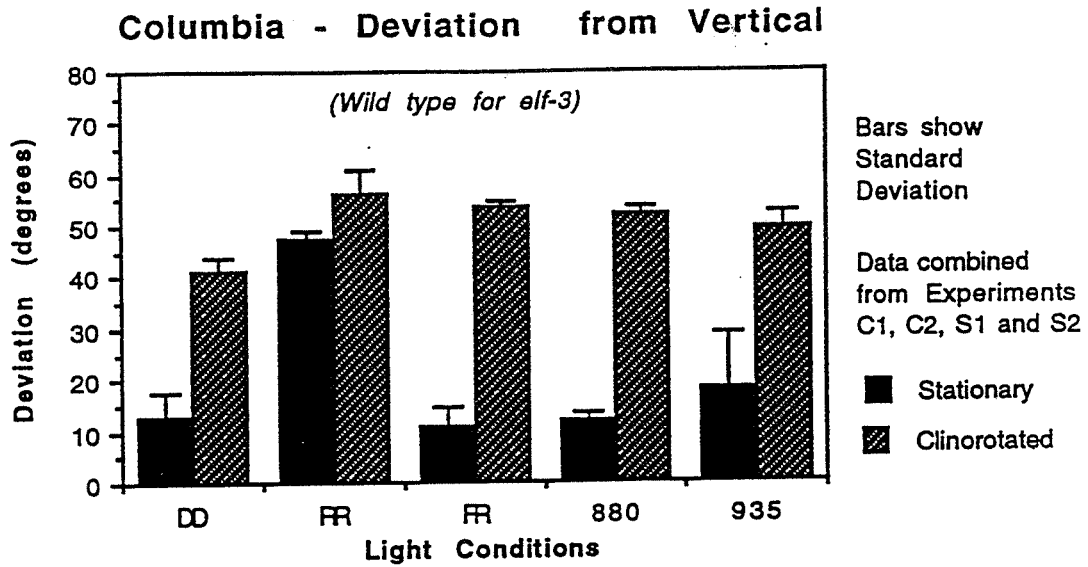


Figure 7

Growth angle of Col and elf-3
in various light conditions with and
without clinorotation

concentrations of phytochrome in *Arabidopsis* are too low for accurate measurement of phytochrome *in vivo* and so we were forced to make these measurements in oat seedlings. Table 1 shows the results of 15 min. irradiations of oat coleoptiles with each of the LED light sources. Since phytochrome is synthesized as Pr in the dark, there is no Pfr evident in dark-grown, etiolated plants (6d DD) or in plants that had been sham irradiated in a box with the LEDs turned off (6d DD + 15 min. DD LED). The far-red LEDs produce about 7.5 % Pfr because of the overlap in the absorption spectra of Pr and Pfr in the far-red (6d DD + 15 min. FR LED). The red LEDs (6d DD + 15 min. RR LED) produced 86 % Pfr, which is the maximal theoretical photoequilibrium obtainable due to the spectral overlap. Neither of the infra-red LEDs produced any measurable Pfr following 15 min. of irradiation. It is possible that some Pfr would have been formed with longer irradiations, but this is technically difficult to test because of the need to irradiate on ice. An attempt will be made to first irradiate the coleoptiles with red light followed by infra-red light to see if the photoequilibrium can be lowered.

TABLE 1

Phytochrome Measurements of 1.0 g Fresh Weight
Oat Coleoptiles Following Irradiation with
15 min. of Light from Various LED Sources

TREATMENT 6d DD + 15 min.	TOTAL PHYTOCHROME ($\Delta\Delta\Delta \times 10^{-3}$)	Pfr (% of P _{tot})
DD	49.53	0.0
Far-Red LEDs	51.66	7.4
Red LEDs	60.59	86.0
880 nm LEDs	58.43	0.0
935 nm LEDs	60.21	0.0

IV SUMMARY COMMENTS

Although the results presented in this report are to some extent disappointing in the sense that they failed to confirm an interaction between the infra-red LEDs and gravity perception, they provide a much clearer definition of the observations made in oat seedlings. The two possible explanations for those observations were that (1) the infra-red LEDs produced contaminating radiation of shorter wavelength and (2) that phytochrome could be excited by the infra-red wavelengths emitted by the infra-red LEDs. Both of these possibilities can be ruled out in *Arabidopsis* since the infra-red LEDs had no effect on either growth or gravity perception. This does not rule out the possibility that oat is more sensitive to infra-red radiation and shows a response that cannot be detected by *Arabidopsis* or that the phytochrome system in oats is different than that in *Arabidopsis*. It does suggest; however, that the observed effects in oat seedlings may not be mediated by phytochrome but by some pigment that is present in oat but not in *Arabidopsis*.

Finally, the most unexpected result found during this study was that hypocotyl elongation in hy-3, which lacks phytochrome B, nevertheless was inhibited by red light. We believe that this is due to the very high irradiances that were achieved by the red LEDs which were 5-7 times higher than those used earlier. Apparently at such high irradiances another species of phytochrome is able to assume the function normally mediated by phytochrome B. This may be phytochrome A, even though hy 8-2 is also inhibited by red light, because hy 8-2 has normal levels of phytochrome B. It may; however, be mediated by one of the other species of phytochrome (phy C, D or E) that have no known function. We will perform fluence response tests with red light to establish whether hy-3 simply has an altered sensitivity. Understanding this response is important since red light irradiances that will be used for life cycle experiments for the Space Station will be well above the $100 \mu\text{mol m}^{-2} \text{s}^{-1}$ used in this study.

V. REFERENCES

1. Sharrock, R.A. and P.H. Quail. Novel phytochrome sequences in *Arabidopsis thaliana*: Structure, evolution, and differential expression of a plant regulatory photoreceptor family. *Genes Dev.* Vol. 3. 1989. pp. 1745-1757.
2. Smith, H. and G.C. Whitelam. Phytochrome, a family of photoreceptors with multiple physiological roles. *Plant Cell Environ.* Vol. 13. 1990. pp. 695-707.
3. Parks, B.M. and P.H. Quail. *hy8*, a new class of *Arabidopsis* long hypocotyl mutants deficient in functional phytochrome A. *Plant Cell* Vol. 5. 1993. pp. 39-48.
4. Somers, D.E., R.A. Sharrock, J.M. Tepperman and P.H. Quail. The *hy3* long hypocotyl mutant of *Arabidopsis* is deficient in phytochrome B. *Plant Cell* Vol. 3. 1991. pp. 1263-1274.
5. Zagotta M.T., S. Shannon, C. Jacobs and D. Ry Meeks-Wagner. Early flowering mutants of *Arabidopsis thaliana*. *Aust J Plant Physiol* Vol. 19. 1992. pp. 411-418.
6. Nagatani, A., J.Chory and M.Furuya. Phytochrome B is not detectable in the *hy3* mutant of *Arabidopsis*, which is responding to end-of-day far-red light treatments. *Plant Cell Physiol.* Vol. 32(7). 1991. pp. 1119-1122.
7. Reed, J.W., P. Nagpal, D.S. Poole, M. Furuya and J. Chory. Mutations in the gene for the Red/Far-Red light receptor Phytochrome B alter cell elongation and physiological responses throughout *Arabidopsis* development. *Plant Cell* Vol. 5. 1993. pp. 147-157.
8. Liscum, E. and R.P. Hangarter. Genetic evidence that the red-absorbing form of phytochrome B modulates gravitropism in *Arabidopsis thaliana*. *Plant Physiol.* Vol. 103. 1993. pp. 15-19.
9. Johnson, C.F., C.S. Brown, R.M. Wheeler, J.C. Sager, D.K. Chapman and G.F. Deitzer. Infra-red light -emitting diode radiation causes gravitropic and morphological effects on dark-grown oat seedlings. (In Preparation)
10. Mian, A. and S. Chuang. Dark cycle monitoring of biological specimens on Space Station Freedom. Soc. Automotive Engineers Technical Paper #921393. 1992.

11. Dehesh, K., C Franci, B.M. Parks, K.A. Seeley, T.W. Short, J.M. Tepperman and P.H. Quail. *Arabidopsis HY8* locus encodes phytochrome A. *Plant Cell* Vol. 5. (1993) pp. 1081-1088.
12. Koornneef, M., E. Rolff and C.J.P. Spruit. Genetic control of light-inhibited hypocotyl elongation in *Arabidopsis thaliana* (L.) Heynh. *Z. Pflanzenphysiol.* Vol. 100. 1980. pp. 147-160.
13. Whitelam, G.C. and H. Smith. Retention of phytochrome-mediated shade avoidance responses in phytochrome-deficient mutants of *Arabidopsis*, cucumber and tomato. *J. Plant Physiol.* Vol. 139. (1991). pp. 119-125.
14. Reed, J.W., A. Nagatani, T.D. Elich, M. Fagan and J. Chory. Phytochrome A and Phytochrome B have overlapping but distinct functions in *Arabidopsis* development. *Plant Physiol.* Vol. 104. (1994) pp. 1139-1149.

VI. APPENDIX

Running Head:

PRELIMINARY DRAFT

INFRA-RED RADIATION EFFECTS ON OAT SEEDLINGS

Author to whom all correspondence should be sent:

Corinne F. Johnson
Mail Code BIO-3
The Bionetics Corporation
Kennedy Space Center, FL 32899

email: johnsonc@lssf.ksc.nasa.gov
(voice) 407-853-7703
(fax) 407-853-4220

12-57

PRELIMINARY DRAFT

Infra-red Light-emitting Diode Radiation Causes Gravitropic and Morphological Effects on Dark-Grown Oat Seedlings

Corinne F. Johnson¹, Christopher S. Brown¹, Raymond M. Wheeler², John
C. Sager², David K. Chapman¹, and Gerald F. Deitzer³

¹*The Bionetics Corporation, Code BIO-3, Kennedy Space Center, FL 32899,* ²*National
Aeronautics and Space Administration, NASA/MD-RES, Kennedy Space Center, FL 32899,*

³*University of Maryland, Department of Horticulture and Landscape Architecture, 2102
Holzapfel Hall, College Park, MD 20742*

Date of Manuscript Receipt: _____

Date of Manuscript Acceptance: _____

¹ This work was supported by the National Aeronautics and Space Administration (NASA) through the Life Sciences Support Contract (NAS10-11624) to The Bionetics Corporation, at the Kennedy Space Center, and by The University of Pennsylvania, under the NASA contract (NAG2-574) for International Microgravity Laboratory-1, Gravitational Plant Physiology Facility, SLS-42. The oat seeds were a gift of Svalof Weibull AB International of Sweden.

² Abbreviations: IR, infra-red; LED, light-emitting diode; nm, nanometer (wavelength); cv., cultivar;

ABSTRACT

Oat (*Avena sativa* cv Seger) seedlings were irradiated with two sources of infra-red (IR) light-emitting diode (LED) radiation (peak wavelengths 880 and 935 nm) passed through a visible-light blocking filter (blocks wavelengths below 800 nm). IR LED irradiated seedlings exhibited differences in growth (i.e., reduction in mesocotyl tissue length, increase in coleoptile length and advanced leaf emergence) when compared to seedlings grown in darkness at the same temperature. Further, IR LED irradiated seedlings exhibited an orthogravitropic response in the mesocotyl while dark-grown seedlings exhibit a diagravitropic response. The oat seedlings in this study perceived IR LED radiation. These findings stress the importance of careful verification testing before the use of IR LEDs as a safe-light for photosensitive plant response experiments.

INTRODUCTION

Infra-red (IR) light-emitting diodes (LEDs) have been used in several plant experiments as a "safe-light" source for IR sensitive cameras (1-3, 5, 7, 13). Dark photography was preferred in these experiments on circumnutation and gravitropism because it allowed plant movements to be observed while eliminating the complicating phototropic responses caused by flash (or light) photography. An IR camera system for dark cycle monitoring of biological specimens also has been recommended for the NASA Space Station (9). The IR LEDs in this viewing system provide illumination to the IR camera in the near infra red (780 - 1000 nm) region of the spectrum. Because of the relatively narrow band-width of the LED radiation, and because the IR LED wavelengths are outside the visible region of the electromagnetic spectrum, it has been assumed their use in dark photography systems would have no effects on plants.

In previous studies, we have tested IR LEDs and found them safe with regard to phototropic influences on dark-grown oat seedlings. However, mesocotyl tissue of oat seedlings grown under long-duration exposure to IR LED radiation (filtered through an IR-transmitting, visible-light-blocking filter) exhibited an apparent orthogravitropic response whereas the dark-grown oat seedlings' mesocotyl exhibited an apparent diagravitropic response.

Two possible explanations for the observations are considered. One possibility addressed here is that both the IR LEDs and the visible-blocking filter may provide extremely minute, but sufficient quantities of red light wavelengths to the plants to account for the observed gravitropic responses. Phytochrome, has been implicated in red light-induced gravitropism (8, 11, 12) and the observed morphological changes in the seedlings (suppressed mesocotyl growth and advanced leaf emergence) are consistent with known phytochrome-induced changes (4, 6). However, the absorption spectra of purified oat phytochrome (P_{fr}) includes a "tail" which extends into the near infrared region (10). Thus, a second possible explanation is that IR light, rather than red, through absorption by P_{fr} is causing the observed response.

In this report, we describe two series of experiments which demonstrate that the radiation from IR LEDs is not imperceptible to dark-grown oat seedlings. Also described is the analysis of the LED spectral quality output. (For clarification, when IR light and IR radiation are discussed here, this only refers to the spectral radiation in the near-infrared portion of the electromagnetic spectrum.)

MATERIALS and METHODS

Plant Material and Growth

Oat (*Avena sativa* cv Seger) seeds were planted in a moistened peat/vermiculite mix (Metro-Mix 220, Grace Sierra Horticultural Products Company, Milapitas, CA) so that the brush of the seed was even with the soil line. Seeds were planted with the seed's point-of-attachment directed downward into the soil, and the seed coat crease oriented 90-degrees from the direction of IR LED irradiation. The germinating oat seedling, when grown in the dark, directs shoot growth away from the seed in the direction of the seed coat crease. This directional growth (possibly a nastic response) was exploited to differentiate between an apparent phototropic response and a morphological growth pattern. By uniformly orienting the seeds, the natural direction of coleoptile growth was 90 degrees from the IR light source. For the first set of experiments, seeds were planted in 147 cm (6 inch) standard plastic pots, covered with aluminum foil to retain soil moisture. Holes were punched through the aluminum foil to provide openings for the seeds. In the second set of experiments, seeds were planted in soil trays made of black anodized aluminum as described by Johnsson *et al* (7). The soil trays were placed inside light-tight plant modules with windows made of IR transmitting, visible-light-blocking acrylic (Rohm and Haas acrylic # 2650 Rohm and Haas, Philadelphia, PA). The plant chambers were maintained at a temperature of 22.5 ± 1 °C in all experiments.

Experimental

In the first set of experiments, the IR LED radiation of either 935 nm or 880 nm, (depending on treatment) was passed through a clear acrylic window inside a 245 cm x 368 cm wooden dark box. The wooden dark boxes were placed inside a temperature controlled growth chamber. The seedlings received continuous IR LED treatment from time of planting to age 120 hours. Controls were grown in a dark box identical to the IR LED treatment boxes. The 880 nm LEDs used in the study were made of aluminum gallium arsenide (Honeywell # 840-3470-001, Micro Switch Division, Richardson, TX) and provided a fluence rate of $90 \mu\text{mol}\cdot\text{m}^{-2}\cdot\text{s}^{-1}$. The 935 nm IR LEDs used were made of gallium arsenide (Honeywell # 840-3445-004, Micro Switch Division, Richardson, TX) and provided a fluence rate of $65 \mu\text{mol}\cdot\text{m}^{-2}\cdot\text{s}^{-1}$. In both 935 nm and 880 nm LED boxes, one-hundred LEDs were arranged in a 21 cm square matrix. There were 20 seeds planted per pot with one pot per treatment. This experiment was performed 5 times.

In the second set of experiments, to increase our confidence that neither red nor far-red light

were contaminating the experimental set-up (through very minute amounts possibly being emitted by the IR LEDs) the 880 nm LED treatment was eliminated and an IR filter was added to the 935 nm LED system. The IR transmitting visible-light-blocking filter-windows on the plant modules provided a cut-off of light wavelengths below 800 nm. Oat seedlings were grown for 58 hours in darkness, then exposed to 935 nm IR LED radiation passed through the IR filter from age 58 to 84 hours. At the temperature of 22.5 °C, the seedlings are just emerging above the soil line at age 58 hours. This shorter growth time (and shorter length) allowed the seedlings to be grown inside the small (but available) light-tight IR-filter plant modules, as described above. The IR transmitting filters reduced irradiance from the 935nm LEDs to a fluence rate of 15 $\mu\text{mol}\cdot\text{m}^{-2}\cdot\text{s}^{-1}$. Dark controls were also grown inside the light-tight modules, wrapped in aluminum foil to block IR radiation from entering through the IR filter windows. There were 9 seeds per plant module, and 2 plant modules per treatment. This experiment was performed 8 times.

Measurements

Plants were removed from the treatment dark boxes and photographed from the side using an IR sensitive CCD camera (Model 4TN2505, General Electric, USA). The image was digitized and stored on computer. Plants were then removed from their containers and length of coleoptile, mesocotyl and leaf tissue were measured. Plant angle measurements were made from the digitized image of the seedlings with the aid of an Apple Macintosh computer image analysis program (NIH Image). In the first set of experiments, tip-to-base angles were measured in the longer, 120 hour old seedlings. In the second set of experiments, the angle of orientation with respect to vertical was measured along the bottom third of the seedling shoots (mesocotyl tissue region) in the shorter, 85 hour old seedlings. Measurements of light quality were made with an LI-1800 spectroradiometer (LiCor, Lincoln, NE). The spectroradiometer scanned between 300 - 1100 nm, in 2 nm intervals, to determine the spectral quality and quantity of the LEDs. The dark control box was also measured to establish a baseline and to confirm that there was no light contamination in the visible or IR range.

RESULTS

Plant growth responses

As expected, growth of the dark-grown seedlings was uniformly directed away from the seed in the direction of the seed coat crease. Also as expected, there was no phototropic bending response of the seedlings was observed in any of the treatments.

In the first set of experiments, growth measurements of the 120 hour-old seedlings showed seedlings grown in the presence of 880 nm IR LEDs were shorter and had a lower percentage of mesocotyl tissue than seedlings grown under 935 nm LEDs or in darkness (Table I). Although total lengths of dark-grown seedlings and 935 nm seedlings were not significantly different, seedlings grown in the presence of 935 nm LEDs had a lower percentage of mesocotyl tissue than the dark-grown controls. The 880 nm IR LED treated seedlings were more advanced in leaf emergence and unfurling than 935 nm IR LED treated seedlings or dark-grown seedlings. Angle measurements show that there was no significant difference in seedling tip-to-base angles between the two IR irradiated treatments. However, both the 935 nm and 880 nm LED treatment seedling angles were significantly different from the dark-grown seedling angles (Figure 1) at the 0.05 confidence level (Table I.)

In the second set of experiments, growth measurements of the 85 hour old seedlings showed oat seedlings grown in the presence of IR radiation (935 nm) were shorter and had significantly less mesocotyl tissue than seedlings grown in darkness (Table I). Angle measurements show that seedlings treated with 935 nm IR LED radiation passed through an IR filter grew straighter than dark-grown seedlings .

Light quality measurements

Spectroradiometer measurements show that no visible light (300 - 700 nm) was present in either IR system or the dark control (Figure 2). Closer examination of the tail regions of the spectral irradiance curves (Figure 3) show that the 880 nm LED source begins radiating quantities of less than $0.1 \mu\text{mol m}^{-2} \text{s}^{-1}$ over the range of wavelengths below 800 nm and the 935 nm LED source begins radiating quantities of less than $0.1 \mu\text{mol m}^{-2} \text{s}^{-1}$ below 900 nm. Measurements of the Dark Treatment Box were made. The average value recorded for darkness measurements on the spectroradiometer was $9.0\text{E}-05 \pm 3.3\text{E}-04$. (n= 4000 data points, 5 each at even numbered nanometers between 300 - 1100). Log graphs plotted to accentuate irradiance in the tail sections of the curves show that the 880 nm LEDs began to radiate at 770 nm (Figure 4). When passed through an IR filter the 880 nm source yielded measurable radiation at 800 nm. Also shown in the log graph, the 935 nm LEDs began to radiate at 880 nm. When passed through an IR filter, the 935 nm source yielded measurable radiation at 890 nm.

Through the spectroradiometer readings, it was noted that the LEDs which were marketed to have peak wavelengths of 880 and 935 nm had peak wavelengths higher than their marketed

values. For simplicity throughout this paper they are referred to by their catalog values of 880 nm and 935 nm LEDs, however, average measured peak wavelengths were actually 916 nm and 958 nm, respectively. Average band width at half-height for the 880 nm LEDs was 94 nm. Average band width at half-height for the 935 nm LEDs was 50 nm.

To further characterize the IR filter, measurements were made using the 880 nm LEDs as a source. Without the IR filter, the 880 nm LEDs yielded an average of $0.050 \mu\text{mol m}^{-2} \text{s}^{-1}$ in the (far-red) region from 770-780 nm. This was reduced when the IR filter was used in combination with the 880 nm LEDs to $0.004 \mu\text{mol m}^{-2} \text{s}^{-1}$ in the (far-red) region from 770-780 nm. The IR filters only slightly changed the starting wavelengths for light emission. The filter did little to change the light quality, but did significantly decrease the light quantity. This effectively reduced the measurable light in the tail cut-off regions, thus slightly increasing the starting measurable emission wavelength.

Discussion and Conclusions

The results of this study show that long duration exposure of *Avena sativa* L. Seger to IR LED radiation is perceptible to oat seedlings. The plants were not affected phototropically (i.e., the IR LED irradiated plants did not bend towards the LEDs); however, the IR LED irradiated seedlings' mesocotyl tissue displayed an orthogravitropic response while dark-grown plants exhibited a diagravitropic response.

Suppression of mesocotyl tissue development and advanced tissue unfurling, known to be phytochrome mediated responses (4, 6) were observed in the IR LED-treated seedlings. Thus, if the phytochrome system is being activated by some component of the IR LED/IR filter system, then either a minute amount of far-red light is emanating from the system; causing a very low fluence response, or the phytochrome may be being activated in the near infrared region as well. The spectroradiometer data shows that the 880 nm LEDs may yield minute quantities of far-red, however, no measurable far-red light was detected from the 935 nm LED source. This supports the latter hypothesis, that is, phytochrome may be being activated in the near infrared region by the 935 nm LEDs, and both the far-red and near infra-red regions by the 880 nm LEDs. This is consistent with the findings of Liscum and Hangarter (8), suggesting that absorption by the P_{fr} form of phytochrome and the subsequent photoconversion to the P_r form is responsible for the observed gravitropic response.

The mesocotyl tissue's orthogravitropic response was activated by both the 880 and 935

LEDs, however, the response appeared more pronounced in the 880 treated seedlings, demonstrating an increase in response as the wavelength of the light gets closer to the visible.

Although the precise wavelengths of radiation causing the effect are yet to be identified, the observation is important for investigators using IR LEDs as a study tool for dark-viewing.

References

1. Brown A.H. and D.K. Chapman (1977), Effects of Increased Gravity Force on Nutations of Sunflower Hypocotyls, *Plant Physiol.* 59:636-640
2. Brown, A.H., D.K. Chapman, R.F. Lewis and A.L. Venditti (1990) Circumnutations of Sunflower Hypocotyls in Satellite Orbit. *Plant Physiol.* 94: 233-238
3. Chapman D.K. and A.H. Brown (1979), Residual nutational activity of the sunflower hypocotyl in simulated weightlessness. *Plant and Cell Physiol.* 20(2):473-478
4. Downs R. et al (1957) *Botan. Gazzette* 118:199
5. Eidesmo T., A.H. Brown, D.K. Chapman, and A. Johnsson (1991) Tropistic responses of Avena seedlings in simulated hypogravity. *Microgravity Science and Technology IV*:199-206
6. Hopkins, W and W. Hillman (1965) *Planta* 65:157
7. Johnsson, A., Chapman, D.K., Brown, A.H., Johnson-Glebe, C.F., Karlsson, C. and Heathcote, D.G. (1993) Gravity sensing in oat coleoptiles: scatter in growth orientation under different g-conditions. *Plant, Cell and Environment* 16:749-754
8. Liscum E. and R.P. Hangarter (1993) Genetic Evidence that the Red-Absorbing Form of Phytochrome B Modulates Gravitropism in *Arabidopsis thaliana*. *Plant Physiol.* 103:15-19
9. Mian, A. and S. Chuang (1992) Dark Cycle Monitoring of Biological Specimens on Space Station Freedom, Society of Automotive Engineers Technical Paper #921393

10. Quail , P.H. in *Plant Biochemistry* (1976) eds. J. Bonner and J.E. Varner, Academic Press, New York pp684 after Anderson, G.R., E.L. Jenner and F.E. Mumford (1970) *Biochim. Biophys. Acta* 221:69
11. Quail PH, WR Briggs (1978) Light-enhanced geotropic sensitivity in maize roots: possible involvement of phytochrome, *Carnegie Inst Wash Year Book*, 77:336-339
12. Tepfer DA, HT Bonnett (1972) The role of phytochrome in the geotropic behavior of roots of *Convolvulus arvensis* *Planta* 106:311-324
13. Zachariassen E., A. Johnsson, A.H. Brown, D.K. Chapman, C.F. Johnson-Glebe (1987) Influence of the g-force on the circumnutations of sunflower hypocotyls. *Physiol. Plant.* 70:447-452

TABLE I. Plant growth and angle data. Students' t-test groupings: Averages \pm Standard Errors shown. Means of each column followed by the same letter are not significantly different at the 0.05 level. Test series #1 and #2 data statistically analyzed separately.

Treatment	Total Height	Leaf length	Percent mesocotyl	Average seedling tip-to-base angle (degrees)
First set of Experiments (Plant age 120 hours)				
	(mm)	(mm)	(%)	
Dark	100.1 \pm 2.2 x	0 x	54.6 \pm 1.4 (x)	146.4 \pm 5.8 x
935 nm	98.4 \pm 2.8 x	0 x	35.6 \pm 1.1 (y)	86.0 \pm 3.5 y
880 nm	88.1 \pm 2.4 y	7.4 \pm 1.3 y	17.7 \pm 0.9 (z)	91.8 \pm 2.6 y
Second set of Experiments (Plant age 84 hours)				
	(mm)	(mm)	(%)	
Dark	37.6 \pm 2.1 a	0 a	60.6 \pm 0.5 (a)	159.8 \pm 4.1 (a)
935 nm LED + IR Filter	32.6 \pm 1.8 b	0 a	48.9 \pm 1.6 (b)	127.3 \pm 5.7 (b)

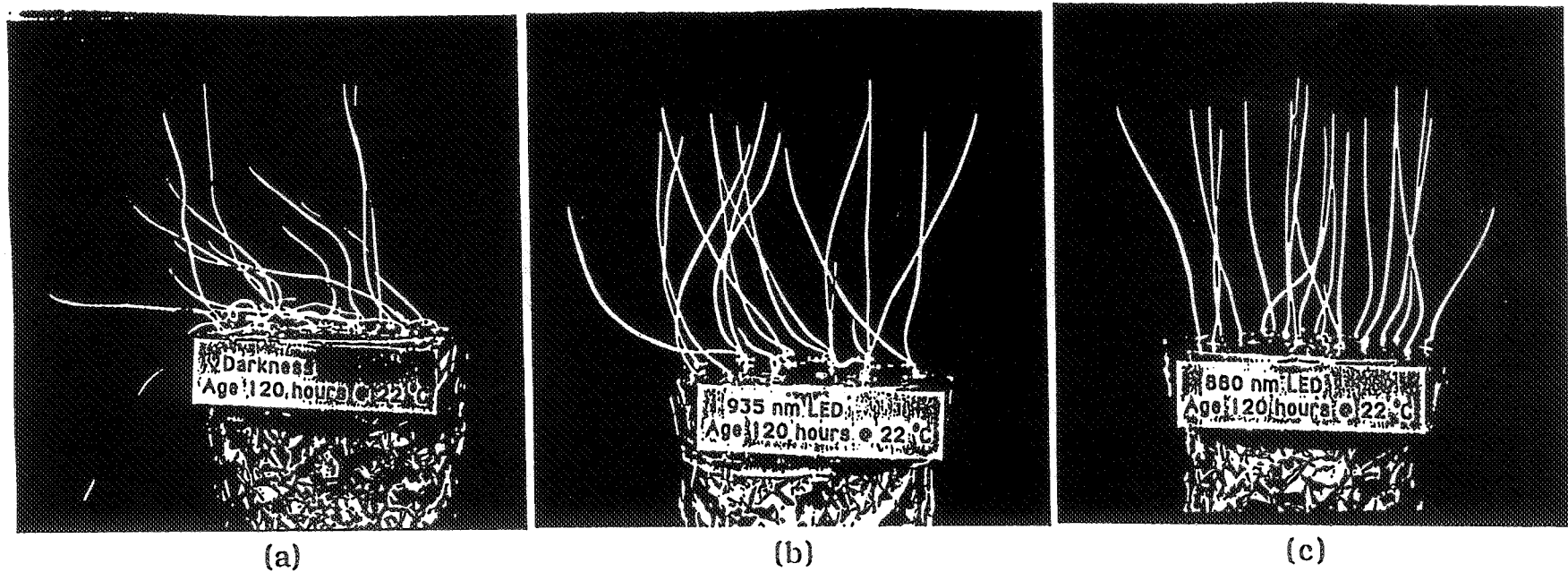


FIGURE 1. *Avena sativa* seedlings, age 120 hours, grown at 22.5 °C under continuous (a) darkness, (b) 935 nm IR LED irradiation, and (c) 880 nm IR LED irradiation

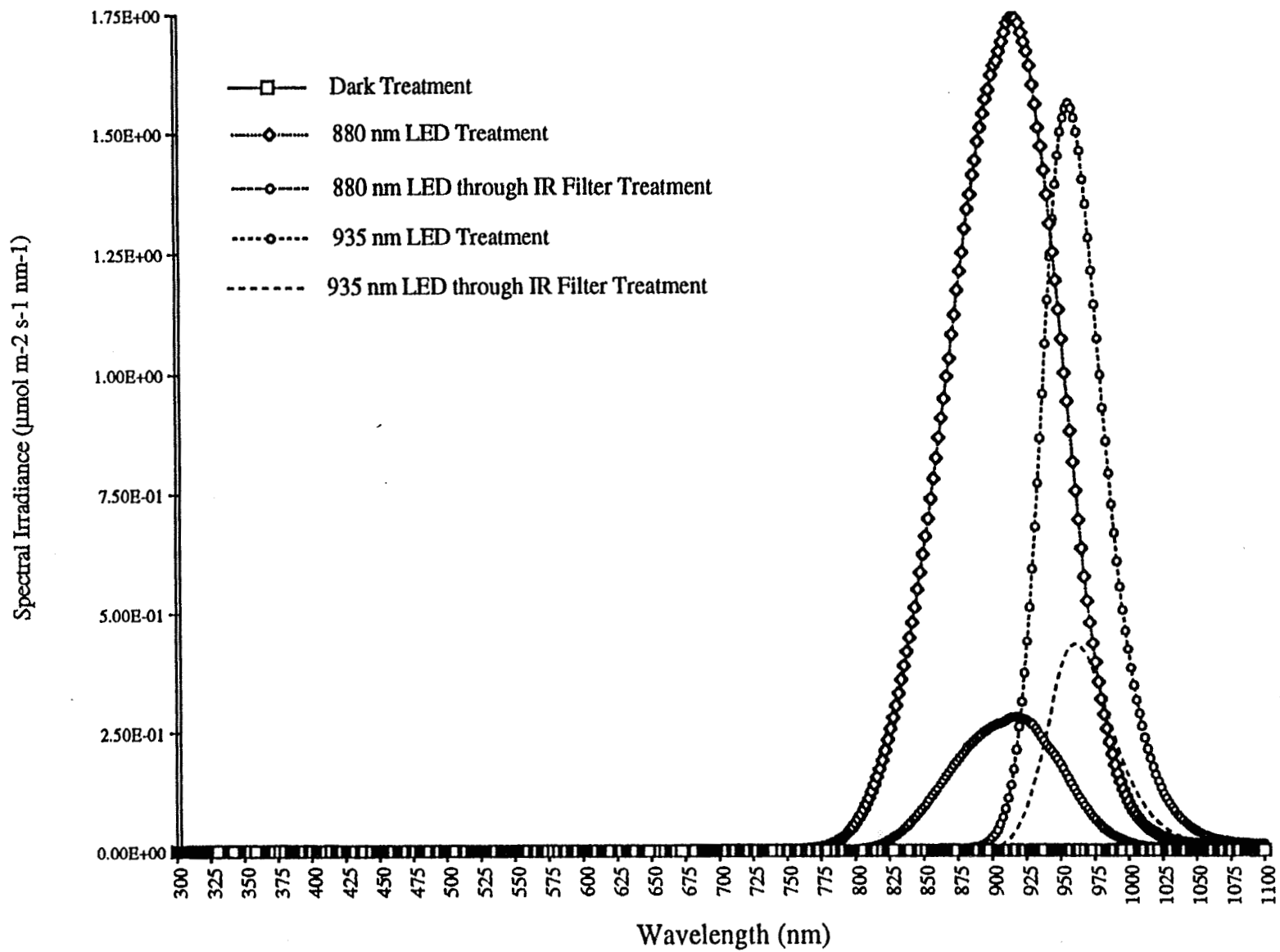


FIGURE 2. Linear analysis of spectral output from spectroradiometer

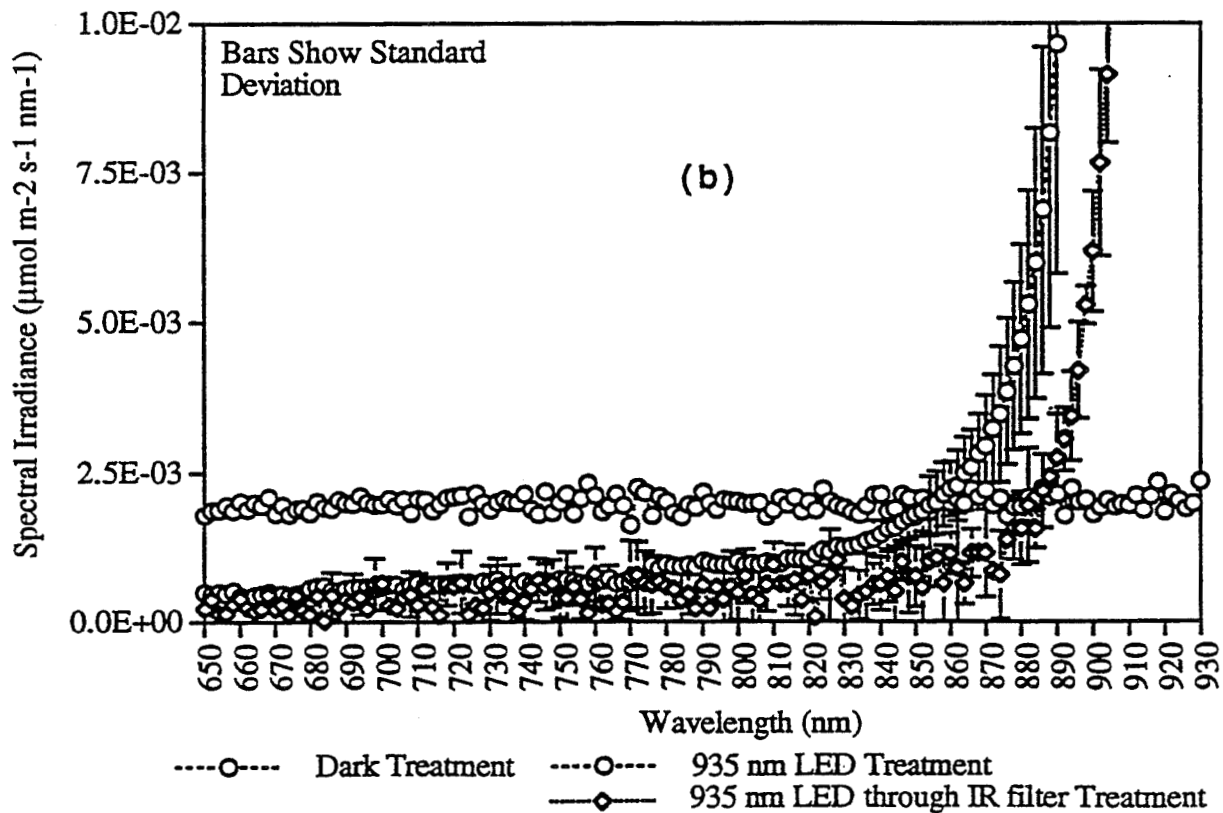
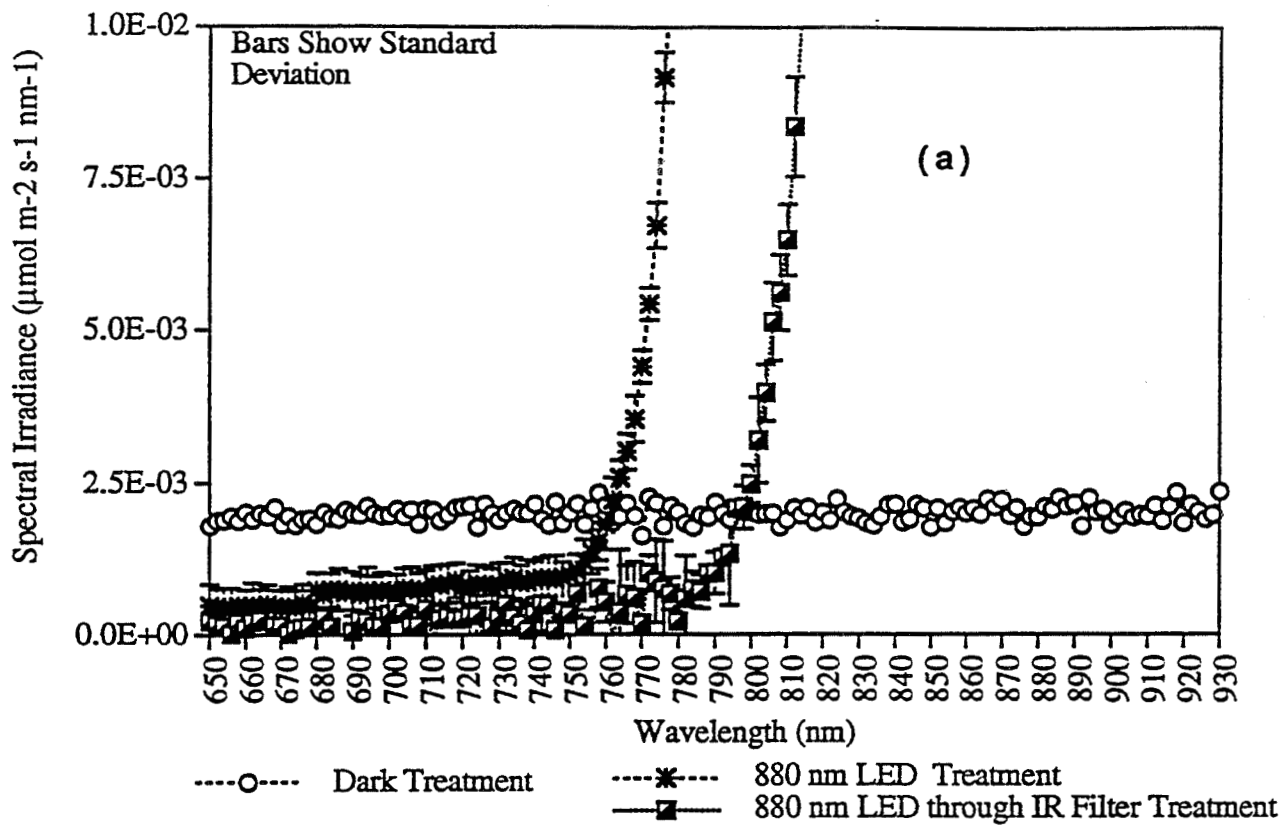


FIGURE 3. Linear graphs from spectroradiometer, close-up of tail regions for (a) 880 nm LEDs (with and without IR Filter) and (b) 935 nm LEDs (with and without IR Filter)

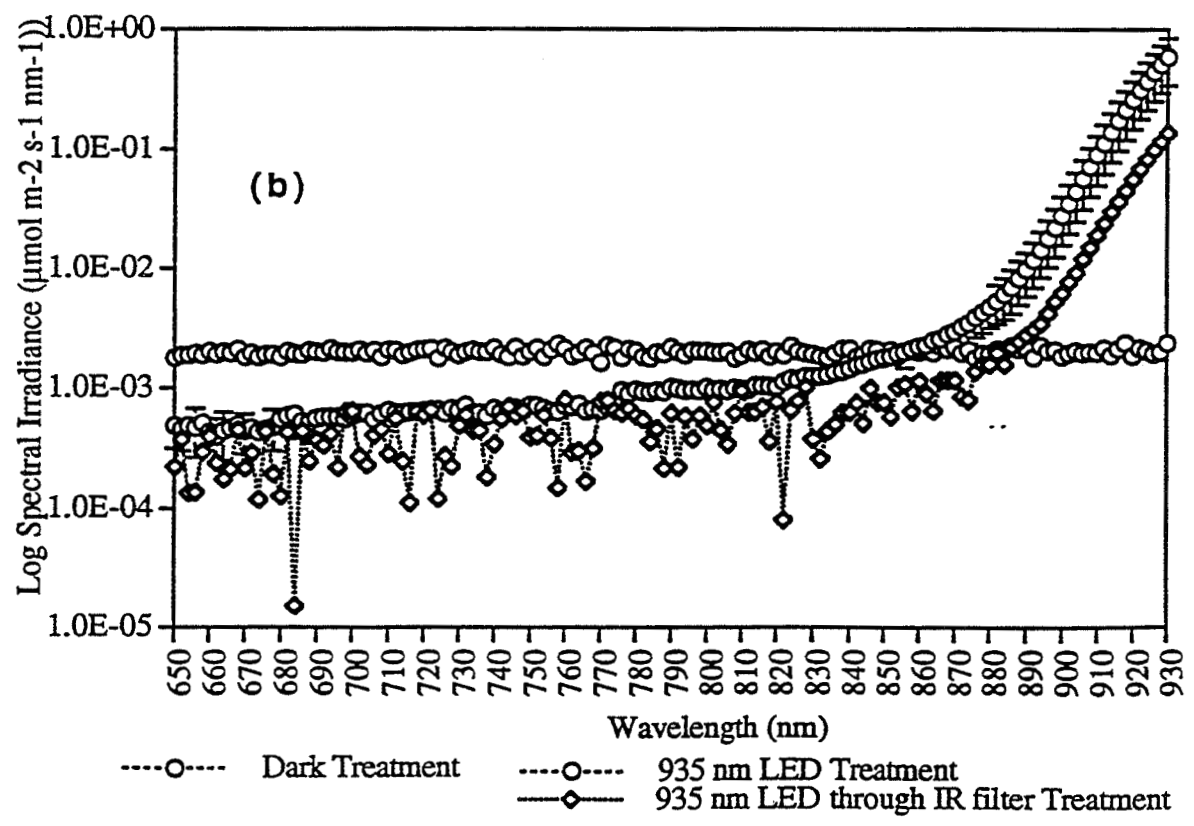
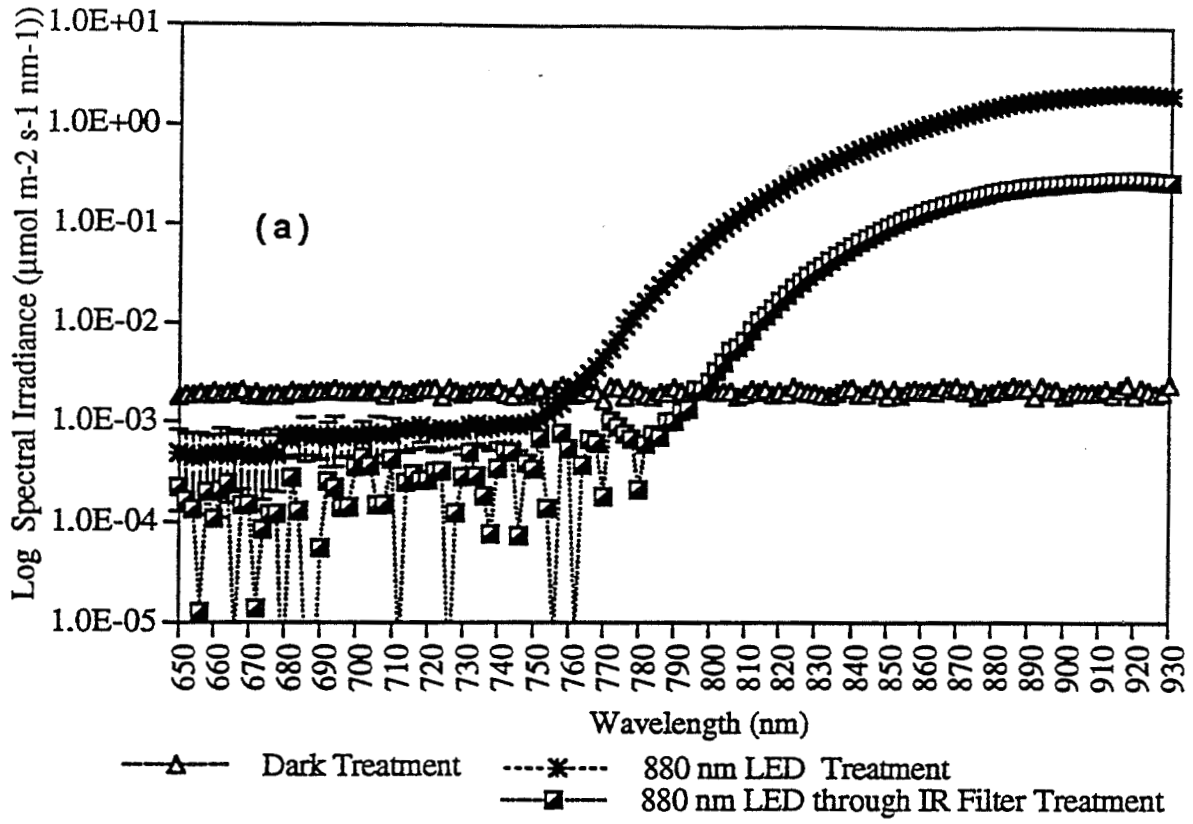


FIGURE 4. Log scale graphs from spectroradiometer, close-up of tail regions for (a) 880 nm LEDs (with and without IR Filter) and (b) 935 nm LEDs (with and without IR Filter)

1994 NASA/ASEE SUMMER FACULTY FELLOWSHIP PROGRAM

351485
117 759

JOHN F. KENNEDY SPACE CENTER
UNIVERSITY OF CENTRAL FLORIDA

58-47

33968

p. # 30

LIGHTNING STUDIES USING LDAR AND
COMPANION DATA SETS

PREPARED BY:	Dr. Gregory S. Forbes
ACADEMIC RANK:	Associate Professor
UNIVERSITY AND DEPARTMENT:	The Pennsylvania State University Department of Meteorology
NASA/KSC	
DIVISION:	Communications and Instrumentation
BRANCH:	Instrumentation and Measurements
NASA COLLEAGUE:	Carl Lennon
DATE:	August 15, 1994
CONTRACT NUMBER:	University of Central Florida NASA-NGT-60002 Supplement: 17



ACKNOWLEDGEMENTS

Participation in the NASA/ASEE Summer Faculty Fellowship Program has been an enjoyable and professionally stimulating experience. Appreciation is extended to all those who support this program financially, and to the many individuals who made presentations or gave tours to the Faculty Fellows. Particular thanks are extended to Dr. Loren A. Anderson, Co-Director of the NASA/ASEE Summer Faculty Fellowship Program, and to Kari L. Stiles, Administrative Assistant, who coordinated the program extremely well.

It was a great pleasure to work with Carl Lennon and others associated with the Lightning Detection and Ranging (LDAR) system in TE-CID-3. Carl Lennon is to be congratulated for the development of the LDAR system, which shows great capabilities in revealing the presence of electrical discharges within, and emanating from, thunderstorms. His support and encouragement of the applied research reported here is appreciated. The author benefitted from discussions with Launa Maier, who has vast knowledge of thunderstorms and their electrical processes.

The author is very appreciative of the efforts of the NYMA employees, Steve Schaefer and Phil Gardner, who operate the LDAR system and archive its data, and patiently dealt with many data requests and the increased computer load while the data were being processed. Steve was particularly helpful in retrieving data for the studies described below.

Many groups and individuals helped provide companion data sets for use in the study. Bart Hagemeyer (MIC), Dave Sharp (SOO) and Steve Hodanish, all of the National Weather Service Office in Melbourne, assisted in WSR-88D radar data acquisition. Phil Gemmer of EG&G and Hal Herring, Susan DeRussey and Val Valek of CSR provided field mill and wind tower (surface mesonet) data. Jim Medina (TE-CID-1) and Mike Moore (NYMA) helped acquire KSC wind profiler data. Gerry Talley of TE-CID-2 and Al Cater (LSOC) provided LLP data and roof camera video data. Greg Taylor and Mark Wheeler of the Applied Meteorology Unit (AMU; ENSCO) helped acquire Patrick AFB radar data using the McGill radar display system.

Two graduate students participated in the summer research project: Steven G. Hoffert, a graduate student in meteorology at Penn State University and Lt. Nathan E. Drummond of the Air Force Institute of Technology and the Ohio State University Department of Geography and Atmospheric Science. They assisted in cloud photography, radar data retrieval, and took the lead in obtaining and implementing radar display software and overlaying LDAR data on the radar imagery. Steve also served as liaison to the National Weather Service Office in Melbourne in their process of learning to use LDAR data in operational weather forecasting and kept track of the meteorological scenarios in which thunderstorms were developing. Their participation helped make the summer research program a success. John Madura, Chief, Weather Projects Office (TM-LLP-2), provided financial support for the participation of Steve Hoffert.

The processing of large quantities of data from diverse sources required considerable computer support. Mark Sorger and Carol Lundberg of EG&G provided exceptional service in loading data onto the KSC computer system (KSDN). John Kiriazes and Steve Tam of TE-CID-3 helped provide access to the Internet, and helped the graduate students gain access to computer workstations. Art Person of Penn State provided computer assistance via e-mail. Workstations in the Wave Analysis Lab were used to display radar data and LDAR overlays, and the assistance of Tom Henning (NGTS) is appreciated. Radar display software was written by and obtained from Dave Priegnitz, Institute of Atmospheric Sciences, South Dakota School of Mines and Technology.

The author looks forward to a continued interaction with Carl Lennon, Launa Maier, Steve Schaefer, Phil Gardner, and others using LDAR data for weather applications, including Robin Schumann (ENSCO) and Frank Merceret of the AMU. Our goal is to help the operational weather forecasters of the 45th Weather Squadron--detached out of Patrick AFB, USAF Space Command--who provide KSC with operational weather support from the Cape Canaveral Forecast Facility.

ABSTRACT

Research was conducted to use the KSC Lightning Detection And Ranging (LDAR) system, together with companion data, in four subprojects: weather forecasting and advisory applications of LDAR, LDAR in relation to field mill readings, lightning flash and stroke detection using LDAR, and LDAR in relation to radar reflectivity patterns and KSC wind profiler vertical velocities. The research is aimed at developing rules, algorithms, and training materials that can be used by the operational weather forecasters who issue weather advisories for daily ground operations and launches by NASA and the United States Air Force.

During the summer of 1993, LDAR data was examined on an hourly basis from 14 thunderstorm days and compared to ground strike data measured by the Lightning Location and Protection (LLP) system. These data were re-examined during 1994 to identify, number, and track LDAR-detected storms continually throughout the day and avoid certain interpretation problems arising from the use of hourly files. An areal storm growth factor was incorporated into a scheme to use current mappings of LDAR-defined thunderstorms to predict future ground strikes.

During the summer of 1994, extensive sets of LDAR and companion data have been collected for 16 thunderstorm days, including a variety of meteorological situations. Detailed case studies are being conducted to relate the occurrence of LDAR to the radar structure and evolution of thunderstorms. Field mill (LPLWS) data are being examined to evaluate the complementary nature of LDAR and LPLWS data in determining the times of beginning and ending of the ground strike threat at critical sites. A computerized lightning flash and stroke discrimination algorithm has been written that can be used to help locate the points of origin of the electrical discharges, help distinguish in-cloud, cloud-ground, and upward flashes, and perhaps determine when the threat of ground strikes has ceased. Surface wind tower (mesonet), radar, sounding, and KSC wind profiler data will be used to develop schemes to help anticipate the timing and location of new thunderstorm development. Analysis of this data will continue in graduate student research projects.

SUMMARY

Lightning Detection and Ranging (LDAR) data have been examined from thunderstorms during the summers of 1993 and 1994. The 1993 data set, consisting of 33 hours of data from 14 days, has been extensively examined to determine the locations of cloud-ground strikes relative to the areas experiencing LDAR events, which are sometimes related to ground strikes and to the more frequent in-cloud and cloud-cloud discharges. Extensive software was written to cluster the LDAR data points into LDAR-defined thunderstorms, number them, and track their movements. The locations of ground strikes detected by the KSC Lightning Location and Protection (LLP) system were then compared to the LDAR storms. Ninety-eight percent of the ground strikes occurred within the boundaries of the LDAR storms or within 2 km of their edges. The 2 km margin allows for modest position mislocations by the remote sensing systems (primarily LLP) and for tilted ground strikes whose lower portions are not typically detected by the LDAR system. For individual storms, LDAR events occur aloft, on average, 4-5 minutes before the first ground strike. Typically the first LDAR events are centered near 8 km.

An extrapolation scheme which used existing LDAR storms and their movements to predict future ground strike locations was examined. Modest success was obtained for forecasts of less than 10 minutes duration. An areal storm growth factor was also incorporated into the scheme, giving somewhat improved results in forecasts longer than 5 minutes. Beyond 10 - 20 minutes, however, the extrapolation scheme would not prove acceptable as an automated warning tool. Further analysis revealed that this type of scheme performed reasonably well once the day's thunderstorm activity was well underway. However, during the first half hour--when the number of thunderstorms is rapidly increasing--the forecast problem is one of anticipation of where new thunderstorm cells will form, rather than one of extrapolation of existing storms.

Software was written to examine and intercompare companion meteorological data sets and begin to address the problem of new thunderstorm cell development. These include LPLWS (Launch Pad Lightning Warning System--field mills), radar, KSC wind profiler, and surface mesonet (wind tower) data. Data sets have been obtained and initial case studies performed to test the software. Analyses of these data sets will continue.

LDAR has been superimposed on radar to relate the evolution of the storm lightning pattern to thunderstorm structure. Initial examples have been presented showing the location of the first LDAR events in storms with respect to radar reflectivity patterns, typically at a location just above the highest reflectivity core. The LDAR pattern at the beginning of a microburst-producing storm has been documented. The quasi-stratiform radar reflectivity pattern accompanying a broad, diffuse in-cloud flash has been shown.

Field mill readings are being examined to determine critical values of electric field at the time of beginning and end of the threat of lightning at critical sites. This relates to a forecast problem concerning the likelihood of lightning from electrified anvil or debris clouds. Examples are shown.

Software was written to identify individual flashes and strokes contained within the volume of LDAR data. This can be used to help identify isolated ground strikes from anvil using LDAR data. The points of origin of the LDAR-detected flashes and strokes can be used to help identify the three-dimensional positions of the positive and negative charge centers within thunderstorms, and can be related to radar depictions of the storm precipitation structure in these regions. Examples are shown.

The generation of training materials has also been an objective of the project. In addition to the material within this report, seminars were given to operational weather forecasters of the National Weather Service and the United State Air Force 45th Weather Squadron. Copies of the viewgraphs and slides from these presentations have been made available to these groups, to the Applied Meteorology Unit, and to the NASA Weather Projects Office.

TABLE OF CONTENTS

<u>Section</u>	<u>Title</u>	<u>Page</u>
I	INTRODUCTION	7
1.1	The LDAR and LLP Systems and Data Processing	7
1.2	Past Results and Current Objectives	9
II	WEATHER FORECASTING AND ADVISORY APPLICATIONS OF LDAR	10
2.1	Potential Mesoscale and Synoptic Climatology Applications	10
2.2	LDAR Lead Times	10
2.3	Evolution of LDAR in Thunderstorms	10
2.4	Prediction of Future Ground Strikes by Extrapolation	12
2.5	Ground Strikes from Anvils	13
III	LDAR IN RELATION TO FIELD MILL READINGS	15
3.1	Intercomparison of LDAR, LLP, and Field Mill Readings	15
3.2	Case Study of Field Mill Lightning Hazard Thresholds	15
IV	LIGHTNING FLASH AND STROKE DETECTION USING LDAR	17
4.1	Lightning Flash/Stroke Identification Algorithm; Noise Identification	17
4.2	Thresholds for Flash and Stroke Detection	17
V	LDAR IN RELATION TO RADAR REFLECTIVITY PATTERNS AND KSC WIND PROFILER VERTICAL VELOCITIES	22
5.1	Intercomparison of LDAR to Radar	22
5.2	KSC Wind Profiler Vertical Velocities in Relation to a Layered LDAR Structure	26
VI	CONCLUDING REMARKS	28
	REFERENCES	29

LIST OF ILLUSTRATIONS

<u>Figure</u>	<u>Title</u>	<u>Page</u>
Figure 1-1	LDAR cubes superimposed on LDAR data points used in LDAR storm classification	8
Figure 2-1	Frequency of lightning occurrence based on 1993 LDAR sample ..	11
Figure 2-2	Hypothetical limits to accuracy of extrapolation forecasts of lightning ground strikes	14
Figure 3-1	Field mill readings as a function of time in relation to the distances to the nearest LDAR and LLP lightning events ...	16
Figure 4-1	Perspective view of all LDAR data points during minute 0106 UTC of day 154, 3 June 1993	18
Figure 4-2	Perspective view of flash 2	19
Figure 4-3	Perspective view of flash 4	20
Figure 5-1	South-north cross-section of thunderstorm with LDAR overlay, from 1948 UTC on day 210, 29 July 1994	23
Figure 5-2	Constant-altitude display of radar reflectivities with LDAR overlay at 7 km from 1958 UTC on day 210, 29 July 1994 ..	24
Figure 5-3	Constant-altitude display of radar reflectivities with LDAR overlay at 6 km from 2153 UTC on day 210, 29 July 1994 at 6.0 km	25
Figure 5-4	Time-height section of LDAR events over the KSC wind profiler site in relation to patterns of updraft and downdraft	27

I. INTRODUCTION

The Kennedy Space Center (KSC) is located in one of the regions of the United States (and even the world) that encounters the most lightning strikes to ground per unit area (refs. 1,2,3). The possibility of lightning at the surface or aloft is, of course, a hazard that must be avoided during launches. On a daily basis, however, there are many operations at KSC which must be curtailed if there is a threat of a lightning strike to ground in the vicinity. The accuracy and timeliness of lightning advisories, therefore, has both safety and economic implications. The ultimate goal of the research described in this report is to provide information that can be used to improve the process of real-time detection and warning of lightning by weather forecasters who issue lightning advisories.

Special networks of remote sensing equipment have been established to provide highly accurate information concerning lightning in the vicinity of KSC: the Lightning Location and Protection (LLP) system, the Lightning Detection and Ranging (LDAR) system, and a Launch Pad Lightning Warning System (LPLWS). In addition, a Catenary Wire Lightning Instrumentation System (CWLIS) detects electrical surges in wires at the launch pads when struck by lightning. The first two systems detect lightning signatures. LPLWS, by contrast, responds not only to lightning but also detects electric fields at the surface induced by electrified clouds, thunderstorms, and other atmospheric conditions. Data from the LLP, LPLWS, and LDAR systems were used in this study.

1.1 THE LDAR AND LLP SYSTEMS AND DATA PROCESSING

The LLP system (ref 4) detects lightning ground strikes through use of a network of magnetic direction finding antennae which sense electromagnetic disturbances triggered by lightning in a broad band of frequencies. Individual antennae detect a particular ground strike at different azimuth angles, and the location of the ground strike is essentially determined by finding the point of intersection of lines drawn from the antennae toward the source of the disturbance. The LLP system is approximately 90% efficient in detecting ground strikes near KSC, with position accuracy of about 1 km.

The LDAR system was developed by Carl Lennon and colleagues at KSC TE-CID-3 (ref 5). Its antennae detect lightning-induced disturbances at 66 MHz (VHF) frequency. This system uses a time of arrival (TOA) approach, and achieves extremely accurate timing through use of the Global Positioning System (GPS). The lightning-induced disturbance, travelling at the speed of electromagnetic propagation, arrives at different antennae at slightly different times. The three-dimensional position of the lightning source is determined by essentially converting these time offsets into distance differences, and then performing a triangulation. The LDAR system began real-time operation in June, 1992.

The LDAR system can generate up to 10,000 data points per second, yielding numerous data points per lightning flash. Tests of the position accuracy of the LDAR data by Launa Maier have shown that within 10 km of the central antenna, 95% of the data points are accurate to better than 200m, and 50% are accurate to better than 100m. Dots on Figure 1-1 illustrate a sample plot of LDAR data points (events) during one minute, projected to their positions at the surface. Raw LDAR data points are represented by a time and by x, y, and z positions relative to the LDAR central site. Some of the studies during 1994 used raw LDAR data.

Also shown in Fig. 1-1 is a squared-off portrayal of the area experiencing LDAR events. The squares represent post-processed LDAR data used in other facets of this research. LDAR data were composited into a four-dimensional array, consisting of the number of LDAR events within a minute and a volume. During 1993 (ref. 6) the volume was a cube having sides of length 1 km. Array elements extended from 52 km west of the LDAR central site to 52 km east, from 40 km south to 40 km north, and from 0 to 20 km in elevation. During 1994, the volumes used were rectangular wafers 1 km² in cross-section and covering the same domain, but 0.25 km in vertical thickness, extending from 0 to 22 km.

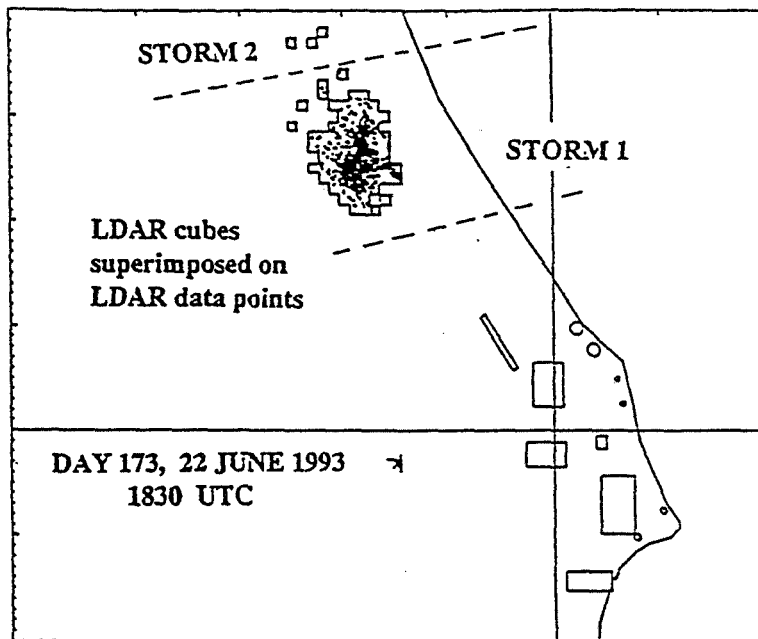


Figure 1-1. LDAR cubes superimposed on LDAR data points used in LDAR storm classification. Only a portion of the -52:52 by -40:40 km domain is shown.

Contiguous and adjacent LDAR volumes were then clustered together to form LDAR-defined storms. LDAR volumes separated by more than 3 km from a neighbor become part of a separate storm, as depicted in Fig. 1-1. Additional software examines the classified storms, discards as spurious data any storms occupying less than 4 km³, and numbers storms consistently from minute to minute. During 1993, data files were one hour in duration, such that storm number continuity could be lost between successive hours. Software has now been implemented to number storms consistently throughout a multi-hour case.

The storm numbering process uses the LDAR event-density-weighted mean horizontal position of the LDAR storm center or "centroid" and its variations with time. In this procedure, certain time and distance limits are empirically invoked to deal with numbering of intermittent LDAR storms and storms that split or merge. LDAR storms are assigned a new number if their centroid does not fall within 6 km of the position of an existing storm from an earlier time. Thus, a storm resulting from a merger of two storms could be assigned either one of the existing storm numbers--in the case of a large storm "absorbing" a smaller one--or be assigned a new number--if the composite centroid was more than 6 km from either of those of the previous storms. In the case of intermittent storms, a 10-minute preceding period is searched. Storm area, depth, volume, LDAR event density, and other parameters are monitored with time. Algorithms have been written to track LDAR-defined storms through examination of the rates of change of their centroid positions. Additional details can be found in Reference 6.

1.2 PAST RESULTS AND CURRENT OBJECTIVES

This was the second summer of study involving research to utilize lightning detection and ranging (LDAR) data, together with companion data sets, aimed at developing rules, algorithms, and training materials that can be used by the operational weather forecasters who issue weather advisories for daily ground operations and launches by NASA and the United States Air Force. Research during 1993 enabled the development of a computerized scheme for clustering the LDAR data into groups of data points associated with individual thunderstorms (as described above), tracking these LDAR-defined storms, and comparing the positions of the LDAR-detected lightning to those of other remote sensing systems. It was determined that LDAR-detected discharges aloft within the storm precede ground strikes by about 5 minutes in the region within 60 km of KSC, making LDAR a very useful tool for issuing very-short-term weather advisories and warnings. By recognizing and including storm movement in a forecast scheme, mappings of current LDAR data points can be used to make forecasts of future cloud-ground strikes.

Research during 1993 showed, however, that beyond about 10 minutes areal storm growth and the development of new thunderstorm cells became increasingly important factors in the prediction of future lightning ground strikes. Hence, the focus of the 1994 research was to include a storm growth factor in the forecast scheme, and to begin to examine companion meteorological data sets that could ultimately be used in forecast schemes to help the forecasters anticipate new thunderstorm formation. In addition, forecasters must determine when the lightning threat at a site has ended--a task made difficult because electrified anvil clouds are often left behind above a site long after the core of the storm has exited the region. Thus, work was begun to examine this problem.

Research summarized in this report was conducted in parallel as four subprojects: (1) weather forecasting and advisory applications of LDAR, (2) LDAR in relation to field mill readings, (3) lightning flash and stroke detection using LDAR, and (4) LDAR in relation to radar reflectivity patterns and KSC wind profiler vertical velocities. Each of these subprojects is summarized briefly below.

II. WEATHER FORECASTING AND ADVISORY APPLICATIONS OF LDAR

2.1 POTENTIAL MESOSCALE AND SYNOPTIC CLIMATOLOGY APPLICATIONS

Figure 2-1 shows a mapping of the frequencies of occurrence of LDAR events above the -52:52 by -40:40 km domain during the 1993 sample, consisting of 33 hours of LDAR data from 13 days in June and July and mainly between the hours of 1500 and 2100 UTC. Numbers represent the percentage of time (minutes) with LDAR data above each 1 km² area of the domain. Dramatic gradients in frequency, such as the couplet 15-25 km west of KSC, suggest the meso-gamma-scale importance of river breeze circulations and land-water distributions on summer thunderstorm formation in this area. While the detail in the pattern in this limited sample is undoubtedly impacted by individual cases, the overall pattern nevertheless is indicative of a general tendency for cells to develop more frequently over regions west of KSC. It is also known (e.g., ref 7) that the timing and pattern of thunderstorm development is strongly a function of the prevailing wind direction. Sounding data has been collected, and will be used together with surface, radar, and other data in studies aimed at improving prediction of thunderstorm formation.

2.2 LDAR LEAD TIMES

The lead time between first appearance of LDAR events in a storm and first ground strike was computed in several ways. In the 1993 study, 27 storms were examined that occurred during the first hour of the day when storms were in the domain. The average lead time was 5.26 minutes, and 11% of the storms had ground strikes during the first minute of LDAR event existence.

Once storms were renumbered consistently throughout the case (rather than independently by hour) in 1994, all hours were used to recompute lead time, resulting in a larger sample and one typical of all new storm formations. To avoid storms already in existence and moving into the domain, only LDAR storms with centroids in a smaller domain were used: -48:48 by -36:36. In addition, storms "newly formed" by the objective scheme as a result of merging or splitting cells were eliminated by ignoring new storms forming within 6 km of pre-existing LDAR storms. For the 88 storms defined in this manner, the mean lead time was 4.01 minutes, with 28% of the storms producing ground strikes during the first minute of LDAR activity. Lead times in the sample ranged from 0 to 20 minutes.

It should be pointed out that from a forecaster's perspective the 4-5 minute lead times cited here pertain to the relatively uncommon situation in which thunderstorms develop directly above a forecast site. Thus, LDAR more typically provides a longer lead time by pointing out that thunderstorms are developing within the region and may soon pose a threat to a forecast site.

2.3 EVOLUTION OF LDAR IN THUNDERSTORMS

LDAR storms in the renumbered 1993 sample were examined to identify common features of LDAR pattern evolution. Starting with the 88 storms forming within the network, as described above, the sample size was reduced to 59 by elimination of short-lived storms (duration less than 6 minutes). Of the remaining storms, the mean duration was 25 minutes, with one storm lasting 94 minutes. This is a reasonable value for individual thunderstorms, and the objective numbering scheme tends to exclude broad, long-lived mesoscale storm systems formed through mergers.

A noticeable aspect of the LDAR storm evolution was that the early and late stages of their existence tended to be episodic. Gaps of several minutes between flashes were typical within the 5 minutes following the first minute of LDAR activity, and again during the last 10 minutes.

LDAR events first occurred near 8 km in most storms. The mean height of the center of storms' first LDAR events was 7.9 km, with no center below 3.25 km or above 11.25 km. Seventy-four percent of the centers developed between 7.25 and 9.75 km. These altitudes suggest the importance of an in-cloud temperature of

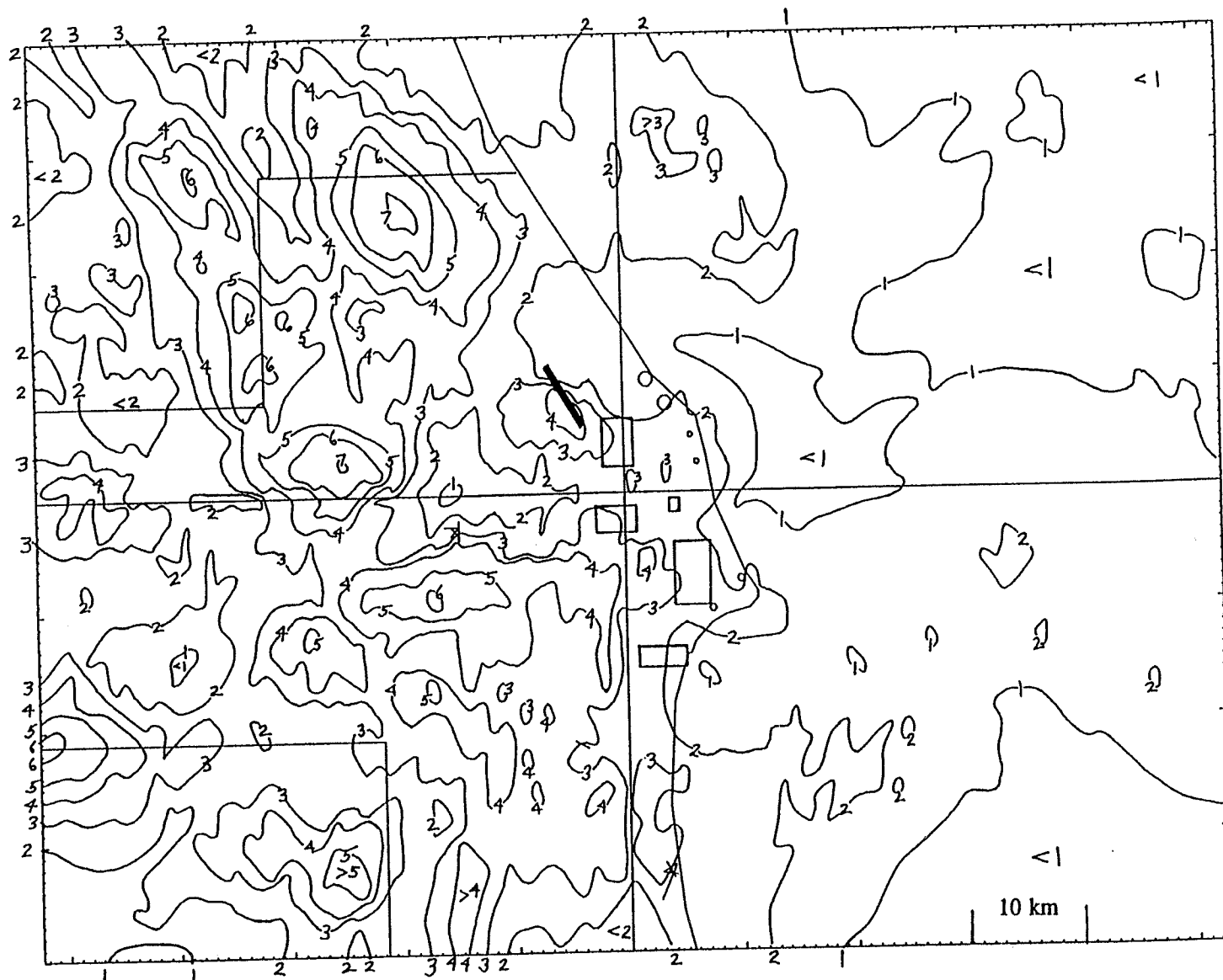


Figure 2-1. Frequency of lightning occurrence per square kilometer per minute, using LDAR data from the 1993 sample: 33 hours on 13 days. Numbers are in percent.

-15 to -20 °C, at which mixed-phase precipitation and electrification processes are likely.

The individual LDAR storm tended to grow vertically and horizontally rather rapidly, expanding its areal cross-section by a factor of 3 during the first 10 minutes, a total factor of 5 by 20 minutes, and a total factor of 10 by about 60 minutes. No distinct trend was seen in the limited number of storms with longer durations. It should be pointed out that mesoscale convective events can last much longer, and grow much larger, due to the development of mesoscale clusterings of cells into squall lines or mesoscale convective systems and known to contain mesoscale circulations different from those of individual thunderstorms. Such merger processes typically result in assignment of new storm numbers via the objective numbering scheme. Thus, those mesoscale phenomena have been excluded from the composites.

2.4 PREDICTION OF FUTURE GROUND STRIKES BY EXTRAPOLATION OF LDAR STORMS

Based upon the 1993 sample, within the concurrent minute, 85% of the LLP-measured ground strikes fell inside the bounds of the LDAR-defined storms and 98% inside or within 2 km of the edge. The latter 2 km strip allows for (1) tilted flashes not detected at low levels by LDAR and (2) location inaccuracies largely attributed to LLP positioning. LDAR event rates decline markedly below 3 km, at least partly due to the increased importance of return strokes at these levels which--due to their more continuous rather than pulsed emission characteristics--are not amenable to detection by LDAR.

An extrapolation scheme was developed in 1993 to determine the percentage of future ground strikes that could be successfully predicted by extrapolating existing LDAR patterns with storm motion vectors. It was determined that by a forecast time of about 15 minutes, half of the future ground strikes would be missed, due to a combination of existing storm growth and new storm formation.

During 1994 an additional factor was added to the extrapolation scheme, allowing expansion (or occasional contraction) of storm area by extrapolation of the storms' growth rate histories. The historical record was chosen to be equal in time to the desired forecast period, or as long as possible if the storm was not that old. Growth rates were computed and applied based upon the rate of change of the width of the LDAR storms in the x and y directions, expressed as percentage changes relative to the start time size.

Table 2-1 shows the results of the augmented extrapolation scheme. Incorporation of an areal expansion factor increased the percentage of ground strikes falling within the bounds of the LDAR storm at all forecast times. The growth factor had no effect on the percentage of ground strikes within 2 km of storm edge for forecasts of durations to 5 minutes, and yielded only modest improvements at longer forecast intervals. The main conclusion is that anticipation of non-systematic growth, and particularly development of new thunderstorm cells, becomes critical in making forecasts for duration longer than 15 minutes.

Further examination of the issue of ground strike predictability via extrapolation of LDAR gave a bit more room for optimism and shed light on the nature of the prediction problem. Figure 2-2 shows the practical limits on predictive skill via extrapolation schemes as a function of time during the convective episode. Here an episode begins at the time of first LDAR occurrence within the -52:52 by -40:40 km domain, rather than being linked to an individual storm. To develop the graphs, it was hypothesized that a perfect prediction could be made of the future positions and sizes of LDAR storms, such that only new thunderstorm formation was not accounted for. Of course, this is more easily assumed than achieved.

The inference to be drawn from Fig. 2-2 is that the worst forecast problems tend to come early in the convective portion of the day, particularly during the first half hour when relatively few storms are already in existence and new ones are forming frequently. After about the first 90 minutes of the convective period,

sufficient numbers of storms are in existence that their extrapolation can lead to increased success rates, but perhaps never to a point of acceptability in a 20-30 minute forecast.

TABLE 2-1

**PREDICTION OF FUTURE CG STRIKES BASED UPON
EXTRAPOLATION OF EXISTING LDAR STORMS,
WITH AND WITHOUT CONSIDERATION OF
GROWTH/DECAY FACTOR OR AGE OF EPISODE**

% OF LLP EVENTS FALLING WITHIN PREDICTED AREA

FORECAST TIME	NO GROWTH FACTOR		RECENT GROWTH EXTRAPOLATED	
	INSIDE EDGE	WITHIN 2 km	INSIDE EDGE	WITHIN 2 km
3 min	71	88	80	87
5	64	84	74	83
10	44	67	61	72
15	31	50	49	59
20	20	35	39	48
30			23	31

2.5 GROUND STRIKES FROM ANVILS

There is great interest in knowing when and if ground strikes emanate from thunderstorm anvils, since they frequently persist over a forecast site long after the convective tower portion of the thunderstorm has passed. A preliminary study was conducted using LDAR and LLP data to determine the frequency of ground strikes from anvils. This study was done by defining an altitude corresponding to an anvil base, and then defining LDAR anvil areas as those having no LDAR events at lower elevations. However, this method excludes from consideration not only the cases where the lower LDAR events emanate from in-cloud lightning, but also excludes the cases of ground strikes from anvil detected by LDAR (thus, yielding LDAR data points at sub-anvil levels). Thus, this task was postponed until an LDAR flash detector could be developed to identify the latter situations. This project is described in section IV.

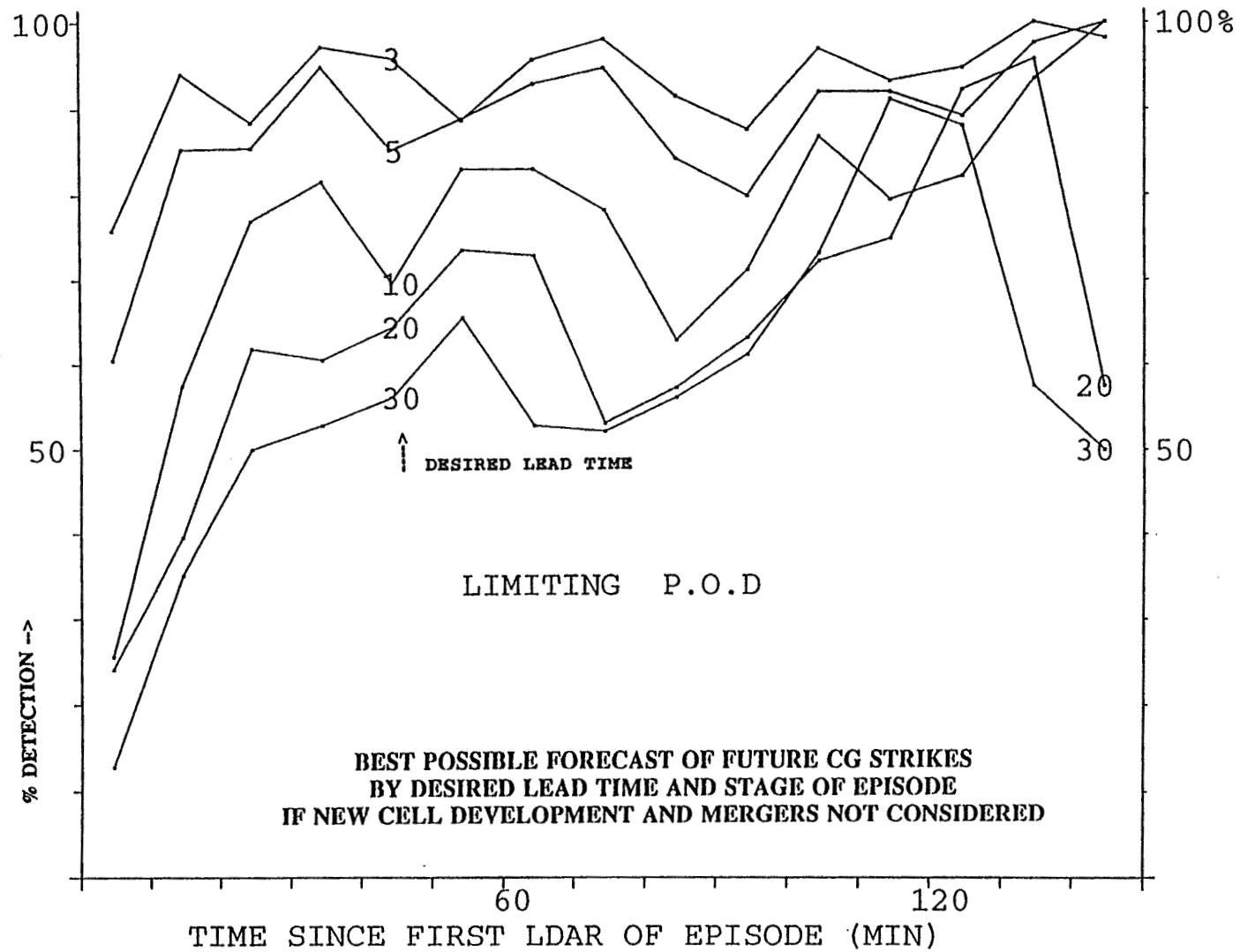


Figure 2-2. Hypothetical limits to accuracy of extrapolation forecasts of lightning ground strikes as a function of time since the first LDAR event in the domain and forecast duration.

III. LDAR IN RELATION TO FIELD MILL READINGS

3.1 INTERCOMPARISON OF LDAR, LLP, AND FIELD MILL READINGS

Vertical electric fields at the surface are measured by an "old" and a new, upgraded network of electric field mills deployed over KSC and surroundings. The lower portion of Figure 3-1 shows a time series of electric field readings. These values are from old mill 20, just northeast of the LDAR central site. Readings become increasingly negative as the negative charge center builds within overhead or nearby thunderstorms, as shown through 2015 UTC. A positive surface electric field can exist beneath the lower positive charge center that sometimes develops near cloud base in heavy rain areas, and at distances beyond about 10 km from the thunderstorm where the surface electric field is dominated by the upper positive charge center within the thunderstorm anvil, as shown after about 2115 UTC. The value of the surface electric field is, therefore, a function of the magnitudes and elevations of the charge centers in nearby thunderstorms and their distances from the site. The presence of screening layers and spatial and temporal variations of atmospheric conductivity are further complicating factors (see ref 8 for a review). Dramatic, nearly discontinuous changes in electric field associated with lightning strokes and flashes are also registered in the electric field readings, such as the spike near 2049 UTC.

Shown in the upper segments of Fig. 3-1 are plots of the horizontal distances from the field mill site to the nearest LDAR and LLP lightning discharge events as a function of time (one value per minute). In this situation a thunderstorm was located west of KSC and heading southward, and its ground strikes remained 9.25 km (5 n.mi.) or more distant from the site. Several flashes aloft were recorded directly overhead by LDAR, however, resulting in spikes within the field mill trace. In the figure, small squares at 15 km indicate that the nearest event was at a distance of more than 15 km, whereas the absence of a data point indicates no events within the -52:52 by -40:40 km domain during the minute.

3.2 CASE STUDY OF FIELD MILL LIGHTNING HAZARD THRESHOLDS

The main emphasis of these intercomparison studies, which are ongoing, is to determine the threshold field mill values typically associated with the beginning and end times of heightened ground strike threat at a site, and triggered lightning threat to a launched vehicle. In a case study from 21 June 1994, Julian day 172, the average field mill reading was -1958 kV/m at the time when LDAR events first came within 9.25 km (5 n.mi.) of a site, and -1237 kV/m at the time when LDAR events last were detected within that distance. A reading of more than +/- 1 kV/m is currently used as an indicator of lightning threat.

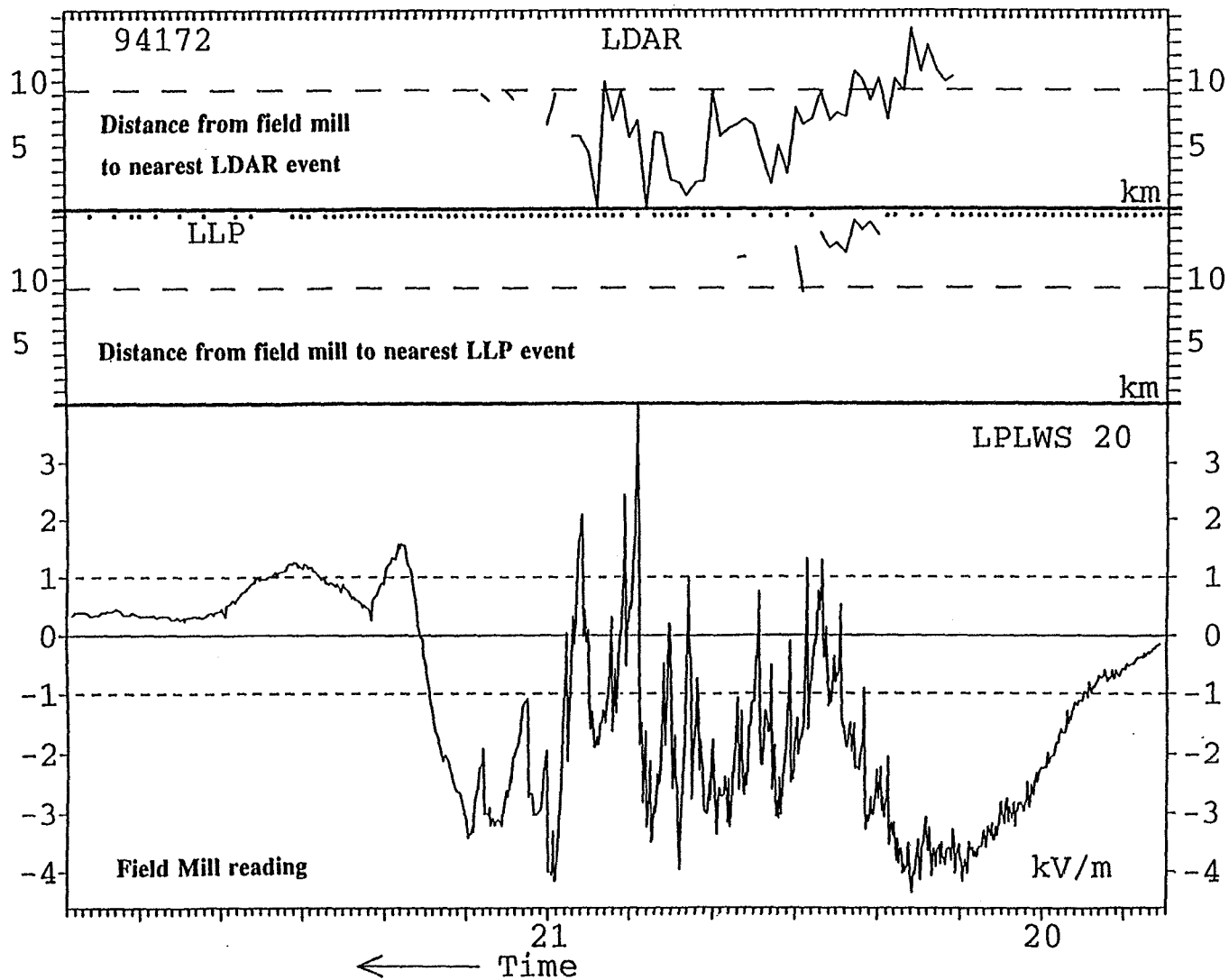


Figure 3-1. Field mill readings as a function of time for site 20 on 21 June 1994, day 172, from 1945 to 2159 UTC, in relation to the distances to the nearest LDAR and LLP lightning events.

IV. LIGHTNING FLASH AND STROKE DETECTION USING LDAR

4.1 LIGHTNING FLASH/STROKE IDENTIFICATION ALGORITHM; NOISE IDENTIFICATION

LDAR data are recorded sequentially in time, but more than one lightning stroke and flash can be in progress and detected essentially simultaneously, from separate storms and even from within the same storm. A computerized scheme was developed to separate a file of LDAR data events into numbered groupings of data points associated with distinct flashes (or strokes; for a distinction, see discussion below). Data points falling within specified time and distance limits are classified as a distinct flash (or stroke).

The algorithm looks at each LDAR data point in the file, beginning with the first data point (record 1), which is assigned as part of flash 1. The algorithm then performs a four-dimensional "buddy" search, forward in time throughout the specified threshold interval. All future data points are assigned (numbered) as part of the same flash if they fall within the time and distance separation thresholds. The algorithm then goes on to deal with the next data point (record 2). If it is initially numbered, then all unnumbered buddies found in the forward search are assigned its number. If the data point is initially unnumbered, then it is assigned the number of the first numbered buddy found. If no buddies are found within the time and distance thresholds, then the data point is defined as part of a new flash and assigned the next unused flash number. Numbered buddy data points at forward times never are reassigned a different flash number. The algorithm continues with the third and all subsequent records until each data point in the file has been assigned a number. Additional options then permit a renumbering to separate major flashes (affiliated with more than a specified number of LDAR events), minor flashes, and noise (one-event "flashes").

The distinction between a flash and a stroke is somewhat imprecise, but the term flash is typically used to represent a time integral of about one-half second, comparable to the image of lightning seen by the human eye or in a photograph. In reality such a lightning flash is composed of a branching stepped leader, one or more return strokes, and often a dart leader. Since LDAR does not normally detect return strokes, the "strokes" cited in this research take on a somewhat different meaning.

Figures 4-1, 4-2, and 4-3 illustrate the implementation of the flash identification algorithm during one interesting minute in which a readily identifiable in-cloud flash passed over KSC. Fig. 4-1 maps all the LDAR data points during the minute 0106 UTC on day 154 of 1993. Figure 4-2 shows the data points clustered into a flash identified as number 2 (of 5 during the minute) by the algorithm when thresholds are set at 400 msec and 4.0 km. The flash consists of 737 LDAR data points.

4.2 THRESHOLDS FOR FLASH AND STROKE DETECTION

A detailed human inspection of the sequence of data points comprising flash 2 of Fig. 4-2 reveals that this flash was comprised of several distinct branches or strokes, of which three were major. The first of these began just south of KSC and headed to the northwest, to near the northernmost point of the flash. Just before the first stroke terminated to the north, another major stroke began near KSC and eventually reached the most northwestern point of the flash. These strokes were primarily horizontal or upward. While the second major stroke was halfway to its western termination, the third major stroke began south of KSC and headed south and west, reaching the most southwestern point of the flash. Several smaller strokes were also identified in the region south-southwest of KSC. The use of 100 msec and 2.0 km thresholds resulted in two of the smaller strokes being identified as separate entities, as indicated in the figure, with a loss of 57 LDAR events. The use of 50 msec and 2.0 km thresholds divided this flash (and the several other flashes subjected to painstaking human inspection) into its distinct "strokes".

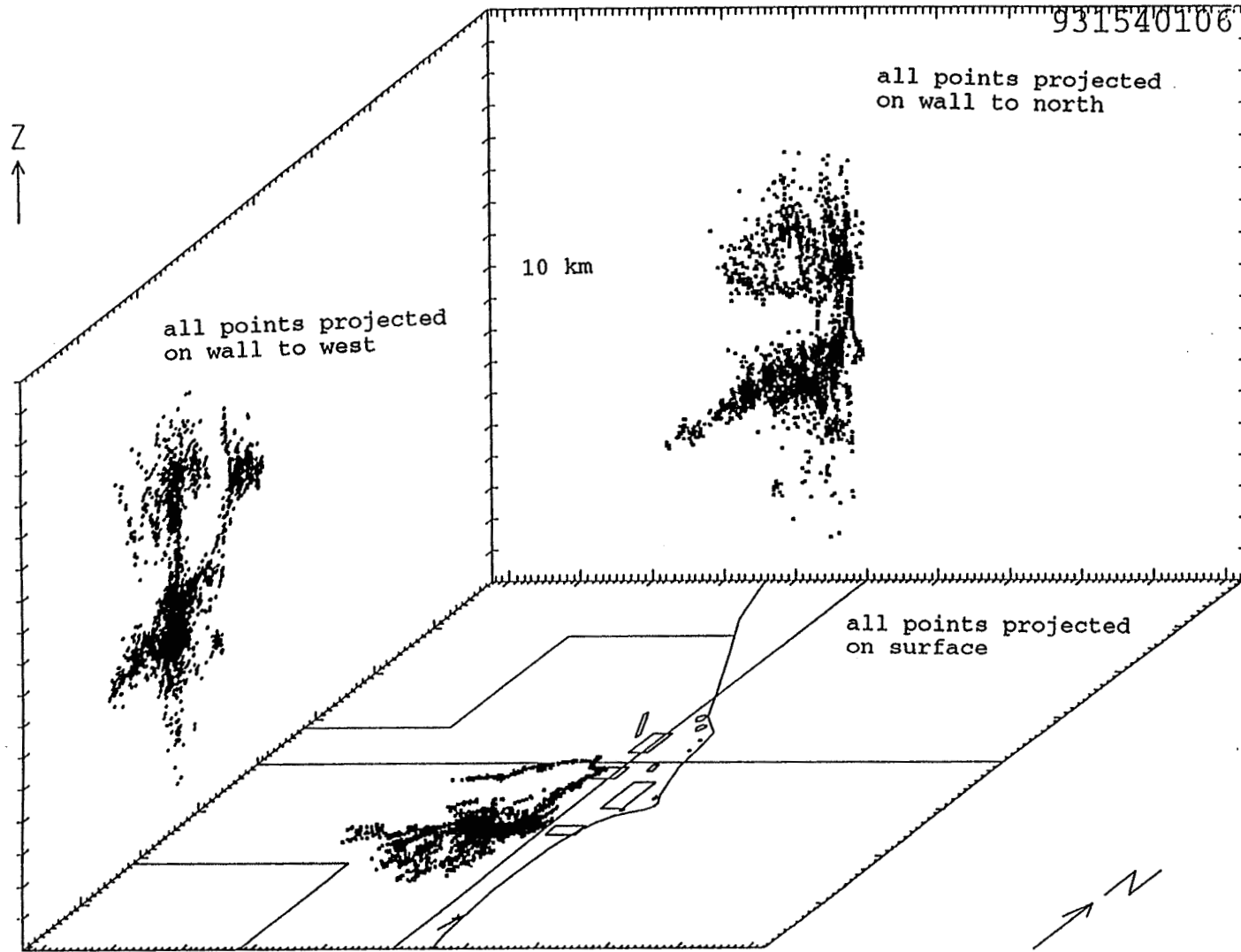


Figure 4-1. Perspective view of all LDAR data points during minute 0106 UTC of day 154, 3 June 1993.

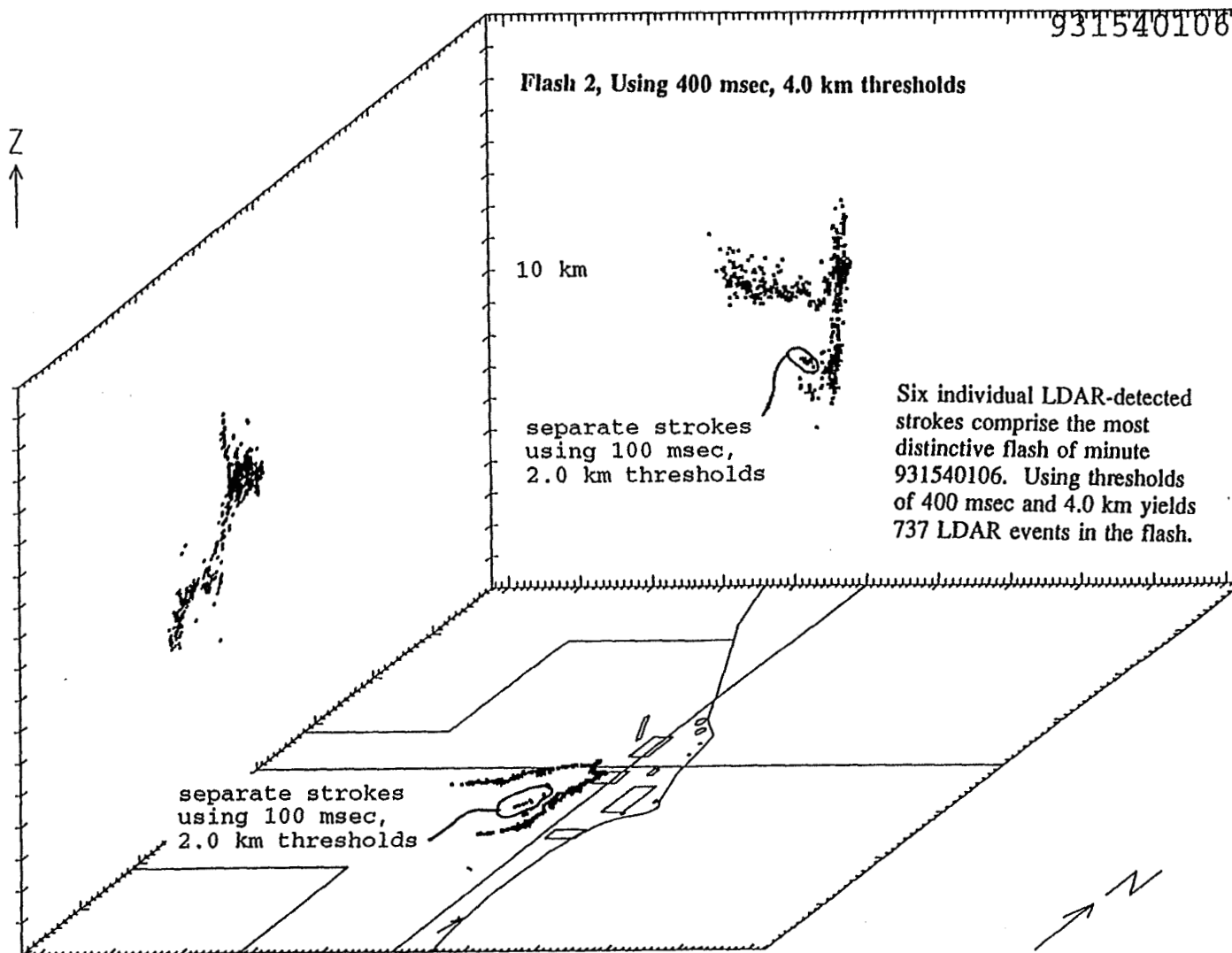


Figure 4-2. Perspective view of flash 2 out of 5 major flashes within the events of Fig. 4-1, using 400 msec and 4.0 km thresholds. These thresholds yield one major flash of duration 933 msec and consisting of 737 LDAR events. Reanalysis of Fig. 4-1 using 100 msec and 2.0 km thresholds separates this flash into two flashes, losing the 57 LDAR events as annotated.

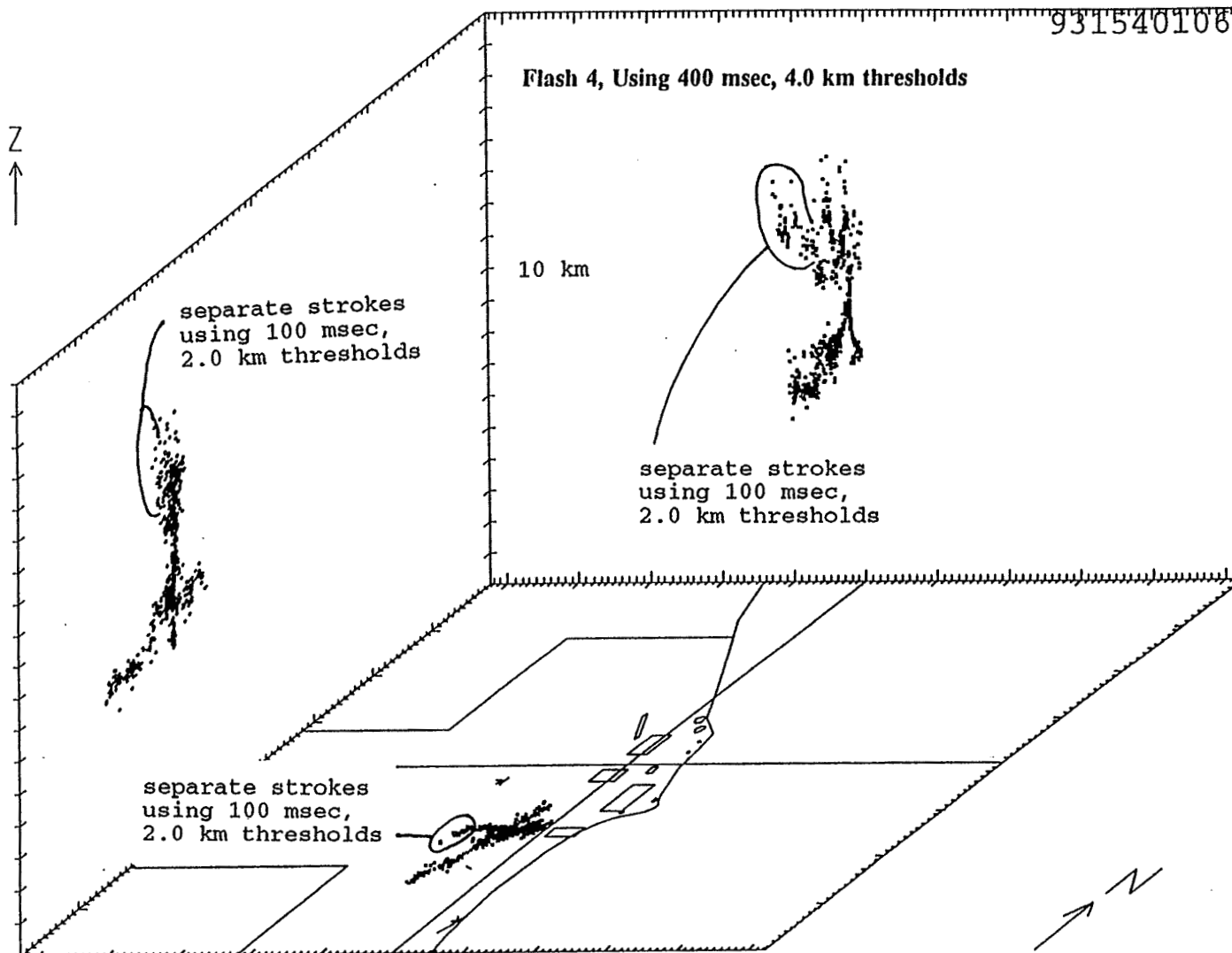


Figure 4-3. Perspective view of flash 4 out of 5 major flashes within the events of Fig. 4-1, using 400 msec and 4.0 km thresholds. Use of 100 msec and 2.0 km thresholds separates this flash into two flashes, as depicted.

Figure 4-3 shows one of the other flashes (number 4 of 5 during the minute), with thresholds of 400 msec and 4.0 km. When 100 msec and 2.0 km thresholds are used, the flash is divided into two flashes, numbers 25 and 26 of the minute, as depicted. Use of 50 msec and 2.0 km thresholds would further subdivide the flash into strokes, several of which are readily discernible in the figure.

Motivation for development of the flash identification algorithm arose during the course of several of the subtasks researched above. One is a need to isolate flashes from anvil to ground from mid-level, in-cloud flashes in order to improve understanding of the occurrence of ground strikes from anvils using LDAR. Time did not permit a return to this task after the algorithm was developed, but it will be pursued in the future.

Another motivation was the question by the author of whether there might be a variation within thunderstorms of the number and ratio of major and minor flashes, and whether this might be of value to forecasters in determining the relative likelihood of ground strikes from a storm, within different portions of the same storm, or as a function of time during the storm. In practice, the number of minor flashes depends upon what threshold is set on the minimum number of LDAR events within the flash and upon the time and distance thresholds which, when set small, tend to break major flashes into more numerous strokes. With 400 msec and 4.0 km thresholds, about 10% of the events in the small sample studied to date are classified as within minor flashes. In some minutes the minor flashes are more prevalent. Additional study is needed.

V. LDAR IN RELATION TO RADAR REFLECTIVITY PATTERNS AND KSC WIND PROFILER VERTICAL VELOCITIES

5.1 INTERCOMPARISON OF LDAR TO RADAR

Because the development of lightning is affiliated with the microphysics and storm-scale dynamics of the precipitation formation process, radar--which detects the location and approximate precipitation rates within stratiform and convective storms--is a tool fundamental to lightning forecasting. Radar data from the McGill radar at Patrick AFB and the NWS Doppler weather radar (WSR-88D) at Melbourne, FL are being used in conjunction with LDAR and other companion data to examine storm structural and electrical evolution on an ongoing case study basis.

In studies performed thus far, hardcopies of radar cross-sections of storms were obtained, and software was written to overlay LDAR data onto the sections. Raw LDAR data points have been plotted in the section for the same volume sampled by the radar, namely a strip 1.85 km (1.0 n.mi.) wide. Because the radar cross-section is interpolated from a sequence of scans at progressively increasing elevation angles, it represents a reflectivity composite over a 5-minute interval. LDAR data are overlaid from a single minute near the end of the composite period, such there could be a small mismatch at lower elevations.

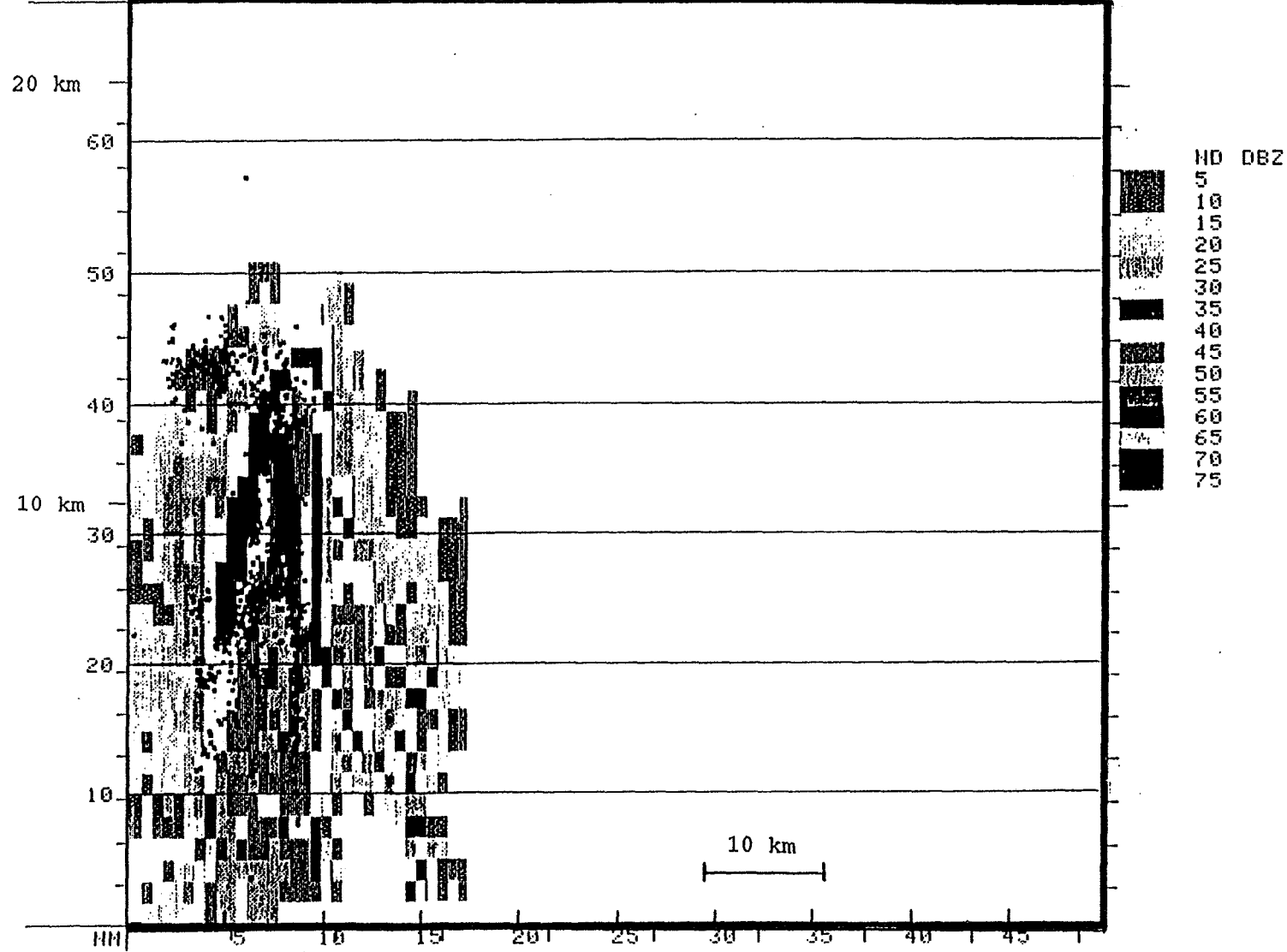
Figure 5-1 shows an example of such a cross-sectional overlay, though the color does not reproduce well in black and white. It is from a mature thunderstorm at 1948 UTC on day 210, 29 July 1994. A core of 50-57 dBZ reflectivity, indicative of heavy precipitation, is suspended aloft in the layer between 4 and 9 km (13 - 29 kft) near the center of the radar echo pattern associated with the storm. The radar reflectivity pattern with the anvil is partially truncated at the left edge of the diagram, where the radar tilt sequence does not reach elevation angle sufficiently near vertical to detect storm top.

Also shown in Fig. 5-1, a vertical column of LDAR data points extends upward from near the top of the reflectivity core at 8 km to about 13 km (42 kft), where the LDAR pattern begins to flatten into a more horizontal layer affiliated with the storm anvil. It seems likely that the LDAR column between 8 and 13 km represents in-cloud flashes between the negative and positive charge centers of the thunderstorm. The location of the negative charge center just above the core of heaviest reflectivity would be consistent with its affiliation with the mixed phase (ice and supercooled water) precipitation region of the storm, containing large drops and possibly graupel. Below 4 km at least two strings of LDAR points reveal cloud-ground strokes within and along the gradients just outside of the heavy precipitation core.

Graduate student Nathan Drummond obtained color radar display software via the Internet from Dave Priegnitz of the South Dakota School of Mines and Technology and implemented it onto workstations in the Wave Analysis Lab of TE-CID-3. Nathan and graduate student Steve Hoffert obtained archived Doppler radar data from the WSR-88D at Melbourne for several cases and Hoffert converted LDAR data to a form that could be overlaid on horizontal radar displays. Because raw LDAR data plots would often obscure much of the details of the radar display, only one LDAR data point per square kilometer is superimposed. An LDAR point was plotted if there were any LDAR data points within the square kilometer column of depth 0.75 km centered on the radar display altitude.

Figure 5-2 shows an example of a radar image with LDAR overlay, from 1958 UTC on day 210, 29 July 1994 at 7.0 km. This depicts the first LDAR events associated with a thunderstorm that produced a microburst--a strong small-scale downdraft and near-surface outflow--which caused damage on Merritt Island about 25 minutes later. The LDAR events at this time are centered just above and slightly downwind (to the north-northeast) of the reflectivity core. A younger cell just west of the microburst storm has not yet produced any LDAR events. Elsewhere on the figure, LDAR events are associated with moderate and heavy precipitation intensity regions of active thunderstorms south through west-northwest of KSC.

ALT KFT | MAX = 570BZ | ALT = 19KFT | (AZ/R) = 341/ 24 | 07/29/94 19:48



227

Figure 5-1. South-north cross-section of thunderstorm with LDAR overlay, from 1948 UTC on day 210, 29 July 1994. Shadings indicate different radar reflectivities, though the colors have not reproduced well in black and white. Dots represent LDAR data points within the same volume scanned by the radar.

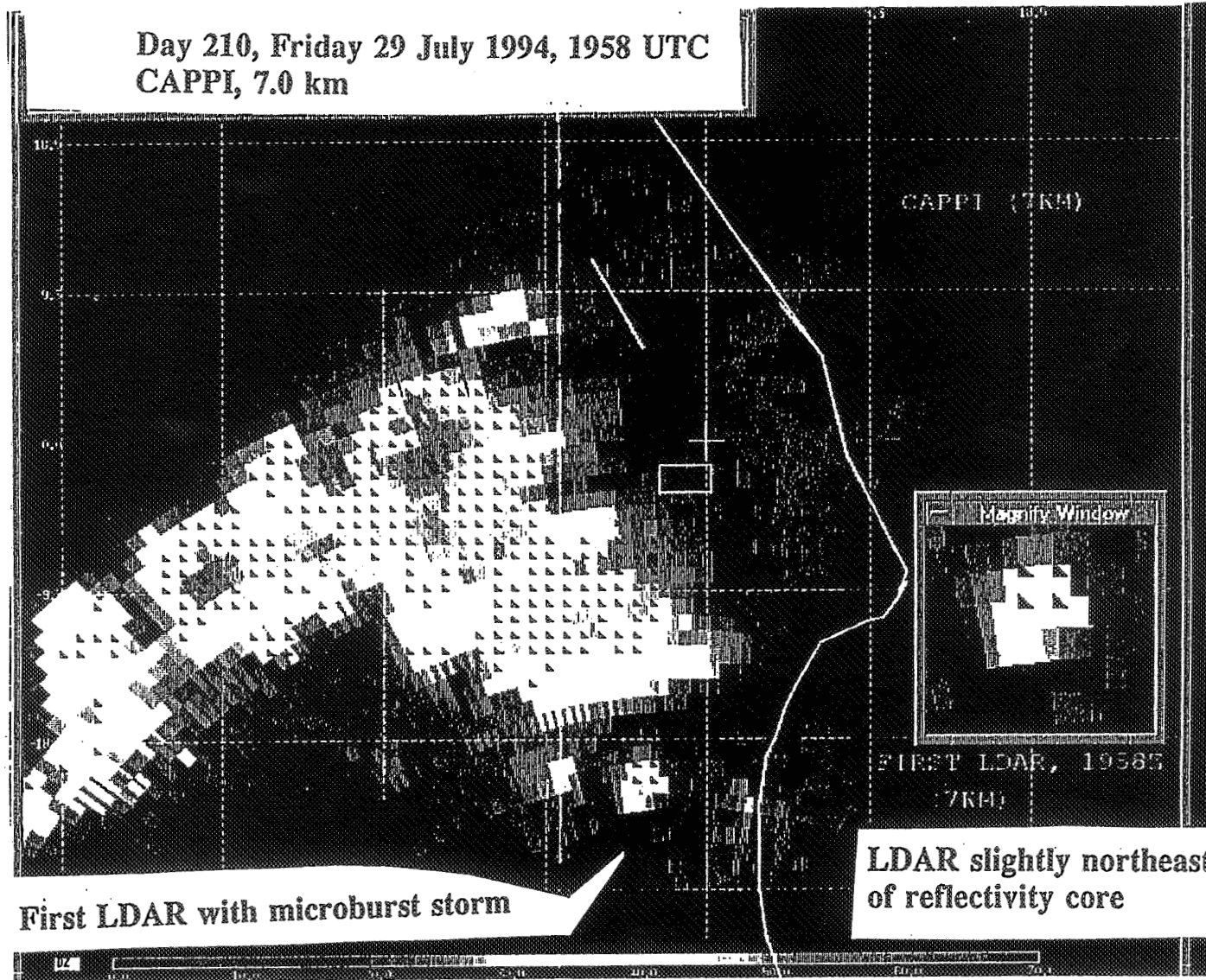


Figure 5-2. Constant-altitude display of radar reflectivities with LDAR overlay (triangles) at 7 km from 1958 UTC on day 210, 29 July 1994. Gray regions inside of white areas have highest reflectivities, about 60 dBZ.

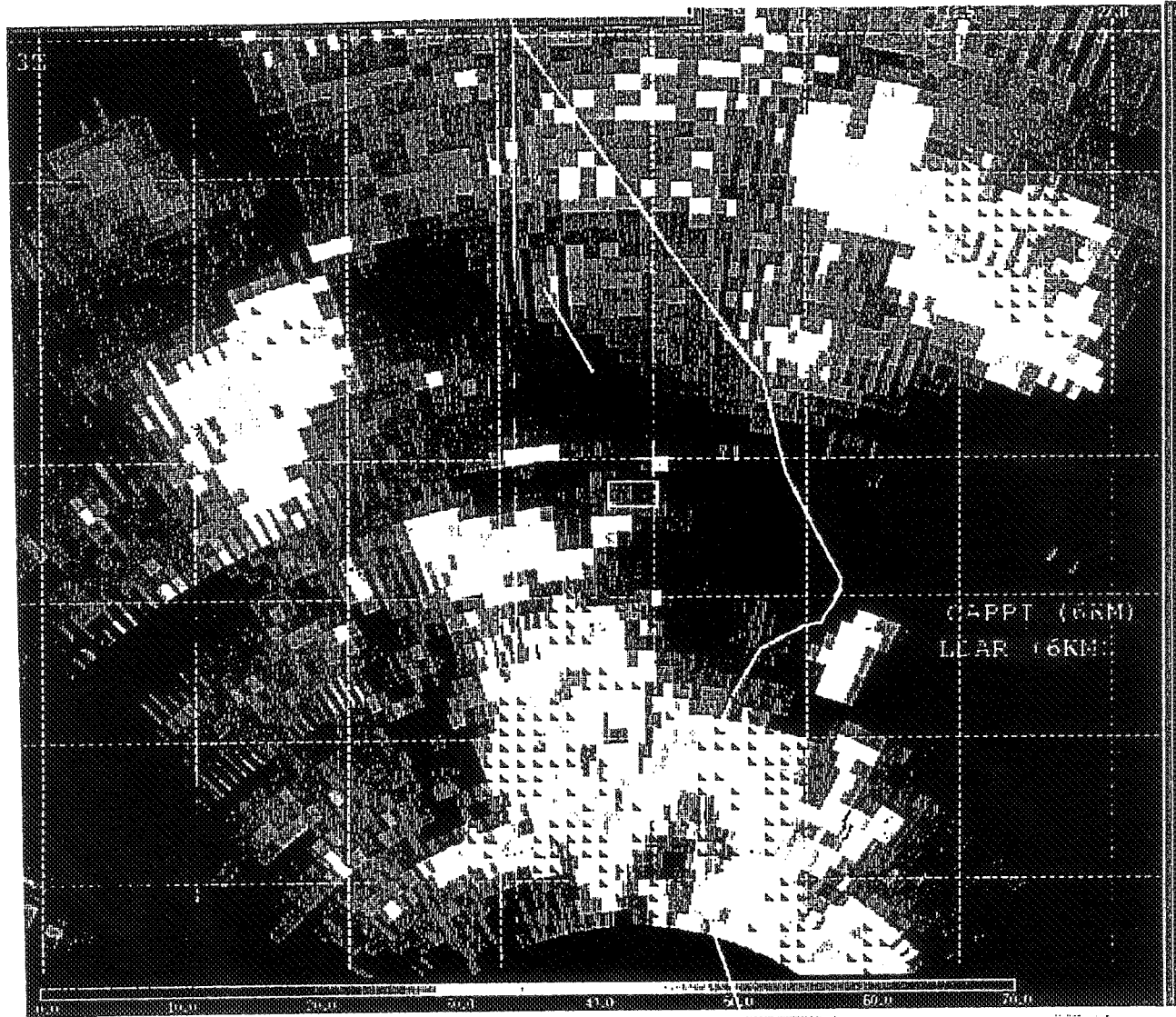


Figure 5-3. Constant-altitude display of radar reflectivities with LDAR overlay at 6 km from 2153 UTC on day 210, 29 July 1994 at 6.0 km. Reflectivities are now mostly 40 dBZ or less, except in a 60 dBZ core offshore about 10 km south of Cape Canaveral. A broad, diffuse flash extends to the west-northwest within quasi-stratiform echo rearward of that storm.

Figure 5-3 shows an example of a radar image with LDAR overlay at a later time, 2153 UTC, at 6 km. At this stage of the episode, many of the strong convective towers have weakened or disappeared, and the remaining precipitation is becoming more stratiform. LDAR activity is becoming organized into progressively more diffuse layers, with occasional quasi-horizontal branching flashes extending even tens of kilometers. One of these is depicted in the lower half of the figure. Presumably these flashes are in association with electrified cloud layers generated earlier in the day and left behind after the active portions of the storms have decayed or exited the region. However, the pockets of higher reflectivity within these regions still suggest that there may be pockets of upward vertical velocity and modest charge generation processes in progress.

5.2 KSC WIND PROFILER VERTICAL VELOCITIES IN RELATION TO A LAYERED LDAR STRUCTURE

Time-height series of vertical velocities measured by the KSC wind profiler confirm the existence of pockets of upward motion in the stratified cloud of the type mentioned in discussion of Fig. 5-3. Thunderstorm cells on 29 July 1994 moved toward the north-northeast, such that the cores of the major cells of Fig. 5-2 took a track passing west of the KSC wind profiler, located just east of the north end of the Shuttle Landing Facility. Thus, for much of the time the wind profiler site was under the influence of anvil and stratified debris clouds east of the thunderstorm cores.

Figure 5-4 shows the time-height section of LDAR events within 1 km of the wind profiler site as a function of time during the afternoon of 29 July 1994. Superimposed on the figure are outlines of discernible upward velocities, together with arrows showing locations of maximum upward and downward vertical motions. During the period between about 2005 and 2130 UTC, two layers of LDAR events existed over the profiler site, descending with time. The layers were initially centered near 12 and 8 km and descended to below 9 and 5 km, respectively, while becoming more diffuse. This descent could be affiliated with the fallout of charged ice crystals slowly descending from aloft. The mean descent rate is about 0.8 m/s, somewhat less than the fallspeed of ice crystals, however.

Evident in Fig. 5-4 is that the pattern of upward vertical velocities also slopes downward with time, parallel to the LDAR layers. The LDAR layers are generally affiliated with updraft, though somewhat cellular in nature. Between the layers there was a rather continued downward motion. The presence of updraft in association with the LDAR layers may explain why the net layer descent rate was slower than ice crystal terminal velocities if, indeed, that is the meteorological context. The presence of cellular updrafts within the quasi-stratiform region may also explain the dynamics through which the layers were able to remain electrically active. Additional investigation is merited.

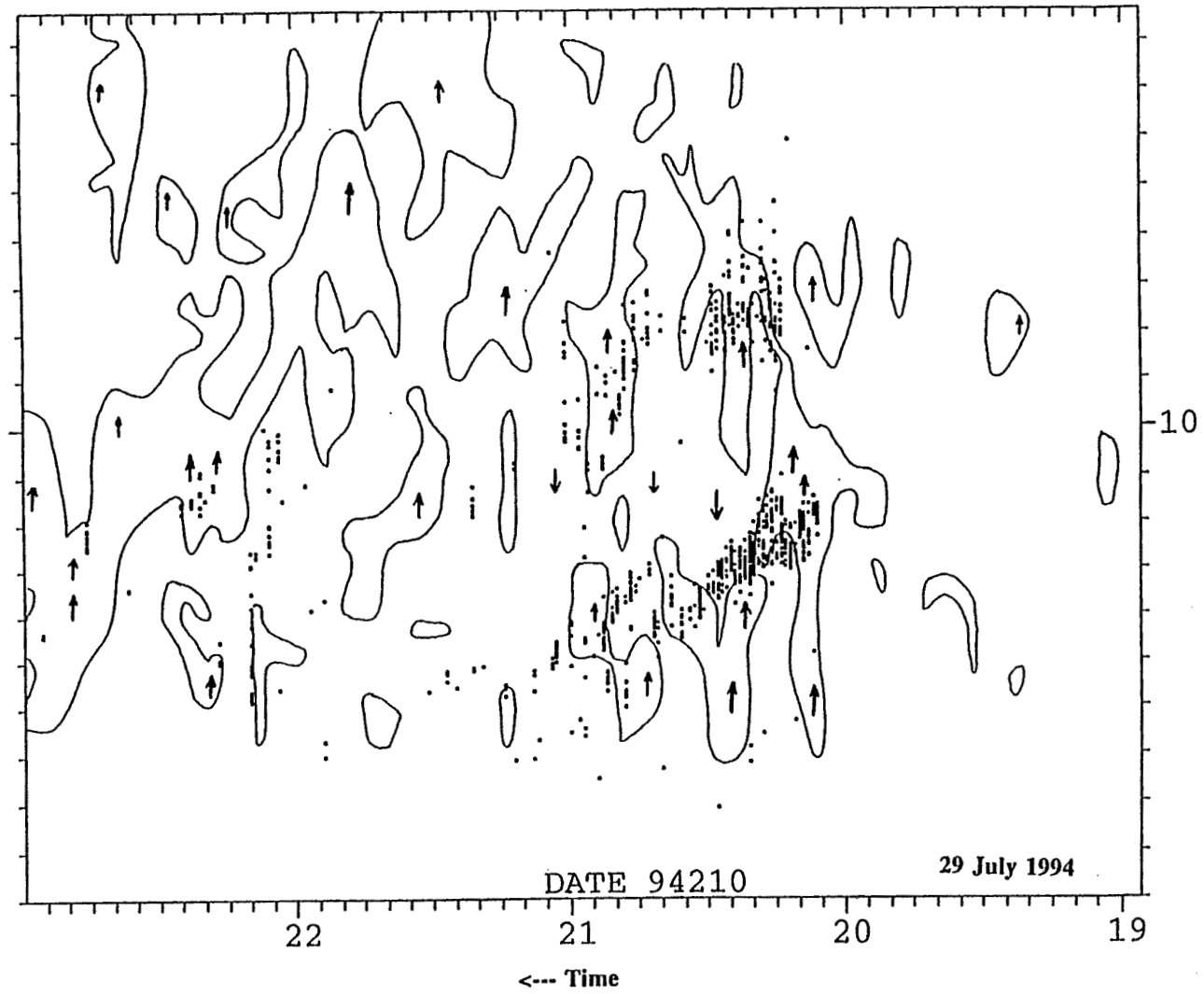


Figure 5-4. Time-height section of LDAR events above the KSC wind profiler and outlined areas of discernible upward vertical velocities between about 1900 and 2300 UTC on day 210, 29 July 1994. Arrows depict vertical velocity maxima, which peaked at 3.3 m/s.

VI. CONCLUDING REMARKS

The task of issuing lightning advisories is a formidable one, involving a diversity of situations. In some instances the forecast problem is one of anticipating the time and location of formation of the first thunderstorms cells of the day, or determining when and if new cells will form near a forecast site, given that storms already exist elsewhere. At other times the problem is one of anticipating the movement, growth, merger, flanking cell development, or dissipation of existing thunderstorms. Yet another problem arises in knowing when and if to cancel lightning advisories while, because of vertical wind variations or other factors such as mesoscale convective systems, electrified clouds persist over a site adjacent to or following the passage of deep thunderstorm cells. The nature of the forecast problem can evolve rapidly during the day, and can be different in one weather regime from another. The forecasters are to be congratulated for their successes in a difficult job.

Operational weather forecasters involved with the space program have at their disposal a host of tools helpful in solving the above problems: radar, satellite, LDAR, field mills (LPLWS), LLP, surface mesonet (wind towers), soundings, wind profiler, and even mesoscale numerical model forecast data. Each of these platforms can contribute useful information individually. Because of the deadlines of operational decision-making, forecasters often may not have time to leisurely contemplate the interrelationships and complementary natures of these diverse pieces of information, or to re-examine past cases for clues toward future success. The goal of this ongoing research is to supplement the efforts of the forecasters by developing guidelines, approaches, and techniques involving diverse types of data that can be useful in operational weather forecasting. Based upon the studies to date, the author has given presentations to operational forecasters and provided software and training materials for use in ongoing technology transition activities.

The author looks forward to a continuing cooperation with NASA, the Applied Meteorology Unit, the National Weather Service, and other groups also performing studies with similar goals. A meeting of the participants was held in early August as a first step in coordinating these efforts.

REFERENCES

1. Maier, M.W., A.G. Boulanger, and R.I. Sax: An initial assessment of flash density and peak current characteristics of lightning flashes to ground in South Florida. NUREG/CR-1024, U.S. Nuclear Regulatory Commission, 1979.
2. MacGorman, D.R., M.W. Maier, W.D. Rust: Lightning strike density for the contiguous United States from thunderstorm duration records. NUREG/CR-3759, U.S. Nuclear Regulatory Commission, 1984.
3. Maier, L.M., E.P. Krider, and M.W. Maier: Average diurnal variation of summer lightning over the Florida Peninsula. *Mon. Weather Rev.*, 112(6), June, 1984, pp. 1134-40.
4. Krider, E.P., A.E. Pifer and D.L. Vance: Lightning direction-finding system for forest fire detection. *Bull. Amer. Meteorological Soc.*, 61, 1980, pp. 980-86.
5. Lennon, C. and L. Maier: Lightning mapping system. NASA CP-3106, Vol, II, 1991 International Aerospace and Ground Conference on Lightning and Static Electricity, 1991, pp. 89-1 to 89-10.
6. Forbes, G.S.: Lightning studies using LDAR and LLP data and applications to weather forecasting at KSC. 1993 Research Reports, NASA/ASEE Summer Faculty Fellowship Program (C.R. Hosler, C. Valdes, T. Brown, eds.), NASA CR-194678, Grant NGT-60002 Supplement 11, 1993, pp. 165-194.
7. Holle, R.L., A.I. Watson, R.E. Lopez, R. Ortiz: Meteorological aspects of cloud-to-ground lightning in the Kennedy Space Center region. Preprints, AIAA 26th Aerospace Sci. Meeting, Reno, NV, 1988, 12pp.
8. Uman, M.A.: *The Lightning Discharge*. Academic Press, NY, 1987, 377pp

351490
111 760

1994 NASA/ASEE SUMMER FACULTY FELLOWSHIP PROGRAM

JOHN F. KENNEDY SPACE CENTER
UNIVERSITY OF CENTRAL FLORIDA

59-25

33969

P. # 28

INVESTIGATION OF NEW HYPERGOL SCRUBBER TECHNOLOGY

PREPARED BY:	Dr. Barbara H. Glasscock
ACADEMIC RANK:	Associate Professor
UNIVERSITY AND DEPARTMENT:	California State Polytechnic University, Pomona Chemical and Materials Engineering
NASA/KSC	
DIVISION:	Materials Science
BRANCH:	Materials and Chemical Analysis
NASA COLLEAGUE:	Gale Allen
DATE:	August 19, 1994
CONTRACT NUMBER:	University of Central Florida NASA-NGT-60002 Supplement: 17



ACKNOWLEDGMENTS

I would like to express my sincere appreciation to the Office of Educational Affairs, NASA Headquarters, Washington, D.C. and the American Society for Engineering Education (ASEE) for their sponsorship of the 1994 NASA/ASEE Summer Faculty Fellowship Program at Kennedy Space Center. My summer research experience at KSC has been stimulating and rewarding and I know that I will carry with me to my home university many of the new ideas I have gained here.

The program was well organized and ran smoothly, thanks to the administrative efforts of the folks at the University of Central Florida, in particular Dr. Loren A. Anderson and Ms. Kari Stiles.

A special thanks to Gale Allen, my NASA Colleague, for suggesting this work as a summer project and for her enthusiasm along the way. I am grateful to Lee Underhill and Orlando Melendez, both of the Chemical Analysis Section, for their collaboration on several aspects of the project, especially to Orlando for his work on Stability Study #2. I would like to acknowledge all of the members of the Chemical Analysis Section and thank them for their stimulating discussions in the lab, the lunchroom, and over a computer screen.

ABSTRACT

The ultimate goal of this work is to minimize the liquid waste generated from the scrubbing of hypergolic vent gases. In particular, nitrogen tetroxide, a strong oxidizer used in hypergolic propellant systems, is currently scrubbed with a sodium hydroxide solution resulting in a hazardous liquid waste. This study investigated the use of a solution of potassium hydroxide and hydrogen peroxide for the nitrogen tetroxide vent scrubber system. The potassium nitrate formed would be potentially usable as a fertilizer. The hydrogen peroxide is added to convert the potassium nitrite that is formed into more potassium nitrate. Small scale laboratory tests were conducted to establish the stability of hydrogen peroxide in the proposed scrubbing solution and to evaluate the effectiveness of hydrogen peroxide in converting nitrite to nitrate.

SUMMARY

Small scale laboratory tests were conducted to evaluate the stability of hydrogen peroxide (H_2O_2) in alkaline mixtures, some of which included nitrate and nitrite salts, and which were adjusted to different pH levels. These mixtures simulated the proposed scrubber liquor for removing nitrogen tetroxide (N_2O_4) from the scrubbing of hypergolic vent gases. Currently the N_2O_4 vent gas is scrubbed with a sodium hydroxide (NaOH) solution resulting in a hazardous liquid waste. This study investigated the use of a solution of potassium hydroxide (KOH) and hydrogen peroxide (H_2O_2) for the nitrogen tetroxide vent scrubber system with a goal of producing a solution of potassium nitrate (KNO_3) that could be used as a fertilizer.

A series of three different stability studies were conducted. In the first study a 2^4 factorial experimental design was used to compare the effect of four variables (pH, nitrite concentration, nitrate concentration, and sodium (Na^+) or potassium (K^+) as the cation) on the response variable, % H_2O_2 decomposed. It was found that the most significant effect was the pH; an average of 65% of the H_2O_2 disappeared at pH = 9 and only 4% disappeared at pH = 6 after 68 hours at room temperature. The potassium salts may have a slight stabilizing effect over the sodium salts. It also appears that when there was nitrite present in the original solution, a significant portion of the nitrite reacted with the hydrogen peroxide to yield nitrate.

The second stability study considered the effect of pH on the stability of H_2O_2 in the absence of any salts. The decomposition rate of H_2O_2 at pH = 9 and pH = 13 was comparable, but surprisingly pH = 11 exhibited a higher decomposition rate. Thus the decomposition rate as a function of pH appears to go through a maximum at a pH around 11. The decomposition rate was very high initially and then leveled off with time when expressed as %decomposed/hour.

The third stability study was a 2^3 factorial experimental design to compare the effect of three variables (pH, H_2O_2 concentration, Na^+ or K^+), with levels of nitrate and nitrite held constant, on the response variable, % H_2O_2 decomposed. It again appears that some of the nitrite is converted to nitrate.

In addition, preparations were made to conduct small scale scrubbing experiments to measure the efficiency of the solutions on removing N_2O_4 from gaseous nitrogen, but time limitations prevented the completion of this part of the work.

In conclusion, a mixture of potassium hydroxide and hydrogen peroxide shows promise as a scrubbing liquor for N_2O_4 because of its ability to convert the nitrite in solution to nitrate, thus producing a solution that may be useful as a feed stream to a fertilizer manufacturer.

TABLE OF CONTENTS

ACKNOWLEDGEMENTS	2
ABSTRACT	3
SUMMARY	4
LIST OF FIGURES.....	6
LIST OF TABLES	7
ABBREVIATIONS	8
1. INTRODUCTION.....	9
1.1 BACKGROUND	9
1.2 SCRUBBER SYSTEM.....	9
1.3 CHEMISTRY.....	10
2. PROPOSED SCRUBBER LIQUOR.....	12
2.1 COMPOSITION.....	12
2.2 CONCERNS	12
2.2.1 PRESENCE OF NITRITES.....	12
2.2.2 STABILITY OF HYDROGEN PEROXIDE	12
2.2.3 EFFICIENCY OF SCRUBBER LIQUOR	12
2.2.4 SOLUBILITY OF POTASSIUM NITRATE.....	13
2.2.5 CAPACITY OF SCRUBBER LIQUOR.....	13
3. MATERIALS AND METHODS	15
3.1 STABILITY STUDIES	15
3.1.1 STABILITY STUDY #1	15
3.1.2 STABILITY STUDY #2	16
3.1.3 STABILITY STUDY #3	16
3.2 SCRUBBER EFFICIENCY EXPERIMENTS.....	17
4. RESULTS AND DISCUSSION.....	18
4.1 STABILITY STUDY #1.....	18
4.2 STABILITY STUDY #2.....	20
4.3 STABILITY STUDY #3.....	23
5. CONCLUSIONS	26
APPENDIX A. SEPARATION OF THE H₂O₂ AND NO₂⁻ INTERACTIONS WITH KMNO₄	27
REFERENCES	28

LIST OF FIGURES

FIGURE 1. VENT GAS SCRUBBER SYSTEM	10
FIGURE 2. SCRUBBER EFFICIENCY EXPERIMENTS.....	17
FIGURE 3. TABULAR DISPLAY OF STABILITY STUDY #1.....	19
FIGURE 4. RESPONSE PLOT FOR STABILITY STUDY #1	20
FIGURE 5. DISTRIBUTION OF H₂O₂ AFTER 68 HOURS IN STABILITY STUDY #1 ...	20
FIGURE 6. STABILITY STUDY #2 - EFFECT OF PH ON DECOMPOSITION RATE OF H₂O₂	21
FIGURE 7. STABILITY STUDY #2 - DECOMPOSITION RATE VS. TIME	22
FIGURE 8. TABULAR DISPLAY OF STABILITY STUDY #3.....	24
FIGURE 9. RESPONSE PLOT FOR STABILITY STUDY #3	25
FIGURE 10. DISTRIBUTION OF H₂O₂ AFTER 68 HOURS IN STABILITY STUDY #3.	25

LIST OF TABLES

TABLE 1. SOLUBILITY OF NaNO_3 AND KNO_3 IN WATER AT 25°C	13
TABLE 2. MAXIMUM CAPACITY OF SCRUBBING LIQUORS.....	14
TABLE 3. STABILITY STUDY #1 - 2^4 DESIGN MATRIX	15
TABLE 4. STABILITY STUDY #3 - 2^3 DESIGN MATRIX	16
TABLE 5. STABILITY STUDY #1 RESULTS	19
TABLE 6. STABILITY STUDY #2 RESULTS	21
TABLE 7. STABILITY STUDY #3 RESULTS	24

ABBREVIATIONS

cc	cubic centimeter
cfm	cubic feet per minute
g	grams
gpm	gallons per minute
H ₂ O	water
H ₂ O ₂	hydrogen peroxide
K ⁺	potassium ion
KMnO ₄	potassium permanganate
KNO ₂	potassium nitrite
KNO ₃	potassium nitrate
KOH	potassium hydroxide
mg	milligram
ml	milliliter
MMH	monomethyl-hydrazine
N	Normality (equivalents/liter)
NO	nitric oxide
NO ₂	nitrogen dioxide
NO ₂ ⁻	nitrite ion
NO ₃ ⁻	nitrate ion
N ₂ O ₃	dinitrogen trioxide
N ₂ O ₄	nitrogen tetroxide (dinitrogen tetroxide)
Na ⁺	sodium ion
NaNO ₂	sodium nitrite
NaNO ₃	sodium nitrate
NaOH	sodium hydroxide
ppm	parts per million
wt%	weight percent
[]	concentration

1. INTRODUCTION

1.1 BACKGROUND

Hypergolic fuels are used at Kennedy Space Center (KSC) and Cape Canaveral Air Force Station (CCAFS) for propulsion in Space Shuttle Orbiters, satellites, etc. During on-ground servicing involving hypergols, such as transfer between storage tank and orbiter, the excess hypergols are purged and flushed from tanks and transfer lines using gaseous nitrogen. There is no storage capability for this vent gas mixture of nitrogen and hypergol and it must be scrubbed, i.e. the hypergol removed, before being released to the atmosphere. This scrubbing is accomplished by bubbling the gaseous stream through a liquid that will react with the hypergol to convert it into a water soluble species, thus removing it from the gas stream. The liquid waste stream can then be disposed.

The two primary hypergols currently used in the space program are monomethylhydrazine (MMH) as the fuel and nitrogen tetroxide (N_2O_4) as the oxidizer. The MMH vent gas is scrubbed with a citric acid solution and the N_2O_4 vent gas is scrubbed with a sodium hydroxide (NaOH) solution. The spent scrubber solution for the N_2O_4 vent gas constitutes the second largest hazardous waste stream at the Kennedy Space Center and is the subject of this study.

1.2 SCRUBBER SYSTEM

The currently used scrubber solution for the N_2O_4 vent gas is 25 wt.% NaOH. Because there is no storage capability for the vent gas, a scrubber system is required at each location where the N_2O_4 gas is handled and as a result, there are at least ten separate scrubbing systems in the KSC/CCAFS complex. Figure 1 shows the schematic for one such system.

The scrubber liquor is held in a 750 gallon tank and is pumped at a rate of 80 to 200 gpm to a distributor in the piping which divides the flow equally to the tops of four gas scrubbing columns. The liquor flows in parallel, downward through the columns and is returned to the tank. The N_2O_4 vent gas flows in series through the four gas scrubbing columns, entering from the bottom and exiting the top of each column. The vent gas only passes through the gas scrubbing train once, but the scrubbing liquor is recirculated until the scrubbing capacity has been determined to be sufficiently exhausted. The gas scrubbing columns are packed with polypropylene Pall rings to enhance the contact between the gas and liquid.

The concentration of N_2O_4 in the vent gas and the flow rate before entering the scrubbing system can vary widely depending on the conditions and the operation that generated the vent gas. Typically the vent gas associated with loading N_2O_4 on the shuttle orbiter when it is on the launch pad results in high levels of N_2O_4 and high volumes of vent gas because of the large quantity of N_2O_4 being handled. Concentrations of N_2O_4 in the vent gas can range from 100,000 ppm to 900,000 ppm at flow rates of 10 to 400 cfm.

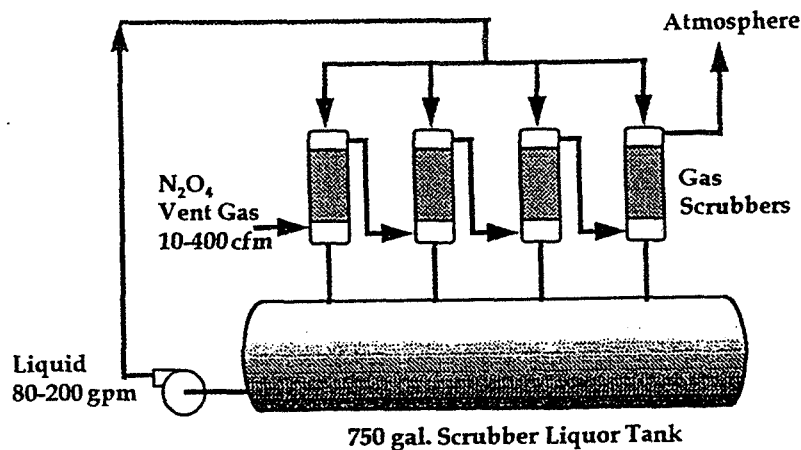


Figure 1. Vent Gas Scrubber System.

The efficiency of the vent gas scrubber system can be calculated as shown in equation (1),

$$\text{Efficiency} = 100\% \times ([N_2O_4]_{in} - [N_2O_4]_{out}) / [N_2O_4]_{in} \quad (1)$$

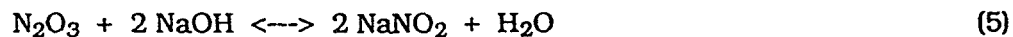
where $[N_2O_4]_{in}$ represents the concentration of N_2O_4 in the feed gas and $[N_2O_4]_{out}$ represents the concentration of N_2O_4 in the exit gas released to the atmosphere.

1.3 CHEMISTRY

The reaction chemistry of nitrogen tetroxide gas reacting with aqueous solutions of alkali is extremely complex when one considers all of NO_x species that may be present in the gas phase and their varying solubilities and reactivities in the liquid phase. Nitrogen tetroxide (N_2O_4) is a dimer of nitrogen dioxide (NO_2) and both exist in equilibrium, the amounts determined by the temperature, pressure, and concentration of the system. Nitric oxide (NO) will also be present as a byproduct of the liquid phase reactions. Some of the more important chemical reactions in the gas phase and in the liquid phase for the current $NaOH$ system are shown below, although others are known to occur also.

Gas Phase Reactions



Liquid Phase Reactions

Reaction #4 is the primary liquid phase reaction and if it were the only reaction occurring, equal moles of NaNO_2 and NaNO_3 would be formed. However because of the other liquid phase reactions occurring, the moles of NaNO_3 is always greater than the moles of NaNO_2 .

The reactions for a solution of KOH instead of NaOH are expected to be similar to the above reaction for NaOH , however the rates and equilibrium concentration may be different.

2. PROPOSED SCRUBBER LIQUOR

2.1 COMPOSITION

The proposed scrubber solution would utilize potassium hydroxide (KOH) rather than sodium hydroxide (NaOH) because the potassium nitrate (KNO_3) produced is more attractive to the fertilizer industry than the corresponding sodium salt.

In addition, hydrogen peroxide will be explored as an additive in the hopes of converting the nitrites to nitrates according to the following reaction.



Thus, the new scrubbing liquor under study would contain 10 to 25 wt.% KOH and 0 to 10 wt.% H_2O_2 .

2.2 CONCERNS

As promising as this proposed scrubbing liquor appears, there are a number of concerns that will need to be addressed before it could be adopted.

2.2.1 PRESENCE OF NITRITES

In order for the spent scrubbing liquor to be successfully used in the fertilizer industry, it needs to be essentially free of nitrites and contain only nitrates. As shown previously (equations 2 to 7) it is expected that a mixture of nitrite and nitrate will be produced. Molar ratios of $\text{NaNO}_3 / \text{NaNO}_2$ in the range of 2 to 16 are typical in the absence of H_2O_2 . It is hoped that the hydrogen peroxide can drive this ratio even higher. This will be a key evaluation criteria for the proposed scrubbing liquor.

2.2.2 STABILITY OF HYDROGEN PEROXIDE

Hydrogen peroxide undergoes homogeneous decomposition in the presence of catalysts and alkali as shown in the following reaction.



Solutions of H_2O_2 are most stable at a pH of about 4.0 to 5.0. Thus, it will be of major concern whether the H_2O_2 will last long enough in a basic solution to react with the nitrites.

The stability usually increases with increasing concentration of H_2O_2 and decreases with temperature as would be expected.

2.2.3 EFFICIENCY OF SCRUBBER LIQUOR

As previously discussed, the efficiency of the vent gas scrubber system is calculated as was shown in equation (1),

$$\text{Efficiency} = 100\% \times ([\text{N}_2\text{O}_4]_{\text{in}} - [\text{N}_2\text{O}_4]_{\text{out}}) / [\text{N}_2\text{O}_4]_{\text{in}} \quad (1)$$

Any scrubber liquor must be able to meet the requirements for reducing the emissions of N_2O_4 .

2.2.4 SOLUBILITY OF POTASSIUM NITRATE

One possible constraint of the potassium system that may not be readily apparent is the solubility limit of potassium nitrate. The solubilities of NaNO_3 and KNO_3 in water at 25°C are shown in the table below in the standard units of g./100 ml. saturated solution, and using the densities of the solutions, have been converted to wt%.

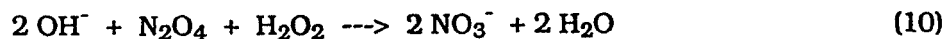
Table 1. Solubility of NaNO_3 and KNO_3 in Water at 25°C .

at 25°C	Solubility, g./100 ml	Density, g./cc	Solubility, wt%
NaNO_3	92.1	1.5	61.4
KNO_3	27.7	1.16	23.8

It can be seen that NaNO_3 is almost three times more soluble than KNO_3 in water. It is not known what the effect of the other species in the scrubbing system might have on solubility or if concentrations approaching the solubility limits would be reached. Nonetheless, this concern warrants further consideration as it would be extremely undesirable to have solids precipitating in the scrubbers or piping.

2.2.5 CAPACITY OF SCRUBBER LIQUOR

The capacity of the scrubbing liquor can be described as how much N_2O_4 could be absorbed by one tank batch of liquor. Assuming the limiting factor is the solubility of the nitrate and that we have been successful in converting all of the nitrite to nitrate, then one can calculate how much hydroxide would have reacted to reach that limit as shown in equation (10). In addition, one can calculate how much N_2O_4 would have been absorbed or reacted to reach that limit. Using the solubilities presented in the previous section and assuming a batch size of 650 gallons, the numbers shown in Table 2 are generated.



As shown in Table 2, the NaOH solution can theoretically hold over three times as much N_2O_4 as the KOH solution, due to the solubility differences in their nitrate salts and the difference in molecular weights. It is interesting to note that the solubility limit for the sodium system would be reached if 28 wt% NaOH reacted to form NaNO_3 , which is greater than the 25 wt% NaOH currently used as a scrubbing liquor. Thus all of the NaOH in the current solution of 25 wt% could form NaNO_3 with no precipitate forming. In actuality not all of the NaOH is consumed and currently the more soluble NaNO_2 is also formed so the system is far from the solubility limit. However, the proposed potassium system could operate near the solubility limit for KNO_3 , limiting the overall capacity.

Table 2. Maximum capacity of scrubbing liquors.

at 25°C	Wt% hydroxide reacting to reach NO ₃ solubility limit	Maximum capacity kg. N ₂ O ₄ absorbed at solubility limit
NaOH	28 wt% NaOH	940 kg N ₂ O ₄
KOH	13 wt% KOH	310 kg N ₂ O ₄

This concern will be somewhat mitigated if the spent scrubbing liquor containing KNO₃ can be used as a fertilizer rather than being classified as a hazardous waste. So that even if more scrubbing liquor must be used, this increased cost will be partially offset by not incurring a disposal fee and perhaps by income from the fertilizer company.

3. MATERIALS AND METHODS

3.1 STABILITY STUDIES

The goal of the stability studies was to measure the stability or the rate of decomposition of hydrogen peroxide as a function of time, at different pH levels and with different levels of salts present. The nitrate and nitrite salts serve to simulate a partially used scrubbing liquor.

3.1.1 STABILITY STUDY #1

In the first study a 2^4 factorial experimental design was used to compare the effect of four variables (pH, $[\text{NO}_2]$, $[\text{NO}_3]$, Na^+ or K^+), each at 2 levels, on the response variable, % H_2O_2 decomposed. The design matrix for this study is shown below in Table 3.

Table 3. Stability Study #1 - 2^4 Design Matrix.

Test #	Cation - = Na^+ + = K^+	pH - = 6 + = 9	NaNO_2 or KNO_2 - = 0 wt% + = 5 wt%	NaNO_3 or KNO_3 - = 0 wt% + = 5 wt%
1	-	-	-	-
2	-	-	-	+
3	-	-	+	-
4	-	-	+	+
5	-	+	-	-
6	-	+	-	+
7	-	+	+	-
8	-	+	+	+
9	+	-	-	-
10	+	-	-	+
11	+	-	+	-
12	+	-	+	+
13	+	+	-	-
14	+	+	-	+
15	+	+	+	-
16	+	+	+	+

To prepare the solutions, first the appropriate quantities of nitrite and nitrate salts were weighed on a Metler balance and then added to a 250ml Erlenmeyer flask. Next a small amount of deionized water was added to dissolve the salts. Then 9 ml of nominally 50 wt% H_2O_2 stock solution was added to the flask. The H_2O_2 stock solution had a density of 1.1935 g/ml and was determined to contain 48.3 wt% H_2O_2 by standard titration with 0.1N KMnO_4 . Thus 5.173 g. of H_2O_2 was added to each flask. The pH of each solution was adjusted by the addition of NaOH or KOH solutions as appropriate and/or addition of H_2SO_4 solution. Simultaneously while achieving the desired pH, the final total net weight was made to total 100 g. The pH was measured with a glass electrode pH probe,

calibrated at pH = 7. The starting weights of all of the solutions were noted and aluminum foil was placed loosely on the top of each flask to keep out contaminants and minimize evaporative water losses, yet allow the O₂ from the decomposition of the H₂O₂ to escape. A "blank" was also prepared that contained only 100 g. of water, and capped in the same manner, to measure the weight loss due to water evaporation.

After 68 hours the flasks were all weighed again, the weight loss corrected for the water evaporation, and the remaining weight loss being due to O₂ escape from decomposition of H₂O₂. Using stoichiometry, the quantity of H₂O₂ that decomposed can be calculated from the O₂ lost as was shown in equation (9). Samples were taken from each flask and titrated with 0.1N KMnO₄ to determine the quantity of H₂O₂ remaining. The H₂O₂ that is unaccounted for by these methods is postulated to have reacted with the nitrite as expressed in equation (11).

$$[\text{H}_2\text{O}_2]_{\text{reacted}} = [\text{H}_2\text{O}_2]_{\text{initial}} - [\text{H}_2\text{O}_2]_{\text{decomposed}} - [\text{H}_2\text{O}_2]_{\text{remaining}} \quad (11)$$

The one difficulty encountered in this method was the discovery that the KMnO₄ used in the titration analysis for H₂O₂ also reacted with any nitrites that were still present. This was corrected for mathematically as explained in the appendix.

3.1.2 STABILITY STUDY #2

The second stability study considered the effect of pH on the stability of H₂O₂ in the absence of any salts. Solutions were prepared similarly to Study #1, except that no salts were added. Erlenmeyer flasks of 125ml capacity were used to prepare solutions totaling 30 g. in weights. To each flask was added 3ml of the stock H₂O₂ solution, netting 1.73g H₂O₂ in each solution. The pH was then adjusted with KOH solutions or pellets. For measuring pH levels at 11 and 13, the probe was calibrated at pH = 10. The flasks were loosely capped with aluminum foil and samples withdrawn at different time intervals for titration with 0.1N KMnO₄ for determination of H₂O₂ remaining.

3.1.3 STABILITY STUDY #3

The third stability study was a 2³ factorial experimental design to compare the effect of three variables (pH, [H₂O₂], Na⁺ or K⁺), with levels of nitrate and nitrite held constant, on the response variable, %H₂O₂ decomposed. The design matrix for this study is shown below in Table 4.

Table 4. Stability Study #3 - 2³ Design Matrix.

Test #	Cation - = Na ⁺ + = K ⁺	pH - = 9 + = 11	H ₂ O ₂ - = 2.3 wt% + = 5.2 wt%
1	-	-	-
2	-	-	+
3	-	+	-
4	-	+	+
5	+	-	-
6	+	-	+
7	+	+	-
8	+	+	+

The quantity of nitrate and nitrite salts added was that necessary to achieve (40 mg ion)/ml, which roughly corresponds to 5 wt.% salt. It was felt that a better comparison could be achieved if the ions were present in equal concentrations rather than the salts being in equal concentration. PH levels of 9 and 11 were chosen for this study. Two levels of H_2O_2 were used as indicated in Table 4, the lower value being approximately just enough to react with the nitrite present. Solutions were prepared and handled in a manner similar to the procedure described for Stability Study #1.

3.2 SCRUBBER EFFICIENCY EXPERIMENTS

In addition, preparations were made to conduct small scale scrubbing experiments to measure the efficiency of the solutions on removing N_2O_4 from gaseous nitrogen. A gas mixture of N_2 and N_2O_4 flowed from a pressurized cylinder, with the flow controlled by a needle valve and the flowrate monitored by a rotameter. Next the gas passed through the scrubbing liquor contained in a midget impinger. After the impinger it was possible to capture a sample of the exit gas in glass sampler for later analysis. A simplified diagram of the equipment is shown in Figure 2.

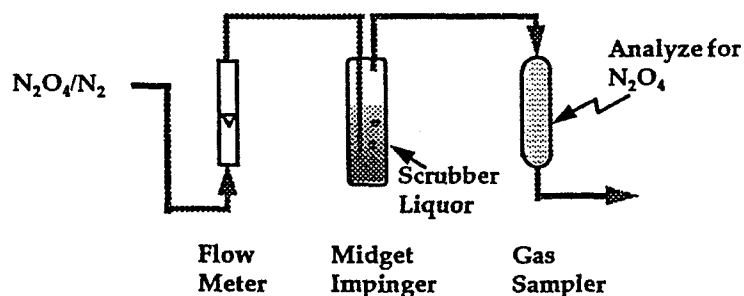


Figure 2. Scrubber Efficiency Experiments

This arrangement was to allow comparison of the efficiency of different scrubbing liquors and at different gas flow rates, but time limitations prevented the completion of this part of the work.

4. RESULTS AND DISCUSSION

4.1 STABILITY STUDY #1

In the first study a 2^4 factorial experimental design was used to compare the effect of four variables (pH, $[\text{NO}_2]$, $[\text{NO}_3]$, Na^+ or K^+) on the response variable, % H_2O_2 decomposed. The design matrix was presented earlier in Table 3 and the data and overall results are presented in Table 5. The weight lost was measured after 68 hours at room temperature.

The fraction H_2O_2 decomposed was determined from the weight loss, attributable to the O_2 escaping and was assumed to be more accurate than the fraction H_2O_2 remaining as determined by titration with 0.1N KMnO_4 . Thus, for example, in Run #1 originally there was 5.17 g. H_2O_2 with 0 g. H_2O_2 lost as determined by weight loss, therefore it is assumed that 5.17 g. H_2O_2 remain, even though the titration gave a value of 5.02 g. H_2O_2 remaining.

Figure 3 contains a tabular display of the response factor for Stability Study #1, expressed as percent H_2O_2 decomposed. Each cell in the table corresponds to a specific combination of the factors and aids in the analysis of the data. The effect of various factors can be compared by comparing different columns or rows. For example the percent decomposed is significantly higher at pH 9 as shown in the two rightmost columns. An average of 65% of the H_2O_2 disappeared at pH = 9 and only 4% disappeared at pH = 6.

A response plot shown in Figure 4 illustrates the effect of pH on the percent H_2O_2 decomposed. Each data point in the response plots represents an average response from four runs, obtained by holding two of the factors constant. For example for Na^+ as the cation and at a pH = 6, runs #1, 2, 3, and 4 can be averaged together. The first response plot in Figure 4 suggests that potassium salts may have a slight stabilizing effect over the sodium salts, i.e. less decomposed.

The distribution of the fate of the H_2O_2 is shown graphically in Figure 5. The values shown for each set of conditions is the average of the four runs which satisfy those conditions, similar to the treatment for the response plot. It appears that when there was nitrite present in the original solution, a significant portion of the nitrite reacted with the hydrogen peroxide to yield nitrate.

Table 5. Stability Study #1 Results. Runs 1 to 8 contain sodium salts, Runs 9 to 16 contain potassium salts.

Run #	Orig. NaNO3 or KNO3 g.	Orig. NaNO2 or KNO2 g.	Orig. H2O2 g.	Total weight	pH	Weight lost, g. O2	H2O2 decomp. g.	H2O2 remain, wt% (titration)	H2O2 remain, g.	H2O2 rx w/ NO2, g; rx	Fraction of H2O2 decomp	Fraction of H2O2 remain
1	0.00	0.00	5.17	99.9	6.1	0.0	0.00	5.02	5.01		0.00	1.00
2	5.01	0.00	5.17	99.9	6.0	0.1	0.21	5.11	5.10		0.00	0.96
3	0.00	5.01	5.17	102.9	6.1	0.3	0.64	2.39	2.45	2.08	0.40	0.47
4	5.01	5.00	5.17	100.1	6.1	0.1	0.21	2.42	2.42	2.54	0.49	0.47
5	0.00	0.00	5.17	100.0	9.2	2.1	4.46	0.43	0.42		0.00	0.14
6	5.01	0.00	5.17	101.3	9.0	1.7	3.61	1.15	1.15		0.00	0.30
7	0.00	5.02	5.17	100.0	9.0	1.6	3.40	0.27	0.27	1.50	0.29	0.05
8	5.00	5.00	5.17	100.0	9.0	1.6	3.40	0.16	0.16	1.61	0.31	0.03
9	0.00	0.00	5.17	101.0	5.9	0.0	0.00	4.94	4.99		0.00	1.00
10	5.01	0.00	5.17	100.7	5.9	0.2	0.43	4.91	4.93		0.00	0.92
11	0.00	5.01	5.17	100.1	6.0	0.0	0.00	2.99	2.99	2.18	0.42	0.58
12	5.00	5.01	5.17	100.0	5.9	0.1	0.21	2.99	2.99	1.97	0.38	0.58
13	0.00	0.00	5.17	100.0	9.1	1.3	2.76	2.20	2.17		0.00	0.47
14	5.01	0.00	5.17	101.6	9.1	1.5	3.19	1.89	1.89		0.00	0.38
15	0.00	5.01	5.17	101.1	9.1	1.4	2.98	0.15	0.15	2.04	0.40	0.03
16	5.00	5.00	5.17	99.6	9.1	1.4	2.98	0.04	0.04	2.15	0.42	0.01

		pH				
		6		9		
		Nitrate		Nitrate		
Cation	Na ⁺	Nitrite	0%	5%	0%	5%
			0%	0	4	86
		5%	12	4	66	66
	K ⁺	Nitrite	0%	0	8	53
		5%	0	4	58	58

Figure 3. Tabular Display of Stability Study #1. Response is the percent H₂O₂ decomposed.

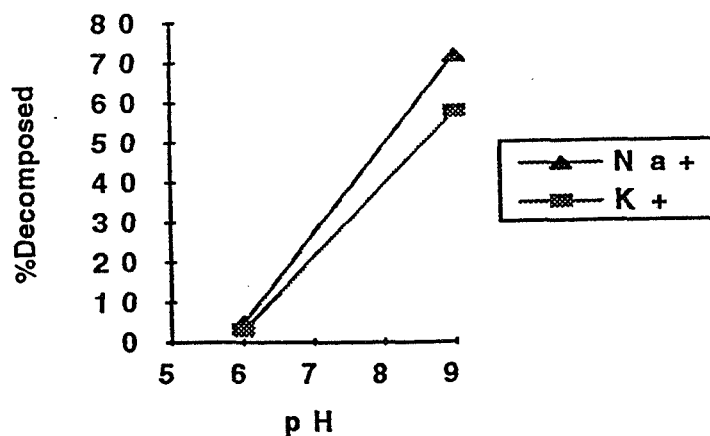


Figure 4. Response Plot for Stability Study #1.

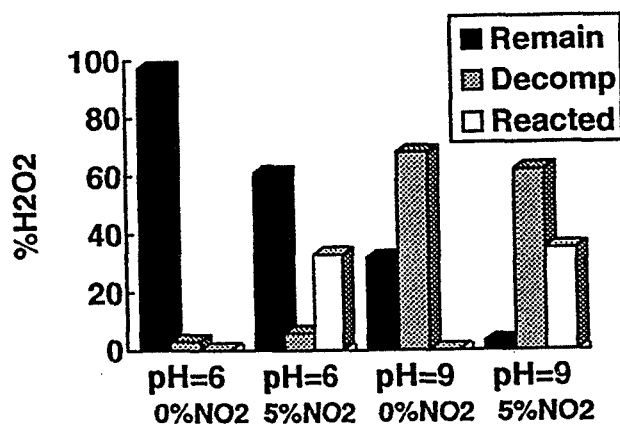


Figure 5. Distribution of H₂O₂ after 68 hours in Stability Study #1.

4.2 STABILITY STUDY #2

The second stability study considered the effect of pH on the stability of H₂O₂ in the absence of any salts. Solutions for this study were prepared at two different times, first a set of three solutions at pH = 9, 11, and 13; later a set of six samples were prepared consisting of duplicates at each of the pHs. Samples were withdrawn from the solutions at various times and titrated with KMnO₄ to determine the H₂O₂ concentration. The starting concentration was assumed to be the calculated concentration based on weighed and pipetted amounts. The rate of decomposition can be calculated as the percent decrease in concentration divided by the elapsed time. This data is presented in Table 6.

Table 6. Stability Study #2 Results.

ph	time	H2O2	rate
	hours	wt%	%dec/h
9	0	5.66	
9	1	3.71	34.45
9	2	3.57	18.46
9	5	3.21	8.66
9	22	2.32	2.68
9	24	2.25	2.51
11	0	5.66	
11	1	1.95	65.55
11	2	1.38	37.81
11	5	1.18	15.83
11	22	0.94	3.79
11	24	0.86	3.53
13	0	5.66	
13	1	3.52	37.81
13	2	3.34	20.49
13	22	2.17	2.80
13	24	2.03	2.67
9.04	0	5.73	
9.04	1	5.22	8.90
9.04	48	2.87	1.04
9.04	72	1.74	0.97
9.24	0	5.73	
9.24	18	2.26	3.36
9.24	48	1.248	1.63
9.24	72	0.47	1.27
10.96	0	5.71	
10.96	1	2.12	62.87
10.96	18	1.08	4.50
10.96	48	0.79	1.80
10.96	72	0.34	1.31
11.09	0	5.75	
11.09	1	2.09	63.65
11.09	18	1.34	4.26
11.09	48	0.86	1.77
12.97	0	5.72	
12.97	18	3.18	2.47
12.97	48	2.39	1.21
12.97	72	1.79	0.95
13.1	0	5.35	
13.1	1	4.5	15.89
13.1	48	2.03	1.29
13.1	72	1.99	0.87

An interesting observation during this work was that when all of the samples at pH = 11 were titrated soon after preparation, over 60% of the H₂O₂ had already disappeared. In Figure 6 all of the data is plotted as decomposition rate vs. pH. The decomposition rate of H₂O₂ at pH = 9 and pH = 13 was comparable, but surprisingly pH = 11 exhibited a higher decomposition rate. Thus the decomposition rate as a function of pH appears to go through a maximum at a pH around 11.

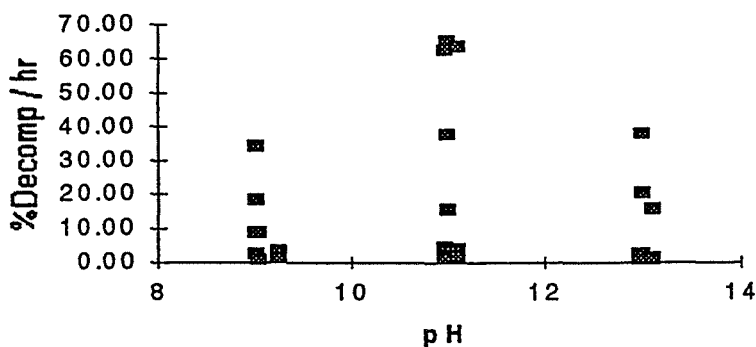


Figure 6. Stability Study #2 - Effect of pH on Decomposition Rate of H₂O₂.

The highest values for the decomposition rates at all pH values occurred at the shortest intervals of time. This can be seen better in Figure 7, decomposition rate as a function of time. The decomposition rate was very high initially and then leveled off with time when expressed as %decomposed/hour.

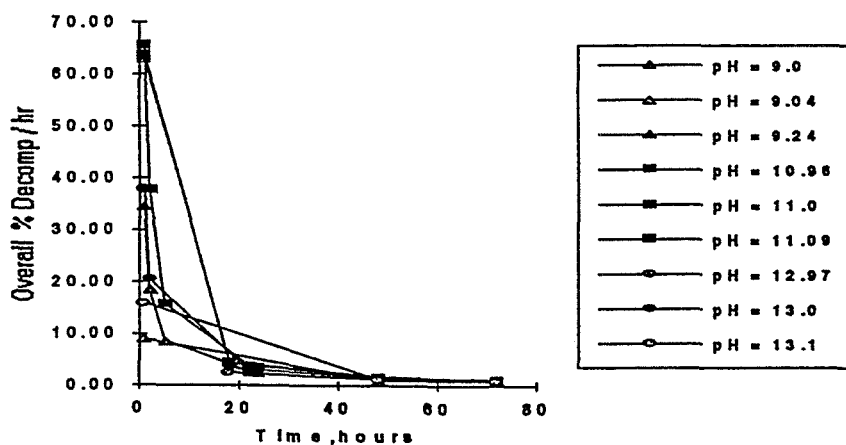


Figure 7. Stability Study #2 - Decomposition Rate vs. Time

4.3 STABILITY STUDY #3

The third stability study was a 2^3 factorial experimental design to compare the effect of three variables (pH, $[H_2O_2]$, Na^+ or K^+), with levels of nitrate and nitrite held constant, on the response variable, % H_2O_2 decomposed. The design matrix was presented earlier in Table 4 and the data and overall results are presented in Table 7. The weight lost was measured after 68 hours at room temperature. As in Stability Study #1, the fraction H_2O_2 decomposed was determined from the weight loss, attributable to the O_2 escaping and was assumed to be more accurate than the fraction H_2O_2 remaining as determined by titration with 0.1N $KMnO_4$. Both the H_2O_2 and the nitrite react with the $KMnO_4$ during the titration, but this has been corrected for, as explained in the appendix.

Figure 8 contains a tabular display of the response factor for Stability Study #3, expressed as percent H_2O_2 decomposed. Each cell in the table corresponds to a specific combination of the factors. The effect of various factors can be compared by comparing different columns or rows. There does not appear to be any strong trends in this data.

A response plot shown in Figure 9 illustrates the effect of pH on the percent H_2O_2 decomposed. Each data point in the response plots represents an average response from two runs, obtained by holding two of the factors constant. No explanation is obvious as to why the two lines in Figure 9 cross.

The distribution of the fate of the H_2O_2 is shown graphically in Figure 10. The values shown for each set of conditions is the average of the two runs which satisfy those conditions. It does appear that a significant portion of the hydrogen peroxide reacted with the nitrite to yield nitrate.

Table 7. Stability Study #3 Results. Runs 1 to 4 contain sodium salts, Runs 5 to 8 contain potassium salts.

Run #	g. NaNO3 or KNO3	g. NaNO2 or KNO2	Initial weight	Orig. g. H2O2	pH	Weight lost g. O2	H2O2 decomp. (g)	Titration sample g.	ml titrate	g. H2O2 rx w/NO2	% H2O2 Decomp	% H2O2 React	% H2O2 Remain
1	5.00	5.45	100.12	2.31	9.28	0.547	1.16	0.835	7.95	0.856	50.4%	37.1%	12.4%
2	5.00	5.45	100.15	5.19	9.02	2.031	4.32	0.885	9.5	0.579	83.2%	11.2%	5.6%
3	5.00	5.46	101.41	2.31	10.89	0.618	1.31	0.673	5.05	0.968	57.0%	42.0%	1.1%
4	5.00	5.46	100.34	5.19	10.93	1.055	2.24	0.662	4.75	2.131	43.2%	41.1%	15.7%
5	5.93	6.73	99.50	2.31	9.03	0.417	0.89	0.733	6.2	1.385	38.4%	60.1%	1.5%
6	5.93	6.73	100.05	5.19	9.11	1.867	3.97	0.709	6.45	1.206	76.5%	23.2%	0.3%
7	5.93	6.73	100.23	2.31	10.96	0.545	1.16	0.742	7.1	1.119	50.2%	48.5%	1.2%
8	5.93	6.73	101.52	5.19	10.93	1.084	2.30	0.759	6.5	2.223	44.4%	42.9%	12.7%

		pH			
		9		11	
Cation		H ₂ O ₂		H ₂ O ₂	
		2.3%	5%	2.3%	5%
Na ⁺		50	83	57	43
K ⁺		38	76	50	44

Figure 8. Tabular Display of Stability Study #3. Response is the percent H₂O₂ decomposed.

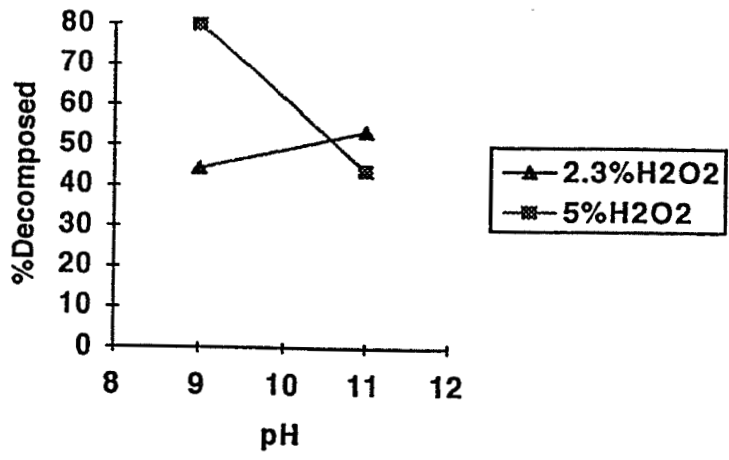


Figure 9. Response Plot for Stability Study #3.

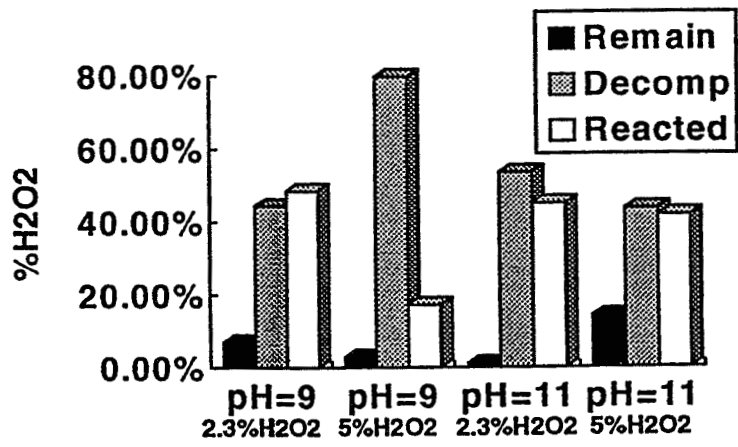


Figure 10. Distribution of H₂O₂ after 68 hours in Stability Study #3.

5. CONCLUSIONS

Small scale laboratory tests were conducted to evaluate the stability of H_2O_2 in alkaline mixtures, some of which included nitrate and nitrite salts, and which were adjusted to different pH levels. These mixtures simulated the proposed scrubber liquor for removing N_2O_4 from the scrubbing of hypergolic vent gases. Currently the N_2O_4 vent gas is scrubbed with a sodium hydroxide (NaOH) solution resulting in a hazardous liquid waste. This study investigated the use of a solution of potassium hydroxide (KOH) and hydrogen peroxide (H_2O_2) for the nitrogen tetroxide vent scrubber system with a goal of producing a solution of NO_3 that could be used as a fertilizer.

A series of three different stability studies were conducted. In the first it was found that the most significant effect was the pH; an average of 65% of the H_2O_2 disappeared at pH = 9 and only 4% disappeared at pH = 6 after 68 hours at room temperature. It also appears that when there was nitrite present in the original solution, a significant portion of the nitrite reacted with the hydrogen peroxide to yield nitrate. The second stability study found that the decomposition rate of H_2O_2 as a function of pH appears to go through a maximum at pH 11. In the third stability study it again appears that some of the nitrite is converted to nitrate.

In conclusion, a mixture of potassium hydroxide and hydrogen peroxide shows promise as a scrubbing liquor for N_2O_4 because of its ability to convert the nitrite in solution to nitrate, thus producing a solution that may be useful as a feed stream to a fertilizer manufacturer.

Appendix A

Appendix A. Separation of the H_2O_2 and NO_2^- Interactions with KMnO_4 .

The following two material balances can be used to solve for the H_2O_2 remaining and the H_2O_2 that reacted with NO_2^- .

Hydrogen Peroxide Material Balance:

$$\text{g. H}_2\text{O}_2 \text{ initial} - \text{g. H}_2\text{O}_2 \text{ decomp.} = \text{g. H}_2\text{O}_2 \text{ remain} - \text{g. H}_2\text{O}_2 \text{ reacted w/ NO}_2^- \quad (\text{A.1})$$

KMnO₄ Material Balance:

$$\text{total ml. titrate} = \text{ml. titrate for NO}_2^- + \text{ml. titrate for H}_2\text{O}_2 \quad (\text{A.2})$$

Let the two unknowns be expressed as

$$x = \text{g. H}_2\text{O}_2 \text{ remain} \quad (\text{A.3})$$

$$y = \text{g. H}_2\text{O}_2 \text{ reacted w/ NO}_2^- \quad (\text{A.4})$$

Now developing equation for (ml. titrate for NO_2^-):

$$\text{g. NO}_2^- \text{ remain} = \text{g. NO}_2^- \text{ initial} - \text{g. NO}_2^- \text{ reacted} \quad (\text{A.5})$$

and the (g. NO_2^- reacted) can be related to "y" (g. H_2O_2 reacted w/ NO_2^-) from the reaction stoichiometry:

$$\text{g. NO}_2^- \text{ reacted} = y (\text{MW NaNO}_2) / (\text{MW H}_2\text{O}_2) \quad (\text{A.6})$$

Expressions can also be developed to relate the (g. NO_2^- remain) to the (ml. titrate for NO_2^-) and to relate the (g. H_2O_2 remain) to the (ml. titrate for H_2O_2) based on the titration sample size.

Thus the two material balances, equations (A.1) and (A.2), can be written with only the two unknowns "x" and "y", all other values being known. It is just a matter of algebraic manipulation to solve for "x" and "y".

The one problem with this correction is that the NO_2^- does not react completely with the KMnO_4 , but most of it does. It was determined by titration without H_2O_2 that 68% to 78% of the NO_2^- reacts with the KMnO_4 , thus a correction factor was used to account for the partial reaction of NO_2^- with KMnO_4 .

References

- Ardon, Michael, *Oxygen, Elementary Forms and Hydrogen Peroxide*, W. A. Benjamin Publ, New York, 1965.
- Chopp, R. J., H. Dev, P. Condorelli, B. J. Jody, "Effects of Packing Material, Caustic Strength, By-Product Level, and Temperature on an Oxidizer Scrubber", Report IITRI C06567-TR2, IIT Research Institute, 1984.
- "Evaluation of Hypergolic Emissions Control Technologies", Report NAS 10-10715, Research Triangle Institute, 1984.
- Felts, W. Keith, "Air Pollution Testing of Hypergolic fuel - Vapor Scrubbers at Cape Canaveral Air Force Station, Florida", Report ESL-TR-80-58, Engineering Science, 1981.
- "Hypergolic Nitrogen Tetroxide Vapor Scrubber, Phase 1 Test Report", Report KSC-DD-777, Planning Research Corporation, 1983.
- "Hypergol Oxidizer Vapor Scrubber Report, Phase IV and Phase V Test Results", Report KSCE-824-0014, EG&G Florida, 1989.
- "Hypergolic Vapor Scrubber, Phase II (N₂O₄) & Phase III (MMH), Modification and Test Project", Report KSC-E-3084, EG&G Florida, 1986.
- Kirk-Othmer Encyclopedia of Chemical Technology*, 3rd edition, volume 18, John Wiley and Sons, New York, 1982.
- Moen, Ronald D., Thomas W. Nolan, Lloyd P. Provost, *Improving Quality Through Planned Experimentation*, McGraw-Hill, New York, 1991.
- Schumb, W. C., et al., *Hydrogen Peroxide*, Reinhold Publishing Corp., New York, 1955.
- Thomas, J., et al., "Improved Hypergolic Vapor Removal Systems", Report NAS 10-10106, Florida Institute of Technology, 1982.
- Weast, Robert C., ed., *Handbook of Chemistry and Physics*, The Chemical Rubber Co., Cleveland, Ohio, 1965.

N95-18176

351493

111761

1994 NASA/ASEE SUMMER FACULTY FELLOWSHIP PROGRAM

JOHN F. KENNEDY SPACE CENTER
UNIVERSITY OF CENTRAL FLORIDA

510-81

33970

P. 50

APPLYING COSTS, RISKS AND VALUES EVALUATION (CRAVE) METHODOLOGY
TO ENGINEERING SUPPORT REQUEST (ESR) PRIORITIZATION

PREPARED BY:	Dr. Prafulla N. Joglekar
ACADEMIC RANK:	Professor
UNIVERSITY AND DEPARTMENT:	La Salle University Management Department
NASA/KSC	
DIVISION:	Shuttle Project Engineering
BRANCH:	Process Integration
NASA COLLEAGUE:	Art Beller
DATE:	August 5, 1994
CONTRACT NUMBER:	University of Central Florida NASA-NGT-60002 Supplement: 17

Acknowledgments

I am thankful to the NASA/ASEE fellowship program for this second year of research opportunity. Although my intention this year was to apply the Costs Risks and Values Evaluation (CRAVE) methodology to specific software development projects, at the instance of Bob Lang, Director of Vehicle Engineering, I decided to apply my methodology to the problem of prioritization of Engineering Support Requests (ESR). In retrospect, this choice of the area of application turns out to be more productive in demonstrating the applicability of my methodology, and in providing concrete recommendations for improvement in the decision processes at KSC. I am thankful to **Bob Lang**, both for focusing my attention on ESRs and for his patience in listening to my final presentation to management.

I appreciate the generosity, and candidness of the many NASA and Lockheed employees I interviewed this summer. I have very freely used many of their ideas in this report without explicitly crediting them for the same. But I do want to thank them for the same. Special thanks are due to **Mark Allison** (LSOC D/17-12, GSE PEO), **Jim Haggard** (TV-PEO-32), and other members of the GSWT steering committee for making almost all of their files and data available to me.

As they did last year, **Loren Anderson** (UCF), and **Kari Stiles** (UCF), again provided valuable and very effective administrative support, as well as educational and entertainment opportunities. **Gene Thurston's** (TV-PEO-1) constant encouragement and guidance allowed me to cope with project re-direction(s) and keep my enthusiasm undiminished. I express my heartfelt gratitude to each one of these special individuals.

Finally, once again, **Art Beller** (TV-PEO-12) has proved to be an outstanding mentor, thinker, facilitator, and a close friend. He provided any and all help I needed, professional as well as personal. Words are inadequate to express my gratitude to him.

APPLYING
COSTS, RISKS, AND VALUES EVALUATION (CRAVE) METHODOLOGY
TO
ENGINEERING SUPPORT REQUEST (ESR) PRIORITIZATION

Executive Summary

Given limited budget, the problem of prioritization among Engineering Support Requests (ESRs) with varied sizes, shapes, and colors is a difficult one. At the Kennedy Space Center (KSC), the recently developed 4-Matrix (4-M) method represents a step in the right direction as it attempts to combine the traditional criteria of technical merits only with the new concern for cost-effectiveness. However, the 4-M method was not adequately successful in the actual prioritization of ESRs for the fiscal year, 1995 (FY95). This research identifies a number of design issues that should help us develop better methods. It emphasizes that given the variety and diversity of ESRs one should not expect that a single method could help in the assessment of all ESRs. One conclusion is that a methodology such as Costs, Risks, and Values Evaluation (CRAVE) should be adopted. It also is clear that the development of methods such as 4-M requires input not only from engineers with technical expertise in ESRs but also from personnel with adequate background in the theory and practice of cost-effectiveness analysis.

At KSC, ESR prioritization is one part of the Ground Support Working Teams (GSWT) Integration Process. It was discovered that the more important barriers to the incorporation of cost-effectiveness considerations in ESR prioritization lie in this process. The culture of integration, and the corresponding structure of review by a committee of peers, is not conducive to the analysis and confrontation necessary in the assessment and prioritization of ESRs. Without assistance from appropriately trained analyst(s) charged with the responsibility to analyze and be confrontational about each ESR, the GSWT steering committee will continue to make its decisions based on incomplete understanding, inconsistent numbers, and at times, colored facts. The current organizational separation of the prioritization and the funding processes is also identified as an important barrier to the pursuit of cost-effectiveness. Perhaps the greatest barrier is that, at the working level, KSC's culture is so preoccupied with technical concerns that it seems almost oblivious to any cost concerns, let alone cost-effectiveness concerns. It is recommended that we must urgently begin to change that culture and seek a better balance between these two concerns.

Abbreviations and Acronyms List

4-M	The 4-Matrix method
AHP	Analytic Hierarchy Process
ASW	Advanced software
CBA	Cost Benefit Analysis
CRAVE	Costs, Risks, and Values Evaluation
DE	Design Engineering
ESR	Engineering Support Request
GSWT	Ground Systems Working Teams
GTD	Global Technology Deployment
KSC	Kennedy Space Center
OPF	Operations Processing Facility
O&M	Operations and Maintenance
SF	Shop Floor
TV	Technical Vehicle Engineering Directorate at KSC

Table of Contents

<u>Section</u>	<u>Title</u>	<u>Page</u>
1.	BACKGROUND	1
2.	THE TASK THIS YEAR	3
3.	BARRIERS AND CORRESPONDING RECOMMENDATIONS	5
	REFERENCES	7
	Exhibits, Tables, and Figures	8
APPENDIX A	A Critique Of The 4-Matrix (4-M) Method Of ESR Assessment	17
	Attachments A-1, A-2, & A-3	26
APPENDIX B	Comments On Selected ESRs from the CRAVE Perspective	36

1. BACKGROUND

1

“Our team pledges the highest level of performance at the lowest possible cost within the framework of absolute dedication to safety and quality to meet the National Space Initiatives and challenges of today and the 21st Century.”

From p.3 of the March 24, 1994 document,
Implementation of the KSC 1994 Strategic Management Plan

To keep this pledge, at KSC, decisions such as which engineering support requests (ESRs) to fund and at what level must be based on sound cost-benefit / cost-effectiveness analyses (CBA). Toraskar and Joglekar [1993] have shown that although CBA theory contains rich concepts and sound principles, its practice is often based on overly simplified and narrow techniques supplemented with numerous convenient but incorrect assumptions. Consequently, often the practice of CBA is trapped in the type of vicious circle [See **Exhibit 1**] I observed last year, here at KSC, in the context of advanced software decision-making [Joglekar, 1993].

In order to break out of such vicious circles, we must use a methodology such as Costs, Risks, and Values Evaluation (CRAVE). A methodology is a way of thinking — armed with certain fundamental principles and concepts — and a way of analyzing available decision alternatives using situationally appropriate techniques and tools from a large body of methods consistent with the fundamental principles and concepts. A methodology focuses on both the techniques and the processes used in relevant decision-making. Joglekar and Toraskar [1994] have explained exactly what CRAVE is, and how it is supposed to work. **Exhibit 2** captures Joglekar and Toraskar’s prescription for the process of applying CRAVE written in the context of global technology deployment (GTD) decisions. The six-stage process emphasizes some of the fundamentals of CRAVE, such as

- the need for context articulation,
- the recognition that cost-benefit estimation is in itself a costly process and sometimes the benefits of estimation do not justify the costs,
- the recognition that it is not necessary to force quantification on certain consequences that are truly non-quantifiable
- the recognition that measurement and valuation should not be confused as one and the same; valuation of a consequence is in the eye of the beholder, and hence a multi- perspective analysis is more desirable than a single perspective analysis.

As **Exhibit 3** shows, CRAVE retains some of the fundamental principles and looks forward to the use of many rich typologies and concepts of classical CBA. Yet, CRAVE attempts to overcome the typical flaws in the practice of traditional CBA. **Exhibit 4** shows how CRAVE differs from classical CBA practice. [For a fuller understanding of CRAVE, see Joglekar and Toraskar, 1994].

2. THE TASK THIS YEAR

This year, Bob Lang, Director of Vehicle Engineering, asked me to

- (a) See how CRAVE could be applied to the problem of ESR prioritization, and
- (b) Recommend a method for future use.

Given that task, I tried to understand:

1. What exactly an ESR is, how varied ESRs are from one another, and what kinds of peculiarities characterize some of the ESRs;
2. What explicit and implicit criteria are currently used in the prioritization of ESRs; and
3. What process is currently used in the prioritization of ESRs.

Clearly, my understanding of these three topics was not a linear but a parallel process, with the understanding of one topic influencing the understanding of other topics, and vice versa. It follows that readers who want to truly grasp my total understanding may want to read this report and its appendices at least twice in its entirety.

Briefly, an ESR is a proposal to upgrade an equipment or a facility used in the "ground processing" (all the work done between one landing and the next launch) of a space shuttle. An ESR seeks one or more of desired goals such as improving flight safety, improving safety of ground processing operations, overcoming system obsolescence, avoiding schedule delays, and reducing processing costs. At KSC, there are over thirty engineering systems (represented by their GSWT teams) that are together seeking funding for some 200 different ESRs, each costing anywhere between a few thousand to a few million dollars. Given limited resources, only a few of these ESRs can be fully or partly funded in any given year.

The benefits sought by some ESRs are considered so critical to the strategic objectives of KSC that these ESRs are designated as Category 1 (i.e., mandatory), and they are implemented expeditiously. This research is focused on the prioritization of Category 2 (i.e., desirable but optional) ESRs, where cost-effectiveness analysis ought to be useful. However, as **Appendix A** explains, historically, even Category 2 ESRs were prioritized by using a system called "P-cut rating," which extended the notion of "required" versus "desirable" within Category 2. Cost-effectiveness considerations were simply left out. (See **attachments A-1 and A-2**).

Therefore, I was pleasantly surprised to know that, to incorporate cost-effectiveness considerations in the prioritization of Category 2 ESRs, recently, GSWT steering committee had developed a new approach, named "the 4-Matrix (4-M) method." (See **Attachment A-3**). Clearly, the 4-M method represents a step in the right direction, and its designers must be applauded for their courage in breaking away from the tradition of focusing exclusively on the technical merits of an ESR.

On the other hand, it seems that the designers had no help from anyone with the proper background in the theory and practice of cost-effectiveness analysis. Consequently, the design shows numerous flaws detailed in **Appendix A**, including:

1. The 4-M method ignores two over-riding considerations at KSC, namely safety and obsolescence.
2. The 4-M method actually focuses on two primary factors:
 - (a) Expected annual impact on flow schedule, and
 - (b) Payback period.
3. A multiplicative model is inappropriate for the 4-M method.
4. The design of the rating categories and score ranges is inappropriate.
5. The absence of relevant probability considerations on the Cost Assessment Worksheet is inappropriate.
6. The language is ambiguous, and instructions / explanations are lacking.

As a consequence of these design flaws, the 4-M method was not successful in assisting the prioritization of FY95 ESRs. **Table 1** and **Figures 1, 2, and 3** confirm this lack of success by showing that there is no relationship between the steering committee's actual priorities and either the cost or the payback or the ESR scores.

These and other design flaws are also manifest in the assessments of specific ESRs reviewed in **Appendix B**. As can be seen, the design of 4-M leads to a variety of instances of misrepresentations and overestimation of the benefits. At the same time, there are instances of ESRs for which 4-M worksheets are very difficult to use. Some of the comments in **Appendix B** further show that we seem to aggravate the problem of comparing ESRs by lumping together ESRs costing \$4M with those costing \$4K. **Figure 4** graphically shows how a single one of the top 17 ESRs accounts for over 66% of the funding needed by all 17 put together. Clearly, ESRs requiring capital expenditures ought to be evaluated and funded separately from ESRs requiring a few thousand dollars.

Most importantly, the variety of sizes, shapes, and colors of ESRs captured by **Appendix B** makes it clear that the presumption of being able to create a single method to fit all ESRs is unrealistic. What we need is a methodology, and not a method. A methodology allows for the use of several different methods of analysis depending on the nature of the technical system, the type of modification sought, and the relevant costs and benefits. Despite the shortcomings of the 4-M method, we must not abandon the pursuit of cost-benefit analysis, or return to the arbitrary decision making of the past. Instead, we must evolve towards the adoption of a methodology such as Costs, Risks, and Values Evaluation (CRAVE).

In any case, the most important reasons for the lack of success of the 4-M method lie in the GSWT integration process. The latter part of **Appendix A** discusses these process issues in depth. Here, by way of conclusion, I simply want to list several process related barriers to the application of CRAVE, and my recommendations to management for overcoming those barriers.

BARRIERS AND CORRESPONDING RECOMMENDATIONS

Barrier 1.

We are trying to develop a single method to assess all ESRs.
 However, ESRs come in a variety of sizes, shapes and colors.
 Their assessment calls for a **methodology** -- a collection of methods, along with
 the knowledge of which one to use when.

Recommendation:

Adopt CRAVE.

Barrier 2.

We leave the development of a cost-benefit analysis (CBA) method to engineers
 who do not have the necessary background in the theory and practice of CBA.

Recommendations:

Get expert help.
 Develop internal expertise through training.

Barrier 3.

The culture of "integration" (and the corresponding structure of review by a
 committee of peers) is not conducive to the analysis and confrontation necessary
 for objective assessment of each ESR, and the subsequent rational prioritization
 among them.

This is true whether the assessment criteria include cost considerations or not.

Recommendation:

Let the GSWT steering committee be assisted by appropriately trained, objective
 analysts, charged with the responsibility to analyze and be confrontational about
 each ESR.

Barrier 4.

Organizational separation of the prioritization, funding, and implementation processes is not conducive to the pursuit of cost-effectiveness.

Recommendation:

To the extent possible, centralize the authority to prioritize, fund, and monitor implementation of ESRs.

At least, coordinate sufficiently to make sure that decisions in these three processes are based on the same criteria, and on an appreciation of each others' reasoning and deliberations.

Barrier 5 (The Most Important One).

At the working level, KSC's culture is almost oblivious to any cost concerns, let alone cost-effectiveness concerns.

Recommendation:

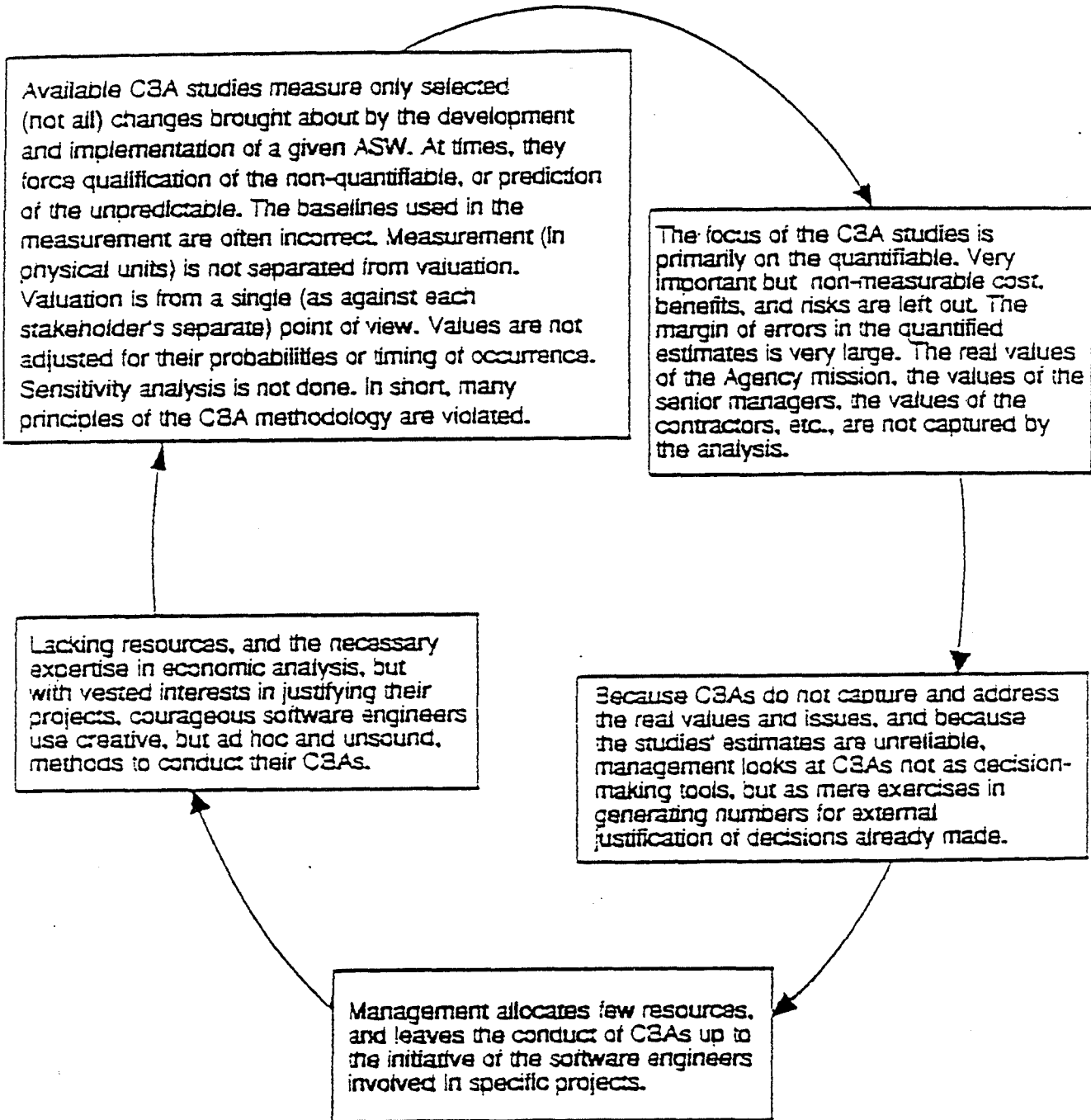
Begin to change the culture by

- insisting on a discussion of costs, and paybacks at meetings to review priority list, and at funding decision meetings,
 - tracking and monitoring the estimated and actual costs of ESRs approved in prior years,
 - setting up a program of training in CBA / CRAVE concepts and principles.
-
-

REFERENCES

- **Toraskar, Kranti & Joglekar, Prafulla (1993)**, "Applying Cost Benefit Analysis (CBA) Methodology for Information Technology Decisions," in R. Banker, R. Kauffman, M. Mahmood (eds.), *New Perspectives on the Strategic and Economic Value of Information Technology Investment*, Harrisburg, PA: Idea Publishing Group, January 1993, pp. 119-142.
- **Joglekar, Prafulla (1993)**, "Cost Benefits of Advanced Software: A Review of Methodology used at Kennedy Space Center," in E. Hosler and C. Valdes (eds.) *NASA/ASEE Summer Faculty Fellowship Program, Contractor Report No. CR-194678*, Kennedy Space Center, FL., October 1993, pp. 229-267.
- **Joglekar, Prafulla & Toraskar, Kranti (1994)**, "Costs Risks, and Values Evaluation (CRAVE): A Methodology for Global Technology Deployment Decisions," in A. Chakravarti (ed.) *Proceedings of Symposium on Emerging Paradigms in Globalizing Technology, Manufacturing, and Service Operations*, Goldering Institute, Tulane University, New Orleans, LA., January, 1994, pp. 1-39.

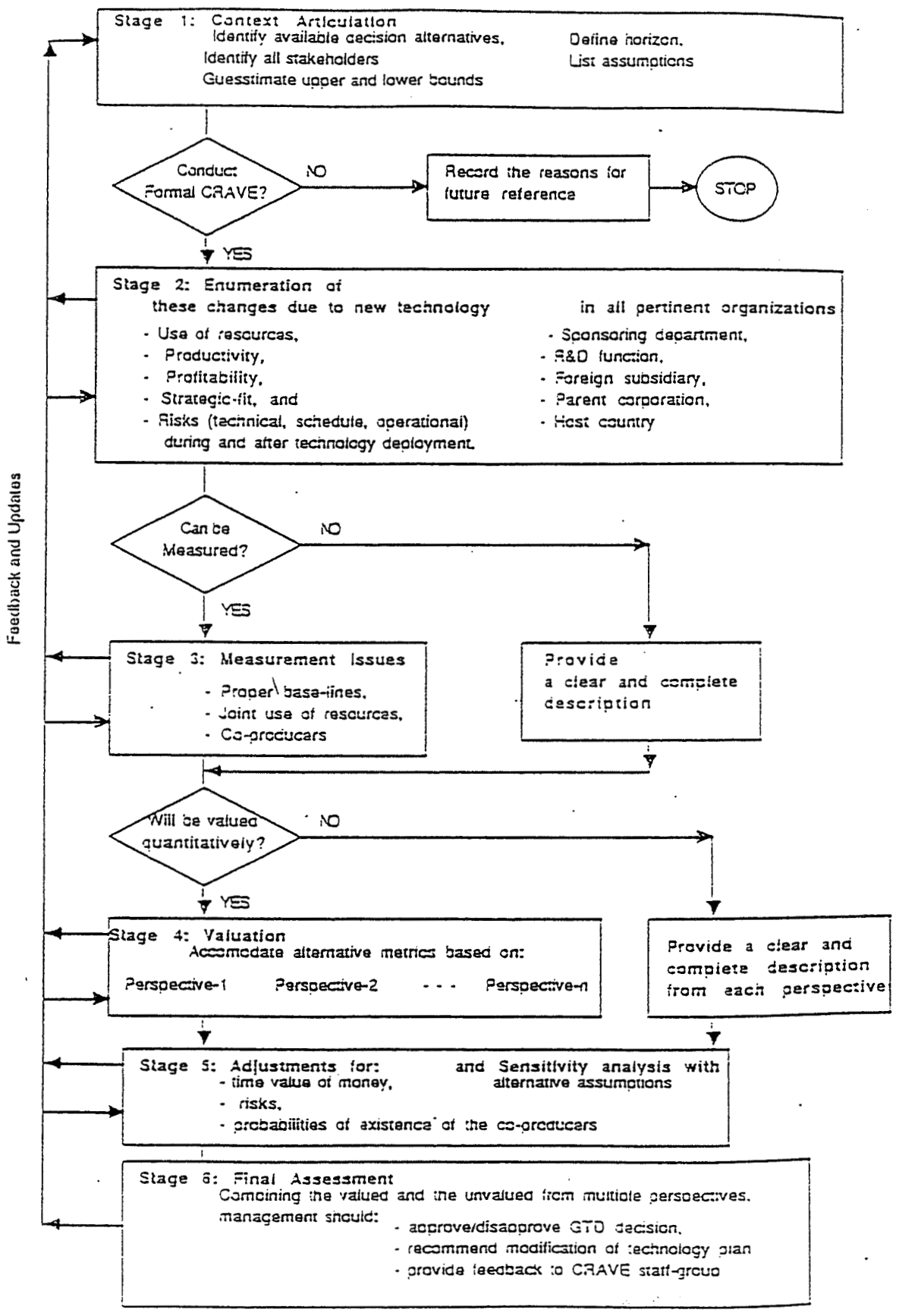
The Vicious Circle



Small illegible text at the bottom left corner.

Exhibit 2

A Process for Applying CRAVE Methodology to GTD Decisions



ORIGINAL PAGE IS OF POOR QUALITY

Some Commonalties in CBA and CRAVE Methodologies

1. **Fundamental principles such as:**
 - Formal and explicit analysis
 - Accounting for all incremental costs and benefits
 - Accounting for costs and benefits to whomsoever they accrue
 - Adjusting for time value of various costs and benefits
 - Explicit recognition of assumptions, and performance
of sensitivity analysis for alternative assumptions

2. **Use of typologies of costs and benefits such as:**
 - Fixed and variable.
 - Direct and indirect,
 - Obvious and hidden,
 - Primary, secondary, tertiary
 - One-time and recurrent
 - Controllable and non-controllable

3. **Use of rich concepts such as:**
 - Opportunity costs
 - Pareto-superiority
 - Joint use of resources
 - Cause-effect versus multi-producers-single-product relationships

**A COMPARISON OF CURRENT CBA PRACTICE
 WITH CRAVE METHODOLOGY**

CBA PRACTICE	CRAVE METHODOLOGY
Justification focus	Decision Assistance focus
Retrospective	Prospective
Technique-oriented	It is a methodology
Single-perspective assessment	Multi-perspective assessment
Consolidation of multiple stakeholders' criteria (possibly AHP type)	No simple consolidation (concept of Pareto superiority)
Forced quantification of the non-quantifiable	Quantification only when possible
Left to the proponents of specific GTDs	Actively directed by the MNC managers / decision makers
Left to non-experts with certain recipes	Guided by a methodologist
Potential for advocacy ignored	Potential for advocacy actively managed
Economic values only	Economic and non-economic values
Risks of non-existence of co-producers ignored	Risks of non-existence of co-producers explicitly accounted for
Consideration of internal risks only	Consideration of both internal and external risks
Stringent financial criteria Short-sighted perspective	More realistic criteria Balanced perspective
Product-oriented (i.e. C/B ratio, or IRR)	Process-oriented
Zero valuation of non-quantified intangibles	Explicit consideration of non-quantified intangibles
Measurement and valuation confused with one another	Measurement separated from valuation
Evaluating given alternatives	Helping construction of better alternatives
Often unrealistically long horizons	Well-defined, reasonably long but limited horizons
Ad hoc methods and assumptions	Consistent methodology and assumptions

Table 1						
Summary Data on The Steering Committee's Top 17 ESRs						
Priority #	ESR #	Costs (\$' 000)	Payback (months)	ESR Score	Category / P-cut	Old Category
1	k15040	\$108	12	144	2-s	1-s
2	k15813	\$16	17	80	2-s	1-M
3	k15399	\$29	3,484	36	2-s	
4	k14453	\$3,800	63	60	2	1-M
5	k11794	\$340	0	375	2	1-s
6	k15783	\$305	NA	60	2	1-M
7	k15505	\$4	NA	40	2-s	
8	k15836	\$58	7	240		
9	k15569	\$35	264	9		
10	k15825	NA	NA	60	P4-3	
11	k14887	\$22	10	180		
12	k15317	\$470	12	240	P4-1	
13	k15818	\$46	7	180		
14	k15835	\$2	3	256		
15	k14213	\$84	84,000	30		
16	k15626	\$472	34	40		
17	k15602	\$26	16	60		

FIGURE 1

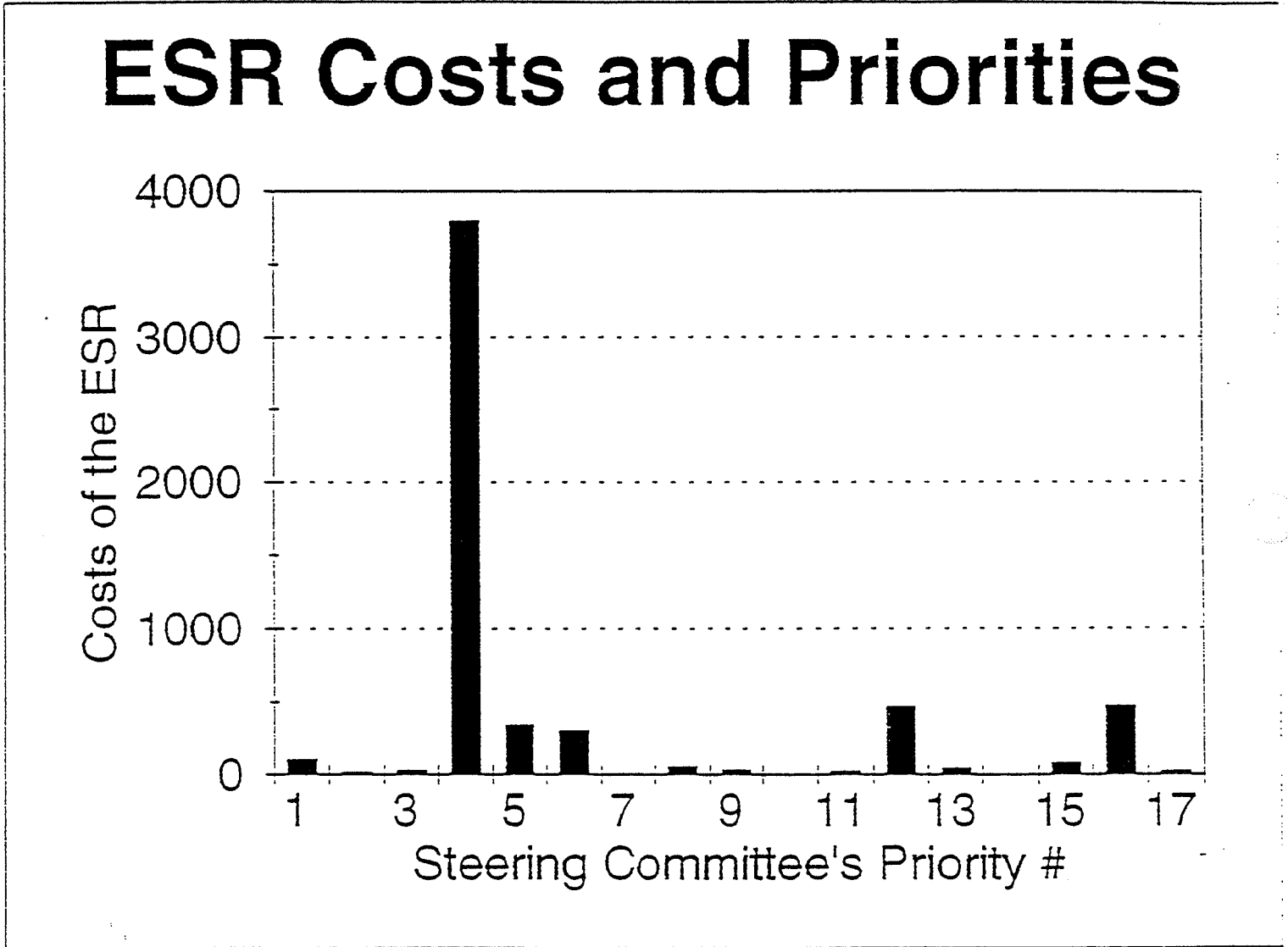


FIGURE 2

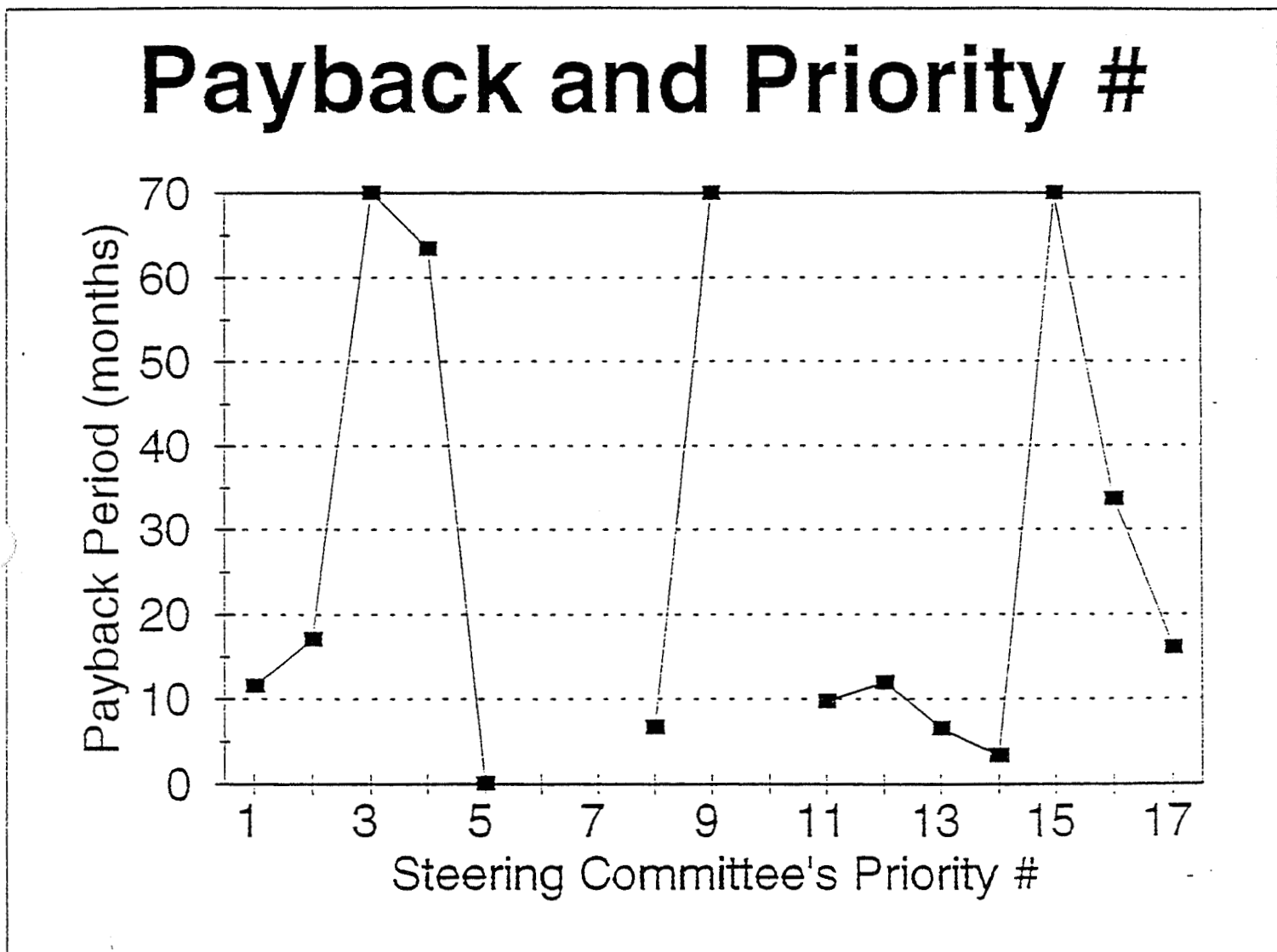


FIGURE 3

ESR Scores and Priority #s

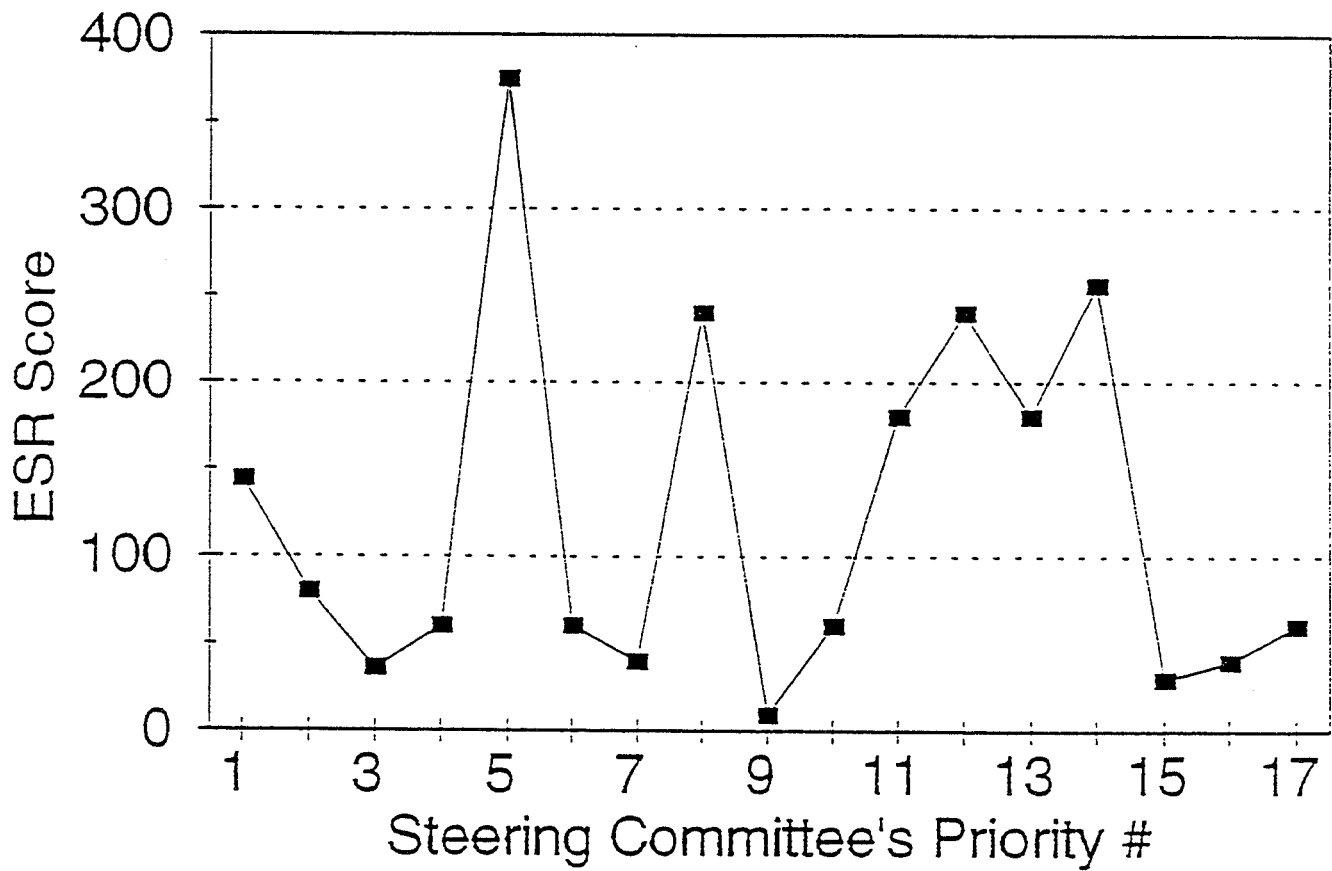
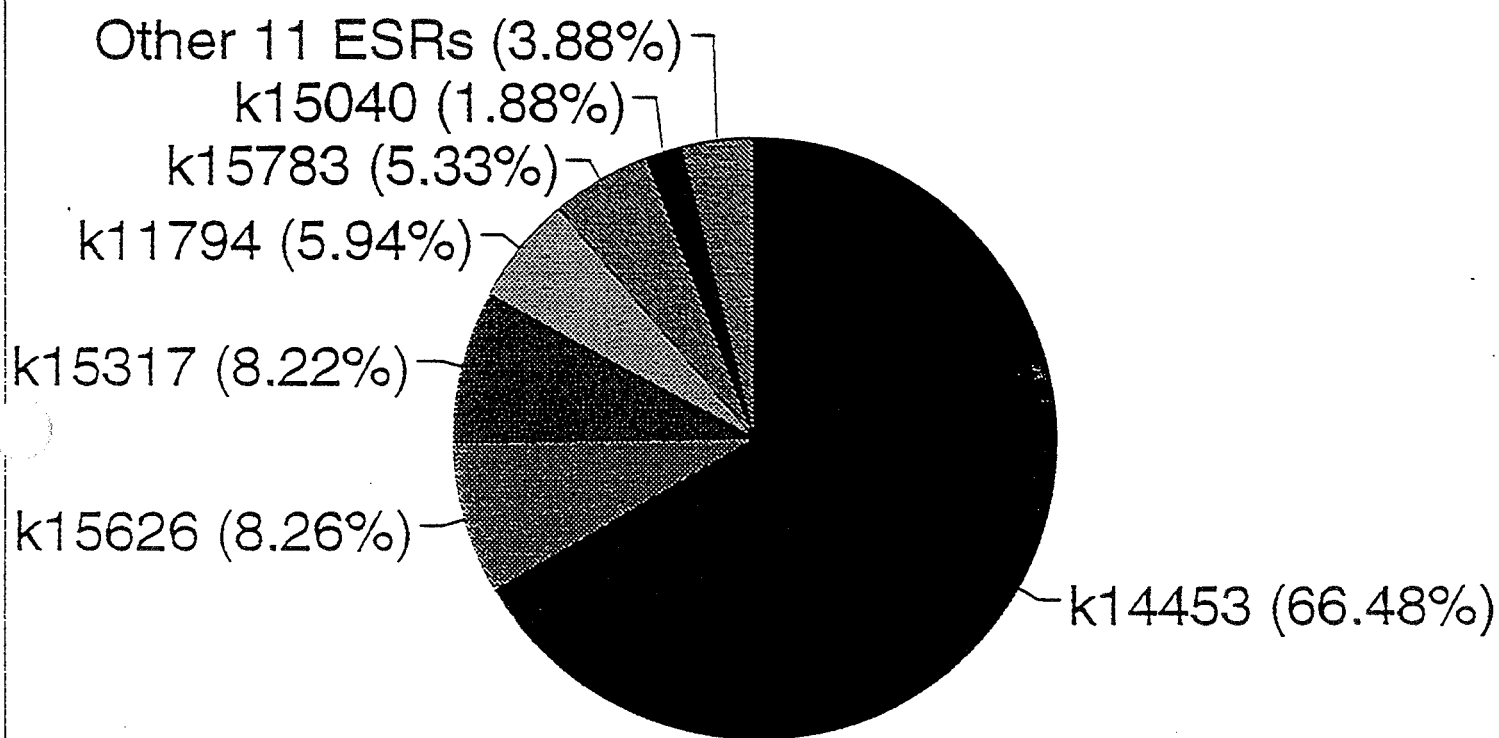


FIGURE 4

ESR Shares of Total Costs



A Critique of the 4-Matrix (4-M) Method of ESR Assessment

by
Praf Joglekar

The Ground Systems Working Teams (GSWT) Steering Committee has a difficult task: Prioritization among hundreds of worthy Engineering Support Requests (ESR). These ESRs come from some 31 different vehicle, payload, and facility systems. Individual ESRs cost anywhere between a few thousand to a few million dollars, and seek one or more of KSC's goals of improving safety, avoiding delays in flow-critical activities, reducing obsolescence, and reducing operations and maintenance (O&M) costs. At the same time, an important concern at KSC is that the modifications done by one engineering system must not adversely affect the functioning of other engineering systems vital to the processing of the shuttle. Thus, the process of ESR prioritization is actually called, **"GSWT Integration."** Attachment A-1 describes this process and its ground rules as of August 1993.

To understand the first ground rule, it should be realized that there is a system of designating ESRs as either Category 1 (i.e., mandatory) or Category 2 (i.e., highly desirable, but not mandatory). Suffixes such as S, M, or E are added to these categories to indicate whether ESR attempts to address a safety, or management, or environmental requirement. The ultimate authority for all ESR category designation rests with the Ground Review Board (GRB). The funding and approval of Category 1 ESRs is outside the GSWT process, which focuses on prioritizing within Category 2 ESRs.

To compare ESRs with one another and prioritize them is similar to comparing and rank-ordering hundreds of apples, oranges, bananas, strawberries, and watermelons, fruit by fruit! Each fruit comes in a variety of sizes, shapes, colors, and ripening stages. To complicate the matter further, the fruits come in a variety of semi-transparent packages designed to exaggerate their attractiveness. Some fruits sell by the pound, other by the piece, still other by the package. For some quantity discounts are available, for some others their are cost-premiums associated with the timing of purchase. We want to maximize the nutritional value, the taste, the flavor and still be within our budget, which will be determined at future dates by several different funding authorities!

As I understand it, in the past, this comparison and rank-ordering was not a major problem. We had resources to buy plenty of each kind of fruit. Even ESRs that were not funded in a given year were seen as simply deferred for implementation in a year or two. Thus, as described in Attachment A-1, we prioritized ESRs on the basis of their **technical merit** (perhaps a euphemism for subjective judgment based on such inputs as which team makes the best presentation, who is championing an ESR, which team is screaming the loudest, etc.), with **practically no regard to what they cost.**

To assist the steering committee in its assessment of the technical merits, GSWT teams were encouraged to assign a "P-cut" rating to individual ESRs. Attachment A-2 presents the P-cut definitions. Although, the GSWT steering committee is charged to consider only Category 2 (desirable but not mandatory) ESRs, the P-cut system extended the concept of mandatory versus desirable nature of ESRs to several levels within Category 2 by focusing on the reasons underlying the modifications sought by the ESRs, and within Category 2 ESRs getting P1, P2, or P3 ratings were seen as required!. The differences in the costs of various ESRs were not seen as an important consideration, and even highly cost-efficient ESRs (those promising a payback in less than one year) received a low priority of P4-2, practically ensuring that we will never get around to these ESRs with the limited available funds.

Over the last three years, the resources available for NASA, in general, and for ESRs in particular have shrunk dramatically. Now, we must be cost-conscious and choose between competing ESRs systematically and rationally. In other words, **today we must base our decisions not only on technical merit but also on cost-effectiveness considerations.** Recognizing this need for cost-effectiveness considerations, the GSWT Steering Committee recently developed and implemented a method called **the 4-Matrix (4-M) method of ESR assessment.** See Attachment A-3 for the description of the method, the forms used, and the accompanying instructions.

The designers of 4-M method must be applauded for their courage in breaking away from the established culture at KSC which is oblivious to any cost considerations, let alone consideration of cost-effectiveness. 4-M represents a first attempt at bringing a degree of rationality to the process of rank-ordering ESRs. This method must evolve and lead to a sounder methodology in the future. The critique here is intended to assist in that evolution. It must not undermine the credit for a pioneering effort on the part of the designers of 4-M.

I had the opportunity to study how the 4-M method worked in the steering committee's rank-ordering of the top 17 Vehicle Engineering (TV) related ESRs for FY95. Table 1 summarizes the data on cost, payback period, and ESR score, for each of the top 17 ESRs. In addition, I have included the Category / P-cut rating, where available. Finally, I was told that some of these top 17 ESRs were originally in Category 1 but were downgraded to Category 2. The Column "Old Category" reports this information.

As can be seen from Table 1, an ESR's priority does not seem to be related to either the size of the project (as defined by its cost), or its payback period, or the ESR score. **Figures 1, 2, and 3** graphically demonstrate the lack of these relationships. In short, the steering committee's priority order cannot be explained by any of these factors. It follows that the 4-M method does not seem to help in the rank-ordering of ESRs. There are several reasons why. Here, these reasons are grouped in two major areas: issues pertaining to the **design** of the 4-M method, and those pertaining to the GSWT **process.**

DESIGN ISSUES:

1. **The 4-M method ignores two over-riding considerations at KSC, namely SAFETY and OBSOLESCENCE.**

There is no factor to assess the severity of the consequences of potential mishaps caused by the existing equipment or facilities in terms of injury to personnel, or damage to the orbiter or the payloads. Nor is there a factor to assess the obsolescence and lack of supportability of the existing equipment or facilities. Thus, in addition to the ESR scores, the GSWT Steering Committee has to consider these factors. Since at KSC, safety is indeed our Number 1 concern, it is natural that we give a high priority to safety related ESRs regardless of their 4-M scores. The "category" and "old category" information in Table 1 confirms this. ESRs that had an Old Category 1, and those with 2-s designation seem to be at the top of the list of 17 regardless of their costs, ESR scores, or payback periods.

2. **The 4-M method actually focuses on two primary factors:**
 - (a) **Expected annual impact on flow schedule, and**
 - (b) **Payback period.**

Note that three of the four factors in the 4-M method, namely

- i. Frequency of Operation
- ii. Processing Impact/ Improvement
- iii. Likelihood of Occurrence

when multiplied together, basically give us a score for the **expected annual impact on flow schedule.**

The **payback period** is calculated separately in the Cost Assessment Worksheet.

3. **A multiplicative model is inappropriate for the 4-M method.**

In theory, if **all incremental costs, risks, and benefits can be identified, measured, and valued in dollar terms, the calculated *Payback* period should be the sole criterion for rank-ordering ESRs. The shorter the *Payback*, the more desirable the ESR.**

However, often it is difficult, if not impossible, to measure and value in dollar terms factors such as *Safety Improvement, Obsolescence Reduction, and Avoidance of Schedule Delays*. In that case, it makes sense to use a **factor scoring and weighting method**. But the scores on such factors should not be multiplied with each other or with the score on *Payback*. What we need is a weighted average of the scores. The weights have to be carefully chosen to reflect the values of the organization. A method called the **Analytical Hierarchy Process (AHP)** is most helpful in the development of proper weights, and KSC should explore its application.

4. **The design of the rating categories and score ranges is inappropriate.**

4-M's multiplicative approach is particularly inappropriate since, by design, the score for *Expected Schedule Impact* can range from 1 to 100 while the score for *Payback* can range only from 1 to 5. Thus, 4-M is biased towards minimizing the importance of *Payback*. This bias is further accentuated by the fact that all ESRs providing a longer than 2-year payback (including those that may never payback) receive a rating of 1, while ESRs providing a payback within 3 months receive a rating of only 5. I believe this is totally inappropriate.

The way I see it, provided the payback calculations are reasonably valid and accurate, all ESRs promising a payback within one year deserve to be immediately funded. That will have more money (or other resources) at the end of the year than we had at the beginning, and those increased resources would be available for the pursuit of our other goals such as increased safety. Even ESRs promising a payback within 4 years are highly desirable. They represent better than 20% per year compounded rate of return. On the other hand ESRs that take longer than 5 years to payback should be considered undesirable unless they promise significant improvements on one or more of the non-quantifiable dimensions of safety, obsolescence, or schedule.

Thus, I believe that 4-M's design of the rating categories as well as possible range of scores for the *Payback* factor are inappropriate.

An important attribute of properly designed rating categories is that they are **mutually exclusive** (i.e., non-overlapping) and **collectively exhaustive** (i.e., no possibility should be left out). Unfortunately, in 4-M we see **both** of these attributes **violated**:

- The critical path (i.e., serial flow) nature of an operation seems to be **double-counted**, once in the *Frequency of Operation* factor, and again in the *Processing Impact/Improvement* factor.
- The categories in the *Likelihood of Occurrence* factor provide **no room for the rating** of a mishap that is expected to happen no earlier than 18 months and no later than 24 months. Thus, the categories here are **not collectively exhaustive**.
- Given that we have already accounted for the frequency of an operation, the likelihood of occurrence factor should refer to likelihood *per operation*, rather than likelihood *per year*. This is a second example of **double-counting** certain factors.

5. **The absence of relevant probability considerations on the Cost Assessment Worksheet is inappropriate.**

Many ESRs are designed to avoid potential mishaps likely to be caused by existing equipment or facilities, and hence will contribute their estimated savings in "annual corrective manhours and materials" only with the probability of occurrence of the mishap.

The expected savings are the product of this probability times the estimated savings. Yet, the Cost Assessment Worksheet does not require an estimation of the relevant probability. Consequently, the computation implicitly assumes that the mishap would occur with certainty. The net result is that typically, 4-M's Cost Assessment Worksheet underestimates the payback period. (For an example, see comments on *k15836* in Appendix B).

6. The language is ambiguous, and instructions / explanations are lacking.

One well-known short-coming of cost-benefit analysis is that it can easily become *an instrument of intentional or unintentional biases* introduced by the champions and advocates of specific projects. Therefore, in designing a cost-benefit assessment method, one has to be extra careful and try to minimize opportunities for the introduction of such biases, and convenient misinterpretations of the words and phrases chosen. Unfortunately, 4-M is fertile with many opportunities for the introduction of such biases:

- One factor is defined simply as "*Processing Impact / Improvement*," without any further instruction. The designers of 4-M assume that there will never be an ESR that will actually negatively impact the flow schedule. But the fact is, in some cases for the sake of safety, we may introduce new procedures that could actually delay a shuttle's serial flow. For such an ESR, the designers of 4-M would like to see that the lowest rating of 1 is used. However, the lead engineer who knows that the concerned operation is a serial one, refuses to use a 1 or a 2. Indeed, one cannot blame a lead engineer whose ESR introduces a 24-hour serial delay if he/she chose to rate the ESR as a "5."
- 4-M asks that an operation's frequency be rated either as a "5 Multiple times per flow / month," or as a "4 Once per flow / month." Given the ambiguity in the phrase "per flow / month," we just cannot blame a champion, whose ESR truly deserves a "4," if he/she rates it a "5." After all, if the operation is once a month, then it is clearly multiple times per flow since a flow lasts for several months. If the operation is once per flow, given the overlapping nature of several shuttle flows, in many months in a year the operation may be done multiple times a month!
- The designers of 4-M use the phrase "likelihood of occurrence" to refer to the "*probability that a mishap or 'problem condition' would occur unless an ESR was implemented*". Yet, several lead engineers I have talked to assume it to mean the "*probability that the operation will be done within the next so many flows*." (See comments on *k15813* in Appendix B).
- Among those who realize that "likelihood of occurrence" referred to the probability of a mishap, many say that faced with the choice between rating their ESR a "3 Could happen within next 4 flows / 6 months" or a "2 Could happen within next 8 flows / 12 months," they invariably choose a "3" rather than a "2." As one lead engineer puts it,

PROCESS ISSUES:

1. KSC culture is not cost-conscious.

The greatest single barrier to the implementation of any method of cost-effectiveness analysis at KSC is KSC's culture which is **almost oblivious to any cost concerns, let alone cost-effectiveness concerns**. In the GSWT process this lack of cost-consciousness is evident in many ways:

- As Table 1 and my Appendix B comments on *k14453* show, **the GSWT process does not distinguish between a \$4K ESR and a \$4M ESR**.
- Note from Table 1 that the steering committee has included *k15825* in its list of Top 17 ESRs **even though there is no rough order of magnitude (ROM) estimate** of its cost. In other words, the ESR could cost anywhere between a few thousand to a few million dollars, and it would still be Priority #10 on the list.
- At the Thursday morning meetings of the steering committee, often a report is given on the status of ESRs approved in prior years. While that report includes information on which ESRs are complete, which ones are behind schedule and by how much, etc., **there is no information on the original cost estimates and actual expenditures** on the various ESRs. In fact, I am told that the way our accounting system is set up, it just cannot track and monitor ESR by ESR expenses.
- At the June 28, 1994 meeting to review TV's FY 95 priority list, **management did not raise any questions about costs, paybacks, or the 4-M scores of any of the ESRs**. The steering committee also did not make any attempt to defend its priority list using any one of these cost-related considerations.

Given this culture, **most engineers do not take ESR cost estimates seriously**. Even those who are charged with arriving at the estimates freely admit that their **estimates could be wrong by 50-60%**. Others put the expected margins of errors to be as high as 80-100%! Given that, for many ESRs, benefits are inherently more difficult to quantify and measure, sometimes we even see instances of carelessly exaggerated claims. (See Appendix B comments on *k11794*). Others see no need to even attempt to quantify the benefits of their ESRs, or report any 4-M scores. They know very well that as long as their ESR can claim to be a "mission-stopper," it will be funded regardless of costs. Some team members speculated that the 4-M method **creates the paperwork necessary to pretend to Washington DC that we are cost-conscious**.

Thus, I was not surprised that many teams had not read 4-M instructions carefully, and made such elementary mistakes as addition in place of multiplication, or reporting payback in years as payback in months (See Appendix B comments on *k15040*).

2. Organizational separation of the prioritization, funding, and implementation processes is not conducive to the pursuit of cost-effectiveness.

The second most important reason why any method of cost-effectiveness analysis would be very difficult to implement in the GSWT process is the organizational separation of the process that does the prioritization from the process that provides the funding, which in turn, is separated from the process that ensures actual implementation of an ESR. While GSWT teams and steering committee are asked to prioritize the ESRs, they have no authority to actually fund or implement any ESR. **The consequences of this separation are:**

- **It perpetuates the culture of a lack of cost-consciousness**, and GSWT teams and steering committee are likely to continue to focus exclusively on technical merit and ignore all cost considerations.
- **It causes considerable frustration for the teams and the steering committee** insofar as the funding mechanism can override the priorities set by the GSWT integration process, and the implementation mechanism (i.e., Design Engineering [DE] and Shop Floor [SF]) can easily re-arrange those priorities by allocating or not allocating the necessary manpower to specific ESRs. Furthermore, even if the steering committee wants to use cost-effectiveness as an important criterion, given that our long standing culture is so deeply ingrained throughout KSC, DE and/or SF may continue to use technical merit as the sole criterion in deciding which ESRs to work first, if at all.
- Both, the total manpower spent, and the calendar time needed, for all this prioritization, funding, and implementation is inordinately high. In other words, **the bureaucracy is perpetuated.**

3. The culture of integration is not conducive to the analysis and confrontation necessary in a rational prioritization among competing investment alternatives.

At KSC, the ESR prioritization process is called "GSWT integration process," and it is left to a committee consisting of representatives of several GSWT teams (i.e., a committee of peers). This is consistent with KSC's long standing tradition of decision-making by consensus developing teams. The GSWT integration process should help ensure that one team's ESR does not interfere with the functioning of other team's systems. However, it may not be the most productive process for prioritization among competing demands on limited resources. Appendix B clearly shows that for a rational prioritization of ESRs, we need considerable analysis and confrontation.

As members of "an integration process," individuals on the steering committee are inclined to respect the expertise and trust the integrity and judgment of individual teams. For example, from Attachment A-1, page 2, note that a team's internal priorities of its ESRs

are not to be questioned by the steering committee. Yet, as is clear from Appendix B, these teams have no expertise in cost-benefit estimation. Consequently, a team's cost-benefit estimates may be way off the mark, and its internal priorities may be based on such erroneous estimates. On the other hand, GSWT teams do have substantial vested interests in making their ESR look as attractive as possible. Consequently, a team may be misrepresenting the true benefits (see Appendix B comments on *k15040*), or overestimating the magnitude of those benefits (see Appendix B comments on *k15813*, *k11794*, and *k15836*).

4. The need for a properly trained and impartial analyst to assist the steering committee.

Of course, even if we renamed the GSWT Steering Committee as "ESR Prioritization Committee," we will not get the necessary degree of analysis and confrontation from this committee, for several reasons:

- First, most members of the committee do not have the necessary background or training to do the kind of analysis I have done.
- Second, given that
 - a) serving on the steering committee is only one tenth of one's job, and
 - b) the number of ESRs to consider is very large
(48 were considered in prioritizing the TV list),
 no one has the time to check the claims, the assumptions, and the computational accuracy of each one of the ESRs.
- Third, in a structured team, members of the team could be assigned to check out specific ESRs, ensuring that each ESR is checked by one or more team members. In a committee of peers, such a division of labor is very difficult.
- Finally, a committee of peers thrives on the collegiality of its members. Such a committee hates confrontational members, and no individual is likely to volunteer to be a confrontational member.

Thus, if the GSWT steering committee truly wants to use cost-effectiveness as a criterion in its prioritization of ESRs, it must seek assistance from a **properly trained, impartial analyst who is charged to be confrontational about every ESR**, its logic, cost-benefit estimates, computational accuracy, etc.

“Almost anything that could happen over the next 12 months, could also happen over the next 6 months, except perhaps an increase in my salary.”

- Although the instructions are to *multiply* the scores on the four matrices to obtain the total score, the use of *the word “total” seems to have led some teams to add* the scores on the four matrices. (See comments on *k15813* in Appendix B).
7. **The presumption of being able to create a single method to fit all ESRs is unrealistic.**

When we force different discipline engineers to all use particular forms, and a given set of cost categories, we soon discover that our method does not quite fit all the systems we are trying to evaluate. There are many tell-tale signs that the 4-M method does not fit all ESRs.

- 7 (15%) of the top 48 ESRs for FY95 were submitted without an attempt to fill out either of the two forms of the 4-M method.
- 6 (13%) more filled out the ESR score form, but not the Cost Assessment Worksheet.
- Regardless, 3 of these “defiant” 13 wound up on the Steering Committee’s list of the top 17 ESRs.
- Those who did fill in the forms, often had to modify the cost assessment worksheet to report the some of the unique costs or benefits of their system.
- For more specific examples of the inapplicability of 4-M method, see Appendix B.

The variety of technical disciplines the ESRs originate in, the diversity of benefits they seek, the variety of risks they reduce, the many different types of costs they impose, together suggest that to evaluate and rank-order these ESRs, **what we need is a methodology, and not a method.** A methodology allows for the use of several different methods of analysis depending on the nature of the technical system, the type of modification sought, and the relevant costs and benefits. Thus, despite the shortcomings of the 4-M method, we must not abandon the pursuit of cost-benefit analysis, or return to the arbitrary decision making of the past. Instead, **we must evolve towards the adoption of a methodology such as Costs, Risks, and Values Evaluation (CRAVE).**

GSWT INTEGRATION PROCESS

0 GROUND RULES

0 ONLY CATEGORY 2, 2E, OR 2S ESR'S ARE CONSIDERED

0 TECHNICAL MERIT IS THE ONLY CRITERIA USED TO EVALUATE ESR'S THROUGHOUT THE INTEGRATION PROCESS

0 THE INTEGRATION PROCESS STARTS WITH THE TEAM LIST.

0 THE GSWT TEAM CONSISTING OF A NASA & LSOC SE AND AN SDE FROM GSDE PRIORITIZE THE ESR'S WITHIN THEIR SYSTEM BY TECHNICAL MERIT AND FISCAL YEAR.

0 THE NEXT LEVEL OF INTEGRATION (CALLED THE TV LIST) OCCURS ONCE A YEAR .

0 THE GSWT STEERING COMMITTEE (S/C) REPRESENTATIVES FROM TV, 17-01, AND 15-01 TAKE THE TEAM LISTS FROM THEIR RESPECTIVE ORGANIZATIONS AND INTEGRATE THESE ESR'S INTO A SINGLE LIST.

293

8-19-93

1

 **Lockheed**
Space Operations Company

ATTACHMENT A-1

26

GSWT INTEGRATION PROCESS

- 0 THE PROCESS WORKS AS FOLLOWS;
- 0 THE #1 PRIORITY ESR FROM EACH TEAM'S LIST ARE LAID ON THE TABLE. THIS IS A TOTAL OF 22 ESR'S.
- 0 THE ESR'S ARE GROUPED BY P-CUT AN INDEX ASSIGNED TO THE ESR BY THE GSWT TEAM. IT INDICATES THE SEVERITY OF THE IMPACT OF **NOT** DOING THE REQUESTED MODIFICATION.
- 0 USING THE P-CUT, THEIR UNDERSTANDING OF THE PROBLEM CONDITION AND THEIR EXPERIENCE AS A GUIDE, THE THREE S/C REP'S SELECT WHAT THEY CONSIDER TO BE THE MOST IMPORTANT ESR FROM THE ITEMS ON THE TABLE.
- 0 THE #2 PRIORITY FROM THAT TEAM (WHOSE ESR WAS SELECTED AS MOST IMPORTANT) IS THEN BROUGHT UP ON THE TABLE AND COMPETES AGAINST THE OTHER 21 ESR ALREADY ON THE TABLE.
- 0 THIS PROCESS CONTINUES UNTIL A SET NUMBER OF ITEMS HAVE BEEN SELECTED. THIS IS THE TV LIST.

294

GSWT INTEGRATION PROCESS

- 0 THE TV LIST IS THEN SUBMITTED TO THE ENGINEERING DIRECTORS FROM 17-01 AND 15-01, THE LSOC CHIEF ENGINEER, THE TV ENGINEERING DIRECTOR, AND ALL TV DIVISION CHIEFS.

- 0 A MEETING IS CONVENED TO ALLOW REDLINES TO THE LIST TO BE DISCUSSED AND INCORPORATED.

- 0 DURING THIS TIME, THE SUPPORT OPS AND TE ORGANIZATIONS ARE PERFORMING THE SAME INTEGRATION FOR ESR'S FROM THEIR TEAMS USING A SIMILAR PROCESS. THEIR EFFORT COMPILES THE TE LIST.

- 0 THE LAST STEP IN THE INTEGRATION IS PERFORMED BY THE GSWT S/C INTEGRATION TEAM AND RESULTS IN THE FYXX GSWT INTEGRATED PRIORITY LIST.

- 0 THIS TEAM CONSISTS OF THE S/C REPRESENTATIVES FROM TV, TE, 30-0, AND 17-01 (ALSO REPRESENTING 15-01). THE S/C CHAIRMAN ATTENDS AND ACTS AS A TIE BREAKER IF REQUIRED.

295

GSWT INTEGRATION PROCESS

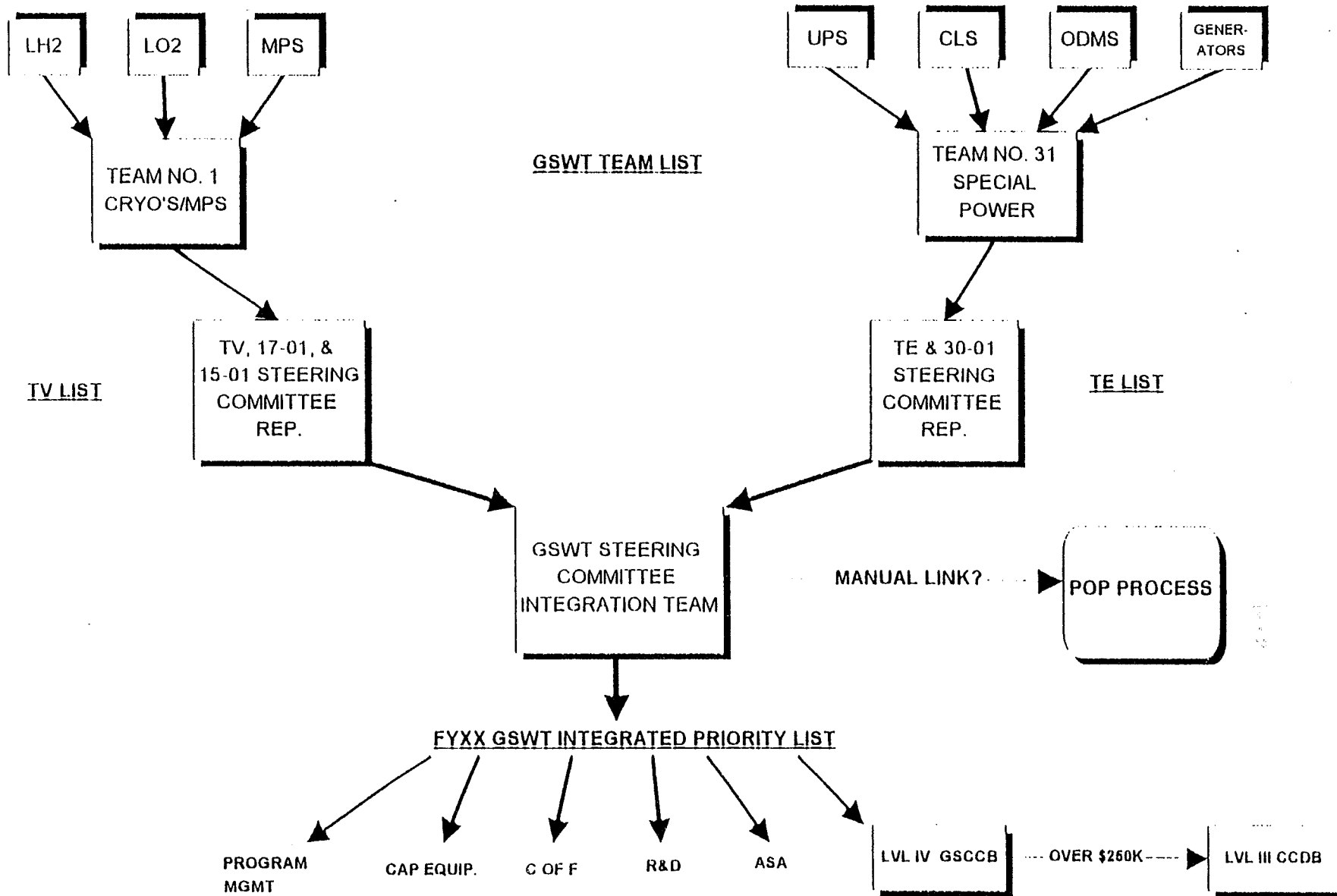
- 0 THE TV AND TE LISTS ARE USED AT THIS LEVEL AND THE INTEGRATION PROCESS IS THE SAME AS EARILER EXCEPT THERE ARE ONLY 2 ESR'S ON THE TABLE AT ANY GIVEN TIME.
- 0 THE NUMBER OF ITEMS TO COMPRISE THE LIST IS DETERMINED BY THE TEAM AT THE START OF THE PROCESS AND THE INTEGRATION CONTINUES UNTIL THIS NUMBER IS REACHED.
- 0 WHEN THE PROCESS IS COMPLETE THE LIST IS DISTRIBUTED BY THE STEERING COMMITTEE CHAIRMAN.

296

8-19-93

4

GSWT INTEGRATION PROCESS



GSWT TEAM LIST

TV LIST

TE LIST

MANUAL LINK?

POP PROCESS

FYXX GSWT INTEGRATED PRIORITY LIST

PROGRAM MGMT

CAP EQUIP.

C OF F

R&D

ASA

LVL IV GSCCB

OVER \$260K

LVL III CCDB

GSWT STEERING COMMITTEE - PRIORITY DEFINITIONS

REQUIRED ITEMS THAT ARE:

- P1-1 - Requirements dictated by drawing, specification, or directive to support a specific mission effectivity
- P1-2 - Modifications required to support a specific flight system/payload requirement dictated by drawing, specification, or directive
- P1-3 - Modifications which prevent potential loss of life, severe injury, or significant damage to flight hardware where no procedural or operational workarounds exist
- P1-4 - Modifications which prevent significant (> 8 hrs) processing impact

REQUIRED ITEMS THAT:

- P2-1 - Meet upgraded design requirements (with hazardous implications)
- P2-2 - Correct design deficiencies in primary system (with hazardous implications)

REQUIRED ITEMS THAT:

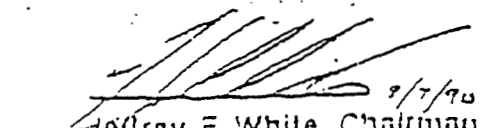
- P3-1 - P1 or P2 item where workaround is possible
- P3-2 - Correct design deficiencies in backup systems
- P3-3 - Meet upgraded requirements
- P3-4 - Correct design or documentation inconsistencies
- P3-5 - Reduce the potential of injury to personnel or potential damage to flight hardware where a procedural or operational workaround exists.

DESIRABLE ITEMS THAT ARE NEEDED TO:

- P4-1 - Prevent obsolescence-caused problems
- P4-2 - Enhance operations with short-term payback (less than 1 year)
- P4-3 - Improve processing operations to reduce schedule risk.

DESIRABLE ITEMS WITH NO QUANTIFIABLE EFFECT ON PROCESSING BUT WILL:

- P5-1 - Create improved practices or efficiencies
- P5-2 - Enhance processing with long-term payback (more than 1 year)
- P5-3 - Upgrade systems to align with current Government regulations.


 Dorrroy F. White, Chairman
 -GSWT Steering Committee

ORIGINAL PAGE IS
 OF POOR QUALITY

ATTACHMENT A-3

LOCKHEED SPACE OPERATIONS COMPANY
INTERDEPARTMENTAL COMMUNICATION

DATE: March 29, 1994
CONTROL NUMBER: 3201-94-049

TO:	Distribution	DEPT. NO.	BLDG. NO.	MAIL CODE	
FROM:	J. F. White	DEPT. NO. 32-01	BLDG. NO. LST-2	MAIL CODE LSO-042	PHONE 383-2200 Ext. 2759
SUBJECT:	REPLACEMENT OF THE P-CUT DURING ESR PRIORITIZATION				

Currently a P-CUT is assigned to each ESR as it is entered in CMDS. The P-CUT is useful to the Steering Committee Integration Team during the yearly prioritization process, but has not been helpful to the GSWT's in prioritizing the ESRs on their individual team lists.

The GSWT Steering Committee is introducing a new methodology to use in determining the priority of ESRs within the GSWT system that will replace the P-CUT. This new system called "the 4-matrix method" is simpler and more straight forward and should benefit your GSWT in evaluating where an ESR should fit on your respective team lists. A copy of the method is attached and a brief description of each major matrix follows:

Frequency of Operation:

Each ESR has a problem condition or event that is described in Block 16 of the ESR form. This problem condition is normally the result of the performance of some operation such as a particular sequence of an OMI or WAC. This matrix correlates the number of times this operation occurs per flow or month to a numerical value. The more frequent the occurrence the higher the value.

Processing Impact/Improvement:

This matrix equates the Block 16 problem to a Vehicle processing impact. This impact should be a direct result of the problem condition, a "single point failure" scenario rather than relying on a series of failures to cause a worst case situation.

Likelihood of Occurrence:

This matrix concerns the probability of the problem condition or event occurring within a given time frame. A higher potential of occurrence is assigned a higher value in the matrix.

ORIGINAL PAGE IS
OF POOR QUALITY

TO: Distribution

- 2 -

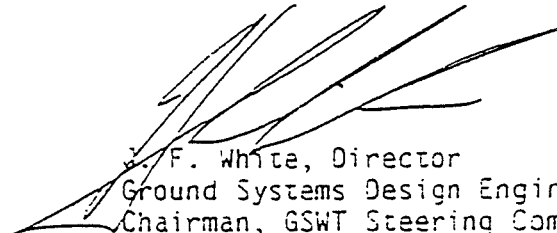
3201-94-049

Cost Assessment:

The first step in performing this matrix is to fill out the ESR Evaluation-Cost impact sheet. This data is similar to the ROM data that has been required in the past. When the sheet is complete, you will have calculated the months to pay back required to perform the "Cost Assessment" matrix. On the "Cost Assessment" matrix, select the appropriate pay back period and numerical value associated with the pay back period.

Multiply the numerical values obtained from the four matrices together to obtain a score for the ESR under evaluation. This score, when compared to the scores on other ESRs on your list, should help you understand where this ESR should be prioritized.

Please implement this system immediately. Beginning with the upcoming FY95 Integrated Priority Process starting in April of this year, at least the top three priorities on your team list need to have been evaluated and selected using the 4-matrix method. (Retain the work sheets for these three ESRs to provide background data to support your priority). This process is to be used on all new ESRs. Use the attached sheets to perform this evaluation. Update the CMDS P-CUT field for these first three with the numerical score obtained from the matrices. In the summer, the GSWT data fields in CMDS will be revised to allow you to input this information directly into CMDS. Also, SP! BM-310 (2)K is in the process of being revised to reflect this change. In the interim, make the changes to your team list using the attached information. If you have any questions, contact your GSWT Steering Committee Representative.



J. F. White, Director
Ground Systems Design Engineering
Chairman, GSWT Steering Committee

JFW:lm

Attachments: A/S

ORIGINAL PAGE IS
OF POOR QUALITY

ESR ASSESSMENT CRITERIA

SCORE

FREQUENCY OF OPERATION

- 5 Multiple Times Per Flow/Month
- 4 Once Per Flow/Month - Critical Path
- 3 Once Per Flow/Month - Non Critical Path
- 2 1-5/OMDP/2 Years
- 1 Contingency Operation Only

PROCESSING IMPACT/IMPROVEMENT

- 5 More Than 24 Hour Serial Flow Time
- 4 More Than 8 Less Than 24 Hour Serial Flow Time
- 3 Less Than 8 Hour Serial Flow Time
- 2 More Than 24 Hour Parallel Flow Time
- 1 Less Than 24 Hour Parallel Flow Time

LIKELIHOOD OF OCCURRENCE

- 4 Expected To Happen Within The Next Flow/Month
- 3 Could Happen Within The Next Flows/6 Months
- 2 Could Happen Within Next 12 Flows/18 Months
- 1 Not Expected To Happen In The Next 16 Flows/2 Years

COST ASSESSMENT (SCORE FROM REVERSE SIDE)

- 5 Payback Within 3 Months
- 4 Payback Between 3 and 6 Months
- 3 Payback Between 6 and 12 Months
- 2 Payback Between 1 and 2 Years
- 1 Payback Longer Than 2 Years

TOTAL

Determine the appropriate classification of the ESR within each category. Multiply the score of each category together to determine the ESR rating. The rating will be compared with other ESR's to prioritize next year's modification budget. The ratings will be independently verified during the GSWT Integration Process.

ORIGINAL PAGE #
OF POOR QUALITY

COST ASSESSMENT WORKSHEET

COST OF PROPOSAL: (ROM)

Engineering _____ M.H. @ \$40.00 \$ _____
 Material _____ \$ _____
 Labor _____ M.H. @ \$40.00 \$ _____
 FPC _____ \$ _____

 TOTAL COST \$ _____ (A)

****BENEFIT OF PROPOSAL***

OPERATIONAL SAVINGS: (ANNUAL)

(_____ M.H. (Old Way) - _____ M.H. (New Way) X \$40.00 = \$ _____
 (_____ Consumables (Old) - \$_____ Consumables (New) = \$ _____
 (\$_____ Energy (Old) - \$_____ Energy (New) = \$ _____

 TOTAL _____ (B)

MAINTENANCE SAVINGS: (ANNUAL)

(P.M. M.H.s/Yr (Old) _____ - P.M. M.H.s/Yr (New) X \$40.00 = \$ _____
 (P.M. Mat'l (Old) _____ - P.M. Mat'l (New) _____) = \$ _____
 Corrective M.H. (Old) _____ - Corrective M.H. (New) _____ X \$40.00 = \$ _____
 (Corrective Mat'l (Old) _____ - Correctible Mat'l (New) _____) = \$ _____

 TOTAL _____ (C)

OTHER SAVINGS (ANNUAL) \$ _____ (D)

PAYBACK:

$$P = \frac{A}{B + C + D} \times 12 = \text{_____ Months To Payback}$$

If savings are negative for any factor, add total algebraically.

To be used with ESR Assessment Matrix

**Comments on Selected ESRs from the
Costs, Risks, and Values Evaluation (CRAVE) Perspective**

by
Praf Joglekar

Costs, Risks, and Values Evaluation (CRAVE) is a methodology. That is, it is a way of thinking — armed with certain fundamental principles and concepts — and a way of analyzing available decision alternatives using situationally appropriate techniques and tools from a large body of methods consistent with the fundamental principles and concepts. A methodology focuses on both the techniques and the processes used in relevant decision-making.

Consequently, the first step in applying CRAVE to the problem of ESR rank-ordering is to understand the complexity, diversity, and situational specificity of the ESRs in terms of

- a) the magnitudes of costs, risks, and benefits involved,
- b) the degree to which these magnitudes could be quantitatively measured,
- c) the degree to which related decisions affect an ESR's costs and benefits,
- d) the degree to which sub-decision elements (such as the timing of implementation or availability of quantity discounts) affect the pertinent costs and benefits, and
- e) any other critical elements.

Only when we understand this complexity and diversity can we create a suitable adaptation of the CRAVE methodology to ESR prioritization. Towards that end, I studied several ESRs in terms of the modifications they were proposing, their estimated costs, risks, benefits, ESR scores, payback periods, etc. I talked to several lead engineers, ESR champions, steering committee members, accounting professionals, and third parties familiar with specific ESRs and/or familiar with the GSWT process.

The following comments reflect my informed assessments of the selected ESRs, as well as my observations about the ESR prioritization process. Some readers may find these comments too cryptic, but of necessity, I have assumed that readers are reasonably familiar with the selected ESRs and their respective 4-M assessments.

*K14453. "New Hydraulic Pump Units"***1. An ESR that does not belong.**

In terms of costs, this ESR stands out as the most important one to analyze carefully. Insofar as its estimated costs (\$3.8M for Option A and \$2.8M for Option A1) exceed the combined costs of all 16 remaining ESRs on TV's FY95 priority list (See Figure 4), it is unfair and irrational to treat this as just another ESR to be rank-ordered as Priority 1, or 4 (as the Steering Committee did), or 17. Thus, in my opinion this ESR does not belong to the GSWT prioritization process. If a comparison with other ESRs must be done, the appropriate question would be whether or not the benefits of this ESR exceed the sum total of the benefits of all remaining ESRs. But such a comparison would be similar to asking whether the value of buying a house exceeds the value of feeding and clothing ourselves for several years. With that kind of a comparison, we would never buy a house!

In our personal lives, although some sacrifices in the amounts we spend on food and clothing are necessary to buy a house, through devices such as a mortgage, we manage to buy a house without starving. Similarly, organizations must find ways to spend on capital equipment without jeopardizing their short-term survival. The best way to do that is to set aside two separate funds for capital expenditures and operational expenditures, and to avoid any comparison of a project in the capital expenditure category with projects in the operational expenditure category.

At KSC, we do have different funds and funding mechanisms to take care of capital versus operational items. Unfortunately, in the GSWT prioritization process, we have not stopped comparing capital ESRs with operational ESRs.

2. Let them fight with their equals.

If at all, I would have compared this ESR with others costing \$1M or more.

3. Widely different cost estimates.

As I dug deeper into this ESR, I came across several different cost estimates ranging from \$1.8M to 3.8M without much explanation for why the estimates were so widely different. I was told not to be surprised if it ends up costing \$5M by the time it is actually implemented. More importantly, it seems that with the accounting system at KSC, even in retrospect, we may never find out how much an ESR really costs. The most disturbing thing for me is the fact that the GSWT Steering Committee concerns itself neither with the magnitude of the cost estimates nor with the reliability of those estimates. Finally, I am disturbed to note that KSC culture is so oblivious to cost consideration.

4. **If I were King:**

If I were King, considering that

- a) this ESR offers a payback from its quantified benefits (from savings in reduced PRs and reduced O&M expenses) within six to eight years,
- b) additionally, it offers intangible benefits such as avoidance of flight-critical delays, reduction of noise, and reduction of electric shock hazard, that have not been quantified,
- c) the current equipment is 17 years old and it must be replaced within the next two or three years, and
- d) proper timing (coordinated with the construction of Fluid Support Stations in the two OPF bays) is very important in the case of this ESR, and can save as much as \$1M,

I would have approved this ESR for FY94. Perhaps it is still not too late.

K15040. PGHM Anti-Free Wheel Mod

1. **Disguised motivation.**

It seems that the GSWT team's real motivation is to modernize and automate PGHM operations — a very desirable goal. However, knowing the KSC culture of approving primarily (perhaps only) safety related ESRs, the champions of this ESR have framed its justification in terms of avoiding potential damage to cryogenic or hypergolic payloads. The fact is that given the precautions we take and the manpower we allocate to PGHM operations, the likelihood of Z wheel operations causing any major damage to payload is one in several thousand.

2. **Inconsistent cost and payback estimates.**

Although an October 1993 study estimates the cost of this ESR to be \$49K, the ESR score calculations are based on a cost of \$108K. No one on the GSWT Steering Committee is charged specifically with the responsibility to identify and correct such inconsistencies. Indeed, the steering committee does not know how much expenditure it is authorizing by putting an ESR on its priority list.

Similarly, the GSWT team seems to have made a mistake in reporting that this ESRs payback as *11.6 months when they meant 11.6 years!* Once again, the mistake went undetected by the steering committee.

3. **Bite the bullet or forget it!**

I am not an engineer, but it seems to me that if we are going to spend \$108K, we ought to attain a much greater degree of automation than replacing a ball and screw mechanism with a machine screw!

K15813. EPDM Cover Installation Tool

1. The steering committee does catch some mistakes.

Instead of *multiplying*, the GSWT team had *added* the scores on the four matrices. The steering committee corrected that mistake. The steering committee also seems to have challenged the team's claim of a rating of 4 on the Processing Impact factor and corrected it to a rating of 2.

2. Likelihood factor incorrectly rated.

On the other hand, the steering committee seems to have missed the fact that the GSWT team interpreted this factor to mean "likelihood that the operation will be performed" rather than "likelihood that a mishap or problem condition would occur."

3. Operational savings overestimated.

A reality check suggests that the estimated saving of eight man-hours per EPDM cover installation exceeds the actual man-hours currently required for this operation! A payback period of four years may be more accurate. Of course, that is sufficient considering the reduction in the risk of damaging the covers — a benefit not quantified in the payback calculation.

K153991. Main Door Windlocks Pin Insertion

1. Isn't there a cheaper way?

While it makes sense to avoid a broomstick approach (particularly in the Space Program), certainly the replacement should not cost \$28K.

2. Look for economies of scale.

This ESR highlights the need to make certain changes in Pad A and Pad B configurations simultaneously rather than one at a time. Had we done that, the incremental cost of the device for Pad A could have been of the order of \$5K rather than \$28K.

K11794. An Additional Winch to Recover from ESP/IECP Platform Tilt

1. Counting benefits that are impossible to obtain through the proposed ESR.

This ESR estimates the payback period for its investment to be .067 months (or two days)! To me this ESR represents the case of a carelessly exaggerated claims. An assumption

underlying this claim is that by recovering from a tilt of the ESP/ECP platform we will save the cost of an SSME (\$60M). The fact is, the damage due to the tilt would be already done and straightening out the platform will not in itself save the SSME. We will have to undertake all the necessary repairs, and tests as well. If having an additional winch would prevent a potential tilt, then we could count the avoided damage times the probability that the damage would occur in the absence of the new winch as a saving due to this ESR.

Another implied assumption in this payback calculation is that a ESP/ECP platform tilt will occur with certainty. Although with aging winches, the probability of a tilt occurring is increasing, I would say that it is still of the order of one in a hundred.

Yes, we need to refurbish our aging winches, but this is hardly a rational way of justifying that. I am most surprised that the steering committee did not challenge these payback calculations.

2. Inadequacy of the cost assessment worksheet

It is clear that 4-M's design of the Cost Assessment Worksheet cannot accommodate the capture of all relevant risk and benefits associated with this ESR.

3. Why insist on an exact duplicate of existing winches?

I am told that for the \$340K cost of this ESR, instead of buying one winch that duplicates existing winches in form and function, one could easily buy four commercial off-the-shelf (COTS) winches that incorporate better technology and avoids single point failures.

Such a purchase of four new winches would allow us

- a) to use them together for the safest hoisting of crucial loads, and
- b) to disassemble, inspect, and refurbish at least ten of the existing twelve winches, with parts to spare from the other two.

4. The option generating nature of CRAVE.

The suggestion in Comment 3 above shows that the CRAVE methodology not only helps in the assessment of a given ESR, it has the potential to generate better options.

K15783. KU-Band DEMOD Replacement.

1. Internal inconsistency.

On the one hand, this ESR claims a processing improvement of more than 24 hours of serial flow time. On the other hand, it says that there will be no monetary payback. This seems inconsistent. Surely there must be a quantifiable lower bound on the value of a 24-hour serial flow improvement.

2. The importance of establishing upper and lower bounds on the values of certain types of benefits.

It seems important that a trained cost-benefit analyst should establish upper and lower bounds for the value of the various categories in the Processing Impact/Improvement factor. This is a very doable task, and it should help us in more rigorous and quantitative assessments of many ESRs.

3. Work around possible.

As it turns out, this ESR will not contribute to an improvement of 24 hours of serial flow time. This is because when the DEMOD does not work, we do have a way to communicate between firing room and OPF. The trouble is that communication involves routing through JSC and satellite, etc. Commercially, such a communication could cost as much as \$100 per minute. Luckily, NASA does not have to pay anybody for this communication. However, we may be impeding or slowing down other vital communication that truly needs the satellite system. Considering all these factors and the fact its estimated cost is \$305K, I found this ESR to be the most difficult one to decide on.

K15505. Additional HPD Platforms

1. We must develop a simpler and speedier low cost mod (LCM) process.

This is one of the least costly (\$4K) of the ESRs I studied. It seems unfair to burden such low cost proposals with the same degree of rigor of assessment and rank-ordering as ESRs costing ten or a hundred times its cost.

2. Estimate minimum benefits in quantitative terms.

Although this ESR made no attempt to calculate its payback period, it would have been easy to obtain a lower bound on the benefits and an upper bound on that payback. Given that two injuries have occurred during the last two years, the average cost of these injuries can be seen as the minimum savings brought by this ESR. Of course, one of my presumptions is that we have reasonable records from Personnel Department to be able to estimate the costs of those injuries.

3. If I must rank-order the sample of ESRs I have studied:

Considering the facts that

- a) we have already spent the money for the design of the platforms,
- b) the incremental costs of the remaining work are so small, and

c) it will avoid the types of injuries to workers that have occurred twice during the last two years, this ESR would be my Priority #1.

4. Why re-evaluate?

What I do not understand is why this ESR is being re-evaluated at this stage. The original version of this ESR calling for the design and implementation was estimated to cost \$35K, and we have already done the design work. I would have assumed that implementation of that design would not be a new decision point!

15836. Replace Diver Operated Plug (DOP) s/n 4

1. Reasonably quantifiable costs, risks, and benefits.

This a good example of ESRs whose costs, risks, and benefits are reasonably quantifiable. The use of the 4-M ESR score in such cases would be **totally inappropriate**. The sole criterion for rank-ordering among these ESRs should be the payback period—the shorter the better.

2. Benefits overestimated.

This ESR claims a payback in seven months by estimating an annual saving of \$103K when the cost of a new DOP is only \$58K. Based on available information, I would re-estimate the benefits as below:

The last time DOP s/n 4 failed was two years back. So let us assume that its probability of failure in a year is 0.5. In the event of a failure, we would spend

One day of sea labor	\$7,700
One day of sea boat rental	5,000
PR Generation & Disposition	1,600
Materials & Labor to Fix DOP s/n 4	<u>19,800</u>
	\$34,100

Thus, assuming that a new DOP will have zero probability of failure, the purchase of a new DOP will help us avoid a cost of \$34K with a probability of 0.5. Hence, the expected savings are $(.5)(34K) = 17K$ per year. This gives us a payback of 41 months.

To the extent that the probability of DOP s/n 4 failing goes up from year to year, the payback period may be shorter than my calculation indicates. But certainly it is not as short as seven months. Of course, as I have indicated elsewhere, if the payback is four years or less, I

consider an ESR to be desirable. Such ESRs should be prioritized in the increasing order of their (correctly estimated) payback periods.

3. Look for economies of scale.

Here is another example illustrating the need to take advantage of economies of scale. We will need one more DOP within a year or two. It would be considerably cheaper if we ordered two at a time, rather than one now and one a year or two later.

4. The need for a qualified analyst to assist GSWT Steering Committee.

I do not expect a steering committee to be able to do the kind of reassessment of benefits I have done in Comment 2 above. I believe that if we are serious about incorporating cost-effectiveness considerations in our ESR prioritization, the steering committee must be assisted by a properly trained and impartial analyst whose charge is to challenge the GSWT teams' logic and the numbers on each ESR.

K15818. Digital Control Cards for LOX Pumps

1. An ESR we cannot afford not to invest in.

This ESR proposes to spend \$46K in order to save three cold flows (LOX) per year, worth \$25K per flow. Assuming these numbers are correct, KSC must take \$46K from its liquid oxygen (LOX) budget to fund this ESR immediately, so that we will save \$29K this year and we will have \$75K extra in future years for other desirable projects.

2. Use the right funding source.

As I see it, this ESR should be funded from the LOX budget. It should not compete with other ESRs for other sources of funds. Any comparison of this ESR with other ESRs would be unfair to both.

K14515. Prime Backup HGDS Infinite Zero Gas Source

1. Not on GSWT steering committee's priority list, very correctly.

This ESR is not one of the Top 17 on TV's list, but it is on the "open ESR" database. Yet, I have included it in this review primarily because I want to make the following points.

2. Reasonably quantifiable costs and benefits.

From the data on this ESR, it seems clear that the costs, risks, and benefits are reasonably quantifiable, and hence payback ought to be the sole criterion for this ESRs rank-ordering.

3. **An ESR that deserves to be rejected once and for all, closed, and deleted from the database.**

This ESR proposes to spend \$118K to be able to use facility GN2 gas in place of ultra pure GN2 in everyday standby purge operations, so as to obtain an estimated savings of \$7K per year. There are no other intangible benefits associated with this ESR. Thus, this ESR will take 16 years to payback!

I believe that such ESRs ought to be rejected once and for all, closed, and deleted from the "open ESR database" so that the GSWT steering committee is not burdened with its consideration year after year, and our computer systems are not burdened with carrying unnecessary data.

1994 NASA/ASEE SUMMER FACULTY FELLOWSHIP PROGRAM

111 7-62
351495

511-37

JOHN F. KENNEDY SPACE CENTER
UNIVERSITY OF CENTRAL FLORIDA

33971

p. 26

DESIGN OPTIMIZATION OF A BRUSH TURBINE
WITH A CLEANER/WATER BASED SOLUTION

PREPARED BY:	Dr. Rhyn H. Kim
ACADEMIC RANK:	Professor
UNIVERSITY AND DEPARTMENT:	University of North Carolina at Charlotte Department of Mechanical Engineering and Engineering Science
NASA/KSC	
DIVISION:	Mechanical Engineering
BRANCH:	Special Projects
NASA COLLEAGUE:	Rudy Werlink
DATE:	August 5, 1994
CONTRACT NUMBER:	University of Central Florida NASA-NGT-60002 Supplement: 17



ABSTRACT

Recently, a fluid turbine which has a brush attached to it has been designed and tested with water as fluid. The purpose of the turbine-brush is to clean up fouling in a tube. The Montreal Protocol prohibits the use of CFC products from refrigeration industry or from industry in general as a cleanser in 1996. Alternatives for the cleansers, devices or a combination of alternative devices with a cleanser should be found. One of the methods is to develop a device which cleanses fouling with a cleaning medium. In this paper, we describe a turbine connected with a brush. However, the turbine with the brush should be simple and easy to install. This device is a combined small liquid turbine with a brush. The turbine is activated by the liquid flowing through the tube. Then the turbine turns the brush cleaning fouling along the tube. Based on the energy conservation and the Bernoulli equation along with an empirical relationship of drag force obtained from an experimental apparatus, a relationship of the rotational speed, the number of blades, and geometric variables of the turbine-brush was obtained. The predicted rotational speeds were compared with the experimental observations. Further work was recommended for improvements.

SUMMARY

One of methods of cleaning fouling in a tube will be a turbine-brush unit to replace R113 as a cleanser after 1995. The turbine-brush consists of a turbine and a brush with a connector between the two. The turbine-brush was created in KSC, NASA and demonstrated its rotational motion while it was held at a position.

Objective of the program is to optimize the geometry of the turbine-brush including the blade angle, the number of blades, and arrangements of the connector and brush, flow rates, rotational speeds, diameters of tubing and performance of cleaning before a final product is designed and manufactured.

As an initial step, a relationship among the above variables was developed based on the energy conservation law and the force momentum theorem. Numerical values of an existing turbine-brush are used with the relationship to predict the rotational speed. Predicted rotational speeds are compared with observed rotational speeds. These two differ in one order of magnitude.

The drag coefficients were computed based on the incoming velocity. From the open literature, we did not find any information of its drag force coefficients, because this may be the first device to do the cleaning in the tube with the fluid as driving energy source. Possible alternative coefficients useable for the turbine-brush are those for a spinning sphere or a disk and cylinder connected in tandem. From the experimental results, the force was measured and its coefficient was calculated. As a result, the equation relating the variables produced the angular velocity.

While it rotates, the flow downstream of the turbine-brush is a combination of a usual turbulent one dimensional flow with a forced vortex motion due to the turbine motion within the connector and brush then one more complicated form of forced vortex motion takes place downstream of the brush. A laminar sublayer flow was assumed to pass through the gap between the turbine-brush and the wall of the tubing.

A simple numerical model was developed. One hundred sixty eight volume elements were constructed in order to use in a three dimensional unsteady flow conditions. Boundary conditions, properties, turbulence model, and so on have to be supplied to run and yield a result.

Further work is recommended as follows: (1) a coded program of computation is recommended for various parameters of the turbine-brush, (2) measurement of drag force coefficients in the wide range of the volume rates, (3) study of constraints under which the relationship derived be optimized including the degree of the reaction of the turbine, (4) experiments be performed with a different forms of the brush, (5) a numerical simulation be continued with the model to determine a feasibility of the numerical scheme for the turbine-brush in the future.

TABLE OF CONTENTS

Section	Title	Page
	Cover/Title Page	
	Abstract	
	Summary	
	List of Figures	
	Nomenclature	
I	INTRODUCTION	
II	ANALYSIS	
2.1	Drag Force and its Coefficient	
2.2	Energy Conservation Law	
2.3	Application of the Derived Equation	
2.4	Numerical Simulation	
III	EXPERIMENTAL INVESTIGATION	
3.1	Type of Probes and Their Locations	
3.2	Data from Experiments and Computed V_1, C_D	
IV	RESULTS AND DISCUSSIONS	
4.1	Angular Velocity and frequency	
4.2	Coefficients of Drag Forces	
4.3	Constraints under Which Optimum Values Are Obtained	
4.4	Numerical Simulation	
V	RECOMMENDATION	
VI	CONCLUDING REMARKS	
VII	APPENDIX	
	A DERIVATION OF KINETIC ENERGY OF ROTATING ELEMENTS	
	B DERIVATION OF ROTATIONAL WORK DUE TO CENTRIFUGAL FORCE	
	C THE NEWTON-RAPHSON METHOD FOR FINDING ROOTS OF A POLYNOMIAL	
VIII	REFERENCES	

LIST OF FIGURES

- Fig.1 Dimensions of Turbine-Brush
- Fig.2 Control Volume and a Schematic Diagram of a Turbine-Brush Unit
- Fig.3 Finite Volume Element Structure
- Fig.4 Experimental Apparatus and Probe Locations
- Fig.5 Inlet and Exit Vector Diagram and Combined Vector Diagram
- Fig.6 Mass Moment of Inertia, Centrifugal Force Friction Force
- Fig.7 Radii of Turbine-Brush, (a) Turbine and its Housing, (b) Connector, (c) Brush

NOMENCLATURE

A	Area of tube cross-section, m^2
B	Width of the brush, or the length of turbine-brush sections, m
C_D	Drag coefficient
d	Diameter of the tube, m
F	Force, N
g_c	Constant defined by the force:unity is the SI unit
H	Enthalpy, kJ/s
h	specific enthalpy, kJ/kg
K.E.	Kinetic energy, kJ/kg
m_f	Mass rate, kg/s
p	Static pressure, N/m^2
P.E.	Potential energy, kJ/kg
Q	Heat transfer rate, J/s
r	radii of the rotating elements, m
u	Specific internal energy, kJ/kg
U	Tangential Velocity, m/s
V	Fluid velocity, m/s
v	Specific volume, m^3/kg
W	Rate of work, kJ/s

Greek Letters

α	Turbine angle
β	Weight adjusting factor
π	3.14
ρ	Density, kg/m^3
Σ	Summation
ω	Angular velocity, /s
μ	Dynamic viscosity, $N s/m^2$

Subscripts

1-2	representing the length between p_1 and p_2
1-4	representing the length between p_1 and p_2
b.b.	Brush Base
b.h.	brush and its hub
br	Brush
D	Drag force
f	Fluid
in	Entering section
out	exiting section
shaft	shaft work
skin.f.	Shear force
rot.	Referring to rotational parameters
tension	Tension of a wire
tur	turbine

I. INTRODUCTION

CFC refrigerants/cleasers will not be allowed to use in cleaning fouling in tubes starting in 1996. In this paper, we describe a device which will clean fouling in tubes. The device consists of two parts; a turbine and a brush with a connecting part. Details of the turbine, brush and the connector are shown in Fig.1(Werlink,1993). The turbine has four blades with 70 degree wide and there is a spacing of 20 degrees between the blades. These blades are installed in a direction of 45 degree from the axial direction. A connector links the turbine with a brush.

The brush is made of nylon fibers so very densely structured that fluid may not pass through. It is possible to consider that the friction in the gap between the turbine and the tube wall and brush and wall may be of a nature of a laminar flow. However, the drag force of the turbine-brush unit is very complicated. At a glance, the unit may be assumed to be a spinning sphere(Goldstein) or a disk connected to a cylinder in tandem(Blevins). While a cleanser water solution passes through a tube, more or less, the friction force may be reduced due to the fact that the cleanser is a material made of long chain structured polymers(Sellin and Moses). On the other hand, a constant vortex motion provided by the turbine followed by a swirling motion of the fluid within the connector and the brush, again, a vortex motion due to the brush rotation are very complicated and difficult to analyze exactly.

The combined vortex and turbulent flow may be analyzed by superimposing two separate flow characteristics together, i.e., an axial turbulent flow passing through the geometry of the turbine-brush and a rotational flow within the turbine-brush configuration may be analyzed separately and results should be superimposed.

In this project, preliminary results were obtained based on simplifying assumptions and measurements of drag forces. Based on the assumptions, the energy conservation law was used along with the force momentum theorem tying up with the drag force in terms of pressure drops across the turbine-brush. By doing so, the speed of the unit in rotational motion was predicted and compared with the experimental results.

II. ANALYSIS

2.1 Drag Force and its Coefficient

Consider a control volume shown in Fig.2. Certain assumptions are needed to deal with the flow phenomena for a first order approximation solution. The assumptions used for the fluid

are(Munson et al.):

1. One-dimensional incompressible steady flow
2. No heat transfer from or to the flow, and $t_{in} = t_{out}$.
3. Fully developed turbulent flow
4. The tube has a uniform internal diameter.
5. The fluid has constant dynamic and thermal properties.
6. Fluid passing through the brush section is a negligible amount.
7. The drag force of the turbine-brush held at a position will be the same as it moves, once the tension force is taken into account in computing the drag coefficient.

Based on the force-momentum theorem, the sum of forces in the horizontal direction is the same as the rate of momentum change(Munson, et.al):

$$\Sigma F = (m_f/g_c)(V_{out} - V_{in}) \quad (1)$$

The sum of forces are collection of the tension force, static forces, the drag force and the skin friction forces(Fig.2):

$$- F_{tension} + (p_1 - p_2)A + F_D - F_{skin.f.1-2} = (m_f/g_c)(V_2 - V_1) \quad (2)$$

where p's are the static pressures measured at the upstream and downstream of the turbine-brush. If the static pressures at the stations 1 and 4 are used equation(2) becomes(Fig.4):

$$-F_{tension} + (p_1 - p_4)A + F_D + F_{skin.f.1-4} = (m_f/g_c)(V_4 - V_1) = 0$$

because V_4 is the same as V_1 for a fully developed flow at the station 4 in the tube. From the above, we obtain F_D :

$$F_D = F_{tension} + (p_4 - p_1)A - F_{skin.f.1-4}$$

By the definition of the drag coefficient, C_D , the drag force is given by:

$$F_D = \rho_f V_1^2 A C_D / (2g_c)$$

$$C_D = [F_{tension} + (p_4 - p_1)A - F_{skin.f.1-4}] / (\rho_f V_1^2 A / 2g_c) \quad (3)$$

The coefficient, C_D is computed from equation(3) with $F_{tension}$, p_4 , p_1 , and V_1 which come from experiments. The skin friction force is in terms of viscosity, the velocity gradient at the laminar sublayer in the gap between the turbine and tube wall and the brush and tubing wall. The friction force in the axial direction has a form:

$$F_{skin.f.1-4} = \mu_f V_1 (2\pi B_{1-4}) \quad (4)$$

2.2 Energy Conservation Law

Consider the energy conservation on the control volume shown in Fig.2(Moran and Shapiro):

$$Q - W = (K.E. + P.E. + H)_{out} - (K.E. + P.E. + H)_{in} \quad (5)$$

where Q is the heat transfer rate, W , the mechanical work and K.E. and P.E. are the kinetic and potential energy, respectively and H is enthalpy defined by:

$$H = m_f h; \quad h = u + p/\rho, \quad m_f = \text{mass rate} \quad (6)$$

Applying the usual assumptions to liquid steady flows, i.e., no heat transfer, temperature being unchanged, i.e., $t_{in} = t_{out}$, and the density being constant, the above equation is written as follows:

$$-W = (m_f/g_c) [(V_2^2/2 + p_2 v) - (V_1^2/2 - p_1 v)] \quad (7)$$

The rate of work in equation(7) includes the shaft work and the friction work as the unit rotates:

$$W = W_{shaft} + W_{skin.f.} \quad (8)$$

Since the rotational force comes from the motion of the blades, all of energy of fluid is assumed to turn the turbine-brush, the shaft work will have a form:

$$W_{shaft} = J_{tot} \omega^2 / 2 \quad (9)$$

where ω is the angular velocity and J_{tot} is the sum of the moment of inertia about the axial direction. The sum of the moments consists of moments of inertia of the turbine, J_{tur} , the connectors, $J_{conn.}$, brush hub, $J_{b.h.}$ and the brush, J_b .

$$J_{tur} = (\rho t)_{tur} (\pi/2) (r_4^4 - r_1^4) (\alpha/360) N \beta_{tur} \quad (10)$$

$$J_{conn.} = (\rho t)_{conn.} (\pi/2) (r_3^4 - r_2^4) \beta_{conn.} \quad (11)$$

$$J_{b.h.} = (\rho B)_{b.h.} (\pi/2) (r_3^4 - r_2^4)_{b.h.} \quad (12)$$

$$J_b = (\rho B)_b (\pi/2) (r_3^4 - r_2^4)_b \quad (13)$$

where ρ is the density, t is the thickness, α is the angle of the blade, and β is a number adjusting the geometry with respect to one of the components of the turbine-brush, N , the number of blades, and r 's are radii, respectively (See details in derivations of APPENDIX).

Since the turbine-brush unit is held in a position but rotates, the friction work due to the translation motion is negligible. The friction between the brush and surface of the tube wall is due to the force normal to the centrifugal force. This force should be multiplied by the tangential velocity of rotation (See details in derivation of APPENDIX):

$$W_{br,rot} = (2\pi/3g_c)\mu_{dry}(\rho B)_{br}\omega^3 r_7(r_7^3 - r_2^3)_{br}\beta_{b.h.} \quad (14)$$

The magnitude of the dry friction coefficient between the turbine the brush and the tube wall is 0.35 (Baumeister and others). Since the flow in the gap between the tube wall and turbine housing is laminar, the work against the rotational motion is:

$$W_{rot.} = (2\pi/3g_c)\mu_f(\rho B)_{tur}\omega^3 N r_4(r_4^3 - r_1^3)_{tur}\beta_{tur} \quad (15)$$

After collecting all of these terms, equations (2), (3), (4), (9-15) and substituting into equation (7), a relationship of important variables such as the angular velocity, the speed of the unit along the tube, and the number of the blades is shown as follows.

$$\begin{aligned} c_1 r_7(r_7^3 - r_3^3)\omega^3 + c_2 r_4(r_4^3 - r_1^3)N\omega^3 - c_3(r_4^4 - r_1^4)N\omega^2 - \\ (c_4 + c_5)(r_3^4 - r_2^4)\omega^2 - c_6(r_7^4 - r_3^4)\omega^2 \\ + c_7(r_6 + r_1)^2\omega^2 - c_8 = 0 \end{aligned} \quad (16)$$

where

$$c_1 = (2\pi/3g_c)\mu_{dry}(\rho B)_{br.}\beta_{b.h.} \quad (17a)$$

$$c_2 = (2\pi/3g_c)\mu_f(\rho B)_{tur}\beta_{tur}(\alpha/360) \quad (17b)$$

$$c_3 = (\pi/2)(\rho B)_{tur}\beta_{tur}(\alpha/360)/2g_c \quad (17c)$$

$$c_4 = (\pi/2)(\rho t)_{conn.}\beta_{conn.}/2g_c \quad (17d)$$

$$c_5 = (\pi/2)(\rho B)_{b.h.}/2g_c \quad (17e)$$

$$c_6 = (\pi/2)(\rho B)_b/2g_c \quad (17f)$$

$$c_7 = m_f/(8g_c) \quad (17g)$$

$$c_8 = - (m_f/2g_c)V_1^2 C_D + F_{tension}V_1 \quad (17h)$$

where $\beta_{b.h.}$ is a factor adjusting the geometry for the brush and hub, $\beta_{conn.}$ a factor adjusting the geometry for the connector, and β_{tur} is a factor adjusting the geometry for the turbine. $V_2^2 = V_{2trans.}^2 + V_{2rot.}^2$, $V_1^2 \approx V_{2trans.}^2$, $V_{2rot.} = ((r_6 + r_1)/2)\omega$ were also used in equation(16). Subscripts 1, and 2, here refer to the inlet and outlet, respectively.

2.3 Application of the Derived Equation

For the number of blades, $N=4$, r 's being read from Fig.1, listed in Table 1, equation(16) becomes a third degree polynomial in ω at a given volume rate, .i.e., $V_1 = \text{constant}$:

$$a_3\omega^3 + a_2\omega^2 - a_0 = 0 \quad (18)$$

where a 's are expressed as follows:

$$a_3 = c_1r_7(r_7^3 - r_3^3) + c_2r_4(r_4^3 - r_1^3)N \quad (19a)$$

$$a_2 = c_7(r_6 + r_1)^2 - [c_3N(r_4^4 - r_1^4) + (c_4 + c_5)(r_3^4 - r_2^4) + c_6(r_7^4 - r_3^4)] \quad (19b)$$

$$a_0 = c_8 \quad (19c)$$

where C_D is assumed to depend on the incoming velocity, V_1 and constant determined from the experiments. Table 1 summarizes all of the numbers in the above computations.

Table 1 Values of material properties, geometry and flow properties

Turbine	Brush	Brush Hub	Connector
$r_1=0.00381m$			
	$r_2=0.00508$	$r_2=0.00508$	$r_2=0.00508$
	$r_3=0.00762$	$r_3=0.00762$	$r_3=0.00762$
$r_4=0.01905$			
$r_5=0.02159 m$			
$r_6=0.02301 m$			
$r_7=0.0254 m$	$r_7=0.0254 m$		
$t=0.0015875 m$			$t=0.0015875$
$B=0.0047625 m$	$B=0.008382 m$	$B=0.008382 m$	$B=0.00254$
$\rho=7900 \text{ kg/m}^3$	$\rho=1121.625 \text{ kg/m}^3$	$\rho=4800 \text{ kg/m}^3$	$\rho=7900 \text{ kg/m}^3$

The density and viscosity of fluid are $\rho=997 \text{ kg/m}^3$ and $\mu=885 \times 10^{-6} \text{ Ns/m}^2$.

2.4 Numerical Simulation

A software NEKTON(Fluent,Inc.) was made available on a DEC workstation in the Branch through the KSC Telnet network. NEKTON is a finite element based fluid problem solver that is capable of analyzing flows of three dimensional unsteady nature. This is a result of a spectral element method developed by Professor Patera of MIT and commercialized by Fluent,Inc.

The flow domain of the turbine-brush is a cylinder with a length of $11d$, d being the diameter of the cylinder. At the location of $3d$ from the entrance, the turbine-brush of $2d$ long is placed. The location of the exit is then $6d$ away downstream from the turbine-brush which may be the minimum distance for which a fully developed flow at the exit is warranted.

Starting from the entrance, 21 surface elements were constructed. These elements were moved up to the next position along the cylinder length, thereby, became volume elements. At the location of the turbine brush, the surface was divided into different concentric elements from the previous fluid elements so that these elements are identified as rotating elements at given locations. The connector and brush sections were made into volume elements in a similar manner to the turbine section(Fig.3).

At present, 168 finite volume elements were constructed for the flow domain and stored in the SUN workstation network at UNC-Charlotte. Additional variables to be supplied are boundary conditions, fluid properties, rotating boundary conditions, turbulence model, and deformation information for each element. This is a very crude model for the turbine-brush. However, this would yield important an insight so that an analyzer can determine whether a numerical study may be of help in the turbine-brush development.

III. EXPERIMENTAL INVESTIGATION

3.1 Type of Probes and Their Locations

Fig.4 shows an experimental apparatus. A hydrant with a control valve supplies water to the test section of a transparent tubing of i.d., 2 in. The valve controls the flow rate. The turbine-brush unit is held by a wire and a load cell transducer measures the tension force of the wire. The pressure ports are shown as p_1 , p_2 , p_3 , and p_4 . The rotation speed was measured by picking up pulses from a

rotating magnet which is placed in a turbine blade. The sampling rate was 49.98 per second. The load cell and pressure transducers have the measuring ranges as shown in Table 2.

Table 2 Transducer Ranges

Transducers	ranges	Accuracy in F.S.
Load cell	0-50 lb	0.1 %
p ₁	14.7-60 psia	0.02%
p ₂	14.7 - 50psia	0.02%
p ₃	12.0 - 30psia	0.02%
p ₄	12-30 psia	0.02%

A PC and labview software display and record the data in an ASCII file in a monitor and disk. A typical data set is shown in Table 3.

3.2 Data from Experiments and V₁, F_D Computation

Applying the force-momentum theorem to the turbine-brush held at a point produces an equation in the form:

$$-F_{\text{tension}} + (p_1 - p_2)A + F_{\text{Drag}} - F_{\text{skin.f.1-2}} = (m_f/g_c)(V_2 - V_1) \quad (2)$$

where the first two quantities of the left hand side of the equality and V₁ are known and the drag force is given by $F_{\text{Drag}} = C_D \rho_f V_1^2 A / 2g_c$, A being the cross section area of the tube. From this equation V₂ is obtained. Computation yielded that V₂'s are within a range of 95 percent of V₁. Table 3 summarizes data from the experiments, computed velocities and the drag forces. The quantities in parentheses are the numbers in the Pound-Inch system.

The reading devices have ranges of uncertainties within 0.10 percent, yielding an uncertainty of about 1.0 percent for the measurement system.

Table 3 Summary of Flow Rates, Pressures, Tension Force and Drag Force

Flow Rate	p_1	p_2	p_3	p_4	$F_{tension}$	V_1	Drag Force
m^3/s (gpm)	kpa (psi)	kpa (psi)	kpa (psi)	kpa (psi)	N (lbs)	m/s (ft/s)	N (lbs)
.0037 (58.5)	21.86 (3.17)	10.34 (1.50)	1.014 (0.147)	2.64 (0.38)	39.44 (8.86)	1.822 (5.98)	0.468 (.105)
.0047 (74.47)	21.79 (3.16)	10.76 (1.56)	1.048 (0.152)	2.64 (0.38)	41.15 (9.25)	2.32 (7.61)	0.53 (2.36)
.0052 (82.00)	20.80 (3.02)	10.74 (1.60)	1.50 (0.218)	2.81 (0.41)	39.41 (8.86)	2.01 (6.58)	0.655 (2.97)

IV. RESULTS AND DISCUSSION

4.1 The Angular Velocity

In the computation procedure, the geometry factors were used; $\beta_{b.h.} = 72$, $\beta_{conn.} = 72$, and $\beta_{tur} = 0.65$. Table 4 shows the computed and observed frequencies for three cases.

The predicted and the observed frequencies do not agree well. The predicted values are of magnitude of one order higher than the observed values. This means that the mass of the rotating system has been estimated less than it should be and that the sum of the inertia of rotating parts of the turbine-brush should be estimated more carefully, rather than using the geometry factors.

One of the assumptions used was the flow in the gap between the turbine-brush and the tube wall is a laminar sublayer. This may not be true. Estimating the frictional work in the rotating motion of the turbine-brush may not be accurate, particularly with the brush. More data are needed for the drag coefficients in a wide range of the volume rates to know whether the deviation between the two values of the angular velocities would be greater in the high Reynolds number side.

4.2. Coefficients of Drag Forces

From Table 3, the drag coefficients were computed for three different flow rates. The Reynolds numbers and the coefficients are listed in Table 4. Further computed results will be compiled for a later report.

Table 4 Coefficients of Drag forces at Flow Rates

Flow Rate m ³ /s (gpm)	Re	C _D	f _{pred.}	f _{observed}
0.0037(58.5)	1.08x10 ⁵	0.14	43.98	7.0
0.0047(74.47)	1.37x10 ⁵	0.43	47.41	7.0
0.0052(82.00)	1.19x10 ⁵	0.20	47.86	7.0

The difference between the incoming velocity and the moving speed of the turbine-brush is very little. The drag coefficient changes from 0.14 to 0.4 in the Reynolds number range at 10⁵. The coefficient of the turbine-brush is compared to those of the spinning sphere(Goldstein), and the disk connected to a cylinder in tandem. The drag coefficients of the turbine-brush is less than the spinning sphere and the disk connected to a cylinder(Blevins).

4.3 Constraints under which optimum values are obtained

An important constraint among others seems to be the degree of the reaction of the turbine-brush, which is defined as(Shepherd):

$$R = [(U_1^2 - U_2^2) + (V_{r2}^2 - V_{r1}^2)] / (2g_c E) \quad (20)$$

where E is defined as:

$$E = [(V^2 - V_2^2) + (U_1^2 - U_2^2) + (V_{r2}^2 - V_{r1}^2)] / (2g_c) \quad (21)$$

where all of the symbols used are denoted in Fig.5. The absolute velocity V is resolved into a component V_m passing through the axis(a radial velocity) and a tangential component V_u. The reaction is an indication of energy transfer from the fluid to the turbine. For example, R = 0 implies that there is no change of static head or pressure in the rotor and such a machine is called an impulse type. In general, the term reaction alone is used whenever the turbine is not purely impulse, but for the special case of steam turbines, it has come to imply 50 percent or half degree of the reaction. The turbine of the turbine-brush has a degree of the reaction between 0 and 50 percent. This aspect of the degree of reaction for the turbine-brush should be studied further.

Other important constraints are the optimum radii of the structure because these determine the weight of the turbine-brush, consequently the rotating inertia. The structure of the connector seems to be a very important constraint. A new arrangement and structure of the brush will be important. All of these variables are related with the geometry factors. The more accurate these are, the better predictions seem to be made.

Strictly speaking, the actual application of this device in cleaning fouling, the device will travel along the tube, not held at a place. The current experimental apparatus holds the turbine-brush at a point, thus the drag coefficient might be different from those obtained from the apparatus in which the turbine-brush was held at a point. A series of this type of experiments should be carried out in the future.

4.4 Numerical Simulation

The numerical analysis be continued to establish a feasibility study. This type of the feasibility study may be needed to justify the required time for a coding a new program or justify using a commercially available code, if needed.

V. RECOMMENDATION

Further work is recommended as follows.

1. Determine the weights of the turbine-brush as a unit and individual components. This will help determine the mass moment of inertia of the turbine-brush and mass adjusting factors, because these control the prediction of the rotation speed.
2. More drag force measurements may be needed from low volume rates. Additional experiments would tell us whether the prediction is reliable in the low or high velocity side of the flows.
3. Investigation of the constraints under which the relationship derived be optimized including the degree of the reaction of the turbine. Because of the brush attached to the turbine, this may be a brand new study.
4. Different forms of brushes be attached and experimented for a possible reduction of the drag force. Rather than the radial brush, attach fibers in the connector along the axial direction so that the fibers get stretched due to the centrifugal force in rotation. This would reduce the drag force and enhance the rotational speeds. This kind of fiber arrangement could be beneficial for a smaller diameter.

5. Computation procedures be coded for the current verification of the equation as well as its future use.

6. Numerical analysis with constructed elements be carried out to determine feasibility for further numerical study and to know whether it could aid the design development activity based on the software NEKTON or a different code or coding a new code.

VI. CONCLUDING REMARKS

Based on the Newton's law of force and the energy conservation law, an equation was derived relating certain number of geometrical variables with flow variables together. Pressure drops across the turbine-brush were measured in order to compute the drag force coefficients. These coefficients were used in the derived equation. This equation provided the rotations per second. These have been compared with the experimental values. They do not agree at all. The reason was discussed in the Results and Discussion section. Further work has been suggested in the Recommendation section.

VII. APPENDIX

A. DERIVATION OF THE KINETIC ENERGY OF THE BLADES

From Figs. 6(a) and 7(a), the mass moment of inertia of the arc element is:

$$dI = r^2(dm); \quad dm = \rho(2\pi r dr)t = 2\pi(\rho t)r dr; \quad dI = 2\pi(\rho t)r^3 dr$$

$$I = \int 2\pi(\rho t/g_c)r^3 dr = (\pi/2g_c)(\rho t)(r_2^4 - r_1^4) \quad (A1)$$

where ρ is the density, and t is the thickness of a plate.

Integration of the above with respect to the radius for a blade that has α degree, the outer and inner radii as r_2 and r_1 gives:

$$I_{tur} = (\pi/2g_c)(\rho t)_{tur}(r_2^4 - r_1^4)(\alpha/360) \quad (A2)$$

Thus, the kinetic energy of the N turbine blade is:

$$(\pi/2g_c)(\rho t)_{tur}\omega^2(r_2^4 - r_1^4)N/2 \quad (A3)$$

B. DERIVATION OF THE OF THE ROTATIONAL FRICTIONAL FORCE AND ITS WORK

From Figs.6(a)and 7(b), the centrifugal force of the arc element is:

$$dF_{cent} = r\omega^2(dm); \quad dm = \rho(2\pi r dr)B; \quad \omega = \text{constant} \quad (B1)$$

where ω is the angular velocity of the blade. Integration of the force with respect to the blade angle and radius with the number of blades gives:

$$F_{cent} = (2\pi/3g_c)(\rho t)_{tur}\omega^2(r_4^3 - r_1^3)(\alpha/360)N \quad (B2)$$

The friction force is, then:

$$F_{frict} = \mu_{dry}F_{cent},$$

where μ_{dry} is the dry friction coefficient between the brush and the tube wall. Thus, the rate of the frictional work is:

$$W_{br,rot} = (2\pi/3g_c)\mu_{dry}(\rho B)_{br}\omega^3 r_2(r_7^3 - r_2^3) \quad (B3)$$

C. THE NEWTON-RAPHSON METHOD FOR FINDING ROOTS OF A POLYNOMIAL

Consider a function of x , $f(x) = a_0 + a_1x + a_2x^2$

$$+ a_3x^3 + a_4x^4 + \dots \quad (C1)$$

Suppose an estimated root is x_0 . Then evaluate the function $f(x_0)$, that is:

$$f(x_0) = a_0 + a_1x_0 + a_2x_0^2 + a_3x_0^3 + a_4x_0^4 + \dots \quad (C2)$$

Take the derivative of the function with respect to x and substitute x with x_0 :

$$df(x_0)/dx_0 = a_1 + 2a_2x_0 + 3a_3x_0^2 + 4a_4x_0^3 + \dots \quad (C3)$$

Now make a ratio of $f(x_0)/df(x_0)/dx$, subtract from x_0 and set it as:

$$x_n = x_0 - f(x_0)/df(x_0)/dx \quad (C4)$$

Let us compare x_n with x_0 in terms of their magnitudes; hence the absolute value of the difference is less than a certain number, $\epsilon = 0.01$ for which the accuracy is warranted:

$$|x_n - x_0| \leq \epsilon \quad (C5)$$

then, one of the roots of equation(8) is x_n . For other roots, the above procedure should be repeated for the polynomial(Stoecker).

Using velocities of Table 3 and C_p 's of Table 4 for three cases of experimental results, the roots were found. $\omega = 276.2072, 297.7274,$ and $300.5572,$ respectively. The other two roots are imaginary numbers for the three cases. Thus $\omega = 2\pi(\text{rotation/s})$ produces $43.98, 47.41,$ and 47.86 for rotations per second, which is frequency.

VIII. REFERENCES

1. Werlink, R., Private Communication on Patent Application, KSC, NASA, Nov., 1993, May, 1994
2. Goldstein, S., Modern Developments in Fluid Dynamics, Oxford Press, London, 1938
3. Blevins, R., Advanced Fluid Dynamics Handbook, Van Nostrand Reinhold, New York, 1984, p.333
4. Sellin, R.H., Moses, R.T., Drag Reduction in Fluid Flows, Techniques from Friction Control, Ed. Ellis Horwood limited, 1989
5. Munson, B.R., Young, D.F., Okiishi, T.H., Fundamentals of Fluid Mechanics, 2nd Ed. John-Wiley & Sons, Inc., 1994
6. Moran, M.J., Shapiro, M.J., Fundamentals of Engineering Thermodynamics, 2nd Ed., John-Wiley & Sons, Inc., New York, 1992
7. Baumeister, T., Avallone, E.A., and Baumeister, T, III, Marks' Handbook of Mechanical Engineers, 8th Ed., McGraw-Hill Book co., 1978
8. Fluent Inc., NEKTON, Ver. 2.85, User's Guide, Lebanon, N.H., 1992
9. Shepherd, D.G., Principles of Turbomachinery, Macmillan Co., 1969
10. Stoecker, W.F., Design of Thermal Systems, McGraw-Hill Book Co., 1971

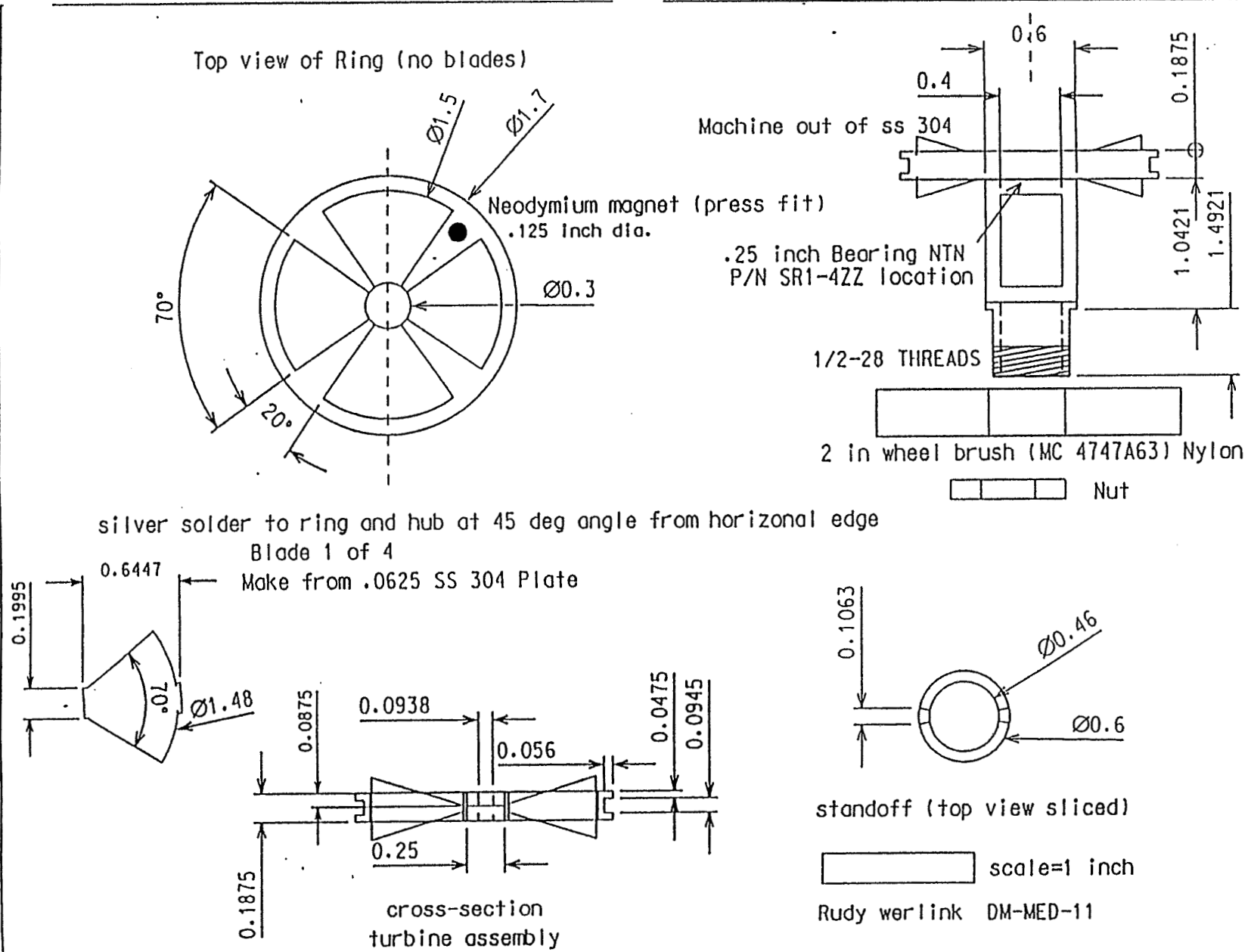


Fig.1 Dimensions of Turbine-Brush

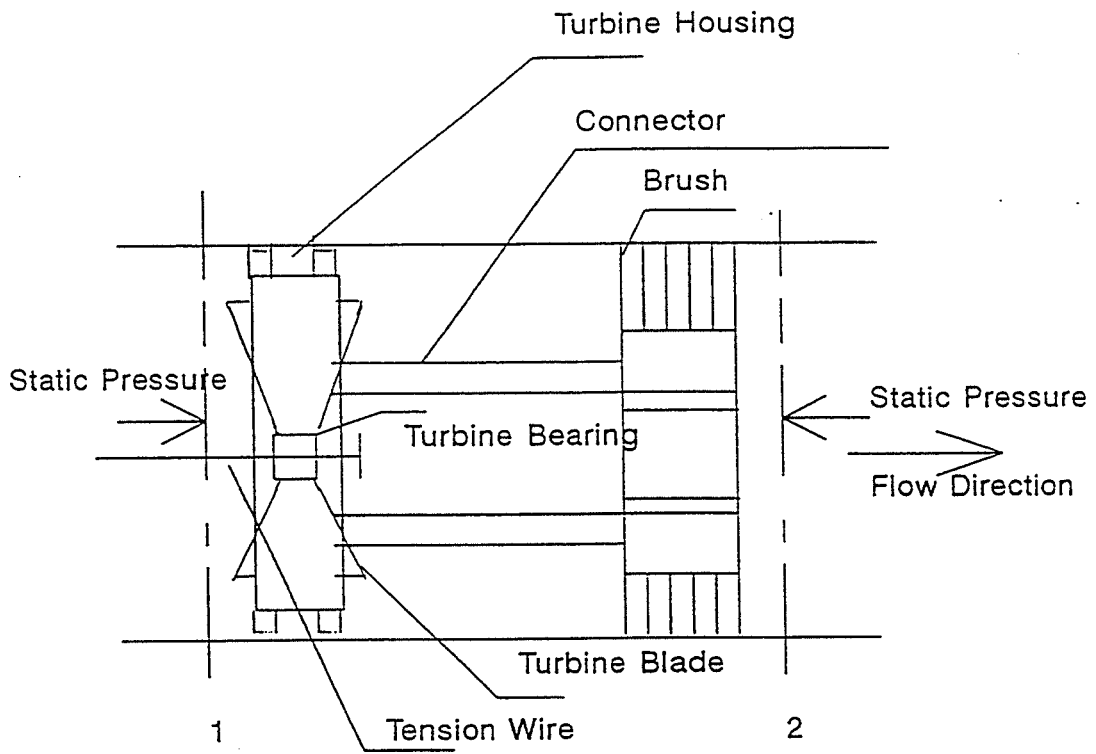


Fig.2 A Control Volume and a Schematic Diagram of a Turbine-Brush Unit

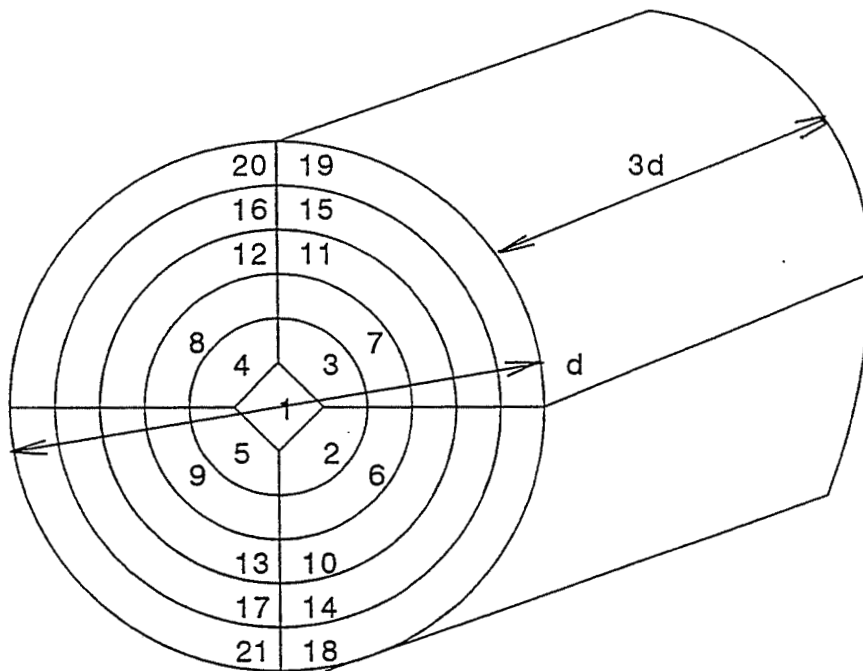


Fig.3 Finite Volume Element Structure

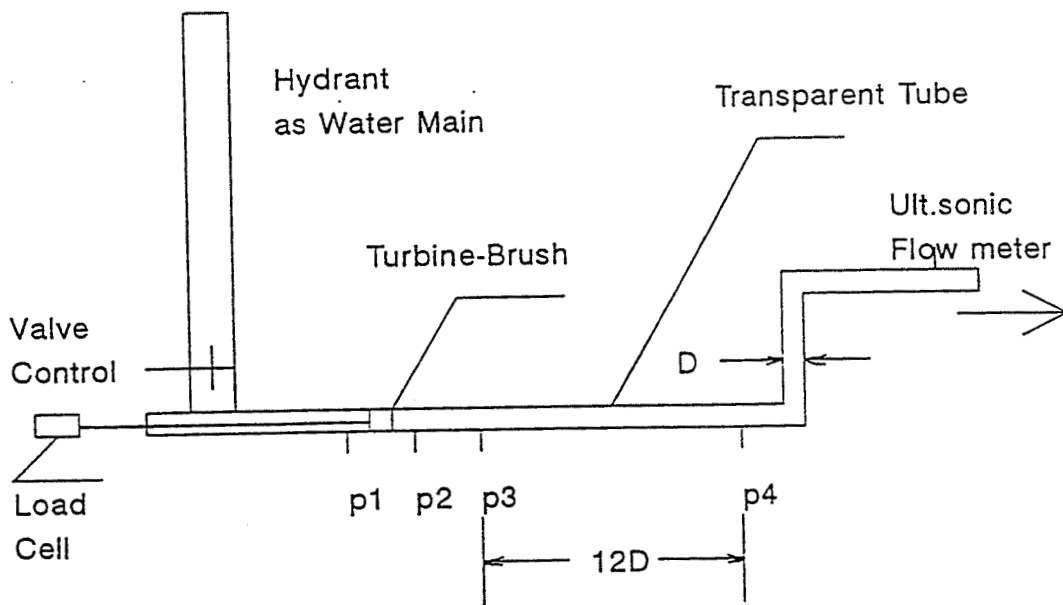
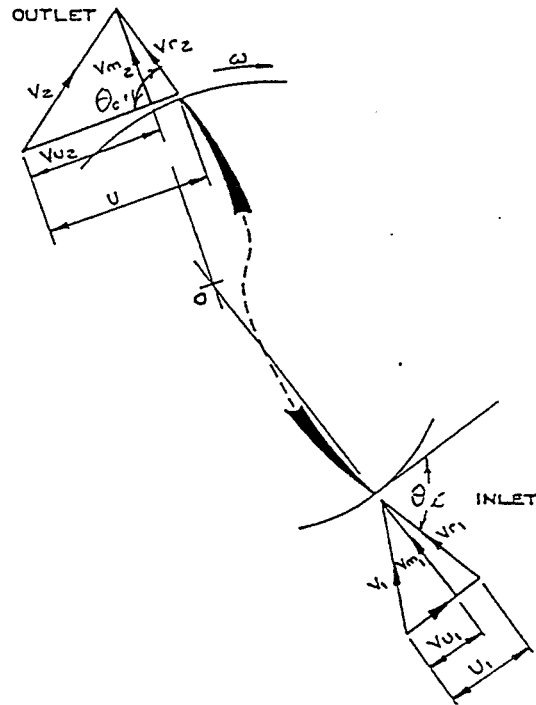
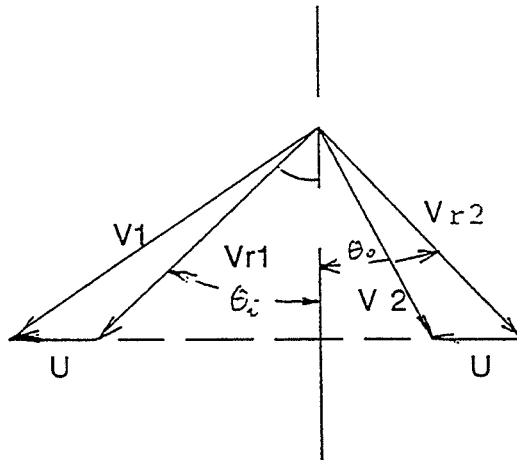


Fig.4 Experimental Apparatus and Probe Locations

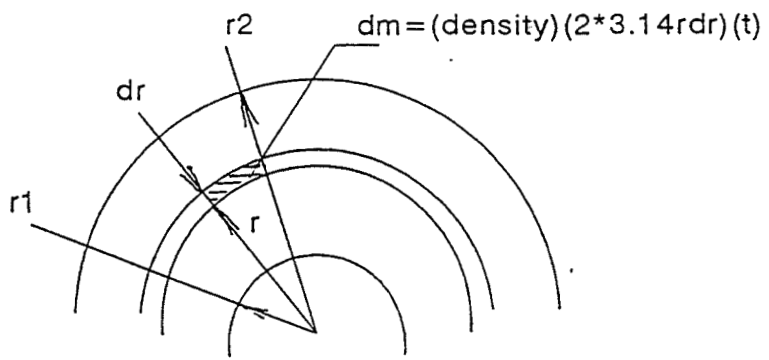


(a) Inlet and Exit Vector Diagram

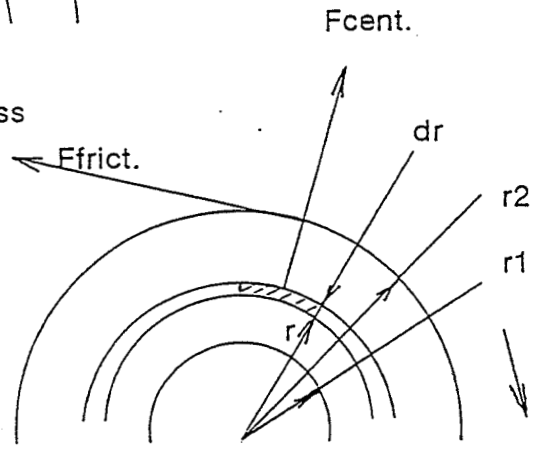


(b) Combined Vector Diagram at Inlet, Exit of a Blade of a Turbine

Fig.5 Inlet and Exit Vector Diagram and a Combined Vector Diagram



(a) Moment of Inertia for Mass



(b) Friction Force due to Centrifugal Force

Fig.6 Mass Moment of Inertia, Centrifugal Force, Friction Force

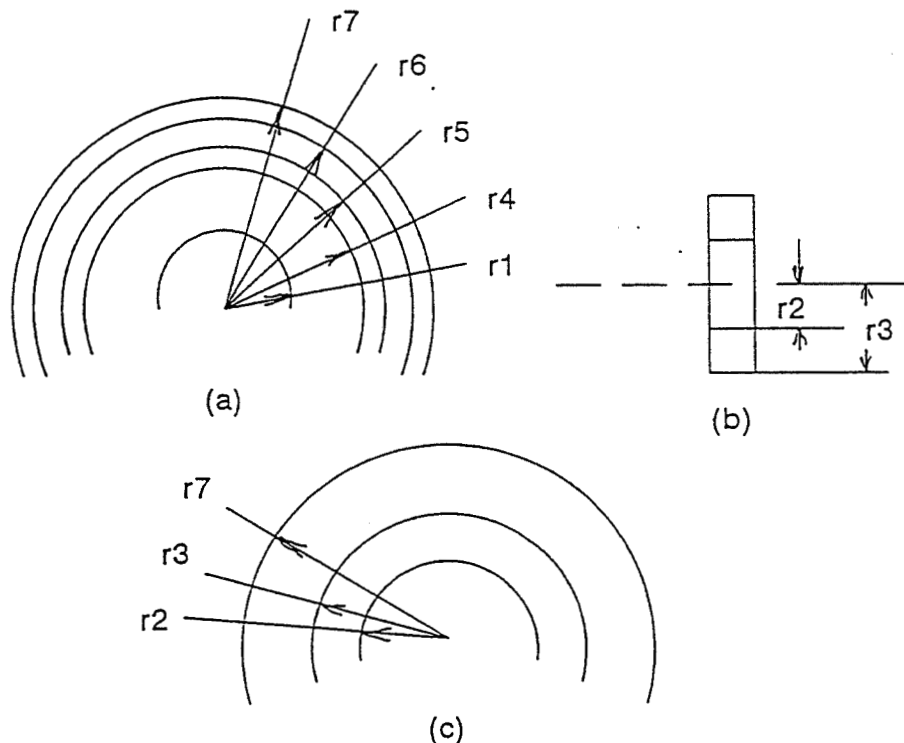


Fig.7 Radii of Turbine-Brush (a)Turbine and its Housing
 (b)Connector,(c)Brush

N95-18178

351497

111763

1994 NASA/ASEE SUMMER FACULTY FELLOWSHIP PROGRAM

**JOHN F. KENNEDY SPACE CENTER
UNIVERSITY OF CENTRAL FLORIDA**

512-37

33972

P.10

RACK INSERTION END EFFECTOR (RIEE) GUIDANCE

PREPARED BY:	Dr. Narasimha S. Malladi
ACADEMIC RANK:	Associate Professor
UNIVERSITY AND DEPARTMENT:	Tuskegee University Department of Mechanical Engineering
NASA/KSC	
DIVISION:	Mechanical Engineering
BRANCH:	Special Projects
NASA COLLEAGUE:	Eduardo Lopez del Castillo
DATE:	August 16, 1994
CONTRACT NUMBER:	University of Central Florida NASA-NGT-60002 Supplement: 17

ACKNOWLEDGMENTS

I gratefully acknowledge the support of Dr. Loren A. Anderson, Kari Styles of University of Central Florida and the staffs of NASA and I-NET whose diligence and friendliness, made my ASEE/NASA Faculty Fellowship program at Kennedy Space Center, productive and enjoyable. Particular thanks to Fred Jankowsky, Bill Jones, Cary Parrish, Todd Graham and Allen Littlefield of NASA and James Spencer and Perry Hartford of I-NET. My NASA colleague Eduardo Lopez has become a good friend and good critic of my work. My special thanks and appreciation are to him for his spontaneous willingness to help in many ways and for his spiritual fellowship. Jim Jennings, Albert Diggs and Evelyn Johnson gave me an opportunity to give lectures on "Fun with Engineering Formulations" to the NASA scholars. These spontaneous lectures helped me develop new and simplified methods for my book "Discovering Statics and Dynamics". My thanks are to all of them. I enjoyed working with the Co-op student Russatta Buford. My thanks are to other NASA fellows and in particular, Dr. Bill Brewer, Dr. Bob Byers and Dr. Alfred Andrawis. Dr. Brewer has provided me company in the high bay, and gave me valuable academic and spiritual fellowship throughout the stay. For all these good things, May God Bless Every One.

ABSTRACT

NASA-KSC has developed a mechanism to handle and insert Racks into the Space Station Logistic Modules. This mechanism consists of a Base with 3 motorized degrees of freedom, a 3 section motorized Boom that goes from 15 to 44 feet in length, and a Rack Insertion End Effector (RIEE) with 5 hand wheels for precise alignment.

During the 1993 NASA-ASEE Summer Faculty Fellowship Program at KSC, I designed an Active Vision (Camera) Arrangement and developed an algorithm to determine (1) the displacements required by the Boom for its initial positioning and (2) the rotations required at the five hand-wheels of the RIEE, for the insertion of the Rack, using the centroids of the Camera Images of the Location Targets in the Logistic Module.

Presently, during the summer of '94, I completed the preliminary design of an easily portable measuring instrument using encoders to obtain the 3-Dimensional Coordinates of Location Targets in the Logistic Module relative to the RIEE mechanism frame. The algorithm developed in '93 can use the output of this instrument also.

Simplification of the '93 work and suggestions for the future work are discussed.

TABLE OF CONTENTS

1. INTRODUCTION
2. THE RIEE MECHANISM
3. DETERMINATION OF THE COORDINATES OF THE SUPPORTS IN THE FRAME OF SCEM
 - 3.1. CONCEPT OF SCEM
 - 3.2 DESIGN OF SCEM
 - 3.3 TYPICAL EQUATIONS FOR A SUPPORT FROM THE OUTPUT SPHERICAL COORDINATES (R, θ_2, θ) , OF SCEM
4. ALIGNMENT OF RIEE ROTATION AXIS AND RACK INSERTION
5. CONCLUSIONS AND RECOMMENDATIONS
6. REFERENCES

RACK INSERTION END-EFFECTOR (RIEE) GUIDANCE

Narasimha S. Malladi, 1994 NASA-ASEE Summer Faculty Fellow,
Tuskegee University.

1. INTRODUCTION:

Towards an efficient guidance of the RACK INSERTION END-EFFECTOR (RIEE) Mechanism, a Spherical Coordinate Encoder Module (SCEM) has been designed to determine the X, Y & Z coordinates of the Rack Supports with respect to the Boom, by measuring the Spherical Coordinates of the Rack Supports relative to the Rack Interface Plate.

This work is in continuation of the '93 Summer work that resulted in the Conceptual Development of an Active Vision Alignment System (AVAS) to determine the above X, Y & Z coordinates, using a vision system attached to the Rack Interface Plate.

The X, Y & Z coordinates obtained as above, will become inputs to a program that determines the displacements required by Boom and the Handwheels of the RIEE to:

- 1) Align the RIEE relative to the Logistic Module to Prepare for Final insertion. and
- 2) Translate the Rack Rotation Axis and rotate the Rack about it for Final Insertion.

The following sections contain description of concepts, derivation of equations, the preliminary design details of SCEM and the alignment procedures for the RIEE.

2. THE RIEE MECHANISM

The RIEE is a space mechanism with 5 degrees of freedom. It has 12 links and 15 joints. It is used to align the axis of rotation of the Rack and perform the final insertion of the Rack into the Logistic Module. The Boom carrying the RIEE, has 4 degrees of freedom. Figures 1 & 2 show the RIEE in two positions as per drawing # 82K03931.

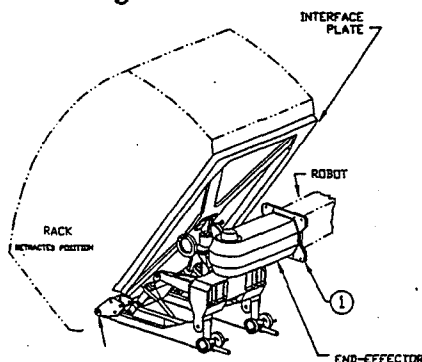


Figure 1. RIEE in Retracted Position

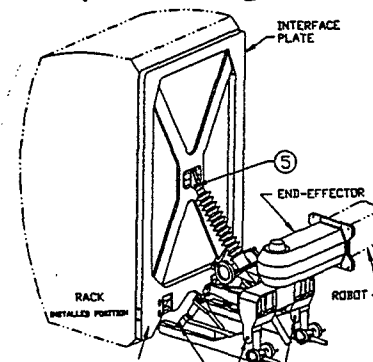


Figure 2. RIEE in Installed Position

3. DETERMINATION OF THE COORDINATES OF THE SUPPORTS IN THE FRAME OF SCEM.

To insert the rack we have to know the positions of the rack support points on the logistic module, shown as lower support points in Figure 3 below. In the following Analysis expressions are derived for the coordinates of the left and right support points by getting the spherical coordinates of the support points by scem. The figure shows typical relationship of a SCEM to a support in the yz plane of the boom coordinate system containing the RIEE. The RIEE mechanism has 2 end-effector points on the left and right sides shown by the letter E and top end-effector point P. Different views of this mechanism can be studied in the set of drawings # 89K03931. The points shown in the figure carry prefixes "R" for right and "L" for left in the discussion that follows.

RIEE MECHANISM SCHEMATIC

(Not to scale)

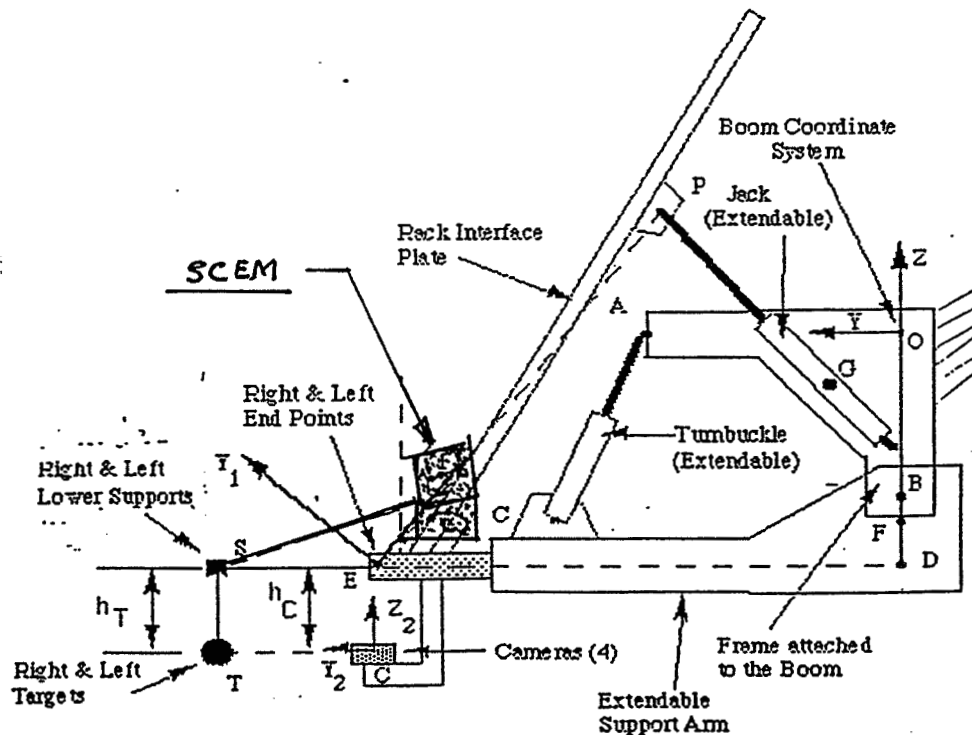


Figure 3

3.1 CONCEPT OF SCYM:

The concept of SCYM as shown in Figure 4 is provided by NASA Colleague Eduardo Lopez. It essentially contains a Wire or Tape Pool in an encasement attached to a mount with a shaft that can rotate on a rotating base. The rotating base has a shaft, whose axis is perpendicular to the shaft of the mount, rotating on a portable base. To each of the shafts of the rotating mount and the rotating base, a code wheel is attached. The encoders attached to the Rotating and the portable bases measure the rotation angles of the mount and the rotating base. The intersection of the two shaft axes form the origin of the SCYM coordinate system. The wire or tape length measured by a suitable encoder is the radial coordinate.

CONCEPT OF SCYM

Mike Brudee & Eduardo Lopez del Castillo
NASA - KSC

5/1/94

Eduardo Lopez del Castillo 5/6/94

this code wheel is attached to a roller that rotates as wire is deployed.

The wire will roll-up on a spring loaded reel (can't be seen on this figure).

- everything mounted on or above part labeled A can rotate about X-axis.
- everything mounted on or above part labeled B can rotate about Y-axis as well as X-axis

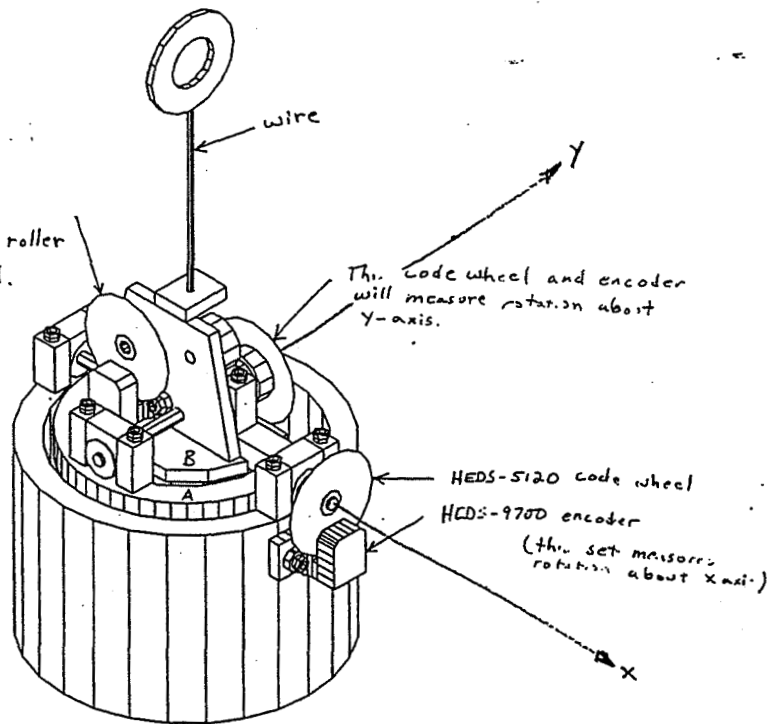


Figure 4

3.2 DESIGN OF SCEM:

Figure 5 shows the assembly drawing of the SCEM. The major parts and the material employed are listed below. The SCEM is connected to a Computer.

S. N.	Part	No. Off	Material/Part No.
01	Portable Base	1	Oil Impregnated Cast Nylon McMASTER 8664K24 (page 2487)
02	Rotating Base	1	Oil Impregnated Cast Nylon
03	Tape Mount	1	Lexan
04	Base Shaft	1	Aluminum
05	Mount Shaft	1	Aluminum
06	Cover	2	Lexan
07	Code wheel	2	HP-HEDG-6120 # U08
08	Encoder	2	HP-HEDS-9000 Option U00
09	Tape Encoder	1	NEWARK-87F6454-HOA709-001
10	Tape	1	STANLEY-12ft tape

The origin of the Spherical Coordinate System is at O, the intersection of the axes of the two rotating shafts. The angle of the tape Length is measured from the Z axis by the top encoder reading the Vertical code wheel. The angle from x axis, in the xy plane is measured by the bottom encoder reading the Horizontal Code wheel. The part drawings are not included here to conserve the space. They are submitted to NASA Colleague, Eduardo Lopez,

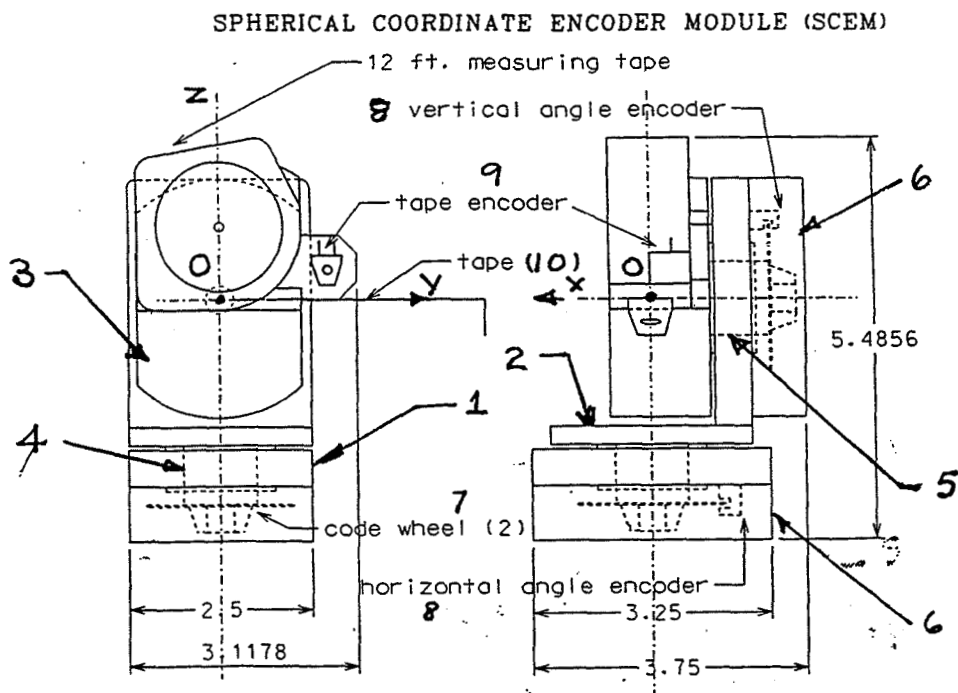


Figure 5. The assembly drawing of SCEM

3.3 TYPICAL EQUATIONS FOR A SUPPORT FROM THE OUTPUT SPHERICAL COORDINATES (R, θ_z, θ) , OF SCEM.

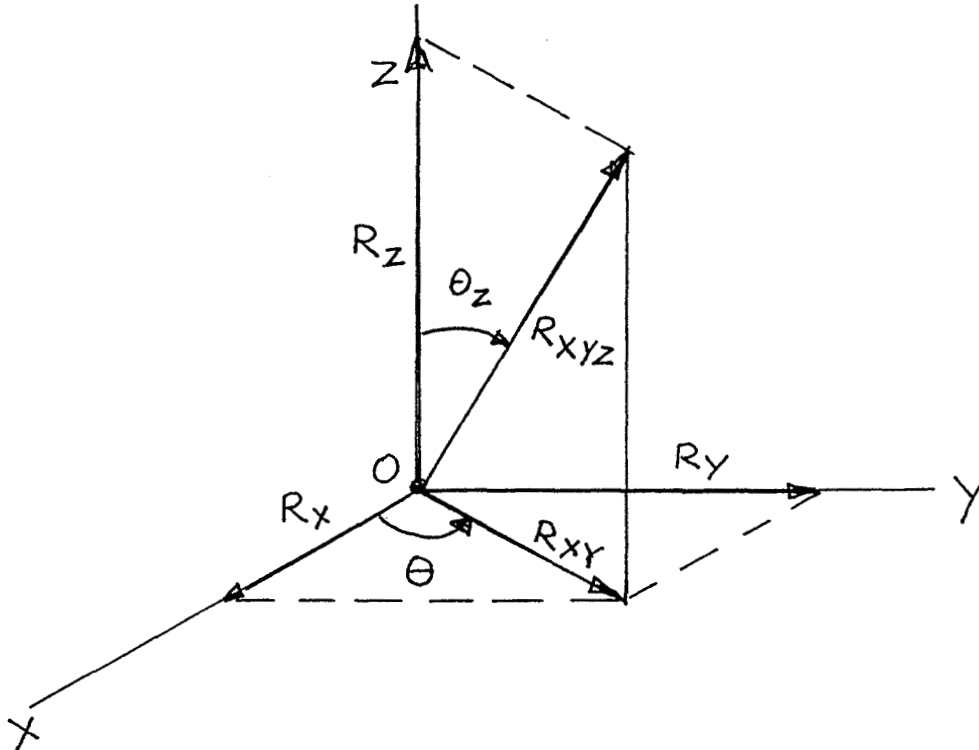


Figure 6. Spherical Coordinates, Space Vector and its components.

$R_{xyz} = | R |$; R_{xyz} is Radius of Space Vector given by the length of the tape.

$$R_{xy} = | R_{xyz} \sin \theta_z | ;$$

θ_z is the angle of R_{xyz} from z axis.
 θ_z is given by the Vertical Code Wheel.

$$R_x = R_{xy} \cos \theta ;$$

θ is the angle of R_{xy} from x axis.
 θ is given by the Horizontal Code Wheel.

$$R_y = R_{xy} \sin \theta$$

$$R_z = R_{xyz} \cos \theta_z$$

The x, y, z coordinates of the supports in the Boom Coordinate System are obtained by applying further transformations, that were discussed in detail in my 1994 NASA/ASEE report available with my NASA Colleague Eduardo Lopez.

4. ALIGNMENT OF RIEE ROTATION AXIS AND RACK INSERTION

Figure 7 below, shows the views of the left and right support points LS and RS with their centerpoint CS and the RIEE rotation axis points LE and RE with their centerpoint CE before and after alignment.

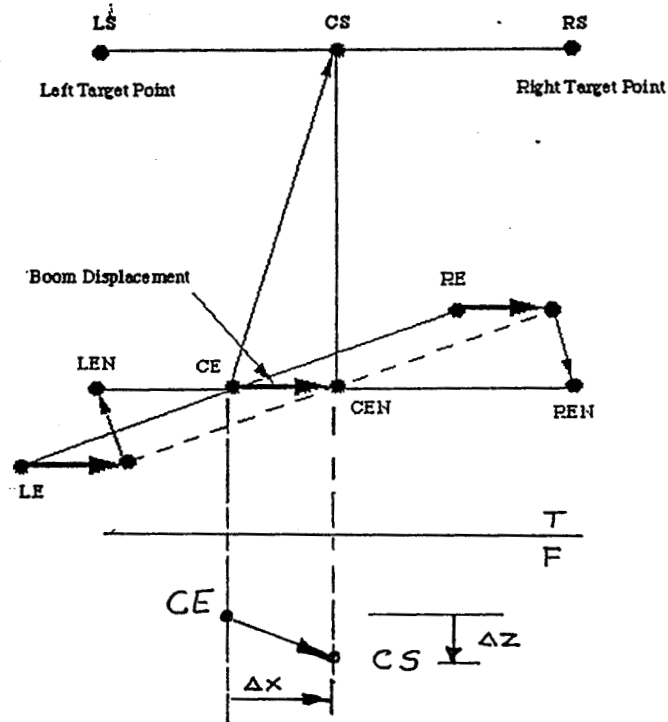


Figure 7. RIEE Rotation Axis Alignment

The following are the steps for the RIEE Alignment and Rack Insertion.

1. The Centers of Module Supports and RIEE Ends are made to have same X and Z coordinates by moving the boom.
2. Ends of RIEE are moved so that the Module Support Axis and RIEE Rotation Axis are Parallel.
3. Check by Repeating Measurements and correct by Repeating 1 & 2.
4. Move the RIEE so that the support and RIEE rotation axes are at proper distance.
5. Rotate the Rack on the RIEE rotation axis, gently into final position.

The above steps were discussed in the 1994 report with typical numerical values.

5. CONCLUSIONS AND RECOMMENDATIONS:

In this report the design of a Spherical Coordinate Encoder Module (SCEM), the equations for the rectangular coordinates of the Supports measured by SCEM, and alignment procedures were discussed. Equations derived in last years report for the alignment will also hold good for alignment with SCEM. The sperical targrts (see Figure 3) suggested last year for the vision system AVAS, can be simplified as Colored Dots.

Both SCEM and AVAS will be useful in a variety of Payload Transfer applications. The author, with 8 years of his US Industry Design and Development Experience is willing to help on the hardware and software Prototype Development projects of these systems.

6. REFERENCES:

A. KSC drawing set # 82K03931 and associated drawings.

B. Narasimha S. Malladi, "RACK INSERTION END-EFFECTOR (RIEE) AUTOMATION", 1993 NASA/ASEE Summer Faculty Report to KSC.

1994 NASA/ASEE SUMMER FACULTY FELLOWSHIP PROGRAM

JOHN F. KENNEDY SPACE CENTER
UNIVERSITY OF CENTRAL FLORIDA

111764
351498
513-51
33973
A-30

ETHYLENE DYNAMICS IN THE CELSS BIOMASS PRODUCTION CHAMBER

PREPARED BY:	Dr. Allen L. Rakow
ACADEMIC RANK:	Associate Professor
UNIVERSITY AND DEPARTMENT:	Colorado State University Department of Agricultural and Chemical Engineering
NASA/KSC	
DIVISION:	Biomedical Operations and Research
BRANCH:	Biological Research and Life Support
NASA COLLEAGUE:	John Sager
DATE:	August 24, 1994
CONTRACT NUMBER:	University of Central Florida NASA-NGT-60002 Supplement: 17

ACKNOWLEDGEMENTS

I am greatly appreciative of the support which I received from everyone in the CELSS group. Their dedication and enthusiasm was an inspiration to me and made my task extremely pleasant. In particular, John Sager , Gary Stutte , and Ray Wheeler made it all possible. John helped me to define the problem and Gary went out of his way to ensure that I got the data and information necessary for model development. Ray, along with Gary, spent many hours discussing BPC characteristics. Barbara Peterson collected and analyzed the GC data and Jim Bledsoe and Russ Fortson helped with control room data format and chamber components. Last, but not least , Callen Coiner made it extremely pleasant to walk through the door each morning.

ABSTRACT

A material balance model for ethylene was developed and applied retrospectively to data obtained in the Biomass Production Chamber of CELSS in order to calculate true plant production rates of ethylene. Four crops were analyzed ; wheat, lettuce, soybean, and potato. The model represents an effort to account for each and every source and sink for ethylene in the system. The major source of ethylene is the plant biomass and the major sink is leakage to the surroundings. The results , expressed in the units of ppb/day, were converted to nl of ethylene per gram of plant dry mass per hour and compare favorably with recent glasshouse to belljar experiments.

SUMMARY

During crop production (lettuce, wheat, soybean and potato) in the CELSS Biomass Production Chamber (BPC) ethylene can accumulate in the air space and affect plant viability. The chief source of ethylene is the plants which reside in plastic trays containing circulating nutrient solution and the main sink is chamber leakage. There are a variety of other sources and sinks, however, they are small in comparison with the plants and leakage. Accordingly, a material balance model was developed and applied to historical data from the BPC. The data consists of chamber concentration in ppb plotted against time in days. Each plot was curve fitted to obtain an expression for concentration as a function of time. The first derivative was used in the model as the accumulation rate. Production rates in ppb/day were then calculated by adding time averaged leakage rates to the accumulation rate. The time averaging of leakage rates poses a problem in calculating a continuous production rate because some of the leakage is discrete, e.g., door openings and closings. For lettuce the peak production rate was approximately 30 ppb/day whereas wheat had a peak rate of about 80 ppb/day. These numbers were converted to nl/gram-dry mass/hr (46 for lettuce and 15.6 for wheat) and compare favorably with recent glasshouse to bell jar experiments for lettuce and wheat. In addition a dosing experiment was conducted under static conditions wherein 60 ml of pure ethylene was injected into the upper chamber and ethylene concentration was tracked for 18 hours. The ethylene level varied considerably in the 400-700 ppb range. For perfect mixing a level of 1000 ppb was expected. Several explanations can be put forth to account for the lower than expected value. One in particular should be further investigated, i.e., dispersion rates in the BPC under both static and dynamic conditions could shed light on the existence of concentration gradients in the system and the validity of the perfect mixing assumption.

TABLE OF CONTENTS

I.	Introduction
II.	Material Balance Model
III.	Ethylene Sources and Sinks
3.1	Plants
3.2	Materials
3.3	Ambient Air
3.4	Gas Cylinders
3.5	Nutrient Solution
3.6	Removal Systems
3.7	Dosing
3.8	Sampling
IV.	Analysis
V.	Discussion of Results
VI.	Conclusions and Recommendations
VII.	References

LIST OF ILLUSTRATIONS

Figure

1	Ethylene Sources and Sinks
2	Static Leakage Test Data
3	Dynamic Leakage Test Data
4	Door Opening Leakage Test Data
5	Dose Test
6	Crop Data
7	Lettuce Concentration Data
8	Lettuce Production Rate
9	Wheat Concentration Data
10	Wheat Production Rate
11	Potato Concentration Data
12	Potato Production Rate
13	Soybean Concentration Data
14	Soybean Production Rate
15	Crop Drymass Data

I. Introduction

Ethylene is an important plant hormone which is produced and possibly consumed by plants during their growth cycle. There has been concern over its potential detrimental effect on plant health in closed systems where appreciable levels can build up in the air space of a plant production chamber. For example, parts per billion to parts per million levels can cause one or more of the following: leaf epinasty, flower abortion, stem swelling, adventitious roots, leaf chlorosis, or fruit ripening. Should NASA decide to control ethylene levels in future CELSS (Closed Ecological Life Support Systems) development efforts, or attempt to measure plant production rates of ethylene in closed systems, it will be imperative to account for all ethylene flows in the system. In other words a material balance model is of paramount importance to ethylene quantification. The work described herein is an attempt to develop a working model to include all sources and sinks in the BPC (Biomass Production Chamber).

The material balance is based on the principle of conservation of mass and is applied to the air space in the BPC to compute the transient concentration of ethylene assuming a well mixed chamber. The main sources and sinks in the chamber are the plants, solid materials, and any leakage from or to the chamber. The solid materials can be both sources and sinks, since ethylene can be adsorbed on surfaces as well as outgassed from plastics and sealants. Leakage from or to the chamber has three basic routes: door openings, incomplete sealing of the chamber, and HVAC seals. Experiments were conducted to establish leakage rates for these three modes and the results are employed in the model calculations. In addition, a literature search on off-gassing and binding characteristics of construction materials was initiated to generate rates for the model calculations. Experiments were also conducted in the BPC during which ethylene was measured using gas chromatography. In these experiments there were no plants present in the chamber in order to determine ethylene-material interactions. This information is useful in building the materials component of the model.

With a good understanding of leakage and material interactions, the model was used to analyze previous data obtained in the BPC for lettuce, potato, wheat, and soybean tests. The results are interpreted and discussed in view of ethylenes role in plant physiology.

II. Material Balance Model

A typical plant growth experiment conducted in the BPC includes the measurement (Gas Chromatography with Photoionization Detector through sampling port) of ethylene concentration (ppb) in the chamber air space at daily intervals. Although concentration gradients can exist in the chamber, during these experiments the air handling units were operational and good circulation was maintained (~ 400 cubic meters/min for 113 cubic meters of total BPC volume). Therefore, it is assumed that the chamber air space is perfectly mixed. This means that any ethylene produced is instantaneously distributed throughout the air space. It is also assumed that there are no chemical reactions taking place within the air space itself which could either produce or consume ethylene. If one can account for all sources and sinks of ethylene in the BPC other than from or to the plants, and if the accumulation rate is measured (from concentration vs. time data), then the plant production rate can be obtained by difference.

The general starting equation in words is : Rate of Accumulation = Rate of Input - Rate of Output + Rate of Generation - Rate of Consumption. If the right hand side is negative then Decumulation occurs and the ethylene concentration decreases with time. Since there is no generation or consumption within the air space the word equation reduces to Rate of Accumulation = Rate of Input - Rate of Output. The input and output terms are the various sources and sinks in the BPC and the accumulation term using the perfect mixing assumption is:

$$\text{Accumulation} = \frac{VdC}{dt}$$

where V is the volume of the chamber air, C is the concentration of ethylene in ppb, and t is time in days. In the following section expressions are developed for the various input and output terms in order to complete the balance so that the production rate can be calculated.

III. Ethylene Sources and Sinks

The sources and sinks are depicted in Figure 1 and are described in detail in this section.

3.1 Plants

The production of ethylene by plants and other microorganisms was first observed sixty years ago(1). However, there is a dearth of data on whole, unadulterated plants in closed chambers. Corey et al.(2) recently measured ethylene evolution by plants grown in closed environments. Lettuce and wheat were grown in a glasshouse and then transferred to sealed bell jars for measurement of ethylene. For lettuce the production rate ranged from 20 to 200 nl/g dm/hr, whereas wheat ranged from 5 to 30 nl/g/hr. Care must be taken in comparing these results with the BPC, since the plant mass to head volume ratio in a bell jar is different from the ratio in the BPC. (The BPC has a high volume to plant area ratio of ~5.6:1)

3.2 Materials

There are two mechanisms for material exchange; outgassing and sorption. In a Lockheed study (3) the steady-state outgassing rate of ethylene for all Space Station equipment was estimated to be 1.2 mg/day. On a per mass of non-metallic material basis this rate is 0.000214 mg ethylene/kg/day; however, it is based in part on tests conducted at 322 degrees Kelvin which is about 30 degrees higher than BPC temperatures. Even if the BPC materials outgassed at this rate it would be less than 1 ppb/day. According to Johnson (4) , however, there should be negligible outgassing in the BPC since the major plastic components are PVC and ABS, not polyethylene. Also, Johnson claims that ethylene is outgassed in significant amounts from polymers only at highly elevated temperatures (with other degradation products). Therefore, in the material balance for the BPC (substantial plant mass and minimal outgassing conditions) outgassing will be neglected.

With regard to sorption , an experiment was conducted in the BPC which involved the measurement of ethylene concentration in the head space , with no plants present and the air handler in the off mode. The leakage rate under these conditions was determined to be 1% per day (see Figure 2 and section 3.3), therefore, the exchange of ethylene between the air space and any material surfaces in the biochamber could be ascertained. Over an 8-hour period under the static conditions of the chamber the ethylene concentration remained fairly constant. This suggests that the material-gas interface may have been saturated with ethylene. In a related experiment conducted by Dubay (5) 7500 ng of ethylene were injected into a 65-liter chamber consisting of a PVC tray covered with plexiglass. At 6 hours an equilibrium was established between the air space and surfaces of the chamber such that the concentration of ethylene in the air space was 47 ppb. The difference between the amount injected and the amount in the air space divided by the estimated surface area of the chamber yields 3237 ng ethylene/ square meter of surface adsorbed at equilibrium. In order to establish whether the surface could have adsorbed additional molecules, it would have been necessary to inject more ethylene into the chamber after

the 47 ppb equilibrium. However, this result is a good upper limit for the amount of ethylene adsorbed by the plastic in the BPC since 47 ppb is sufficiently higher than the average concentration in the BPC during a typical plant cycle. Also, based on the work of Kamiya et al. (6), lower surface concentrations can be calculated for ethylene sorbed by polybutadiene.

Using a value of 70 square meters for the total plastic air interface in the upper chamber the surface can sorb about 3 ppb. Since a typical plant growth cycle is a minimum of 30 days, the amount adsorbed averaged over the entire plant cycle is less than 0.1 ppb/day. Thus sorption will be neglected in this study since ethylene production rates are subsequently shown to range from a few ppb/day all the way up to 80 ppb/day.

3.3 Ambient Air

There are three conditions that exist in the BPC which have a major bearing on leakage of air from the system when plant growth occurs. In the normal mode of operation during plant growth, the chamber door is closed and sealed and sealant is applied to all necessary areas such that the only leakage route is most probably through the air handling unit. The other two modes are a closed, unsealed chamber and an open chamber resulting from an open door. In an average plant growth cycle the normal mode is maintained for 98% of the time. The closed, unsealed state is estimated to exist for 1.6% of the cycle and the door is in the open state 0.4% of the time. In order to measure the leakage rate for each of these modes experiments were conducted to track the concentration of injected carbon dioxide over time. For a well mixed air space the rate of carbon dioxide decline should equate with the leakage rate. The carbon dioxide decay (Figures 3 and 4) yields the following rates: closed and sealed-10% of the chamber volume per day; closed and unsealed-77%; and open chamber-13,100%. Linear combination of these rates results in an overall leakage rate of 63% of the chamber volume per day. It is this rate which will be used in the material balance model even though it is an average, continuous rate, i.e., leakage occurs in a non-continuous manner during 2% of the cycle.

3.4 Gas Cylinders

Carbon dioxide is metered into the BPC on a daily basis to maintain a constant level for plant growth. A typical rate is approximately 200 liters per day from a gas cylinder. According to Eastwell et al. (7), carbon dioxide cylinders contain 20 ppb of ethylene although no ethylene was found in cylinders used in the BPC at the 10 ppb detection limit. Twenty ppb would introduce about 0.1 ppb/day of ethylene to the BPC upper chamber. Therefore, this source shall be neglected in this study.

3.5 Nutrient Solution

Ethylene is soluble in water so the nutrient solution that is circulated through the plant trays represents a sink for ethylene. The Henry's Law constant for ethylene at 0 degrees C is 5,520 atm/mole fraction. If the concentration of ethylene in the air space were 100ppb then the equilibrium mole fraction of ethylene in water would be 0.0000000002. For 250 liters of

nutrient solution (14,000 gmoles water) the water would hold 28×10^{-8} gmoles ethylene. At STP this corresponds to 627×10^{-8} liters of ethylene. The chamber volume is 56,000 liters, therefore, the total sink would be 0.1 ppb. Since the nutrient solution (contains 100 liters of condensate) is recycled and has a lower capacity for ethylene than pure water it represents a negligible sink for ethylene and is ignored in this study.

3.6 Removal Systems

There are a variety of contaminant control methods such as catalytic convertors, activated carbon adsorption and bypass configurations. Currently, potassium permanganate is used to remove ethylene from the BPC, however, during the experiments to measure ethylene production rates, it was not employed so removal is not included in the material balance calculations. If a removal system is employed during the growth cycle it can be incorporated into the material balance if a rate expression is available for the method employed. Removal would then behave as a sink in the balance equation.

3.7 Dosing

The upper chamber of the BPC was maintained in a closed, sealed state with the air handlers off after 60ml of pure ethylene was injected by hand into the air space. A small circulating fan was operated to disperse the gas. Ethylene level was then measured by GC with photoionization detector. Ethylene fluctuated between 400 and 700 ppb during an 18 hour period (Figure 5). If all the ethylene injected were uniformly dispersed in the BPC a concentration of 1000 ppb would be expected (even higher levels could be expected if the injected ethylene didn't reach the ducts of the air handler units). Perhaps some ethylene escaped in exiting the BPC after injecting the ethylene and/or the fan was inadequate for dispersion purposes resulting in stagnant pockets of undiluted ethylene. Based on the previous calculation for the sorption sink, it is unlikely that the missing ethylene sorbed to the surfaces inside the BPC.

Dosing did not occur during the experiments (historical data) presented in Figure 6 so it is not included in the material balance calculation in this study. It could be included in future experiments and calculations as a spike, or instantaneous change in the chamber concentration if the dose instantaneously disperses throughout the chamber. Then the type of analysis outlined in the next section can be applied to plant response.

3.8 Sampling

The chamber air is continuously sampled for carbon dioxide. The sampling rate is .75 liters per minute and the ethylene, in all likelihood, is completely consumed as it hits the platinum catalyst within the sampler at high temperature. This rate is equivalent to 1.9% leakage and will affect the production rate by about 0.4 ppb/day on average. It is not included in the analysis, but could easily be incorporated by adjusting the leakage rate.

IV. Analysis

The objective is to calculate ethylene production rates for different crops in the BPC. The first step in the calculation involves a curve-fit of the concentration vs. time data for different crops in order to develop an expression for the accumulation rate (proportional to the derivative of the curve). The leakage rate can then be added to the accumulation rate to yield the production rate. The data to be analyzed is presented in Figure 6.

The first step in the analysis involved an eyeball smoothing of the data in Fig.6 followed by an equation fit to the smoothed curve using Sigma Plot. An expression for the first derivative of the equation was then calculated and used to compute the accumulation rate for different times. Then the leakage rate expression was added to the accumulation rate to give the instantaneous production rate during the plant growth cycle. The following is an example for lettuce:

For lettuce the production rate is assumed to be first order in C(ppb), i.e., production rate (P) is equal to a constant times the concentration of ethylene at any time, t(days) , i.e., $P=k C/V$. The leakage rate (L) is also first order, i.e., $L=.63 C$, where $V=56,000$ liters (upper chamber volume). The material balance equation for lettuce then becomes

$$V \frac{dC}{dt} = kC - .63VC$$

or , dividing both sides by V:

$$\frac{dC}{dt} = (k/V - .63) C$$

If we let $a=(k/V-.63)$ and if at time zero $C=1$ ppb then $C= \exp(a t)$.

This last equation is used to fit the data with $a= 0.1235$ giving the best fit(Fig.7). The value of a from the curve fit can now be used to solve for the production rate constant, k. Then at any time t the production rate in ppb/day can be computed simply by multiplying k/V by the concentration at t. The results for four different times are

t, days	P, ppb/day	L, ppb/day
0	.75	.63
10	.85	.71
20	8.9	7.5
30	30.5	25.5

and are plotted in Figure 8.

Similar computations were made for the three other crops and the results for these rates are presented in figures 9 through 14. For any crop as long as the production rate is greater than the leakage rate accumulation occurs and the concentration rises in the chamber. When P is equal to L the concentration remains constant and when L becomes larger than P the concentration declines.

V. Discussion of Results

It is important to keep in mind that the leakage rate was taken to be continuous, i.e., any sudden leakage (e.g., door opening) was distributed uniformly over the entire growth cycle. Sudden leakage, such as a door opening for one minute, can cause a 10% drop in chamber concentration and may explain some of the variation in the concentration verses time data , especially for wheat. Therefore, at certain times during the cycle the production rate may have been higher or lower (perhaps even negative, i.e., the plants could have consumed ethylene during a period of declining concentration or may even have sorbed ethylene) than the calculated values. On the other hand, if ethylene production is not dependent on concentration in the BPC, i.e., if it correlates with plant growth in an independent manner , then the leakage rate will not affect the production rate. For this reason it would be desirable to conduct an experiment at different continuous leakage rates , to determine any dependency. Also, it is desirable to avoid door openings for as long a period as possible (e.g., 7-10 days for wheat as the peak is approached) to reduce concentration variations.

The results for ethylene production can be converted to peak rates per dry biomass and compared with other data on ethylene production. Figure 15 shows the dry biomass for the different crops. The peak value for lettuce is about 3 kg of dry mass for the total of upper and lower biochambers. Therefore the upper value is taken to be 1.5 kg of drymass, i.e., one half of the total. At the peak lettuce is producing 30 ppb/day or 1,680,000 nl/day. This yields a value of 46 nl/g dm /hr , which is in the range of Corey's (2) data. Similarly, for wheat a value of 15.6 nl/g/hr is obtained which also falls within Corey's range. Since Corey found rates as high as 200 nl/dryg/hr for lettuce , this might suggest that the glasshouse to bell jar experiments were more stressful to the crop and more ethylene was produced accordingly.

VI Conclusions and Recommendations

The ethylene production rates calculated here are in good agreement with the limited closed system data in the literature. Whether ethylene production correlates best with plant growth and is independent of concentration in the BPC or whether a concentration dependent kinetic model (e.g., first order) best describes the system remains an open question. This question might be resolved by conducting experiments at different continuous leakage rates as previously mentioned or by dosing the chamber. In a dose experiment, concentration independence (plant biomass correlation) would be established if the production rate is unaltered by injection of ethylene. However, in the dose experiment where 60 ml of pure ethylene was injected into the BPC, there were problems in accounting for all the ethylene injected. Therefore, it would be desirable to perform dispersion experiments, perhaps using solid carbon dioxide, to establish diffusional patterns in the BPC to determine whether concentration gradients exist. This could be done in both the static and dynamic modes (air handlers on) to confirm the ideal mixing assumption of the model. If ethylene can be injected and accounted for in the dynamic mode then a dose experiment could resolve the concentration dependency question.

VII References

- 1) Abeles , F.B. , P. W. Morgan , and M. E. Saltveit, Jr. Ethylene in Plant Biology. 2nd Edition. Academic Press. 1992.
- 2) Corey K. A. , Z. Y. Tan , R. M. Wheeler , and A. V. Barker. Ethylene Evolution By Plants Grown in Closed Environments. submitted to Journal of Life Support and Biosphere Sciences.
- 3) Lockheed Missiles and Space Company. Development of a Preprototype Trace Contaminant Control System. NASA Contract NAS 9-14897. March 31, 1977.
- 4) Johnson, H. Personal Communication from NASA WSTF. July, 1994.
- 5) Dubay D. T. Gaseous Emissions From Plants in Controlled Environments . NASA/ASEE Summer Faculty Fellowship Program Report. KSC. 1988
- 6) Kamiya, Y, K. Terada , K. Mizoguchi, and Y. Naito. Sorption and Partial Molar Volumes of Organic Gases in Rubbery Polymers. Macromolecules. Volume 25. 1992. pp4321-4324
- 7) Eastwell K. C. , P. K. Bassi , and M. E. Spencer. Comparison and Evaluation of Methods for the Removal of Ethylene and Other Hydrocarbons from Air for Biological Studies. Plant Physiology. Vol. 62. 1978. pp. 723-726.

Ethylene Sources and Sinks

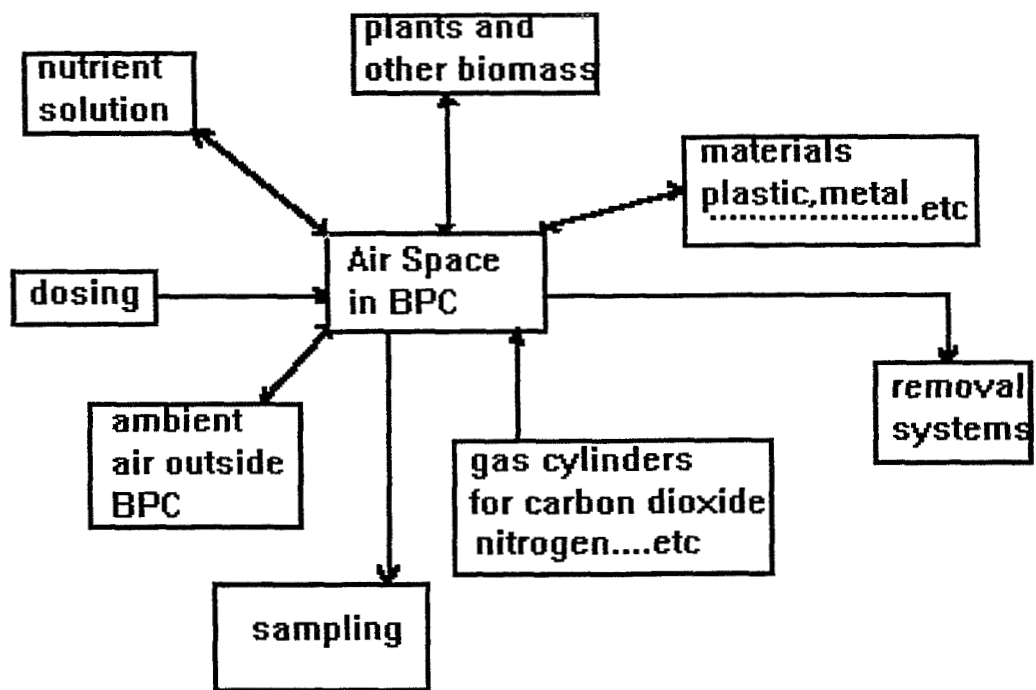


Figure 1

Upper Chamber Multivariate Trends
20Jun94 12:00 - 21Jun94 16:00

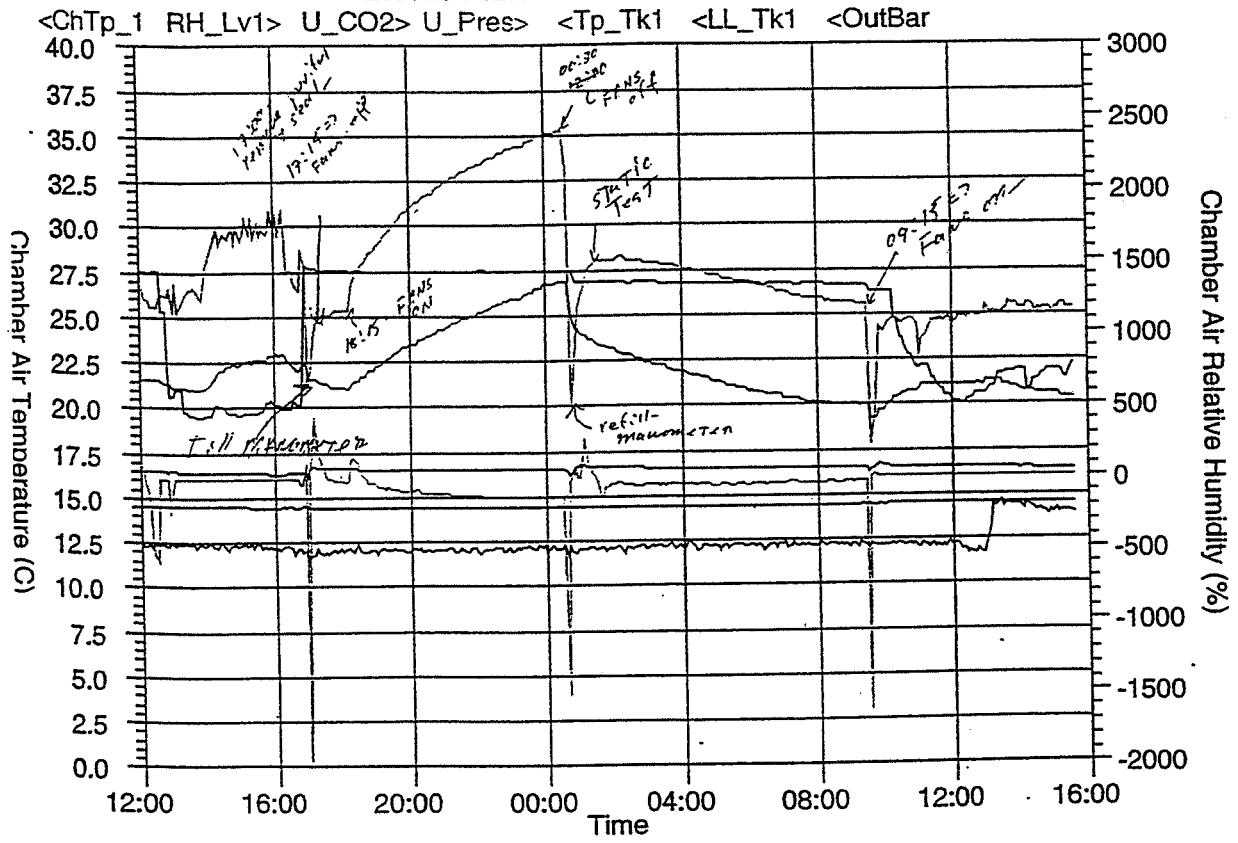


Figure 2

Upper Chamber Multivariate Trends
 17Jun94 12:00 - 21Jun94 00:00

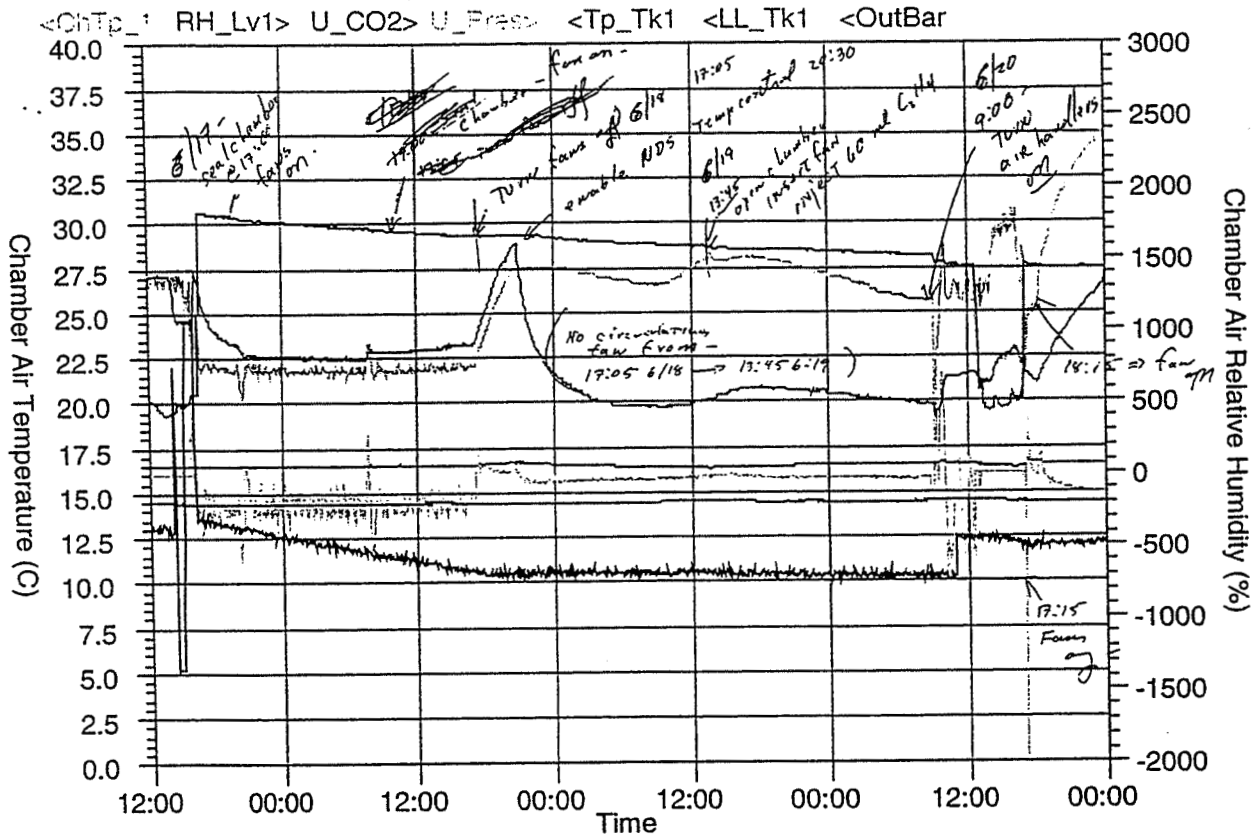


Figure 3

Chamber Air Carbon Dioxide Concentration
29Jun94 11:10 - 29Jun94 17:10

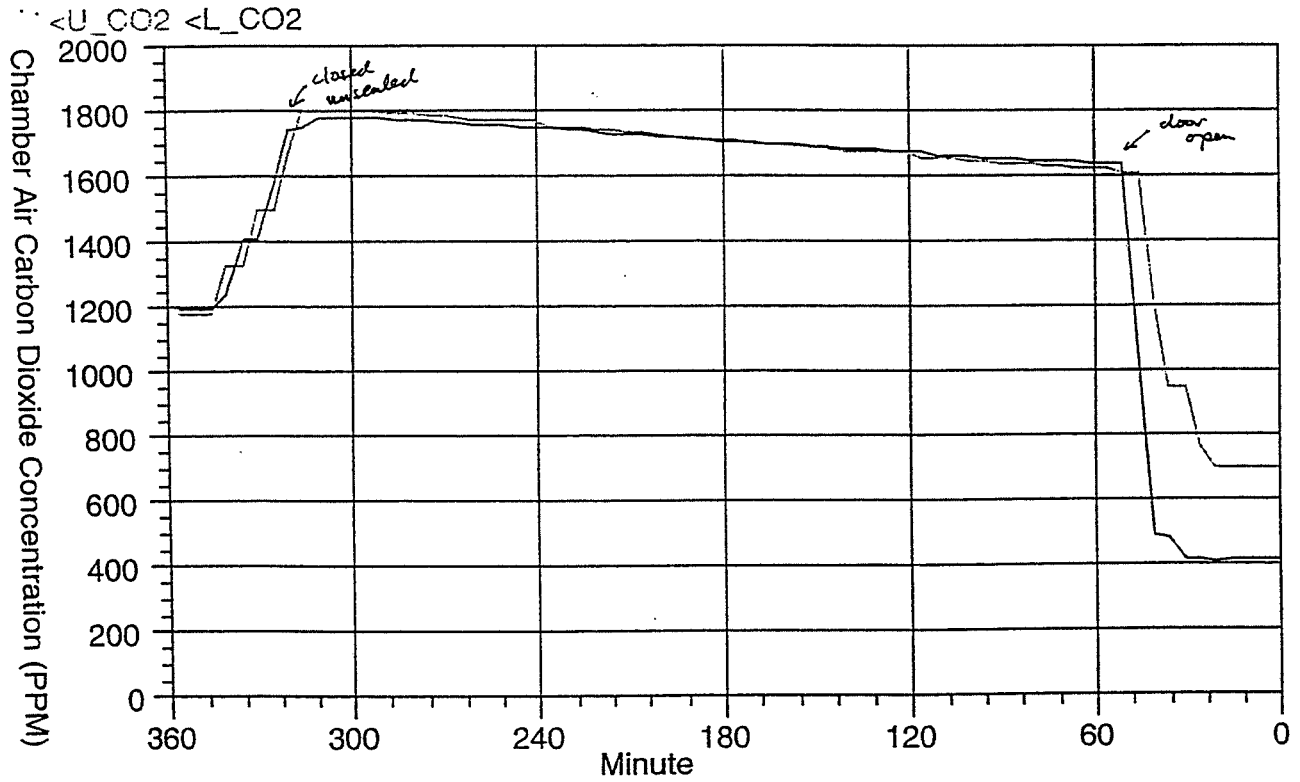


Figure 4

ethylene concentration in BPC
dose test(60ml) 6/19/94

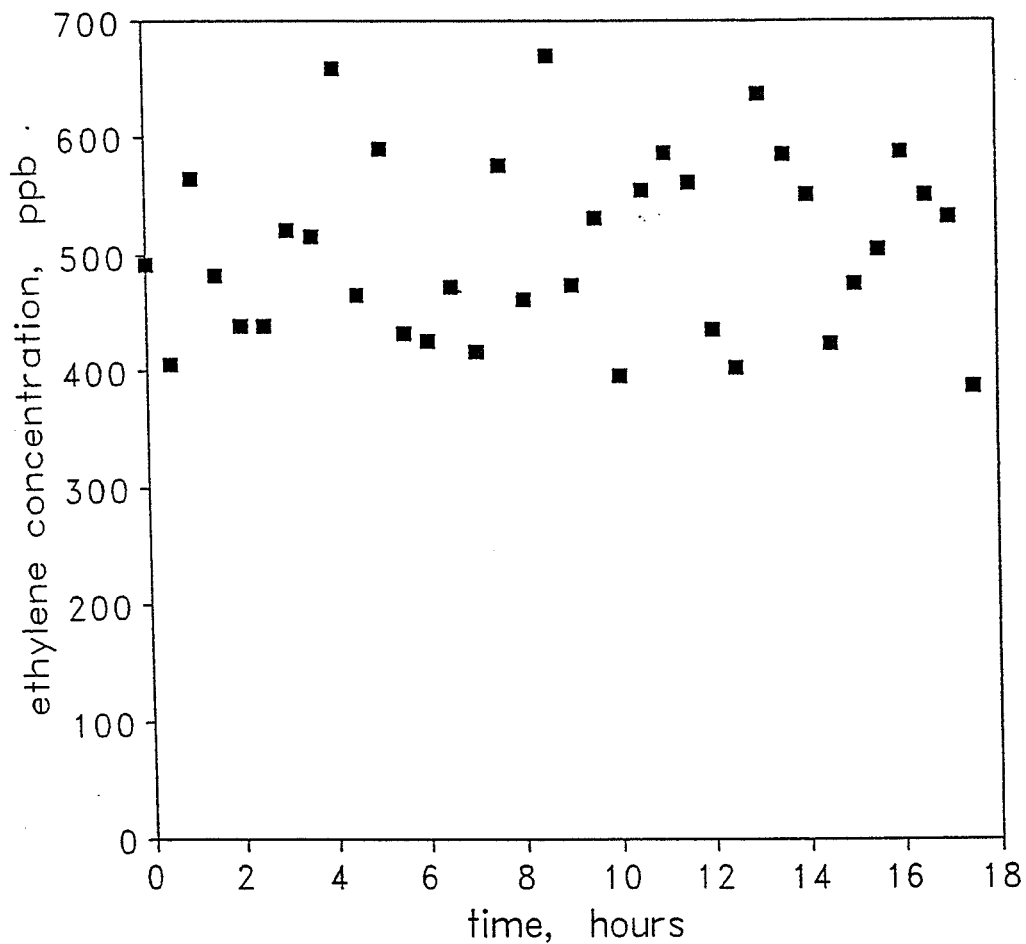


Figure 5

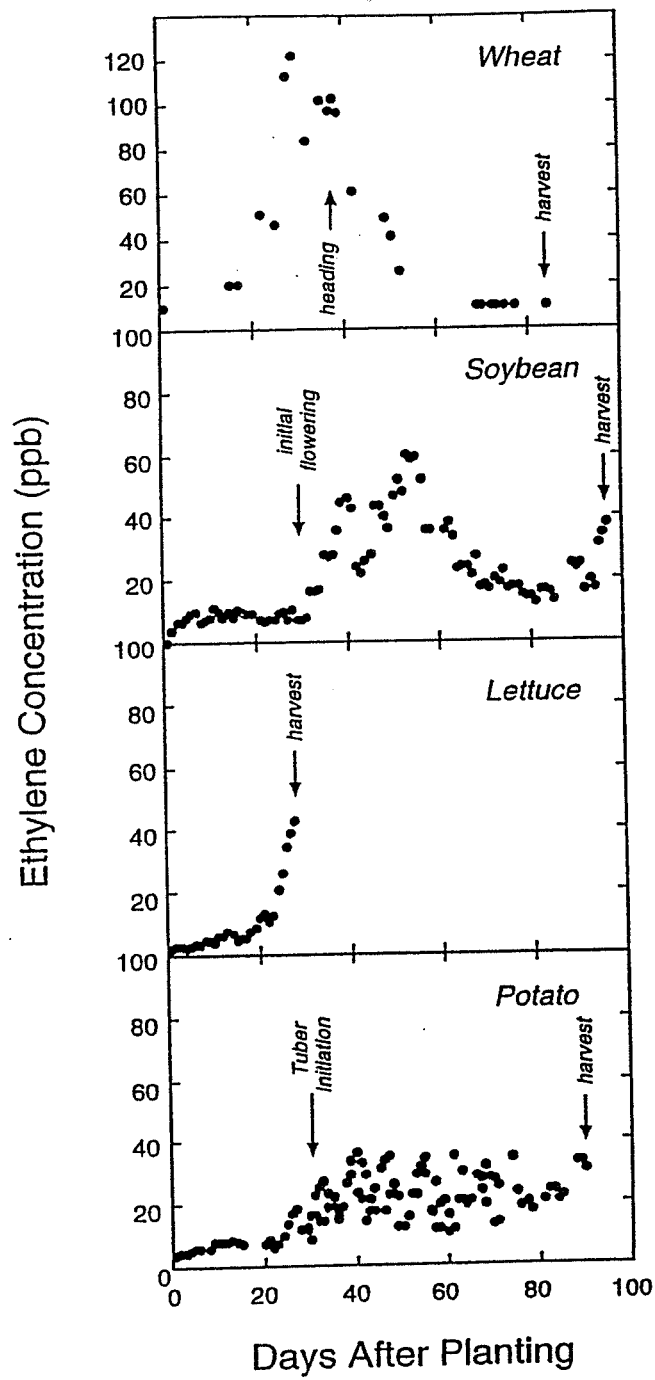


Figure 6

Ethylene Concentration in BPC (Lettuce)

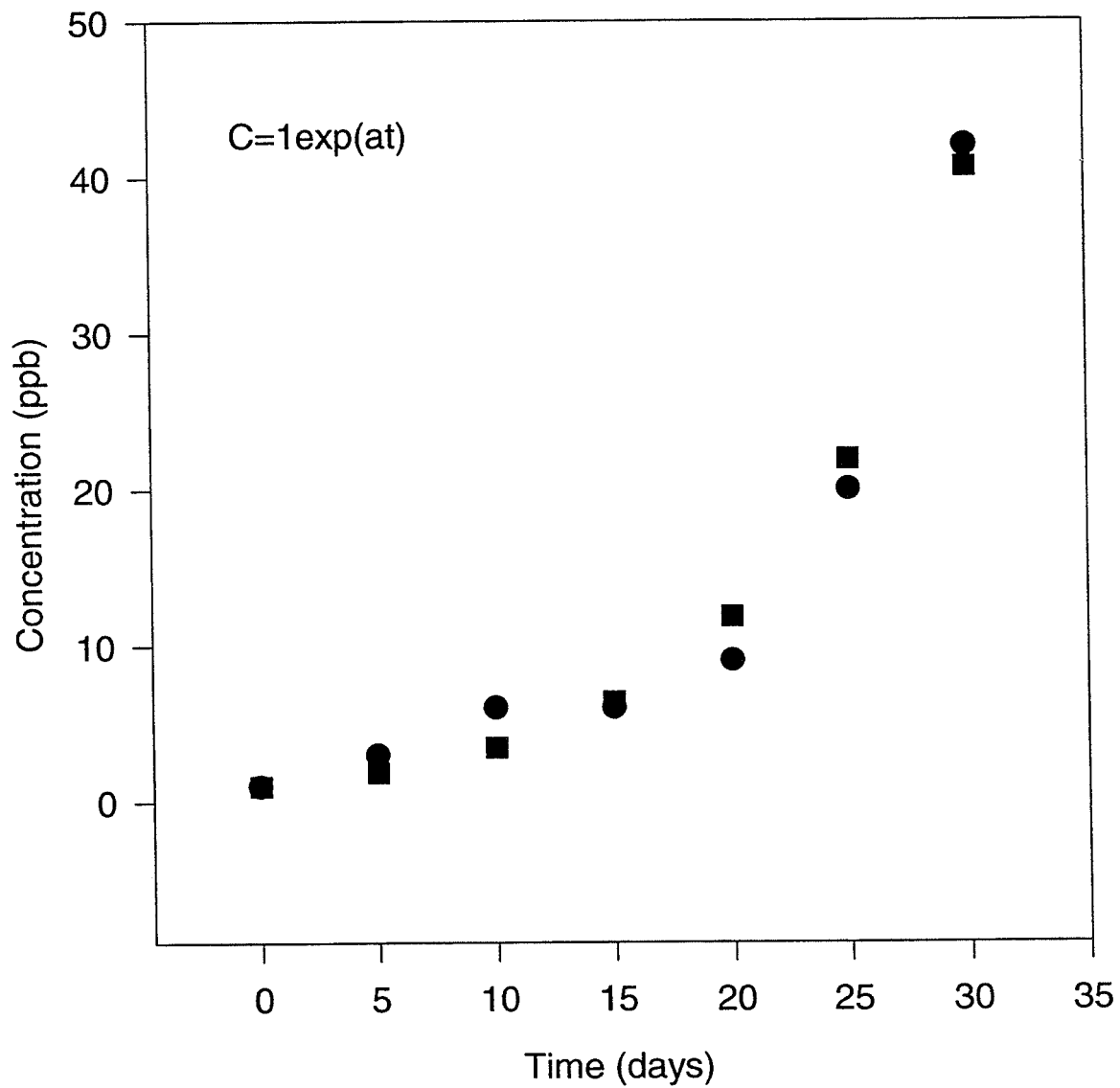


Figure 7

Ethylene Production Rate (Lettuce)

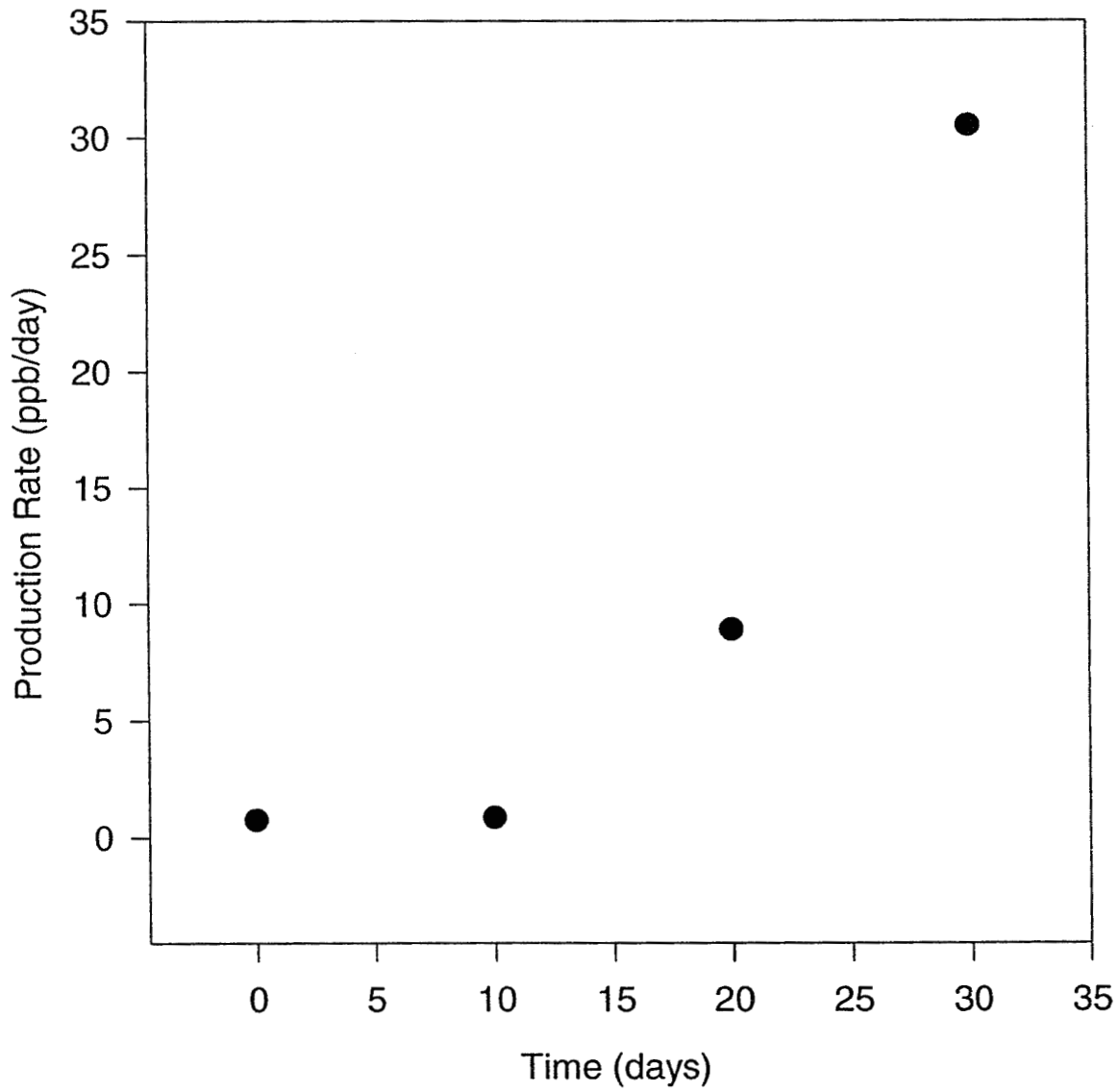


Figure 8

Ethylene Concentration in BPC (Wheat)

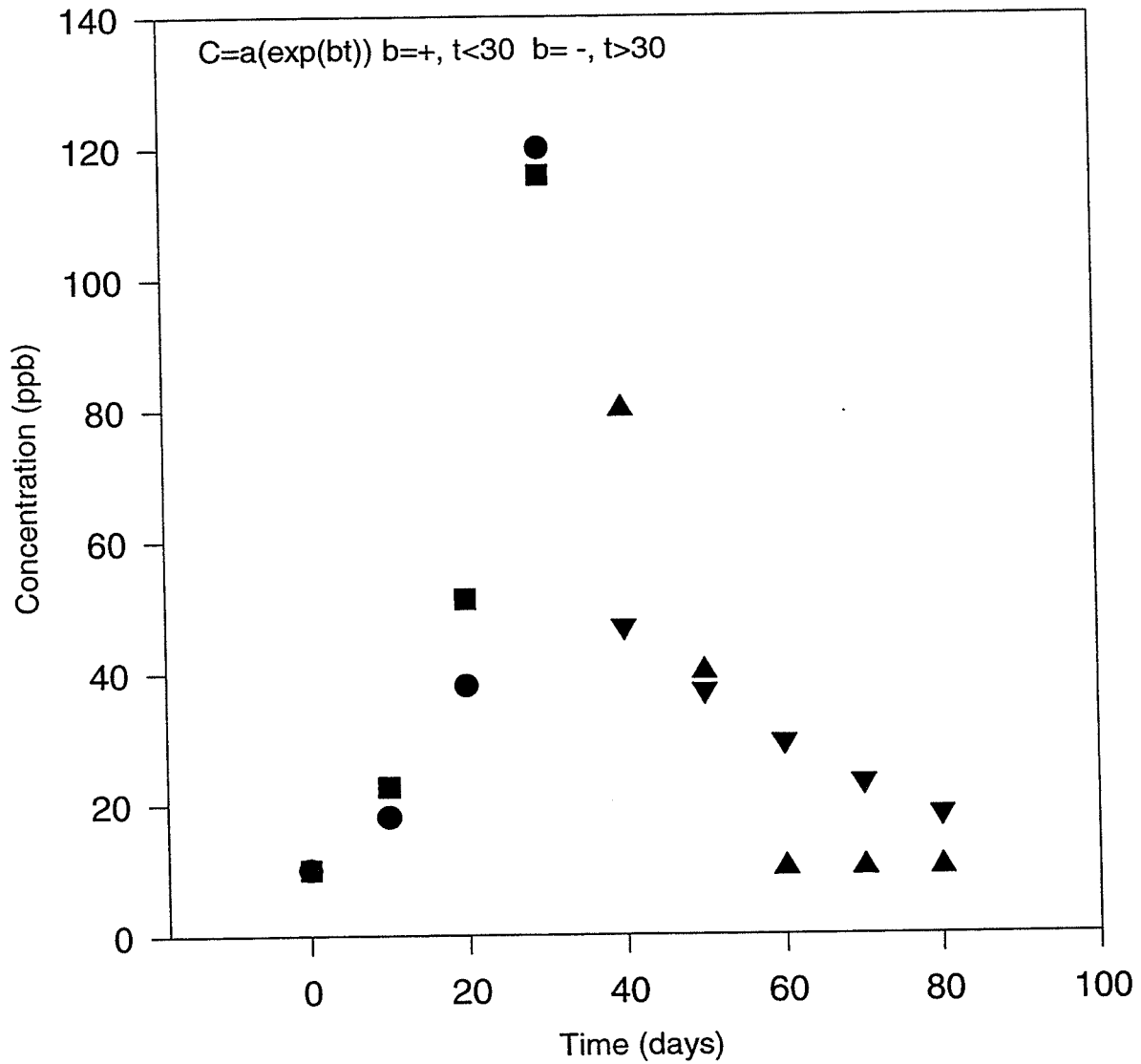


Figure 9

Ethylene Production Rate (Wheat)

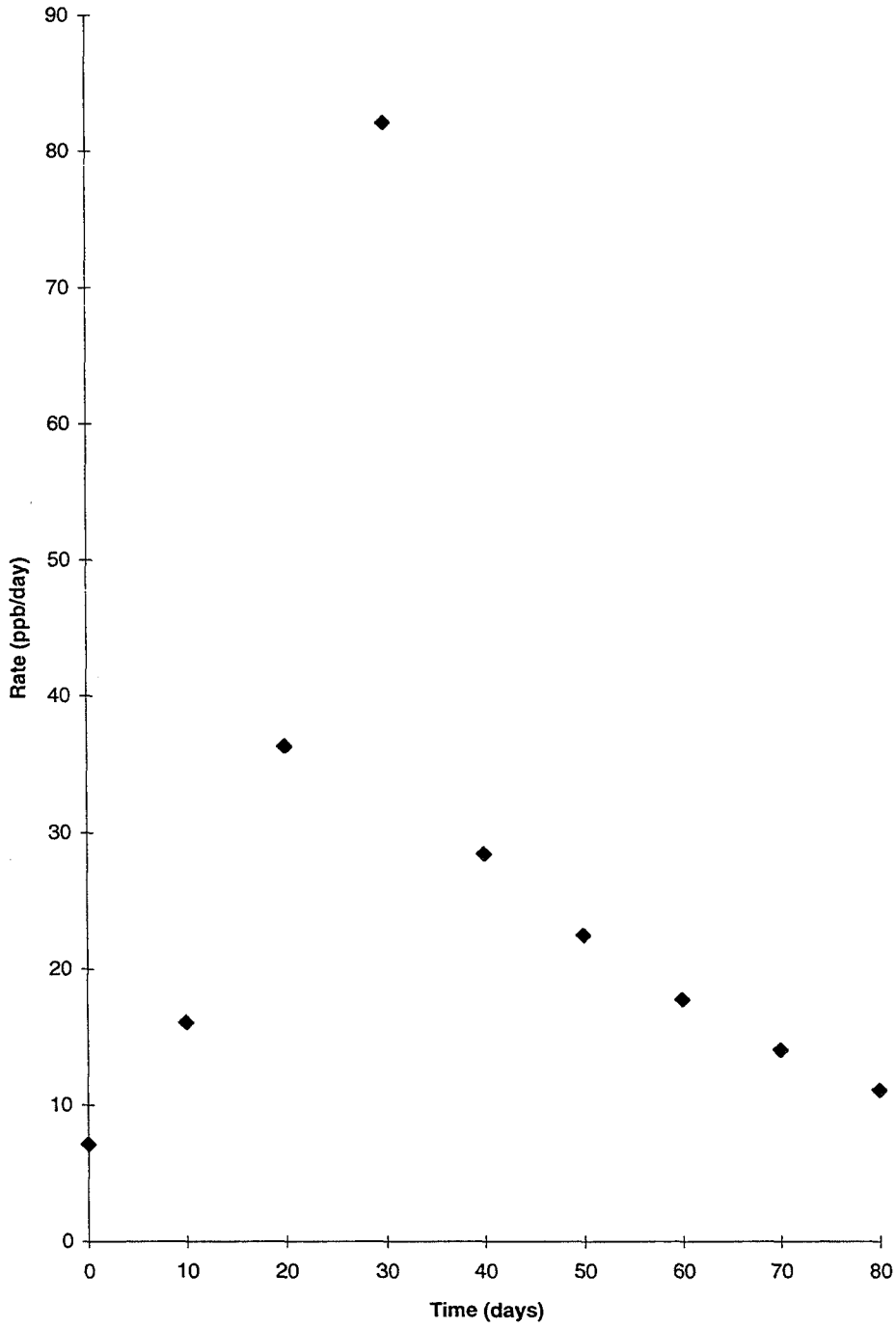


Figure 10

Ethylene Concentration in BPC (Potatoes)

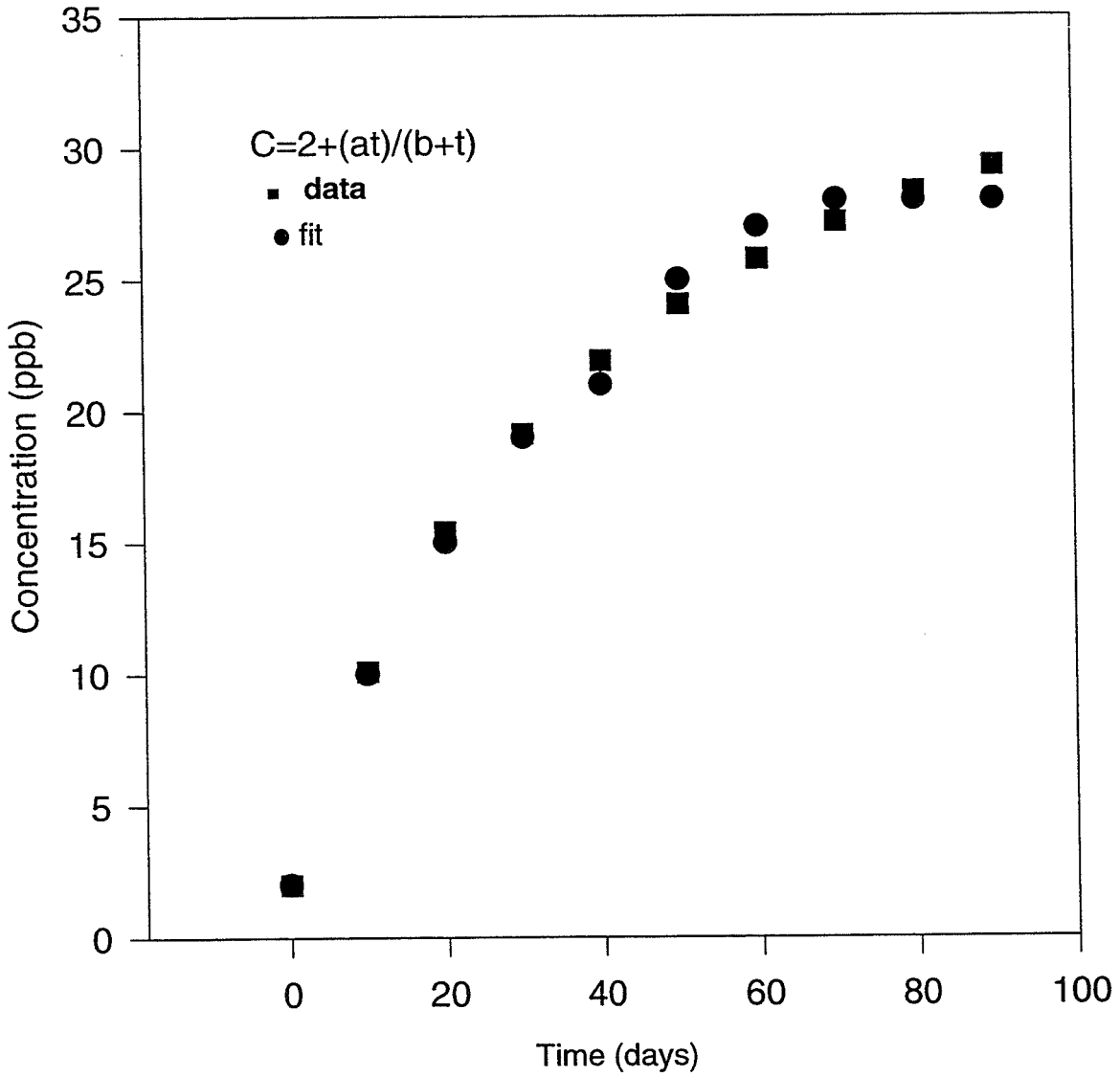


Figure 11

Ethylene Production Rate (Potatoes)

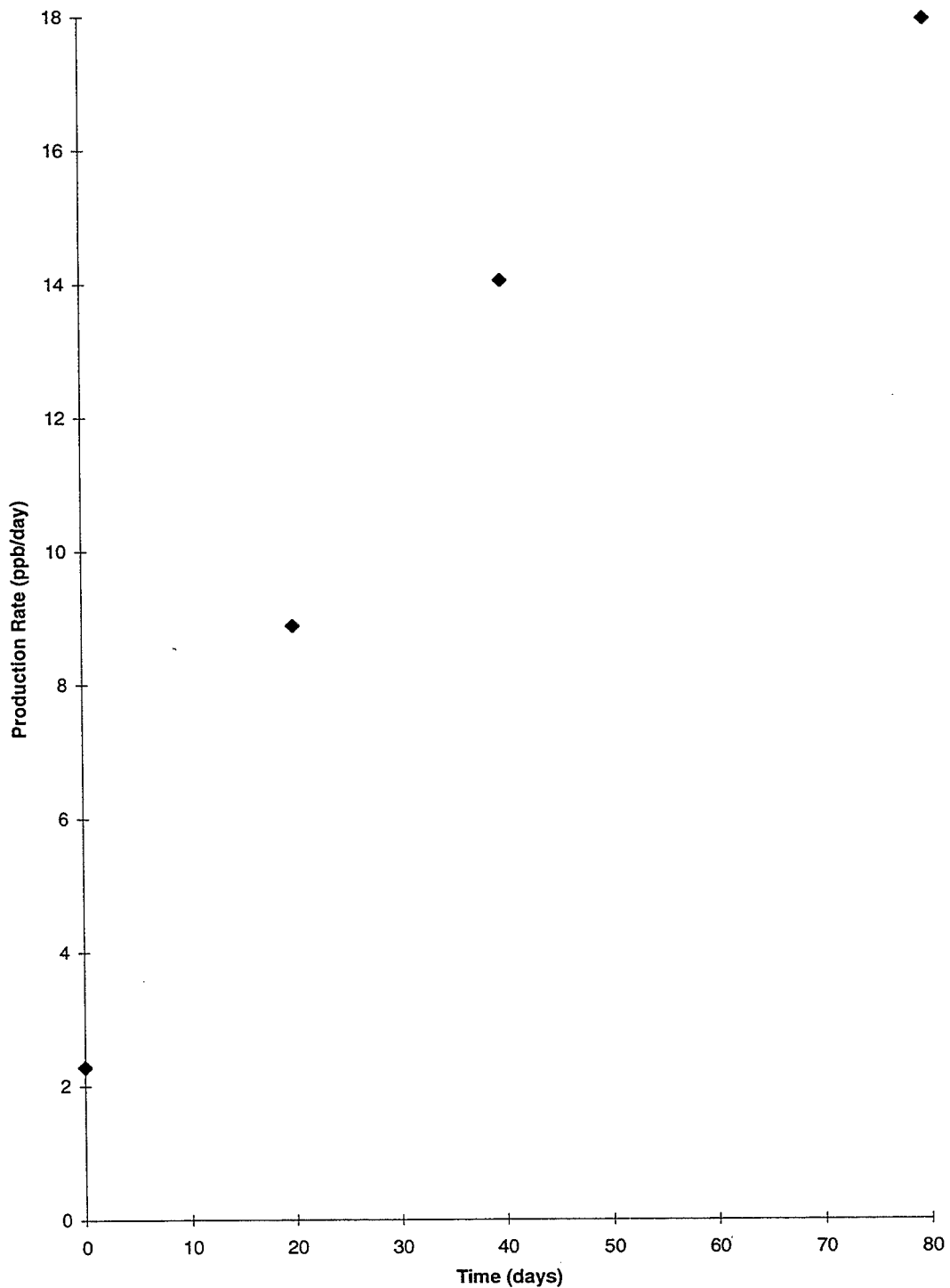


Figure 12

Ethylene Concentration in BPC (Soybean)

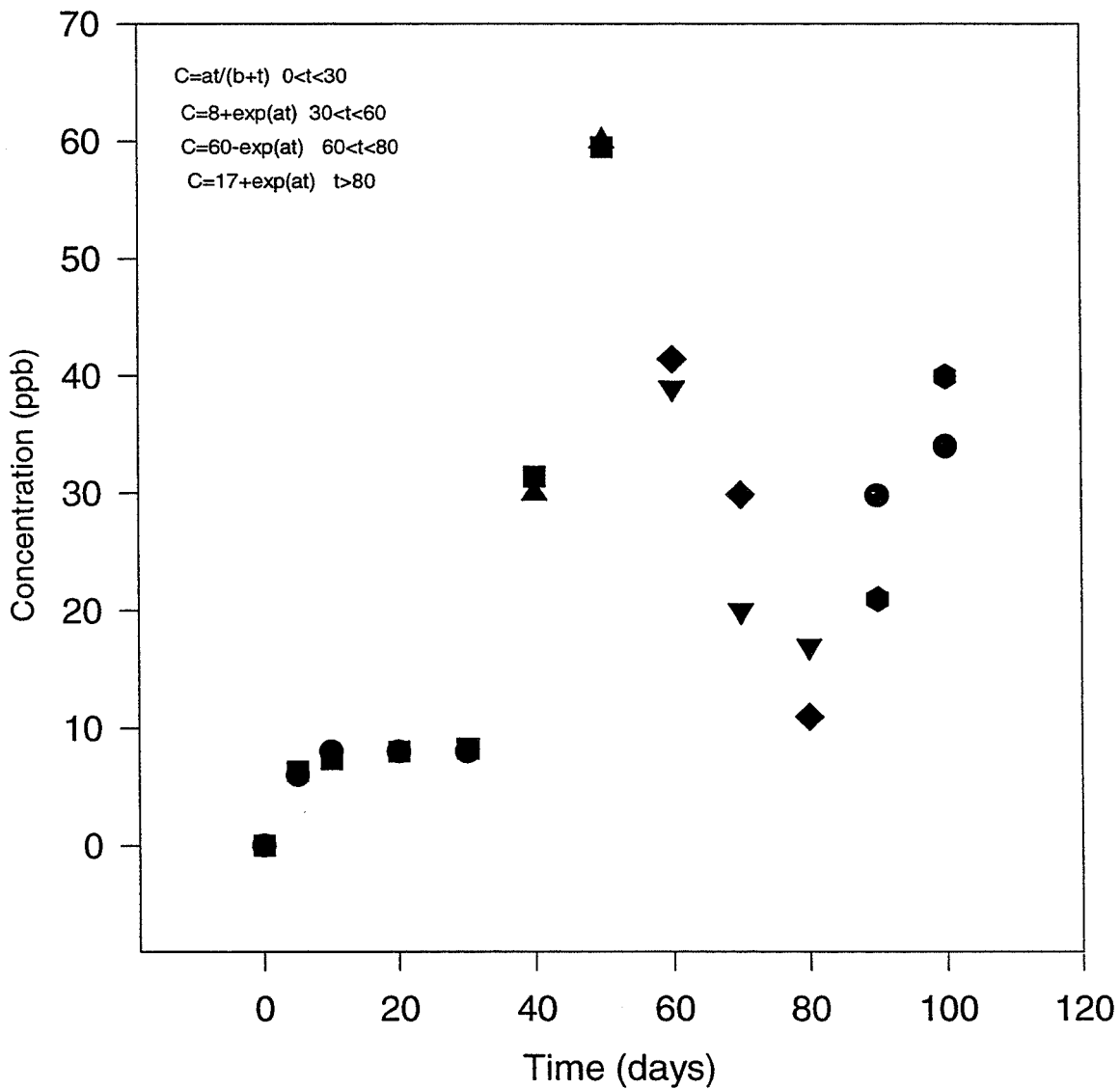


Figure 13

Ethylene Production Rate (Soybean)

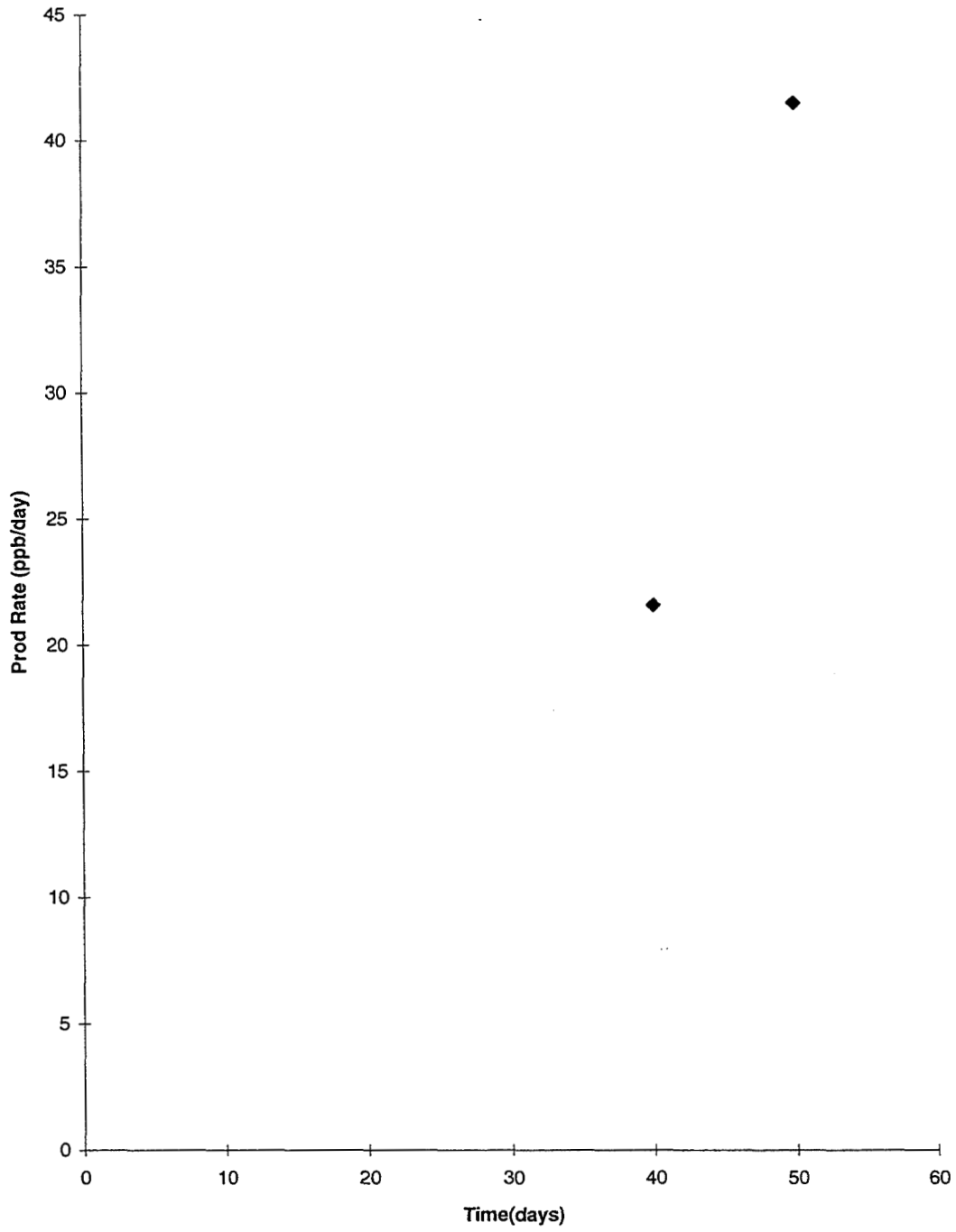


Figure 14

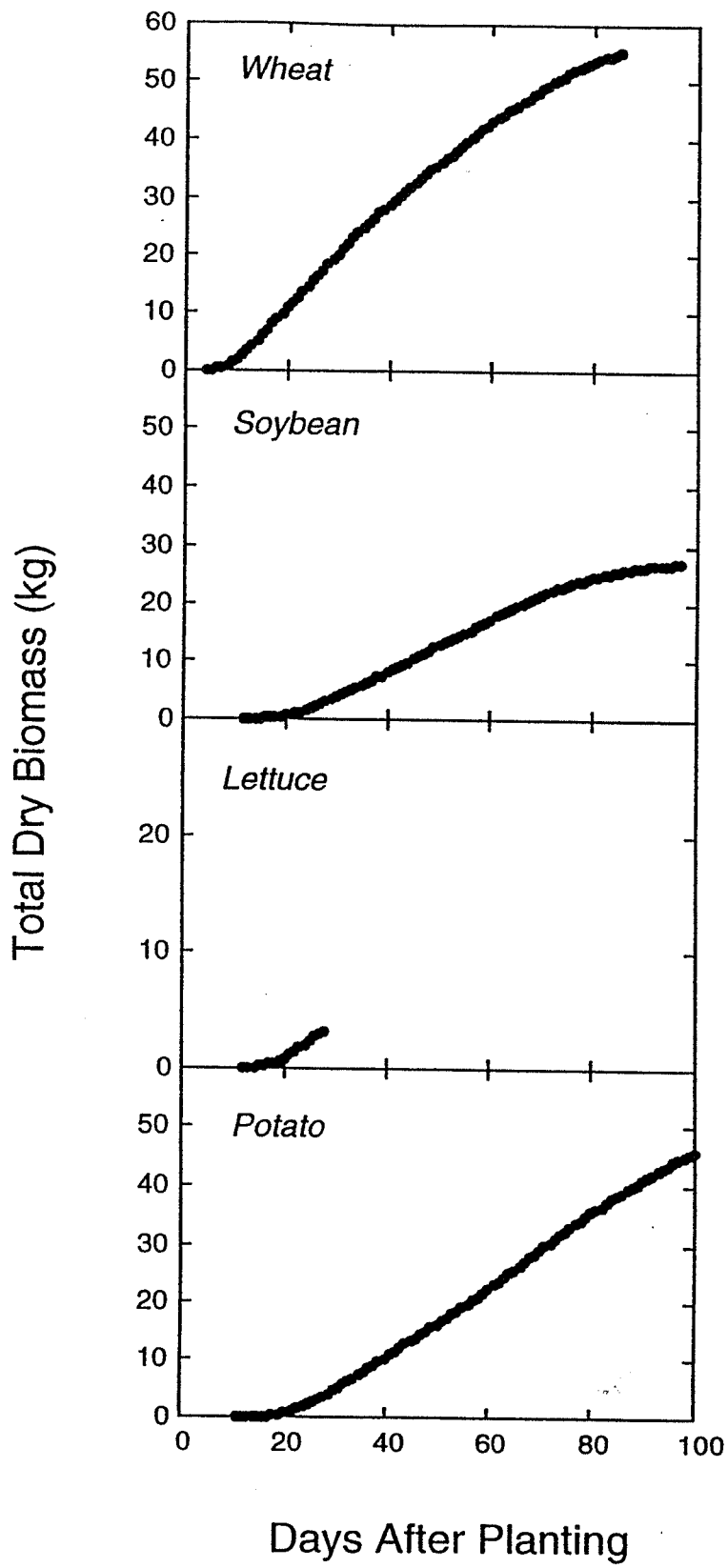


Figure 15

1994 NASA/ASEE SUMMER FACULTY FELLOWSHIP PROGRAM

JOHN F. KENNEDY SPACE CENTER
UNIVERSITY OF CENTRAL FLORIDA

111765
351501
514-26
33974 40
p - 39

MECHANICAL BEHAVIOR OF PRECIPITATION HARDENABLE STEELS
EXPOSED TO HIGHLY CORROSIVE ENVIRONMENT

PREPARED BY:	Dr. Ferdinand Rosa
ACADEMIC RANK:	Professor
UNIVERSITY AND DEPARTMENT:	University of Puerto Rico Mechanical Engineering Department
NASA/KSC	
DIVISION:	Materials Science Laboratory
BRANCH:	Failure Analysis and Materials Evaluation
NASA COLLEAGUE:	Rupert Lee
DATE:	August 5, 1994
CONTRACT NUMBER:	University of Central Florida NASA-NGT-60002 Supplement: 17

ACKNOWLEDGEMENTS

I would like to express my appreciation for being selected to participate in the NASA/ASEE Summer Fellowship Program. To Dr. Loren Anderson [University of Central Florida] and to Mr. Warren Camp [NASA] my congratulations, for their capable administration of the program.

I also want to thank my NASA colleague Dr. Rupert Lee for his invaluable assistance during this summer. To Mr. Peter Marciniak, Mr. Dean Lewis, and all the rest of the people in the Materials Section my thanks for their unconditional help.

My gratitude goes also to Ms. Kari Stiles and Ms. Maria Smith for their dedication and invaluable assistance during my stay at Kennedy Space Center.

Last but not least I want to thank Mr. Scott Murray, Mr. William (Irby) Moore, and Mr. Cole Bryant for making me feel at home during this summer.

ABSTRACT

Unexpected occurrences of failures , due to stress corrosion cracking (SCC) of structural components , indicate a need for improved characterization of materials and more advanced analytical procedures for reliably predicting structures performance .

Accordingly , the purpose of this study was to determine the stress corrosion susceptibility of 15 - 5 PH steel over a wide range of applied strain rates in a highly corrosive environment . The selected environment for this investigation was a 3.5 % NaCl aqueous solution. The material selected for the study was 15 - 5 PH steel in the H 900 condition . The Slow Strain Rate technique was used to test the metallic specimens .

SUMMARY

The catastrophic failure of some structural components, at Kennedy Space Center, due to environmentally assisted cracking has raised questions regarding the reliability of those structures. To that effect NASA has initiated a comprehensive program to identify materials which are immune to cracking under the above mentioned conditions, and recommend them for future applications.

The purpose of this study was to determine the behavior of some Precipitation Hardenable steels when exposed to a highly corrosive environment under different loading situations. The material used in this study was a 15 - 5 PH steel in the H 900 condition and the selected environment was a 3.5 % NaCl aqueous solution. The Slow Strain Rate techniques was used to test the material. Slow Strain Rate tests were done at 8×10^{-5} in/min.

Results show that the 15 - 5 PH steel is susceptible to stress corrosion cracking in a 3.5 % NaCl solution, and for the geometry used in these tests the stress intensity factor is of the order of 70 $\text{Ksi}\sqrt{\text{in}}$.

TABLE OF CONTENTS

- 1.0 INTRODUCTION**
 - 1.1 BACKGROUND**
 - 1.2 STRESS CORROSION CRACKING MECHANISM**
 - 1.3 LINEAR ELASTIC FRACTURE MECHANIC**
 - 1.4 SLOW STRAIN RATE TECHNIQUES**
- 2.0 MATERIALS AND PROCESSES**
 - 2.1 MATERIALS**
 - 2.2 EQUIPMENT**
 - 2.3 EXPERIMENTAL PROCEDURE**
- 3.0 RESULTS AND DISCUSSIONS**
- 4.0 CONCLUDING REMARKS**
- 5.0 RECOMMENDATIONS**
- 6.0 APPENDICES**
 - 6.1 APPENDIX A**
- 7.0 REFERENCES**

LIST OF FIGURES

FIGURE	TITLE
1	Stress Intensity Factor vs Specimen Thickness Typical Curve-----
2	Crack Growth Rate vs Stress Intensity Factor Typical Curve-----
3	Load vs Crack - Mouth Opening Displacement Curve-----
4	Tensile Stress vs Crack Depth Diagram Illustrating the Regions of no - Crack , Subcritical Crack Growth , and Catastrophic Failure-----
5	Photomicrograph of 15 - 5 PH Steel in the H 900 Condition Showing Precipitates Distribution-----
6	Compact Tension (CT) Type , Fracture Toughness Specimen-----
7	Typical Fatigue Crack Produced in Samples Prior to Exposure to Corrosive Environment-----
8	Load - Displacement Curve of 15 - 5 PH Steel Strained at a Constant Strain Rate of 8×10^{-5} in./min .-----
9	SEM of Fracture Surface of SCC Specimen . a) Fast Fracture Region , b) Stress Corrosion Region-----

LIST OF FIGURES (Cont .)

- 10 Plastic Fracture Surface of 15 - 5 PH Steel Exposed to a 3.5 % NaCl Solution , Showing Regions of Fatigue , Stress Corrosion , and Fast Fracture-----**
- 11 Fracture Propagation in C-T Specimens of 15 - 5 PH Steel Exposed to a 3.5 % NaCl Solution at a Constant Strain Rate of 8×10^{-5} in./min.-----**
- 12 Stress Intensity as a Function of Initial Crack Length for Dry and Wet Specimens -----**
- 13 Maximun Stress Intensity as a Function of Initial Crack Length for Dry and Wet Specimens-----**

LIST OF TABLES

TABLE	TITLE
1	Nominal Composition of 15 - 5 PH Steel-----
2	Heat Treatment of 15 - 5 PH Steel-----
3	Mechanical Properties of 15 - 5 PH Steel-----
4	SCC Properties of 15 - 5 PH Steel-----

1.0 INTRODUCTION

1.1 BACKGROUND

The solid rocket boosters used to launch the space shuttle, use ammonium perchlorate as fuel and release approximately seventeen (17) tons of hydrochloric acid into the atmosphere in each launching. This acidification of the marine atmosphere has led to severe problems and premature failure of various structural components and critical equipment [1] at the launching facilities at Kennedy Space Center (KSC).

The fact that some structural components have failed catastrophically due to environmentally assisted cracking, has raised questions with regards to the reliability of those structures. Even if catastrophic failures are rarely observed in practice, when they occurs, they may be more costly in terms of life and property damage than other types of failures. To that effect NASA has been working in a comprehensive program to identify materials which are not susceptible to cracking in the launch - pad's environment when stressed, and recommend them for future applications.

1.2 STRESS CORROSION CRACKING MECHANISM

Delayed failure of structural components subjected to an aggressive environment may occur under statically applied stresses well below the yield strength of the material. Failure under these conditions is caused by stress corrosion cracking (SCC) and has long been recognized as an important failure mechanism.

Although many tests have been developed to study this mode of failure the underlying mechanism for SCC are yet to be resolved [2,3,4] and quantitative design procedures against its occurrence are yet to be established. These difficulties are caused by the complex chemical, mechanical, and metallurgical interactions; the many variables that affect the behavior; the extensive data scatter [5,6]; and the poor correlation between laboratory test results and service experience.

Experimental procedures for SCC tests of pre-cracked specimens may be divided in two general categories. They are Time-to-Failure tests and Crack-Growth-Rate tests. The Time-to-Failure tests are similar to the conventional stress-corrosion tests for smooth or notched specimens. The Crack-Growth-Rate tests are more complex and requires more sophisticated instruments than do the Time-to-Failure tests. However data obtained by using Crack-Growth-Rate tests should provide information necessary to enhance the understanding of the kinetics of SCC and verify the threshold behavior K_{ISCC} .

Cracking of materials may be either intergranular or transgranular and may progress at velocities between 10^{-9} to 10^{-1} in/sec . Three broad categories of stress corrosion mechanism can be identified:

1. Pre-existing path mechanism - This mechanism relates the cracking susceptibility to the chemical activity of the grain boundaries (i.e. - precipitates).
2. Strain assisted active path mechanism - This mechanism is related to the rupture of a protective film at the crack tip, followed by metal dissolution by the corrosive environment.
3. Absorption mechanism - This mechanism is based on the chemisorption of an environmental specie on the crack tip which reduces the surface energy, and therefore reduces the local fracture strength of the metal lattice.

1.3 LINEAR ELASTIC FRACTURE MECHANIC

The application of Linear Elastic Fracture Mechanics (LEFM) concepts has met with considerable success in the study of SCC [7,8] , because environmentally enhanced crack growth and the stress intensity factor can be used to characterize the mechanical component of the driving force in SCC.

The critical stress intensity factor or fracture toughness (K_{IC}) represents the inherent ability of a material to withstand a given stress - field intensity at the tip of a crack and to resist progressive tensile crack extension under plane strain conditions. Plane strain conditions requires that:

$$B \geq 2.5 (K_{IC} / S_{YS})^2, \text{ where :}$$

B = specimen thickness

S_{SY} = tensile strength

For materials that are susceptible to crack growth in a particular environment this threshold value is called K_{ISCC} and represent the value below which crack propagation does not occur for a given material - environment combination under plane strain conditions (See Fig. 1).

Stress corrosion crack growth rates have been investigated in various material - environment combination , and the results suggest that the crack growth rate as a function of the stress intensity factor can be divided in three different regions (See Fig. 2). In region I the rate of crack growth is strongly dependent on the magnitude of the stress intensity factor , such that small changes in K results in large changes in crack growth rates . Region I also exhibit a stress intensity factor (K_{ISCC}) below which cracks do not propagates under sustained loads for a given material - environment system . In region II crack growth rates , for many systems , is moderately dependent on the magnitude of K and for some systems , like high strength steel in gaseous hydrogen , crack growth rate is independent of K . The crack growth rates in region III increases rapidly with K and approaches the K_{IC} of the material .

The usefulness of Fracture Mechanics for defining SCC tendencies in high strength metals is derived from the ability to use the parameter K_{ISCC} for calculating the stress - flaw size combination necessary for the initiation of cracks growth . The value of K_{ISCC} is calculated from the load vs crack - mouth - opening displacement curve (See Fig. - 3) . From that graph the stress intensity factor for the specific material - geometry - environment (K_Q) will be calculated according to the following equation :

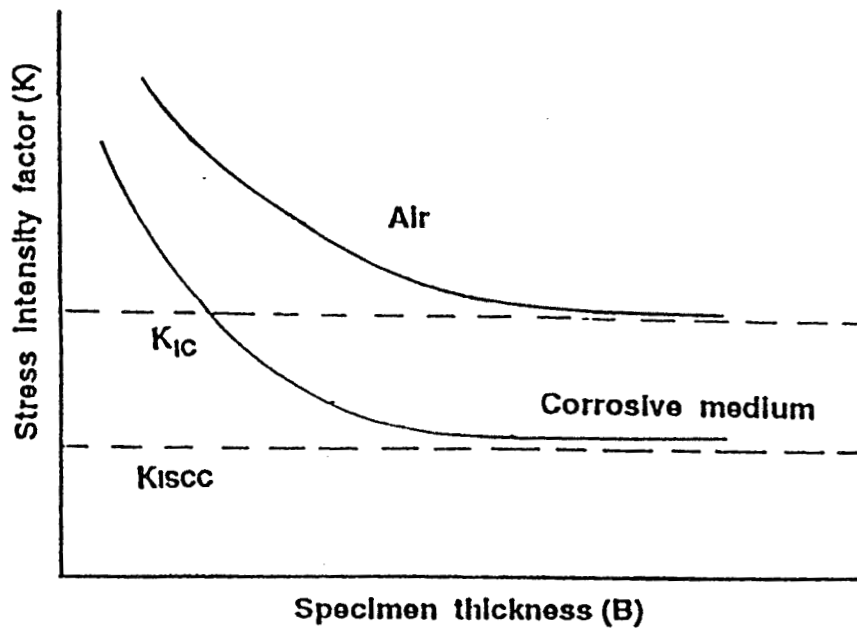


Fig. - 1 Stress Intensity Factor vs Specimen Thickness Curve

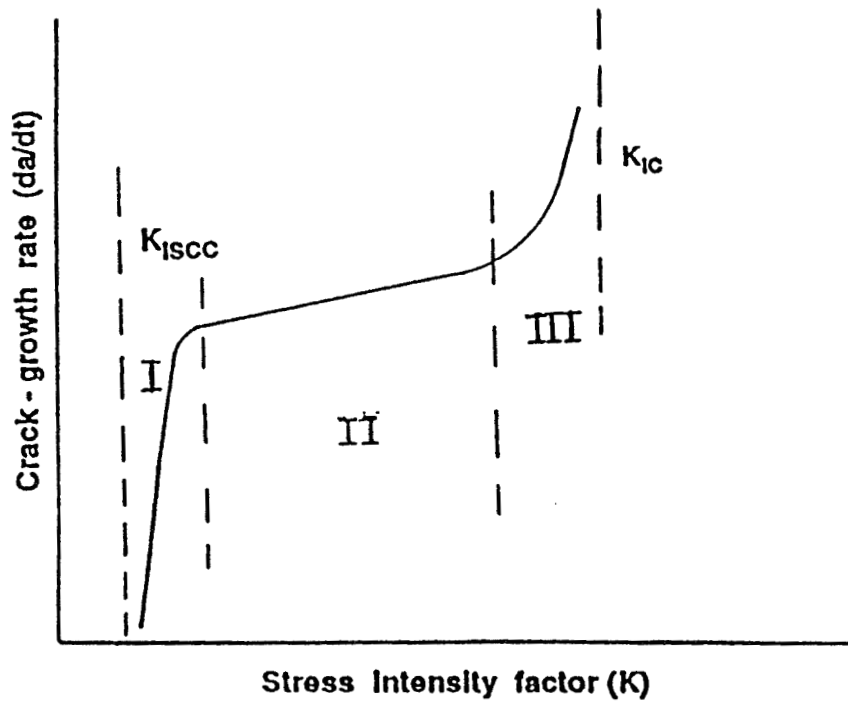


Fig. - 2 Typical Curve Of Crack-growth Rate vs Stress Intensity Factor

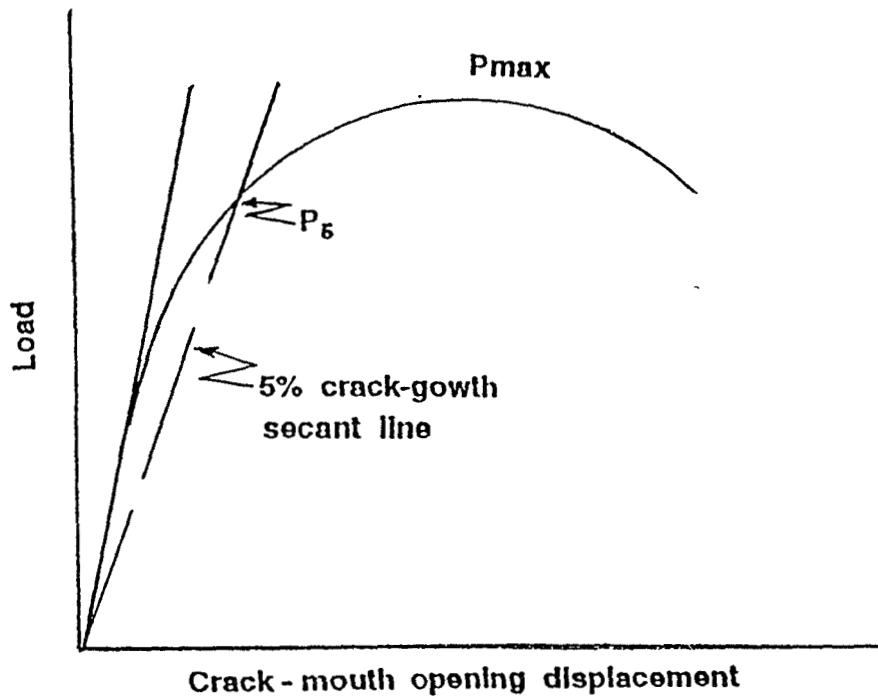


Fig. - 3 Load vs Crack-mouth Opening Displacement Curve

$K_Q = [P/B\sqrt{W}] \cdot f(a/W)$ where :

B = specimen thickness

W = specimen width

a = crack length

$P_Q = P_5$ if the load at every point in the graph preceded P_5 (See Fig. 3)

$P_Q = P_{max}$ if there is a maximum load preceding P_5 in the graph (See Fig. 3), and

$$f(a/W) = [(2+k)(.886+4.64k-13.32k^2+14.72k^3-5.6k^4)]/[1-k]^{3/2}$$

where : $k = a/W$.

The value of K_Q will be equivalent to K_{IC} or K_{ISCC} if :

$P_{max}/P_5 \leq 1.10$, and

B and a $\geq 2.5(K_Q/S_{ys})^2$, where :

$S_{ys} = 0.2\%$ yield strength

If the two constraints previously discussed are not satisfied, then the test is not valid for determining K_{IC} or K_{ISCC} , and a new test have to be done using a thicker specimen, usually 1.5 time thicker.

The application of the Fracture Mechanics approach to design concepts relies on the definition of the boundary lines on the Stress vs Crack-Depth diagram. Figure - 4 shows the no - crack - growth, the the subcritical - crack - growth, and the catastrophic - failure regions. The boundaries are experimentally definable, with limits imposed by S_{ys} and S_U for smooth specimens and K_{IC} and K_{ISCC} for pre - cracked samples (S_U is the maximum tensile strength of the material).

Whether or not a component will crack, from the time of commissioning will depend on the tensile stress - crack - size combination. If the initial stress intensity associated with this combination is greater than K_{ISCC} , its lifetime or inspection periodicity may be determined by integration of the appropriate crack - velocity vs stress intensity curve.

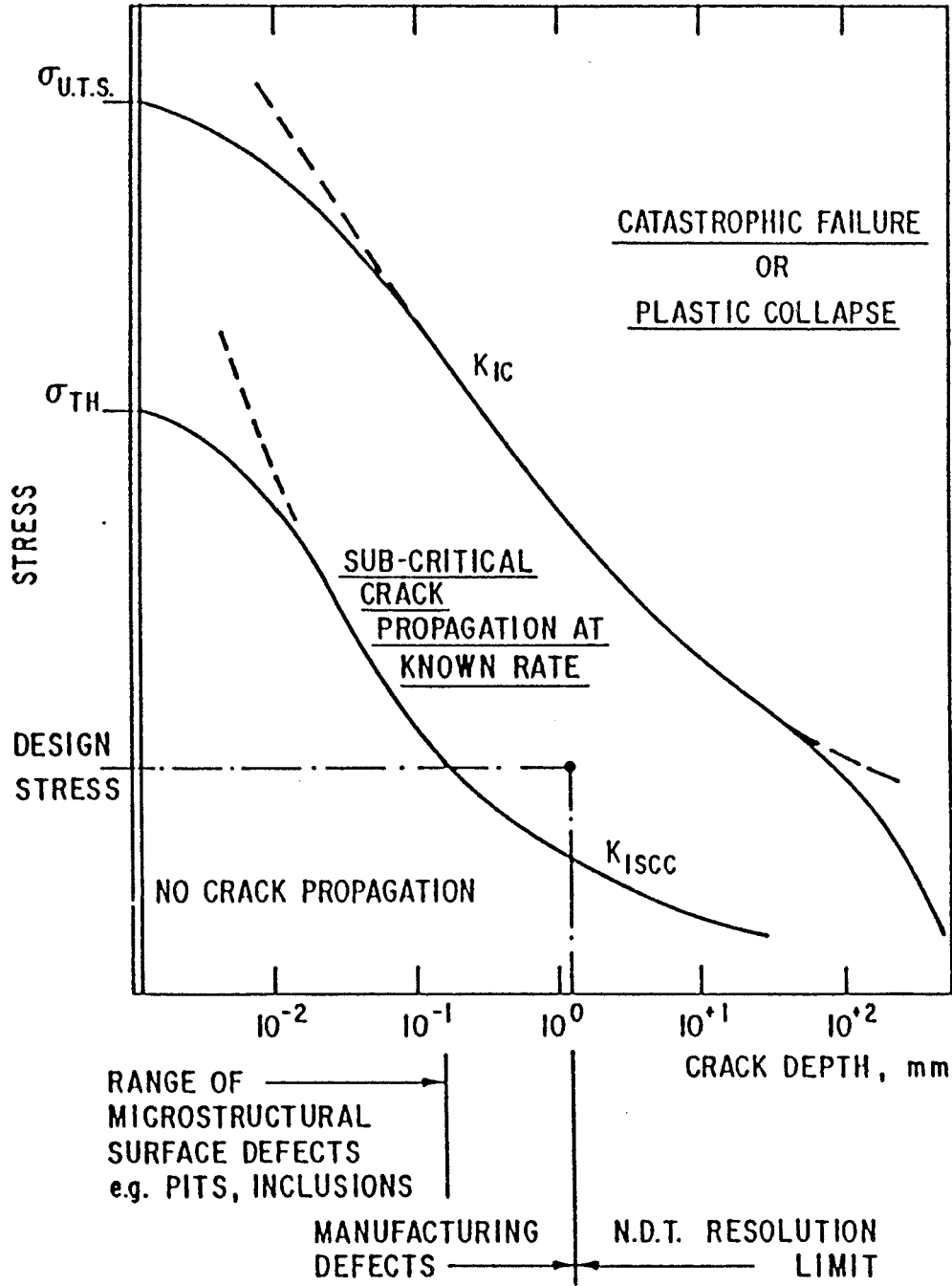


Fig. 4 Tensile stress/crack depth diagram, illustrating the regions of no crack growth, subcritical crack growth, and catastrophic failure.

1.4 SLOW STRAIN RATE TECHNIQUES

Before the early 1969's, constant load and constant strain testing on smooth and notched specimens of various configurations became very popular. However the 60's produced two accelerated test techniques based on different mechanical approaches [9,10]. One of the techniques involved testing statically - loaded mechanically - precracked specimens using Linear Elastic Fracture Mechanics concepts. The second involved the Slow Strain Rate Testing of smooth specimens. These testing methods have often produced SCC in materials, where older techniques have failed to do so.

More recently the Constant Strain Rate test have become widely accepted as a quality control or screening technique quite apart from their usefulness in mechanistic studies. The prime justification for this technique is that it accelerates a known rate determining step in the cracking mechanism of ductile alloys - aqueous environment system (i.e. oxide - rupture rate). The Constant Strain Rate technique is a method to assess the susceptibility of metals and their alloys to SCC. It provides a rapid laboratory method to determine the SCC susceptibility of the material in environments in which other tests do not readily promote SCC. The results are positive in that failure occurs in a ductile manner or prematurely in a brittle mode if SCC occurs. It is not surprising then that good correlations are observed between SCC susceptibility rated by this technique and by more protracted methods involving static loads.

Several properties are used to define and compare the severity of SCC of materials and aggressiveness of environments. Generally a measure of the time to failure, or reduction in ductility in a corrosive environment is compared to the behavior of the material in an environment which does not promote that condition, for example air. Increased severity of SCC is indicated by shorter times to failure or reduced ductility, as measured by reduction in area or reduction

in elongation . The presence or absence of SCC on the fractured specimen can be unequivocally determined only by metallographic examination . Results of those examinations can be presented quantitatively by comparing the number or length of secondary stress corrosion cracks .

Strain rate is one of the most important single parameter in evaluating SCC susceptibility of any metal or alloy in a given environment . If strain rate is too high , fracture of the material will be mostly mechanic (ductile) because the corrosion process cannot keep pace with the straining process . On the other side if the strain rate is too low , SCC may be prevented due to repassivation of the exposed base metal , which may be too fast compared to the frequency of the film rupture event . It has been observed that strain rates in the range of 10^{-5} to 10^{-1} S⁻¹ tend to promote SCC in most cases .

2.0 MATERIALS AND PROCEDURES

2.1 MATERIALS

The materials used in this investigation consist of 15 - 5 PH steel in the H 900 condition . The nominal chemical composition is shown in Table - 1 , and the thermal conditions are shown in Table - 2 . A summary of the mechanical properties of the material is shown in Table - 3 . Figure - 5 shows the distribution of precipitates in the samples .

Compact tension (CT) specimens were machined from the as - received material , according to ASTM E 399 - 83 standard . Specimens were

Table - 1 Nominal Composition Of 15-5 PH Steel

Cr	Ni	Cu	Mn	Si	Cb+Ta	C
14.0- 15.0	3.5- 5.5	2.5- 4.5	1.0- Max	1.0- Max	0.15- 0.45	0.07- Max

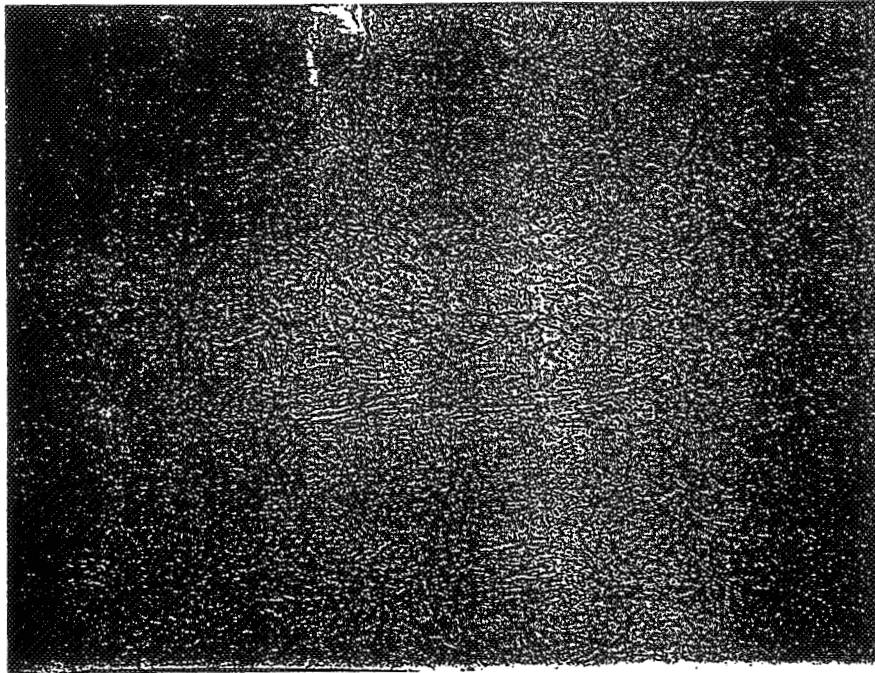
Table - 2 Heat Treatment Of 15-5 PH Steel

Temper	Heat Schedule
Solution Treated	1900 F for half (.5) hour Oil quench
H 900	900 F for one (1) hour Air cooled

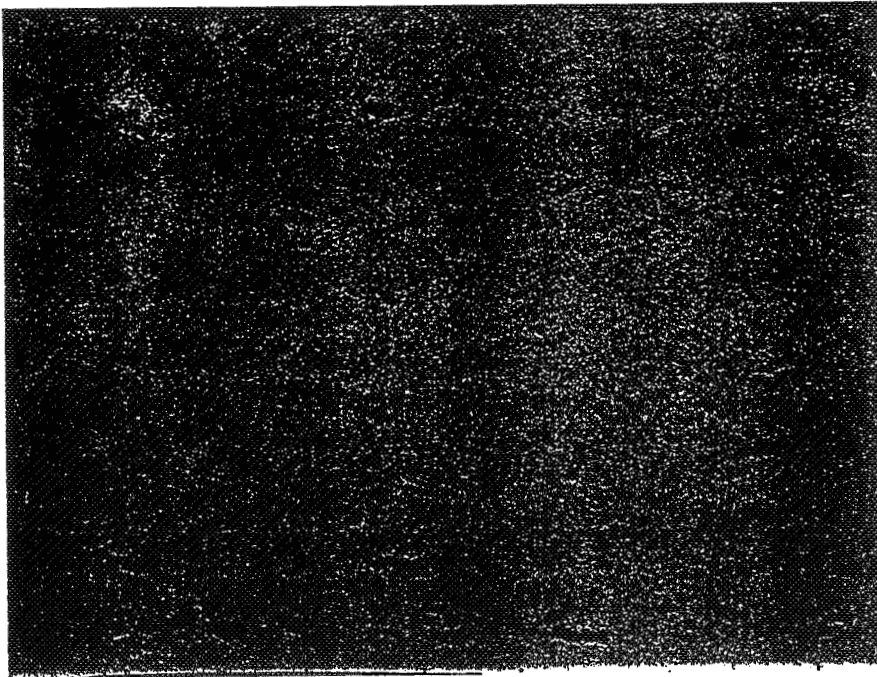
Table - 3 Mechanical Properties Of Vacuum Melted 15-5 PH Steel

Temper	Su	Sys	% Elong	% R.A.	Hardness
H 900	199.6	178.9	17	61	HB 401

Su = Tensile Strength (KSI)
Sys = 0.2% offset yield strength (KSI)
R.A. = Reduction in area
HB = Brinell hardness



Mag.-100X



Mag.-500X

Fig.-5 Photomicrograph Of 15-5PH Steel In The H900 Condition Showing The Precipitate Distribution.

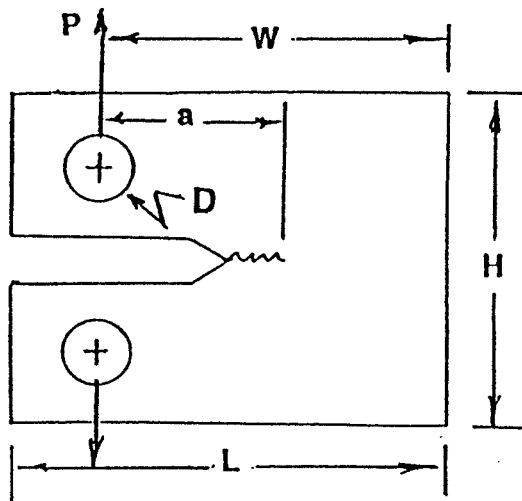
cleaned to eliminate grease and other impurities from the machining operation and then were fatigued to produce the starting crack required in this type of test. The specimen configuration is shown in Figure - 6. The specimens were then loaded into the testing machine and strained under different conditions.

2.2 EQUIPMENT

Test were conducted in a Satec's MATS II Universal Testing Machine equipped with "Nuvision II" software package for automating the system. The minimum strain rate applied by the machine was 8×10^{-5} inches per minutes. The crack - mouth opening was measured with a double cantilevel beam type extensometer.

2.3 TESTING PROCEDURE

All the Slow - Strain - Rate $K_{I,SCC}$ tests involved in this investigation were conducted in a 0.375 - in. thick, C-T specimen in accordance with ASTM method E - 399 - 83. The specimens were fatigue pre-cracked in air prior to loading in the corrosive environment (See Fig. - 7). Test were conducted at a strain rate of 8×10^{-5} in/min in air and in a 3.5 % NaCl solution. A curve of applied load vs crack - mouth opening, similar to the one shown in Figure - 8 was obtained. From the graphs the stress intensity factor (K_Q) for the material was calculated.



$H = 1.2W$
 $L = 1.25 W$
 $D = 0.25W$
 $a = \text{crack length}$
 $P = \text{applied load}$

Fig. --6 Compact - Tension (CT) Type Fracture Toughness Specimen

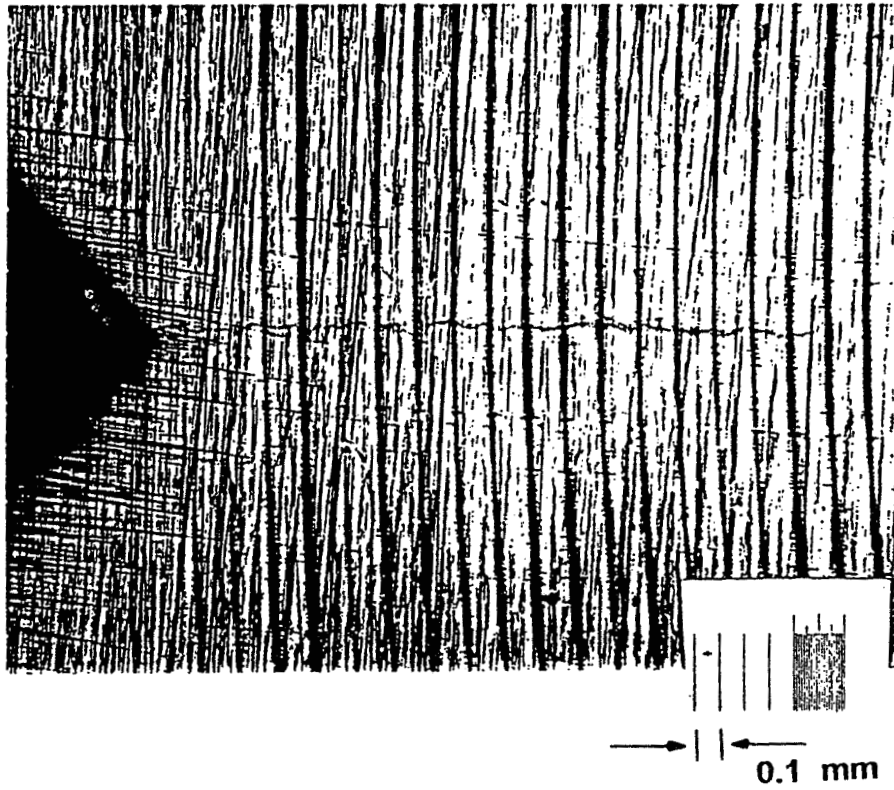


Fig. - 7 Typical Fatigue Crack Produced in Samples Prior to Exposure to Corrosive Environment .

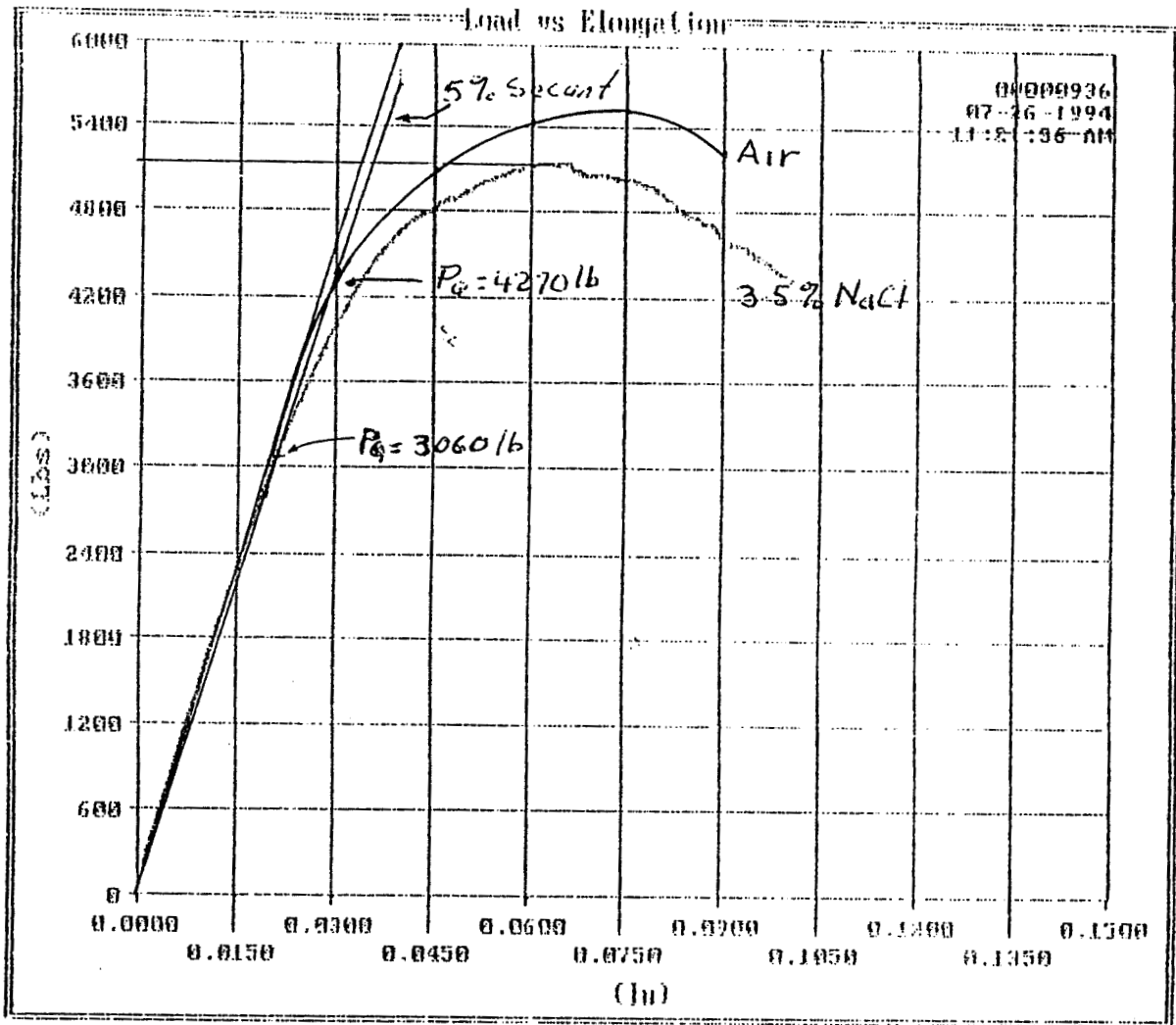


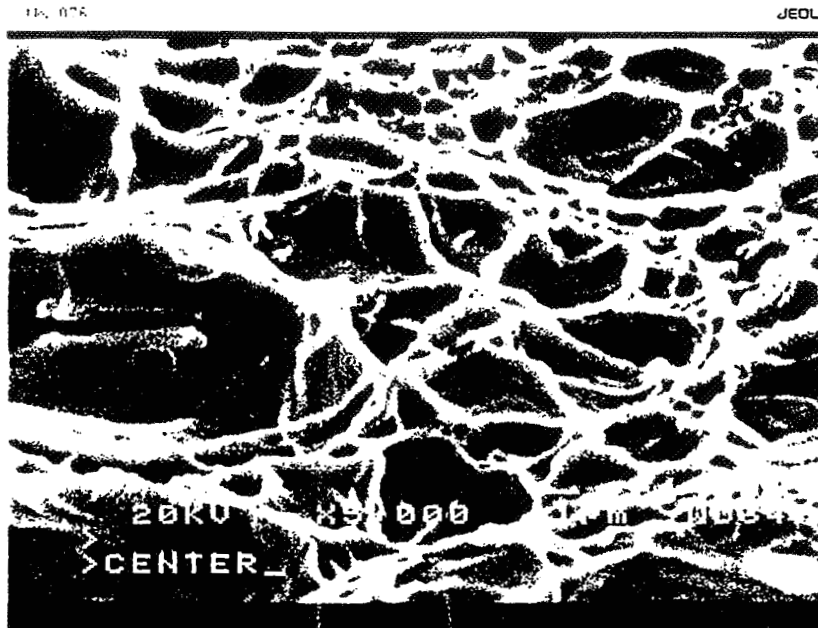
Fig. - 8 Load - Displacement Curve of 5 - 15 PH Steel Strained at a Constant Strain Rate of 8×10^{-5} inches / min .

3.0 RESULTS AND DISCUSSION

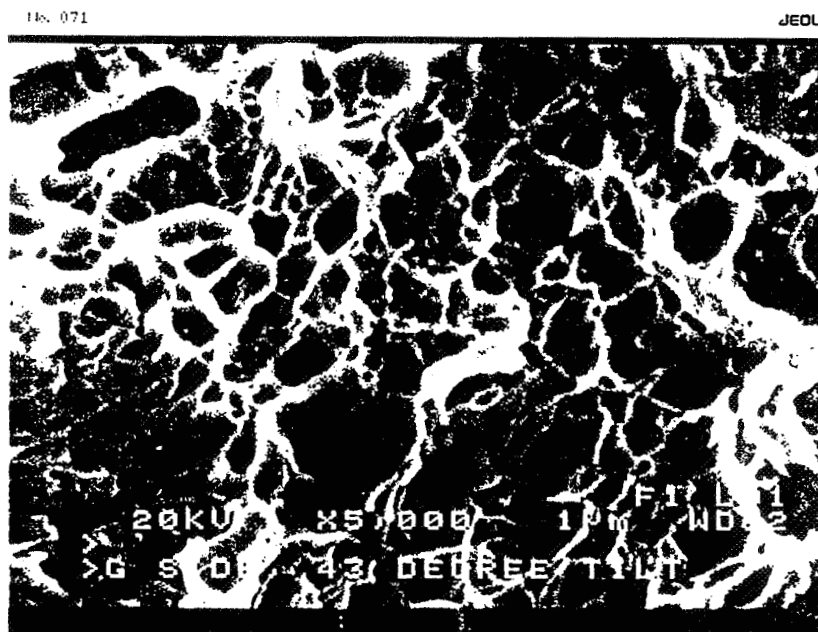
3.1 GENERAL

In order to standardize the technique used to establish the point of deviation on the load - crack opening displacement curve associated with the onset of subcritical crack growth , a 5 % secant offset procedure similar to that used for K_{IC} testing (ASTM method 399-83) was employed . Specifically a line with a slope 5 % less than the slope of the linear load - displacement record is used to define the load (P_Q) and the displacement at the onset of crack growth .

Fig. - 8 represent a load - mouth opening displacement record of the Constant Strain Rate test involved in this investigation . In air the first deviation from linearity occurred at about 4270 lb. and the load continued to increase up to 5599 lb. before fracture occurred . In the 3.5 % NaCl solution , deviation from linearity started at about 3060 lb. and load increased to 5131 lb. before development of rapid unstable crack growth . Because of high K values associated with these tests, deviation from linearity , may be the result of either subcritical crack growth , plastic yielding , or a combination of both mechanism . In SEM studies of the fracture surface , (Fig. - 9) , no subcritical cracks were observed , but an increase in the number of voids formed , can be observed in the stress corrosion region as compared to the fast fracture region .



a



b

Fig. - 9 SEM of Fracture Surface of SCC Specimen . a) Fast Fracture Region , b) Stress Corrosion Region .

Structural materials whose toughness levels are such that they exceed the plane - strain limits , exhibit elastic - plastic fractures with varying amounts of yielding prior to fracture . The tolerable flaw sizes at fracture vary considerable but can be fairly large . Fracture is usually preceded by the formation of large plastic zones ahead of the crack . Fig. - 10 is typical of this type of behavior where failure occurs mainly by general yielding . The direction of the crack propagation can be observed in Fig. - 11 and confirm also , the previews observations .

Table - 4 is a summary of the SCC properties of 15 - 5 PH steel in air and in a 3.5 % NaCl solution tested at a strain rate of 8×10^{-5} in/min . In Figs. - 12 & 13 the changes in stress intensity factors as a function of initial crack length can be observed . For the samples exposed to the corrosive environment the value of K_Q , (K_{ISCC} apparent) , is approximately 70 Ksi In and is independent of initial crack length . For the samples tested in air there is a big decrease in the K value as a function of increasing initial crack length .

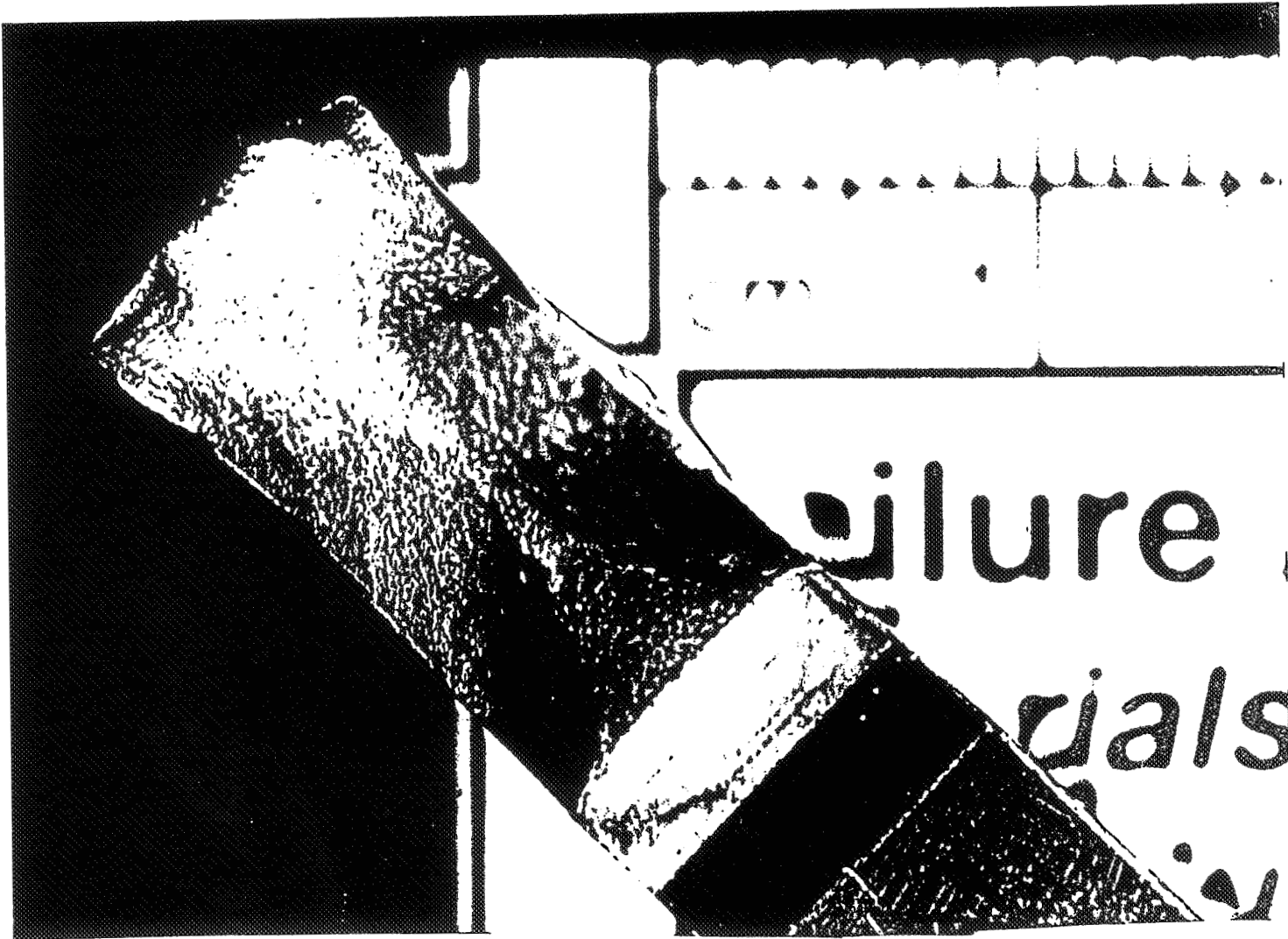


Fig. - 10 Plastic Fracture Surface of 15 - 5 PH Steel Exposed to a 3.5 % NaCl Solution , Showing Regions of Fatigue , Stress Corrosion , and Fast Fracture .

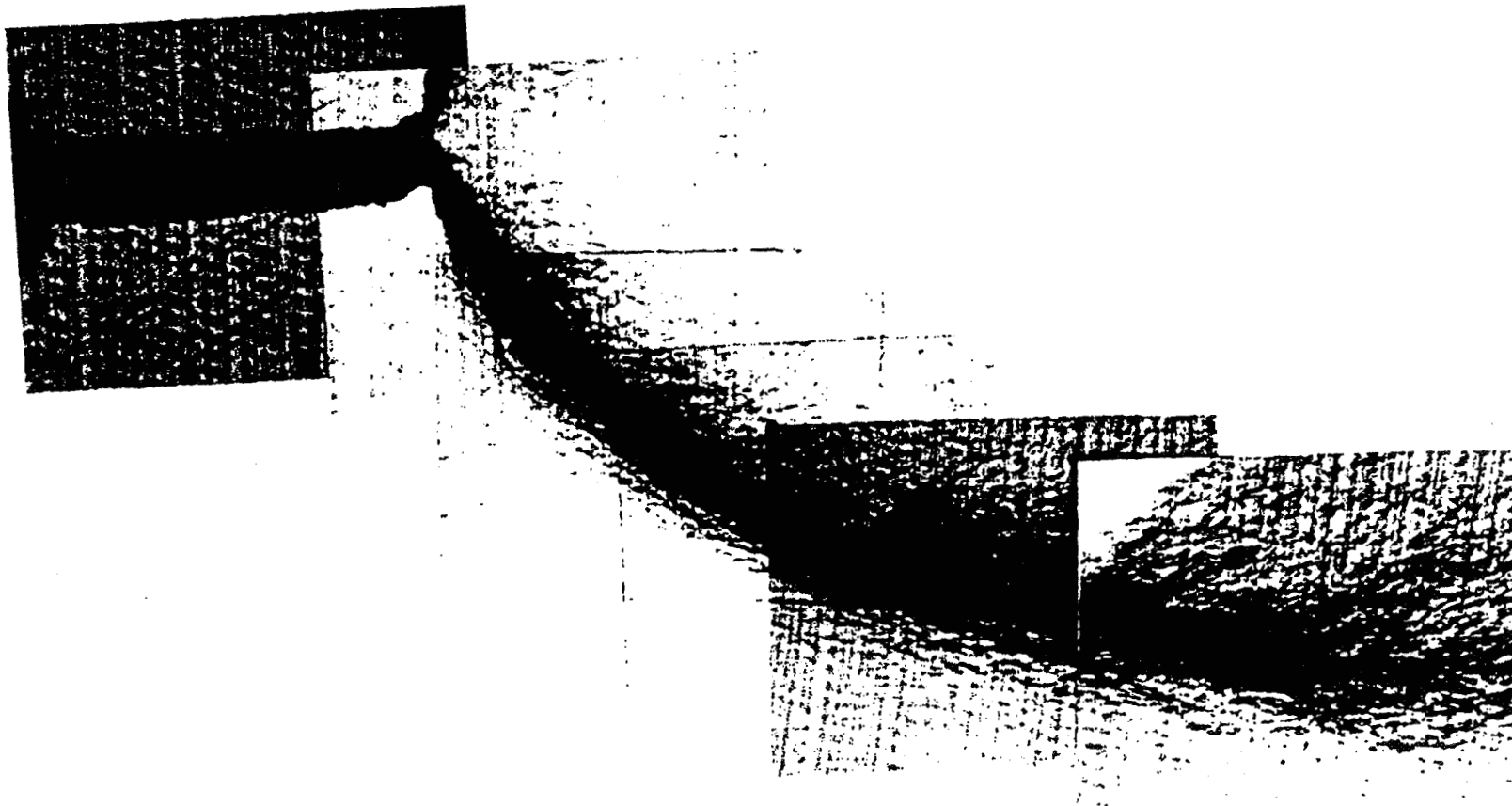


Fig. - 11 Fracture Propagation in C-T Specimens of 15 - 5 PH steel
Exposed to a 3.5 % NaCl Solution at a Constant Strain
Rate of 8×10^{-5} inches / min .

Table - 4 SCC Properties of 15 - 5 PH Steel

Sample	Solution	a in .	P_Q lb .	P_{max} lb .	K_Q ksi in	K_{max} ksi in
A - 1	Air	0.910	2780	3351	72.1	86.9
C - C	Air	0.780	4270	5599	95.7	125.4
G - G	3.5 %NaCl	0.800	2920	4810	68.2	112.4
H - H	3.5 %NaCl	0.780	3060	5131	68.6	115.0
I - I	3.5 %NaCl	0.753	3380	5639	71.1	118.6

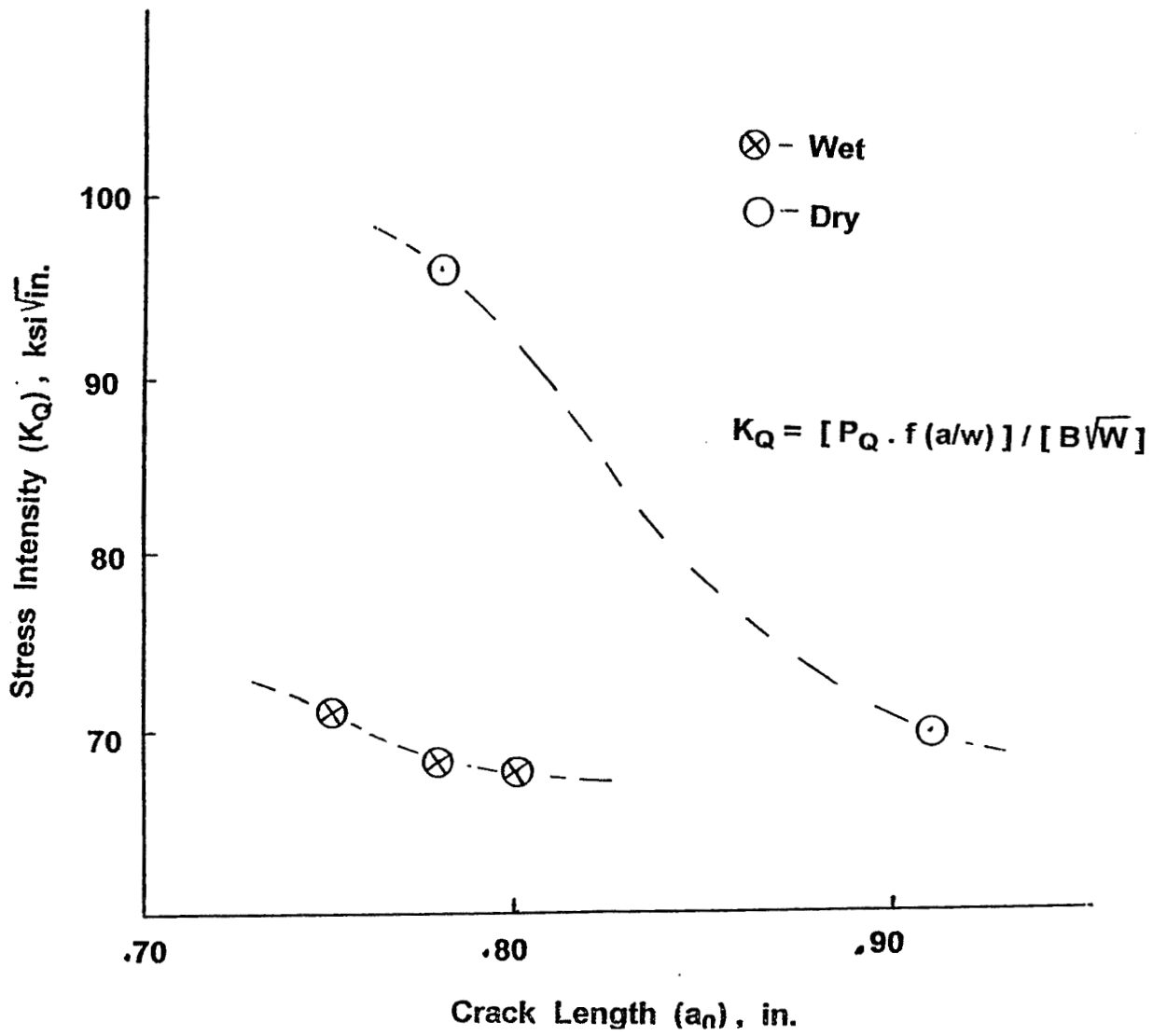


Fig. - 12 Stress Intensity as a Function of Initial Crack Length for Dry and Wet Specimens .

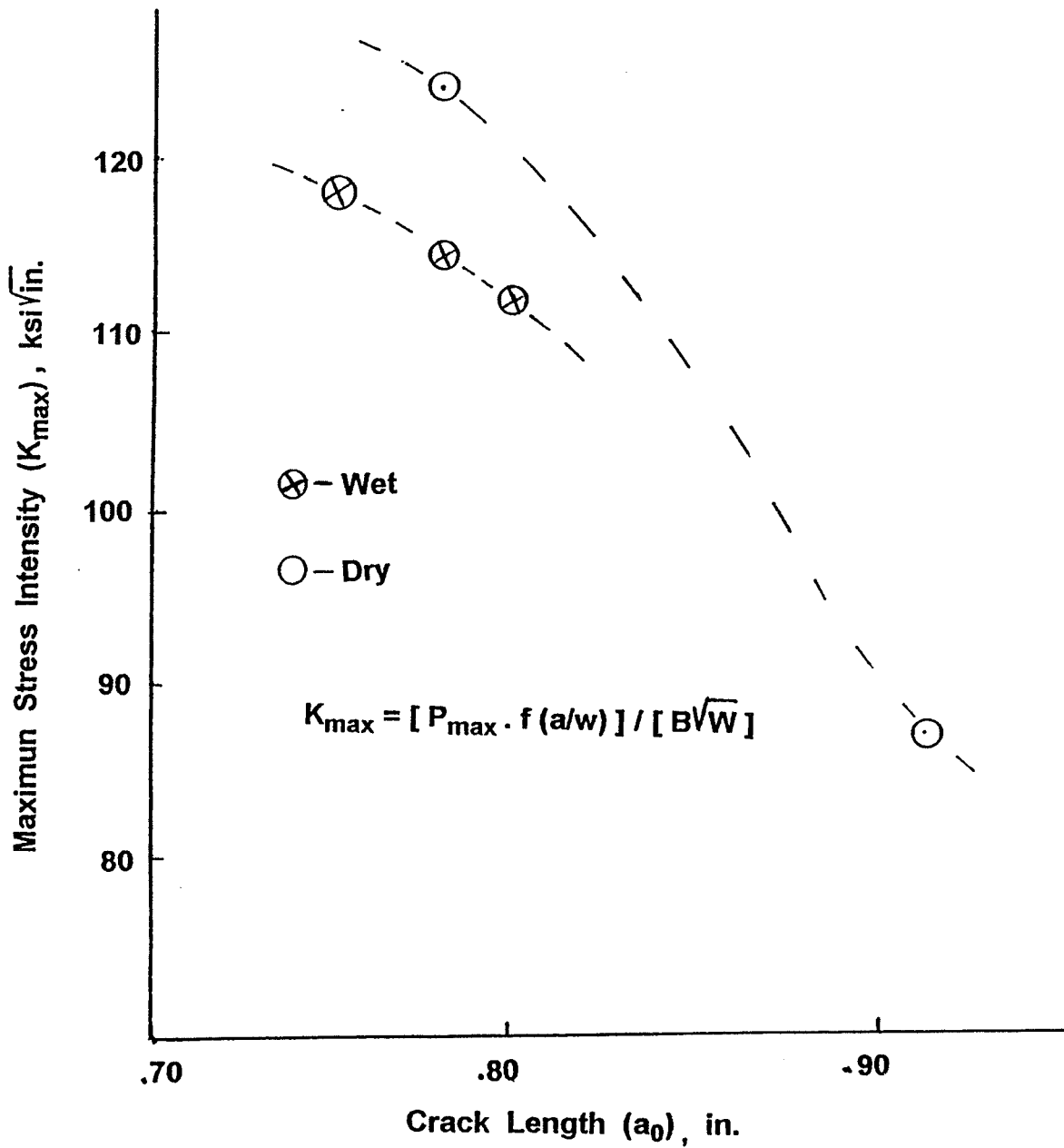


Fig. - 13 Maximum Stress Intensity as a Function of Initial Crack Length for Dry and Wet Specimens.

4.0 CONCLUDING REMARKS

The primary design criterion for most large structures is still based on strength and stability requirements such that nominal elastic behavior is obtained under conditions of maximum load. Usually the strength and stability criteria are achieved by limiting the maximum design stress to some percent of the yield strength. In many cases fracture toughness is also an important design criterion, and yet specifying a notch toughness criterion is much more difficult.

The maximum allowable flaw size in a member has been shown to be related to the notch toughness and yield strength of a material as follow :

$$a = c (\text{critical } K / \text{yield strength})^2$$

Thus the critical K and yield strength, becomes a good index for measuring the relative toughness of structural materials. It is desirable that the structure tolerate large flaws without fracturing, therefore the use of materials with high K / S_{ys} ratio is a desirable condition.

Constant Strain Rate techniques provides a rapid laboratory method to determine the stress intensity factor (K), and the susceptibility of materials to stress corrosion cracking. Absolute results are obtained because failure occurs either in a ductile manner or prematurely by a

brittle mode when SCC is present. A decrease in the value of (K) is indicative of SCC susceptibility to a given environment if all other parameters are kept constant. The absence of SCC assures that the material can be used safely under the specific conditions examined. If SCC is observed, judgement is necessary, because the material still can provide sufficient useful life in service. The data obtained from these tests besides being useful for materials selection provides also for a better understanding of the SCC mechanism.

5.0 RECOMMENDATIONS

Due to the broad scope of this project the proposed testing program could not be finished during the summer. So it is suggested that this investigation be continued and if possible be expanded to cover other areas like :

- Testing at other temperatures
- Testing at other heat treatment conditions
- Testing at atmospheric conditions under static loads

Other sample geometries should be tested to determine the effect of geometry on the test's results.

A similar set of experiments can be done using other types of Precipitation Hardenable steels.

6.0 APPENDICES

6.1 APPENDIX A

Manufacturer certification of quality and properties of 15 - 5 PH steel .

5123823	CUST. NO.	BILL TO	2110	286	SHIP TO
ANDERSON SHUMAKER CO		ANDERSON SHUMAKER CO		ANDERSON SHUMAKER CO	
824 S. CENTRAL AVE		824 S. CENTRAL AVE		824 S. CENTRAL AVE	
CHICAGO IL 60644		CHICAGO IL 60644		CHICAGO IL 60644	
PRODUCT NUMBER	TEST LOT ID	SALES ORDER NO.	PURCHASE ORDER NO.		
32280-18157	4083-7-B1262A01	23689	735		

SHIP LOT ID: 4083-7-B1262A01 MET LOT NO.: B1262A

15-5 PH SEMI FINISH BILLET STNLS XM-12 VAC CE FQ OA FOR FORGE

AMS 2300G * AMS 2315C EX ONE TEST SAMPLE >6" OK * AMS 5659G TYPE 1 EX
 COND A HDNS WVD * ASME SA705 B9ED TYPE XM-12 COND H900T ANAL & MECH PROP
 CPBLTY ONLY * ASTM A564-89 TYPE XM-12 COND H900T ANAL & MECH PROP CPBLTY
 ONLY * ASTM A705-89 TYPE XM-12 COND H900T ANAL & MECH PROP CPBLTY ONLY *
 MIL-I-45208A * MIL-STD-2154 (SUPERCEDES MIL-I-8950) TYPE II (CONTACT) PER
 ARMCO UTP 7 REV 4 *

LINE: 1 SIZE: 8.00000"RCS SHAPE: 16' 0" TO 20' 0"MIN/MAX WEIGHT: 4,420#

ANAL: REGULAR PARENT HEAT NO: 626233
 C: 0.050 MN: 0.540 F: 0.020 S: 0.004 SI: 0.380 CR: 14.91
 NI: 4.57 MO: 0.080 CU: 3.580 CB: 0.310 SN: 0.009 W: 0.003
 CO: 0.040 AL: 0.004 N: 0.034 TI: 0.004 Y: 0.080 TA: 0.008
 B: 0.00130 MULT: 5. MULT X C: 0.250
 CB+TA LOWLIM: 0.250 CB+TA: 0.318

TYPE ANAL: PRODUCT ANALYSIS HEAT NO: 4083-7 *
 C: 0.047 MN: 0.350 F: 0.024 S: 0.004 SI: 0.390 CR: 14.86
 NI: 4.70 MO: 0.070 CU: 3.430 CB: 0.360 CO: 0.043 N: 0.024
 TA: 0.008
 MULT: 5. MULT X C: 0.235 CB+TA: 0.368

TYPE ANAL: TOP HEAT NO: 4083-7 *
 C: 0.047 MN: 0.350 F: 0.024 S: 0.004 SI: 0.390 CR: 14.86
 NI: 4.70 MO: 0.070 CU: 3.430 CB: 0.360 CO: 0.043 N: 0.024
 TA: 0.008
 MULT: 5. MULT X C: 0.235 CB+TA: 0.368

AS SHIP TEST: OVERAGE HTL: 2-920199
 B HRDNS: 293. B HRDNS (P/F): OK TEMP: 1300.
 HOURS: 2. MINS: 0. QUENCH: AIR
 CAPABILITY TEST: H900T
 B HRDNS: 401. B HRDNS (P/F): OK TEMP: 900.
 HOURS: 1. MINS: 0. QUENCH: AIR
 OFFSET %: 0.20 UTS KSI: 198.7 .2% YLD STR KSI: 180.9
 % EL 2" OR EQ: 8.0 % RED OF AREA: 20.60

PHYSICAL:
 FERRITE PCT: <1 FERRITE (P/F): OK MACRO 604 CL 1: A
 MACRO 604 CL 2: A MACRO 604 CL 3: A MACRO 604 CL 4: A
 MACRO 604 (P/F): OK MFLUX FREQUENCY: 0.00 MFLUX SEVERITY: 0.00
 MAGNAFLUX (P/F): OK

413 METALLURGICAL RELEASE *[Signature]* 1/20/93

5123823	CUST. NO.	BILL TO	2110	286	SHIP TO
ANDERSON SHUMAKER CO 824 S. CENTRAL AVE CHICAGO IL 60644		ANDERSON SHUMAKER CO 824 S. CENTRAL AVE CHICAGO IL 60644			
PRODUCT NUMBER	TEST LOT ID	SALES ORDER NO.	PURCHASE ORDER NO.		
32280-18157	4083-7-B1262A01	23689	735		

MATERIAL OVERAGED 1300 DEG F 2 HRS @TEMP 12 HRS T.T. AIR COOLED
 Material Ultrasonic tested per MIL-STD-2154 (SIZES 0"-10" INCL - CL A, OVER 10" - CL B) TYPE II (supercedes MIL-I-8950) per ARMCO UTP 7 REV 4 (SIZES 0"-10" INCL - CL A, SIZES OVER 10" - CL B) (CONTACT) and was found Heat treated at TIME, TEMP and QUENCH indicated above.

Material electric furnace melted, AOD refined, VAC ARC remelted. Melted and manufactured in the U.S.A.
 No welding or weld repair performed on this material.
 ASAP certifies conformance to NRC 10CFR PT 21, and 10CFR PT 50 APP B.
 This material was manufactured and tested in accordance with the noted specifications, and is in conformance with those specification requirements
 ASAP certifies that this material is manufactured free from mercury, radium, alpha source and low melting metal or alloy contamination.
 This material was produced in accordance with the Quality Assurance Program, Quality Assurance Manual, Issue 5 Rev 0 dtd 6/1/92.
 All testing procedures were conducted in accordance with the latest ASTM standards or applicable specifications.
 The recording of false, fictitious or fraudulent statements or entries on this document may be punished as a felony under federal statutes including Federal Law, Title 18, Chapter 47. This certified test report has been delivered to a consignee of material purchased from ASAP. To avoid the possibility of its misuse on the redelivery of this report to a third party it must be recertified by and under the name of such consignee.
 The chemical analyses and physical or mechanical test report are correct as contained in the records of the Corporation.

E. Famularo
 E. FAMULARO, CERTIFICATION CLERK

**METALLURGICAL
 RELEASE** *Jos 1/20/93*

MSi Metallurgical Services Inc.

1201 S. Ninth Avenue
Maywood, Illinois 60153
708-343-3444

Anderson Shumaker Company
824 S. Central Ave.
Chicago, IL 60644

Report No.: 9274-1
Date: 2-5-93
Order No.: 7401

Attention: Mr. Steven Tribble

SUBJECT

Tensile and hardness testing of one (1) test bar identified as 15-5 PHVAC, Condition H900, Heat #4083-7, Job #10553, AMS 5659.

TEST RESULTS***Tensile Testing**

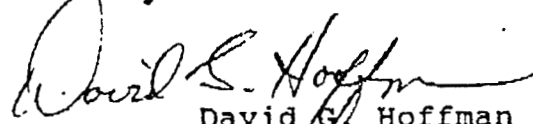
Tensile Strength, psi	199,600
Yield Strength, psi (.2% offset)	178,900
% Elongation in 2"	17
% Reduction of Area	61

Hardness Testing

Hardness, HB	401
--------------	-----

* Testing performed in accordance with ASTM E8-91 and E10-84.

Respectfully Submitted,
Metallurgical Services Inc.



David G. Hoffman
Senior Metallurgical Engineer

MSi Metallurgical Services Inc.
1201 S. Ninth Avenue
Maywood, Illinois 60153
708-343-3444

Anderson Shumaker Company
824 S. Central Ave.
Chicago, IL 60644

Report No.: 9274-2
Date: 2-5-93
Order No.: 7401

Attention: Mr. Steven Tribble

SUBJECT

Free ferrite examination of one (1) test bar identified as 15-5 PHVAC, Condition H900, Job #10553, Heat #4083-7, AMS 5659.

TEST RESULTS*

Free Ferrite Examination

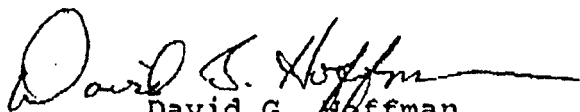
One (1) 15-5 PHVAC stainless steel sample was examined for percentage of free ferrite in accordance with Aerospace Material Specification (AMS) 2315A. The sample was sectioned perpendicular to the direction of rolling as identified in paragraph 3.1.6. The sample was metallographically prepared in accordance with ASTM E3-80 and examined in the etched condition at a magnification of 250X.

The microstructure was rated for percentage of free ferrite in accordance with the occupied squares method as outlined in paragraph 3.2.1. The worst field determined by metallographic examination was photographed at 250X and rated using a transparent grid overlay. A total of fifteen squares were used in the free ferrite calculation. The percentage of free ferrite was determined in accordance with paragraph 3.2.1.1. The results are as follows:

Percentage Free Ferrite

.92

Respectfully Submitted,
Metallurgical Services Inc.


David G. Hoffman
Senior Metallurgical Engineer

DGH/mj

7.0 REFERENCES

- 1-Kundalgorke, S.G.- "Effect Of Strain Rate And Temperature On The Stress Corrosion Cracking Tendency Of Engineering Alloys In Acidified Water", M.S. Thesis, Florida Atlantic University, Boca Raton, Fla., Dic.1992.
- 2-Ford, F.P.- "Stress Corrosion Cracking", Report No. 80CRD141, General Electric, Technical Information Series, Class I, Schenectady, N.Y., June 1980.
- 3-Swann, P.R.- "Stress Corrosion Failure", Scientific American, Feb.1966, Pag.121-135.
- 4-Parkins, R.N.- "Stress Corrosion Spectrum", Br. Corrosion J., Vol.7, Jan.1972, Pag.15-28.
- 5-Clarke Jr, W.C.-"Applications And Properties Of 15-5PH Steel" Source Book On Stainless Steel, A.S.M., Metals Park, Ohio, 1976.
- 6-Jaske, C.E.; Payer, J.H.; Balint, V.S.-"Corrosion Fatigue Of Metals In Marine Environments", MCIC 81-42, Batelle's Columbus Labs., July 1981.
- 7-Campbell, J.E.; Gerberich, W.W.; Underwood, J.H.-Editors- "Application Of Fracture Mechanics For Selection Of Metallic Structural Materials", A.S.M., Metals Park, Ohio, 1982.
- 8-Barsom, J.M.; Rolfe, S.T.-"Fracture & Fatigue Control In Structures - Applications Of Fracture Mechanics", 2nd Ed., Prentice Hall Inc., 1987.
- 9-Craig, H.L.; Editor- "Stress Corrosion - New approaches" A.S.T.M.-STP 610; Philadelphia, Pa., 1976.
- 10-Brown, B.F.; Beachem, C.D.-"A Study Of The Stress Factor In Corrosion Cracking By Use Of The Precracked Cantilever Beam Specimen", Corrosion, 5, 1965.

1994 NASA/ASEE SUMMER FACULTY FELLOWSHIP PROGRAM

JOHN F. KENNEDY SPACE CENTER
UNIVERSITY OF CENTRAL FLORIDA

11766
351502
515-35
33975
p- 30

MODELING AND MEASUREMENT OF THE PERFORMANCE OF A BRANCHED
CONDUIT SAMPLING SYSTEM IN A MASS SPECTROMETER LEAK DETECTOR

PREPARED BY:	Dr. John M. Russell
ACADEMIC RANK:	Associate Professor
UNIVERSITY AND DEPARTMENT:	Florida Institute of Technology Program in Aerospace Engineering
NASA/KSC	
DIVISION:	Electronic Systems
BRANCH:	Ground Support Equipment
NASA COLLEAGUE:	Frederick Adams Carolyn McCrary
DATE:	August 5, 1994
CONTRACT NUMBER:	University of Central Florida NASA-NGT-60002 Supplement: 17



ACKNOWLEDGEMENTS

I am indebted to my NASA colleagues RICK ADAMS and CAROLYN MCCRARY for suggesting the problem addressed herein, for authorizing the allocation of work space, equipment, and technical assistance at the Hazardous Gas Detection Laboratory, and for continued interest, encouragement, and council during my summer stay.

I am indebted to Messers. LARRY LINGVAY, RICH HRITZ, and GUY NAYLOR of the Hazardous Gas Detection Lab for setting me up at a workbench in Room 117 of the Engineering Development Lab, for checking me out on the use of several kinds of equipment (including the Alcatel ASM 110 Turbo CL mass spectrometer leak detector, the MKS Baratron and Granville Phillips pressure gauges, the Sierra Instruments flow controller, cylinders of compressed calibration gas and thier regulators, three different reservoir type leak detectors, and numerous fittings, flanges, caps, tubes, and tools) and for responding to all my requests for support with the utmost speed, skill, and enthusiasm.

I am also indebted to Mr. DAVID FLOYD of the I-NET company for lending me a Macintosh IIfx computer, for attaching it to the local area network, and for making sure that it can send print commands to his own laser printer.

Finally, I am indebted to Dr. LOREN ANDERSON and Mrs. KARI STILES for thier able admistration of the details of this year's Faculty Summer Fellow Program.

ABSTRACT

In the leak testing of a large engineering system, one may distinguish three stages, namely leakage measurement by an overall enclosure, leak location, and leakage measurement by a local enclosure. Sniffer probes attached to helium mass spectrometer leak detectors are normally designed for leak location, a qualitative inspection technique intended to pinpoint where a leak is but not to quantify its rate of discharge. The main conclusion of the present effort is that local leakage measurement by a leak detector with a sniffer probe is feasible provided one has: (a) quantitative data on the performance of the mass separator cell (a device interior to the unit where the stream of fluid in the sample line branches); and (b) a means of stabilizing the mass transfer boundary layer that is created near a local leak site when a sniffer probe is placed in its immediate vicinity. Theoretical models of the mass separator cell are provided and measurements of the machine-specific parameters in the formulas are presented. A theoretical model of a porous probe end for stabilizing the mass transfer boundary layer is also presented.

SUMMARY

As I wrote in abstract printed nearby, "Sniffer probes attached to helium mass spectrometer leak detectors are normally designed for leak location, a qualitative inspection technique intended to pinpoint where a leak is but not to quantify its rate of discharge". Most long range sniffer probe sampling systems are of branched conduit type. In such a system, sampled gas enters the tip of the sniffer probe, passes down the length of a long hose, and discharges into a so-called *mass separator cell*, a chamber with one inlet and two outlets. A typical chamber pressure in the mass separator cell is 0.18 atm.

One outlet from the mass separator is across the face of a permeable membrane (also called a *window*), on the other side of which is the very low pressure (say 10^{-7} to 10^{-8} atmospheres) typical of the analysis cell of a mass spectrometer leak detector. The meter reading on the leak detector is affected only by the portion of the sampled gas that passes across this permeable window. The rest of gas that enters the mass separator cell is exhausted to the low pressure port of mechanical vacuum pump. Since the inlet end of the sampling line is at atmospheric pressure, sampled gas will not flow through it unless the pressure at the outlet end is less than one atmosphere. In the present instance, the mechanical vacuum pump furnishes this low pressure at the outlet end of the sampling line.

Thus, of all the gas sniffed by the sniffer probe, only a small portion (say one six-hundredth to one eight hundredth) passes across the window of the mass separator cell where it is measured. The *internal supply-to-sample flowrate ratio* (ISSFR) (also called the *permeation ratio*) is the ratio of the rate of transport of helium *into the probe tip* to the rate of helium transport *across the separator cell window*. One must, of course, have quantitative knowledge of the ISSFR before one can relate the meter reading on a leak detector to the rate of transport of helium into the probe tip.

An interesting question that arises in this context is whether the ISSFR is a constant of the machine, or whether the IFFSR exhibits a functional dependence upon one or more parameters. To address this question, one must model the transport of helium across the mass separator window. If one assumes that the transport of helium across the window is a diffusion phenomenon, then one may argue that the rate of transport is directly proportional to the partial pressure of helium in the mass separator chamber and that the factor of proportionality is $\kappa A/h$, in which κ is the diffusivity of helium in the window material (in, say, $(\text{cm})^2/\text{s}$), A is the effective cross sectional area of the window (in, say $(\text{cm})^2$), and h is the window thickness (in, say, cm).

The present investigation yields formulas for the ISSFR in terms of $\kappa A/h$ and various flow parameters. It also furnishes results of measurements of $\kappa A/h$ under a variety of circumstances to determine whether it is indeed a constant of the machine. The results indicate that $\kappa A/h$ varies slightly with changes in chamber pressure of the mass separator, but that the variations are much weaker than the corresponding variations in other flow parameters.

The ratio of the rate of transport of helium from a leak to the rate of capture of that helium by the sniffer probe is the *external supply-to-sample flowrate ratio* (EFFSR). The present investigation involved the determination of the EFFSR in some simple cases (where a plain probe end is held close to a pinhole leak of known discharge rate) and found values in the range 0.20 to 0.95, though the results are extremely sensitive to currents of air in the laboratory where the tests are conducted.

Stabilization of the mass transfer boundary layer (the region of exceptionally high concentration of helium near the point leak) by a sponge, pad, or other medium through which the sampled gas is forced to seep promises significant reductions in the variations of the EFFSR due to currents in the room air. This report furnishes a model of the mass transport boundary layer when the porous medium exhibits either of two symmetries (cylindrical or spherical). The recommendations include follow-on research on the development of porous medium probe ends for stabilization of the mass transfer boundary layer.

TABLE OF CONTENTS

<u>Section</u>	<u>Title</u>	<u>Page</u>
	ACKNOWLEDGEMENTS	ii
	ABSTRACT	iii
	SUMMARY	iv
	LIST OF TABLES	vi
	LIST OF FIGURES	vi
I	INTRODUCTION	1-1
1.1	The need for leak testing	1-1
1.2	Stages in a generic leak testing program	1-1
1.3	Internal plumbing of a particular mass spectrometer leak detector with an branched conduit sampling system	1-2
1.4	Internal and external supply-to-sample flowrate ratios and their significance in the interpretation of probe measurements	1-3
1.5	Objectives of the present effort	1-5
II	THE MASS SEPARATOR CELL: PERFORMANCE PARAMETERS AND THEIR MEASUREMENT	2-1
2.1	Gradient-flux relationship in a generic diffusion process	2-1
2.2	Diffusion of helium across the mass separator window	2-1
2.3	Two steady flow methods for measuring the parameter $\kappa A/h$ of a mass separator window	2-2
2.3.1	A method that employs two reservoir type leaks and ultra high purity nitrogen	2-2
2.3.2	A method that employs one reservoir type leak and air	2-5
2.4	A time dependent flow method for measuring the parameter $\kappa A/h$ of a mass separator window	2-7
III	SOME OBSERVATIONS OF EXTERNAL SUPPLY-TO-SAMPLE FLOWRATE RATIO (STANDARD PROBE TIP)	3-1
3.1	Probe end inserted loosely in opening of reservoir leak	3-2
3.2	Probe end held at a forty-five degree angle to a flat surface with a pinhole leak	3-2
3.3	Probe shaft held flush against a flat surface with a pinhole leak about 4mm from the probe end	3-2
IV	CONCEPT OF A DRAFT DAMPER TO MINIMIZE DISPERSAL OF LEAKED HELIUM IN THE ROOM AIR	4-1
4.1	Preliminary remarks	4-1
4.2	Padded diaphragm probe end	4-2
4.3	Porous probe end in the form of a spherical wedge	4-3
V	CONCLUSIONS AND RECOMMENDATIONS	5-1
5.1	Conclusions	5-1
5.3	Recommendations	5-1
	REFERENCES	6-1

LIST OF TABLES

<u>Number</u>	<u>Title</u>	<u>Page</u>
1	Measurements of $\kappa A/h$ with an apparatus involving two reservoir leaks.....	2-5
2	Measurements of $\kappa A/h$ with an apparatus involving one reservoir leak and air.....	2-6
3	Measurements of the decay of $(p_{\text{He}})_{\text{window}}$ with respect to t	2-8

LIST OF FIGURES

<u>Number</u>	<u>Title</u>	<u>Page</u>
1	Internal pumping of a leak detector featuring a sniffer probe and a branched conduit sampling system.....	1-3
2	Schematic diagram of apparatus for tests involving two reservoir leaks.....	2-3
3	Window diffusivity parameter $\kappa A/h$ versus chamber pressure in the mass separator cell.....	2-5
4	ISSFR versus chamber pressure in the mass separator cell.....	2-5
5	Window diffusivity parameter $\kappa A/h$ versus chamber pressure in the mass separator cell.....	2-6
6	A closed container with a porous stopper.....	2-7
7	Probe held in various attitudes relative to flange of a reservoir leak.....	3-1
8	Structure of the diffusion boundary layer within a padded diaphragm probe.....	4-3
9	Structure of the diffusion boundary layer within a draft damper shaped like a hemisphere.....	4-5

SECTION ONE

INTRODUCTION

1.1 THE NEED FOR LEAK TESTING

The storage and transport of fluid is intrinsic to many engineering devices. The ability of such a device to carry out a given mission and to do so safely is often contingent on *leak tightness*. Accordingly, inspection for leak tightness constitutes a significant portion of the time devoted to between-flight testing of the space shuttle orbiter.

1.2 STAGES IN A GENERIC LEAK TESTING PROGRAM

A useful compendium of the technology for leakage testing was prepared in 1968 by J. WILLIAM MARR on behalf of the General Electric Company and was published as a NASA Contractor's Report under the title *Leakage testing handbook* (Ref. 1). In the leak testing of a large engineering system, one may distinguish three stages: (i) leakage *measurement* by an *overall* enclosure; (ii) leak *location*; and (iii) leakage *measurement* by a *local* enclosure.

The between-flight testing of the space shuttle main engine compartment conforms to a paradigm of this sort. Thus, in stage (i), one may seal off all but two openings of the engine compartment. These openings serve as the inlet and the outlet for *purge gas*. Suspect fluid lines in the compartment are pressurized with *tracer gas* such as helium. Leaked helium then becomes a trace contaminant in the effluent. The concentration of this effluent contaminant may be measured by helium mass spectrometry. When data from such measurements are combined with information about the rate of transport of purge gas, one can deduce the total rate of discharge of tracer gas through all of the leaks in all of the fluid lines that had been pressurized with tracer gas. The foregoing description is a rough representation of the *Helium Signature Test* (Ref. 2) that operations personnel at Kennedy Space Center routinely carry out.

One advances to stage (ii) of the leak test program whenever leakage measurement by an overall enclosure reveals the presence of at least one out-of-specification leak somewhere. A hand-held

probe attached to the collection system of a helium-mass-spectrometer leak detector—a *sniffer probe*—is a standard device for the location of such individual leaks. According to the classical paradigm as described by MARR, such a *leak-location* effort yields *qualitative* information—whether tracer gas is or is not leaking from a suspect leak site—but does not provide *quantitative* information about the rate of discharge through a leak, once located.

The reason why a generic sniffer probe does not actually measure the discharge rate from an individual leak is obvious. Even if the leak detector is calibrated so as to give accurate information regarding the rate of transport of helium into the probe tip, the user does not know what portion of the tracer gas discharged from the leak actually enters the probe tip and what remaining portion is dispersed in the surrounding environment. In the Final Report of a Summer Faculty Research Fellowship (Ref. 3), the present author suggested the term *external supply-to-sample flowrate ratio* (ESSFR) for the ratio whose numerator is the rate of discharge of tracer gas from the leak and whose denominator is the rate of transport of tracer gas into the probe tip.

To continue the discussion of the classical paradigm for leak testing a large test object, suppose that leakage measurement by an overall enclosure (stage (i)) has indicated the presence of an out-of-specification leak somewhere and that inspection of the test object by a sniffer probe (stage (ii)) has pinpointed the location of a local leak site. One thus advances to stage (iii), namely leakage measurement by a local enclosure. In the classical paradigm, such testing involves the installation of a vacuum bag around the leak site to prevent dispersal of the leaked tracer gas into the surrounding environment. If one is confident that all or nearly all of the leaked tracer gas enters the sampling line of the leak detector, then one can make a quantitative measurement of the discharge through the individual leak.

The cramped quarters of the main engine compartment of the shuttle orbiter, the complexity of cable bundles and plumbing therein, and the general inaccessibility of leak sites render the installation of vacuum bags in the main engine compartment ex-

tremely awkward. Thus, vacuum-bag testing in the main engine compartment amounts to a *heroic measure* that operations personnel resort to only when circumstances make it unavoidable.

One may try to estimate the rate of discharge of tracer gas from a local leak site from information furnished by a sniffer probe, provided one is willing to accept the uncertainties associated with poor understanding of the external supply-to-sample flowrate ratio. Some routine inspection procedures employed by operations personnel in the leak testing of the main engine compartment of the space shuttle orbiter are of this latter kind. Acceptability Criteria pertaining to such inspections are described in SPECIFICATION number MF0001-003 titled "Proof pressure and leak detection—Aerospace plumbing systems and assemblies" prepared by D. R. SUEME & K. R. RAVAL on behalf of Rockwell Corporation (Ref. 4).

1.3 INTERNAL PLUMBING OF A PARTICULAR MASS SPECTROMETER LEAK DETECTOR WITH A BRANCHED CONDUIT SAMPLING SYSTEM

Helium mass spectrometer leak detectors equipped with sniffer probes employ sampling systems that one may group into two broad classes according to their internal plumbing. To understand why this plumbing has the form that it has, one must provide some background on the general layout of mass spectrometer leak detectors.

Every helium mass spectrometer leak detector has an *analysis cell*, which acts as a transducer whose signal is proportional to the partial pressure of a particular gas species identified by the charge-to-mass ratio of its positively charged ion. The analysis cell operates only if the gas in it is rarified, *i.e.* if the mean free path is large compared to the spatial dimensions of the device. The total pressure in the analysis cell must thus be on the order of 10^{-7} atm or less. Thus, every mass spectrometer leak detector has a *high vacuum envelope* containing an analysis cell into which some sampled gas must pass if its partial pressure (or, more precisely, if an electrical signal proportional to the partial pressure) is to be measured.

In a typical mass spectrometer leak detector, a sequence of vacuum pumps maintains the very low

pressure in the high vacuum envelope. One pump within that sequence has an input port whose pressure is about the same as that of the analysis cell. I will call that port the *lowest pressure port*. The pumping system is designed so as to maintain near constancy (under normal operating conditions) of the volume transport rate $\dot{\Delta}_{\max}$ through the lowest pressure port. The product of $p_{\text{He,ac}}\dot{\Delta}_{\max}$, in which $p_{\text{He,ac}}$ is the partial pressure of helium in analysis cell, is a measure of the flowrate of helium through the high vacuum envelope*. If $\dot{\Delta}_{\max}$ is indeed constant, then the flowrate $p_{\text{He,ac}}\dot{\Delta}_{\max}$ is proportional to $p_{\text{He,ac}}$, which, in turn, is proportional to the electrical signal generated by the analysis cell. In this respect, the electrical signal generated by the analysis cell is a measure of the flow rate of helium through the high vacuum envelope. Thus, a modern designer of a leak detector may feel justified in equipping his or her device with a *leak flowrate meter*, whose signal is proportional to the electrical current through the target electrode in the analysis cell, but whose scale is demarcated in flowrate units such as $\text{atm}\cdot(\text{cm})^3/\text{sec}$.

The pumping system in any leak detector has a limited capacity and this limit places a ceiling on the rate at which sampled gas may be admitted into the high vacuum envelope without exceeding the 10^{-7} atm ceiling on the total pressure there. The simplest type of sniffer probe sampling system is one in which all of the sampled gas that enters the probe tip is admitted into the high vacuum envelope of the leak detector. This arrangement is described by the term *direct conduit* sampling system. Owing to the limitations on pumping capacity described in the opening sentence of this paragraph, the rate of flow through the probe in a direct conduit sampling system must be very low. In addition, the sampling hose that runs from the sniffer probe to the leak detector must be part of the high vacuum envelope itself. To avoid excessive leakage by permeation of atmospheric gasses through the hose, it must have a rather thick wall and a rather short length.

In recent years a second kind of sampling system has appeared on the market, whose conduit is

* The beginning of subsection 1.3 below provides some motivation for the representation of flowrate through a streamtube as the product of pressure at a particular cross section with volume transport rate across that section.

branched rather than direct. Thus, sampled gas flows through the sampling line into the chamber of a *mass separator cell* which has one inlet and two outlets. Gas flows through the sampling hose owing to the difference in pressure between atmospheric pressure at the probe tip and the somewhat lower pressure (say 0.18 atm) in the mass separator chamber. Since the sampling hose is not part of the low pressure envelope of the leak detector, it is not subject to the limitations on wall thickness and hose length described in the previous paragraph. Hoses in use in the orbiter processing facility, for example, are made of PVC plastic, have an outside diameter of about 0.5 cm and a length of 100ft.

Of the two outlets from the chamber of the mass separator cell, one is a permeable membrane or *window*, across which a small portion of the sampled gas diffuses. The window is a rigid partition that separates the mass separator chamber from the high vacuum envelope of the leak detector. The relatively low diffusive transport of gas across the window prevents the sampled gas from overwhelming the pumping system for the high vacuum envelope. In a branched conduit sampling system, the overwhelming portion of the sampled gas is exhausted into the low pressure port of a mechanical vacuum pump whose high pressure end vents to the atmosphere. One may thus proclaim

The distinctive feature of branched conduit sampling system: *The electrical signal generated by the analysis cell (and displayed on a flow rate meter) is proportional to the rate of transport of helium across the mass separator window, not to the (much larger) rate of transport of helium through the probe tip.*

Fig. 1 is a schematic diagram showing the internal plumbing of a particular helium mass spectrometer leak detector manufactured by Alcatel (type ASM 110 Turbo CL). Point A is the tip of the sniffer probe; point B is a quick disconnect which enables the sniffer probe hose to be detached from the leak detector cabinet; point C is the inlet to the mass separator chamber; point D is the upstream end of the high vacuum conduit that starts at the mass separator window; path DEF is the portion of the sample conduit that passes through the high vacuum envelope; device FG is a turbomolecular pump whose inlet is the lowest pressure port described earlier; path GH is a moderate vacuum conduit; device H is the low pressure stage of a vane

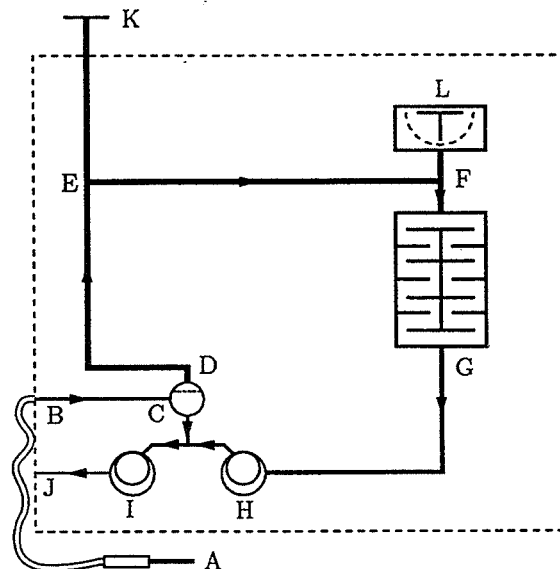


Fig. 1. Internal plumbing of a leak detector featuring a sniffer probe and a branched conduit sampling system.

pump system consisting of two identical stages; device I is the high pressure stage of the pair; station J is the exhaust to the room; device L is the analysis cell; and point K is the a direct input port to the high vacuum envelope (which is capped during normal operation of the sniffer probe).

Most of the sampled gas follows the circuit ABCIJ (the end of which is exhausted to the room), but some of it follows the circuit ABCDEFGHIJ. Only the latter portion affects the signal displayed on the leak flowrate meter.

1.4 INTERNAL AND EXTERNAL SUPPLY-TO-SAMPLE FLOWRATE RATIOS AND THEIR SIGNIFICANCE IN THE INTERPRETATION OF PROBE MEASUREMENTS

Before one can interpret the terms internal supply-to-sample flowrate and external supply-to-sample flowrate, one must clarify what one means by the term *flowrate*. Let $\dot{\Delta}$ (in, say, $(\text{cm})^3/\text{s}$) be the rate of transport of fluid volume across a particular cross section of a streamtube. Let ρ^* (in, say, $\text{gm-mole}/(\text{cm})^3$) be the molar density of the fluid averaged over the same cross section. Then the

product $\rho^* \dot{\Delta}$ has the dimensions of gm-mole/s and represents the rate of transport of matter across the streamtube. According to the law of conservation of mass, however, the rate of transport of matter (and thus the product the product $\rho^* \dot{\Delta}$) is the same for all cross sections of the streamtube (even if ρ^* and $\dot{\Delta}$ vary from one station to the next) and is an intrinsic property of the streamtube.

According to the equation of state of an ideal gas,

$$p = \rho^* \mathcal{R} T, \quad (1.1)$$

in which p is the pressure (in, say atm), T is the absolute temperature (in, say, °K), and \mathcal{R} is the universal gas constant, whose numerical value is*

$$\mathcal{R} = 82.0560 \frac{\text{atm} \cdot (\text{cm})^3}{\text{gm-mole} \cdot ^\circ\text{K}}. \quad (1.2)$$

If one multiplies (1.1) by $\dot{\Delta}$, one obtains

$$p \dot{\Delta} = \rho^* \dot{\Delta} \mathcal{R} T. \quad (1.3)$$

It follows that $p \dot{\Delta}$ is directly proportional to the rate of transport of matter $\rho^* \dot{\Delta}$ through the streamtube with a factor of proportionality $\mathcal{R} T$ that depends only on the absolute temperature. Following the standard convention in the leak testing literature, I will refer, here and elsewhere, to the expression $p \dot{\Delta}$ as the *flowrate* through a streamtube.

In subsection 1.2 above, I defined the external supply-to-sample flowrate ratio (ESSFR) to be "the ratio whose numerator is the rate of discharge of tracer gas from the leak and whose denominator is the rate of transport of tracer gas into the probe tip". Thus,

$$\text{ESSFR} = \frac{(p_{\text{He}} \dot{\Delta})_{\text{leak}}}{(p_{\text{He}} \dot{\Delta})_{\text{probe}}}. \quad (1.4)$$

By similar reasoning, one may define the *internal supply to sample flowrate ratio* (ISSFR) (also called the *permeation ratio*) by the expression

$$\text{ISSFR} = \frac{(p_{\text{He}} \dot{\Delta})_{\text{probe}}}{(p_{\text{He}} \dot{\Delta})_{\text{window}}}, \quad (1.5)$$

* The numerical value for the gas constant was computed from reference values in the *U.S. Standard Atmosphere 1976* (Ref. 5, p3)

in which the subscript in the denominator refers to the streamtube passing through the mass separator window. The flowrate meter on the leak detector furnishes the value of $(p_{\text{He}} \dot{\Delta})_{\text{window}}$.

Suppose that one has a mixture of *calibration gas* whose helium concentration $c_{\text{He}} = p_{\text{He}}/p_{\text{mix}}$ is known (here p_{He} is the partial pressure of helium in the mixture and p_{mix} is the total pressure of all the gases in the mixture). Then

$$p_{\text{He}} = c_{\text{He}} p_{\text{mix}}. \quad (1.6)$$

If one multiplies both sides by the volume transport rate of gas mixture into the probe tip $\dot{\Delta}$, one obtains

$$(p_{\text{He}} \dot{\Delta})_{\text{probe}} = c_{\text{He}} (p_{\text{mix}} \dot{\Delta})_{\text{probe}}. \quad (1.7)$$

Suppose, further, that one can measure the flowrate $(p_{\text{mix}} \dot{\Delta})_{\text{probe}}$ of calibration gas through the probe tip by a suitable flowmeter. Then both factors in the right member of (1.7) are measurable or known, and so helium transport rate $(p_{\text{He}} \dot{\Delta})_{\text{probe}}$ through the probe tip is expressible in terms of measurable quantities. It follows that the numerator and the denominator in the right member of (1.5) are both measurable and (1.5) furnishes the corresponding value of ISSFR.

It is not obvious that the relation between $(p_{\text{He}} \dot{\Delta})_{\text{window}}$ and $(p_{\text{He}} \dot{\Delta})_{\text{probe}}$ is one-to-one. Even if the relationship is one-to-one, it is not obvious that the relationship is linear. One of the objectives of the present research effort was to determine set of parameters upon which ISSFR depends. Chapter II below addresses this objective in detail.

From the foregoing definitions, one may deduce that

$$\begin{aligned} (p_{\text{He}} \dot{\Delta})_{\text{leak}} &= \frac{(p_{\text{He}} \dot{\Delta})_{\text{leak}}}{(p_{\text{He}} \dot{\Delta})_{\text{probe}}} \cdot \frac{(p_{\text{He}} \dot{\Delta})_{\text{probe}}}{(p_{\text{He}} \dot{\Delta})_{\text{window}}} \cdot (p_{\text{He}} \dot{\Delta})_{\text{window}} \\ &= \text{ESSFR} \cdot \text{ISSFR} \cdot (p_{\text{He}} \dot{\Delta})_{\text{window}}. \end{aligned} \quad (1.8)$$

If one has a good model of the action of the mass separator cell, one can relate ISSFR to measurable quantities and to constants of the machine and if the flowrate meter is properly adjusted, one can read $(p_{\text{He}} \dot{\Delta})_{\text{window}}$ from the flowrate meter. Equation (1.8) indicates that one still needs to know the value of ESSFR before one can use a sniffer probe to measure $(p_{\text{He}} \dot{\Delta})_{\text{leak}}$.

The most serious obstacle to the determination of ESSFR is its dependence upon air currents in the environment where the test is taken. If, for example, there is a draft in the room where a sniffer probe is held up to a point leak source, then one would expect the sniffer probe to capture a smaller fraction of the leaked tracer gas (leading to a larger value of ESSFR) than it would capture if there were no such draft. The dynamics of the flow in the neighborhood of a stock sniffer probe and a point leak source in the presence of arbitrary drafts is complicated enough to preclude any quantitative prediction of ESSFR in general. Section III below describes some observations of ESSFR in various conditions, namely (i) when the leaked gas emerges from a duct into which the probe shaft can be inserted; (ii) when the leak is from a point source on a flat surface and the probe is placed at a 45° angle to that surface; and (iii) when the leak is from a point source on a flat surface and the probe shaft is laid flat against the surface with the probe tip some 4mm away from the point source. In all these cases, the value of ESSFR depended upon room drafts, but was in the range $0.20 < \text{ESSFR} < 0.95$.

Fortunately, with modifications of the environment through which the tracer gas passes one may expect to reduce the uncertainties considerably. Suppose, for example, that tracer gas leaks from a point on a planar surface. One may construct a hemispherical sponge with a hole along its axis of symmetry that just fits the shaft of the sniffer probe (so the probe tip is at the center of the flat face of the sponge). If one places the sponge flush against the leak surface and centered on the leak, then one may expect the flow of air through the sponge to be affected far more by friction within the sponge than by room drafts. In this respect, one may expect that the use of porous medium probe ends may stabilize the *mass transfer boundary layer*, i.e. the region containing helium rich air in the vicinity of the point leak against which the probe tip has been placed.

A second objective of the present research effort was thus to determine (analytically) the distribution of helium through a porous medium probe end. Section IV of this report addresses this objective in detail.

1.5 OBJECTIVES OF THE PRESENT EFFORT

As I have pointed out in the preceding subsection, the present research effort addressed two main objectives, namely

1. To determine the set of parameters upon which the internal supply-to-sample flowrate ratio (ISSFR) depends and to evaluate the machine specific constants in the formula for ISSFR for a particular device.
2. To determine the distribution of helium concentration in the interior of a porous medium probe end of simple form.
3. To indicate how knowledge of the helium distribution in the porous probe end can be used to design probe ends that promise relatively high values of the external supply-to-sample flowrate ratio (ESSFR).

SECTION TWO

THE MASS SEPARATOR CELL: PERFORMANCE PARAMETERS AND THEIR MEASUREMENT

2.1 GRADIENT-FLUX RELATIONSHIPS IN A GENERIC DIFFUSION PROCESS

Let ρ_{He}^* denote the molar density of helium (in, say gm-moles/(cm)³) in some background material (which may, for example, be the mass separator window or air). If ρ_{He}^* is nonuniform, one expects that helium will diffuse in the direction of most rapid decrease of ρ_{He}^* . Let \mathbf{u}_{He} (in, say, (cm/s)) denote the migration velocity of helium through the background material. One expects that \mathbf{u}_{He} will, in general, be a function of both position and time. Now the vector $\nabla\rho_{\text{He}}^*$ (in, say, gm-moles/(cm)⁴) points in direction of most rapid *increase* of ρ_{He}^* and its magnitude $|\nabla\rho_{\text{He}}^*|$ equals the slope of the curve of ρ_{He}^* with respect to arc length in that direction. Thus the vector $-\nabla\rho_{\text{He}}^*$ points in direction of most rapid *decrease* of ρ_{He}^* . The simplest standard model of diffusion thus asserts that

$$\rho_{\text{He}}^* \mathbf{u}_{\text{He}} = -\kappa \nabla \rho_{\text{He}}^*, \quad (2.1)$$

in which κ is the *diffusivity* of helium through the background material. In view of the units of measurement furnished earlier for ρ^* , $\nabla\rho^*$, and \mathbf{u}_{He} one concludes that the corresponding units for κ compatible with (2.1) are (cm)²/s.

2.2 DIFFUSION OF HELIUM ACROSS THE MASS SEPARATOR WINDOW

Suppose that the mass separator window has cylindrical symmetry. Let z be an axial coordinate measured along the axis of symmetry. For definiteness, let the plane $z = 0$ be the face of the window that abuts the mass separator chamber and let the plane $z = h$ be the face that abuts the high vacuum envelope of the leak detector. Thus, helium diffuses in the direction of increasing z and the only non-trivial component of the vector equation (2.1) is the z -component. This component reads

$$\rho_{\text{He}}^* w_{\text{He}} = -\kappa \frac{d\rho_{\text{He}}^*}{dz}, \quad (2.2)$$

in which w_{He} is the z -component of \mathbf{u}_{He} .

Let A be the cross sectional area of the mass separator window. If one multiplies (2.2) by A , one obtains

$$\rho_{\text{He}}^* w_{\text{He}} A = -\kappa A \frac{d\rho_{\text{He}}^*}{dz}. \quad (2.3)$$

Now $w_{\text{He}} A$ is the rate of transport of helium volume, $\dot{\Delta}$, across a typical plane $z = \text{constant}$ internal to the window. One may therefore write (2.3) in the form

$$\rho_{\text{He}}^* \dot{\Delta} = -\kappa A \frac{d\rho_{\text{He}}^*}{dz}, \quad (2.4)$$

In the first paragraph of subsection 1.4 above, I pointed out that $\rho_{\text{He}}^* \dot{\Delta}$ is the rate of transport of helium (in, say gm-moles/s) through a streamtube which, in this case, is the tube bounded by the side edge of the mass separator window.

Consider, now, the region between the plane $z = 0$ and any other plane $z = \text{constant}$ in the window. If the diffusion is steady in time, there is no accumulation of helium between these planes, *i.e.* inward transport of helium across the plane $z = 0$ is balanced by outward transport of helium across the plane $z = \text{constant}$. It follows that

$$(\rho_{\text{He}}^* \dot{\Delta})|_{z=0} = (\rho_{\text{He}}^* \dot{\Delta})|_{z=\text{constant}} \quad (2.5)$$

for any z greater than 0 and less than h . One concludes that the left member of (2.4) is independent of z . If one integrates (2.4) with respect to z from $z = 0$ to $z = h$, one obtains, therefore,

$$\rho_{\text{He}}^* \dot{\Delta} h = -\kappa A (\rho_{\text{He}}^*|_{z=h} - \rho_{\text{He}}^*|_{z=0}), \quad (2.6)$$

In the present application,

$$\rho_{\text{He}}^*|_{z=h} \ll \rho_{\text{He}}^*|_{z=0}, \quad (2.7)$$

which expresses the assumption molar density of helium in the high vacuum envelope of the leak detector (where the total pressure is less than 10^{-7} atm) is very much smaller than the molar density of helium in the mass separator chamber (where the total pressure is some modest fraction of an atmosphere, such as 0.18 atm). In view of (2.7), equation one may approximate (2.6) by the simpler equation

$$\rho_{\text{He}}^* \dot{\Delta} h = \kappa A \rho_{\text{He}}^*|_{z=0}, \quad (2.8)$$

or

$$\rho_{\text{He}}^* \dot{\Delta} = \frac{\kappa A}{h} \rho_{\text{He}}^*|_{z=0}, \quad (2.9)$$

Now the partial density $\rho_{\text{He}}^*|_{z=0}$ of helium on the boundary of the mass separator chamber is related to the partial pressure p_{He} of helium there by an equation analogous to (1.1) *i.e.*

$$p_{\text{He}} = \rho_{\text{He}}^* \mathcal{R}T. \quad (2.10)$$

If one multiplies both sides of (2.9) by $\mathcal{R}T$ and makes use of (2.10), one obtains

$$(p_{\text{He}} \dot{\Delta})_{\text{window}} = \frac{\kappa A}{h} p_{\text{He}}|_{z=0}, \quad (2.11)$$

Equation (2.11) is the model of diffusion across the mass separator window that I have employed in throughout present investigation. The values of A and h are constants for any particular mass separator window. One expects that the diffusivity κ for helium diffusing through the window material should be proportional to some positive power of the absolute temperature T , but not necessarily to anything else. If κ is indeed dependent only on T , then it should not change from one experiment to the next, provided the experiments are all run at the same temperature. Equation (2.11) suggests that $\kappa A/h$ is a basic performance parameter of the machine. I will discuss methods for the determination of $\kappa A/h$ (suitable units for which are $(\text{cm})^2/\text{s}$) in the following subsections.

2.3 TWO STEADY FLOW METHODS FOR MEASURING THE PARAMETER $\kappa A/h$ OF A MASS SEPARATOR WINDOW

2.3.1 A METHOD THAT EMPLOYS TWO RESERVOIR TYPE LEAKS AND ULTRA HIGH PURITY NITROGEN.

Fig. 2, printed nearby, is a schematic diagram of the apparatus that employs two reservoir leaks. The acronyms in the figure have the following interpretations: (i) AC stands for *analysis cell*; TMP stands for *turbomolecular pump*; VP stands for *vane pump*, of which there are two identical stages labeled *first* and *second*; MSC stands for *mass separator cell*; RL stands for *reservoir leak*, of which there are two labeled *internal* and *external* (relative to the high vacuum envelope); PG stands for *pressure gauge*; QD stands for *quick disconnect*;

and FM stands for *flowmeter*, of which there one for the probe and one for the vent.

Both of the reservoir leaks are equipped with hand valves. The purpose of the internal reservoir leak is to validate the zero, peak, and gain setting of the flowrate meter, whose signal is proportional to the electrical current of the helium ion beam, but whose scale is demarcated in units of leak flowrate as (*cf.* the discussion in subsection 1.3 above). One may shut off the hand valve on the external reservoir leak bottle and disconnect the sniffer probe, then adjust the flowrate meter to force agreement between the meter reading and the certification label on the internal reservoir leak bottle. When the agreement is satisfactory, one shuts the hand valve on the internal reservoir leak bottle and thenceforth interprets the meter reading as the measured value of $(p_{\text{He}} \dot{\Delta})_{\text{window}}$.

Once the meter is adjusted and the hand valve on the internal reservoir leak is shut off, one may attach the sniffer probe (keeping the hand valve on the external reservoir leak shut) and begin to flow ultra high purity nitrogen through the sniffer probe line. The arrangement in Fig. 2 is meant to ensure that all of the gas that enters the probe tip is nitrogen and that the pressure of the gas at the probe tip is atmospheric. This condition is achieved if the two flow meters shown are identical, are arranged in the symmetric pattern shown, and if the hand valve on the nitrogen supply regulator is adjusted so that the readings from the two flow meters are equal. In tests under the conditions described in the last paragraph, I have verified that the leak flowrate meter continues to read zero. Thus, any helium contaminant in the ultra high purity nitrogen supply I used this summer is below the noise level in the measurement system.

Next, one opens the hand valve on the external reservoir leak and observes the response of the leak flowrate meter. The effect is usually to release a slug of helium into the system (which produces a transient spike in the flowrate meter reading), followed by a slow decay of the indicated value of $(p_{\text{He}} \dot{\Delta})_{\text{window}}$. One must often wait for a half hour or more for the signal to appear to stabilize at a reasonably steady value. When it does, one may assume that the total number of moles per unit time of gas (both helium and nitrogen) that enter the mass separator cell is equal to $(\mathcal{R}T)^{-1}$ times

$$(p_{\text{He}} \dot{\Delta})_{\text{RL,ex}} + (p_{\text{N}_2} \dot{\Delta})_{\text{probe}}. \quad (2.12)$$

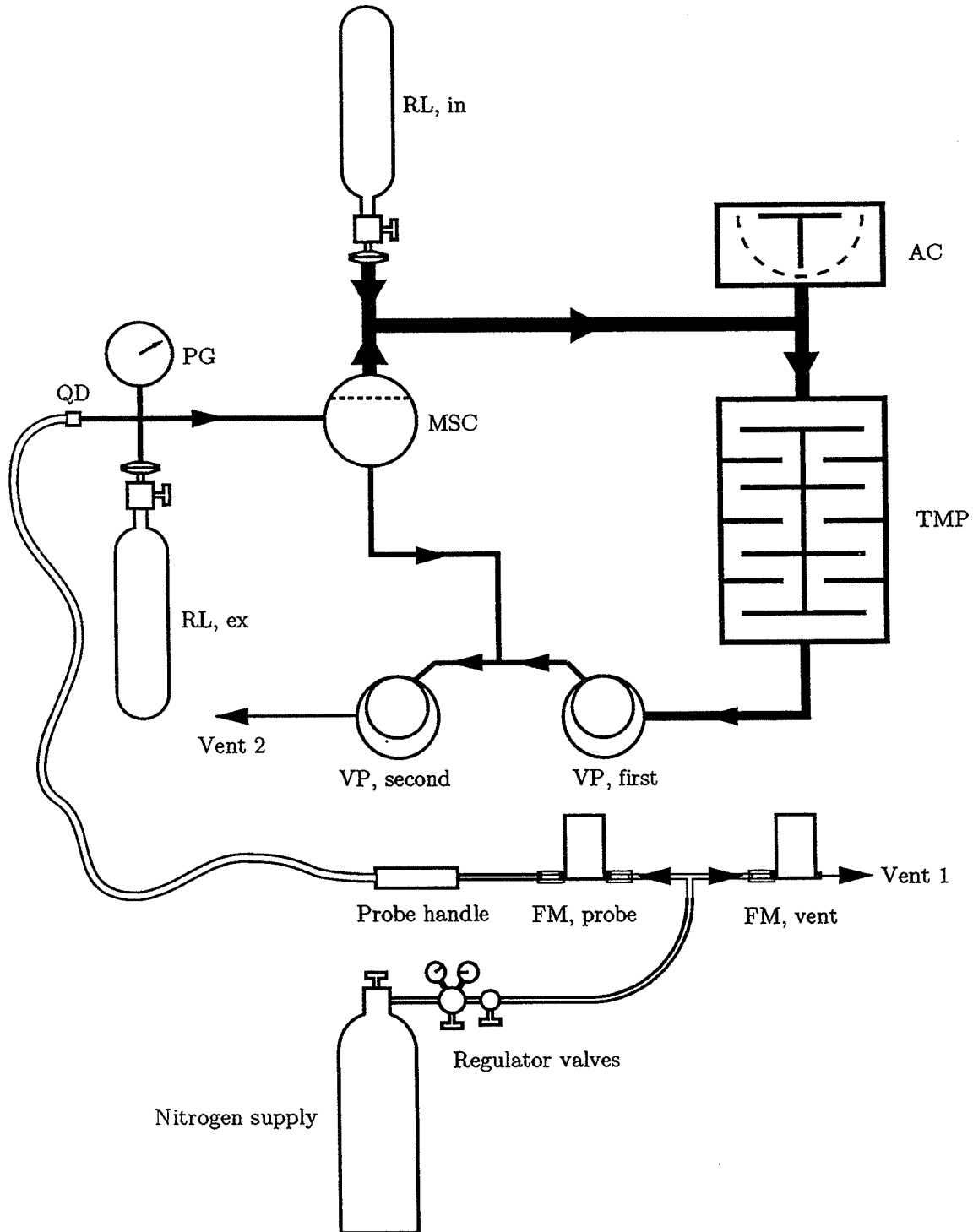


Fig. 2. Schematic diagram of apparatus for tests involving two reservoir leaks

If one assumes that the gas that enters the mass separator cell is a well mixed solution of helium in nitrogen, one may represent the concentration c_{He} of helium in the mass separator chamber by

$$(c_{\text{He}})|_{\text{MSC}} = \frac{(p_{\text{He}})_{\text{chamber}}}{(p_{\text{He}})_{\text{chamber}} + (p_{\text{N}_2})_{\text{chamber}}} \quad (2.13)$$

Now the volume occupied by the helium component of a unit mass of a solution of helium in nitrogen is equal to the volume occupied by the nitrogen component. In particular, there is no need to distinguish between the volume transport rate $\dot{\Delta}$ of helium and nitrogen in the mixture that enters the mass separator chamber. One may thus multiply the numerator and the denominator of (2.13) by the common factor $\dot{\Delta}$ to obtain

$$(c_{\text{He}})|_{\text{MSC}} = \frac{(p_{\text{He}}\dot{\Delta})_{\text{chamber}}}{(p_{\text{He}}\dot{\Delta})_{\text{chamber}} + (p_{\text{N}_2}\dot{\Delta})_{\text{chamber}}} \quad (2.14)$$

Now all of the helium that enters the chamber must come from the external reservoir leak and all of the nitrogen that enters the chamber must come from the probe tip. It follows that

$$(p_{\text{He}}\dot{\Delta})_{\text{chamber}} = (p_{\text{He}}\dot{\Delta})_{\text{RL,ex}} \quad (2.15)$$

$$(p_{\text{N}_2}\dot{\Delta})_{\text{chamber}} = (p_{\text{N}_2}\dot{\Delta})_{\text{probe}} \quad (2.16)$$

In view of (2.15) and (2.16), one may write (2.14) in the equivalent form

$$(c_{\text{He}})|_{\text{MSC}} = \frac{(p_{\text{He}}\dot{\Delta})_{\text{RL,ex}}}{(p_{\text{He}}\dot{\Delta})_{\text{RL,ex}} + (p_{\text{N}_2}\dot{\Delta})_{\text{probe}}} \quad (2.17)$$

The two flowrates in the denominator of (2.17) differ by a large factor. Thus, in the tests I conducted this summer,

$$(p_{\text{He}}\dot{\Delta})_{\text{RL,ex}} = 5.0 \times 10^{-6} \text{ atm}\cdot(\text{cm})^3/\text{sec} \quad (2.18)$$

according to the label on the leak bottle (which had been prepared by the Calibration Laboratory at KSC). If there are no obstructions in the sniffer probe line, the probe flowrate meter registers a typical value of

$$(p_{\text{N}_2}\dot{\Delta})_{\text{probe}} = 3.53 \text{ atm}\cdot(\text{cm})^3/\text{sec} \quad (2.19)$$

The denominator of (2.17) is clearly dominated by the term $(p_{\text{N}_2}\dot{\Delta})_{\text{probe}}$, and one may approximate (2.17) by the simpler expression

$$(c_{\text{He}})|_{\text{MSC}} \approx \frac{(p_{\text{He}}\dot{\Delta})_{\text{RL,ex}}}{(p_{\text{N}_2}\dot{\Delta})_{\text{probe}}} \quad (2.20)$$

I have indicated why one may approximate the fraction (2.17) by the simpler fraction (2.20). By the same token, one may approximate the fraction (2.13) by the simpler fraction

$$(c_{\text{He}})|_{\text{MSC}} \approx \frac{(p_{\text{He}})_{\text{chamber}}}{(p_{\text{N}_2})_{\text{chamber}}} \quad (2.21)$$

It follows from (2.20) and (2.21) that

$$\frac{(p_{\text{He}}\dot{\Delta})_{\text{RL,ex}}}{(p_{\text{N}_2}\dot{\Delta})_{\text{probe}}} = \frac{(p_{\text{He}})_{\text{chamber}}}{(p_{\text{N}_2})_{\text{chamber}}} \quad (2.22)$$

One may rearrange (2.22) to give an explicit formula for the partial pressure of helium in the mass separator chamber, *viz.*

$$(p_{\text{He}})_{\text{chamber}} = \frac{(p_{\text{He}}\dot{\Delta})_{\text{RL,ex}}}{(p_{\text{N}_2}\dot{\Delta})_{\text{probe}}} (p_{\text{N}_2})_{\text{chamber}} \quad (2.23)$$

According to equation (2.11) above,

$$\frac{\kappa A}{h} = \frac{(p_{\text{He}}\dot{\Delta})_{\text{window}}}{p_{\text{He}}|_{z=0}} \quad (2.24)$$

If one assumes that

$$p_{\text{He}}|_{z=0} = (p_{\text{He}})_{\text{chamber}} \quad (2.25)$$

(whose right member is given by (2.23)), one may rewrite (2.24) in the equivalent form

$$\frac{\kappa A}{h} = \frac{(p_{\text{He}}\dot{\Delta})_{\text{window}}(p_{\text{N}_2}\dot{\Delta})_{\text{probe}}}{(p_{\text{He}}\dot{\Delta})_{\text{RL,ex}}(p_{\text{N}_2})_{\text{chamber}}} \quad (2.26)$$

All the terms in the right member of (2.26) are expressible in terms of data one may read from the apparatus illustrated in Fig. 2. Thus: $(p_{\text{He}}\dot{\Delta})_{\text{window}}$ is the the reading on the leak flowrate meter; $(p_{\text{N}_2}\dot{\Delta})_{\text{probe}}$ is the reading of the flowrate meter upstream of the probe tip; $(p_{\text{He}}\dot{\Delta})_{\text{RL,ex}}$ is the flowrate value given on the label of the external reservoir leak (it cf. (2.18) above); and $(p_{\text{N}_2})_{\text{chamber}}$ is the reading of the pressure gauge PG illustrated in Fig 2. If the window performance parameter $\kappa A/h$ is indeed constant, then measurement of the expression in the right member of (2.26) should give nearly the same value, even if the individual terms in that fraction are varied.

Table 1. Measurements of $\kappa A/h$ with an apparatus involving two reservoir leaks

$(p_{\text{He}}\dot{\Delta})_{\text{window}}$ atm·(cm) ³ /sec	$(p_{\text{N}_2})_{\text{chamber}}$ atm	$(p_{\text{N}_2}\dot{\Delta})_{\text{probe}}$ atm·(cm) ³ /sec	$\kappa A/h$ * (cm) ³ /s	ISSFR†
6.0×10^{-9}	0.180	3.53	0.0236	833
6.1×10^{-9}	0.180	3.53	0.0239	820
8.4×10^{-9}	0.066	0.933	0.0238	595
8.12×10^{-9}	0.0637	8.67	0.0221	616
5.79×10^{-9}	0.0861	1.33	0.0179	864
5.61×10^{-9}	0.100	1.67	0.0187	891
5.6×10^{-9}	0.138	2.53	0.0206	893
5.1×10^{-9}	0.180	3.47	0.0196	980
7.05×10^{-9}	0.106	1.87	0.0248	709
6.8×10^{-9}	0.105	1.80	0.0233	735

* Calculated from (2.26) with $(p_{\text{He}}\dot{\Delta})_{\text{RL, ex}} = 5.0 \times 10^{-6}$ atm·(cm)³/sec
 † Here ISSFR = $(p_{\text{He}}\dot{\Delta})_{\text{RL, ex}} / (p_{\text{He}}\dot{\Delta})_{\text{window}}$

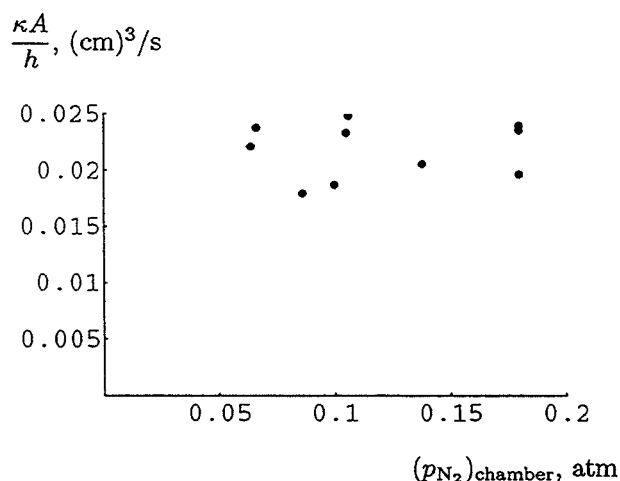


Fig. 3 Window diffusivity parameter $\kappa A/h$ versus chamber pressure in the mass separator cell

One way of artificially varying the values of the individual terms in the numerator and the denominator of the fraction in the right member of (2.26) is to attach a C-clamp to the plastic tubing between the quick disconnect (labeled QD in Fig. 2) and the mass separator chamber. By tightening the C-clamp, the parameters $(p_{\text{N}_2}\dot{\Delta})_{\text{probe}}$ and $(p_{\text{N}_2})_{\text{chamber}}$ both decrease. Table 1 summarizes the results of a test run on July 25, 1994.

The data in Fig. 3 do not indicate any trend that is distinguishable from the scatter. Fig. 4, by

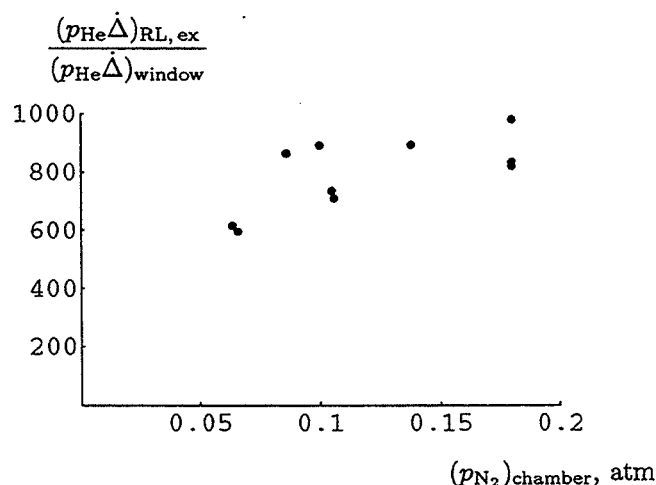


Fig. 4 ISSFR versus chamber pressure in the mass separator

contrast, seems to indicate a slight upward trend of ISSFR with increasing pressure in the mass separator chamber.

2.3.2 A METHOD THAT EMPLOYS ONE RESERVOIR TYPE LEAK AND AIR.

Referring again to Fig. 2, suppose that both the regulator valve on the Nitrogen supply and the hand valve on the external reservoir leak are shut off. In this configuration, the sniffer probe sucks atmospheric air, which then flows into the chamber

of the mass separator cell without any addition of helium. Of course, atmospheric air has some helium in it. According to data furnished in the *U.S. Standard Atmosphere, 1976* (Ref. 5), the ambient helium concentration has the average value

$$c_{\text{He, air}} = 5.24 \times 10^{-6} \quad (2.27)$$

If one assumes that the concentration of helium in air does not change between the probe inlet and the mass separator cell, then

$$(p_{\text{He}})_{\text{chamber}} = c_{\text{He, air}}(p_{\text{air}})_{\text{chamber}} \quad (2.28)$$

If one substitutes this result into (2.25) and substitutes the result of that manipulation into (2.24), one obtains

$$\frac{\kappa A}{h} = \frac{(p_{\text{He}}\dot{\Delta})_{\text{window}}}{c_{\text{He, air}}(p_{\text{air}})_{\text{chamber}}} \quad (2.29)$$

As was the case in the experiment described in §2.3.1 above, one may vary the parameters in the problem by adjusting the tightness of a C-clamp on the tubing between the quick disconnect QD in Fig. 2 and the mass separator cell.

On Friday July 22, 1994, a blockage appeared in the tubing between the mass separator chamber and the second stage of the vane pump (*cf.* Fig. 2). Thus, while the chamber pressure in the mass separator cell does not normally rise above 0.185 atm it did so on that Friday and the following Monday until the blockage seemed to clear itself out. The presence of this blockage (which was accidental) presented an opportunity to take data in the case when the chamber pressure in the mass separator cell is well above the value intended by the designers of the device. Table 2 gives data from some tests in this configuration

Fig. 5 is a plot of some of the data in Table 2. Unlike the data in Fig. 3 above, the window diffusivity parameter $\kappa A/h$ does indicate a trend that is distinguishable from the scatter, in particular a decrease in $\kappa A/h$ in response to increases in the mass separator chamber pressure in the range 0.2 to 0.8 atmospheres. Apparently, if one is to expect constancy of the window diffusivity parameter $\kappa A/h$, one must ensure that the chamber pressure in the mass separator cell does not rise above its normal value when the machine is clean and free of blockages.

Table 2. Measurements of $\kappa A/h$ with an apparatus involving one reservoir leak and air

$(p_{\text{He}}\dot{\Delta})_{\text{window}}$ atm·(cm) ³ /sec	$(p_{\text{air}})_{\text{chamber}}$ atm	$\kappa A/h$ * (cm) ³ /s
3.69×10^{-9}	0.0298	0.0236
1.24×10^{-8}	0.0982	0.0241
1.8×10^{-8}	0.0146	0.0235
4.35×10^{-8}	0.725	0.0114
3.38×10^{-8}	0.499	0.0129
2.96×10^{-8}	0.402	0.0140
2.89×10^{-8}	0.387	0.0142
1.93×10^{-8}	0.219	0.0168
1.84×10^{-8}	0.208	0.0168
1.06×10^{-8}	0.0734	0.0275
9.2×10^{-9}	0.0629	0.0279
9.55×10^{-9}	0.0656	0.0277

* Calculated from (2.29) with $c_{\text{He, air}} = 5.25 \times 10^{-6}$

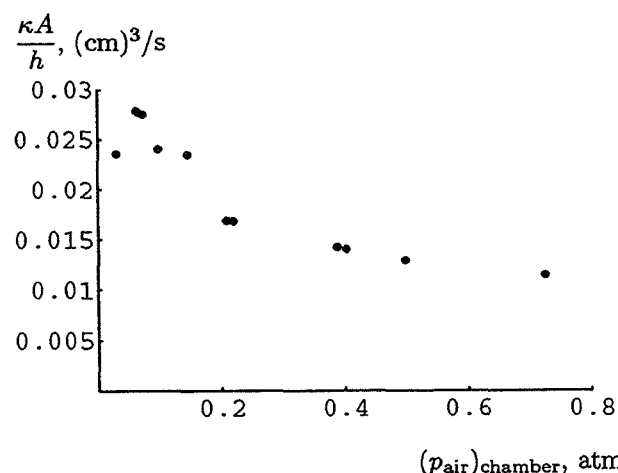


Fig 5. Window diffusivity parameter $\kappa A/h$ versus chamber pressure in the mass separator cell.

I can not think of any good reason why the window performance parameter $\kappa A/h$ should be nonconstant. The best conjecture I can come up with in this instance is that high chamber pressures in the mass separator cell allow relatively higher total pressure in the high vacuum envelope of the leak detector. Such high values of the total pressure in the leak detector may cause the pumping speed

$\dot{\Delta}_{\max}$ (cf. §1.3 above) to be nonconstant. If it is, then one can no longer assume that the reading on the leak flowrate meter (which is really proportional to the partial pressure of helium in the analysis cell) is a constant multiple of the helium flowrate through the mass separator window and the results may be skewed accordingly.

2.4 A TIME DEPENDENT FLOW METHOD FOR MEASURING THE PARAMETER $\kappa A/h$ OF A MASS SEPARATOR WINDOW

Fig. 6 illustrates a closed container with a porous stopper. The container is a model of the mass separator cell when the leads into it and out of it are closed and the stopper is a model of the mass separator window.

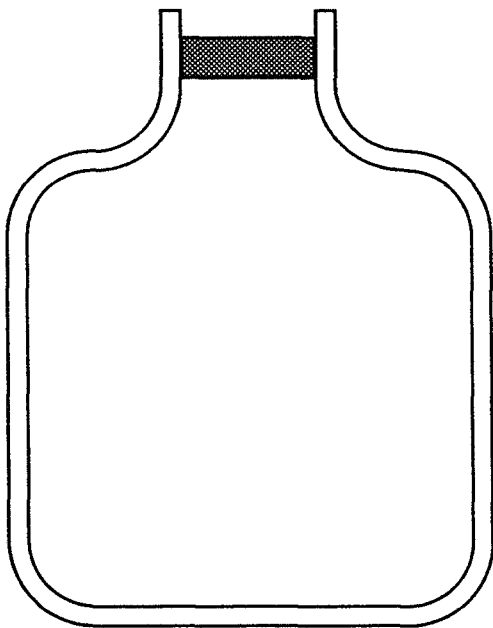


Fig. 6 A closed container with a porous stopper

Let \mathcal{V} be the region interior to the container and let $\partial\mathcal{V}$ be its bounding surface. Let dV denote the differential volume element in \mathcal{V} and let dS denote the differential area element on $\partial\mathcal{V}$. Let \hat{n} denote the outward unit normal vector at a generic point on $\partial\mathcal{V}$ and let \mathbf{u} denote the helium velocity immediately after it enters the stopper. Now the time rate of change of the total number of moles of helium in \mathcal{V} equals the rate of transport of helium

into \mathcal{V} across $\partial\mathcal{V}$, *i.e.*

$$\frac{d}{dt} \left(\iiint_{\mathcal{V}} \rho_{\text{He}}^* dV \right) = \iint_{\partial\mathcal{V}} \rho_{\text{He}}^* \mathbf{u} \cdot (-\hat{n}) dS. \quad (2.30)$$

I will assume, as before, that the absolute temperature in the mass separator cell and the window is effectively constant. If one multiplies (2.30) by $\mathcal{R}T$ and applies the ideal gas law (2.10), one obtains

$$\frac{d}{dt} \left(\iiint_{\mathcal{V}} p_{\text{He}} dV \right) = \iint_{\partial\mathcal{V}} p_{\text{He}} \mathbf{u} \cdot (-\hat{n}) dS. \quad (2.31)$$

Now the right member of (2.31) is just the negative of the flowrate through the mass separator window ($p_{\text{He}}\dot{\Delta}$)_{window}, so

$$\frac{d}{dt} \left(\iiint_{\mathcal{V}} p_{\text{He}} dV \right) = -(p_{\text{He}}\dot{\Delta})_{\text{window}}. \quad (2.32)$$

In view of the basic diffusion model for the window (cf. (2.11)), one may write (2.32) in the equivalent form

$$\frac{d}{dt} \left(\iiint_{\mathcal{V}} p_{\text{He}} dV \right) = -\frac{\kappa A}{h} p_{\text{He}}|_{z=0}, \quad (2.33)$$

where, to recall, the subscript $z = 0$ denotes conditions at the face of the window that looks into the mass separator cell.

Let $\langle p_{\text{He}} \rangle$ denote the spatial average of p_{He} throughout \mathcal{V} , *i.e.*

$$\langle p_{\text{He}} \rangle \equiv \frac{\iiint_{\mathcal{V}} p_{\text{He}} dV}{\iiint_{\mathcal{V}} dV}. \quad (2.34)$$

Let V denote the volume enclosed by the mass separator cell (*i.e.* the denominator in (2.34)). Then one may multiply both sides of (2.34) by V to obtain

$$\langle p_{\text{He}} \rangle V = \iiint_{\mathcal{V}} p_{\text{He}} dV. \quad (2.35)$$

If one substitutes (2.35) into (2.33) to eliminate the integral contained therein, one obtains

$$\frac{d}{dt} (\langle p_{\text{He}} \rangle V) = -\frac{\kappa A}{h} p_{\text{He}}|_{z=0}. \quad (2.36)$$

Now the container is rigid, so V does not change in time. One may therefore move the factor V outside of the time derivative in (2.36) to obtain

$$\frac{d}{dt} (\langle p_{\text{He}} \rangle) V = -\frac{\kappa A}{h} p_{\text{He}}|_{z=0}. \quad (2.37)$$

If one divides both sides of (2.37) by the product $V p_{\text{He}}|_{z=0}$, one obtains

$$\frac{\frac{d}{dt} (\langle p_{\text{He}} \rangle)}{p_{\text{He}}|_{z=0}} = -\frac{\kappa A}{hV}. \quad (2.38)$$

A natural approximation to introduce at this point is

$$\langle p_{\text{He}} \rangle \approx p_{\text{He}}|_{z=0}. \quad (2.39)$$

Before making this approximation, one should point out that it can not hold exactly. To see why it can not, note that the rate at which helium leaves the gas in the container must equal the rate at which helium enters the stopper (or window). If the latter is nonzero, then the former must be nonzero too. In particular, the rate of diffusion of helium from the core region of the container to the stopper must be nonzero. In view of the gradient-flux relation (2.1), a nonzero helium current due to diffusion can only occur if there is a nonzero gradient of helium concentration (or partial pressure) in the container. But if the gradient of helium partial pressure is nonzero in the core region and the helium current due to diffusion is in the direction from the core to the stopper, one expects that the concentration (or partial pressure) of helium should be lower at the stopper (toward which the helium is diffusing) than in the core region (since in any diffusion process, the diffusion current is in the direction from higher to lower concentration). Such considerations lead one to expect that

$$\langle p_{\text{He}} \rangle > p_{\text{He}}|_{z=0}, \quad (2.40)$$

which indicates the algebraic sign of the error introduced by the approximation (2.39).

Having acknowledged the limitations of the approximation (2.39), I am now ready to apply it for what it is worth. Thus, if one eliminates $\langle p_{\text{He}} \rangle$ from (2.38) by means of (2.39), one obtains

$$\frac{d}{dt} (p_{\text{He}}|_{z=0}) \approx -\frac{\kappa A}{hV}. \quad (2.41)$$

Equation (2.41) is now a first order ordinary differential equation for $p_{\text{He}}|_{z=0}$ as a function of t . One may write the general solution of this equation in the form

$$\ln(C p_{\text{He}}|_{z=0}) = -\frac{\kappa A}{hV} t, \quad (2.42)$$

in which C is an arbitrary constant with the dimensions of (pressure)⁻¹. One may evaluate C by introducing the initial condition

$$p_{\text{He}}|_{z=0} = p_0. \quad (2.43)$$

If one evaluates (2.42) at $t = 0$, uses the initial condition (2.43) and solves for C , one finds that $C = p_0^{-1}$. If one substitutes this result back into (2.42) and solves for $p_{\text{He}}|_{z=0}$, one obtains

$$p_{\text{He}}|_{z=0} = p_0 \exp\left(-\frac{\kappa A}{hV} t\right). \quad (2.44)$$

Equation (2.44) indicates that $p_{\text{He}}|_{z=0}$ decreases by one power of e during a time interval t_e defined by

$$t_e = \frac{hV}{\kappa A}. \quad (2.45)$$

If one can determine t_e experimentally, then (2.45) indicates that the experimental value of the window performance parameter $\kappa A/h$ must be

$$\frac{\kappa A}{h} = \frac{V}{t_e}. \quad (2.46)$$

Table 3 gives the results of some measurements of $\kappa A/h$ by this time-decay method.

Table 3. Measurements of the decay of $(p_{\text{He}})_{\text{window}}$ with respect to t

$(p_{\text{He}}\Delta)_{\text{window}} \times 10^8$ atm·(cm) ³ /sec	t s	t_e^* s	$\kappa A/h^\dagger$ (cm) ³ /s
$10e^0 = 10.00$	0	—	—
$10e^{-0.5} = 6.07$	18	—	—
$10e^{-1.0} = 3.68$	34	34	0.018
$10e^{-1.5} = 2.23$	50	32	0.019
$10e^{-2.0} = 1.35$	67	33	0.018
$10e^{-2.5} = 0.82$	90	40	0.015

* t_e is here defined to be the difference between the present t and the value of t when $(p_{\text{He}}\Delta)_{\text{window}}$ was one power of e higher
 \dagger Calculated from equation (2.46) with $V = 0.599 \text{ (cm)}^3$

The mass separator cell was disassembled and the dimensions of its chamber were measured with a precision caliper. The value of container volume V given in Table 3 is the result of these measurements. This figure for V is the sum of the volume of the main cylindrical cavity plus the volumes enclosed by two metal tubes that branch off of it. During a typical test, the tubing to the mass separator cell was briefly exposed to atmospheric air. As soon as a test run was to begin, the tubing branches extending from the cell were stopped off with rubber stoppers.

The values of $\kappa A/h$ found here are lower than those of Table 1 but in the range of those in Table 2. Since each time-decay test was begun by exposing the mass separator cell to atmospheric air, one would expect the measured value of the window performance parameter $\kappa A/h$ to be similar to those in Table 2 with relatively high chamber pressures. Chamber pressures between 0.2 and 0.3 atm in Table 2 do indeed correspond to values of $\kappa A/h$ in the same range as those of the time decay tests.

If I had more time to conduct tests this summer, I would repeat the time decay tests but with a lower starting pressure, (say 0.18 atm). I would also use valves to seal off the leads to the mass separator cell rather than rubber stoppers. Repeated attachment and detachment of the stoppers allowed rubber shavings to be sucked into the tubing branches and to risk fouling the line to the vacuum pump. I would expect the time decay measurements of $\kappa A/h$ in the case of lower starting pressure to more nearly resemble the values in Table 1.

SECTION THREE

SOME OBSERVATIONS OF EXTERNAL SUPPLY-TO-SAMPLE FLOWRATE

RATIO (STANDARD PROBE TIP)

Fig. 7 illustrates three different experimental configurations in which I measured the external supply to sample flowrate ratio.

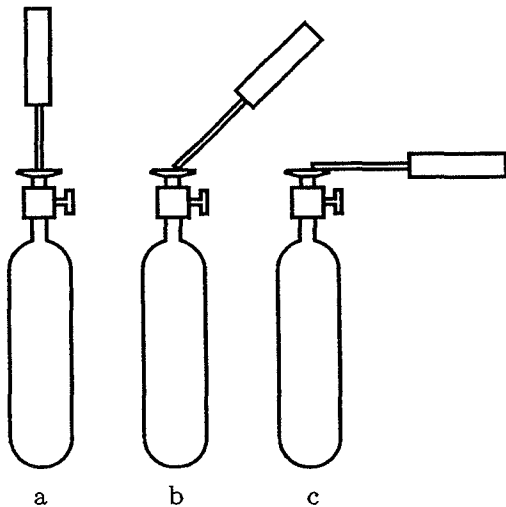


Fig. 7 Probe held in various attitudes relative to flange of a reservoir leak

As a preliminary step, I verified that the probe was drawing atmospheric air without any apparent obstructions. To this end, I measured the flowrate of atmospheric air into the probe tip (with a Sierra flowmeter mounted to the probe end as in Fig. 2 above but with the nitrogen shut off) and obtained the value

$$(p_{\text{air}}\dot{\Delta})_{\text{probe}} = 3.40 \text{ atm}\cdot(\text{cm})^3/\text{sec}. \quad (3.1)$$

I also noted that the chamber pressure in the mass separator cell was 0.179 atm (according to the pressure gauge PG illustrated in Fig. 2). These values are consistent with the normal functioning of the device I had access to this summer (the Alcatel ASM 110 Turbo CL leak detector in Room 117 of the Engineering Development Lab). I also adjusted the zero and the gain of the leak flowrate meter to force agreement between the meter reading and the internal reservoir leak labeled "RL, in" Fig. 2. In these

tests, I employed an internal reservoir leak having the posted leak rate

$$(p_{\text{He}}\dot{\Delta})_{\text{RL,ex}} = 5.05 \times 10^{-8} \text{ atm}\cdot(\text{cm})^3/\text{sec}. \quad (3.2)$$

The choice of reservoir leak ensured that no change in scale of the leak flowrate meter would be required between the time the meter was adjusted and the time the measurements were taken.

With the meter duly adjusted and the internal reservoir leak shut off, I noted that the flowrate meter (with the probe tip exposed to clean air) read

$$(p_{\text{He}}\dot{\Delta})_{\text{window}} = 2.54 \pm 0.05 \times 10^{-8} \text{ atm}\cdot(\text{cm})^3/\text{sec}. \quad (3.3)$$

If one substitutes these data (along with the usual assumption $c_{\text{He,air}} = 5.25 \times 10^{-6}$) into equation (2.29) for the window performance parameter $\kappa A/h$, one finds

$$\frac{\kappa A}{h} = 0.0270 \frac{(\text{cm})^3}{\text{s}}. \quad (3.4)$$

This value is in the range of values in the left margin of Fig. 5.

From the data quoted above, one may also deduce that

$$\begin{aligned} (p_{\text{He}}\dot{\Delta})_{\text{probe}} &= c_{\text{He,air}}(p_{\text{air}}\dot{\Delta})_{\text{probe}} \\ &= 1.785 \times 10^{-5} \text{ atm}\cdot(\text{cm})^3/\text{sec}. \end{aligned} \quad (3.5)$$

It follows that

$$\text{ISSFR} \equiv \frac{(p_{\text{He}}\dot{\Delta})_{\text{probe}}}{(p_{\text{He}}\dot{\Delta})_{\text{window}}} = 703. \quad (3.6)$$

At this point, one should note the change in the flowrate meter reading that one would expect to observe if the probe tip were placed in the vicinity of a reservoir leak and were able to capture all of the leaked helium. The label on the reservoir leak I used indicated

$$(p_{\text{He}}\dot{\Delta})_{\text{RL}} = 5.0 \times 10^{-6} \text{ atm}\cdot(\text{cm})^3/\text{sec}. \quad (3.7)$$

If the probe captured all of the helium discharged from this leak, then the meter reading should increase by

$$\begin{aligned}\Delta[(p_{\text{He}}\dot{\Delta})_{\text{window}}] &= \frac{(p_{\text{He}}\dot{\Delta})_{\text{window}}}{(p_{\text{He}}\dot{\Delta})_{\text{probe}}} \times \Delta[(p_{\text{He}}\dot{\Delta})_{\text{probe}}] \\ &= \frac{1}{\text{ISSFR}} \times (p_{\text{He}}\dot{\Delta})_{\text{RL}} \\ &= \frac{5.0 \times 10^{-6} \text{ atm}\cdot(\text{cm})^3/\text{sec}}{703} \\ &= 7.11 \times 10^{-9} \text{ atm}\cdot(\text{cm})^3/\text{sec}.\end{aligned}\quad (3.8)$$

3.1 PROBE END INSERTED LOOSELY IN THE OPENING OF A RESERVOIR LEAK

The opening of the external reservoir leak in Fig. 7 is large enough for the probe tip to fit loosely in it to a depth of about one inch. I inserted the probe end into this well (*cf.* panel a of Fig. 7) and let the meter stabilize. The stabilized value was

$$(p_{\text{He}}\dot{\Delta})_{\text{window}} = 3.16 \pm 0.07 \times 10^{-8} \text{ atm}\cdot(\text{cm})^3/\text{sec}.\quad (3.9)$$

This value exceeded the clean air reading given in equation (3.3) by

$$\begin{aligned}\Delta[(p_{\text{He}}\dot{\Delta})_{\text{window}}] &= 0.62 \times 10^{-8} \text{ atm}\cdot(\text{cm})^3/\text{sec} \\ &= 6.2 \times 10^{-9} \text{ atm}\cdot(\text{cm})^3/\text{sec}\end{aligned}\quad (3.10)$$

This figure is 87% of the figure for complete capture of the leaked gas given in (3.8) above. Alternatively, the external supply-to-sample flowrate ratio ESSFR is the quotient whose numerator is the figure in (3.8) and whose denominator is the figure in (3.10), *viz.*

$$\text{ESSFR} = \frac{7.11}{6.2} = 1.15.\quad (3.11)$$

Evidently, the shelter provided by the well into which the probe tip was inserted in this test helped to achieve such a low value of ESSFR. If one could arrange that the ESSFR were as small as the value given in (3.11) for general placement of the probe tip, there would be no problem in the use of a sniffer probe for local leakage measurement.

3.2 PROBE END HELD AT A FOURTY-FIVE DEGREE ANGLE TO A FLAT SURFACE WITH A PINHOLE LEAK

In the next test, I covered the well on the reservoir leak with a Band-AidTM *shear spot* (a covering that does not have any perforations). I then punctured the Band-Aid with a pointed object to create a pinhole leak on an otherwise flat surface. I then placed the probe tip as shown in panel b of Fig. 7 and allowed the meter reading to stabilize.

This time, the stabilized value was

$$(p_{\text{He}}\dot{\Delta})_{\text{window}} = 3.03 \pm 0.13 \times 10^{-8} \text{ atm}\cdot(\text{cm})^3/\text{sec}.\quad (3.12)$$

This value exceeded the clean air reading given in equation (3.3) by

$$\begin{aligned}\Delta[(p_{\text{He}}\dot{\Delta})_{\text{window}}] &= 0.49 \times 10^{-8} \text{ atm}\cdot(\text{cm})^3/\text{sec} \\ &= 4.9 \times 10^{-9} \text{ atm}\cdot(\text{cm})^3/\text{sec}\end{aligned}\quad (3.13)$$

This figure is 69% of the figure for complete capture of the leaked gas given in (3.8) above. Alternatively, the external supply-to-sample flowrate ratio ESSFR is the quotient whose numerator is the figure in (3.8) and whose denominator is the figure in (3.13), *viz.*

$$\text{ESSFR} = \frac{7.11}{4.9} = 1.45.\quad (3.14)$$

Evidently, the unsheltered environment of the pinhole leak and the probe tip illustrated in panel b of Fig. 7 allows more helium to disperse to the surrounding air than in the case illustrated in panel a.

3.3 PROBE SHAFT HELD FLUSH AGAINST A FLAT SURFACE WITH A PINHOLE LEAK ABOUT 4mm FROM THE PROBE END

In the third test, placed the probe tip as shown in panel c of Fig. 7 and allowed the meter reading to stabilize.

This time, the stabilized value was

$$(p_{\text{He}}\dot{\Delta})_{\text{window}} = 2.74 \pm 0.11 \times 10^{-8} \text{ atm}\cdot(\text{cm})^3/\text{sec}.\quad (3.15)$$

To allow for the possibility of drift in the instrumentation, I exposed the probe tip to clean air a second time to see if the value returned to the value given by (3.3) above. This time the stabilized value was

$$(p_{\text{He}}\dot{\Delta})_{\text{window}} = 2.49 \pm 0.09 \times 10^{-8} \text{ atm}\cdot(\text{cm})^3/\text{sec}, \quad (3.16)$$

which is satisfactorily close to the value given in (3.3).

This test value given by (3.15) exceeds the clean air reading given in equation (3.16) by

$$\begin{aligned} \Delta[(p_{\text{He}}\dot{\Delta})_{\text{window}}] &= 0.25 \times 10^{-8} \text{ atm}\cdot(\text{cm})^3/\text{sec} \\ &= 2.5 \times 10^{-9} \text{ atm}\cdot(\text{cm})^3/\text{sec} \end{aligned} \quad (3.17)$$

This figure is 35% of the figure for complete capture of the leaked gas given in (3.8) above. Alternatively, the external supply-to-sample flowrate ratio ESSFR is the quotient whose numerator is the figure in (3.8) and whose denominator is the figure in (3.17), *viz.*

$$\text{ESSFR} = \frac{7.11}{2.5} = 2.84. \quad (3.18)$$

Again, the unsheltered environment of the pinhole leak and the probe tip illustrated in panel c of Fig. 7 allows more helium to disperse to the surrounding air than in the case illustrated in panel a.

SECTION FOUR

CONCEPT OF A DRAFT DAMPER TO MINIMIZE DISPERSAL OF LEAKED HELIUM IN THE ROOM AIR

4.1 PRELIMINARY REMARKS

The results of section III above indicate that the external supply-to-sample flowrate ratio (ESSFR) obtained by an unmodified mass spectrometer hand probe held up to a leak may be as low as 1.15 if the probe tip is sheltered from drafts. The aim of the present section is to pursue the implications of this observation. Thus, one may shelter the probe tip from room drafts and inhibit buoyant convection at the same time by surrounding the probe tip with a sponge or other flexible porous material, provided the small pressure gradients needed to cause sniffed air to seep through it are still large compared to pressure gradients associated with the dynamic pressure of room drafts or the buoyant force per unit volume ρg (in which ρ is the mass density of the air and g is the acceleration due to gravity).

In this section, I will solve a convection-diffusion problem for the distribution of helium concentration in the interior of a porous medium probe end in the case when the probe end exhibits either of two symmetries, namely cylindrical or spherical. In each case, one supposes that the end of the sniffer probe is placed as closely as possible to a pinhole leak. Thus, the nonuniformity of helium concentration due to the relatively high concentration near the pinhole leak leads to diffusion of helium in the direction from higher to lower concentration, *i.e.* away from the pinhole leak. At the same time, the inward flow of air to supply the sucking action of the probe causes helium to drift toward the probe tip (which, you will recall, is placed as closely as possible to the pinhole leak). Thus, the helium transport is affected by inward drift with the air and by outward diffusion through it, leading to a steady state nonuniform helium distribution to be determined by solution of a suitable differential equation for the helium concentration as a function of the radial coordinate r in either cylindrical or spherical geometry.

To determine the arbitrary constants in the general solution of such a differential equation, one

must have a boundary condition for the helium concentration at the low- r extremity of the solution domain (*i.e.* the range of values over which the solution is sought). To fix such a boundary condition, consider the steady input-output balance for helium:

$$\rho_{\text{He, air}}^* \dot{\Delta}_{\text{air}} + \rho_{\text{He, leak}}^* \dot{\Delta}_{\text{leak}} = \rho_{\text{He, eff}}^* \dot{\Delta}_{\text{eff}}, \quad (4.1)$$

in which the subscript "air" refers to the room air that enters the porous medium probe end; the subscript "leak" refers to the gas emanating from the leak; and the subscript "eff" refers to the effluent, *i.e.* the gas that enters the sample line of the leak detector. One may write (4.1) in the equivalent form

$$c_{\text{He, air}} \rho_{\text{air}}^* \dot{\Delta}_{\text{air}} + c_{\text{He, leak}} \rho_{\text{leak}}^* \dot{\Delta}_{\text{leak}} = c_{\text{He, eff}} \rho_{\text{eff}}^* \dot{\Delta}_{\text{eff}}, \quad (4.2)$$

in which c_{He} is the nondimensional helium concentration, *i.e.* the ratio whose numerator is the molar density of helium in some mixture and whose denominator is the molar density of the mixture as a whole.

One may also write down an equation of balance for all the gases, namely

$$\rho_{\text{air}}^* \dot{\Delta}_{\text{air}} + \rho_{\text{leak}}^* \dot{\Delta}_{\text{leak}} = \rho_{\text{eff}}^* \dot{\Delta}_{\text{eff}}, \quad (4.3)$$

In equations (4.2) and (4.3), however,

$$\rho_{\text{air}}^* = \rho_{\text{leak}}^* = \rho_{\text{eff}}^* = \frac{p}{\mathcal{R}T}, \quad (4.4)$$

which expresses AVOGADRO'S principle that "equal volumes of gas at the same temperature and pressure have equal numbers of molecules" (*cf.* (1.1) above).

One may thus cancel several common factors in (4.2) and (4.3) to obtain, respectively,

$$c_{\text{He, air}} \dot{\Delta}_{\text{air}} + c_{\text{He, leak}} \dot{\Delta}_{\text{leak}} = c_{\text{He, eff}} \dot{\Delta}_{\text{eff}}, \quad (4.5)$$

$$\dot{\Delta}_{\text{air}} + \dot{\Delta}_{\text{leak}} = \dot{\Delta}_{\text{eff}}, \quad (4.6)$$

If one eliminates $\dot{\Delta}_{\text{air}}$ from (4.5) by means of (4.6), one obtains

$$c_{\text{He, air}} (\dot{\Delta}_{\text{eff}} - \dot{\Delta}_{\text{leak}}) + c_{\text{He, leak}} \dot{\Delta}_{\text{leak}} = c_{\text{He, eff}} \dot{\Delta}_{\text{eff}}. \quad (4.7)$$

If one divides through by $\dot{\Delta}_{\text{eff}}$, one obtains

$$c_{\text{He, air}} \left(1 - \frac{\dot{\Delta}_{\text{leak}}}{\dot{\Delta}_{\text{eff}}} \right) + c_{\text{He, leak}} \frac{\dot{\Delta}_{\text{leak}}}{\dot{\Delta}_{\text{eff}}} = c_{\text{He, eff}} \quad (4.8)$$

As an example, suppose that

$$\dot{\Delta}_{\text{leak}} = 5.0 \times 10^{-6} \text{ atm}\cdot(\text{cm})^3/\text{sec}$$

and $\dot{\Delta}_{\text{eff}} = 3.4 \text{ atm}\cdot(\text{cm})^3/\text{sec}$. Suppose further that $c_{\text{He, air}} = 5.25 \times 10^{-6}$ and $c_{\text{He, leak}} = 1$. Then equation (4.8) yields

$$\begin{aligned} c_{\text{He, eff}} &= 5.25 \times 10^{-6} \left(1 - \frac{5.0 \times 10^{-6}}{3.40} \right) \\ &+ (1) \frac{5.0 \times 10^{-6}}{3.40} \\ &= 6.72 \times 10^{-6} \text{ atm}\cdot(\text{cm})^3/\text{sec} \quad (4.9) \end{aligned}$$

4.2 PADDED DIAPHRAGM PROBE END

Consider a porous medium probe end in the form of a cylinder of thickness h . Let \dot{n} denote the molar transport of helium across a cylinder of radius r (in, say, gm-moles/s). If the flow is steady then helium does not accumulate between coaxial cylinders of different radii. It follows that the transport of helium into the gap between the cylinders must be balanced by the transport of helium out of that gap and one concludes that \dot{n} is independent of r .

Now there will be two distinct contributions to \dot{n} , namely diffusion of helium through the air and drift of helium with the air. Summing these two effects, one obtains

$$\dot{n} = (2\pi r h) \left(-\kappa' \frac{d\rho_{\text{He}}^*}{dr} \right) + (-\dot{\Delta} \rho_{\text{He}}^*) \quad (4.10)$$

In (4.10), the expression $2\pi r h$ is the area of the cylinder of height h and radius r across which helium diffuses. The expression within large parentheses is the intensity of the helium current due to diffusion (in say gm-moles per square centimeter per second). The parameter κ' is the diffusivity of helium in air (not to be confused with the diffusivity of helium in the window material introduced in (2.2) above). MARR (Ref. 1, p93) furnishes a value for κ' , namely $2.7 \text{ (ft)}^2/\text{hr}$, at $T = 0^\circ \text{ Celsius}$. Converting to CGS units, one obtains $\kappa' = 0.6968$

(cm)²/s at that temperature. CHAPMAN & COWLING (Ref. 6, p264) indicate that the diffusivity varies as a positive power of the absolute temperature and furnish the value 1.691 for the exponent. If one takes $T = 300^\circ \text{K}$ as a typical value for the temperature in the laboratory, one finds that the

$$\begin{aligned} \kappa'|_{T=300^\circ\text{K}} &= \kappa'|_{T=273.15^\circ\text{K}} \left(\frac{300}{273.15} \right)^{1.691} \\ &= 0.8165 \text{ (cm)}^2/\text{s} \quad (4.11) \end{aligned}$$

One may rearrange (4.10) to the equivalent form

$$0 = (2\pi r h) \left(-\kappa' \frac{d\rho_{\text{He}}^*}{dr} \right) - \dot{\Delta} \left(\rho_{\text{He}}^* + \frac{\dot{n}}{\dot{\Delta}} \right), \quad (4.12)$$

so

$$0 = (2\pi r h) (-\kappa') \frac{d}{dr} \left(\rho_{\text{He}}^* + \frac{\dot{n}}{\dot{\Delta}} \right) - \dot{\Delta} \left(\rho_{\text{He}}^* + \frac{\dot{n}}{\dot{\Delta}} \right), \quad (4.13)$$

so

$$\frac{d}{dr} \left(\rho_{\text{He}}^* + \frac{\dot{n}}{\dot{\Delta}} \right) = \frac{-\dot{\Delta}}{2\pi h \kappa' r} \frac{1}{\rho_{\text{He}}^* + \frac{\dot{n}}{\dot{\Delta}}}, \quad (4.14)$$

the general solution of which is

$$\rho_{\text{He}}^* + \frac{\dot{n}}{\dot{\Delta}} = A r^{-\dot{\Delta}/(2\pi h \kappa')}, \quad (4.15)$$

in which A is an arbitrary constant.

As $r \rightarrow \infty$, equation (4.15) takes the form

$$(\rho_{\text{He}}^*)_{\infty} + \frac{\dot{n}}{\dot{\Delta}} = 0, \quad (4.16)$$

so

$$\dot{n} = -(\rho_{\text{He}}^*)_{\infty} \dot{\Delta}. \quad (4.17)$$

If one substitutes this expression for \dot{n} into (4.15), one obtains

$$\rho_{\text{He}}^* - (\rho_{\text{He}}^*)_{\infty} = A r^{-\dot{\Delta}/(2\pi h \kappa')}. \quad (4.18)$$

If

$$\rho_{\text{He}}^*|_{r=r_1} \equiv \rho_{\text{He}}^*(r_1), \quad (4.19)$$

one may deduce from (4.18) that

$$\rho_{\text{He}}^*(r_1) - (\rho_{\text{He}}^*)_{\infty} = A (r_1)^{-\dot{\Delta}/(2\pi h \kappa')}. \quad (4.20)$$

If one divides (4.18) by (4.20), one obtains

$$\frac{\rho_{\text{He}}^* - (\rho_{\text{He}}^*)_{\infty}}{\rho_{\text{He}}^*(r_1) - (\rho_{\text{He}}^*)_{\infty}} = \left(\frac{r}{r_1}\right)^{-\Delta/(2\pi h \kappa')} \quad (4.21)$$

If one divides the numerator and the denominator of the left member of (4.21) by the molar density of the mixture of helium and air (which equals $p/\mathcal{R}T$ according to (4.4)), and recalls the definition of concentration (cf. the text immediately after (4.2)), one obtains

$$\frac{c(r) - c_{\infty}}{c(r_1) - c_{\infty}} = \left(\frac{r}{r_1}\right)^{-\Delta/(2\pi h \kappa')} \quad (4.22)$$

One may apply this equation to the design of a padded diaphragm. To illustrate the idea, suppose that the left member of (4.22) is to take the value 0.01 at the radius $r = R = 5r_1$ and that $\dot{\Delta} = 3.40 \text{ (cm)}^3/\text{s}$ and κ' is given by (4.11) above. Then from (4.22), we have

$$\frac{c(R) - c_{\infty}}{c(r_1) - c_{\infty}} = \left(\frac{R}{r_1}\right)^{-\Delta/(2\pi h \kappa')} \quad (4.23)$$

If one solves for h , one obtains

$$\begin{aligned} h &= \frac{\dot{\Delta}}{2\pi \kappa'} \frac{\ln(R/r_1)}{\ln\left(\frac{c(r_1) - c_{\infty}}{c(R) - c_{\infty}}\right)} \\ &= \frac{3.40 \text{ (cm)}^3/\text{s}}{2\pi (0.8165 \text{ (cm)}^2/\text{s})} \frac{\ln 5}{\ln 100} \\ &= 0.2316 \text{ cm} \end{aligned} \quad (4.24)$$

To add further detail to the example, one may identify the radius r_1 with the radius of the smallest disk that can completely cover both the pinhole leak and the probe end. If one imagines that $r_1 = 1 \text{ mm}$, then $R = 5 \text{ mm}$ so the diameter of the padded diaphragm-probe is 1 cm. Such a probe is small enough to be practical, although there is some doubt about usefulness of the device when the test surface is not flat.

4.3 POROUS PROBE END IN THE FORM OF A SPHERICAL WEDGE

Consider next a steady convection-diffusion problem with the helium transport denoted by \dot{n} as before.

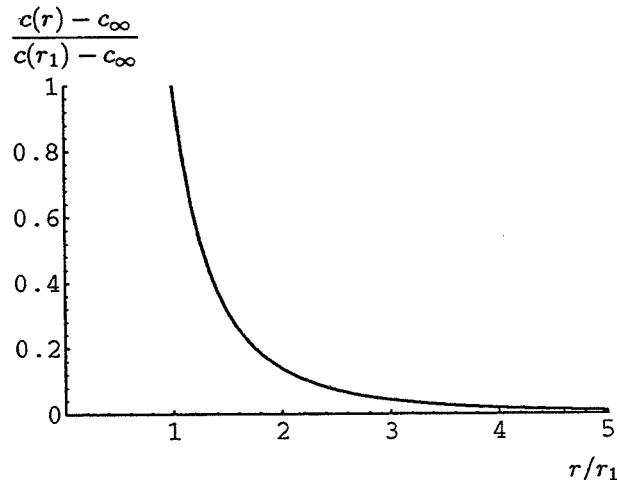


Fig. 8 Structure of the diffusion boundary layer within a padded diaphragm probe (cf. (4.22)) corresponding to the values $\kappa' = 0.8165 \text{ (cm)}^2/\text{s}$, $\dot{\Delta} = 3.40 \text{ (cm)}^3/\text{s}$, $h = 0.2316 \text{ cm}$, and $r_1 = 1 \text{ mm}$.

This time the helium flow is between hemispheres, quarter spheres, or other kinds of *spherical wedges*. For the purposes of the present analysis, the only parameter that distinguishes one kind of spherical wedge from another is the *view factor* Ω , i.e. the fraction of the celestial sphere visible to a hypothetical observer at the center of the wedge. Thus, for the hemisphere $\Omega = 1/2$, for the quarter-sphere, $\Omega = 1/4$, and so on.

Consider now the flow of helium between two concentric spherical wedges. By assuming that the flow is steady, one concludes that inflow of helium into the gap must be balanced by outflow of helium from it. An equation analogous to (4.10) is

$$\dot{n} = (4\pi r^2 \Omega) \left(-\kappa' \frac{d\rho_{\text{He}}^*}{dr} \right) + (-\dot{\Delta} \rho_{\text{He}}^*), \quad (4.25)$$

in which $4\pi r^2 \Omega$ is the area of the spherical wedge of radius r .

One may write (4.25) in the equivalent form

$$0 = (4\pi \Omega \kappa') (-r^2) \frac{d\rho_{\text{He}}^*}{dr} - \dot{\Delta} \left(\rho_{\text{He}}^* + \frac{\dot{n}}{\dot{\Delta}} \right), \quad (4.26)$$

so

$$0 = (4\pi \Omega \kappa') (-r^2) \frac{d}{dr} \left(\rho_{\text{He}}^* + \frac{\dot{n}}{\dot{\Delta}} \right) - \dot{\Delta} \left(\rho_{\text{He}}^* + \frac{\dot{n}}{\dot{\Delta}} \right), \quad (4.27)$$

so

$$\frac{d}{dr} \left(\rho_{\text{He}}^* + \frac{\dot{n}}{\Delta} \right) = \frac{\dot{\Delta}}{(4\pi\Omega\kappa')(-r^2)} = \left(\frac{\dot{\Delta}}{4\pi\Omega\kappa'} \right) \frac{d}{dr} \left(\frac{1}{r} \right), \quad (4.28)$$

the general solution of which is

$$\rho_{\text{He}}^* + \frac{\dot{n}}{\Delta} = A' \exp \left(\frac{\dot{\Delta}}{4\pi\Omega\kappa' r} \right), \quad (4.29)$$

in which A' is an arbitrary constant.

As $r \rightarrow \infty$, (4.29) becomes

$$(\rho_{\text{He}}^*)_{\infty} + \frac{\dot{n}}{\Delta} = A' \quad (4.30)$$

so (4.29) becomes

$$\rho_{\text{He}}^* + \frac{\dot{n}}{\Delta} = \left[(\rho_{\text{He}}^*)_{\infty} + \frac{\dot{n}}{\Delta} \right] \exp \left(\frac{\dot{\Delta}}{4\pi\Omega\kappa' r} \right), \quad (4.31)$$

or, equivalently,

$$\begin{aligned} [\rho_{\text{He}}^* - (\rho_{\text{He}}^*)_{\infty}] + \left[(\rho_{\text{He}}^*)_{\infty} + \frac{\dot{n}}{\Delta} \right] \\ = \left[(\rho_{\text{He}}^*)_{\infty} + \frac{\dot{n}}{\Delta} \right] \exp \left(\frac{\dot{\Delta}}{4\pi\Omega\kappa' r} \right). \end{aligned} \quad (4.32)$$

If one collects common factors of $(\rho_{\text{He}}^*)_{\infty} + \dot{n}/\Delta$ on the right hand side, one obtains

$$\begin{aligned} \rho_{\text{He}}^* - (\rho_{\text{He}}^*)_{\infty} &= \left[(\rho_{\text{He}}^*)_{\infty} + \frac{\dot{n}}{\Delta} \right] \\ &\times \left[\exp \left(\frac{\dot{\Delta}}{4\pi\Omega\kappa' r} \right) - 1 \right]. \end{aligned} \quad (4.33)$$

If one evaluates this equation at $r = r_1$, one obtains

$$\begin{aligned} \rho_{\text{He}}^*(r_1) - (\rho_{\text{He}}^*)_{\infty} &= \left[(\rho_{\text{He}}^*)_{\infty} + \frac{\dot{n}}{\Delta} \right] \\ &\times \left[\exp \left(\frac{\dot{\Delta}}{4\pi\Omega\kappa' r_1} \right) - 1 \right], \end{aligned} \quad (4.34)$$

If one divides (4.33) by (4.34), one obtains

$$\frac{\rho_{\text{He}}^* - (\rho_{\text{He}}^*)_{\infty}}{\rho_{\text{He}}^*(r_1) - (\rho_{\text{He}}^*)_{\infty}} = \frac{\exp \left(\frac{\dot{\Delta}}{4\pi\Omega\kappa' r} \right) - 1}{\exp \left(\frac{\dot{\Delta}}{4\pi\Omega\kappa' r_1} \right) - 1}. \quad (4.35)$$

If one divides the numerator and the denominator of the left member by the common factor ρ_{air}^* , and recalls the definition of concentration given in the text after equation (4.2) above, one obtains

$$\frac{c(r) - c_{\infty}}{c(r_1) - c_{\infty}} = \frac{\exp \left(\frac{\dot{\Delta}}{4\pi\Omega\kappa' r} \right) - 1}{\exp \left(\frac{\dot{\Delta}}{4\pi\Omega\kappa' r_1} \right) - 1}. \quad (4.36)$$

One may use equation (4.36) in the design of a draft damper. Suppose, for example, that ϵ is some given small number, such as 0.01. One may choose the radius of the draft damper such that the left member of (4.36) equals ϵ when $r = r_{\epsilon}$, i.e. r/ϵ is subject to the following constraint

$$\epsilon = \frac{\exp \left(\frac{\dot{\Delta}}{4\pi\Omega\kappa' r_{\epsilon}} \right) - 1}{\exp \left(\frac{\dot{\Delta}}{4\pi\Omega\kappa' r_1} \right) - 1}. \quad (4.37)$$

If one solves (4.37) for r_{ϵ} , one obtains

$$r_{\epsilon} = \frac{\frac{\dot{\Delta}}{4\pi\Omega\kappa'}}{\ln \left\{ 1 + \epsilon \left[\exp \left(\frac{\dot{\Delta}}{4\pi\Omega\kappa' r_1} \right) - 1 \right] \right\}} \quad (4.38)$$

Suppose, for example, that

$$\dot{\Delta} = 3.40 \text{ atm} \cdot (\text{cm})^3/\text{sec},$$

$\kappa' = 0.8165 \text{ (cm)}^2/\text{s}$, and $\Omega = 1/2$. Then

$$\frac{\dot{\Delta}}{4\pi\Omega\kappa'} = 0.6627 \text{ cm}. \quad (4.39)$$

If $\epsilon = 0.01$ and $r_1 = 1 \text{ mm}$, equation (4.38) gives

$$\begin{aligned} r_{\epsilon} &= \frac{0.6627 \text{ cm}}{\ln \left\{ 1 + 0.01 \left[\exp \left(\frac{0.6627 \text{ cm}}{0.1 \text{ cm}} \right) - 1 \right] \right\}} \\ &= 0.3089 \text{ cm} \end{aligned} \quad (4.40)$$

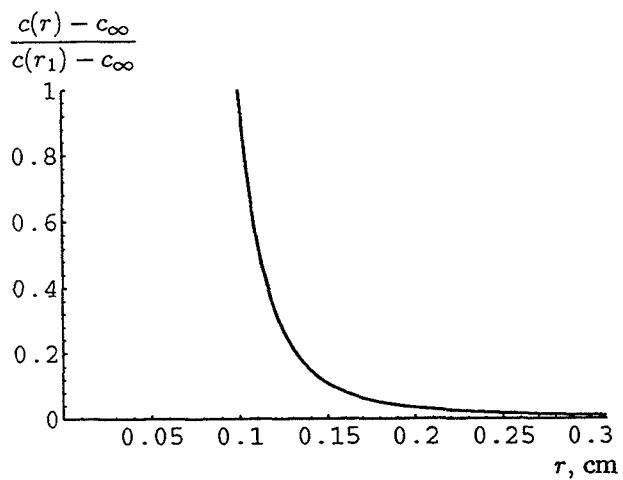


Fig. 9 Structure of the diffusion boundary layer within a draft damper shaped like a hemisphere (cf. (4.36)) corresponding to the values $\kappa' = 0.8165$ $(\text{cm})^2/\text{s}$, $\Delta = 3.40$ $(\text{cm})^3$, $r_1 = 1\text{mm}$, and $\Omega = 1/2$.

SECTION FIVE

CONCLUSIONS AND RECOMMENDATIONS

5.1 CONCLUSIONS

1. The internal supply-to-sample flowrate ratio is not a constant for a given mass separator cell.
2. The window diffusion performance parameter $\kappa A/h$ is a constant of the machine provided the absolute temperature does not change significantly and the total pressure in the mass separator chamber is not above 0.018 atm.
3. The external supply to sample flowrate ratio ESSFR may be as low as 1.15 if the probe tip is sheltered by solid walls (as it is when the test leak is at the bottom of a slender hole into which the probe tip fits). Even if the probe tip is unsheltered, the ESSFR may be as low as three, provided the test leak emerges from a pinhole, the probe tip is placed less than 4mm from it, and the drafts in the room are not artificially large.
4. If a mass spectrometer hand probe is equipped with a porous medium probe end (such as a sponge) and if the sponge is either cylidrically symmetric or spherically symmetric and centered over a point leak, then one may solve the linear convection-diffusion problem for the distribution of helium concentration within the sponge. The solutions are expressible in terms of elementary functions and exhibit boundary layer character (*i.e.* the concentration is largest near the point source but drops off rapidly in the direction away from it). A modest size probe end (whose diameter is one centimeter or less) can shelter the region in which 99% of the drop in helium concentration occurs.
5. For some mass spectrometer leak detectors (including the one I used to conduct the tests I reported in sections II and III above), the leak flowrate meter reading is unreliable unless the zero and gain settings are adjusted with an internal reservoir leak whose order of magnitude matches that of the meter readings in the subsequent tests.

5.2 RECOMMENDATIONS

1. The measurement of the numerical value of the window performance parameter $\kappa A/h$ should be part of the routine qualification a new mass spectrometer leak detector or modification of an old one (*e.g.* after the mass separator cell has been replaced).
2. A pressure gauge should be attached to monitor the chamber pressure in the mass separator cell. Only with this information (and knowledge of the constant value of $\kappa A/h$) can one relate the helium transport rate across the separator window to the concentration of helium in the separator chamber. The pressure gauge for the separator chamber also provides a strong indication of the presence or absence of obstructions in the internal and external fluid transport lines.
3. Followup work should address the optimization of draft dampers to enable local leakage measurement with mass spectrometer hand probes. The present work supplies most of the necessary formulas. What is needed is to fabricate prototypes and test them.
4. In particular, the sensitivity of external supply to sample flowrate (ESSFR) to room drafts should be tested quantitatively. Thus, hand probe equipped with draft dampers should be placed in a wind tunnel and the dependence of the ESSFR upon tunnel speed should be measured.
5. Test should be conducted to determine the repeatability of local leakage measurments made with draft damper equipped hand probes in the case when the measurements are taken by relatively unskilled personnel (such as undergraduate students).
6. Some further work should seek an analytical solution of the convection-diffusion problem of a spherical draft damper equipped hand probe placed in a wind tunnel. The tests mentioned in item 2 above should be compared with such theoretical predictions.

REFERENCES

1. MARR, J. WILLIAM 1968 *Leakage testing handbook*. Prepared by General Electric, Schenectady, N.Y. for Jet Propulsion Laboratory, Pasadena, CA. NASA Contractor Report CR-952, April 1968 (xx + 392 pages, with appendices).
2. BILARDO, VINCENT J., IZQUIERDO, FRANCISCO, & SMITH, R. KENNETH 1987 Development of the Helium Signature Test for orbiter main propulsion system revalidation between flights. AIAA 25th Aerospace Sciences Meeting, Reno, NV, January 12-15 1987. AIAA Paper 87-0293 (9 pages).
3. RUSSELL, J.M. 1993 Interpretation of discrepancies in mass spectrometry data obtained from different experimental configurations. *1993 Research Reports, NASA/ASEE Summer Faculty Fellow Program*, NASA Contractor Report CR-194678, pp 403-432 (edited by E. RAYMON HOSLER, CAROL VALDES, & TOM BARRON).
4. ANONYMOUS 1992 Proof pressure and leak detection—Aerospace plumbing systems and assemblies. Rockwell International specification (prepared by D.R. SUEME, & K.R. RAVAL). SPECIFICATION number MF0001-003 (Code Ident. No. 03953), Sept 27, 1992.
5. ANONYMOUS 1976 *U.S. Standard Atmosphere 1976*, National Oceanic and Atmospheric Administration, National Aeronautics and Space Administration, United States Air Force, number NOAA-S/T 76-1562 (xv+227 pp).
6. CHAPMAN, SYDNEY & COWLING, T.G. *The mathematical theory of non-uniform gases*. 3rd edition, Cambridge University Press, 1970.

1994 NASA/ASEE SUMMER FACULTY FELLOWSHIP PROGRAM

111769
351503
516-80
33976
P-34
36

JOHN F. KENNEDY SPACE CENTER
UNIVERSITY OF CENTRAL FLORIDA

ASSESSMENT OF A CAREER DEVELOPMENT PROGRAM
FOR EXECUTIVE AND MID-LEVEL MANAGERS

PREPARED BY:	Dr. James R. Swanson, Sr.
ACADEMIC RANK:	Associate Professor
UNIVERSITY AND DEPARTMENT:	Embry-Riddle Aeronautical Universtiy Department of Aviation Business Administration
NASA/KSC	
DIVISION:	Human Resources and Management Information
BRANCH:	
NASA COLLEAGUE:	Warren Camp
DATE:	August 26, 1994
CONTRACT NUMBER:	University of Central Florida NASA-NGT-60002 Supplement: 17

TABLE OF CONTENTS

ABSTRACT 3

SUMMARY 4

INTRODUCTION 5

THE RESIDENT MANAGEMENT EDUCATION PROGRAM (RMEP) 7

SPECIFICATION OF MANAGEMENT COMPETENCIES 10

COMPETENCIES REQUIRED OF KSC MID-LEVEL AND EXECUTIVE MANAGERS .. 13

DISCUSSION OF THE RESULTS OF THE SURVEY 19

CONCLUSIONS 21

RECOMMENDATIONS 22

REFERENCES 23

APPENDIX A A-1

APPENDIX B B-1

ABSTRACT

This project sought to validate the competencies required of mid-level and executive managers at the Kennedy Space Center (KSC), in order to enable an assessment of the Resident Management Education Program (RMEP).

Forty (40) statements describing management competencies were presented to a sample of 37 KSC managers, who judged each as essential, useful but not essential, or not needed at each of two management levels.

A content validity ratio (CVR) was calculated for each competency statement at the two management levels. There was general agreement on the validity of 36 or the 40 competency statements.

Based on the content validity ratios and comments from respondents, recommendations for improvement of the RMEP were made.

SUMMARY

The purpose of this study was to examine the management development program for mid-level and executive managers at the Kennedy Space Center (KSC), in view of the changing economic and organizational situation. In particular, the content and activities of the Resident Management Education Program (RMEP) were examined.

A sample of 37 managers who had participated in the RMEP was surveyed. The respondents were presented with 40 statements of managerial competency, derived from previous studies, other federal program sources, and the management literature. They were asked to indicate whether each competency was essential, useful but not essential, or not needed by persons employed at each of two managerial levels: team leaders, and first-line supervisors.

Responses were analyzed by calculating a content validity ratio (CVR) for each competency statement at each management level. This ratio is a measure of the extent of agreement among the respondents that an item (competency statement) is essential to performance of management functions at a particular level. Based on the CVR analysis, it was determined that there is substantial agreement among the respondents with regard to management competencies required of KSC managers. Most of the listed competencies appear to have been addressed in various RMEP sessions in the past, but many of those judged to be most important (i.e., having high CVR values) have not been addressed.

It was also observed that KSC senior management has not been significantly involved in validation of management competencies and also that no formal evaluation of the RMEP has been provided to those senior managers.

Based on the observations and findings of this study, it was recommended that:

1. Senior management participate in a further validation of management competencies.
2. A formal evaluation plan for RMEP be prepared, which will provide for a determination of
 - a. participant opinion with respect to the instructional effectiveness of the program;
 - b. the extent to which participants' subsequent behavior on the job reflects the management competencies that were expected to be attained during the program; and
 - c. opinion of RMEP presenters with respect to preparation of the participants, quality of physical facilities and arrangements, and other factors that might affect the overall quality of the presentation.
3. A design for future RMEP sessions be developed, that will allow for agreement on expected outcomes well in advance of the training sessions.

INTRODUCTION

Several events have converged in recent years to create a situation that challenges the skills of managers in government as well as in the private sector. Chief among these is the general economic condition of the country (and the world), which has led to serious budgetary restrictions and program modifications in all governmental agencies including NASA. Competition from foreign sources, as well as from domestic private industry, has brought about a serious concern for improving the quality of processes and products. This concern has found expression in the Continual Improvement program of NASA and KSC.

As important as the foregoing is the growing sensitivity to matters of diversity and equity in the workplace, and to the changes that must occur if equal opportunity is to be fully realized.

Many managers are still operating in the mode of earlier years when resources were plentiful, employment was high, and little thought was given to conservation issues. This mode does not fit well with changes due to technological advancement, business restructuring, and globalization of activities -- changes that accelerate over time. Executives must be aware of the influence of those and other changes, and they must learn how to deal with the rapidity and scope of such changes. It is not a matter of learning how to manage, and then using that learning throughout one's career. One must also learn how to learn, so that new challenges may be met squarely and overcome to the benefit of the organization.

Cohen (1991, pp. 32-34) said that these challenges await in the next few years:

1. Organizations will have to make maximum use of employee potential, effectively using the skills they currently have. Transfer of learning to new tasks is important.
2. Employees will have to be ready to give up old ways of working without the certainty that a new (or better) way is coming. This will require adaptability, creativity, innovation, courage, a sense of mission or purpose, and other similar skills and competencies.
3. Employees will be held accountable for continuing to improve needed skills.
4. Employees will have to adapt to continuous change, as well as to an increasingly diverse workplace. This will require versatility.
5. Employees must be empowered to make decisions, and organizations must encourage and support that effort.

These challenges can be met by training activities developed around *clusters of competencies* instead of job descriptions. Such training should not be a tool for remediation, but should point the way to continual advanced learning (Cohen, 1991, p. 35).

All managers must be keenly aware of the economic and technical environment in which they work, and must also be aware of actions they should take (or avoid) to accomplish the mission of the organization. This awareness can be fostered and strengthened through the implementation of a well-designed management development program.

The study reported here is an effort to assess the appropriate content of such a program for executive and mid-level managers at the John F. Kennedy Space Center, National Aeronautics and Space Administration.

THE RESIDENT MANAGEMENT EDUCATION PROGRAM (RMEP)

According to McCall, Morrison, and Lombardo (1988, p. 147), management development is

an organization's conscious effort to provide its managers (and potential managers) with opportunities to learn, grow, and change, in hopes of producing over the long term a cadre of managers with the skills necessary to function effectively in that organization.

In describing their idea of a management development program, they said that it should not be viewed as a collection of separate or individual devices such as career planning, mentoring, training courses, rotational assignment systems, and the like. Although those devices are important and useful, they must be used within the general context of management development. These points are implicit in their definition: (1) management development is "organizationally specific" -- that is, it is intended to help managers be more effective within the particular organization; (2) it is a part of a long-term business plan; (3) opportunities for participation must be made available to employees; and (4) it has to be a conscious effort by the organization, in which development opportunities are considered priority activities.

KSC has had a Resident Management Training Program (RMEP) in place for several years. This program was designed for high-performing managers, supervisors and lead personnel in grades 12 through 14 who have been in key lead, management, or supervisory positions for at least two years, and who have not attended the NASA Management Education Program (MEP) at Wallops Island, VA. Current selection practice allows personnel in those grades to attend in anticipation of such assignment. In general, the RMEP satisfies the four points of McCall, Morrison, and Lombardo, listed above.

The stated objectives of the RMEP are (National Aeronautics and Space Administration, 1993):

1. To provide participants with the opportunity to discuss and review current issues affecting KSC and its management with senior KSC managers;
2. To encourage participants to develop Center-wide contacts and thereby to strengthen teamwork throughout the Center;
3. To increase participants' awareness of their own leadership practices and influence strategies;
4. To increase participants' skills in managing interpersonal processes for solving problems and improving performance;
5. To improve participants' skills for leading and working in teams; and

6. To encourage the self-development activities of participants.

The most recent RMEP was organized around a Measurement System for Continual Improvement (CI). (This is not necessarily how future RMEPs will be set up; it was the first one to be so organized.)

The typical RMEP has the following characteristics, which are designed to be specific to KSC:

1. Participation of senior management. Special presentations and discussions are provided by senior management, so that participants have an opportunity to interact with them, learn about their management styles and philosophies, and to address their own concerns with senior managers.
2. Shared experience. Participants have the chance to integrate their conceptual learning and skill training through review and problem-solving discussions.
3. Individual feedback. Several pencil-and-paper instruments are used, both prior to and during the program, to give feedback from co-workers to participants on their supervisory, interpersonal, and influence practices.
4. Behavior modeling and skill training. Through the use of video tapes, participants can view models of management problem situations and solutions. They also have the opportunity to view themselves in role-playing situations.
5. Team development and leadership. Participants focus on procedures and practices leading to the development of superior team leaders.
6. Integration and application. Participants maintain logs of their insights, learning, and opportunities for application. Participants are also requested to develop a plan for improvement and personal development for use following the RMEP.
7. Coordination with supervisors. Participants are expected to discuss their action and development plans and projects with their supervisors following the RMEP. This is an important aspect of the training.

One desirable characteristic is not present in the foregoing list: evaluation of training. Although there are several opportunities for participants to obtain information about themselves and their leadership practices, problem-solving skills and influence strategies, there is no specific provision for feedback to KSC management with respect to whether the participants actually behave differently (i.e., are "better managers") following the RMEP. There is also little evidence concerning the RMEP instruction itself. Both evaluation areas produce vital management information for continual improvement of the training activity. Sepúlveda (1993) had recommended two evaluation forms for

general use, one to be completed by the trainee and the other by the supervisor. The first form appears to be suited to collecting participant opinion, although some minor revisions might be beneficial. The second form (to be completed by supervisors about 6 months following training) was subsequently revised to contain just two items, only one of which deals directly with employee job performance. This form does not contain sufficient information on which to base judgments about performance changes resulting from the RMEP, even in its original design.

SPECIFICATION OF MANAGEMENT COMPETENCIES

Despite the close correspondence to the description of management development activities stated by McCall, Morrison and Lombardo, the RMEP has not been formally organized around any set of competencies that characterize "good management." Consequently, one of the first activities of the present study was to find out whether appropriate descriptions of performance competencies or groups of competencies for KSC managers might be already available. Several sources of "candidate" competencies were found.

Katz (1955) identified three categories into which managerial skills can be grouped: *technical*, *human*, and *conceptual*. Katz said that within each category there exists a hierarchy of skills that can be applied at the various managerial levels in organizations. Each of the managerial levels has needs for each of the skill categories, but the proportions differ as one moves across the levels.

More recently, Sandwith (1993) pointed out that it is not possible to confine the competencies presently required of managers to only three categories. Instead, Sandwith proposed five categories that include Katz's categories, but expand and augment them. Sandwith called these categories "competency domains," and defined them as follows:

1. The **conceptual/creative** domain, which contains the cognitive skills connected with understanding important elements of the job, such as knowing one's role in an organization and how it relates to the roles of others. This domain includes Katz's conceptual category, but also adds a dimension to deal with more recent ideas from cognitive psychology and with creative thought processes.

2. The **leadership** domain, a subdivision of Katz's human skills category, that provides a connection among the **conceptual/creative** and the other domains. According to Sandwith (1993, p. 47), "it is leadership that turns thought into productive action." Skills in this domain are useful both inside and outside the organization.

3. The **interpersonal** domain is another subdivision of the human skills category, and represents the skills managers need for effective interaction with other people. The team emphasis called for by Continual Improvement makes heavy demands upon this domain. All of the communications skills, as well as related skills such as training, delegating, interviewing, etc., are included here.

4. The **administrative** domain is a third subdivision of the human skills category, and applies to organizational activities that lie between the **interpersonal** and the **technical** domains. Sandwith said that skills in this domain do not refer to administrative work in general, but rather to the personnel management and financial management aspects of organizational life (1993, p. 49).

5. Today's **technical** domain, according to Sandwith, is very similar to Katz's technical category. It relates to the actual work that an organization does. Competence in this domain includes skills related to work processes and methods, the use of technology,

Sepúlveda (1992b) conducted a training needs assessment of KSC employees, including mid-level and executive managers. The needs assessment produced a listing of topics based on consensus among the members of a focus group composed of 20 managers who were considered to have great experience in program and project management at KSC. However, the broader management competencies to which each of those topics contribute were not set out. Also, the list of topics was not validated, in the sense that persons outside the focus group were asked to concur in the decisions of that group.

An examination of Sepúlveda's study raises two further concerns. First, only three topics were identified as important for the training of senior executives (higher level competencies); and second, twenty-seven topics were categorized as "useful but not essential" or "no need for training." Examples of topics in the latter category are "Challenge of new roles," "Quality control," "Networking," and "Professional ethics and dealing with conflicts of interest." On the face of it, these topics appear to represent important skills required of managers in the current environment. Since many of the members of the focus group occupy positions that could be considered to be at the executive management level, it is possible that the focus group members assigned importance to the topics based on their personal circumstances, and not on the importance of the topics for senior managers in general.

At the Johnson Space Center in Houston, Texas, Diane DeTroye (personal communication, April 4, 1994) and her associates identified eleven competency areas for four supervisory levels. The supervisory levels identified were: pre-supervisor, first-line supervisor; mid-level manager; and executive. Within each competency category, she described specific competencies required at each of the four levels. The eleven competency categories were: conflict management and negotiation; external orientation; interpersonal effectiveness; written and oral communication; motivation and influence; managing individuals; working with groups; planning, organizing and resource management; technical awareness; personal effectiveness; and problem-solving, analysis, and decision-making.

Another source of competency statements was found in the catalog of management development courses published by the U. S. Office of Personnel Management (1994). This catalog describes the leadership effectiveness framework, which is a model describing competencies "needed by Federal executives, managers, and supervisors to perform effectively in their positions" (p. 33).

Sepúlveda's (1992b) analysis was used as a starting point for the present study. The skills listed by Sepúlveda (pp. 477-478) were condensed into more generic statements that could be located within Sandwith's competency domains. Lists of competencies were compiled from the other sources, and the lists were combined and edited to remove obvious duplications.

These competency statements were then classified into Sandwith's competency domains. Statements that described specific job skills (e.g. operating various kinds of equipment or complying with management instructions or regulations in development of organization budgets) were deleted from the lists or placed into the Administrative or Technical domains. The resulting "grid" of competencies is displayed in Appendix A.

It should be noted that there is substantial overlap among Sandwith's competency domains, and that one might make a good case for classifying a competency statement into a domain other than the ones indicated in the competency grid. The technical and administrative domains were excluded from the present study because those domains relate to performance of specific functions within an organizational unit, rather than to generalized management competencies.

COMPETENCIES REQUIRED OF KSC MID-LEVEL AND EXECUTIVE MANAGERS

In order to better understand the relative importance of the competencies for managerial work at KSC, a survey instrument was designed for administration to managers who had previously participated in the RMEP. Forty (40) competency statements representing competencies in Sandwith's conceptual/creative, leadership, and interpersonal domains were selected for inclusion in the survey.

Although the original intent of the present study was to examine management competencies at mid-level and executive management levels, it was soon found that those categories are difficult to relate to specific positions or salary grades. Consequently, it was decided to classify management levels into two categories: team leaders and first-line supervisors. These categories were selected because of the current flattening of the KSC organizational structure due to downsizing and restructuring, and because they appear to reflect current usage within KSC.

Respondents were asked to read each of the statements and then indicate whether, in their opinion, the competency is (a) essential, (b) useful but not essential, or (c) not needed by team leaders and by first-level supervisors respectively. In addition, the respondents were asked to indicate whether the competency had been addressed in the RMEP in which they participated, and whether they felt that it should be addressed in future RMEPs.

Respondents were also asked to provide general information about their opinions of the RMEP. The survey instrument is reproduced in Appendix B, which also shows the number of respondents who selected each response option. Summaries of responses to the rating scales and open-ended questions are included on page B-1.

With the assistance of the Human Resources Development office, the survey was distributed to a sample of 100 persons currently employed at KSC. Thirty-seven usable responses were received by the date established for return. (Note: a followup memorandum was sent to the non-respondents encouraging them to return their surveys even though the deadline had passed. Surveys received subsequent to that memorandum will be added to the data base for further study.)

In his final report of activity during the summer of 1993, Sepúlveda (1993) briefly discussed the use of the content validity ratio, or CVR, in connection with the evaluation of training. Ford and Wroten (1984) used a content validity approach in establishing statements of knowledge, skill, ability, and other personal characteristics (KSAOs) for use in a police training program, specifically in evaluating the content for such a program once the content domain has been identified.

The content validity ratio (CVR) was proposed by Lawshe (1975) as a means of quantifying consensus among members of a panel attempting to decide whether performance on some test is representative of performance on the job. He said that "content validity is the extent to which

communality or overlap exists between (a) performance on the test under investigation and (b) ability to function in the defined job performance domain" (p. 567). When a content evaluation panel is composed of persons ("experts") who know the requirements of a job, then we can rely on the extent of their agreement to provide a measure of the "relatedness" of the test performance to the job performance requirements.

Lawshe made the following assumptions (p. 567):

1. Any item, performance on which is perceived to be "essential" by more than half of the panelists, has some degree of content validity.
2. The more panelists (beyond 50%) who perceive the item as "essential," the greater the extent or degree of its content validity.

By extension, one can convene a panel whose task it is to decide whether or not some specified performance is essential to successful performance in some job. This was essentially the nature of the investigation for this study, in which individuals who are incumbents in managerial positions and who have participated in a training activity make judgments about the appropriateness of the training for success in a position.

The usefulness of the CVR in this activity derives from these characteristics stated by Lawshe (1975, pp. 567-568):

1. When fewer than half of the panelists say that an item (here, a competency statement) is "essential", the CVR is negative.
2. When exactly half say an item is essential while the remaining half do not, the CVR is zero.
3. When all of the panelists say an item is "essential" the CVR is computed to be 1.00, although it is convenient to adjust it to 0.99 for ease of manipulation.
4. When the number of panelists saying that an item is "essential" is more than half, but less than all, then the CVR is somewhere between 0.99 and 0.00

Table 1 presents the content validity ratios calculated for competencies required for Team Leaders and for First-Line Supervisors, respectively, over the 40 management competency statements contained in the survey instrument (see Appendix B). The same information is presented in Tables 2 and 3, except that the rows have been arranged in descending order of CVR for Team Leaders and First-Line Supervisors respectively.

For Team Leaders, 26 of the 40 competency statements have positive CVRs (i.e., were marked "essential" by more than half of the respondents). For First-Line Supervisors, 36 of the 40 statements have positive CVRs.

The numerical magnitude of a CVR has no direct interpretation other than those described above. However, it can be used to rank order the statements as presented in Tables 2 and 3. When this has been done, a rank-order correlation can be performed to determine whether the panel members generally agree on the importance of the competencies between the two management groups.

A rank-order correlation coefficient (Spearman *rho*) was calculated based on the differences in ranks between CVRs for Team Leaders and First-Line Supervisors. The value of the computed correlation coefficient was 0.80, which is significantly different from zero ($p < .01$). This observation can be interpreted as meaning that the competencies required of managers in the two groups are generally similar. Even though the magnitude of the CVRs has no direct interpretation, an inspection of the data of Tables 2 and 3 reveals that the ratios for First-Line Supervisors are generally smaller than those for Team Leaders. For example, the highest and lowest CVRs for First-Line Supervisors are 0.771 and -0.040 respectively, while for Team Leaders they are 0.943 and -0.500. However, only four of the competency statements were judged to be not essential for First-Line Supervisors (that is, with CVR values less than zero), while 15 were so classified for Team Leaders. This means that the competencies for First-Line Supervisors were less frequently judged "essential" than for Team Leaders, but there was less agreement that the competencies were valid for Team Leaders.

Table 1. Content validity ratios and ranks for 40 competency statements (N=37)

Competency Statement	TL CVR	FLS CVR	Rank by TL CVR	Rank by FLS CVR
1	-0.500	-0.029	40	37
2	0.829	0.892	4	3.5
3	0.657	0.838	8	7
4	0.371	0.838	17.5	7
5	0.886	0.889	2	5
6	-0.486	0.056	39	36
7	0.371	0.611	17.5	25
8	0.643	0.655	11	20
9	0.857	0.786	3	10
10	0.379	0.793	16	9
11	0.357	0.724	19	15
12	-0.185	0.214	31	32
13	-0.111	0.172	28	33
14	-0.143	0.379	29.5	28
15	0.429	0.724	14.5	15
16	0.071	0.724	25	15
17	-0.143	0.351	29.5	29
18	0.714	0.946	6.5	1.5
19	0.943	0.892	1	3.5
20	0.273	0.714	20	17
21	-0.455	-0.231	38	38
22	-0.353	0.111	37	34.5
23	-0.059	0.111	27	34.5
24	0.657	0.676	8	18.5
25	0.143	0.730	24	12
26	-0.040	-0.333	26	40
27	0.450	0.243	13	30.5
28	-0.333	0.622	36	22.5
29	-0.318	-0.294	35	39
30	-0.212	0.622	32	22.5
31	-0.235	0.514	33	26.5
32	0.600	0.730	12	12
33	0.257	0.622	22	22.5
34	0.714	0.622	6.5	22.5
35	0.257	0.730	22	12
36	-0.257	0.243	34	30.5
37	0.257	0.514	22	26.5
38	0.771	0.946	5	1.5
39	0.657	0.838	8	7
40	0.429	0.676	14.5	18.5
Spearman rho -->				0.80

Table 2. Content validity ratios and ranks for 40 competency statements (N=37)
(ordered by CVR rank for team leaders)

Competency Statements	TL CVR	FLS CVR	Rank by TL CVR	Rank by FLS CVR
19	0.943	0.892	1	3.5
5	0.886	0.889	2	5
9	0.857	0.786	3	10
2	0.829	0.892	4	3.5
38	0.771	0.946	5	1.5
18	0.714	0.946	6.5	1.5
34	0.714	0.622	6.5	22.5
24	0.657	0.676	8	18.5
3	0.657	0.838	8	7
39	0.657	0.838	8	7
8	0.643	0.655	11	20
32	0.600	0.730	12	12
27	0.450	0.243	13	30.5
15	0.429	0.724	14.5	15
40	0.429	0.676	14.5	18.5
10	0.379	0.793	16	9
4	0.371	0.838	17.5	7
7	0.371	0.611	17.5	25
11	0.357	0.724	19	15
20	0.273	0.714	20	17
35	0.257	0.730	22	12
37	0.257	0.514	22	26.5
33	0.257	0.622	22	22.5
25	0.143	0.730	24	12
16	0.071	0.724	25	15
26	-0.040	-0.333	26	40
23	-0.059	0.111	27	34.5
13	-0.111	0.172	28	33
14	-0.143	0.379	29.5	28
17	-0.143	0.351	29.5	29
12	-0.185	0.214	31	32
30	-0.212	0.622	32	22.5
31	-0.235	0.514	33	26.5
36	-0.257	0.243	34	30.5
29	-0.318	-0.294	35	39
28	-0.333	0.622	36	22.5
22	-0.353	0.111	37	34.5
21	-0.455	-0.231	38	38
6	-0.486	0.056	39	36
1	-0.500	-0.029	40	37

Table 3. Content validity ratios and ranks for 40 competency statements (N=37)
(ordered by CVR rank for first-line supervisors)

Competency Statements	TL CVR	FLS CVR	Rank by TL CVR	Rank by FLS CVR
38	0.771	0.946	5	1.5
18	0.714	0.946	6.5	1.5
2	0.829	0.892	4	3.5
19	0.943	0.892	1	3.5
5	0.886	0.889	2	5
3	0.657	0.838	8	7
39	0.657	0.838	8	7
4	0.371	0.838	17.5	7
10	0.379	0.793	16	9
9	0.857	0.786	3	10
32	0.600	0.730	12	12
25	0.143	0.730	24	12
35	0.257	0.730	22	12
11	0.357	0.724	19	15
16	0.071	0.724	25	15
15	0.429	0.724	14.5	15
20	0.273	0.714	20	17
40	0.429	0.676	14.5	18.5
24	0.657	0.676	8	18.5
8	0.643	0.655	11	20
30	-0.212	0.622	32	22.5
34	0.714	0.622	6.5	22.5
33	0.257	0.622	22	22.5
28	-0.333	0.622	36	22.5
7	0.371	0.611	17.5	25
31	-0.235	0.514	33	26.5
37	0.257	0.514	22	26.5
14	-0.143	0.379	29.5	28
17	-0.143	0.351	29.5	29
36	-0.257	0.243	34	30.5
27	0.450	0.243	13	30.5
12	-0.185	0.214	31	32
13	-0.111	0.172	28	33
23	-0.059	0.111	27	34.5
22	-0.353	0.111	37	34.5
6	-0.486	0.056	39	36
1	-0.500	-0.029	40	37
21	-0.455	-0.231	38	38
29	-0.318	-0.294	35	39
26	-0.040	-0.333	26	40

DISCUSSION OF THE RESULTS OF THE SURVEY

The responses to the rating scales contained in items 1 and 2 of the survey (see Appendix B, p. B-2) indicate that participants are generally well satisfied with the RMEP. The mean response to item 1, which asked the extent to which participants felt that the RMEP increased their capability to do the jobs they now hold, was 3.75 (maximum 5). The mean response to item 2, asking participants' overall satisfaction with the RMEP, was 4.20 (maximum 5).

Item 3 asked respondents to list the ONE thing that they liked MOST about the RMEP session that they attended. As with any open-ended question, the responses were varied; however, the vast majority of respondents mentioned the value of the sessions in which they were able to meet with senior managers and to discuss issues. Some of the respondents in this group made comments more oriented to their peers, but the opportunity to network with both peers and upper-level managers is an obvious "like" of this sample.

Item 4, another open-ended item, asked respondents to list the ONE thing that they liked LEAST about the RMEP in which they participated. In this case, the responses were much more widely spread. The largest single response (6 respondents) was "disliked nothing." Five respondents stated that they did not like the role-playing exercises (although 8 indicated in item 3 that videotaping of such exercises was positive), and 5 others said that there was not enough time to complete the work (some mentioned the readings, others the project preparation).

Only one respondent mentioned the topic of a specific presentation or session in the list of dislikes. This indicates that it is probably the physical arrangement of the RMEP sessions rather than their content which participants recall negatively. Indeed, the list of "likes" for the 37 respondents is made up exclusively of responses dealing directly with the use or improvement of management competencies that might be valuable on the job at KSC.

At the end of the survey instrument, respondents were asked to describe competencies that should have been included in the list, but that were not. Other comments related to the RMEP were solicited as well. This item was frequently omitted; only 12 survey forms contained responses. No clear trend could be observed in the few suggestions for additional competencies. The "other comments" seem to be in the nature of suggested improvements to KSC management and not, with one or two exceptions, to the RMEP *per se*.

An inspection of Table 1 reveals that, of the 40 competencies subjected to review, only four received negative CVRs for both team leaders and first-line supervisors. Put another way, only

four of the listed competencies were not considered to be essential for managers at either level. These competencies are:

1. Identify and eliminate redundancies within or between KSC organizational units.
21. Tolerate ambiguity in various situations.
26. Integrate the projects and programs of own organization with those of other organizations external to KSC.
29. Champion organizational change.

The number of respondents stating that these competencies were addressed in the RMEP they attended was 4, 8, 10, and 15 respectively. Similarly, the number of respondents stating that the competencies *should be* included in the RMEP was 21, 18, 15, and 23 respectively.

CONCLUSIONS

1. Based on the survey of previous RMEP participants, it appears that there is substantial agreement on management competencies required of team leaders and first-level supervisors. This observation is supported by the significant rank-order correlation coefficient calculated on the content validity ratio ranks for the two groups. This does not imply, however, that the curriculum for the RMEP should be modified to assure that *all* the competencies held to be essential for team leaders and first-level supervisors should be addressed in any particular RMEP. Responses to the open-ended questions included in the survey instrument point toward the perceived high value for participants of networking and discussions with senior managers.

2. Conclusion 1 above notwithstanding, there has been no similar validation of required competencies by senior managers. In other words, there is agreement among RMEP "graduates" that the competencies they were asked about are actually competencies required of KSC managers; but senior managers have not been asked whether they concur that the competencies thought valuable by team leaders and first-level supervisors are actually the competencies they wish their subordinates to display.

3. As mentioned earlier, a serious shortcoming of the RMEP is that few formal evaluation activities have been undertaken. Although in some cases participants have been asked to provide feedback about the program, no attempt has been made to determine the effectiveness of the program as perceived by supervisors; also, there is no formal evaluation of the instructional process for the benefit of the office responsible for the program (currently HM-PER-1).

4. Appendix B reveals that most of the 40 competencies were reported to have been covered in the various respondents' RMEP sessions. Whether this is physically possible is questionable. However, and most important to this investigation, is *how* the competencies were addressed. The subject matter covered by any particular RMEP appears to have been largely left to the discretion of the person(s) conducting the sessions. Based on responses to the first open-ended item on the survey instrument, the tone of the sessions seems to have been appropriately set by the presentations of KSC senior management, but the specifics of how this information is woven into RMEP activities (if at all) have not been made clear.

RECOMMENDATIONS

1. Pursue with senior KSC management a validation of the list of management competencies developed under this project. The validation should address (a) the extent of agreement among senior managers that the specific competencies are appropriate, (b) additions desired by senior management to the list of competencies, and (c) removal of inappropriate statements from the list. In particular, competencies that support the provisions of the strategic plan and the continual improvement plan should be identified, categorized (e.g. into Sandwith's domains), and specified for inclusion in RMEP activities. It is especially important to identify competencies associated with newer management approaches implied by the strategic or continual improvement plans.

2. Devise an evaluation plan for the RMEP that will produce management information to be used in determining (a) participants' opinions the instructional effectiveness of the program and (b) the extent to which participants' subsequent behavior on the job reflects the management competencies that were expected to be attained. The plan should also provide for collecting information from RMEP providers with respect to preparation of the participants, quality of physical facilities, and other factors that might affect the overall quality of the presentation.

3. Develop a design for future RMEP sessions that will allow for agreement on the expected outcomes well in advance of the training. That is, take steps to assure that the objectives for training are consistent with the perceived management needs of Kennedy Space Center, and that the training activities to be offered will reasonably bring about the attitudes and understandings that will promote the management competencies desired. The design should be sufficiently flexible that emerging issues can be dealt with in a timely way.

REFERENCES

- Cocheu, T. (1993.) *Making quality happen: how training can turn strategy into real improvement*. San Francisco: Jossey-Bass, Inc.
- Cohen, S. L. (1993, July.) The challenge of training in the nineties. *Training and development*, 45(7), 31-35.
- Ford, J. K. and Wroten, S. P. Introducing new methods of conducting training evaluation and for linking training evaluation to program redesign. *Personnel Psychology*, 37, 651-665.
- Katz, R. L. (1955, January-February.) Skills of an effective administrator. *Harvard Business Review*, 33, 33-42.
- Kramlinger, T. (1992, July.) Training's role in a learning organization. *Training*, 29(7), 46-51.
- Lawshe, C. H. (1975.) A quantitative approach to content validity. *Personnel psychology*, 28, 563-575.
- Marquardt, M. J. and Reynolds, A. (1994.) *The global learning organization*. Burr Ridge, IL: Richard D. Irwin, Inc.
- McCall, M. W., Lombardo, M. M., and Morrison, A. M. (1988.) *The lessons of experience*. Lexington, MA: Lexington Books.
- National Aeronautics and Space Administration, John F. Kennedy Space Center. (1993.) *KSC Resident Management Education Program* (Participants' notebook). Kennedy Space Center, FL: Author.
- Osbaldeston, M. and Barham, K. (1992, December.) Using management development for competitive advantage. *Long range planning*, 25(6), 18-24.
- Rollins, T. and Fruge, M. (1992, January.) Performance dimensions: competencies with a twist. *Training*, 29(1), 47-51.
- Sandwith, P. (1993, Spring.) A hierarchy of management training requirements: the competency domain model. *Public personnel management*, 22(1), 43-62.

- Senge, P. (1990.) *The fifth discipline*. New York: Doubleday/Currency.
- Sepúlveda, J. A. (1992a.) KSC management training system project final report (training evaluation). In NASA CR-191004, NASA/ASEE Management Science Faculty Fellowship Project, pp. 451-458.
- Sepúlveda, J. A. (1992b.) KSC management training system project final report (needs assessment). In NASA CR-191004, NASA/ASEE Management Science Faculty Fellowship Project, pp. 459-482.
- Sepúlveda, J. A. (1993.) KSC management training system project final report. In NASA CR-194678, NASA/ASEE Management Science Faculty Fellowship Project, pp. 433-464.
- U. S. Office of Personnel Management. (1994?) *Seminars of the management development centers, fiscal year 1995*. Washington, DC: Author.
- Van Wart, M. (1993, Summer.) Providing a base for executive development at the state level. *Public Personnel Management*, 22(2), 269-282.

omit

A-1

APPENDIX A

GENERIC MANAGEMENT COMPETENCIES

Conceptual/Creative Domain	Leadership Domain	Interpersonal Domain	Administrative Domain	Technical Domain
Identifies and eliminates redundancies within and between KSC organizations.	Anticipates, recognizes, manages, and resolves confrontations, disagreements, complaints, and other conflicts in a constructive manner.	Appropriately uses negotiation, persuasion, and/or authority in dealing with subordinates, peers, and supervisors, to meet goals.	Convincingly solicits funding for the agency.	Continuously seeks to improve the quality of services, products, and processes.
Communicates customer expectations and requirements, and ensures that customer needs are met.	Establishes policies, guidelines, plans, and priorities.	Networks with key groups and individuals, including the media, to gain cooperation and exchange information to meet goals.	Plans, prepares, and justifies budgets; allocates resources; and manages the finances of one or more projects within one or more organizational units.	Adapts content and style of communications as appropriate for audiences which may include own organization, KSC, NASA, Congress, the general public, and the media.
Actively seeks customer input and acts as an advocate for customers.	Advocates and supports NASA programs and projects.	Builds and maintains effective positive relationships with customers, contractors, peers, local business leaders, and academia.	Manages procurement and contracting for one or more organizational units.	Presents clear and convincing oral and written material.
Scans the environment for new opportunities, and develops operational strategies to take advantage of such opportunities.	Adapts leadership styles effectively to a variety of individual capabilities and situational demands, including changes in the work environment.	Fosters innovation among others.	Establishes performance measures and monitors the output and quality of projects within the scope of assigned responsibilities.	Asks diagnostic questions, seeks clarification, and provides overall direction on technical areas within directorates.

Conceptual/Creative Domain	Leadership Domain	Interpersonal Domain	Administrative Domain	Technical Domain
Maintains current awareness of laws, regulations, policies, Administration priorities, social and political trends, and other issues affecting NASA in general and KSC in particular.	Improves organizational efficiency and effectiveness.	Actively solicits and listens to the ideas of others.	Develops the capabilities of organizations and individuals to provide for current and future organization needs .	Maintains technical awareness of functions and subfunctions within own organizational unit; understands the consequences and implications of technical decisions.
Seeks alternative solutions to complex problems, identifying the variables involved while distinguishing between relevant and irrelevant information.	Creates an environment that empowers, motivates, and guides individuals and groups. Delegates work appropriately, and establishes performance metrics to meet organizational goals effectively.	Provides effective supervision, including appropriate feedback and coaching or mentoring when necessary.	Effectively promotes affirmative employment, good labor relations, and employee well-being.	Manages and integrates internal technology with technical aspects of other organizations.
Creates, communicates and implements the KSC vision and values.	Uses appropriate influence strategies to get support for team projects, and for the work of team members. Promotes ethical and effective practices.	Fosters cooperation, communication, and consensus among groups.	Demonstrates knowledge of human resource management systems, and ensures effective recruitment, selection, training, performance appraisal, recognition, and corrective or disciplinary action for all subordinates	Manages the integration of various functional roles within own organizational unit (e.g. procurement, budget, finance, engineering, operations, etc.).
Creates a shared vision of the organizational unit; promotes wide ownership.		Provides guidance and support to work group activities throughout KSC. Considers and responds appropriately to the needs, feelings, interests and capabilities of others.	Ensures that subordinates are trained and capable.	Applies new and existing technology to the management of the organization.
		Treats others equitably, and with respect for individual differences.		

Conceptual/Creative Domain	Leadership Domain	Interpersonal Domain	Administrative Domain	Technical Domain
<p>Champions organizational change.</p> <p>Develops objectives and implements strategies, both long- and short-range.</p> <p>Assesses circumstances and draws conclusions about the position of NASA and KSC with respect to NASA Headquarters, the Federal government, the national agenda, the international environment, and the public at large.</p> <p>Develops insights and solutions through identifying and analyzing problems using sound reasoning and other problem-solving techniques applied to the best data available.</p>	<p>Matches organizational skills and abilities to project and program requirements in order to achieve organizational goals.</p> <p>Analyzes risks and takes decisive action in difficult situations when necessary. Effectively plans and manages team and work group meetings to accomplish meeting goals.</p> <p>Serves as a role model by demonstrating personal qualities of professionalism, integrity, flexibility, trust, openness, dependability, initiative, self-confidence, and optimism.</p>	<p>Makes clear and effective oral and written presentations to individuals and groups.</p> <p>Considers differences between directorates or program offices in corporate culture and policy interaction with other organizations.</p> <p>Effectively manages stress.</p> <p>Frames problems for others to solve, and follows up on the resolution of those problems.</p> <p>Provides employment and development opportunities for a diverse workforce.</p>	<p>Maintains internal controls, evaluates programs and projects over time, and makes decisions based on what is best for the organization.</p>	<p>Demonstrates technical proficiency and an understanding of its impact in areas of responsibility.</p>

Conceptual/Creative Domain	Leadership Domain	Interpersonal Domain	Administrative Domain	Technical Domain
<p>Integrates projects and programs of own organization with those of other organizations and functions internal and external to KSC.</p>	<p>Challenges the system and acts as a steward of the public trust.</p>	<p>Realistically assess own strengths, weaknesses, and their impact on others.</p>		
<p>Tolerates ambiguity in situations. Integrates perspectives of multiple disciplines in analyzing problems and in grasping large-scale systems problems.</p>	<p>Ensures the integrity of the organization's processes.</p>	<p>Manages time efficiently.</p>		
<p>Recognizes the value of cultural, ethnic, gender, and other individual differences in the workforce.</p>		<p>Invests in self-development.</p>		
		<p>Encourages subordinates to stay informed about new technology.</p>		

APPENDIX B

Generic Management Competency Validation

As a "graduate" of the Residential Management Education Program (RMEP), we are requesting your help in validating the list of generic management competencies toward which RMEP activities may be directed in the future. In addition, we ask that you answer a few questions about your experience with RMEP, so that future sessions can be improved for every participant. Your responses will be kept confidential, and the results of this validation study will not identify any individual by name or by unit of assignment. Only summary information will be reported.

Please provide a response to each of the following items:

1. On a scale of 1 to 5, with 5 being **highest**, please indicate the extent to which you feel that RMEP increased your capability to do the job that you now hold.
(Mean = 3.75)

1 2 3 4 5

2. On a scale of 1 to 5, with 5 being **highest**, please indicate your *overall* satisfaction with the RMEP. **(Mean = 4.20)**

1 2 3 4 5

3. Considering the RMEP experience as a whole, what ONE thing did you like **MOST** about the RMEP?

videotaping of simulated confrontations and self-evaluations (8)
opportunity for hearing senior management presentations and networking (25)

teaching of management skills (4)

4. Considering the RMEP experience as a whole, what ONE thing did you like **LEAST** about the RMEP.

time away from home
role playing (5)
insufficient time (5)
days too long (3)
evening sessions
(disliked nothing) (6)
the food

immobility (2)
the instructor (3)
(a specific presentation)
group too large
lectures
too many structured exercises
lack of followup

Please go on to the next page

Here is a list of several generic management competencies that might be selected for emphasis at an RMEP session. First, read each competency statement and then make a check mark or an "X" to indicate whether you believe it is **Essential; Useful, but not essential; or Not needed** by Team Leaders. Next, indicate whether you believe the competency is **Essential; Useful, but not essential; or Not needed** by First-Level Supervisors. Then, check to indicate whether (to the best of your recollection) it was addressed at the RMEP in which you participated. Finally, indicate whether you think the listed competency should be addressed at future RMEP sessions.

Competency Statements	For Team Leaders			For First Level Supervisors			Was it addressed in <i>your</i> RMEP?		Should it be addressed in the RMEP?	
	<u>E</u>	<u>U</u>	<u>N</u>	<u>E</u>	<u>U</u>	<u>N</u>	Yes	No	Yes	No
1. Identify and eliminate redundancies within or between KSC organizational units.	8	21	3	17	14	4	4		21	
2. Build and maintain relationships with customers.	32	3	0	35	2	0	24		36	
3. Communicate customer expectations and requirements to supervisors and/or subordinates accurately.	29	6	0	34	3	0	23		35	
4. Recognize, manage and resolve conflicts within or between KSC organizational units.	24	10	1	34	3	0	28		34	
5. Ensure that customer needs are met.	33	2	0	34	2	0	21		34	
6. Scan environment for new opportunities; develop strategies to take advantage of such opportunities.	9	23	3	19	17	0	8		25	
7. Manage stress effectively	24	10	1	29	7	0	14		29	

Competency Statements	For Team Leaders			For First Level Supervisors			Was it addressed in <i>your</i> RMEP?		Should it be addressed in the RMEP?	
	<i>E</i>	<i>U</i>	<i>N</i>	<i>E</i>	<i>U</i>	<i>N</i>	Yes	No	Yes	No
8. Use appropriate influence strategies (e.g. negotiation, persuasion or authority) in working with subordinates, peers, and supervisors.	23	5	0	24	5	0	25		29	
9. Foster cooperation, communication, and consensus within groups and teams.	26	2	0	25	3	0	28		27	
10. Treat subordinates equitably.	20	6	1	26	3	0	21		26	
11. Delegate work appropriately and equitably.	19	9	0	25	4	0	16		26	
12. Create and communicate the KSC vision and values.	11	14	2	17	10	1	10		5	
13. Provide guidance and support to KSC work group activities.	12	12	3	17	10	2	11		22	
14. Advocate and support KSC programs and projects.	12	12	4	20	8	1	13		22	
15. Network with key groups and individuals to gain cooperation and exchange information to meet goals.	20	8	0	25	4	0	24		26	
16. Establish and communicate performance metrics for evaluating work quality.	15	12	1	25	4	0	15		28	

Competency Statements	For Team Leaders			For First Level Supervisors			Was it addressed in <i>your</i> RMEP?		Should it be addressed in the RMEP?	
	<i>E</i>	<i>U</i>	<i>N</i>	<i>E</i>	<i>U</i>	<i>N</i>	Yes	No	Yes	No
17. Maintain a current awareness of law, regulation, policy, Administration priorities, and other issues affecting NASA in general and KSC in particular.	15	16	4	25	10	2	10		20	
18. Create an environment that empowers, motivates, and guides individuals and groups.	30	5	0	36	1	0	30		35	
19. Actively solicit and listen to the ideas of others.	34	1	0	35	2	0	31		34	
20. Improve organizational effectiveness and efficiency.	21	10	2	30	5	0	21		33	
21. Tolerate ambiguity in various situations.	9	14	10	10	16	8	8		18	
22. Encourage subordinates to become and remain informed about new technology.	11	20	3	20	13	3	11		18	
23. Challenge the system, but act as a steward of the public trust.	16	12	6	20	10	6	14		27	
24. Assess own strengths and weaknesses and their impacts on others.	29	6	0	31	6	0	32		35	
25. Respect individual differences.	29	6	0	32	5	0	30		34	

Competency Statements	For Team Leaders			For First Level Supervisors			Was it addressed in <i>your</i> RMEP?		Should it be addressed in the RMEP?	
	<i>E</i>	<i>U</i>	<i>N</i>	<i>E</i>	<i>U</i>	<i>N</i>	Yes	No	Yes	No
26. Integrate the projects and programs of own organization with those of other organizations external to KSC.	8	19	7	12	22	2	10		15	
27. Bring together the perspectives of multiple disciplines in analyzing problems.	24	11	0	23	13	1	22		29	
28. Manage time effectively.	29	6	0	30	7	0	27		30	
29. Champion organizational change.	3	18	11	12	18	4	15		23	
30. Develop objectives and implement strategies, both long- and short-range.	15	18	2	30	7	0	25		33	
31. Provide employment and development opportunities for a diverse workforce.	13	12	6	28	7	2	21		30	
32. Analyze risks and take decisive action when necessary.	28	7	0	32	5	0	20		24	
33. Frame problems for others to resolve, and follow up on the solutions.	22	13	0	30	7	0	21		32	
34. Plan and manage team and work group meetings effectively.	30	5	0	30	7	0	32		33	
35. Match skills and abilities available in own organization to project and program requirements.	22	13	0	32	5	0	28		32	

Competency Statements	For Team Leaders			For First Level Supervisors			Was it addressed in <i>your</i> RMEP?		Should it be addressed in the RMEP?	
	<i>E</i>	<i>U</i>	<i>N</i>	<i>E</i>	<i>U</i>	<i>N</i>	Yes	No	Yes	No
36. Promote wide ownership of the organizational unit.	13	18	4	23	12	2	18		29	
37. Foster innovation among others.	22	13	0	28	9	0	23		34	
38. Anticipate and resolve confrontations in a constructive manner.	31	4	0	36	1	0	33		35	
39. Respond appropriately to the needs, feelings, interests, and capabilities of others.	29	6	0	34	3	0	32		33	
40. Serve as a role model by demonstrating appropriate personal qualities	25	10	0	31	6	0	29		31	

484

In the space below, please write brief descriptions of management competencies that you feel SHOULD HAVE BEEN included in the foregoing list, but that were not. Other RMEP-related comments are invited as well.

Additional competencies: managing resources; measuring effectiveness; understanding leadership styles; job interview and counseling techniques; synergy; group dynamics; problem-solving; TQM/CI integrated techniques; impact of long- and short-range planning strategies; moral and ethical aspects of managing/leading;

Other comments: Communicate performance expectations and feedback to subordinates effectively & objectively; more emphasis on being coach for IDP development; there is a need for upper management to practice what they preach; RMEP ... must be continued. ... More emphasis [on] career development for women and minorities with a true positive objective approach....;send this out sooner or do it at the end of RMEP; ...spend additional time discussing resource management and empowerment.

1994 NASA/ASEE SUMMER FACULTY FELLOWSHIP PROGRAM

111768
351504

JOHN F. KENNEDY SPACE CENTER
UNIVERSITY OF CENTRAL FLORIDA

517-103
33977
P-24

ENHANCEMENTS TO THE KATE
MODEL-BASED REASONING SYSTEM

PREPARED BY:	Dr. Stan J. Thomas
ACADEMIC RANK:	Associate Professor
UNIVERSITY AND DEPARTMENT:	Wake Forest University Department of Mathematics and Computer Science
NASA/KSC	
DIVISION:	Engineering Development
BRANCH:	Artificial Intelligence
NASA COLLEAGUE:	Peter Engrand
DATE:	August 12, 1994
CONTRACT NUMBER:	University of Central Florida NASA-NGT-60002 Supplement: 17

Acknowledgements

I would like to thank Peter Engrand of NASA as well as Charlie Goodrich, Bob Merchant and Steve Beltz of INET for their cooperation and technical support this summer. I would also like to extend both compliments and thanks to Dr. Anderson, Dr. Hosler and Ms. Stiles for their professional management of the summer faculty program.

Abstract

KATE is a model-based software system developed in the Artificial Intelligence Laboratory at the Kennedy Space Center for monitoring, fault detection, and control of launch vehicles and ground support systems. This report describes two software efforts which enhance the functionality and usability of KATE. The first addition, a flow solver, adds to KATE a tool for modeling the flow of liquid in a pipe system. The second addition adds support for editing KATE knowledge base files to the Emacs editor. The body of this report discusses design and implementation issues having to do with these two tools. It will be useful to anyone maintaining or extending either the flow solver or the editor enhancements.

Summary

The Knowledge-based Autonomous Test Engineer (KATE) system is a model-based software system which has been developed in the Artificial Intelligence Laboratory at the Kennedy Space Center over the last decade. It is designed for monitoring, fault detection, and control of launch vehicles and ground support systems.

This report commences with a brief introduction to the fundamental principles behind the operation of KATE. Emphasis is placed on the structure and importance of KATE's knowledge-base. We then describe two software efforts implemented this summer to enhance the functionality and usability of KATE. The first addition, called a flow solver, adds to KATE a tool for modeling the flow of a non-compressible liquid in a system of pipes. The program was developed in C++ in such a way that it can be called from within KATE or used independently as a tool for solving flow problems. The second enhancement is a collection of Emacs-LISP functions which comprise a major editing mode for working with KATE knowledge base files. These functions add domain-specific features to Emacs in order to ease the task of building KATE models.

The body of this report discusses design and implementation issues having to do with these two software systems designed and prototyped this summer. It will be useful to anyone maintaining or extending either the flow solver or the editor enhancements.

TABLE OF CONTENTS

<u>Section</u>	<u>Title</u>
I	AN INTRODUCTION TO MODEL-BASED REASONING
1.1	Basic Principles
1.2	Knowledge-bases
1.2.1	The KATE Knowledge-base
1.2.1.1	High level system knowledge
1.2.1.2	Middle level system knowledge
1.2.1.3	Low level system knowledge
1.2.1.4	Database files
II	THE FLOW SOLVER
2.1	Problem Description
2.2	Newton's Method
2.3	The SGOS Flow Solver
2.4	Implementation of the Flow Solver
2.5	Future Work
III	THE EMACS KATE MODE
3.1	Design Specifications
3.2	Implementation
3.3	Future Work
IV	REVIEW

LIST OF ILLUSTRATIONS

<u>Figure</u>	<u>Title</u>
1-1	Overview of Model-based Reasoning
2-1	Abstract Flow Network
2-2	Example Flow Network
2-3	Comparison of Results

AN INTRODUCTION TO MODEL-BASED REASONING

1.1 BASIC PRINCIPLES

The basic concepts of model-based reasoning are very simple. A computer simulation model of a physical system is constructed from a knowledge-base representing the components of the system and their interconnections. The physical system, which is assumed to have numerous sensors, is put into operation. As the physical system operates, sensor readings are compared to their predicted values from the simulation model. As long as there are no significant discrepancies between predicted values and actual sensor readings, nothing is done. When a significant discrepancy occurs, the model-based reasoning system can carry out whatever actions are needed to alert a human that a problem has occurred. This aspect of model-based reasoning is simply known as monitoring.

If model-based reasoning systems were only capable of monitoring, they would be of limited utility. Fortunately, model-based reasoning systems such as KSC's Knowledge-based Autonomous Test Engineer (KATE) have other abilities. Among the most interesting is failure diagnosis. Once a significant discrepancy has been identified in the monitoring stage, KATE utilizes its internal representation of the physical system in an effort to identify failures which could have led to the conflict between predicted values and actual sensor values. A significant difference between this reasoning process and traditional process control techniques is KATE's ability to include sensors themselves in the diagnostic process. A high-level overview of the monitoring process and its relation to diagnosis is illustrated in Figure 1-1.

In addition to their ability to monitor and diagnose complex systems, model-based reasoning systems such as KATE have the potential for several other very useful functions. If the computer has the ability to issue commands to the physical system, it should be possible to describe a desired state of the physical system and have the reasoning system determine what commands to issue to achieve that state. If the physical system has redundant pathways and components, as is frequently the case in NASA systems, the model-based system can often determine how to utilize redundant hardware in order to continue operation of the physical system after some component or components have failed. It is also possible to have such a model-based reasoning system construct an explanation of the steps taken to identify a failed component or to achieve a specific objective.

In addition to their operational use, model-based reasoning systems have great potential as training tools. An instructor can create failure scenarios in the simulation environment to test the student's ability to respond to failures of the actual hardware.

Another potential use for model-based reasoning systems is to determine the adequacy of the sensors in a complex system before it is built. For a more in-depth introduction to model-based reasoning see [1].

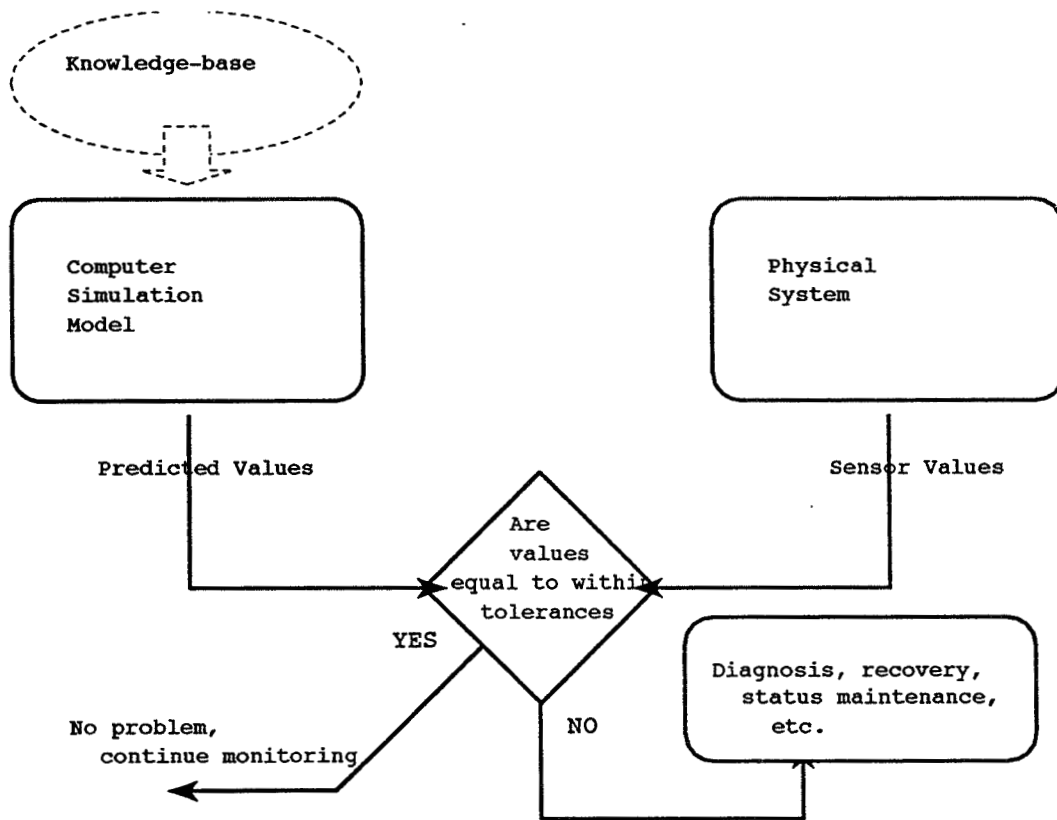


Figure 1-1. Overview of Model-based Reasoning

1.2 KNOWLEDGE-BASES

In order for a model-based reasoning system to function, it must have information about the structure and operation of the physical system to be modeled. We call such information about the real world the system's knowledge-base. As characterized in [2] for the KATE system:

The KATE knowledge base contains vital information about the physical system that KATE is controlling or monitoring. This information is the raw material used by KATE to construct a simulation model that mimics the system's structure and function. Objects in the model have a one-to-one correspondence with parameters, commands, sensors, and other components in the physical system. The knowledge-base is referenced by

KATE in the same way that schematic diagrams and operating specifications are used by system engineers.

1.2.1 THE KATE KNOWLEDGE-BASE. In order to lay the groundwork for topics discussed later in this report, we elaborate upon the organization of KATE's knowledge-base—a three-level hierarchical structure. Such hierarchical structures are typical of the organization of knowledge-bases used for model-based reasoning systems.

1.2.1.1 High level system knowledge. The so-called "top-level" of KATE's knowledge base represents information about very broad classes of system components. For the systems with which KATE is currently used, these classes are commands, measurements, components, pseudo objects, display function designators and so called synchronization objects. For operational efficiency, generic knowledge about the structure and function of these high level classes of objects is hard-coded into the C++ implementation of KATE. This means that changes to KATE's top-level knowledge of system component classes require possibly extensive modifications to the source code. Fortunately, such changes occur infrequently.

1.2.1.2 Middle level system knowledge. The so-called "mid-level" of KATE's knowledge-base represents information about specific types of system components. For example, this class contains knowledge about components such as pumps, relays, valves, and tanks in addition to pseudo objects such as pressures and admittances. Each middle level class is an example of some top-level class previously defined and inherits properties from the top-level class. Again, for efficiency reasons, the mid-level of KATE's knowledge-base is represented in C++ header and source code files which are compiled into the corpus of KATE at compile time. However, modifications to the content of this level have no effect on the body of the KATE system, only the classes of components available for subsequent modeling. This level of the knowledge-base has a regular, predictable, organization and syntax which makes it easy to extend.

1.2.1.3 Low level system knowledge. The lowest level of KATE's knowledge-base is stored in what are referred to as "flatfiles". This is the information about the actual physical components in a system being modeled. Each object at this level is an instance of some mid-level class and inherits properties from that abstract class, which inherits knowledge from its parent class.

The flatfiles representing low-level knowledge are text files (ASCII files) with a well-defined keyword-based syntax. They are read by KATE at run-time in order to construct an internal representation of the physical system to be modeled.

1.2.1.4 Database files. The current practice of those building KATE knowledge bases is to work with a collection of what we will refer to as "database" or .db files. A single real-world system may be modeled using dozens or hundreds of database files. Under control of what we will refer to as a "project" or .kb file, collections of database files are compiled into a single "flatfile" representing a single KATE model. Database and project files are the files which the model builder directly constructs and edits using a text editor such as Emacs. They are discussed in more detail in Section III of this document.

II

THE FLOW SOLVER

2.1 PROBLEM DESCRIPTION

The first KATE enhancement developed this summer is known as the "flow solver". It adds to KATE the ability to model fluid flows in a network of pipes by specifying the connectivity, pipe admittances, external pressure values and static head pressures for the pipes composing the network. The internal pressures and flows in the pipes are calculated in such a way as to conserve flow at each interior node in the network while simultaneously meeting the boundary conditions imposed by the external pressures. Conservation of flow laws lead to a system of non-linear equations. This non-linearity makes the flow solver a challenging program to implement. The size of the network depends only upon the number of interior nodes in the network and can be of any size—however performance of the flow solver slows as the network grows.

Even though the flow solver code is expected to be used initially for modeling flow in the shuttle liquid oxygen (LOX) loading system, it applies to any flow system meeting the following fundamental requirements:

- o The fluid in the system is assumed to be incompressible.
- o The network is always full of liquid.
- o The interior unknown pressures to be solved for, the P_i , are pressures at the junction of exactly three pipe sections.
- o The fundamental flow law for a pipe with ends denoted k and l is

$$FLOW = A_{k,l} * \sqrt[D]{P_k - P_l}$$

where $A_{k,l}$ is the admittance of the pipe section from k to l , P_k and P_l are the pressures at the ends of the pipe and

$\sqrt[D]{X} = \text{sign}(X) * \sqrt{|X|}$. $\sqrt[D]{X}$ is herein referred to as the directed square root of X .

- o There is conservation of flow at every junction. That is to say that the flow into each junction must be equal to the flow out of that junction.
- o The admittance for every pipe is known in advance.
- o The pressure at every "external" pipe end is known in advance.

In Figure 2-1 we illustrate the general form of the systems our flow solver can solve. Even though the connection topology is very simple, many real-world piping systems can be represented in this form. In the figure, the P_i represent known pressures

whereas the $P_{?j}$ represent unknown pressures to be solved for by the flow solver. The $A_{i,j}$ represent known admittance values. In order to simplify our diagrams and the discussion we do not include references to static head pressures induced by height differences between pipe ends; however our computer programs incorporate head pressure data in a straightforward way. Although we refer primarily to solving for unknown pressures in this figure and in subsequent discussion, it should be obvious that solving for the flow in a pipe of known admittance is trivial (see equation above) once the two end pressures are known.

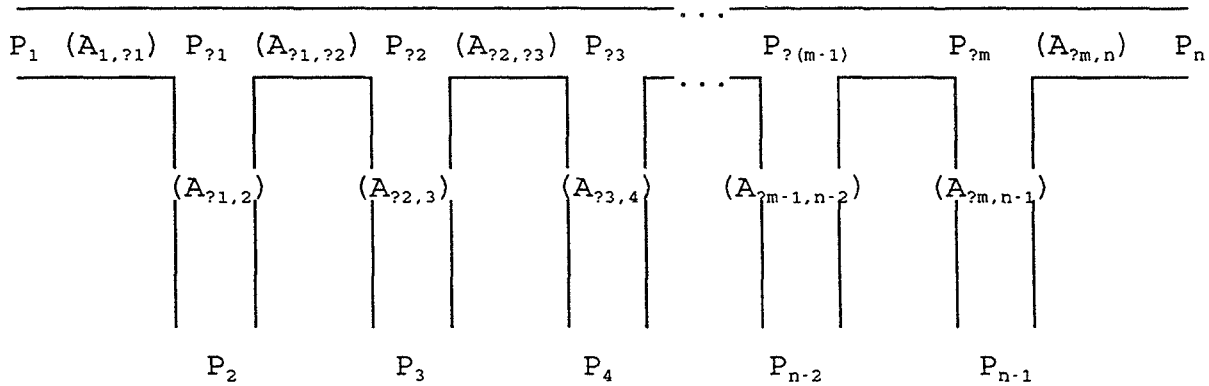


Figure 2-1. Abstract Flow Network

In Figure 2-2 we show an example network with seven known pressures and five unknown pressures. The pressure and admittance values shown were arbitrarily chosen but are illustrative of the kinds of values that might be encountered in a real pipe system.

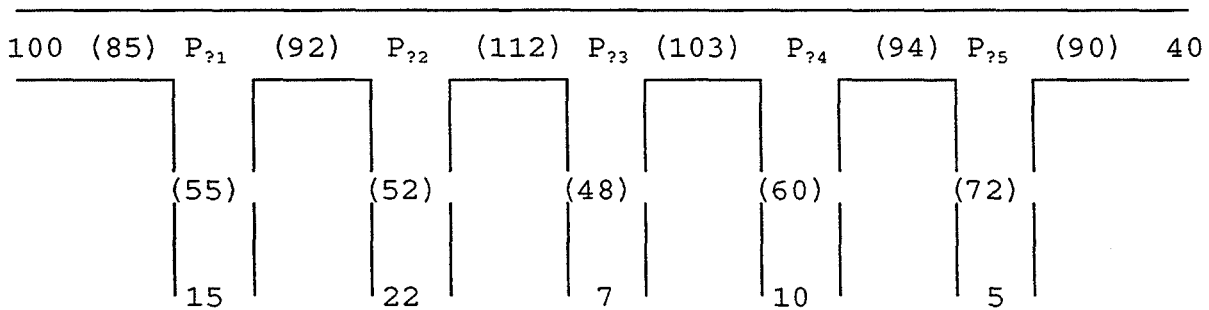


Figure 2-2. Example Flow Network

For a system with m unknown pressures out of a total of n pressures altogether, finding the m unknown pressures leads to solving a system of the form

$$\begin{aligned}
A_{1,1} * \sqrt[D]{P_1 - P_1} + A_{1,2} * \sqrt[D]{P_1 - P_2} + \dots + A_{1,n} * \sqrt[D]{P_1 - P_n} &= 0 \\
A_{2,1} * \sqrt[D]{P_2 - P_1} + A_{2,2} * \sqrt[D]{P_2 - P_2} + \dots + A_{2,n} * \sqrt[D]{P_2 - P_n} &= 0 \\
&\vdots \\
A_{m,1} * \sqrt[D]{P_m - P_1} + A_{m,2} * \sqrt[D]{P_m - P_2} + \dots + A_{m,n} * \sqrt[D]{P_m - P_n} &= 0
\end{aligned}$$

for unknown pressures P_1, P_2, \dots, P_m . In the type of pipe systems we are restricting ourselves to there will only be three non-zero entries in each row but in more general systems, with less restricted interconnections, more non-zero terms would occur. Nonetheless, the problem of determining the unknown pressures in a pipe network reduces to solving systems of non-linear equations of this form, systems which have no closed-form algebraic solution.

2.2 NEWTON'S METHOD

The most commonly used method to solve systems of non-linear equations is the multi-dimensional variant of the well-known Newton's method for finding roots of equations. We briefly review the familiar one-dimensional Newton's method and then describe the higher dimension variant. For an in-depth discussion of these methods, see [3].

Assume that we have a known function $f(x)$ for which we want to find x values for which $f(x) = 0$. Within some neighborhood of x , f can be expanded in a Taylor's series

$$f(x + \delta) = f(x) + f'(x) \delta + \frac{f''(x)}{2} \delta^2 + \dots$$

By neglecting the δ^2 and higher terms we obtain a simple equation for the corrections δX that move $f(x)$ closer to 0, namely the well known recurrence relation

$$x_{i+1} = x_i - \frac{f(x_i)}{f'(x_i)}$$

which is so widely used for iteratively finding roots of non-linear functions.

The multi-dimensional variant of Newton's Method is based on the same principle, the primary difference being the calculation of the derivative of the function. Assume we are given a system of n functional relations f_i in variables x_1, x_2, \dots, x_n , denoted $f_i(x_1, x_2, \dots, x_n) = 0$, for $i=1, 2, \dots, n$. Let X denote the vector of unknown x_i values. Then in some neighborhood of X , each f_i can be expanded in a Taylor's series

$$f_i(X + \delta X) = f_i(X) + \sum_{j=1}^N \frac{\partial f_i}{\partial x_j} \delta x_j + O(\delta X^2)$$

By neglecting the δX^2 terms and higher we obtain a set of linear equations for the corrections δX that move all the function values closer to 0 simultaneously, namely

$$\sum_{j=1}^n A_{ij} \delta x_j = B_i$$

where

$$A_{ij} \equiv \frac{\partial f_i}{\partial x_j}, \quad B_i \equiv -f_i$$

so the problem reduces to one of solving a linear system $A(\delta x) = B$ and updating X iteratively until convergence. The matrix A , known as the Jacobian, is a matrix of partial derivatives which plays a role analogous to that of $f'(x)$ in the one-dimensional case.

A number of observations are in order at this point. First of all, solving a system of non-linear equations by this method is an iterative process. At each step, a linear system must be solved in order to determine the changes to be made to the elements of the vector X . Fortunately, for the class of network flow problems we want to solve, it is possible to arrange the equations in such a way that the system to be solved at each step is tridiagonal. Solving a tridiagonal system of linear equations can be done very efficiently. The process only grows in time linearly with the number of unknowns. Secondly, Newton's method converges very rapidly and predictably as long as the initial X vector values are within a "reasonable" neighborhood of the solution vector. If the initial X vector does not meet this condition then convergence is unreliable.

At this point in our work we had some difficulty finding a reliable heuristic for obtaining good starting values to use for Newton's method. Fortunately a fast, reliable, method of getting starting values for the X vector was found and that is the subject of the next section.

2.3 THE SGOS FLOW SOLVER

The Shuttle Ground Operations Simulator (SGOS) is a software system used for training, testing and validation at KSC. Beginning in the summer of 1979 an effort was made by Dr. Roy Jones and Dr. Richard Ingle of UCF to implement a flow solver in the SGOS environment [4]. Mathematically, the technique they implemented was that of using a piecewise linear approximation to the directed square root function in order to iteratively find an approximate solution to the system of equations

introduced in section 2.1. In other words, each appearance of $\sqrt[D]{X}$ in the earlier system of equations is replaced by a linear function of the form $m \cdot X + b$ where the value of the slope m and the intercept b depend upon the actual value of X . We thus replace the original non-linear system by a linear system of the form

$$\begin{aligned} A_{1,1} * f(P_1 - P_1) + A_{1,2} * f(P_1 - P_2) + \dots + A_{1,n} * f(P_1 - P_n) &= 0 \\ A_{2,1} * f(P_2 - P_1) + A_{2,2} * f(P_2 - P_2) + \dots + A_{2,n} * f(P_2 - P_n) &= 0 \\ &\vdots \\ A_{m,1} * f(P_m - P_1) + A_{m,2} * f(P_m - P_2) + \dots + A_{m,n} * f(P_m - P_n) &= 0 \end{aligned}$$

where $f(x)$ is a linear function whose slope and intercept depend upon x . The algorithm is as follows:

- 1) Divide the X axis into a small number of intervals, for example, six intervals. Within each interval determine the appropriate slope and intercept value to approximate the directed square root within that interval.
- 2) Generate random or heuristically chosen starting values for the unknowns x_1, x_2, \dots, x_n .
- 3) Repeat the following for some fixed number of iterations or until all the x_i values stay within the same x -axis interval for two consecutive iterations:
 - 3a) Construct a linear system using the current x_i approximations as appropriate. The system will be of the form $A(\delta x) = B$ where the A and B matrices are derived from known coefficients in the system. The δx values represent changes to be applied to the unknown x_i 's.
 - 3b) Solve the linear system for the δx values using whatever technique is available.
 - 3c) Update the x_i vector values.
- 4) Test the current solution values for x_1, x_2, \dots, x_n by plugging these values into the system and determining the error. Each equation's left and right hand side values should be 0.
- 5) If the solution obtained is acceptable then terminate, otherwise go back to step 1 and subdivide the X axis into a greater number of intervals.

This algorithm rapidly obtains approximate solutions to the original system of non-linear equations. Acceptable solutions are usually obtained in a few dozen iterations using from six to ten sub-intervals of the X -axis.

For our purposes we implemented the above algorithm with several refinements and enhancements. For example, our starting X values are chosen to be within the known upper and lower bounds of the external pressures of the pipe network. We use a very efficient LU decomposition technique to solve the linear system as mentioned in step 3b. Our implementation also generates solutions with differing numbers of sub-intervals and selects the solution with the smallest total error in the system, an improvement over the SGOS version of the algorithm.

We use this algorithm in two ways. First of all, we use it to compute starting values to be utilized by the multi-dimensional Newton's method. Secondly, we retain the SGOS solution values in the unlikely event that Newton's method does not converge or will not work due to being given a singular matrix to solve. Such situations have not occurred in our testing of Newton's method to date but the availability of the SGOS solution values is, nonetheless, felt to be an important fall back.

2.4 IMPLEMENTATION OF THE FLOW SOLVER

The flow solver was implemented in approximately fifteen hundred lines of C++ code. The basic outline of the program is as follows:

- 1) Gather vectors containing the known pressures, known admittances, and optionally, static head pressures. These inputs can be obtained interactively from the keyboard or passed as parameters from the KATE system.
- 2) Generate starting values for the unknown pressures by averaging the external known pressures. The known external pressures give us useful upper and lower bounds for the unknown pressures.
- 3) Use our implementation of the piecewise linear approximation concept, as in SGOS, to get approximately correct starting values for the unknown pressures.
- 4) Use the multi-dimensional Newton's method approach to obtain a highly accurate solution for the unknown pressures.
- 5) In the unlikely event of a problem in step (4), return the approximate solutions obtained in step (3), otherwise return or report the best solution found.

Although there are many steps to this process, the program returns extremely good solutions, with errors less than 10^{-12} , very quickly, on the size of systems expected to be encountered in practice.

It is instructive to compare the results obtained from the SGOS algorithm with those obtained in step (4) above from Newton's method. In typical experiments, the SGOS values are plus or minus 1% of the value obtained by Newton's method. This

statement causes one to ask whether or not the additional work of using Newton's method is necessary. In Figure 2-3 we tabulate the results of applying both the SGOS algorithm and the complete Newton's method algorithm above to the example flow system from Figure 2-2. The values have been rounded to two decimal places for ease of reporting. Though randomly selected, these results are typical of those found repeatedly when comparing the two algorithms. Note that the absolute differences between the SGOS solutions and the Newton's method solutions are typically in the third or fourth significant digit. However, when the pressure values are used to calculate flows, these differences become greatly magnified. The non-linear nature of the flow network and the interdependent nature of the overall network result in very small errors in unknown pressures translating to sizable errors in flow. Given that these calculations of unknown pressures may be repeated hundreds or thousands of times by KATE during the LOX loading period, one begins to see that even small flow errors could cause the flow model to differ considerably from the actual flow by the end of the simulation period.

Unknown Pressure	SGOS Solution	SGOS Flow Error	Newton's Method Solution	Newton's Method Flow Error
1	41.58	-2.08	41.69	$<10^{-13}$
2	25.93	0.54	25.96	$<10^{-13}$
3	20.48	-0.19	20.52	$<10^{-13}$
4	19.80	3.25	19.84	$<10^{-13}$
5	20.92	-6.47	21.05	$<10^{-13}$
	Total Abs Error	12.53		$<10^{-12}$

Figure 2-3. Comparison of Results

The flow solver code has been interfaced with KATE and testing will soon be underway using recorded LOX loading data from previous launches.

2.5 FUTURE WORK

The flow solver program meets all the design requirements originally set out. The only major enhancement that may be needed is the ability to work with pipe networks with a more general topology than the "straight-line" systems now targeted. As stated previously, the current design assumes that each interior unknown pressure

is connected to exactly three other pressures and at least one of those is always a known exterior pressure. Solving more general classes of networks will require work primarily in the data interface and in implementing a technique for collapsing clusters of connected unknown pressures into a single unknown. The data interface may require some type of adjacency matrix or adjacency list to represent the interconnections of the network. Performance of the program will also degrade markedly because Newton's method will require solving general $N \times M$ matrices rather than the current tridiagonal systems.

III

THE EMACS KATE MODE

3.1 DESIGN SPECIFICATIONS

Constructing a KATE knowledge-base is a critically important and time-consuming task. Starting with the predefined top-level KATE classes and a predefined library of mid-level components, the model builder proceeds along the following lines:

- o Gather together schematics and engineering documents for the physical system to be modeled.
- o Study the target system to gain an understanding of its principal components and their interactions.
- o Determine whether or not the existing middle level component classes are adequate for the system to be modeled. If not, add new component classes. This requires at least some C++ code to be written.
- o Construct database (.db) files for the components, commands and measurements in the physical system. Real world systems may contain over one hundred such files, each containing dozens or hundreds of entries.
- o Specify the interconnections among the components in the database files.
- o Construct a project (.kb) file to be used to coordinate the processing of all the various files which go into making the end product, a "flatfile" which can be loaded into KATE.
- o Add pseudo objects to represent logical functions of groups of components in the system.
- o Run a "make" program to compile together all the various database files describing a model and create a single flatfile from them.

Until now there have been no software tools available to assist the KATE model builder. Most of the work is done using a text editor, frequently Emacs, and there is no way for the model builder to view the model under construction except as a collection of text files. We have designed and implemented a number of enhancements to the Emacs editor to make the job of the model builder easier.

The goals for this work were as follows:

- o Design and implement an improved editing environment for building KATE models. The more the system knows about the structure of knowledge bases, the better.

- o No editing abilities should be forsaken in this environment. That is, the environment must have all the features of a sophisticated editor such as cut and paste, configurable pull-down menus, mousing abilities, undo, backup, and rollback.
- o The editing environment should be portable across all the platforms that KATE runs on. That currently means Unix, Linux and Microsoft Windows.
- o The editing environment must be a stand-alone program. It should not be necessary to have KATE installed or operating on the machine where editing is being done.
- o The editor should be able to construct graphical diagrams showing the interconnections between various components in a complete or partially complete model.
- o The editing environment must be able to use the organizational information present in project (.kb) files to assist the model builder in organizing complete models and generating flatfiles for them.
- o The editing environment should not be built on top of a commercial editor product. When KATE is made available to the general public this editing environment should be freely distributable.

3.2 IMPLEMENTATION

After considering several possible alternatives, including developing an editing environment from scratch, and considering the limited time available to the investigator, it was decided that most of the design goals would best be met by implementing an editing environment as an extension to the GNU-Emacs editor. Emacs is arguably the world's most sophisticated and powerful text-editing environment. It is implemented primarily in Emacs-LISP, a subset of Common LISP and is, in fact, as much a programming environment as a text editor. Recent versions of Emacs support menus, mouse operations, practically unlimited undo capabilities and can even take advantage of some of the features of the X-Windows system. Emacs runs on practically all Unix platforms and is now available for DOS and Microsoft Windows. And it is distributed at no cost to the end user.

In the Emacs terminology we elected to implement an Emacs "major-mode". We have programmed Emacs to automatically recognize when database (.db), project (.kb), or flatfile (.flatfile) files are loaded and make the transition into what we call "kate-mode". One of the primary features of this mode is that tables called tag tables and tables of input connections are automatically constructed as the database files and flatfiles are loaded. These tables form the basis for what might be thought of as a cross-referencing feature of the Emacs environment, called tagging. No matter what file the model builder is editing, he/she can, with only a few keystrokes, quickly find

the file and section of code where an object is defined. This feature can be used not only for matching object names exactly but also for partial, substring, or apropos matches.

A second major feature of kate-mode is the ability to quickly generate simple hierarchical tree drawings representing the connections between an arbitrary object and its upstream and downstream neighbors. This feature works very rapidly because the requisite connection information is constructed once as the files in a project are loaded and then stored in a buffer for later access.

Another kate-mode feature is the ability to compile a collection of database files into a flatfile under control of a project file from within the editor. This process is currently done by a LISP program run on a Symbolics system, requiring several sequential steps to be carried out by the model builder on different platforms. Making this compilation process an integral part of the editor will in itself save a great deal of effort.

There are a number of other features of kate-mode which are expected to make it very useful. For example, the model builder need not be aware of any of the LISP programming being used to make his/her environment easier to use. Much of the operation of kate-mode occurs automatically and is totally invisible to the end user. The non-automatic features can be assigned to Control or Escape key sequences or can be utilized by typing in the name of a function which will then prompt the user for any necessary parameters. The system also attempts to save as much tag and connection information as it can between editor runs in order to save time when restarting or continuing an editing session.

3.3 FUTURE WORK

The current version of kate-mode is approximately fourteen hundred lines of Emacs-LISP code. Additional features can be added by anyone familiar with LISP programming. Incorporating new features can be done in a modular and straightforward way without a negative impact on existing features. We feel that the original design goals have, for the most part, been achieved. The display of the input connection relationships among objects is perhaps the weakest aspect of the current implementation. The information to create the diagrams has been extracted and can be accessed very quickly but it is just very difficult to display structural relationships using only character graphics. The information could be passed to a program running externally to Emacs which would display the connections graphically in a separate window. However, we have not had the time to pursue this idea. Ideally, the model builder should be able to manipulate the graphical representation, for example adding or modifying input connections, and have these actions reflected in the corresponding database files. This too could be done using Emacs as the "control

center" to modify the underlying text files with actions performed in another process supporting a graphical interface, but we have not yet looked into the details.

IV

REVIEW

We have presented the design criteria and described the implementations of the two software projects undertaken this summer. In the case of the flow solver and the editor enhancements we feel that we have made very useful enhancements to both the development and application environments for KATE. We believe both tools will prove to be of great utility to future KATE users.

REFERENCES

- [1] Steven L. Fulton and Charles O. Pepe, "An Introduction to Model-Based Reasoning", *AI Expert*, January 1990, pp. 48-55.
- [2] Charles O. Pepe, et. al., *KATE - A Project Overview and Software Description*, Boeing Aerospace Report, Boeing Aerospace Operations, Mail Stop FA-78, Kennedy Space Center, Florida.
- [3] Burden, R.L, Faires, J.D., and Reynolds, A.C., *Numerical Analysis*, Prindle, Weber, and Schmidt, Boston, MA, 1981.
- [4] Ingle, R.M., *Modeling Fluid Networks Using the SGOS Flow Solver*, Lockheed Space Operations Technical Report, 35SM-FS01-06, August, 1984.

1994 NASA/ASEE SUMMER FACULTY FELLOWSHIP PROGRAM

JOHN F. KENNEDY SPACE CENTER
UNIVERSITY OF CENTRAL FLORIDA

111769
351505
SIB-24
33978
P-12

OUTGASSING OF SOLID MATERIAL INTO VACUUM
THERMAL INSULATION SPACES

PREPARED BY:	Mr. Pao-lien Wang
ACADEMIC RANK:	Associate Professor
UNIVERSITY AND DEPARTMENT:	University of North Carolina at Charlotte Department of Engineering Technology
NASA/KSC	
DIVISION:	Mechanical Engineering
BRANCH:	Special Projects
NASA COLLEAGUE:	Frank Howard
DATE:	August 4, 1994
CONTRACT NUMBER:	University of Central Florida NASA-NGT-60002 Supplement: 17

TABLE OF CONTENTS

ACKNOWLEDGMENTS

ABSTRACT

SUMMARY

<u>Section</u>	<u>Title</u>
1.	INTRODUCTION
2.	OBJECTIVE AND TASKS OF PROJECT
2.1	Objective
3.	RESULTS AND DISCUSSIONS
3.1	Principle materials investigated
3.1.1	Insulation materials
3.1.2	Tank material
3.2	Outgassing rate of vacuum space materials collected from literature search
3.2.1	Outgassing characteristics of the vacuum materials
3.2.1.1	Aluminum foil
3.2.1.2	Aluminized mylar
3.2.1.3	Glass fiber paper
3.2.1.4	Stainless steel
3.3	Calculation example
3.3.1	Sample problem
3.3.2	Solution
4.	CONCLUSIONS
	REFERENCES

ACKNOWLEDGMENTS

I would like to thank NASA/ASEE Summer Faculty Fellowship Program, Dr. Gary Lin of Kennedy Space Center, and Dr. Loren Anderson of the University of Central Florida, for offering me with the opportunity to work on this challenging and rewarding project. Special thank should be extended to Dr. Gary Lin and my colleague Mr. Frank S. Howard for their help, guidance, and encouragement throughout the project. The friendliness and helpfulness of Ms. Kari Stiles is also very much appreciated.

ABSTRACT

Many cryogenic storage tanks use vacuum between inner and outer tank for thermal insulation. These cryogenic tanks also use a radiation shield barrier in the vacuum space to prevent radiation heat transfer. This shield is usually constructed by using multiple wraps of aluminized mylar and glass paper as inserts. For obtaining maximum thermal performance, a good vacuum level must be maintained with the insulation system. It has been found that over a period of time solid insulation materials will vaporize into the vacuum space and the vacuum will degrade. In order to determine the degradation of vacuum, the rate of outgassing of the insulation materials must be determined.

Outgassing rate of several insulation materials obtained from literature search were listed in tabular form.

SUMMARY

1. Outgassing rate of different insulation materials for cryogenic tanks are listed in Tabular form. (All data obtained through literature search)
2. Pressure increased in vacuum space of a tank during a five year period is provided.
3. An example outgassing problem is worked.

1. INTRODUCTION

Many cryogenic storage vessels use inner and outer tanks with a vacuum pumped between the tanks to prevent convection heat transfer from the wall of the outer tank to the wall of inner tank. Most cryogenic tanks also use a multilayer insulation in the vacuum space to protect from radiation heat transfer. Multilayer insulation is used extensively in applications where high thermal resistance is required, such as the insulation of cryogenic tanks. Multilayer insulation consists of many thermal radiation shields arranged in series, usually interleaved with a low conductance spacer material to reduce thermal conduction between shields. To achieve maximum thermal resistance a great many shields in series are required. Many of the shields are made by vacuum depositing of aluminum on one or both sides of mylar substrates with nominal thickness in the range 0.25 - 2.0 mils. A spacer material is used between the reflective aluminum mylar shields, commonly made of thin glass fiber. Because of the many layers required, the total surface area can be extremely high, making the multilayer insulation a significant outgas source. Multilayer insulation outgassing can affect overall system performance. It has been found that over a period of time multilayer materials and the tank material will vaporize into a vacuum space in the form of hydrogen. Newer tanks use palladium monoxide to convert the hydrogen to water which may be absorbed as a getter. Older tanks do not have a method of removing the out gassed hydrogen and the vacuum degrade with time. In order to estimate the vacuum level on old tanks without vacuum gages, outgassing rate of the insulation materials and the tank material must be determined.

2. OBJECTIVE AND TASKS OF PROJECT

2.1 Objective

The objective of this task was to make literature searches into vacuum technology and attempt to derive data and/or equations to determine or estimate the rate outgassing for insulation materials used in cryogenic tanks. This will enable determining the degradation of vacuum levels of tanks which never had palladium monoxide installed.

3. RESULTS AND DISCUSSIONS

3.1 Principle materials investigated

3.1.1 Insulation materials

- a. Aluminum foil or aluminized mylar
- b. Glass fiber paper

3.1.2 Tank material

- a. Stainless steel (Such as series 304)

3.2 Outgassing rate of vacuum space materials collected from literature search

The literature search include a view of 1476 technical documents. Useful data was found in only seven documents listed as references.

Outgassing rate of different materials, their sample preparations, test conditions, references, and remarks are listed in Table 1.

TABLE 1. OUTGASSING RATE OF VACUUM MATERIALS

<u>Ref. No.</u>	<u>Material</u>	<u>Outgassing Rate*</u>	<u>Sample, condition, and Remarks</u>
1	Plain double aluminized mylar as received	8.87 x 10 ⁻⁸ (0.13 - 19.0) 5.6 x 10 ⁻¹⁰ (10 - 19.9)	Mylar film, 0.00025-in. thick; with a vacuum deposited 500 A film of aluminum on each side; made by Norton Metallized Products Division. Tested at 297 K. (Outgassing rate range - from 5.00 x 10 ⁻⁷ to 4.00 x 10 ⁻¹²).
1	Crinkled double-aluminized mylar. As received	2.38 x 10 ⁻⁷ (0.1 - 13.17) 5.0 x 10 ⁻¹¹ (9.17 - 13.17)	Mylar film 0.00015-in. thick; with a vacuum deposited 500 A film of aluminum on each side; crinkled to reduce contact area and maintain separation; made by National Metallizing Division, Standard Packaging Corp. Tested at 297 K. (Outgassing range - from 1.25 x 10 ⁻⁶ to 2.00 x 10 ⁻¹¹).
1	Mylar, as received	1.24 x 10 ⁻⁷ (.017 - 25) 4.43 x 10 ⁻¹¹ (11.67 - 25)	Polyethylene terephthalate film, 0.00025-in. thick; density, 0.051 lb/in ³ ; made by E. I. du Pont de Nemours, Inc. Tested at 197 K. (Outgassing rate range - from 5.40 x 10 ⁻⁷ to 1.00 x 10 ⁻¹¹).
1	Superfloc	3.16 x 10 ⁻⁷ (0.15 - 13) 8.80 x 10 ⁻¹¹ (9.67 - 13)	Mylar film 0.00025-in. thick with a vacuum-deposited 500A film of aluminum on both sides; small tufts of Dacron epoxied to on side at about 0.5-in. spacing. (Outgassing rate range - from 1.60 x 10 ⁻⁶ to 4.00 x 10 ⁻¹²).
2	Double aluminized mylar	5.43 x 10 ⁻⁸ (0.1 - 1000) 4.27 x 10 ⁻¹² (60 - 1000)	Sample, 182.9 cm. x 3,048 cm., with a total surface area of 1.115 x 10 ⁶ cm. ² . Weight of sample is 455.97 gram. Tested at 296 K. (Outgassing rate range - from 9.00 x 10 ⁻⁷ to 5.50 x 10 ⁻¹³).
3	Aluminum foil	1.85 x 10 ⁻¹¹	Testing temperature - 900 F, Testing pressure - 10 ⁻¹⁰ Torr
3	Glass fiber	0	Testing temperature - 1000 F, Testing pressure - 10 ⁻³ Torr
4	Mylar	2.3 x 10 ⁻¹⁰	24 h at 95% Relative humidity
5	Crinkled single-aluminized mylar	2.43 x 10 ⁻⁹	Sample, 1-in. thick and 6-in. diameter disk; Purge gas, nitrogen; test chamber pressure 10 ⁻⁵ - 10 ⁻⁶ Torr

Table 1 (Continued)

<u>Ref. No.</u>	<u>Material</u>	<u>Outgassing Rate*</u>	<u>Sample, condition, and Remarks</u>
6	304 stainless steel	2.00×10^{-12}	Sample cleaned by glass-bead shot blasting; baked 30 h at 250 C; outgassing rate after 24 h at room temperature.
7	304 stainless steel	2.00×10^{-10}	Test chamber material; testing pressure, 1 atmosphere to 10^{-7} Torr

- * 1.) Unit of outgassing rate is in Torr-L./sec.cm.². Outgassing rate, q = Volume of gas at a known pressure and temperature that passes a plane in a known time/unit area,

$$q = pV/A$$

Where p = pressure (Torr), V = volume of gas flow/unit time (L./sec.) and A = unit area (cm.²)

- 2.) Numbers in parenthesis indicate data average between evacuation hours.

3.2.1 Outgassing characteristics of the vacuum materials

3.2.1.1 Aluminum foil

The work by R. L. Reid in 1969⁽³⁾ was the only document found on aluminum foil. Sample was tested at 900 F and 10^{-10} Torr. Reid measured an outgassing rate of 1.8×10^{-11} Torr-L./sec.cm.². This value will be chosen for outgassing rate of aluminum foil.

3.2.1.2 Aluminized mylar

Outgassing rate of 10^{-12} Torr-L./sec.cm.² for aluminized mylar was chosen from recent work by Todd⁽²⁾ (1993). It was an average between 60 and 1000 hour range.

3.2.1.3 Glass fiber paper

According to the work of Reid⁽³⁾, the outgassing rate of glass fiber paper was assigned to be zero.

3.2.1.4 Stainless steel

From the work of Young⁽⁶⁾, and Erikon⁽⁷⁾, the outgassing rates of stainless steel were documented as 10^{-10} Torr-L./sec.cm.² for unbaked sample, and 10^{-12} Torr-L./sec.cm.² after baked for 30 hours at 250 C. An average value of 10^{-11} Torr-L./sec.cm.² will be chosen for stainless steel.

The following outgassing rates were chosen for calculation of vacuum level of tank;

- 1.) Aluminum foil = approximately 10^{-11} Torr-L./sec.cm.².
- 2.) Aluminized mylar = approximately 10^{-12} Torr-L./sec.cm.².
- 3.) Glass fiber paper = approximately 10^{-11} Torr-L./sec.cm.².
- 4.) Stainless steel = approximately 10^{-11} Torr-L./sec.cm.².

Except stainless steel these averaged outgassing rates are very much agreed with Ludlow's(9) recommendation.

3.3 Calculation example

The following problem example is given to illustrate how the outgassing rates found in the literature searches can be used to estimate the vacuum pressure decrease in a cryogenic tank.

3.3.1 Sample problem

A cryogenic tank has an inner tank diameter of 2.5 feet and an outer tank diameter of 3 feet. The inner tank length is 20 feet. The tank uses 25 layers of multilayer insulation containing double aluminized mylar and glass fiber paper. The aluminized mylar is 0.00025 inches thick. The thickness of the glass fiber paper used as spacers is 0.0006 inches providing a total thickness of one layer of insulation material of 0.00085 inches. No getter is used in the vacuum space. Neglecting the thickness of the tank walls, estimate the outgassing after a five year period.

3.3.2 Solution

Outgassing of the 3-ft. tank is calculated as follows:

1. Surface area of outer tank = $\pi(3.0 \text{ ft.})(20 \text{ ft.}) = 188.5 \text{ ft.}^2$
2. Surface area of inner tank = $\pi(2.5 \text{ ft.})(20 \text{ ft.}) = 157 \text{ ft.}^2$
3. Vacuum space volume = $(\pi/4)(D_o^2 - D_i^2)(L.) = 0.7854[(3)^2 - (2.5)^2](20)$
 $= 43.2 \text{ ft.}^3$
4. Volume of insulation materials
 $= \pi(2.5 \text{ ft.})(0.00085 \text{ in.})(1 \text{ ft./12 in.})(25)(20 \text{ ft.})$
 $= 0.278 \text{ ft.}^3$
5. Net volume of vacuum space = $43.2 \text{ ft.}^3 - 0.278 \text{ ft.}^3 = 42.92 \text{ ft.}^3$
 $= 1,216 \text{ L.} \quad (1 \text{ cu ft.} = 28.33 \text{ L.})$

6. Outgassing from Mylar in the vacuum space

$$\begin{aligned}\text{Inner area of tank} &= 188.5 \text{ ft.}^2 = (188.5 \text{ ft.}^2)(929 \text{ cm.}^2/\text{ft.}^2) = 175,117 \text{ cm.}^2 \\ \text{Surface area of 25 layers of Mylar (2 sides)} &= 2 \times 25 \times 175,117 \text{ cm.}^2 \\ &= 8,755,825 \text{ cm.}^2\end{aligned}$$

Outgassing of mylar for five years period (10^{-12} Torr-L./sec.cm.² was chosen for aluminized mylar, see Table 1, Ref. 2)

$$\begin{aligned}&= 8,755,825 \text{ cm.}^2(10^{-12} \text{ Torr-L./sec.cm.}^2)(3.15 \times 10^7 \text{ sec./year})(5 \text{ year}) \\ &= 1,379 \text{ Torr-L.}\end{aligned}$$

7. Outgassing from stainless steel in the vacuum space

$$\begin{aligned}\text{Total surface area of stainless steel in the vacuum space} &= 188.5 \text{ ft.}^2 + 157 \text{ ft.}^2 \\ &= 345.5 \text{ ft.}^2 \\ &= 320,970 \text{ cm.}^2\end{aligned}$$

Outgassing of stainless steel for five years period

$$\begin{aligned}&= 320,970 \text{ cm.}^2(10^{-11} \text{ Torr-L./sec.cm.}^2)(3.15 \times 10^7 \text{ sec./year})(5 \text{ year}) \\ &= 508.8 \text{ Torr-L.}\end{aligned}$$

8. The total outgassing of the sample tank vacuum containing double aluminized mylar is

$$1,379.0 + 508.8 = 1,888 \text{ Torr-L.}$$

9. Pressure increase in the tank with a 1,219.4 L. vacuum volume during 5 years period

$$= 1,888 \text{ Torr-L.} / 1,219.4 \text{ L.} = 1.548 \text{ Torr or } 1,548 \text{ microns}$$

4. CONCLUSIONS

This study resulted in the following conclusions:

1. For a 3-ft. diameter and 20 ft. long tank, the pressure increase in the vacuum space for a time period of five years was calculated to be 1.548 Torr or 1,548 microns.
2. The calculated results were based on the estimated outgassing rates, so that the accuracy of actual pressure rise in the vacuum space can not be predicted.
3. Outgassing is controlled by almost 10 different parameters, it is quite obvious that a theoretical prediction of outgassing is very difficult and almost impossible. On this ground, to derive a mathematical equation to estimate the outgassing rate was not attempted during the summer project.
4. For more reliable results on outgassing rate, a laboratory test at KSC is highly recommended.

REFERENCES

1. Glassford, A. P. M., "Outgassing Behavior of Multilayer Insulation Materials," *Journal of Spacecraft*, Vol. 7, No. 12, 1964, pp.1464-1468.
2. Todd, Robert J., Pate, David, and Welch, Kimo M., "Outgassing Rate of Reemay Spunbonded Polyester and DuPont Double Aluminized Mylar," BNL-49345, August 1993.
3. Reid, R. L., DeWitt, W. D., and Gibbon, N. C., "Outgassing of Multifoil Insulation Materials in Sealed Vacuum Systems," *Journal of Vacuum Science and Technology*, Vol. 6, No. 1, 1969, pp. 217-221.
4. Elsey, R. J., "Outgassing of Vacuum Materials - II," *Vacuum*, Vol.25, No. 8, 1975, pp. 347-361.
5. Lin, J. T. "Analysis of Gas Flow through a Multilayer Insulation System," *AIAA Journal*, Vol. 11, No. 7, 1973, pp. 995-1000.
6. Young, R. J., "Outgassing Characteristics of Stainless Steel and Aluminum with Different Surface Treatments," *Journal of Vacuum Science and Technology*, Vol. 6, No. 3, 1968, pp. 398-400.
7. Erikson, E. D., Beat, T. G., Berger, D. D., and Frazier, B. A., "Vacuum Outgassing of Various Materials," UCRL-89299 Rev.- 1, *Vacuum Society & Technology*, December 20, 1983.
8. Perkins, W. G., "Permeation and Outgassing of Vacuum Materials," *Journal of Vacuum Science and Technology*, Vol. 10, No. 4, July/Aug. 1973, pp. 543-556.
9. Ludtke, Paul R., "A Study of the Vacuum Insulated Transfer Lines at Kennedy Space Center," *National Bureau of Standard Report 10705*, September 22, 1971.
10. Glassford, A. P. M. and Liu, C. K., "Outgassing Rates of Multilayer Insulation," NASA-N79-25051, 1978.
11. Zwaal, A., "Outgassing Measurements on Materials in Vacuum Using a Vacuum Balance and Quartz Crystal Balances," NASA-N79-25053, 1978.

1994 NASA/ASEE SUMMER FACULTY FELLOWSHIP PROGRAM

111770
5/9-32

JOHN F. KENNEDY SPACE CENTER
UNIVERSITY OF CENTRAL FLORIDA

33979
24
1-22
35/500

FEASIBILITY STUDY OF TRANSMISSION OF OTV CAMERA CONTROL
INFORMATION IN THE VIDEO VERTICAL BLANKING INTERVAL

PREPARED BY:	Mr. Preston A. White III
ACADEMIC RANK:	Professor
UNIVERSITY AND DEPARTMENT:	Southern College of Technology Electrical and Computer Engineering Technology
NASA/KSC	
DIVISION:	Communications
BRANCH:	
NASA COLLEAGUE:	Larry Hand
DATE:	August 30, 1994
CONTRACT NUMBER:	University of Central Florida NASA-NGT-60002 Supplement: 17

ACKNOWLEDGMENTS

Like most engineering efforts, the studies reported herein were the result of a team effort and the contributions of the rest of the team need to be acknowledged. The author is especially grateful to his NASA colleague, Larry Hand, for providing the author with the opportunity to make this small contribution to the ongoing operations at KSC. And thanks to the other NASA contributors: Po T. Huang, for your clear explanations of how this work fits into the big picture and for the use of your personal library, John Kassak, for helping this novice understand the OTV system, Robert Stute, for the use of your computer and Amy Farland for your help with paper work and scheduling.

All of these studies were performed in KSC's Fiberoptic and Communications Laboratory, a admirable facility staffed with first-rate contract personnel without whom this research would not have been possible. Special thanks go to F. Houston Galloway for his patience and support, to David Wedekind for obtaining the test items and for his LabVIEW expertise and to Robert Swindle for his help with the test equipment.

Finally, the able administration of this NASA/ASEE Summer Fellowship Program ensured that this summer's experience would be rewarding and memorable for all involved. Kari Stiles, Dr. Loren Anderson and Dr. Ramon Hosler from the University of Central Florida and NASA's Warren Camp and Maria Smith managed a wonderful program.

Thank you.

Please allow the author to add a personal note to Dr. Anderson: Loren, you'll be missed, have a great retirement.

ABSTRACT

The Operational Television system at Kennedy Space Center operates hundreds of video cameras, many remotely controllable, in support of the operations at the center. This study was undertaken to determine if commercial NABTS teletext transmission in the vertical blanking interval of the genlock signals distributed to the cameras could be used to send remote control commands to the cameras and the associated pan and tilt platforms. Wavelength division multiplexed fiberoptic links are being installed in the OTV system to obtain RS-250 short-haul quality. It was demonstrated that the NABTS transmission could be sent over the fiberoptic cable plant without excessive video quality degradation and that video cameras could be controlled using NABTS transmissions over multimode fiberoptic paths as long as 18.2 km.

SUMMARY

The Operational Television network at Kennedy Space Center is tasked with supporting all of the operations at the center. There are approximately 150 OTV cameras at pads 39A and 39B. These cameras and their associated pan and tilt platforms are remotely controllable from the OTV control room which is located 8-km distant in the Launch Control Center. The OTV network is currently being upgraded to wideband multimode fiberoptic video transmission. It is desirable to upgrade the camera and pan and tilt control loops as well. Previous work has shown that electrical multiplexing of the control data and the camera video had some unattractive characteristics.

This study was undertaken to explore the feasibility of using commercial teletext equipment to insert the camera control commands and camera environment telemetry in the vertical blanking interval (VBI) of the OTV video signals. It was determined that the North American Basic Teletext System standard (NABTS) was the most appropriate standard for this application. A data encoder and a decoder that conform to NABTS were obtained for these studies. These devices possess RS-232 ports to interface with the source and user of the teletext data.

It was found that the encoder and decoder could be used to send data from one personal computer to another, both through coaxial cable and over OTV wideband fiberoptic links.

An Ikegami color camera and associated remote control unit were obtained for camera-control over VBI tests. After some problems, unique to the devices under test were found and rectified, it was shown that the video camera could be controlled using data transported by VBI-teletext equipment over coaxial cable or through OTV wideband fiberoptic links.

TABLE OF CONTENTS

I	INTRODUCTION	1-1
1.1	Operational Television at KSC	1-1
1.2	OTV Upgrade	1-1
1.3	Previous Trials With Multiplexed Video and Data	1-1
1.3.1	Data On Aural Subcarriers	1-1
II	VERTICAL BLANKING INTERVAL	2-1
2.1	Structure of the VBI	2-1
2.2	Data in the VBI	2-1
III	NORTH AMERICAN BASIC TELETEXT SYSTEM	3-1
3.1	NABTS	3-1
3.2	NABTS Data Transmission	3-1
3.2.1	NABTS Data Line	3-2
3.2.2	NABTS Data Packet	3-3
3.2.3	Higher Level Protocols	3-3
3.2.4	Forward Error Control	3-3
IV	VBI TRANSMISSION TESTS	4-1
4.1	NABTS Data Transmission Equipment	4-1
4.2	NABTS Data Transmission Tests	4-2
4.2.1	Data Transport	4-2
4.2.2	Video Impairment Test	4-3
4.2.3	Fiberoptic VBI Data Transmission Test	4-4
4.3	Camera Command Transmission Tests	4-5
4.3.1	Camera Control Via NABTS	4-5
4.3.2	Camera Control Across A Fiberoptic Link	4-6
4.3.3	Camera Control And Video Transmission Using WDM	4-7
V	CONCLUSION	5-1
5.1	Summary of Results	5-1
5.2	Concluding Comments	5-1
APPENDIX A STRUCTURE OF THE VERTICAL BLANKING INTERVAL		A-1

LIST OF FIGURES

Figure 2-1	Closed Caption Data.....	2-1
Figure 3-1	NABTS Timing and Amplitudes ^[1]	3-2
Figure 3-2	NABTS Data Line Structure ^[1]	3-2
Figure 3-3	Actual NABTS Transmission	3-3
Figure 3-4	Hamming Code for NABTS Prefix ^[1]	3-4
Figure 4-1	Ultech Universal Data Encoder.....	4-1
Figure 4-2	Norpak VBI Receiver	4-2
Figure 4-3	VBI Data Transmission Tests	4-3
Figure 4-4	Fiberoptic VBI Data Transmission Test	4-4
Figure 4-5	Camera Control via NABTS	4-6
Figure 4-6	Camera Control Across a Fiberoptic Link	4-6
Figure 4-7	Camera Control and Video Transmission Using WDM	4-7
Figure A	Structure of the Vertical Blanking Interval ^[1]	A-1

LIST OF TABLES

Table 2-1	Comparison of Some VBI Data Transmission Standards.....	2-2
Table 3-1	Correspondance Between OSI and NABTS	3-1
Table 4-1	Video Performance of the UDE400 Encoder.....	4-4
Table 4-2	Video Performance of the UDE400 Encoder and Wideband Fiberoptic Transmission System	4-5

[1] ANSI/EIA. *Recommended Practice for Teletext: North American Basic Teletext Specification (NABTS)*. EIA-Standard 516. May 1988

ABBREVIATIONS AND ACRONYMS LIST

ANSI/EIA	American National Standards Institute Electronic Industries Association
ASCII	American Standard Code for Information Interchange
BS	Byte Synchronization sequence, the third byte in NABTS synchronization sequence
CATV	Community Antenna Television
CCTV	Closed Circuit Television
CDSC	Communications Distribution and Switching Center building
CS	Clock Synchronization sequence of two bytes which begins a NABTS data line
CSA	Canadian Standards Association
DTR	Data Terminal Ready line in RS232
EDL	Engineering Development Laboratory building
FEC	Forward Error Control (or Correction)
HC240	model number for an Ikegami color video camera
IRE	units used to measure video signal amplitudes
I/O	input/output
LAN	Local Area Network
LCC	Launch Control Center building
MAC	Multiplexed Analog Components, a type of video signal
NABTS	North American Basic Teletext Specification (ANSI/EIA 516)
NAPLPS	North American Videotext/Teletext Presentation Level Protocol Syntax
NTSC	National Television Systems Committee, a television standard used in N. America and Japan
OTV	Operational Television at KSC
OSI	Open Systems Interconnect, the standard reference model for data communications
P1, P2, P3	Prefix bytes 1, 2 and 3 in the NABTS data packet, specify the data channel number
PAL	Phase Alternating Line, a television standard used in Europe
PC	Personal Computer
PDC	Programme Delivery Control, a UK teletext-like service for controlling VCRs
PROM	Programmable Read-Only Memory
PS	Packet Structure byte, the last byte in the NABTS data line prefix
PTCR	Pad Terminal Connection Room
P/T	Pan and Tilt
RCU240	model number for the remote control unit for the Ikegami HC240 camera
SECAM	Sequential Avec Memoire, a television standard used in France
SID	Station Identification Code sometimes transmitted in the USA on line 20
SS	Synchronization Sequence which begins a NABTS data line
TM10-9	model number for an Ikegami video monitor
TSG100	model number for a Tektronix NTSC video generator
TTX645	model number for a Norpak NABTS decoder
UDE400	model number for an Ultech NABTS encoder
VBI	Vertical Blanking Interval, the first 21 lines of an NTSC video field
VABR	Vehicle Assembly Building Repeater building
VIRS	Vertical Interval Reference Signal
VITS	Vertical Interval Test Signal
VM700A	model number for a Tektronix Video Parameter Measuring Set
VPS	Video Program System, a teletext-like service used in Germany to control VCRs
WDM	Wavelength Division Multiplexer
WST	World System Teletext
5000RX ,TX	model number for the receiver , transmitter modules used in the OTV wideband fiberoptic transmission system

I

INTRODUCTION

1.1 OPERATIONAL TELEVISION AT KSC

The operational television (OTV) system is used to support the operations at Kennedy Space Center (KSC). The OTV network consists of more than two hundred cameras which feed images to the control room in the Launch Control Center (LCC). Within the control room, a 196x512 video switcher allows easy reconfiguration of the network to meet the changing needs of the users. A genlock signal is distributed to the OTV cameras to synchronize the video streams and the switch. Many of the cameras, particularly the 150 cameras at pads 39A and 39B, are remotely controllable from the control room where operators can adjust camera settings such as exposure, zoom and focus and can move the camera's pan and tilt (P/T) platform.

At present the camera and P/T control data is sent from the control room to the pads using modems and dated telephone technology. The control data is converted to discrete electrical signals in room 204 in the pad base and are fed to the cameras on separate wire pairs. Coaxial cables carry the genlock to the camera and the video from the camera. The numerous video streams originating at the pad cameras are multiplexed and carried to the control room using conventional coaxial-cable CATV frequency-division-multiplexing broadband equipment located in the PTCR. The distance from the pads to the control room (8-km maximum) necessitates that the broadband signals be amplified several times along the path.

1.2 OTV UPGRADE

KSC has begun an OTV upgrade that will improve the video quality available from the pad cameras and will reduce maintenance by simplifying the OTV network. Camera video will be migrated to multimode fiberoptic paths that will transport two video streams per fiber using 1300/1550-nm wavelength division multiplexing (WDM). Wideband (12-MHz) fiberoptic transmitter and receiver modules have been installed in pad room 204 and the LCC. The wide bandwidth of the optical fiber equipment can be used to transport more than the video; so it would be very desirable to be able to include the camera control data (and perhaps camera environment telemetry) along the existent fiberoptic paths.

1.3 PREVIOUS TRIALS WITH MULTIPLEXED VIDEO AND DATA

1.3.1 DATA ON AURAL SUBCARRIERS. Several trials, aimed at transmitting some combination of multiplexed video and data, preceded this work. In one case, audio carrier transmission modules from the same manufacturer that produces the OTV wideband fiberoptic transmitters and receivers were obtained. These devices are used to combine two audio channels with one video channel video for transmission. Laboratory adjustments to these audio modules placed the aural carrier frequencies above 9 MHz and a 8.5 MHz low pass filter was used to further isolate the video. Modems were used to insert data streams on the aural carriers. This trial successfully resulted in two full-duplex data channels operating at or above 2400 bit/s multiplexed with one bidirectional video channel. Further testing confirmed that the video still met short-haul specifications. Although technically successful, it was thought that this solution was not appropriate for field installation since it required too much equipment and exhibited unacceptable drift in the aural subcarrier frequencies.

Equipment from other vendors, designed to combine video and data for fiberoptic transport, was tested but found unacceptable usually due to the inability of the video to meet short-haul standards.

II

VERTICAL BLANKING INTERVAL

2.1 STRUCTURE OF THE VBI

The NTSC video standard used in North America has 525 horizontal scan lines divided equally into two fields. The first 21 lines in each field make up an area that does not carry any video information and is not shown on video receivers. Together, these lines are known as the vertical blanking interval (VBI). The first nine lines in the vertical blanking interval transmit special pulses which are used to synchronize the vertical scanning of the video receiver with the top of the transmitted image. Lines 10 through 21 of the vertical interval are unused for either vertical sync or for the video image and are therefore available to carry other information. Neither the USA nor Canada regulates the usage of the VBI. The structure of the VBI can be seen in the figure in Appendix A.

2.2 DATA IN THE VBI

Worldwide, several standards have been developed and are currently in use for transporting signals of various types in the VBI. These standards were developed to meet a wide range of needs of and market opportunities for TV originators, broadcasters, CATV and CCTV operators. Beginning in the late 1970s and expanding since then, many different types of information have been transmitted in the VBI.

Some of the first signals to have been inserted in the VBI are the vertical interval test signal and the vertical interval reference signal (VITS & VIRS). These are analog test signals, normally transmitted on lines 17, 18 and 19 in both fields, enable receiving equipment to assess transmission degradation.

A digital VBI signal that is now ubiquitous in the USA is *closed-captioning* (for the hearing impaired). In 1991 the FCC ordered that all TV receivers sold in the USA after July 1, 1993 must be capable of decoding and displaying closed-caption data. Closed-captioning transmits a NRZ signal, on line 21, field 1, of the VBI. To meet this limited need and to keep costs low, closed-captioning uses a low data rate, transmitting a synchronizing preamble and 2 bytes (7 data bits, 1 parity bit) of information per line. This gives a maximum data rate of ≈ 840 bit/s. Figure 2-1 shows an example of closed-caption data on line 21.

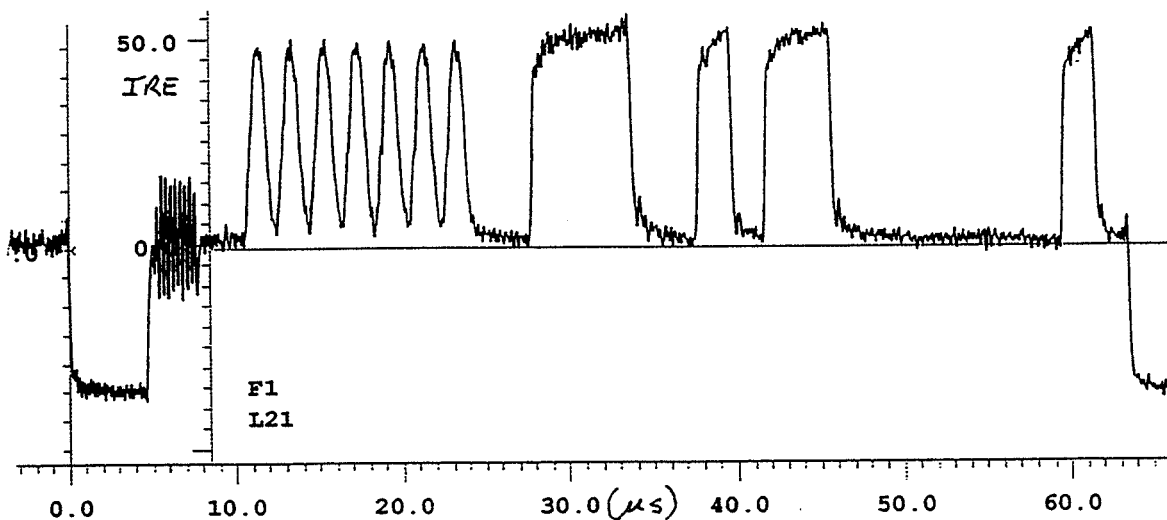


Figure 2-1 Closed Caption Data

Another example of a specialized digital VBI signal that is sometimes broadcast in the USA is the station identification code (SID). This is a 48-bit code that is transmitted on line 20, field 1.

Teletext is a general term used to refer to various digital data broadcasting methods developed over the past decade. Incompatible variations on the teletext theme have been standardized in Europe and in North America. Either variety is highly flexible, allowing the transmission of one or many data streams on video lines in the VBI and even extending up to full field teletext where data is transmitted in the video portion of all lines. Teletext in some form in the VBI has become widely used since it becomes part of the video signal, is carried wherever the video reaches and is transported transparently through all of the video equipment and media (although it is often not recorded on VCRs).

In 1988 ANSI/EIA and CSA (Canadian Standards Association) jointly published the *North American Basic Teletext Specification* (NABTS) which specifies the essential technical details for a very robust and flexible high-speed teletext system for use on NTSC signals. NABTS systems have become widely deployed throughout broadcast and CATV systems. It is this system that appears to be most adaptable to KSC's OTV use and will be detailed in the next section of this report.

In Europe teletext standards and systems have generally reached a higher level of development and deployment and been adapted to a wider range of applications than in the USA. *World System Teletext*, WST is the most flexible specification and is widely used to transmit text and graphics. WST can be carried on PAL, SECAM, NTSC and also can be included in MAC systems (either in the VBI or as packet data). In addition, teletext-like automatic VCR programming data is transmitted in Germany as *Video Program System* (VPS) and in the United Kingdom as *Programme Delivery Control* (PDC) codes.

Table 2-1 compares some of the North American and European teletext standards.

Table 2-1 Comparison of Some VBI Data Transmission Standards

Characteristic	Closed Caption	NABTS	WST	VPS/PDC
Data Rate (Mbit/s)	0.00084	5.7273	6.9375	2.5
Data Amplitude	0.5 V	0.7 V	0.46 V	0.5 V
Data Coding	NRZ	NRZ	NRZ	biphase
TV line(s)	21 field 1	VBI or full field	VBI or full field	16 field 1

III

NORTH AMERICAN BASIC TELETEXT SYSTEM

3.1 NABTS

For the application under investigation, NABTS appears to be the most applicable; therefore, this section will present some of the details of this specification. Published as EIA-516, this specification provides the technical description, transmission technique, coding language, and user interface for one-way teletext service applications in North America. As Table 3-1 shows, the first seven chapters of the standards document generally correspond to the seven layers of the open system interconnect (OSI) reference model for data communications.

Table 3-1 Correspondance Between OSI and NABTS

OSI LAYER NAME	CHAPTER	NABTS SPECIFIES
Physical	Data transmission	NTSC physical transmission parameters: timing, bit rate, waveforms, etc.
Data Link	Data Line	structure of 288-bit data line into 24-bit sync sequence, 264-bit data packet
Network	Data Packet	structure of 264-bit (33-byte) data packet into prefix, data block and suffix
Transport	Data Group	structure of data groups (long messages): a series of related data packets
Session	Teletext Record	structure of presentation or application data records
Presentation	Coding of Teletext Record	coding of presentation records (usually 7-bit ASCII)
Application	Application	organizes sets of records (usually into magazines and pages)

For this application, each camera-control message is thought to be short enough to fit in one data line, so that the parameters affecting data transmission of OTV camera-control information are found in the first three chapters of the standards document and will be detailed in the following sections.

3.2 NABTS DATA TRANSMISSION

Data may be transmitted in the video portion of any or all of lines 10 through 21 in the VBI of both fields; thus, the teletext data may use any of the VBI lines not already occupied by VITS, VIR, SID or closed-captioning. Therefore, lines 10 through 16 and 20 are most likely to be used in broadcast applications. In addition, all active lines of both fields of the 525-line NTSC signal may be used when full-field teletext transmission is desired. The transmission data rate is fixed at 5,727,272 bit/s (8/5 times the color sub-carrier frequency). The data are NRZ-coded with nominal amplitudes of 70 IRE for a 1 and 0 IRE for a 0. The timing and amplitudes of the of the data signal are shown in Figure 3-1.

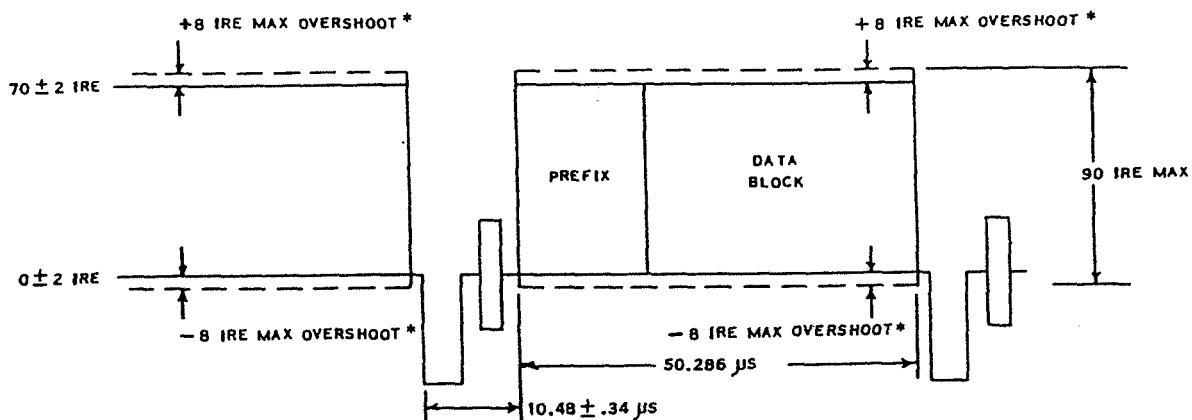


Figure 3-1 NABTS Timing and Amplitudes

3.2.1 NABTS DATA LINE. A teletext *data line* consists of a sequence of 288 bits (36 bytes) which is subdivided into four fields known as the 1) synchronization sequence, 2) prefix, 3) data block and 4) suffix (the suffix may be omitted in some applications). The data line structure is shown in Figure 3-2 and Figure 3-3 shows an example of actual an NABTS transmission.

The synchronization sequence (SS) field consists of a 2-byte clock sync (CS) and a 1-byte framing code (also called the byte-sync, BS). The SS essentially performs the same function as the preamble and start flags that are often used asynchronous LANs. The three remaining fields are known collectively as the *data packet*.

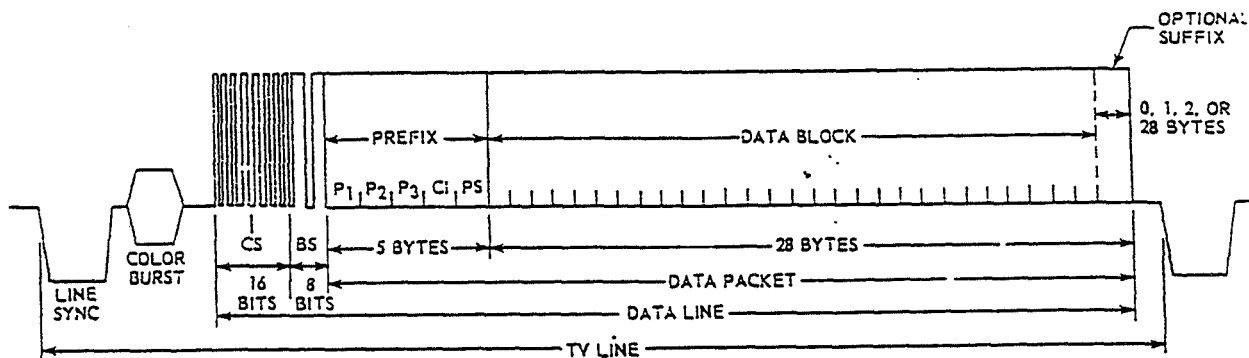


Figure 3-2 NABTS Data Line Structure

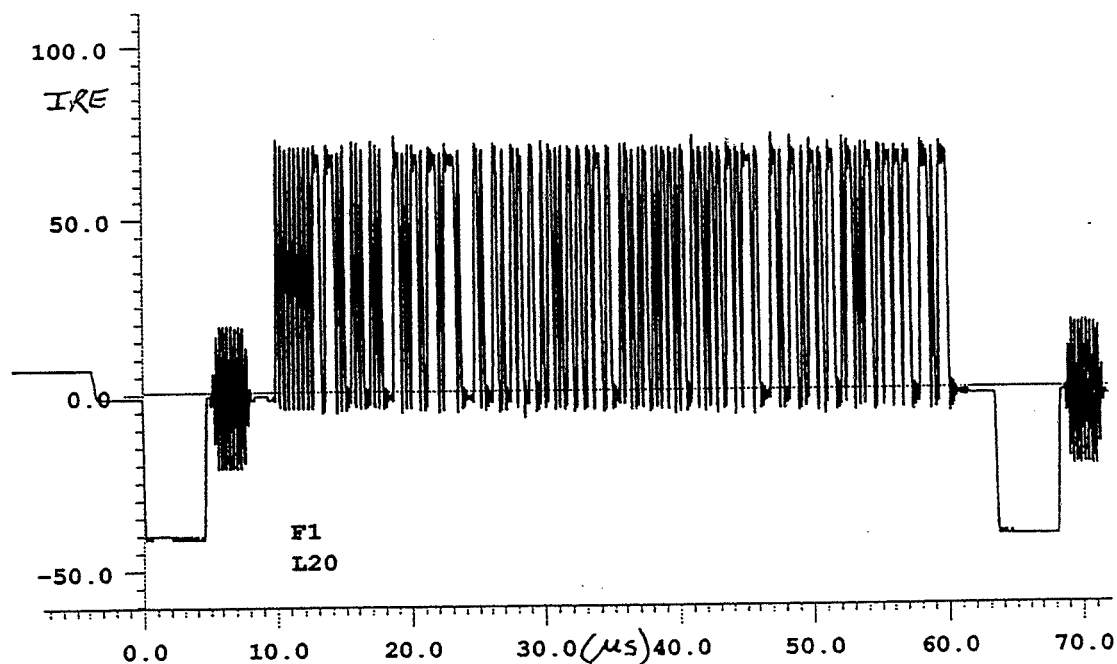


Figure 3-3 Actual NABTS Transmission

3.2.2 NABTS DATA PACKET. The first five bytes of the data packet are reserved for the *prefix*. Each prefix byte is Hamming coded, resulting in 4-bits (1 hex digit) of data and robust error correction capability as shown in Figure 3-4. The first three prefix digits (P1, P2 and P3) combine to form the *data channel* which is essentially similar to a LAN address. Therefore, NABTS supports 4096 distinct data channel addresses (000h - FFFh). The fourth prefix byte is the *continuity index* (CI) which is a modulo-16 sequence number used to detect lost packets in a data channel message stream. The final byte is the *packet structure* byte (PS) which consists of three flags denoting a) if the packet is the first, or *synchronizing*, packet of a multi-packet message (called a *data group*) or a standard packet within a data group, b) if the packet is full of data or not and c) the length of the suffix which can be 0, 1, 2 or 28 bytes.

The *data block* field of the data packet transports the information payload. Depending on the length of the suffix, the data block can carry 28, 27, 26 or 0 bytes per data line. All data-block bytes are transmitted with odd parity. For 26 bytes of payload the resulting data rate is 6240 bit/s/TV line. The payload can consist of upper-layer protocol headers, trailers and information. The suffix, when present, follows the data block and is always positioned at the end of the data line. The suffix is used for error protection of the information payload in the data block or, for a 28-byte suffix, a series of data blocks.

3.2.3 HIGHER LEVEL PROTOCOLS. Much more detail regarding the structure of data groups and the protocols for coding presentation layer records and application layer records are contained in chapters 4 through 7 of the specification document. A related standard document ANSI BSR X3.110 (1983) North American Videotext/Teletext Presentation Level Protocol Syntax (NAPLPS) is used to structure long messages or complex data bases. No further information on these topics is presented in this report since they are not thought to apply to the OTV camera control use addressed in this study.

3.2.4 FORWARD ERROR CONTROL. Since NABTS and other teletext systems are intended to transmit information in only one direction, forward error correction (FEC) is an essential capability since, unlike other

data networks, in ordinary teletext applications the destination cannot request retransmission of erroneous information.

As noted above, the basic NABTS specification provides robust error protection for the 5-byte data packet prefix by the use of Hamming codes. This scheme allows forward error correction of all single-bit errors and detection of multiple errors within a prefix byte. In this way, packets with uncorrectable errors in the critical information in the prefix can be recognized and discarded. However, the error protection afforded to the data block by the small (1 or 2 byte) suffix can provide only error detection. In commercial applications, teletext data robustness is often assured by multiple transmissions of the information streams and programming the receiver to respond only after a predetermined number of identical records have been received. Alternative, proprietary, forward-error-control mechanisms are offered by several NABTS equipment vendors and promise to realize virtually error-free transmission. If one-way NABTS transmissions are used in this OTV application, KSC may need to consider some FEC mechanism to ensure data transmission integrity. However, if two-way transmissions (up-stream camera control and down-stream camera-environment telemetry) are used, then it would be possible for the camera to acknowledge correct transmissions. Further work will need to be performed to assess the probability of NABTS data transmission errors in the field OTV systems

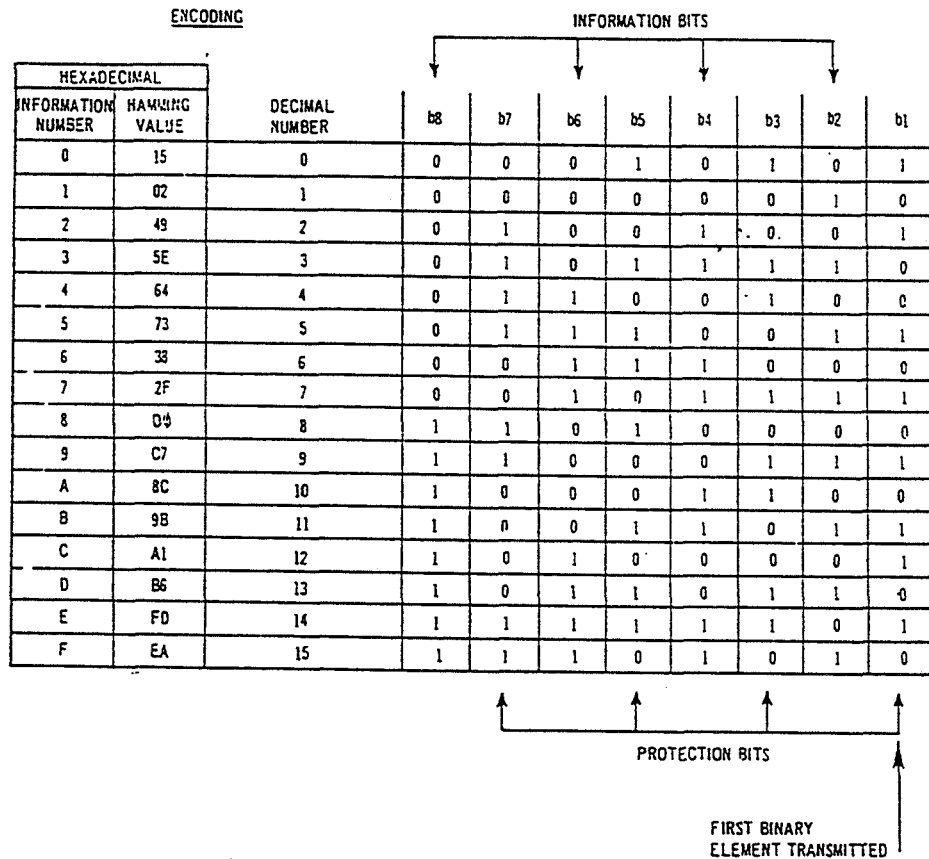


Figure 3-4 Hamming Code for NABTS Prefix

IV

VBI TRANSMISSION TESTS

4.1 NABTS DATA TRANSMISSION EQUIPMENT

A NABTS teletext encoder and a decoder were obtained for the purpose of proof-of-concept testing of the VBI transmission of camera-control signals. The encoder is the model UDE400 Universal VBI Data Encoder manufactured by Ultech. A sketch and block diagram of the UDE400 are provided in Figure 4-1

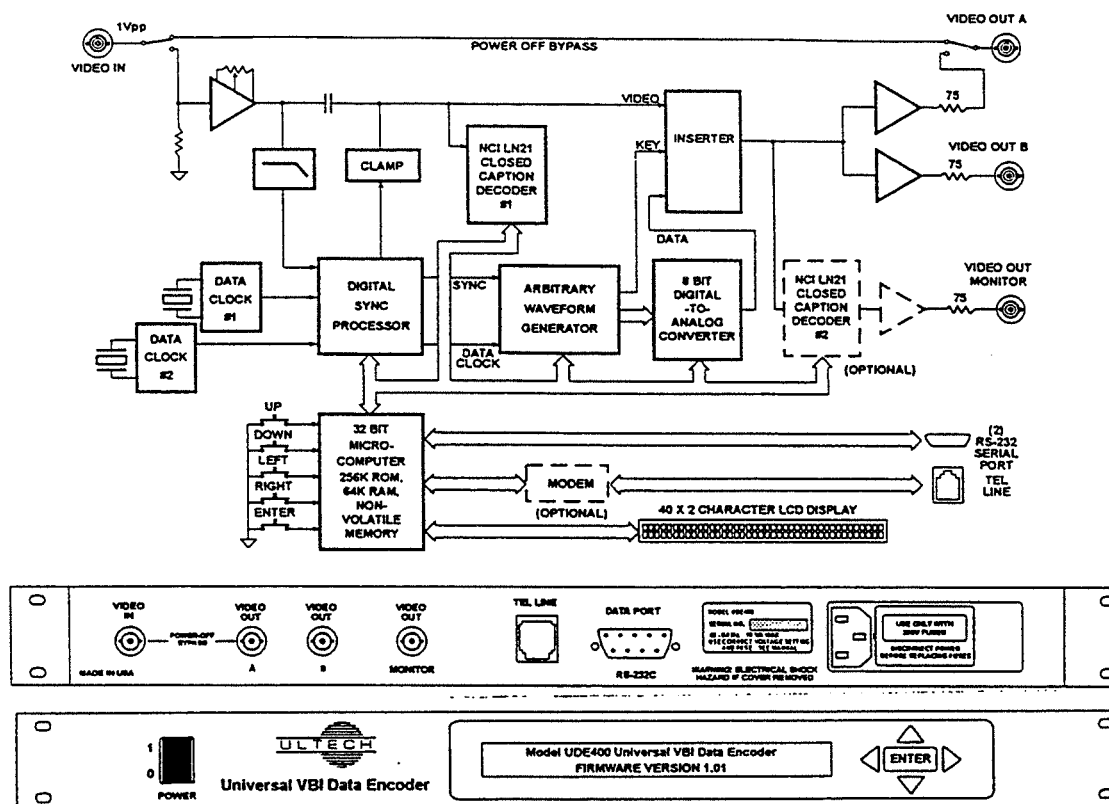


Figure 4-1 Ultech Universal Data Encoder

According to the manufacturer, the UDE400 data encoder is a highly adaptable device. It has the capability of encoding up to 16 unrelated data streams (closed caption, teletext or even arbitrary waveforms) on 16 video lines simultaneously and independently. The device is programmable either from the front panel or by a general purpose personal computer (PC) via its RS232 port, and stores its configuration data in non-volatile memory. Using its powerful internal microprocessor, the device can operate as a stand-alone inserter for one data stream. To utilize 2 to 16 channels, an external PC must be used to input the commands and the data streams. This

encoder can also be used to monitor closed caption data on line 21 and to transcode caption data into the teletext format.

The teletext decoder is the model TTX645 NABTS Standard VBI Broadcast Receiver manufactured by Norpak. Front and back views of the device are shown in Figure 4-2.

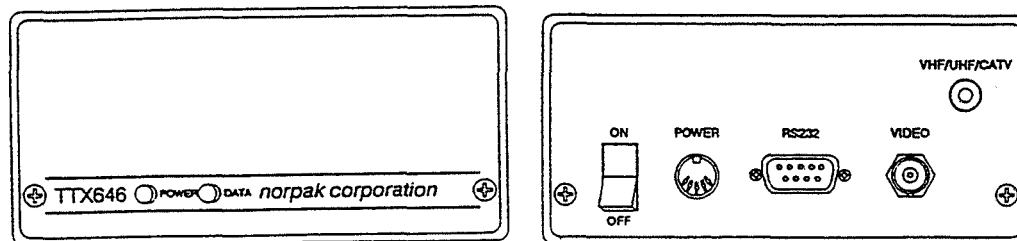


Figure 4-2 Norpak VBI Receiver

According to the manufacturer, the data input to the decoder can be either on baseband video or, by using the device's integral tuner, on an RF-modulated video (off-air or CATV, NTSC or PAL) channel. This receiver/decoder monitors either the VBI or the full field for NABTS data, decodes the data, (optionally) performs forward-error correction on the NABTS data and outputs the information from its RS232 port at bit rates from 50 to 38,400 bit/s. The device is fully programmable via the RS232 connector and stores its configuration information in non-volatile memory.

4.2 NABTS DATA TRANSMISSION TESTS

4.2.1 DATA TRANSPORT. The objective of the first test was to determine that the NABTS encoder and decoder would interoperate and could be used to transport data packets which conform to the NABTS standard. Included with the TTX645 decoder was `SETTTX.EXE`, a program that allowed the use of a PC to configure the decoder. This program did appear to function properly allowing the choice of RS232 port parameters, VBI or full-field data transmission, NABTS data channel number (and two more levels of addressing) and more. The receiver under test could be configured to decode data in one of three modes: 1) process *Alert Records* which are a specialized subset of NABTS complex multipacket records, 2) process NABTS data packets as described in section 3.2.2 of this report and 3) a non-standard *30-byte transparent* mode. All of the tests performed in this study utilized the 30-byte transparent mode which divides the data packet (see Figure 3-2) into a 3-byte Hamming-protected prefix which encodes the data channel number (P1, P2, and P3 bytes), and 30-bytes of transparent (not error-protected) payload. This mode was used due to the fact that the data encoder had been programmed by the manufacturer to utilize this mode exclusively.

Although the UDE400 NABTS encoder is said to be programmable by a PC, this could not be confirmed since neither command protocol information nor interface software were included with the device. The encoder was programmed by Ultech to encode data in the 30-byte transparent mode and to transmit 30-byte packets exclusively. Some configuration parameters could be set utilizing the front panel controls. Specifically, the RS232 interface could be set to operate at 9600, 19,200 or 38,400 bit/s, the VBI line utilized for data transmission could be assigned from line 10 to line 21 in both fields. Proper operation at each of these input stream bit-rates was confirmed.

The configuration for the NABTS data transport test is shown in Figure 4-3. The video source used was the Tektronix 1910 Digital Signal Generator. Two PC's were configured as the data source and the data receiver, interfacing with the encoder and decoder through their respective RS232 ports. The encoder and decoder were directly connected using 75- Ω coax. The program TTX_ENC.EXE, included with the Ultech encoder, produced a continuous stream ASCII characters (codes 30-255) for transmission and Procomm's PCPLUS.EXE was used to inspect the decoded data.

It was found that the encoder and decoder would function properly, allowing data transmission at 9600 baud and 19,200 baud (the only data rates accessible using TTX_ENC.EXE). It was confirmed that the UDE400 encoder, as delivered, could place the NABTS data on any one line from line 10 to line 21. No data errors were observed and no bit-error ratio test was performed since the encoder was originally programmed not to transmit any symbol below ASCII 30.

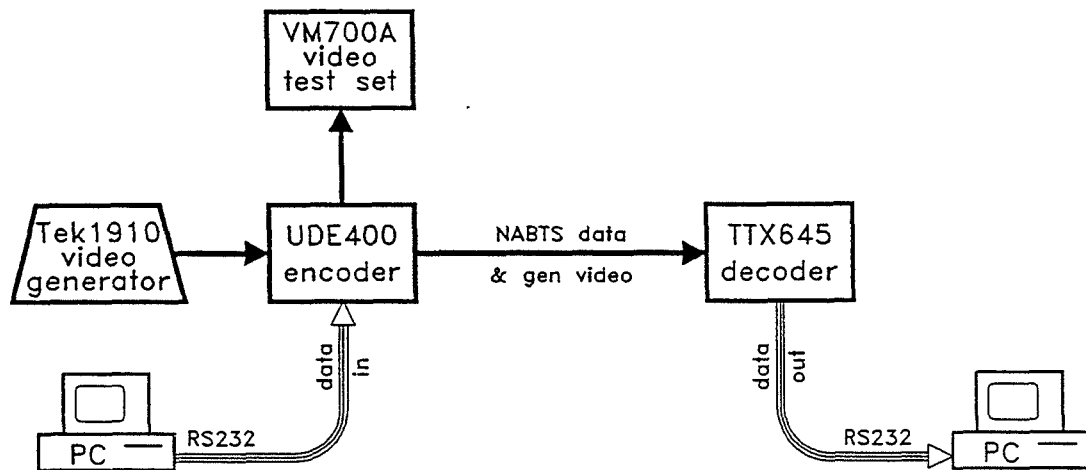


Figure 4-3 VBI Data Transmission Tests

4.2.2 VIDEO IMPAIRMENT TEST. The objective of this test was to measure the degree of video transmission impairment that was due to the insertion and use of the UDE400 VBI data encoder. The test setup was identical to the previous test (Figure 4-3). Video transmission quality was measured utilizing the Tektronix VM-700A Video Measurement Set.

As Table 4-1 summarizes, the insertion of the UDE400 produced no significant quality degradations in the video whether the unit was in bypass mode or was transmitting only the synchronization sequence or inserting data (data inputs at both 9600 and 19,200 baud were tested). Although no test condition violated any preset short-haul limit, there was a noticeable change in the VIRS Chroma Phase and the Relative Burst Phase.

Table 4-1 Video Performance of the UDE400 Encoder

Video Parameter	Encoder			
	in bypass state	sync sequence alone	9600 baud input	19200 baud input
S/N weighted	81.6 dB	81.2 dB	79.8 dB	82.1 dB
Differential Gain	0.71 %	0.79 %	0.79 %	0.77 %
Differential Phase	0.14°	0.14°	0.13°	0.13°
K-factor distortion	0.2 %	0.2 %	0.2 %	0.2 %
Line time distortion	0.1 %	0.2 %	0.2 %	0.2 %
VIRS chroma phase	-0.3°	-3.0°	-3.0°	-3.0°
Relative burst phase	0.10°	3.25°	3.20°	3.18°

4.2.3 FIBEROPTIC VBI DATA TRANSMISSION TEST. The objective for this test was to affirm that there were no unforeseen problems that would prevent the transmission of VBI data by the OTV wideband fiberoptic transmission equipment now being installed at KSC.

As Figure 4-4 shows, for this test a 1300-nm LED-based 5000TX and a 5000RX wideband fiberoptic video transmission system, similar to those being installed at pads 39A and 39B for OTV transmission, was inserted between the VBI data encoder and decoder. Ten meters of multimode fiberoptic patch cord with wavelength division multiplexer (WDM) at each end was used to interconnect the 5000TX and 5000RX.

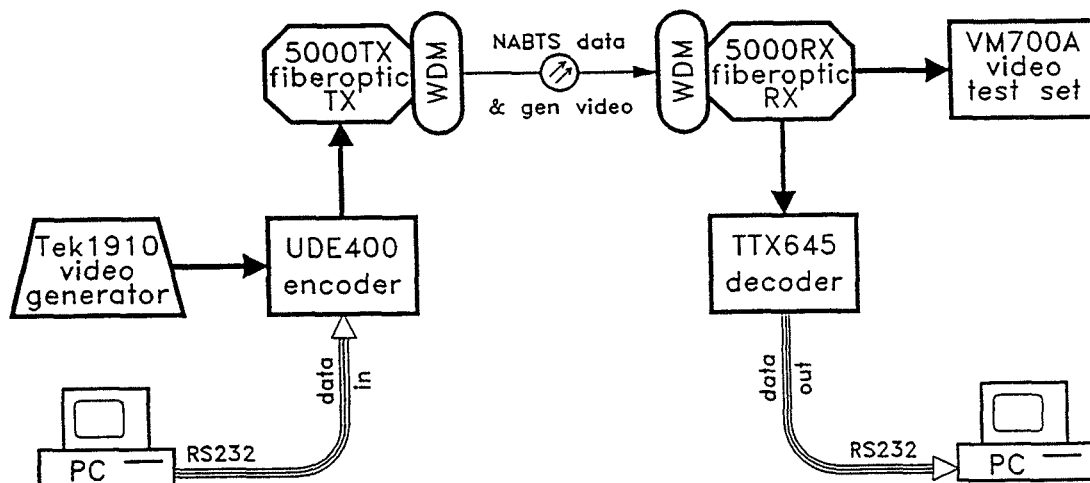


Figure 4-4 Fiberoptic VBI Data Transmission Test

The video performance parameters were measured after passing through the wideband fiberoptic transmission system. Table 4-2 shows the results for these tests with the encoder in one of two states: 1) bypassed and 2) transmitting data continuously using a 9600 baud input. The received data were inspected and no obvious errors were observed; however, no BER test was performed.

Table 4-2 Video Performance of the UDE400 Encoder and Wideband Fiberoptic Transmission System

Video Parameter	Encoder bypassed	Mode 9600 baud input
S/N weighted	69.5 dB	69.0 dB
Differential Gain	1.29 %	1.08 %
Differential Phase	0.18°	0.13°
K-factor distortion	0.9 %	0.9 %
Line time distortion	9.8 %	8.6 %
VIRS chroma phase	-0.2°	-2.9°
Relative burst phase	0.05°	3.02°

4.3 CAMERA COMMAND TRANSMISSION TESTS.

For these tests the objective was to verify that the NABTS encoder and decoder under study can be used to remotely control a video camera. The NABTS encoder and decoder previously tested were used, set for 9600 baud RS232 I/O and operating on line 20 of both fields. Tektronix TSG100 Television Signal Generator was utilized as the video source. The camera to be controlled was an Ikegami HC240 Compact Color Camera. This camera was connected to a matching Ikegami RCU240 Remote Control Unit. The RCU240 performs two functions important to these tests. First, the RCU240 has a standard RS232 port which is meant to accept control commands from a PC and second it translates the control commands to TTL levels which the camera requires. An Ikegami TM10-9 Color Monitor was used to observe the camera output.

A LabVIEW virtual instrument software module, IKI_SET.VI was written to control the shutter speed, the gain, the iris and to turn the camera's color bars on/off. Since 30-byte data packets were required for transmission by the NABTS encoder under test, the camera commands were concatenated and padded to 30-bytes.

All equipment for these tests was located in the Fiberoptics and Communication Laboratory (EDL room 198).

4.3.1 CAMERA CONTROL VIA NABTS. The objective of the first test was to verify that the Ikegami camera could be controlled by commands delivered by the NABTS equipment. The encoder and decoder were directly connected using 75-Ω coax as shown in Figure 4-5.

One handshaking problem between the TTX645 decoder and the RCU240 camera controller was noticed. The RCU240 toggles the DTR pin as data is received but the TTX645 enters a reset state when DTR goes low. In order for the TTX645 to function properly, the DTR line must be held high (<3V).

The Ikegami camera's control protocols required that ASCII 10 (line feed) and 13 (carriage return) terminate all commands. Since the original PROM in the Ultech encoder was programmed not to send any ASCII codes below 30, the encoder in its original state could not send camera commands. Therefore, a second PROM was obtained from the manufacturer that excluded only ASCII codes 1, 17 and 19 from encoding, and this PROM was used for the remaining tests.

After the handshake and PROM problems were rectified, it was observed that the camera's shutter, gain, iris and color bars could be controlled over the NABTS link.

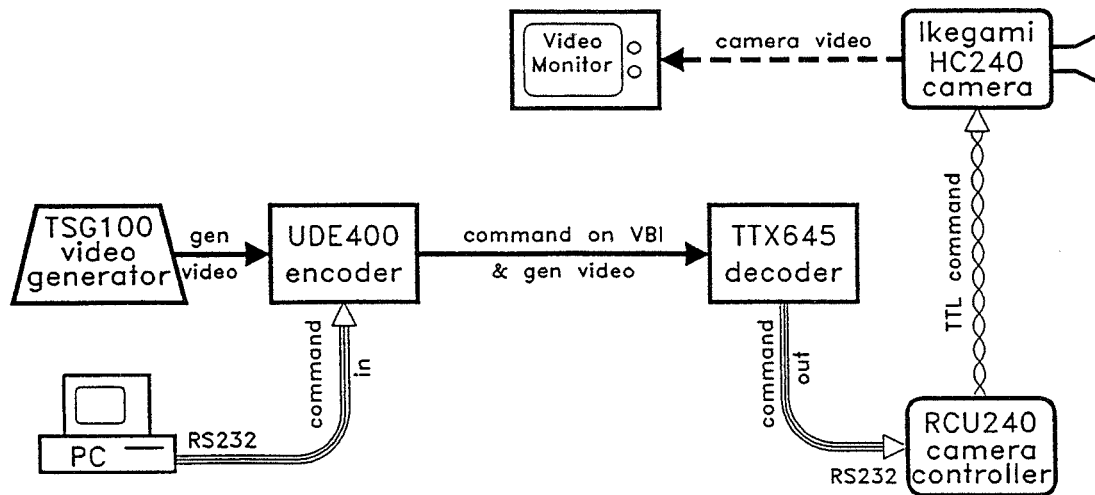


Figure 4-5 Camera Control via NABTS

4.3.2 CAMERA CONTROL ACROSS A FIBEROPTIC LINK. The objective for this test was to determine if the Ikegami camera could be controlled by commands transmitted by VBI data over an OTV wideband fiberoptic link. As Figure 4-6 shows, a 1300-nm LED-based 5000TX and a 5000RX were inserted between the NABTS encoder and decoder. The optical signals were transmitted through a 18.2-km multimode fiber test loop from the from the Fiberoptic Lab through the CDSC to the VABR and return.

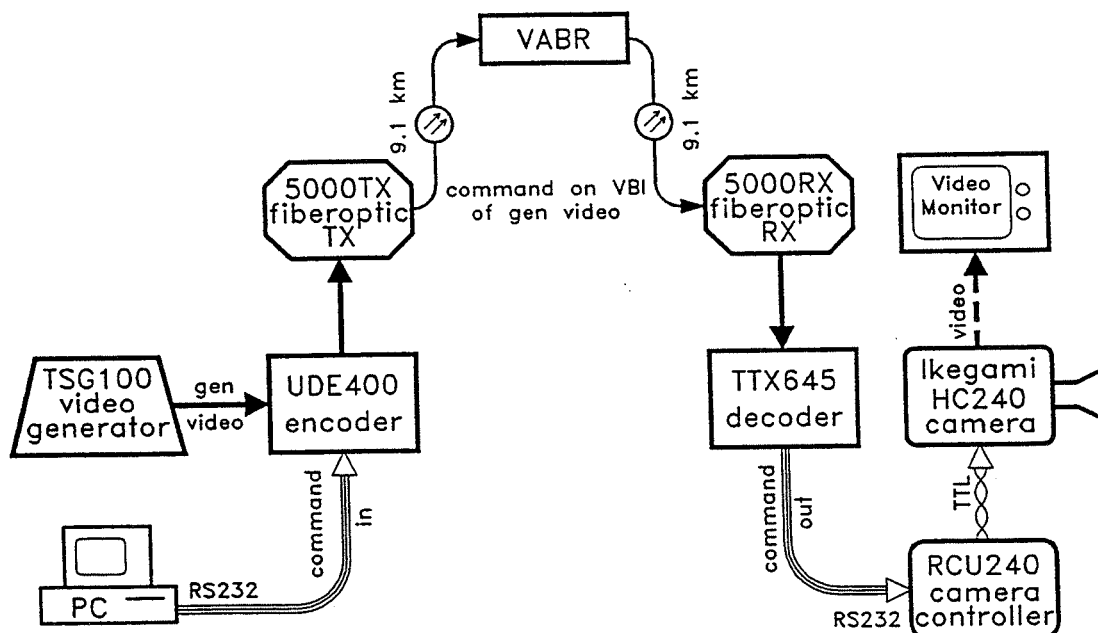


Figure 4-6 Camera Control Across a Fiberoptic Link

It was observed that the camera's shutter, gain, iris and colors bars could be remotely controlled using data transmitted more than 18 km using the OTV fiberoptic equipment.

4.3.3 CAMERA CONTROL AND VIDEO TRANSMISSION USING WDM. The final test in this series required the use of a bidirectional fiberoptic transmission path simulating the OTV WDM wideband fiberoptic links being phased-in at KSC. A 1550-nm LED 5000TX, a second 5000RX and two wavelength division multiplexers (WDMs) were added to allow bidirectional fiberoptic transmission. As Figure 4-7 shows, camera control commands on the VBI of generator video were transmitted using 1550-nm radiation in one direction and camera video was returned at 1300-nm over the same fiber path.

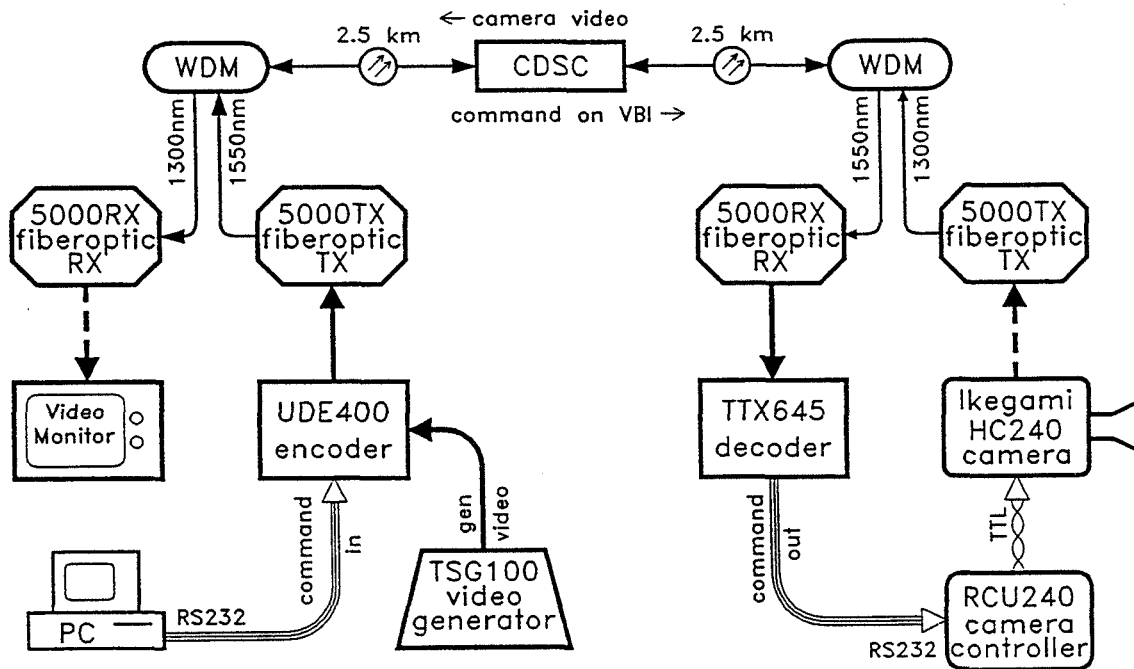


Figure 4-7 Camera Control and Video Transmission Using WDM

At first, an attempt was made to utilize the EDL↔VABR test loops. It was found that the additional loss due to the WDM and additional connectors did not allow that distance. However, it was possible to transmit camera control commands and camera video across the 5.0-km EDL↔CDSC test loops.

V

CONCLUSION

5.1 SUMMARY OF RESULTS

The NABTS encoder and decoder were able to transmit NABTS data with no observable errors at I/O rates of 9600 and 19200 baud. The encoder under test did not cause meaningful degradation of the video signals that were passed through for encoding. The OTV wideband fiberoptic transmission systems were capable of delivering the NABTS encoded video without difficulty, no unusual interactions were found between the OTV wideband system and the encoder or decoder.

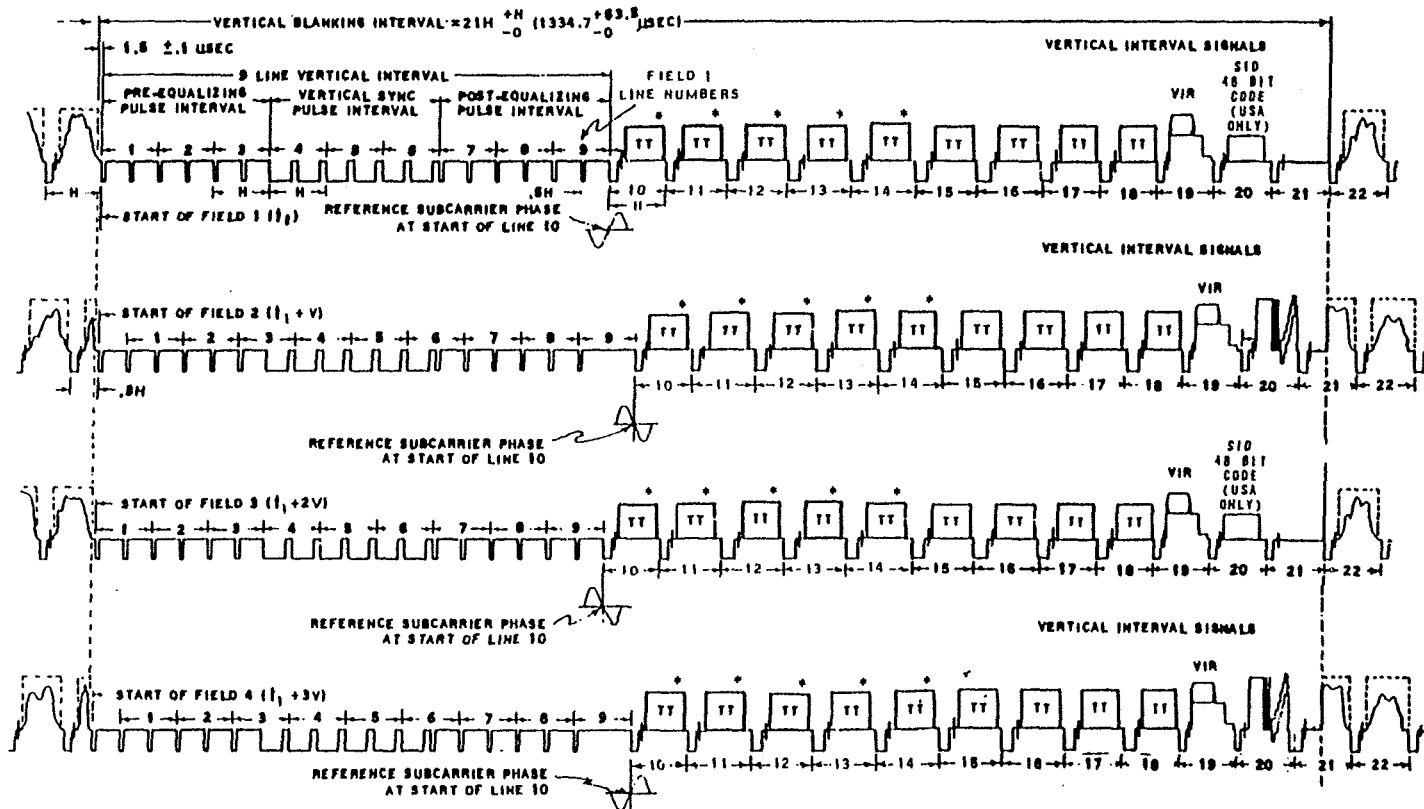
Finally, it was demonstrated that an Ikegami video camera could be controlled using commands delivered at 9600 baud in the VBI of a genlock-like signal and that the OTV WDM wideband fiberoptic equipment could be used to transport the camera control commands through the multimode fiber installed at KSC.

5.2 CONCLUDING COMMENTS

These studies demonstrated that camera control using commands transported in the VBI is feasible using commercially available equipment. It seems reasonable to assume that pan and tilt control could also be realized using this method. A logical next step would be to perform a bit-error ratio test on a system that simulates the LCC to pad environment.

If it remains a goal to return camera environment telemetry data in the VBI of the camera video then a redesign of the NABTS encoder is necessary. The commercial unit used in these tests has many more capabilities than are required for this use and, as currently packaged, is not suitable for deployment at the cameras. Also note that the encoder has a closed-caption (a different format from NABTS) receiver already on board. It seems reasonable to suppose that a NABTS encoder/decoder module with only the limited functions necessary OTV command and telemetry could be economically designed based upon the commercial Ultech encoder.

543/544



NOTE: LINE 20 MAY ALSO BE USED FOR TELETEXT ON BOTH FIELDS

TT = TELETEXT
* = POTENTIAL TELETEXT

APPENDIX A
STRUCTURE OF THE VERTICAL BLANKING INTERVAL

1994 NASA/ASEE SUMMER FACULTY FELLOWSHIP PROGRAM

111771
351507

JOHN F. KENNEDY SPACE CENTER
UNIVERSITY OF CENTRAL FLORIDA

520-61

33980

P. 23
26P

PERFORMANCE EVALUATION OF THE NASA/KSC CAD/CAE
AND OFFICE AUTOMATION LAN's

PREPARED BY:	Dr. George W. Zobrist
ACADEMIC RANK:	Professor
UNIVERSITY AND DEPARTMENT:	University of Missouri - Rolla Department of Computer Science
NASA/KSC	
DIVISION:	Data Systems Division
BRANCH:	CAD/CAE Systems
NASA COLLEAGUE:	Fernando Rico-Cusi
DATE:	August 5, 1994
CONTRACT NUMBER:	University of Central Florida NASA-NGT-60002 Supplement: 17



ACKNOWLEDGMENTS

This is to acknowledge the support of Mr. F. Rico-Cusi and Mr. Hank Perkins of DL-DSD-22 and Mr. Shawn Riley and Mr. Mark Sorger of EG&G. They were very helpful in the initial guidance of this research effort and in obtaining the necessary resources. Ms. Joy Maldonado and Mr. Ed Bertot of DL-DSS-22 are also thanked for additional support.

Additionally, I wish to acknowledge the administrative support of Dr. Loren Anderson and Ms. Kari Stiles, University of Central Florida, and Mr. Bill J. Martin, Program Director, NASA/KSC.

ABSTRACT

This studies objective is the performance evaluation of the existing CAD/CAE network at NASA/KSC. This evaluation also includes a similar study of the Office Automation network, since it is being planned to integrate this network into the CAD/CAE network. The Microsoft mail facility which is presently on the CAD/CAE network was monitored to determine its present usage.

This performance evaluation of the various networks will aid the NASA/KSC network managers in planning for the integration of future workload requirements into the CAD/CAE network and determining the effectiveness of the planned FDDI migration.

SUMMARY

The Computer Aided Design/Computer Aided Engineering (CAD/CAE) network at Kennedy Space Center is composed of segmented Local Area Networks (LAN). These segmented LAN's are to be interconnected through an intelligent switch. At present this LAN is a segmented Ethernet network. The design/engineering workstations are various Intergraph and Digital Equipment Corporation products, mainly. The host is a VAX cluster and there are several Intergraph servers, for plotting/printing/disk storage.

In a NASA/KSC report presented in 1988 the Ethernet peak utilization was under 3% and there were only fourteen Intergraph workstations on the Headquarters LAN. At present utilizations of 80% have been observed in short bursts and 10-25% averaged over longer time periods. There are presently 58 workstations on the NASA/KSC HQ LAN. The Microsoft mail facility and the planned integration of the Office Automation network should have minimal impact, since they have average usage of less than 3-4% at the present time.

An intelligent switch is presently being installed for high speed switching. This is used to bridge multiple LAN's, either FDDI, Ethernet, Token Ring or others. The intelligent switch offers many advantages over shared channel LAN's. The advantages include an increase in the bandwidth, latency (propagation delay) reduction, an increase in connectivity, and better traffic management.

This configuration should increase throughput due to the Ethernet LAN segmentation and the installation of FDDI controllers for the VAX cluster, various Intergraph servers, and several VAX workstations which have a high workload. One also has the option to privatize Ethernet workstations, if the load demands. It should also be noted that other developers have reported that until all workstations are upgraded to FDDI a sizable increase in throughput is usually not recognized, this is due not only to the 10 Mb/s output of the Ethernet controller, but applications are not taking advantage of the higher bandwidth available from FDDI.

Performance data is presented for the 1988 and 1994 CAD/CAE Ethernet configurations and the 1994 Office Automation network. The Microsoft mail facility was also monitored to determine it's impact on the CAD/CAE LAN.

TABLE OF CONTENTS

<u>Section</u>	<u>Title</u>
1.	INTRODUCTION
2.	NASA/KSC CAD/CAE NETWORK CONFIGURATION
3.	LOCAL AREA NETWORK TECHNOLOGY
4.	CONFIGURATION FOR MIGRATION TO FDDI
5.	EXPERIMENTAL ENVIRONMENT
6.	FRAME TRAFFIC
7.	UTILIZATION/%COLLISIONS/STATION%USE/PROTOCOL DISTRIBUTION
8.	MICROSOFT/OFFICE AUTOMATION UTILIZATION
9.	SUMMARY
10.	REFERENCES

LIST OF FIGURES

<u>Figure</u>	<u>Title</u>
1.	Global Statistics - Normal Hours
2.	Global Statistics - Evening Hours
3.	Peak Utilization Snapshot
4(a)	Average Utilization - 30 Minute Slot
4(b).	Average Utilization - 15 Minute Slot
4(c).	Average Utilization - 5 Minute Slot
5.	Frame Length Distribution
6.	Protocol Distribution

LIST OF TABLES

<u>Table</u>	<u>Title</u>
I.	Network Analyzer Data for CAD/CAE Ethernet
II.	Network Analyzer Data for Microsoft Mail
III.	Network Analyzer Data for Office Automation Network

1. INTRODUCTION

The Computer Aided Design/Computer Aided Engineering (CAD/CAE) network at Kennedy Space Center is composed of segmented Local Area Networks (LAN). These segmented LAN's are interconnected through either bridges or routers. At present this LAN is an Ethernet network. The design/engineering workstations are various Intergraph and Digital Equipment Corporation products, mainly. The host is a VAX cluster and there are several Intergraph servers, for plotting/printing/disk storage.

The workstations use the VAX cluster for their work environment. There are various protocols on the LAN, mainly Internet Protocol (IP) and DecNet, with some LAT (a DECnet protocol).

In the sections that follow, the following items will be discussed. A review of the NASA/KSC CAD/CAE network configuration, Ethernet and FDDI principles and nomenclature, intelligent switch concepts and presentation of performance data for of the CAD/CAE and Office Automation networks.

2. NASA/KSC CAD/CAE NETWORK CONFIGURATION

The NASA/KSC CAD/CAE network (1) configuration is composed of a VAXcluster utilizing a Star Coupler tying together a VAX 11/780, VAX 6000-610, and a VAX 6000-510. The VAX 780 and VAX 6510 are to be replaced with an ALPHA 7610 AXP and an ALPHA 4000 AXP, respectively. The VAX cluster is presently interfaced to the workstation environment through an Ethernet LAN, and by Bridges/Routers to workstations that are not situated at the Headquarters building.

The NASA/KSC CAD/CAE LAN presently provides connectivity for the CAD/CAE workstations, which are Intergraph and DEC, and PC's. The network communicates between HQ's, O&C, EDL, CIF, and the Merritt Island Courthouse (MICH) on Broadband Communication Distribution System (BCDS) Channel FM1. There is also a gateway to NSI-DECnet network.

There are several DEC workstations in the Mechanical Engineering area and Boeing has a DEC workstation. These are VAXstation 4060's and 3176's.

The Headquarters CAD/CAE LAN is a segmented Ethernet network and their is presently an FDDI fiber optic ring for the Kennedy Metropolitan Area Network (KMAN). KMAN is to provide connectivity to other sites (in the future) and presently to off-KSC sites.

The rationale for migrating from the present Ethernet configuration to a fiber optic backbone is due to the increase in the number of workstations and the movement of the applications to a windowing environment, extensive document transfers, and compute intensive applications.

In a NASA/KSC report (2) presented in 1988, the Ethernet utilization was 3%, or less, and there were only fourteen Intergraph workstations on the Headquarters LAN. At present utilizations of 80%, or less, have been observed in short bursts and 10-25% averaged over longer time periods. There are presently 58 workstations on the NASA/KSC HQ LAN.

This is then the rationale for obtaining an increase in bandwidth to relieve present congestion and provide the capabilities for future growth. It should be noted that in network communications terminology bandwidth is the amount of data that can be transmitted over a channel in bits/second. This is a different definition than used in electrical engineering terminology.

There are several alternatives for providing greater bandwidth for the CAD/CAE LAN. One is through segmentation, this is a reconfiguration of the LAN network into segments whereby one tries to keep traffic local to the segment and only obtain access to other segments if needed. This results in usage of Bridge/Routers to connect the various segments. Propagation delay will be increased every time a Bridge/Router is introduced into the network. Propagation delay is the amount of time between the time the message is sent from the source to being received by the intended destination. In the LAN being investigated it is presumed that most traffic is between the workstations and the VAXcluster, thereby segmenting would not alleviate the problem to a great degree, since the channel would be utilized between the workstation and the VAXcluster.

Another approach, i.e., as compared to segmentation, is the concept of Intelligent Switching. Intelligent switches are able to accommodate Ethernet and FDDI modes and able to switch, between segmented networks either internally or externally, at a very rapid rate. This not only reduces the propagation delays, but allows one to migrate to FDDI rather than configuring for fiber optics entirely.

They also provide concurrent communications between workgroups and can match different bandwidth LAN's through the switch interface. In general one can achieve a high through-put, low-propagation delay (latency), and transparent communication between end-stations.

In the case of the NASA/CAE LAN this was a reasonable migration for several reasons. One, most of the workstations are not upgradeable to FDDI controllers and the cost would also be prohibitive. Two, the system is not yet saturated but if the workload increases in the future it will be needed. Thirdly, there is a movement to FDDI configurations at NASA/KSC (3).

3. LOCAL AREA NETWORK TECHNOLOGY

Ethernet (IEEE 802.3 Carrier Sense Multiple Access with Collision Detection - CSMA/CD) (4) provides the services of the lower two layers in the International Standards Organization (ISO) Open Systems Interconnection (OSI) model for network protocols.

Ethernet is a carrier sense protocol, i.e., all stations monitor the cable during their transmission, terminating transmission immediately if a collision is detected. When an Ethernet station wishes to transmit a packet a carrier sense is performed forcing the station to defer if any transmission is in progress. If there is no station sensed to be transmitting then the sender can transmit after an appropriate delay. It is possible that two, or more, stations will sense the channel idle at the same time and begin transmitting. This has the possibility of producing a collision. The station will continue monitoring and sense this collision. When a collision is detected the station will stop transmitting and will reschedule a re-transmission at a later time. Re-transmission time is random and is selected using a binary exponential backoff algorithm.

FDDI is a token passing technology that uses a timed token protocol (5). There can be multiple frames on the network which is configured as a logical dual ring, or a dual ring of trees. The media standard is presently optical fiber, although transmission of the packet over copper is also being considered and should be in the standard, in the future. The designation for the later is Copper Distributed Data Interface (CDDI). The bandwidth is 100 Mb/s. Of course the transmission distance for a predetermined db loss is greater with a fiber optic cable, as compared to a copper

cable. There is also concern with cross-talk and radiation with the copper media. These concerns are being addressed, mainly through twisted pair and shielding.

There are various configurations for high speed intelligent switches (6). They are used to interconnect multiple LAN's, either FDDI, Ethernet, Token Ring or others. The intelligent switch offers many advantages over shared channel LAN's. The advantages include an increase in the bandwidth, latency (propagation delay) reduction, an increase in connectivity, and better traffic management.

Depending upon the vendor the switch may/may not interconnect various communication standards internally. Some of the configurations are:

- o Ethernet to Ethernet switching
- o FDDI to FDDI switching
- o FDDI to Ethernet to Token Ring switching externally
- o FDDI to Ethernet switching internally

There are switches which allow only Ethernet to Ethernet or Token Ring to be internetworked by bridging.

The FDDI to FDDI switching configuration is basically a FDDI concentrator. One can typically purchase FDDI line cards with two, or more ports. These ports would support SAS or DAS devices, or presumably SAC or DAC concentrators. Through the purchase of appropriate bridges FDDI and Ethernet segments can be interconnected. These switches can set up concurrent connections to obtain an aggregate throughput much higher than a single segment could obtain. These switches achieve low latency by not utilizing the store and forward concept, but to use cut-through forwarding. This technique forwards a packet as soon as the destination address is determined from the header.

Another type of switch can be called the intelligent switch, in that the internal configuration is such that FDDI can be integrated with Ethernet communications. The concept is to have a collapsed FDDI backbone internal to the switch and be able to bridge from external FDDI or Ethernet stations through the FDDI backbone. There is also the possibility of switching at the module level without going through the FDDI backbone for the Ethernet module. The FDDI module must go through the FDDI backbone internal to the switch.

Each Ethernet module contains ports which can have either Ethernet LAN segments connected or a private Ethernet channel, i.e., an end-station. Ethernet segments attached

to a unique module are switched by an internal bridging function to the appropriate output port. Ethernet segment connections for ports on separate modules must go through the FDDI internal backbone to arrive at the destination address. The same is true for FDDI SAS/DAS connections.

This allows very sophisticated interconnections between dissimilar LAN segments and also allows gradual migration to FDDI devices as bandwidth needs increase. The communication between Ethernet and FDDI is transparent. Due to the usage of the FDDI internal backbone (backplane) there is a maximum of two low latency "hops" between any two stations.

Normally, a switch will have filtering capability based on; source address, destination address, protocol type, or some combination of these attributes. This can be usually done on a per port basis, or workgroup. Some routing functions can be obtained through this capability.

4. CONFIGURATION FOR MIGRATION TO FDDI

The present Ethernet LAN in the Headquarters building is a single segmented LAN with bridge/router connections to other CAD/CAE LAN's and other parts of the KSC network. To provide capabilities for migration to FDDI when resources permit and loading necessitates, the intelligent switching configuration was proposed (3).

This configuration consists of a building switch and the configuration will allow migration to FDDI when workstations are upgraded to FDDI. It will also allow the Ethernet LAN to be segmented, which should provide greater access for each segment to the VAX cluster. Components of the VAX cluster and the various servers have FDDI controllers available and hence will be integrated into the building switch. The connection to the Metropolitan Area Network will be provided by a Router.

The intelligent switch is from the Synernetics Corporation and has four modules available (7):

- o System Processor Module (SPM)
- o FDDI Enterprise Access Module (FEAM)
- o FDDI Concentrator Module (FCM)
- o Ethernet Switching Module (ESM)

The SPM module is dedicated to the management of the system and it continually monitors the system and is used to configure the system. This module is required.

The FEAM provides A/B ports for connecting the switch to an FDDI backbone.

The FCM is an FDDI concentrator and allows one to connect end stations and other intelligent switches to the FDDI backbone.

The ESM has Ethernet connections which can be switched and a fully translational Ethernet to FDDI bridge which can forward messages to other ESM modules or to FDDI stations via the FDDI collapsed backbone internal to the intelligent switch. Messages can be switched between ports on an ESM without going through the FDDI backbone.

5. EXPERIMENTAL ENVIRONMENT

To enable collection of data concerning the traffic on the NASA/KSC CAD/CAE network a network analyzer was used to characterize the traffic. Network analyzers are useful for monitoring, debugging, managing, and characterizing local area networks. Specifically, the analyzer can examine all frames transmitted/received on the network. The analyzer can compute, display, and store statistics about network activity, such as average and peak traffic rates, frame sizes, protocol distribution, and other items.

The network analyzer used for these tests was a Network General Corporation Sniffer Network Analyzer (8). The monitor provides an exact picture of network activity at a given instance, or the activity can be captured in various historical logs.

The following is a partial list of the monitor's capabilities:

- o 1024 stations can be monitored.
- o Alarms for specific stations, or the entire network, can be generated.
- o Real-time traffic and historical information for individual stations, and/or the entire network can be captured.
- o The statistics gathered can be sorted to suit the user.
- o Management reports can be generated.
- o Will automatically store in a file, selected information, at pre-determined time intervals.

The Ethernet monitor can monitor a network continuously for up to 49 days. This monitor can be utilized on an Ethernet (IEEE 802.3) network.

In the following a compilation of frame traffic, average and peak utilization, frame length, protocol traffic is presented for the NASA/KSC CAD/CAE network for the network configuration of 1988 and 1994 and the Office Automation network and Microsoft mail facility.

It should be noted that the 1988 data was captured by an Excelan LANalyzer EX 5000 Series Network Analyzer.

6. FRAME TRAFFIC

The frame traffic on the Ethernet has been observed to be the following, see Figures 1,2:

1994 Traffic

- o 3,500,000 frames during normal work hours (approximately, 7:30 to 15:30)
- o 3,500,000 frames during evening hours

This is approximately a 300% increase over the 1988 traffic (during the normal work hours) and a 270% increase over the 1988 traffic (during the evening hours).

7. UTILIZATION/%COLLISIONS/STATION%USE/PROTOCOL DISTRIBUTION

The Ethernet utilization (and other information) is presented in Table I for a period of a month. This Table has summarized the % Collisions, % Average Utilization, and the three Stations and Protocols with with the highest usage. The data for 1988 showed an average utilization of less than 1%, and a maximum peak utilization of 3 %, or less. While 1994 traffic peak utilizations are not shown in Table I, Figure 3 shows that 80 % peak utilizations have been encountered for 10 second snapshots and 10-25 % utilizations have been observed over longer time periods, see Figure 4. Figure 4(a), (b) and (c) show average utilizations (snapshots) over 30 minute, 15 minute and 5 minute time intervals, respectively.

The distribution of frame lengths is similar to the 1988 distribution, although a larger percentage of the frames are now in the high end of the frame distribution. This implies that more "useful" data is being sent over the network, as compared to "handshaking/acknowledgments", see Figure 5. The protocol distribution has changed from a preponderance of XNS (Xerox Network Systems) to basically Internet

17

protocol (IP). This is due to the type of protocols being utilized by the stations, shifting to IP over the last several years, see Figure 6.

Collisions/CRC alignments cause very few frames to be lost, this is expected when the average utilization rate is low and due to the carrier sense before transmission of Ethernet (see Figures 1 and 2).

It can be seen from Table I and Figure 4, that the average % collisions and average % utilization is well below the thresholds that are stated in the literature (9). These are given as, 10% and 35%, respectively. The peak network utilization for the NASA/KSC has been observed as high as 80%, where the peak utilization as stated in the literature is given as 55%. The thresholds, stated in Reference (9), are values for which network segmentation (or, obtain more bandwidth) is deemed advisable.

8. MICROSOFT/OFFICE AUTOMATION UTILIZATION

Table II shows the Microsoft mail data similar to Table I for the CAD/CAE network. While the Microsoft mail service is already absorbed in the previous data, see Table I, and is presently a minor portion of the network traffic (less than 1% average utilization). The Headquarters Office Automation (OA) network segment is presently a separate network and is planned to be moved to the CAD/CAE network. Table III reflects the impact that this migration might have on the CAD/CAE network. This migration should have minimal impact due to it's present activity (less than 3-4% average utilization, and peak rates in 12-15% range).

9. SUMMARY

The measurements reported reflect only the frame traffic on the CAD/CAE and Office Automation networks, not the actual work effort in a design/office project. The workload in a design/office project is composed of tasks other than workstation interaction and the amount of interaction will depend upon the task.

From the test data obtained in this evaluation one can conclude that there is slack in the CAD/CAE network traffic, with regard to average and peak utilizations. It should be able to accommodate the Office Automation traffic monitored and any increase in Microsoft mail activity.

The planned migration to FDDI utilizing a Synernetics switch, will provide a network configuration that will be

able to provide average and peak utilizations and % collisions well below published thresholds. The Synernetics switch also has the capability to further segment the Ethernet workstations and add FDDI workstations, as they become available, or if traffic warrants further segmentation.

A follow-up to this study is to evaluate the CAD/CAE network after the planned migration to FDDI has been finalized and the Office Automation network traffic has been transferred to the CAD/CAE network.

10. REFERENCES

1. Kennedy Space Center Network Handbook, KSC-DL-3572, March 17, 1993.
2. Zobrist, G. W., "Performance Evaluation of NASA/KSC CAD/CAE Graphics Local Area Network", NASA/KSC Research Report, NASA Grant NGT-60002, October 1988.
3. Zobrist, G. W., "Switch Configuration for Migration to Optical Fiber Network", NASA/KSC Research Report, August 13, 1993.
4. Stallings, W., Handbook of Computer Communications Standards: Volume 2 - Local Network Standards, Howard W. Sams Company, Indianapolis, IN, 1987.
5. Ross, F. E., "FDDI - a Tutorial", IEEE Communications Magazine, Vol. 24, No. 5, May 1986, pp. 10-17.
6. Herman, J. and Serjak, C., "ATM Switches and Hubs Lead the Way to a New Era of Switched Internetworks", Data Communications, March 1993, pp. 69-84.
7. Switching Hubs: An Integral Part of ATM Implementation, Synernetics Corporation, 85 Rangeway Road, North Billerica, MA 01862.
8. Sniffer Network Analyzer-Ethernet Monitor Operations, Network General Corporation, Menlo Park, CA, 1992
9. Stern, Hal, Managing NFS and NIS, O'Reilly & Associates, Sebastopol, CA, 1991

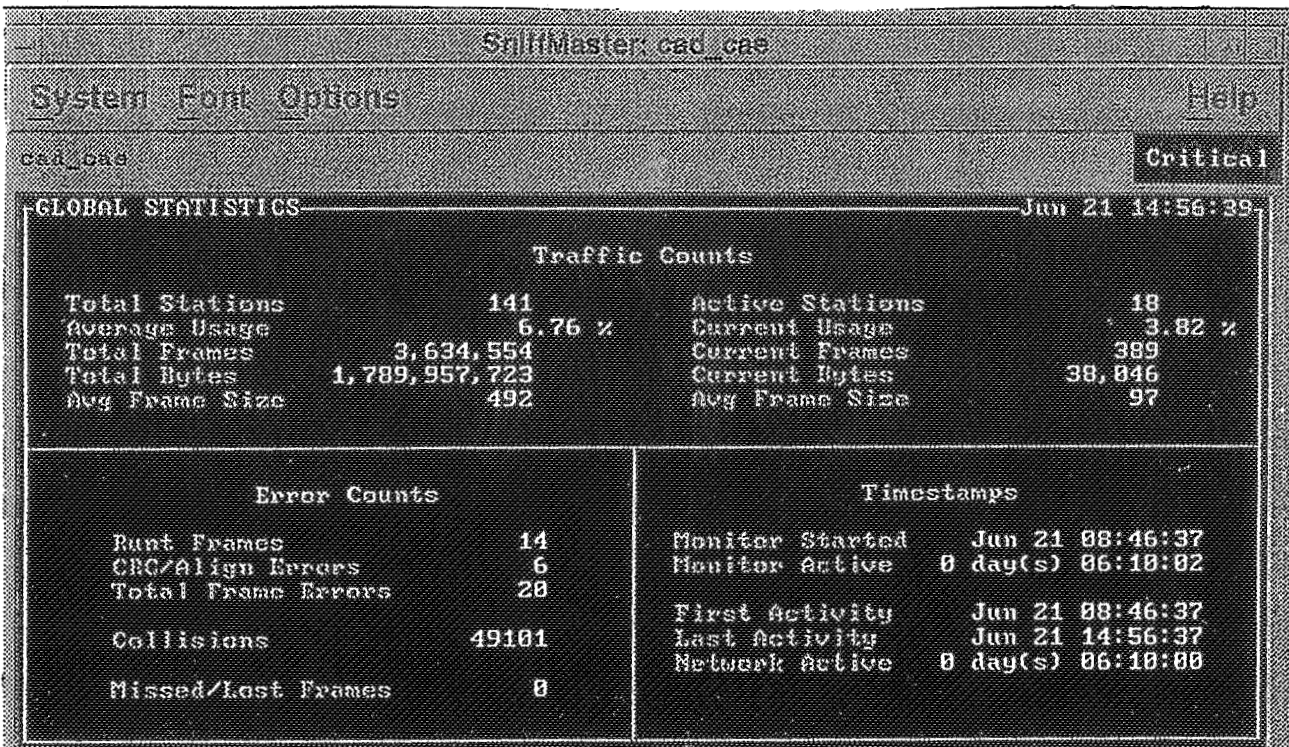


Figure 1. Global Statistics - Normal Hours

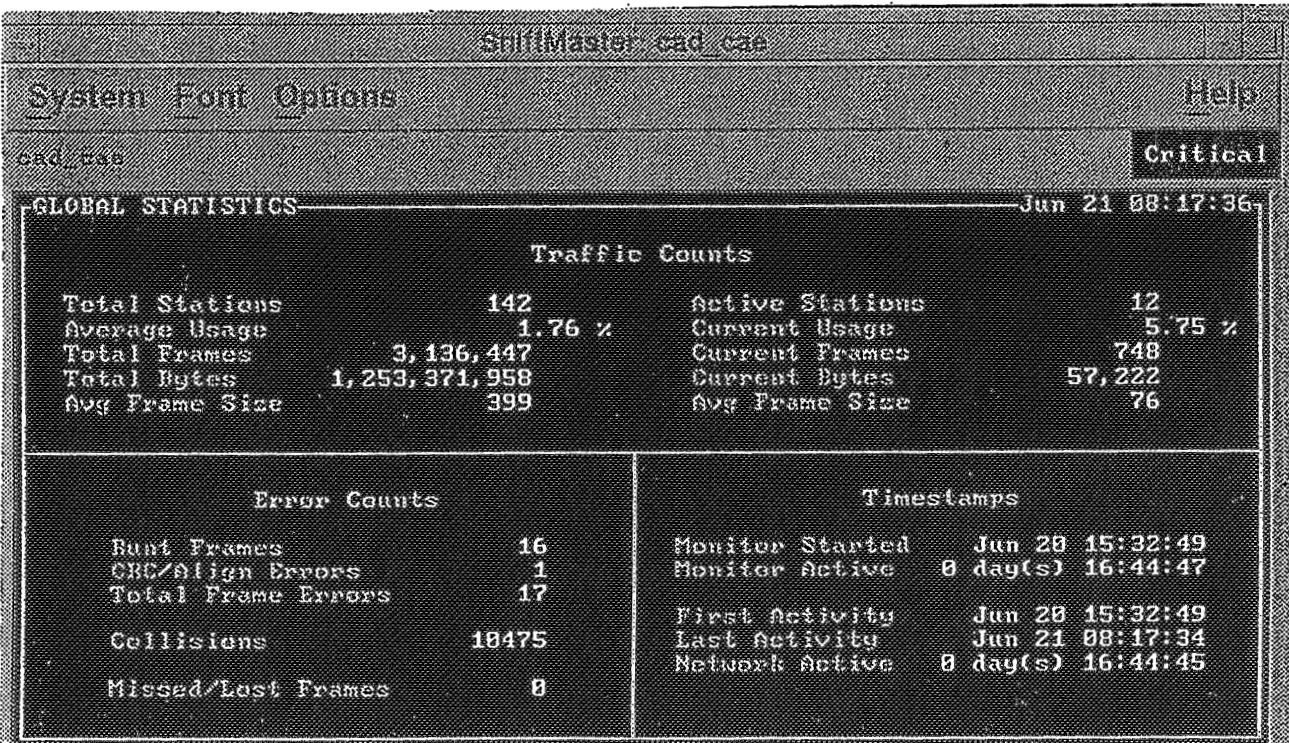


Figure 2. Global Statistics - Evening Hours

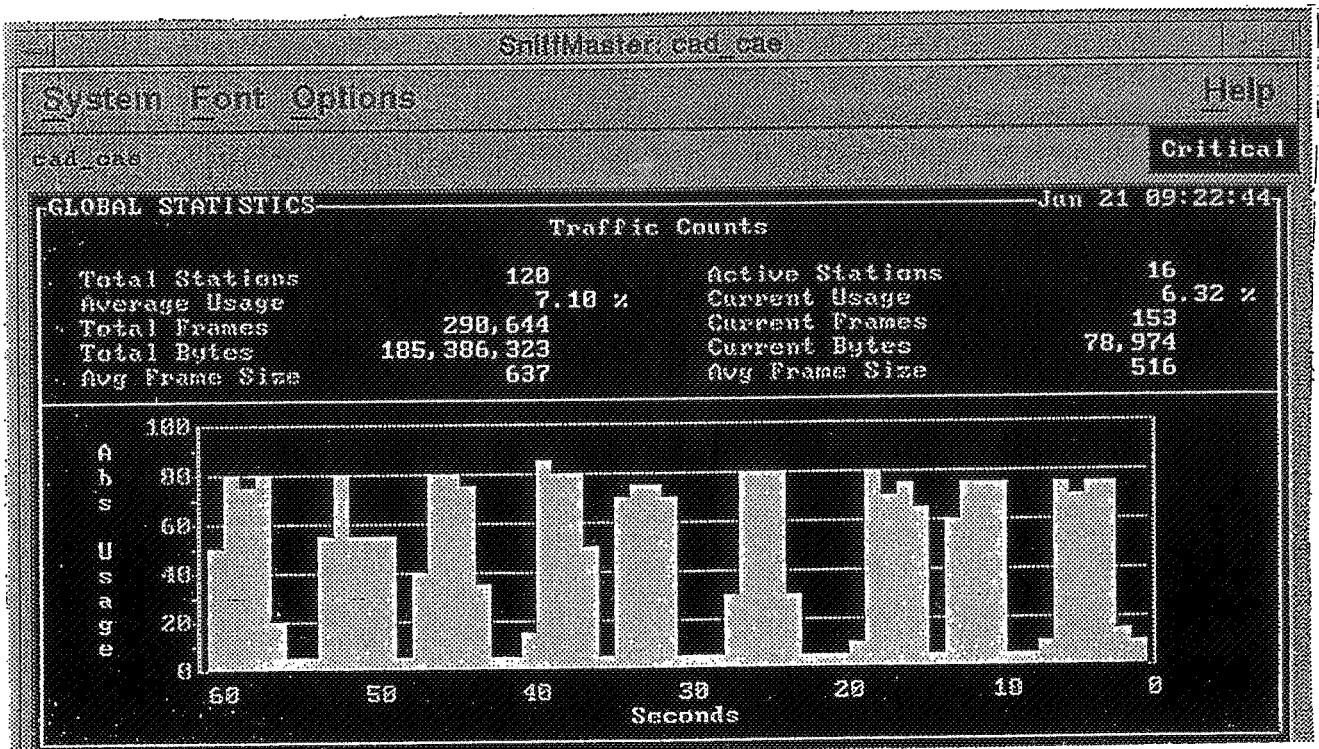


Figure 3. Peak Utilization Snapshot

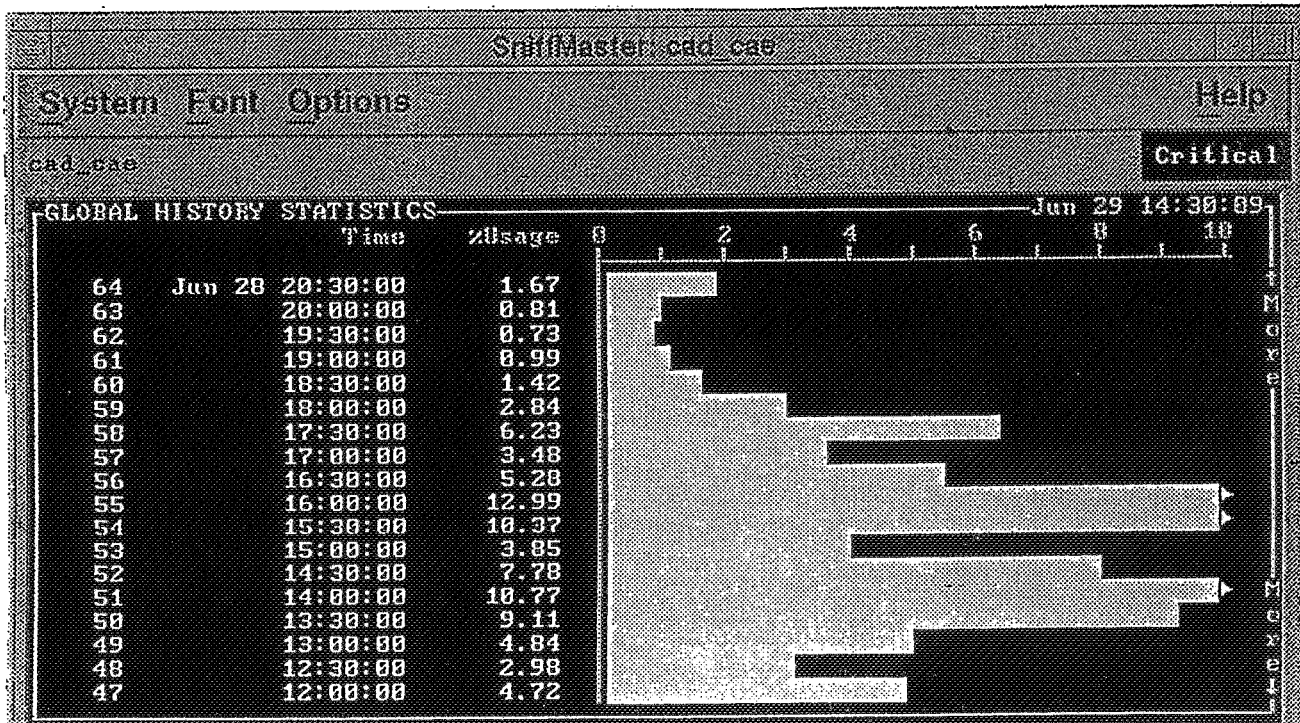


Figure 4(a). Average Utilization - 30 Minute Slot

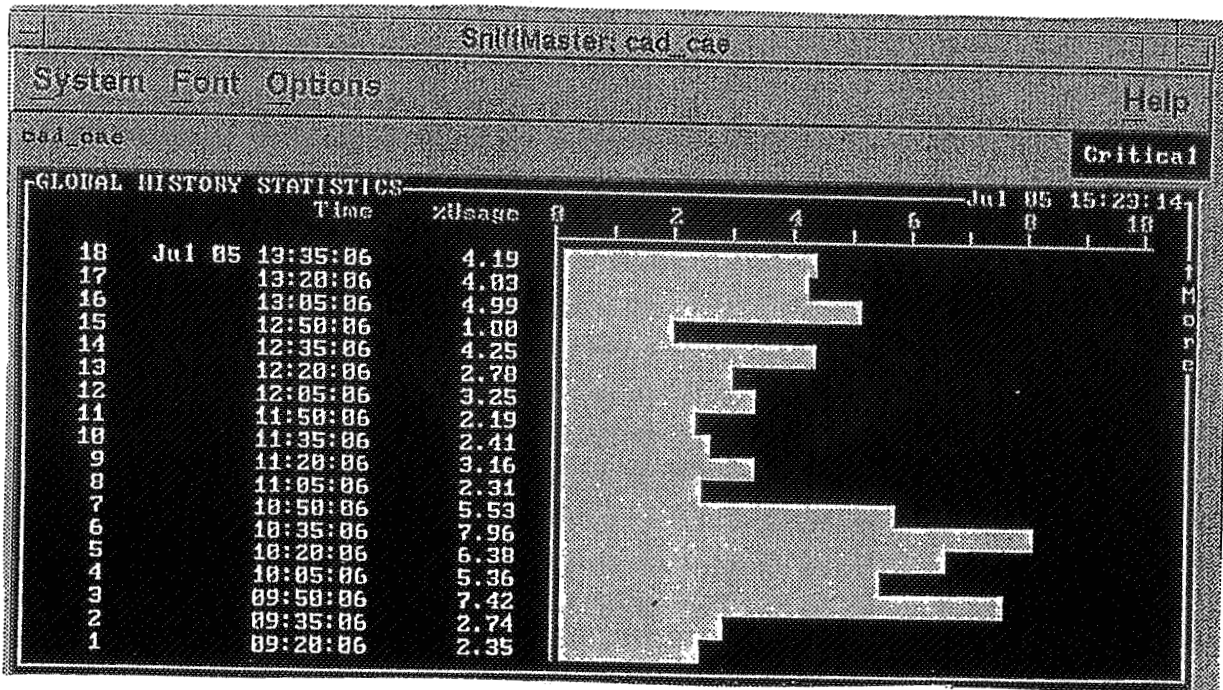


Figure 4(b). Average Utilization - 15 Minute Slot

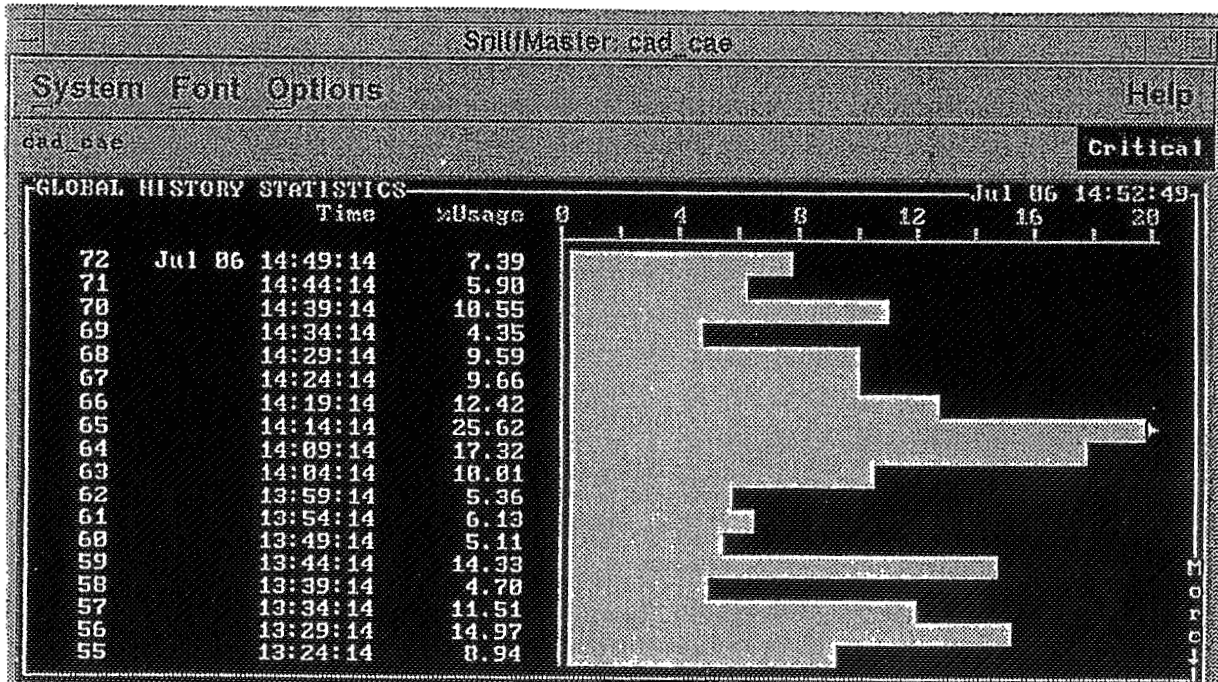


Figure 4(c). Average Utilization - 5 Minute Slot

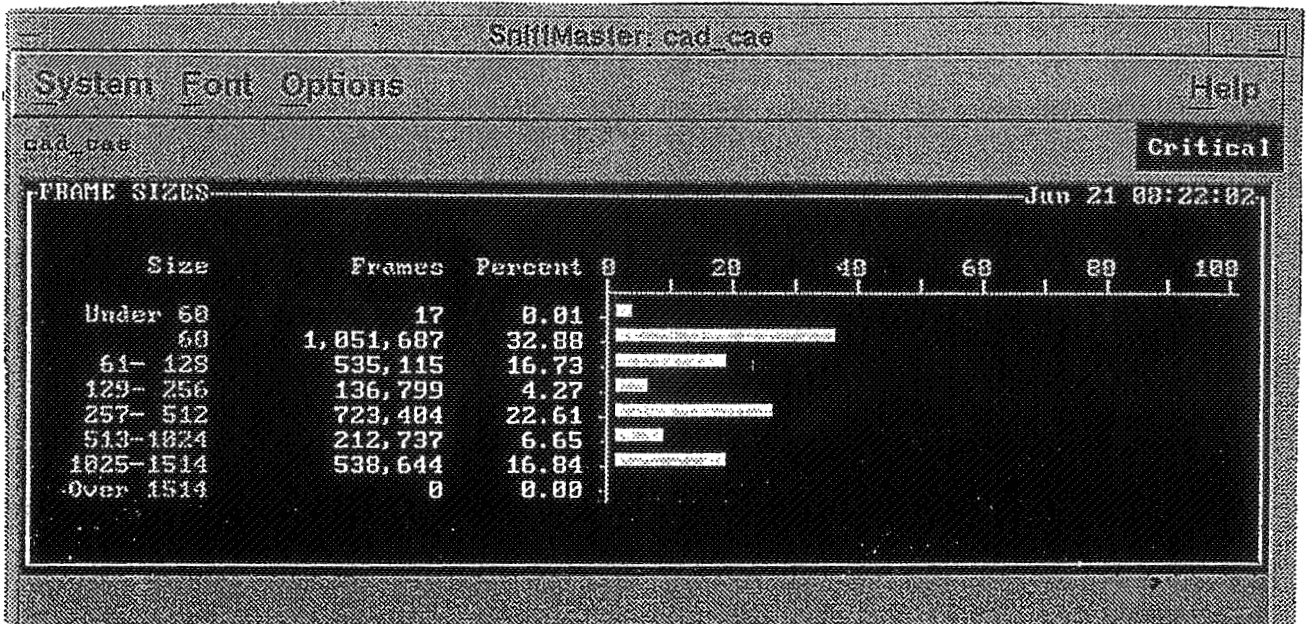


Figure 5. Frame Length Distribution

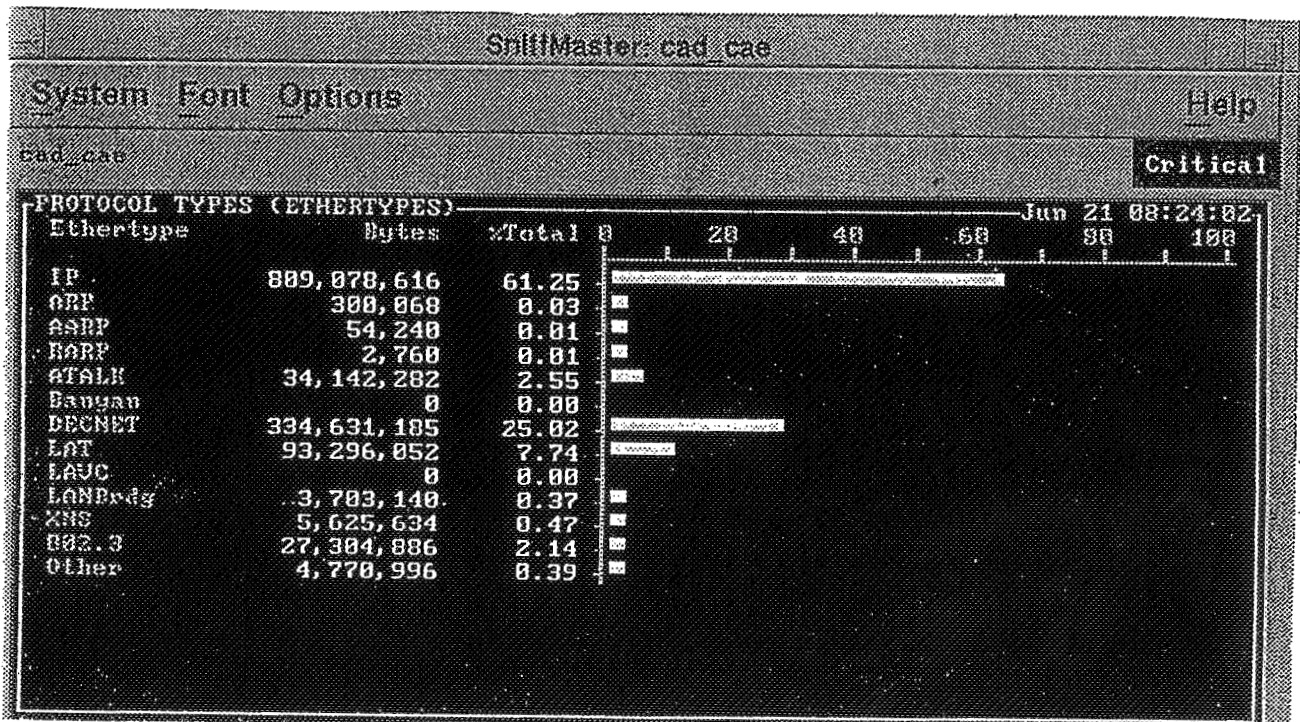


Figure 6. Protocol Distribution

SNIFFER DATA FOR CAD/CAE NETWORK - ETHERNET

COLLECTED BY GEORGE W. ZOBRIST
UNIVERSITY OF MISSOURI-ROLLA

TIME/DATE		%COLLISIONS	%AVE USAGE	STATION	%USE	PROTOCOLS
FROM	TO					
06/03 07:00	06/03 11:00		7.83 %	KSCDL1 PONRTR INTGRn	4.7% 2.3% 2.3%	IP 93% DECNET 2% LAT 3%
06/03 15:00	06/06 09:30		0.80 %	BRDCST SUN PONRTR	0.3% 0.3% 0.3%	IP 80% ATLK 6% DECNET 4%
06/03 10:00	06/10 08:00		3.92%	KSCDL1 PONRTR INTGR	2.2% 0.9% 0.7%	IP 75% DECNET 16% LAT 5%
06/10 09:00	06/13 13:00		1.50%	KSCDL1 BRDCST PONRTR	0.5% 0.3% 0.3%	IP 79% DECNET 10% LAT 4%
06/14 08:30	06/15 08:30	.33%	1.99%	KSCDL1 PONRTR BRDCST	1.0% 0.6% 0.3%	IP 58% DECNET 22% LAT 13%
06/15 09:45	06/15 08:30	.33%	3.0%	KSCDL1 PONRTR BRDCST	2.1% 1.7% 0.3%	IP 44% DECNET 45% LAT 7%
06/16 09:30	06/17 08:30	ovflw	7.0%	KSCDL1 PONRTR CISCO	5.7% 1.7% 0.9%	IP 86% DECNET 8% LAT 3%
06/17 09:15	06/17 15:00	1.0%	6.2%	KSCDL1 INTGR PONRTR	3.7% 1.1% 0.9%	IP 66% DECNET 22% LAT 10%
06/17 15:30	06/20 09:00	0.1%	0.7%	BDCST SUN PONRTR	0.3% 0.3% 0.3%	IP 76% DECNET 6% LAT 5%
06/20 09:00	06/20 15:00	0.7%	4.4%	INTGR KSCDL1 INTGR	1.2% 1.0% 0.9%	IP 76% LAT 14% DECNET 7%
06/20 15:30	06/21 08:15	0.3%	1.8%	KSCDL1 PONRTR INTGR	0.9% 0.4% 0.4%	IP 61% DECNET 25% LAT 8%

Table I.

Network Analyzer Data for CAD/CAE Ethernet

SNIFFER DATA FOR CAD/CAE NETWORK - ETHERNET

COLLECTED BY GEORGE W. ZOBRIST
UNIVERSITY OF MISSOURI - ROLLA

TIME/DATE		%COLLISIONS	%AVE USAGE	STATION	%USE	PROTOCOLS	
FROM	TO						
06/21 08:45	06/21 15:00	1.3%	6.8%	INTGR	4.2%	IP	88%
				INTGR	3.6%	LAT	6%
				PONRTR	1.2%	DECNET	4%
06/21 15:30	06/22 09:30	0.5%	1.9%	KSCDL1	0.8%	IP	65%
				INTGR	0.5%	DECNET	22%
				PONRTR	0.4%	LAT	6%
06/22 10:00	06/29 14:30	OVFLW	3.3%	KSCDL1	1.6%	IP	79%
				INTGR	0.8%	DECNET	13%
				PONRTR	0.8%	LAT	4%
06/29 15:15	06/30 08:00	0.4%	3.2%	KSCDL1	2.2%	IP	38%
				PONRTR	1.7%	DECNET	49%
				INTGR	0.5%	LAT	8%
06/30 14:30	07/01 07:20	OVFLW	9.2%	KSCDL1	7.8%	IP	82%
				INTGR	1.2%	LAT	11%
				CISCO	1.1%	DECNET	4%
07/01 08:00	07/05 09:00	0.2%	1.2%	KSCDL1	0.5%	IP	64%
				PONRTR	0.5%	LAT	18%
				BDCST	0.3%	DECNET	8%
07/05 15:40	07/06 08:20	0.25%	2.0%	KSCDL1	1.2%	IP	51%
				PONRTR	0.4%	DECNET	21%
				KSCDM2	0.4%	LAT	20%
07/06 08:45	07/06 14:30	1.5%	7.4%	INTGR	3.2%	IP	54%
				INTGR	2.4%	DECNET	21%
				KSCDL1	1.7%	LAT	20%

Table I. (cont.) Network Analyzer Data for CAD/CAE Ethernet

CAD/CAE NETWORK TRAFFIC FOR 3COM/MICROSOFT MAIL SYSTEM

COLLECTED BY GEORGE W. ZOBRIST
UNIVERSITY OF MISSOURI-ROLLA

DATE		3COM ACCCE3		3COM AEF52F	
TO	FROM	TOTAL FRAMES/ BYTES	AVE USE%	TOTAL FRAMES/ BYTES	AVE USE%
06/30	07/01	23,277/	.01%	28,299/	0.01%
14:30	07:30	2,847,344		7,355,818	
07/01	07/05	134,533/	.01%	152,719/	0.01%
08:00	09:00	16,465,059		41,425,007	
07/05	07/06	47,077/	.01%	77,003/	0.03%
15:40	08:20	9,083,530		22,585,705	
07/06	07/06	20,281/	.01%	58,635/	0.09%
08:45	15:00	3,927,691		24,108,669	

Table III.

Network Analyzer Data for Microsoft Mail

SNIFFER DATA FOR OFFICE AUTOMATION - ETHERNET

COLLECTED BY GEORGE W. ZOBRIST
UNIVERSITY OF MISSOURI-ROLLA

TIME/DATE		%COLLISIONS	%AVE USAGE	STATION	%USE	PROTOCOLS
FROM	TO					
07/07 14:40	07/11 07:40	1.25%	0.3%	DEC BDCST NOVLL	0.1% 0.1% 0.1%	IP 38% ATLK 32% 802.3 18%
07/11 08:30	07/11 14:45	1.0 %	0.4%	DEC CISCO BDCST	0.2% 0.1% 0.9%	ATLK 47% IP 34% 802.3 11%
07/11 15:20	07/12 08:00	0.2%	0.6%	NOVLL DEC CISCO	0.3% 0.1% 0.1%	IP 52% ATLK 30% 802.3 11%
07/12 08:20	07/12 14:30	0.6%	0.5%	CISCO DEC BDCST	0.3% 0.1% 0.1%	ATLK 40% 802.3 30% IP 23%
07/12 15:30	07/13 08:15	2.0%	0.7%	NOVLL BDCST DEC	0.4% 0.1% 0.1%	IP 60% ATLK 22% 802.3 11%
07/13 08:45	07/13 14:30	0.7%	0.6%	CISCO DEC ADDR	0.3% 0.1% 0.1%	802.3 32% ATALK 32% IP 28%
07/13 15:00	07/14 07:45	2.0%	0.7%	NOVLL DEC BDCST	0.4% 0.1% 0.1%	IP 57% ATLK 26% 802.3 11%
07/14 08:10	07/14 14:40	1.6%	0.5%	CISCO DEC BDCST	0.2% 0.1% 0.1%	ATLK 46% IP 26% 802.3 20%
07/14 15:15	07/15 07:30	0.1%	0.5%	NOVLL DEC CISCO	0.2% 0.1% 0.1%	ATLK 41% IP 40% 802.3 12%
07/15 08:00	07/15 14:30	1.0%	0.7%	CISCO DEC BDCST	0.2% 0.2% 0.2%	ATLK 52% IP 24% 802.3 18%

Table III.

Network Analyzer Data for Office
Automation Network

1994 Research Reports
NASA/ASEE Summer Faculty Fellowship Program

REPORT AUTHORS:

Dr. Alfred S. Andrawis - South Dakota State University
Dr. William V. Brewer - Jackson State University (Mississippi)
Dr. Robert M. Byers - University of Central Florida
Dr. Luz M. Calle - Randolph-Macon Woman's College (Virginia)
Dr. Martha A. Centeno - Florida International University
Dr. Chia-Bo Chang - Texas Tech University
Dr. Gerald F. Deitzer - University of Maryland
Dr. Gregory S. Forbes - Pennsylvania State University
Dr. Barbara H. Glasscock - California State Polytechnic Univ. Pomona
Dr. Prafulla N. Joglekar - La Salle University (Pennsylvania)
Dr. Rhyn H. Kim - University of North Carolina, Charlotte
Dr. Narasimha S. Malladi - Tuskegee University (Alabama)
Dr. Allen L. Rakow - Colorado State University
Dr. Ferdinand Rosa - University of Puerto Rico
Dr. John M. Russell - Florida Institute of Technology
Dr. James R. Swanson, Sr. - Embry-Riddle Aeronautical Univ. (Florida)
Dr. Stan J. Thomas - Wake Forest University (North Carolina)
Dr. Pao-lien Wang - University of North Carolina, Charlotte
Mr. Preston A. White III - Southern College of Technology (Georgia)
Dr. George W. Zobrist - University of Missouri, Rolla

EDITORS:

Dr. Loren A. Anderson - University of Central Florida
Dr. E. Ramon Hosler - University of Central Florida
Mr. Warren Camp - John F. Kennedy Space Center

REPORT DOCUMENTATION PAGE

Form Approved
OMB No. 0704-0188

Public reporting burden for this collection of information is estimated to average 1 hour per response, including the time for reviewing instructions, searching existing data sources, gathering and maintaining the data needed, and completing and reviewing the collection of information. Send comments regarding this burden estimate or any other aspect of this collection of information, including suggestions for reducing this burden, to Washington Headquarters Services, Directorate for Information Operations and Reports, 1215 Jefferson Davis Highway, Suite 1204, Arlington, VA 22202-4302, and to the Office of Management and Budget, Paperwork Reduction Project (0704-0188), Washington, DC 20503.

1. AGENCY USE ONLY (Leave blank)		2. REPORT DATE October 1994	3. REPORT TYPE AND DATES COVERED Contractor Report - Summer 1994	
4. TITLE AND SUBTITLE 1994 Research Reports NASA/ASEE Summer Faculty Fellowship Program			5. FUNDING NUMBERS NASA Grant NGT-60002 Supplement: 17	
6. AUTHOR(S) See attached list				
7. PERFORMING ORGANIZATION NAME(S) AND ADDRESS(ES) University of Central Florida Orlando, Florida 32816-2450 John F. Kennedy Space Center Kennedy Space Center, Florida 32899			8. PERFORMING ORGANIZATION REPORT NUMBER NASA CR-197448	
9. SPONSORING / MONITORING AGENCY NAME(S) AND ADDRESS(ES) National Aeronautics and Space Administration Washington, D.C. 20546			10. SPONSORING / MONITORING AGENCY REPORT NUMBER	
11. SUPPLEMENTARY NOTES				
12a. DISTRIBUTION / AVAILABILITY STATEMENT Unclassified - Unlimited			12b. DISTRIBUTION CODE	
13. ABSTRACT (Maximum 200 words) This document is a collection of technical reports on research conducted by the participants in the 1994 NASA/ASEE Summer Faculty Fellowship Program at Kennedy Space Center (KSC). This was the tenth year that a NASA/ASEE program has been conducted at KSC. The 1994 program was administered by the University of Central Florida in cooperation with KSC. The program was operated under the auspices of the American Society for Engineering Education (ASEE) with sponsorship and funding from the Office of Educational Affairs, NASA Headquarters, Washington, D.C. The KSC Program was one of nine such Aeronautics and Space Research Programs funded by NASA Headquarters in 1994. The NASA/ASEE program is intended to be a two-year program to allow in-depth research by the University faculty member. The editors of this document were responsible for selecting appropriately qualified faculty to address some of the many problems of current interest to NASA/KSC.				
14. SUBJECT TERMS Research and Technology			15. NUMBER OF PAGES 567	
			16. PRICE CODE	
17. SECURITY CLASSIFICATION OF REPORT Unclassified	18. SECURITY CLASSIFICATION OF THIS PAGE Unclassified	19. SECURITY CLASSIFICATION OF ABSTRACT Unclassified	20. LIMITATION OF ABSTRACT UL	